

THEORY OF CRYSTAL STRUCTURES

Basis Functions of the Backprojection Operator

Ya. A. Ilyushin

Moscow State University, Vorob'evy gory, Moscow, 119992 Russia

e-mail: ilyushin@phys.msu.ru

Received August 5, 2004

Abstract—The problem of reconstruction of an unknown object by backprojection in a space of arbitrary dimension $p \geq 2$ is considered. Expressions are obtained to solve the problem in the form of series in multidimensional spherical harmonics. Bases of functions applicable to the expansion of radial components of the series in spherical harmonics are found. © 2005 Pleiades Publishing, Inc.

INTRODUCTION

Backprojection is a method of reconstruction of the structure of an unknown object by its projections [1]. The conditions for the completeness of a set of projections, i.e., the sufficiency for unambiguous reconstruction of an object, were formulated for the three-dimensional reconstruction by Orlov in [2]: a set of projections is complete if the projection directions occupy an area on the sphere of directions, which is intersected by all great circles on this sphere. In a p -dimensional space, the Orlov conditions are reduced to the necessity of intersection of this area by all great circles on a unit p -dimensional sphere, i.e., the central cross sections of this sphere by $(p - 1)$ hyperplanes. More general conditions for the completeness can be found in [3]. In this study, eigenfunctions of the backprojection operator will be investigated for the case when the projection directions occupy the entire sphere of possible directions in a space of arbitrary dimension $p \geq 2$.

BACKPROJECTION INVERSION

As was shown in [4], an arbitrary function of coordinates $f(\mathbf{r})$ in a p -dimensional space and its backprojection $\Sigma(\mathbf{r})$ are related to each other by the expression

$$\Sigma(\mathbf{r}) = f(\mathbf{r}) * \frac{1}{r^{(p-1)}}. \quad (1)$$

For $p > 2$, the solution to this equation with respect to the unknown function $f(\mathbf{r})$ has the form

$$f(\mathbf{r}) = -C_p^{-1} \Delta_p \left(\Sigma(\mathbf{r}) * \frac{1}{r^{(p-1)}} \right), \quad (2)$$

where

$$C_p = (p - 2) \Omega_p \frac{1}{r^{(p-1)}} * \frac{1}{r^{(p-1)}}, \quad (3)$$

the area of the p -dimensional sphere is [5]

$$\Omega_p = 2 \frac{\pi^{(p/2)}}{\Gamma(p/2)}, \quad (4)$$

and Δ_p is the Laplace operator in a p -dimensional space. For odd p , a solution was found in [4, 6]. Here, a solution for even-dimensional spaces will be derived. We will introduce a coordinate system as follows. Let us assume that one of the coordinate axes passes through two singularities of the integrand and go to $(p - 1)$ -dimensional spherical coordinates in the space of other coordinates. Then, the integral of the convolution $r^{(p-1)} r^{*(p-1)}$ will take the form

$$\frac{1}{r^{(p-1)}} * \frac{1}{r^{(p-1)}} = \frac{2^{(p-2)} \Omega_{(p-1)}}{r^{(p-2)}} \times \int_{-\infty}^{+\infty} \int_0^{+\infty} \frac{y^{p-2} dy dx}{((x-1)^2 + y^2)((x+1)^2 + y^2)^{\frac{(p-1)}{2}}}. \quad (5)$$

In this integral, we will pass to elliptical coordinates

$$\begin{aligned} x &= \cos \phi \cosh \xi, \\ y &= \sin \phi \sinh \xi. \end{aligned}$$

Taking into account that the Jacobian of the transition to elliptical coordinates is equal to

$$D(x, y)/D(\phi, \xi) = (\cosh(2\xi) - \cos(2\phi))/2, \quad (6)$$

we can write the integral (5) as

$$\begin{aligned} & \frac{1}{r^{(p-1)}} * \frac{1}{r^{(p-1)}} \\ &= \frac{2^{2(p-2)} \Omega_{(p-1)}}{r^{(p-2)}} \int_0^\pi d\phi \int_0^\infty d\xi \frac{(\sin(\phi) \sinh(\xi))^{(p-2)}}{(\cosh(2\xi) - \cos(2\phi))^{(p-2)}}. \end{aligned} \quad (7)$$

Let ψ be equal to 2ϕ . Then, $\sin^{(p-2)}\phi = ((1 - \cos\psi)/2)^{(p-2)/2}$. In the case of even p , the integrand is an

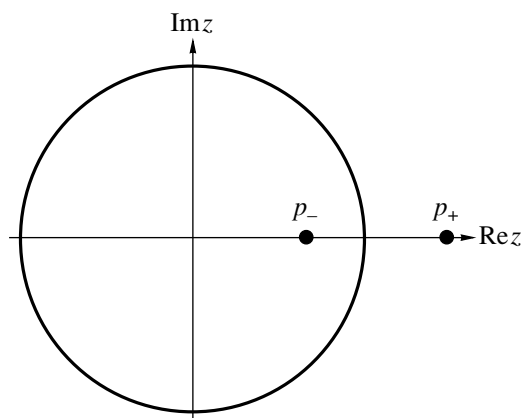


Fig. 1. Calculation procedure for integral (7).

analytic function of ψ , and, after the substitution of $\exp(i\psi) = z$, the integral over ψ is transformed into a contour integral of a rational function z along a unit circle $|z| = 1$ (Fig. 1). The integrand has two poles p_{\pm} of the order $p - 2$ at the points $z = \exp(\pm 2\xi)$. At positive ξ , the pole $z = \exp(+2\xi)$, which is located beyond the contour, does not contribute to the integral. The substitution of the residue at the pole p_- into (7) leads to an integral of a rational function of the variable $\zeta = \exp(2\xi)$. This integral is expressed in terms of elementary functions.

Odd-dimensional spaces were investigated in [6] ($p = 3$) and [4] ($p = 5, 7, 9, 11$). At odd p , the integrand in formula (5) has four poles at the points $y = \pm(1 \pm ix)$. The integral over y can also be taken using the residue theory. The integration contour is shown in Fig. 2. On the arc of the circle, the integrand function decreases as the $-(p - 1)$ power of the arc radius and the integral over the arc tends to zero at $R \rightarrow \infty$. Thus, the integral over y from formula (5) is equal to the sum of residues at the

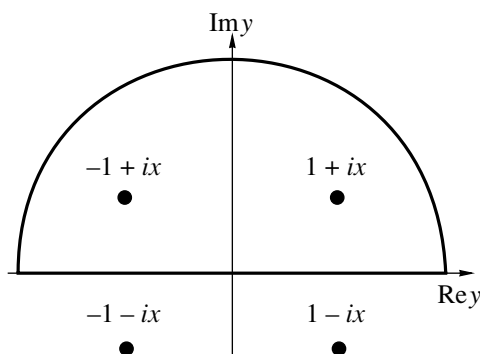


Fig. 2. Calculation procedure for integral (5) at odd p .

two poles $y = (\pm 1 + ix)$, which are within the contour. In this case, we obtain a rational function x , the integral of which can also be calculated. The values of the constant C_p for even and odd dimensions are listed in the table.

EIGENFUNCTIONS OF THE BACKPROJECTION OPERATOR

Relation (2) can be written in the operator form [4]

$$-C_p^{-1} \Delta_p \Sigma \Sigma = -C_p^{-1} \Delta_p \Sigma^2 = I, \quad (8)$$

where I is the identity operator and Σ is the backprojection and summation operator. Therefore, the eigenfunctions of the operator Σ can be found among those eigenfunctions Ψ of the Laplace operator Δ_p that satisfy the Helmholtz equation

$$\Delta_p \Psi + k^2 \Psi = 0. \quad (9)$$

The solutions to this equation have the form [5]

$$\Psi_{\pm}(\mathbf{r}) = S_{nl} z^{1-p/2} J_{\pm(n+p/2-1)}(z), \quad (10)$$

where S_{nl} are generalized spherical harmonics [5, 7, 8], $J_{\nu}(\cdot)$ are the Bessel functions, and $z = kr$. Among these functions, only $\Psi_+(\mathbf{r})$ at real positive values of k^2 are limited within the entire positive real axis. The other solution to the Helmholtz equation, $\Psi_-(\mathbf{r})$, which corresponds to the same eigenvalue, is infinite at zero. It can be shown that the eigenfunctions of the operator Σ must be linear combinations of the functions $\Psi_{\pm}(\mathbf{r})$, and the corresponding eigenvalues can only be equal to $\lambda_{\pm} = \pm \sqrt{C_p/k^2}$. The existence of a positively defined operator, which is a solution to Eq. (8) with respect to Σ , follows from the square-root theorem [9]. The convolution of $\Psi_+(\mathbf{r})$ with the kernel of the operator Σ is also finite

Values of the constant C_p

| p | C_p | p | C_p |
|-----|-------------------------|-----|---|
| 3 | $4\pi^4$ | 4 | $16\pi^4$ |
| 5 | $4\pi^6$ | 6 | $\frac{64}{9}\pi^6$ |
| 7 | π^8 | 8 | $\frac{256}{225}\pi^8$ |
| 9 | $\frac{\pi^{10}}{9}$ | 10 | $\frac{1024}{11\,025}\pi^{10}$ |
| 11 | $\frac{\pi^{12}}{144}$ | 12 | $\frac{4096}{893\,025}\pi^{12}$ |
| 13 | $\frac{\pi^{14}}{3600}$ | 14 | $\frac{16\,384}{108\,056\,025}\pi^{14}$ |

at zero:

$$\begin{aligned} & \Psi_+(\mathbf{r}) * r^{(1-p)} \\ &= k \int_0^\infty S_{nl} d\Omega_p \int z^{1-p/2} J_{\pm(n+p/2-1)}(z) dz \\ &= 2^{1-p/2} k \frac{\Gamma((n+1)/2)}{\Gamma((n+p-1)/2)} \int S_{nl} d\Omega_p. \end{aligned} \tag{11}$$

Hence, the function $\Psi_+(\mathbf{r})$ is the eigenfunction of the operator Σ .

Let us investigate the sign of the eigenvalue for an arbitrary eigenfunction $\Psi_+(\mathbf{r})$. Since the integral of the convolution $\Sigma\Psi_+$ is a homogeneous function with respect to k , we can assume k to be unity without loss of generality.

The following integral representation is valid for Bessel functions [5]:

$$\begin{aligned} & J_{n+p/2-1}(z) \\ &= cz^{p/2-1} \int_{-1}^1 \exp(irt) P_n(t) (1-t^2)^{(p-3)/2} dt, \end{aligned} \tag{12}$$

where

$$c = \frac{(-i)^n}{2^{p/2-1} \sqrt{\pi} \Gamma((p-1)/2)}. \tag{13}$$

With the use of this integral relation and the Funk–Hecke theorem [5, 8], the convolution integral can be written as

$$\begin{aligned} & \Psi_+(\mathbf{r}) * r^{1-p} \\ &= \Omega_{p-1} S_{nl} c \int_0^\infty r^{p-1} (r^2 + \rho^2 - 2\rho r\tau)^{-(p-1)/2} dr \\ & \quad \times \int_{-1}^1 P_n(\tau) (1-\tau^2)^{(p-3)/2} d\tau \\ & \quad \times \int_{-1}^1 P_n(t) (1-t^2)^{(p-3)/2} \exp(irt) dt, \end{aligned} \tag{14}$$

where $P_n(\cdot)$ are the polynomials introduced in [5], which coincide with accuracy to a constant factor with Gegenbauer polynomials. We will restrict our consideration to a three-dimensional space ($p = 3$). For polynomials P_n with even numbers n , integration over r can be

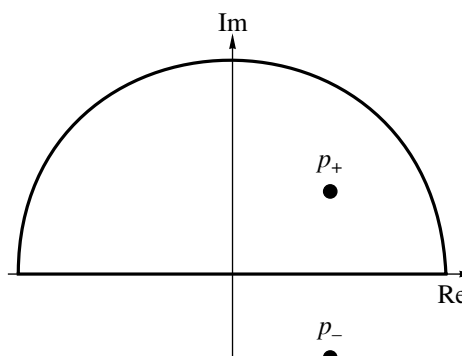


Fig. 3. Calculation procedure for integral (15).

extended to the entire real axis as follows:

$$\begin{aligned} & \Psi_+(\mathbf{r}) * r^{-2} \\ &= 2c\Omega_2 S_{nl} \int_{-\infty}^\infty r^2 (r^2 + \rho^2 - 2\rho r\tau)^{-1}, \\ & \quad \int_0^1 P_n(\tau) \int_0^1 P_n(t) \cos(rt) dt d\tau dr. \end{aligned} \tag{15}$$

Here, $P_n(\cdot)$ coincide with Legendre polynomials at $p = 3$. Note that $\cos(rt) = \text{Re}[\exp(irt)]$.

The integral over r in (15) is a part of the contour integral shown in Fig. 3. The integrand of the integral has two poles $p_\pm = \rho \exp(\pm i\theta)$ in the upper and lower half-planes, respectively. Therefore, integral (15) is equal to

$$\Psi_+(\mathbf{r}) * r^{-2} = 2\pi i \text{Re} s(p_+) + I_R, \tag{16}$$

where I_R is an integral over an arc of radius R , which is a part of the contour. At a large arc radius, I_R is approximately equal to

$$I_R \approx 2c\Omega_2 S_{nl} \text{Re} \left[\int_{-R}^R \exp(irt) \int_0^1 P_n(\tau) \int_0^1 P_n(t) dt d\tau dr \right]. \tag{17}$$

Integration over r leads to the appearance of the rapidly oscillating factor $\sin(Rt)$ in the integral over t ; hence, at $R \rightarrow \infty$, the integral I_R tends to zero according to the Riemann–Lebesgue lemma [10].

Substituting the value of the residue at the pole p_+ into formula (15), we find that

$$\begin{aligned} & \Psi_+(\mathbf{r}) * r^{-2} \\ &= 2c\Omega_2 S_{nl} \text{Re} \left[2\pi i \int_0^1 P_n(\tau) \int_0^1 P_n(t) \frac{\exp(ip_+t) p_+^2}{p_+ - p_-} dt d\tau \right], \end{aligned} \tag{18}$$

where $p_\pm = \rho \exp(\pm i\theta)$ and $\tau = \cos\theta$.

Integrating (18) by parts over t n times, we obtain

$$\Psi_+(\mathbf{r}) * r^{-2} = 4\pi c \Omega_2 S_{nl} \operatorname{Re} \left[\int_0^1 P_n(\tau) \frac{P_+}{P_+ - P_-} \right. \\ \left. \times \sum_{m=0}^n \left(\frac{i}{P_+} \right)^m \{ \exp(ip_+) P_n^{(m)}(1) - P_n^{(m)}(0) \} d\tau \right], \quad (19)$$

where $P_n^{(m)}(\cdot)$ are the m -eth derivatives of Legendre polynomials.

To find the sign of an eigenvalue, it is sufficient to consider the asymptotics of (19) at $\rho \rightarrow \infty$, which is determined by the term with $m=0$. The contribution of the second term in braces contribution is zero. Indeed,

$$-\operatorname{Re} \left[iP_n(0) \int_{\pi/2}^0 P_n(\cos\theta) \exp(i\theta) d\theta \right] \\ = P_n(0) \int_0^1 P_n(\tau) d\tau = 0 \quad (20)$$

for all nonzero even values of n . Taking this fact into account, the integral of the first term in (19) is equal to

$$2c \Omega_2 S_{nl} \pi P_n(1) \operatorname{Re} \left[\int_1^i P_n \left(\frac{z+z^{-1}}{2} \right) \exp(i\rho z) dz \right], \quad (21)$$

where $z = \exp(i\theta)$. The integral is taken over the arc of a unit circle connecting points 1 and $+i$. At large ρ , the asymptotics is determined by the contribution of the final point of the contour $z = i$ [10]:

$$\Psi_+(\mathbf{r}) * r^{-2} \approx 2c \Omega_2 S_{nl} \pi P_n^2(1) \operatorname{Re} \left[\frac{\exp(i\rho)}{i\rho} \right] \\ = 2c \Omega_2 S_{nl} \pi \frac{\sin \rho}{\rho}. \quad (22)$$

Substituting (13) and (4) into formula (22) and comparing the result with the known asymptotics of Bessel functions [11]

$$J_\nu(z) \approx \sqrt{\frac{2}{\pi z}} \cos \left(z - \frac{1}{2} \pi \nu - \frac{\pi}{4} \right), \quad (23)$$

we find that

$$\Psi_+(\mathbf{r}) * r^{-2} = +\sqrt{C_3} \Psi_+(\mathbf{r}) \quad (24)$$

at even values of $n \neq 0$.

For odd n , the extension of integration over r to the entire real axis leads to the expression

$$\Psi_+(\mathbf{r}) * r^{-2} \\ = 2ic \Omega_2 S_{nl} \int_{-\infty}^{\infty} r^2 (r^2 + \rho^2 - 2\rho r \tau)^{-1} dr \\ \times \int_0^1 P_n(\tau) d\tau \int_0^1 P_n(t) \sin(rt) dt. \quad (25)$$

The positivity of the sign of the eigenvalue (24) for odd n is proven similarly.

For the main (spherically symmetric) harmonic $\sin(r)/r$ in a three-dimensional space, the relation $\Sigma \Psi_+ = \sqrt{C_3} \Psi_+$ can be checked directly. Indeed,

$$\frac{\sin(r)}{r} * \frac{1}{r^2} = \int_{R_3} \frac{\sin(r)}{r} \frac{r^2 dr d\phi d\cos\theta}{r^2 + \rho^2 - 2r\rho \cos\theta}. \quad (26)$$

Integration in (26) over r can be extended to the entire real axis as follows:

$$\frac{\sin(r)}{r} * \frac{1}{r^2} \\ = \int_0^{2\pi} d\phi \int_0^1 d\cos\theta \int_{-\infty}^{+\infty} \frac{\sin(r)}{r} \frac{r^2 dr}{r^2 + \rho^2 - 2r\rho \cos\theta}. \quad (27)$$

Integration over the angle ϕ gives 2π since the integrand is independent of ϕ . Taking into account that $\sin(r) = \operatorname{Im} \exp(ir)$, we obtain the expression

$$\frac{\sin(r)}{r} * \frac{1}{r^2} \\ = 2\pi \operatorname{Im} \left[\int_0^1 d\cos\theta \int_{-\infty}^{+\infty} \frac{\exp(ir) r dr}{r^2 + \rho^2 - 2r\rho \cos\theta} \right]. \quad (28)$$

According to Jordan's lemma [12], the integral over r is equal to the sum of residues at the poles above the real axis in the complex plane. Substituting the residue at the pole p_+ into the formula, we have

$$\frac{\sin(r)}{r} * \frac{1}{r^2} = 2\pi^2 \operatorname{Im} \left[\int_{-\pi/2}^0 \exp(ip \exp i\theta) \exp i\theta d\theta \right]. \quad (29)$$

Calculation of the definite integral gives

$$\frac{\sin(r)}{r} * \frac{1}{r^2} = 2\pi^2 \frac{\sin \rho}{\rho} = +\sqrt{C_3} \frac{\sin \rho}{\rho}. \quad (30)$$

The functions $f(\mathbf{r})$ and $\Sigma(\mathbf{r})$ can be expanded in series of spherical harmonics:

$$f(\mathbf{r}) = \sum_{n,l} S_{nl} f_{nl}(r), \quad (31)$$

$$\Sigma(\mathbf{r}) = \sum_{n,l} S_{nl} \Sigma_{nl}(r). \quad (32)$$

Let us assume that the radial parts of the terms of series (31) and (32) belong to the class of functions for which the Hankel transform is determined [13]:

$$\tilde{g}(u) = H\{g(t)\} = \int_0^\infty J_\nu(ut) g(t) t dt. \quad (33)$$

Then, it can be shown that $\Sigma_{nl}(r)$ and $f_{nl}(r)$ are related as follows:

$$f_{nl}(r) = C_p^{-1/2} r^{(1-p/2)} H^{-1}\{kH\{r^{(p/2-1)} \Sigma_{nl}(r)\}\}. \quad (34)$$

For a two-dimensional space ($p = 2$), the relation of type (34) can be checked directly [14] (note that $C_2 = 4\pi^2$).

Since the functions $\Psi_{-}(\mathbf{r})$ are also the eigenfunctions of the operator Σ , one can derive the second relation of the type (34) for $\Sigma_{nl}(r)$ and $f_{nl}(r)$ on the basis of the Y_ν Hankel transform [13].

BASIS FUNCTIONS OF THE BACKPROJECTION OPERATOR

Using the tables of integral transforms [13], one can find series of functions convenient for expansion of $\Sigma_{nl}(r)$ and $f_{nl}(r)$:

$$\Sigma_{nl}(r) = \sum_{m=0}^{\infty} a_{nlm} \Lambda_{nm}(r),$$

where

$$\Lambda_{nm}(r) = \frac{r^n}{2m!} \sqrt{C_p} \frac{\Gamma(m+n+p/2-1/2)}{\Gamma(n+p/2)} \times {}_1F_1(m+n+p/2-1/2; n+p/2; -r^2),$$

$$f_{nl}(r) = \sum_{m=0}^{\infty} a_{nlm} \Phi_{nm}(r),$$

where

$$\Phi_{nm}(r) = r^n \exp(-r^2) L_m^{(n+p/2-1)}(r^2).$$

The basis functions $\Phi_{nm}(r)$ of the initial function $f(\mathbf{r})$ and, accordingly, the basis functions $\Lambda_{nm}(r)$ of its backprojection $\Sigma(\mathbf{r})$ are independent of the index l . By definition of the backprojection (1), the following integral

relation is valid for the main index $n = 0$ and for all $m \geq 0$:

$$\Omega_p \int_0^\infty \Phi_{0m}(r) dr = \Lambda_{0m}(0). \quad (35)$$

Substituting the known value of the integral from the tables of [15] into relation (35), assuming m to be zero, and taking into account (4), we obtain the expression for the constant C_p at an arbitrary value of p :

$$C_p = \frac{4\pi^{p+1}}{\Gamma((p-1)/2)^2}. \quad (36)$$

If we use the orthogonality relation for Laguerre polynomials [15],

$$\int_0^\infty L_m^\alpha(x) L_{m'}^\alpha(x) \exp(-x) x^\alpha dx = \delta_{mm'} \frac{\Gamma(\alpha+m+1)}{m!}, \quad (37)$$

it is easy to construct a conjugate basis for the set of functions $\Phi_{nm}(r)$, i.e., the set of functions

$$\Phi_{nm}^*(r) = \frac{2m!}{\Gamma(n+m+p/2)} r^{(n+p-1)} L_m^{n+p/2-1}(r^2), \quad (38)$$

satisfying the condition

$$\int_0^\infty \Phi_{nm}^*(r) \Phi_{nm'}(r) dr = \delta_{mm'}. \quad (39)$$

Let us now construct a conjugate basis for the set of functions $\Lambda_{nm}(r)$. We will express $\Phi_{nm}(r)$ in terms of $\Lambda_{nm}(r)$ using relation (34) and substitute the resultant function into the orthogonality relation (39). Changing the order of integration in (39), we obtain another orthogonality relation:

$$\int_0^\infty \Lambda_{nm}^*(r) \Lambda_{nm'}(r) dr = \delta_{mm'}, \quad (40)$$

where the functions of the conjugate basis have the form

$$\Lambda_{nm}^*(r) = \frac{2m! r^{p/2}}{\sqrt{C_p} \Gamma(v+m+1)} \times \int_0^\infty L_{m'}^v(z^2) z^{v+1} dz \int_0^\infty J_\nu(ry) J_\nu(yz) y^2 dy. \quad (41)$$

The integrals on the right-hand side of (41) diverge. Let us introduce the regularizing factor $\exp(-\beta z^2)$ into the

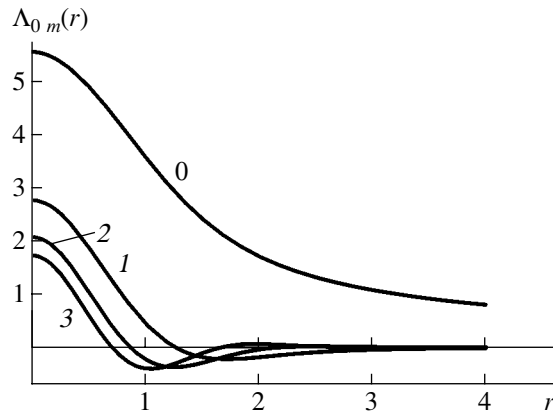


Fig. 4. Basis functions of the backprojection operator for $p = 2$ at $m = 0-3$.

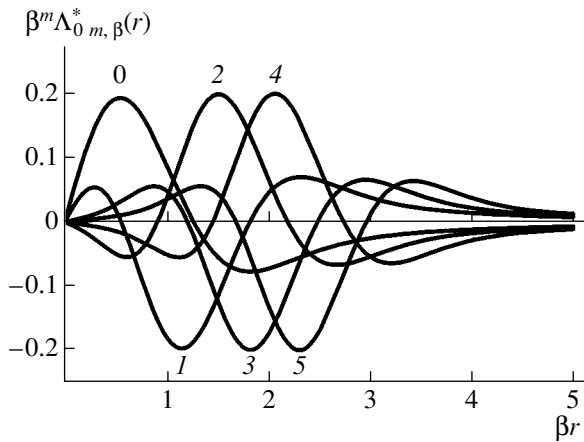


Fig. 5. Conjugate basis functions of the backprojection operator for $p = 2$ at $m = 0-5$.

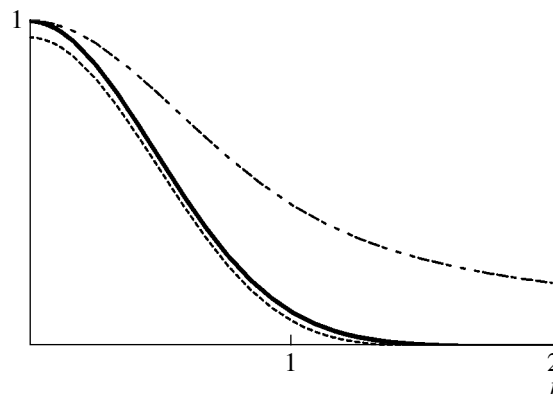


Fig. 6. Reconstruction of a model two-dimensional object.

integrand (41). The thus defined functions $\Lambda_{nm}^*(r)$ will tend to $\Lambda_{nm}^*(r)$ at $\beta \rightarrow 0$ in the sense of weak convergence since relation (40) becomes an exact equality

for all $\Lambda_{nm}^*(r)$ at $\beta = 0$. Using the tables of integral transforms [13], we derive the expression for the conjugate basis functions:

$$\Lambda_{nm,\beta}^*(r) = \frac{2m!r^{p/2}2^{-v-1}\beta^{-v-m-1}(\beta-1)^m}{\sqrt{C_p}\Gamma(v+m+1)}, \quad (42)$$

$$\int_0^\infty J_\nu(ry) \exp\left(-\frac{y^2}{4\beta}\right) L_m^v\left[\frac{y^2}{4\beta(1-\beta)}\right] y^{(v+2)} dy,$$

where $v = n + p/2 - 1$. Substituting the known expression for generalized Laguerre polynomials in terms of the confluent hypergeometric function [15]

$$L_m^v(r) = \binom{m+v}{m} {}_1F_1(-m; v+1; r) \quad (43)$$

into (42) and integrating (42) term by term, we obtain the final result:

$$\Lambda_{nm,\beta}^*(r) = \Gamma\left(\frac{p-1}{2}\right) \frac{2m!}{\pi^{(p+1)/2}} \times \frac{(\beta-1)^m \beta^{(1/2-m)} r^{(n+p-1)}}{\Gamma(n+p/2)}, \quad (44)$$

$$\sum_{q=0}^m \frac{(-1)^q \Gamma(1/2+n+p/2+q)}{(1-\beta)^q (m-q)! q! \Gamma(n+p/2+q)} \times {}_1F_1(1/2+n+p/2+q, n+p/2, -\beta r^2).$$

Figure 4 shows the first four functions $\Lambda_{0m}(r)$ for a two-dimensional space ($p = 2$). In this case, the conjugate basis functions $\Lambda_{0m,\beta}^*(r)$ with a zero main index $n = 0$ have the form

$$\Lambda_{00,\beta}^*(r) = -\frac{\sqrt{\beta} r \exp(-\beta r^2/2)}{\sqrt{\pi}} \times ((-1 + \beta r^2) I_0(\beta r^2/2) - \beta r^2 I_1(\beta r^2/2)),$$

$$\Lambda_{01,\beta}^*(r) = \frac{r \exp(-\beta r^2/2)}{2\sqrt{\pi}\beta} \times ((1 + \beta(2 - 4r^2) + 2\beta^2 r^2(-1 + r^2)) I_0(\beta r^2/2) + 2\beta r^2(1 + \beta - \beta r^2) I_1(\beta r^2/2)).$$

Figure 5 shows the first six conjugate basis functions $\beta^m \Lambda_{0m,\beta}^*(r)$ at $\beta = 10^{-3}$ for $p = 2$. The normalization to β^m is introduced in view of the unlimited increase in the amplitude of the basis functions at $\beta \rightarrow 0$.

Figure 6 shows the reconstruction of the two-dimensional ($p = 2$) model Gaussian profile $f(r) = \exp(-\sigma^2 r^2)$ from the first six basis functions $\Lambda_{0m,\beta}^*(r)$ ($\sigma = 3/2$,

$\beta = 0.3$). The initial Gaussian profile and the reconstruction are shown by solid and dotted lines, respectively. For comparison, the backprojection normalized to unity at the origin of coordinates is shown by a dot-dashed line.

CONCLUSIONS

The problem of reconstruction of an unknown object from the backprojection in a space of arbitrary dimension is solved. The solutions are obtained in the form of expansions in series of multidimensional spherical harmonics. Countable functional bases, convenient for expansion of radial components in series of spherical harmonics, are given.

ACKNOWLEDGMENTS

This study was supported by the Russian Foundation for Basic Research, project no. 03-05-06301. I am grateful to A. Vorontsov for helpful remarks.

REFERENCES

1. B. K. Vainshtein and A. M. Mikhaïlov, *Kristallografiya* **17** (2), 258 (1972) [*Sov. Phys. Crystallogr.* **17**, 217 (1972)].
2. S. S. Orlov, *Kristallografiya* **20** (3), 511 (1975) [*Sov. Phys. Crystallogr.* **20**, 312 (1975)].
3. I. M. Gel'fand, S. G. Gindikin, and M. I. Graev, *Selected Problems of Integral Geometry* (Dobrosvet, Moscow, 2000) [in Russian].
4. Ya. A. Ilyushin and O. A. Terekhova, *Kristallografiya* **45** (5), 784 (2000) [*Crystallogr. Rep.* **45**, 714 (2000)].
5. H. Hochstadt, *The Functions of Mathematical Physics* (Wiley, New York, 1971).
6. Ya. A. Ilyushin, *Kristallografiya* **42** (2), 364 (1997) [*Crystallogr. Rep.* **42**, 323 (1997)].
7. A. F. Nikiforov, S. K. Suslov, and V. B. Uvarov, *Classical Orthogonal Polynomials of a Discrete Variable* (Nauka, Moscow, 1985; Springer, Berlin, 1991).
8. F. Natterer, *The Mathematics of Computerized Tomography* (Wiley, Chichester, 1986; Mir, Moscow, 1990).
9. V. A. Trenogin, *Functional Analysis* (Nauka, Moscow, 1993) [in Russian].
10. M. V. Fedoryuk, *Asymptotics, Integrals, and Series* (Nauka, Moscow, 1987) [in Russian].
11. *Handbook of Mathematical Functions*, Ed. by M. Abramowitz and I. A. Stegun, 2nd ed. (Dover, New York, 1971; Nauka, Moscow, 1979).
12. G. A. Korn and T. Korn, *Mathematical Handbook for Scientists and Engineers*, 2nd ed. (McGraw-Hill, New York, 1968; Nauka, Moscow, 1970).
13. *Tables of Integral Transforms (Bateman Manuscript Project)*, Ed. by H. Bateman and A. Erdelyi (McGraw-Hill, New York, 1954; Fizmatgiz, Moscow, 1970), Vol. 2.
14. H. H. Barrett, *Prog. Opt.* **21**, 219 (1984).
15. I. S. Gradshteyn and I. M. Ryzhik, *Table of Integrals, Series, and Products* (Fizmatgiz, Moscow, 1963; Academic, New York, 1980).

Translated by Yu. Sin'kov

DIFFRACTION AND SCATTERING OF IONIZING RADIATIONS

Numerical Simulation of the Recording of Diffraction Lines with the Bragg–Brentano Focusing

V. V. Korchevskii

Khabarovsk State University of Technology, Tikhookeanskaya ul. 136, Khabarovsk, 680035 Russia

e-mail: kvv@ele.khstu.ru

Received November 3, 2003

Abstract—The role played by different factors in the broadening of X-ray diffraction lines is evaluated using numerical methods. It is demonstrated that, within the kinematical theory of X-ray scattering, the main factors affecting the linewidth are as follows: the angle of reflection, the number of reflection planes, the focus width, the material of the anode of the X-ray tube, and the angle of misorientation of coherent scattering regions. It is established that, in the case where the number of reflection planes is less than 200, the instrumental component of the linewidth does not exceed 5% of the total linewidth. © 2005 Pleiades Publishing, Inc.

INTRODUCTION

The width of a diffraction line is one of the most informative parameters of X-ray diffraction analysis. This parameter is determined by the following factors [1]:

- (i) physical factors responsible for the properties of materials,
- (ii) nonmonochromaticity of X rays, and
- (iii) geometrical factors.

At present, there exist different methods for evaluating the physical factors from the experimental X-ray diffraction lines, and each of these methods has offered its own advantages and disadvantages [2].

In this work, the broadening of X-ray diffraction lines due to the nonmonochromaticity and horizontal divergence of X rays was estimated using numerical simulation methods.

THEORETICAL BACKGROUND

In the framework of the kinematical theory [3, 4], the dependence of the intensity of diffracted radiation on the angle of reflection (measured on an X-ray diffractometer), without regard for the nonmonochromaticity and geometrical divergence of X rays, can be represented in the following form:

$$I(\vartheta) = I_0 f_T P F^2 P(\vartheta) \times \frac{\sin^2 [N \sin 2\vartheta_0 \pi (\vartheta - \vartheta_0) \cot \vartheta_0]}{\sin^2 [\pi (\vartheta - \vartheta_0) \cot \vartheta_0]} \quad (1)$$

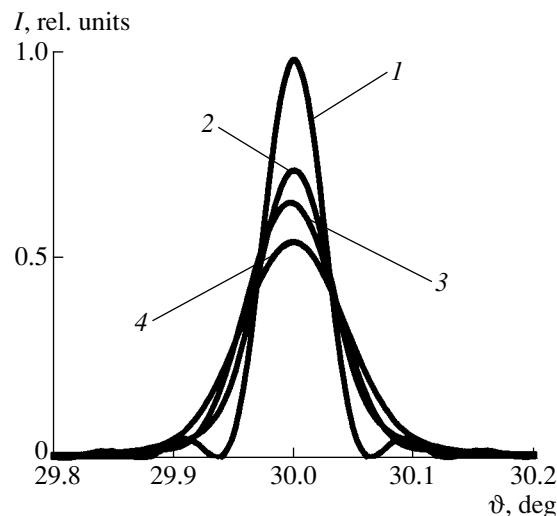
Here, I_0 is the intensity of incident radiation, ϑ is the current value of the angle of reflection, F^2 is the structure factor, ϑ_0 is the Bragg angle of reflection, N is the number of reflection planes in the direction of incident

radiation, f_T is the temperature factor, $P(\vartheta)$ is the Thomson polarization factor, and p is the multiplicity factor.

The theoretical diffraction line, which is calculated from relationship (1) for $N = 600$ and $\vartheta_0 = 30^\circ$, is shown in the figure (curve 1).

The effect of the radiation spectrum on the linewidth can be treated as the convolution of relationship (1) with the characteristic radiation spectrum, which are related by the Wulff–Bragg equation. The radiation spectrum can be described by the dispersion formula [5]

$$I = I_0 \frac{\lambda_0^2}{\lambda_0^2 + \frac{(\lambda_0/\lambda - 1)^2}{(\lambda_0/\lambda_{1/2} - 1)^2}} \quad (2)$$



Theoretical dependences of the intensity of diffracted X rays on the angle of reflection ϑ .

where I_0 is the maximum intensity, and λ_0 and $\lambda_{1/2}$ are the wavelengths corresponding to the maximum intensity and one-half the maximum intensity, respectively.

This convolution can be obtained by combining relationships (1) for different Bragg angles of reflection that are discretely changed in accordance with the X-ray spectrum. The dependence of the intensity of diffracted X rays on the angle of reflection for nonmonochromatic FeK_β radiation at $N = 600$ and $\vartheta_0 = 30^\circ$ is depicted in the figure (curve 2). The parameters characterizing the X-ray spectrum are taken from [5]. The numerical treatment of the constructed convolution has demonstrated that the broadening of the diffraction line due to the nonmonochromaticity of radiation depends on the angle of reflection and on the number of reflection planes. The greatest broadening of the diffraction lines is observed at angles of reflection in the range from 40° to 50° . The increase in the half-width of the diffraction line does not exceed 2% for $N < 200$ and is more than 100% for $N > 2000$.

NUMERICAL SIMULATION

The instrumental distortion of the diffraction line due to the X-ray divergence was estimated by the numerical simulation of the recording of the diffraction line on an X-ray diffractometer with the Bragg–Brentano focusing scheme. The basic idea of this numerical simulation is as follows. The focus of an X-ray tube is considered as a set of point sources. Each of the point sources emits radiation in the form of a set of discrete rays. The discrete rays are incident on the sample at angles of incidence in a certain range. This range is determined by the distances from the focus to the sample and the first slit of the detector, the angle of rotation of the sample with respect to the focus, and the width of the first slit. By combining the discrete rays transmitting through the first slit for particular points of the tube focus, it is possible to determine the angular distribution of the intensities of incident radiation.

Let us assume that the object under investigation is an ideal mosaic crystal that consists of identical coherent scattering regions rotated with respect to the surface through small angles. If the angle of incidence of X rays with respect to the reflection planes of a particular coherent scattering region corresponds to the Wulff–Bragg angle, the X rays are diffracted from the crystal. This radiation will be recorded by a detector only in the case where it is transmitted through the detector slit with a specified width. The angular distribution of the intensities of radiation diffracted from an individual coherent scattering region can be determined from relationship (1). It should be noted that, for this angular distribution, the Bragg angle of reflection is shifted by an angle of misorientation of the coherent scattering region with respect to the Bragg angle of reflection of the total diffraction pattern. The diffraction pattern itself can be represented as the sum of the angular dis-

tributions of the intensities of radiation diffracted from all the individual coherent scattering regions involved.

The above model of the recording of the diffraction pattern of a planar sample on an X-ray diffractometer was implemented in the Dlinewid software package intended for the construction of theoretical diffraction patterns. The Dlinewid software package was used to simulate the dependences of the intensity of diffracted X rays on the angle of reflection under the conditions that corresponded to the geometry of the recording of diffraction patterns on a DRON-3 X-ray diffractometer for $N = 600$ and $\vartheta_0 = 30^\circ$. The dependences thus obtained for monochromatic (curve 3) and nonmonochromatic (curve 4) FeK_β radiation are depicted in the figure.

The results of the numerical treatment carried out with the Dlinewid software package have demonstrated that the broadening of the diffraction line due to the horizontal divergence of the beam depends on a number of parameters, such as the angle of reflection, the number of reflection planes, the focus width, and the material of the anode of the X-ray tube. It should be noted that the effect exerted by these factors on the width of the diffraction line is in qualitative agreement with that observed in the experiments. In particular, the line broadening for $N = 600$ decreases from 86% at $\vartheta_0 = 15^\circ$ to 2% at $\vartheta_0 = 75^\circ$. When the focus width of the X-ray tube is equal to 2 mm, the instrumental broadening of the diffraction lines is as large as 280%. In this case, the $K_{\alpha 1}$ and $K_{\alpha 2}$ diffraction lines merge together. A decrease in the focus width to 0.1 mm leads to a decrease in the instrumental broadening of the diffraction lines to 10%.

The angular dependence of the diffraction line width, with allowance made for the nonmonochromaticity and horizontal divergence of X rays, is represented by a curve with the maximum corresponding to the angles of reflection in the range from 25° to 30° . For parameters $\vartheta_0 < 60^\circ$ and $N > 800$, the width of the diffraction line is predominantly determined by the instrumental factors. For $N < 200$, the instrumental component of the linewidth at angles of reflection in the range from 10° to 80° does not exceed 5%. A change in the material of the anode of the X-ray tube from cobalt to molybdenum results in a change in the broadening of the diffraction line by 10%. Moreover, the diffraction line is broadened by a few percent as the angle of misorientation of the coherent scattering regions increases from 0.001° to 0.300° .

The numerical simulation methods, as applied to the determination of the instrumental component of the error in the X-ray diffraction measurement, provide a means for solving the problem associated with the determination of the parameters N and ϑ_0 directly from the experimental diffraction pattern with the use of the following enumeration procedure. In essence, this procedure consists in enumerating the parameters N and ϑ_0 until the sum of the squares of the deviations of the experimental values from the theoretical dependence

calculated according to relationship (1), with allowance made for the instrumental errors, reaches a minimum value. This procedure is included in the Dlinewid software package.

The diffraction patterns measured for carbon steels on a DRON-3 diffractometer were also processed with the Dlinewid software package. The results of this processing demonstrated that, in the case where the $K_{\alpha 1}$ and $K_{\alpha 2}$ lines cannot be resolved against the background of the second-order lines, the number of reflection planes N is less than 200.

CONCLUSIONS

Thus, the use of numerical methods for simulating X-ray diffraction measurements makes it possible to eliminate the main instrumental errors and to determine

the actual characteristics of the controlled properties of materials from the experimental diffraction patterns.

REFERENCES

1. A. A. Rusakov, *X-ray Diffraction Analysis of Metals* (Atomizdat, Moscow, 1977) [in Russian].
2. S. S. Gorelik, Yu. A. Skakov, and L. N. Rastorguev, *X-ray Diffraction and Electron Diffraction Analyses* (Mosk. Inst. Stali Splavov, Moscow, 1994) [in Russian].
3. V. I. Iveronova and G. P. Revkevich, *Theory of X-ray Scattering* (Mosk. Gos. Univ., Moscow, 1978) [in Russian].
4. D. M. Vasil'ev, *Diffraction Methods for Studying Structures* (Metallurgiya, Moscow, 1977) [in Russian].
5. M. A. Blokhin, *Physics of X-Rays* (Gostekhteorizdat, Moscow, 1953) [in Russian].

Translated by O. Borovik-Romanova

DIFFRACTION AND SCATTERING OF IONIZING RADIATIONS

Numerical Integration Methods for the Takagi–Taupin Equations for Crystals of Rectangular Cross Section

S. I. Kolosov and V. I. Punegov

Syktuykar State University, Oktyabrskii pr. 55, Syktuykar, 167001 Russia

e-mail: punegov@syktsu.ru

Received November 24, 2003

Abstract—Two independent methods for calculation of the rocking curves for laterally bounded crystals are developed. Numerical simulation of diffraction for crystals of different sizes is performed. The results obtained using the dynamical theory of diffraction are compared to those obtained in the kinematic approximation. © 2005 Pleiades Publishing, Inc.

INTRODUCTION

Laterally bounded semiconductor crystal structures are important elements of modern opto-, micro-, and nanoelectronics. There exist different techniques for preparing such structures. In particular, the method of selective epitaxial growth on a profiled substrate is rather promising. There are only a few X-ray diffraction studies of laterally bounded crystals since the resolution available is insufficient, and, thus, analysis of the diffraction data is very time-consuming [1]. As a rule, calculations of diffraction spectra are performed in the kinematic approximation [2, 3] using the finite-element method [2] or explicit formulas [3].

On the other hand, laterally bound crystals may have a size comparable to the extinction length or even exceeding it. The kinematic approximation is no longer valid for such objects. In addition, to calculate the reflectivity of laterally bounded X-ray mirrors, such as grooves of a multilayer diffraction grating, one has to use the dynamical theory of diffraction owing to the strong interaction of X rays with the material.

Calculations of rocking curves within the dynamical theory of diffraction were performed in [4, 5] for perfect crystals of rectangular cross section. However, the rocking curves were calculated in these studies using the procedure based on the Cauchy–Riemann equations. This procedure is very complicated, cumbersome, and, in our opinion, can hardly be applied to processing of experimental data. In addition, the gradual transition from small to semi-infinite lateral crystal sizes was not shown in [4, 5].

In this study, we develop two new independent methods for calculation of rocking curves for laterally bounded crystals of rectangular cross section.

BASIC EQUATIONS

We consider an infinitely long crystal of rectangular cross section with thickness L_z along the OZ axis and

width L_x along the OX axis. A monochromatic plane wave is incident onto this crystal. The plane of incidence of the wave is the XOZ plane. For simplicity, we will consider the reflection from a set of crystallographic planes perpendicular to the OZ plane (Fig. 1). Then, in the two-wave approximation for the symmetric Bragg reflection, the Takagi–Taupin equations have the following form in the Cartesian coordinate system:

$$\begin{aligned} & \left(\cos \theta_B \frac{\partial}{\partial x} + \sin \theta_B \frac{\partial}{\partial z} \right) T(x, z) \\ &= i \frac{\pi}{\lambda} \chi_o T(x, z) + i \frac{\pi}{\lambda} \chi_g CR(x, z), \\ & \left(\cos \theta_B \frac{\partial}{\partial x} - \sin \theta_B \frac{\partial}{\partial z} \right) R(x, z) \\ &= i \frac{\pi}{\lambda} (\chi_o - \alpha) R(x, z) + i \frac{\pi}{\lambda} \chi_g CT(x, z), \end{aligned} \quad (1)$$

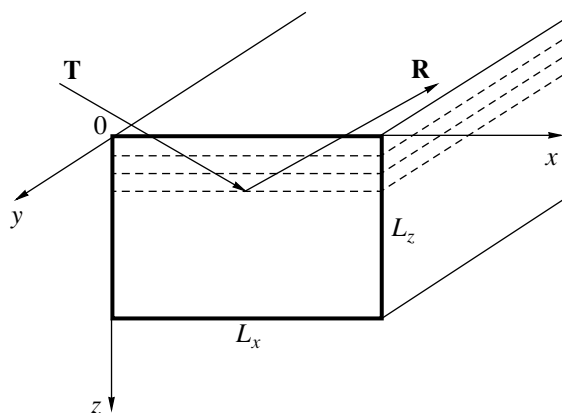


Fig. 1. Schematic of the system. Bold line shows the cross section of the crystal. Dashed lines correspond to the reflecting planes. **T** and **R** are the incident and reflected waves, respectively.

where $T(x, z)$ is the field of the transmitted wave, $R(x, z)$ is the field of the diffracted wave, $\alpha = -2\sin 2\theta_B \Delta\theta$, θ_B is the exact value of the Bragg angle for the crystal under study, $\Delta\theta$ is the deviation of the X-ray incidence angle from the Bragg angle, C is the polarization factor, λ is the X-ray wavelength, and $\xi_{o, g, -g}$ are the Fourier components of the X-ray polarizability.

Let us specify the boundary conditions for the problem stated:

$$\begin{aligned} T(x=0, z) &= 1, & R(x=0, z) &= 0, \\ T(x, z=0) &= 1, & R(x, z=L_z) &= 0. \end{aligned}$$

We introduce dimensionless spatial variables x' and z' :

$$x' = \frac{x}{L_z} \tan \theta_B, \quad z' = \frac{z}{L_z}. \quad (2)$$

Then, Eqs. (1) can be rewritten as

$$\begin{aligned} \frac{\partial T}{\partial x'} + \frac{\partial T}{\partial z'} &= a_1 T + b_1 R, \\ \frac{\partial R}{\partial x'} - \frac{\partial R}{\partial z'} &= a_2 R + b_2 T \end{aligned} \quad (3)$$

with the boundary conditions

$$\begin{aligned} T(x'=0, z') &= 1, & R(x'=0, z') &= 0, \\ T(x', z'=0) &= 1, & R(x', z'=1) &= 0. \end{aligned} \quad (4)$$

Here, the parameters a_1 , a_2 , b_1 , and b_2 are defined as follows:

$$\begin{aligned} a_1 &= \frac{i\pi L_z}{\lambda \sin \theta_B} \chi_o, & a_2 &= \frac{i\pi L_z}{\lambda \sin \theta_B} (\chi_o - \alpha), \\ b_1 &= \frac{i\pi L_z}{\lambda \sin \theta_B} \chi_{-g} C, & b_2 &= \frac{i\pi L_z}{\lambda \sin \theta_B} \chi_g C. \end{aligned} \quad (5)$$

Set of Eqs. (3) with boundary conditions (4) was solved using two methods. The results of numerical calculations by these methods were compared with each other to reveal possible errors.

NUMERICAL SOLUTION ON A MESH

Let us divide the crystal in the direction of the OZ axis into N_z layers with thickness $\Delta z' = 1/N_z$ and introduce a computational mesh with points $z'_j = j\Delta z'$ ($0 \leq j \leq N_z$). For the values of amplitudes at mesh points, we introduce the notation $T_j = T(x', z'_j)$ and $R_j = R(x', z'_j)$. We substitute the derivatives $\partial T/\partial z'$ and $\partial R/\partial z'$ by the symmetric difference derivatives

$$\frac{\partial T_j}{\partial z'} \approx \frac{T_{j+1} - T_{j-1}}{2\Delta z'}, \quad \frac{\partial R_j}{\partial z'} \approx \frac{R_{j+1} - R_{j-1}}{2\Delta z'}$$

for $1 \leq j \leq N_z - 1$. At the boundaries $z' = 0$ and $z' = 1$, it is necessary to use the nonsymmetric difference deriv-

atives:

$$\frac{\partial T_j}{\partial z'} \approx \frac{T_j - T_{j-1}}{\Delta z'}$$

for $j = N_z$ and

$$\frac{\partial R_j}{\partial z'} \approx \frac{R_{j+1} - R_j}{\Delta z'}$$

for $j = 0$.

The values $T_0 = 1$ and $R_{N_z} = 0$ are determined by boundary conditions (4). Then, Eqs. (3) take the form

$$\begin{aligned} \frac{\partial T_j}{\partial x'} &= a_1 T_j - \frac{1}{2\Delta z'} (T_{j+1} - T_{j-1}) + b_1 R_j, \\ \frac{\partial R_j}{\partial x'} &= a_2 R_j + \frac{1}{2\Delta z'} (R_{j+1} - R_{j-1}) + b_2 T_j \end{aligned} \quad (6)$$

for $2 \leq j \leq N_z - 1$, with two additional equations at the boundaries:

$$\frac{\partial T_j}{\partial x'} = \left(a_1 - \frac{1}{\Delta z'} \right) T_j + \frac{1}{\Delta z'} T_{j-1} + b_1 R_j$$

for $j = N_z$ and

$$\frac{\partial R_j}{\partial x'} = \left(a_2 - \frac{1}{\Delta z'} \right) R_j + \frac{1}{\Delta z'} R_{j+1} + b_2 T_j \quad (7)$$

for $j = 0$.

As a result, we obtain a set of $2N_z$ ordinary differential equations with respect to the variable x' with the boundary conditions $T_j(x'=0) = 1$ and $R_j(x'=0) = 0$ (for all values of j).

This set of equations was integrated by the second-order Runge-Kutta method. The integration step $\Delta z'$ was chosen in the range $10^{-2} - 5 \times 10^{-3}$. It was found empirically that the integration step along the OX axis should obey the relation $\Delta x \leq \Delta z$. Thus, using formulas (2), we find $\Delta x' \approx \Delta z' \tan \theta_B$ for variables x' and z' .

APPLICATION OF THE LAPLACE TRANSFORMATION

Let us apply the Laplace transformation with respect to the variable x' to Eqs. (3):

$$\begin{aligned} T(s, z') &= \mathcal{L}[T(x', z')] = \int_0^{\infty} T(x', z') e^{-sx'} dx', \\ R(s, z') &= \mathcal{L}[R(x', z')] = \int_0^{\infty} R(x', z') e^{-sx'} dx'. \end{aligned} \quad (8)$$

Taking into account the boundary conditions $T(x' = 0, z') = 1$ and $R(x' = 0, z') = 0$, we transform the derivatives

$\partial T/\partial x'$ and $\partial R/\partial x'$ as

$$\mathcal{L}[\partial T/\partial x'] = sT(s, z') - 1, \quad \mathcal{L}[\partial R/\partial x'] = sR(s, z').$$

Then, the transformed set of equations takes the form

$$\begin{aligned} \frac{\partial T}{\partial z'} &= (a_1 - s)T + b_1 R + 1, \\ \frac{\partial R}{\partial z'} &= -(a_2 - s)R - b_2 T \end{aligned} \quad (9)$$

with the boundary conditions $T(s, z' = 0) = 1/s$ and $R(s, z' = 1) = 0$. Integrating these equations, we find the solution

$$\begin{aligned} T(s, z') &= (1/s + t)e^{(a_1 - a_2)z'/2} \frac{(\sigma + q)e^{q(1-z')} - (\sigma - q)e^{-q(1-z')}}{(\sigma + q)e^q - (\sigma - q)e^{-q}} \\ &+ rb_1 e^{(a_1 - a_2)(1-z')/2} \frac{e^{qz'} - e^{-qz'}}{(\sigma + q)e^q - (\sigma - q)e^{-q}} - t, \end{aligned} \quad (10)$$

$$\begin{aligned} R(s, z') &= (1/s + t)b_2 e^{(a_1 - a_2)z'/2} \frac{e^{q(1-z')} - e^{-q(1-z')}}{(\sigma + q)e^q - (\sigma - q)e^{-q}} \\ &+ re^{(a_1 - a_2)(1-z')/2} \frac{(\sigma + q)e^{qz'} - (\sigma - q)e^{-qz'}}{(\sigma + q)e^q - (\sigma - q)e^{-q}} - r. \end{aligned} \quad (11)$$

Here, we introduce the notation

$$\begin{aligned} t &= \frac{s - a_2}{b_1 b_2 - (s - a_1)(s - a_2)}, \\ r &= \frac{b_2}{b_1 b_2 - (s - a_1)(s - a_2)}, \\ \sigma &= s - \frac{a_1 + a_2}{2}, \quad q = \sqrt{\sigma^2 - b_1 b_2}. \end{aligned} \quad (12)$$

The amplitudes $T(x', z')$ and $R(x', z')$ are calculated by the formulas

$$\begin{aligned} T(x', z') &= \sum_k \text{Res}[T(s, z'), s_k] e^{s_k x'}, \\ R(x', z') &= \sum_k \text{Res}[R(s, z'), s_k] e^{s_k x'}, \end{aligned} \quad (13)$$

where $\text{Res}[f(z), z_k]$ is the residue of the function $f(z)$ at the pole z_k .

Analysis of solutions for $T(s, z')$ and $R(s, z')$ shows that the poles are the point $s = 0$ and the roots of the equation $(\sigma + q)e^q - (\sigma - q)e^{-q} = 0$. The values of s at which the denominators in the expressions for t and r become zero are removable singularities. The pole $s = 0$ provides a solution for a crystal of infinite length along the OX axis ($L_x = \infty$).

To find the roots of the equation $(\sigma + q)e^q - (\sigma - q)e^{-q} = 0$, we rewrite it as $e^{2q} = (\sigma - q)/(\sigma + q)$. Then, we write the equivalent relation

$$e^{2q} + e^{-2q} = \frac{\sigma - q}{\sigma + q} + \frac{\sigma + q}{\sigma - q},$$

from which the following equations can be easily found:

$$\sinh q = \pm \frac{q}{\sqrt{b_1 b_2}}. \quad (14)$$

These equations have an infinite number of roots $q_k^{(1)}$ and $q_k^{(2)}$, where the superscripts 1 and 2 correspond to Eqs. (14) with positive and negative signs, respectively. The subscript enumerates the roots in the ascending order of their absolute values. The roots of Eqs. (14) were determined numerically by the Newton iteration method. As an initial approximation, it is convenient to take the values

$$q_k^{(1,2)} = \text{arcsinh} \frac{k\pi}{b} \pm (-1)^k k\pi i \quad (k = 1, 2, 3, \dots),$$

where $b = |\sqrt{b_1 b_2}|$.

Then, using the previously introduced notation (12), we find the values of $\sigma_k = \pm \sqrt{q_k^2 + b_1 b_2}$. Here, we choose the sign so as to satisfy the equation $(\sigma + q)e^q - (\sigma - q)e^{-q} = 0$. The values of σ_k with a positive sign can be generally absent for sufficiently thin (along the Z axis) crystals. For thicker crystals, there arise several values of σ_k with a positive real part. Several first even or odd values of k correspond to these values of σ_k . The poles $s^{(1,2)}$ can now be found from the relation $s^{(1,2)} = (a_1 + a_2)/2 + \sigma_k^{(1,2)}$.

When calculating the amplitudes $T(x', z')$ and $R(x', z')$ using formulas (13), it is sufficient to take into account several hundred pairs of poles for only very narrow (along the X axis) crystals ($L_x/L_z < 0.1$), it is necessary to take a number of poles an order of magnitude larger. Note that in the calculation of the rocking curve, the values of $\sigma^{(1,2)}$ are calculated only once since they are determined by the equation involving only the parameters b_1 and b_2 and are independent of the deviation angle $\Delta\theta$.

KINEMATIC APPROXIMATION

In the kinematic approximation, we assume the parameter b_1 to be zero. Then, using Eqs. (10) and (11), we find the following solution:

$$T(s, z') = \left(\frac{1}{s} + \frac{1}{a_1 - s} \right) e^{(a_1 - s)z'} - \frac{1}{a_1 - s}, \quad (15)$$

$$R(s, z') = \frac{b_2}{(s-a_1)(s-a_2)} [1 - e^{(a_2-s)(1-z')}] + \frac{b_2 a_1 e^{a_1-s}}{s(s-a_1)(2s-a_1-a_2)} [e^{(a_2-s)(1-z')} - e^{-(a_1-s)(1-z')}] \quad (16)$$

Performing the inverse Laplace transformation, we obtain the expression for the amplitude $T(x', z')$:

$$T(x', z') = e^{a_1 x'} - (e^{a_1 x'} - e^{a_1 z'}) U(x' - z'), \quad (17)$$

where $U(t)$ is the Heaviside step function

$$U(t) = \begin{cases} 0 & \text{at } t \leq 0 \\ 1 & \text{at } t > 0. \end{cases}$$

The expression for the amplitude $R(x', z')$ can be represented in the form

$$R(x', z') = R_0 + R_1 U(x' - z') + R_2 U(x' + z' - 1) + R_3 U(x' + z' - 2),$$

where

$$R_0 = b_2 \frac{e^{a_1 x'} - e^{a_2 x'}}{a_1 - a_2},$$

$$R_1 = -b_2 e^{a_1 z'} \left[\frac{1}{a_1 + a_2} + \frac{e^{a_1(x'-z')}}{a_1 - a_2} - \frac{2a_1}{a_1^2 - a_2^2} e^{(a_1+a_2)(x'-z')/2} \right],$$

$$R_2 = -b_2 \frac{e^{a_2(1-z')}}{a_1 - a_2} [e^{a_1(x'+z'-1)} - e^{a_2(x'+z'-1)}],$$

$$R_3 = b_2 e^{a_1 + a_2(1-z')} \times \left[\frac{1}{a_1 + a_2} + \frac{e^{a_1(x'+z'-2)}}{a_1 - a_2} - \frac{2a_1}{a_1^2 - a_2^2} e^{(a_1+a_2)(x'+z'-2)/2} \right].$$

RESULTS OF THE CALCULATIONS

A number of problems concerning the choice of stability criteria for the methods described above still remain unsolved. Specifically, we do not know the optimum integration step $\Delta z'$ in the first method at a given set of parameters characterizing the diffraction system and the optimum number of poles in the second method for the same set of parameters. Therefore, calculation of rocking curves was performed simultaneously by both methods. The calculations based on the Laplace transformation require much less computer time in comparison to those using the computational mesh, especially for long (along the OX axis) crystals. The difference may be as high as several tens of or even several hundred times. At the same time, the mesh method is more flexible: it can be much more easily generalized for crystal cross sections that are not rectangular, for example, trapezoidal.

When calculating the rocking curve for a crystal of thickness L_z and width L_x , we first integrated over the crystal surfaces $z = 0$ and $x = L_x$ to find the total reflection amplitude

$$\mathcal{R} = \frac{L_z}{\tan \theta_B} \int_0^{L_x} R(x', 0) dx' + L_z \int_0^1 R(L_x, z') dz',$$

where $L'_x = L_x/L_z \tan \theta_B$. After that, we calculated the intensity of the reflected wave $I = |\mathcal{R}|^2$. In the difference method, we used numerical integration based on the Simpson formula, whereas in the method based on Laplace transformation, this integration was performed analytically.

In our calculations, we used the parameters corresponding to the (111) reflection of $\text{CuK}\alpha_1$ radiation from a germanium crystal.

In Fig. 2, we compare the rocking curves calculated using the dynamical and kinematic approximations for crystals of rectangular cross section with the narrow side along the OX axis ($L_z/L_x \gg 1$, Fig. 2a) and the OZ axis ($L_z/L_x \ll 1$, Fig. 2b). With a further narrowing of the cross section in the corresponding directions, we

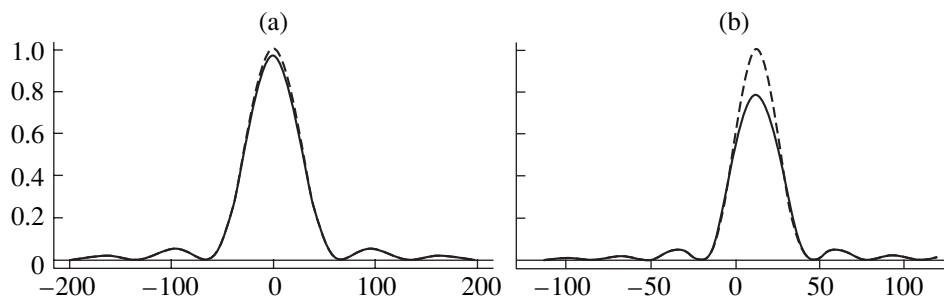


Fig. 2. Rocking curves calculated in the kinematic (dotted curve) and dynamical (solid line) approximations at different ratios of the cross-section sizes L_x and L_z : (a) $L_z = 10 \mu\text{m}$, $L_x = 1 \mu\text{m}$ and (b) $L_z = 0.5 \mu\text{m}$ and $L_x = 50 \mu\text{m}$.

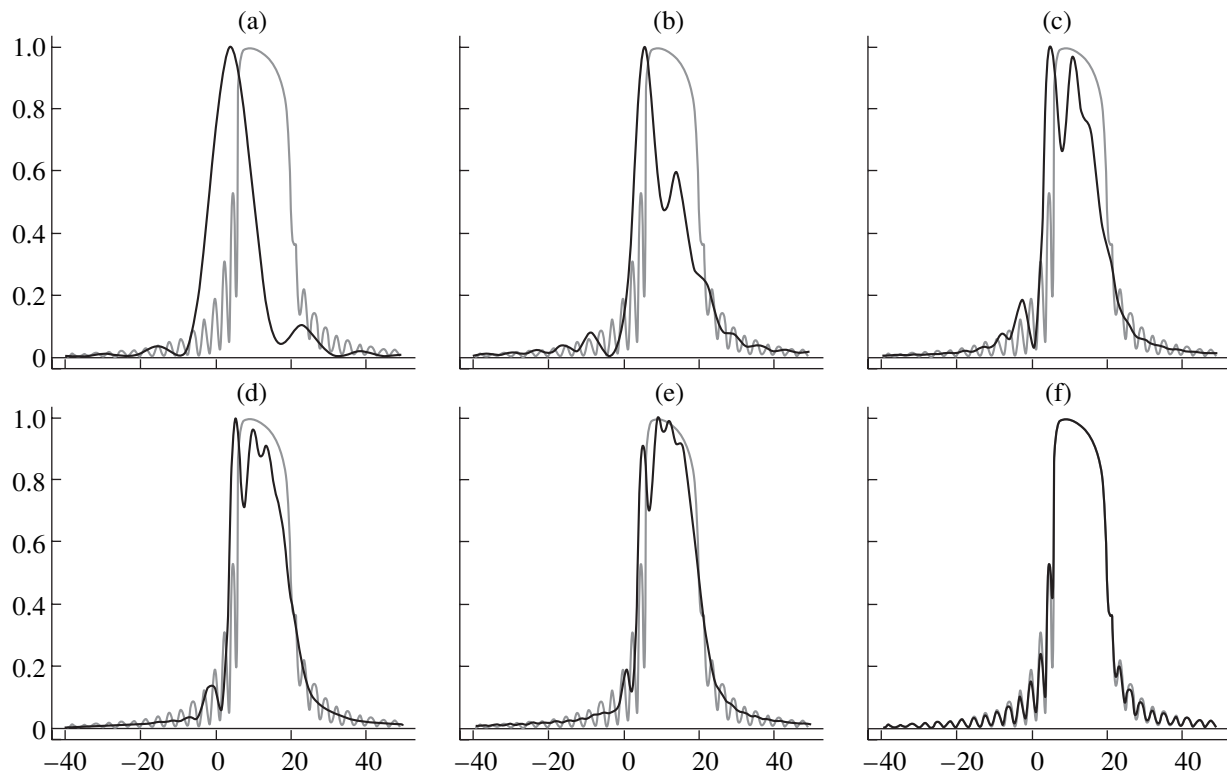


Fig. 3. Rocking curves for a crystal with $L_z = 5 \mu\text{m}$ at different values of L_x . The dotted line is the rocking curve for an infinite plane-parallel plate with $L_x =$ (a) 5, (b) 10, (c) 15, (d) 20, (e) 25, and (f) 150 μm .

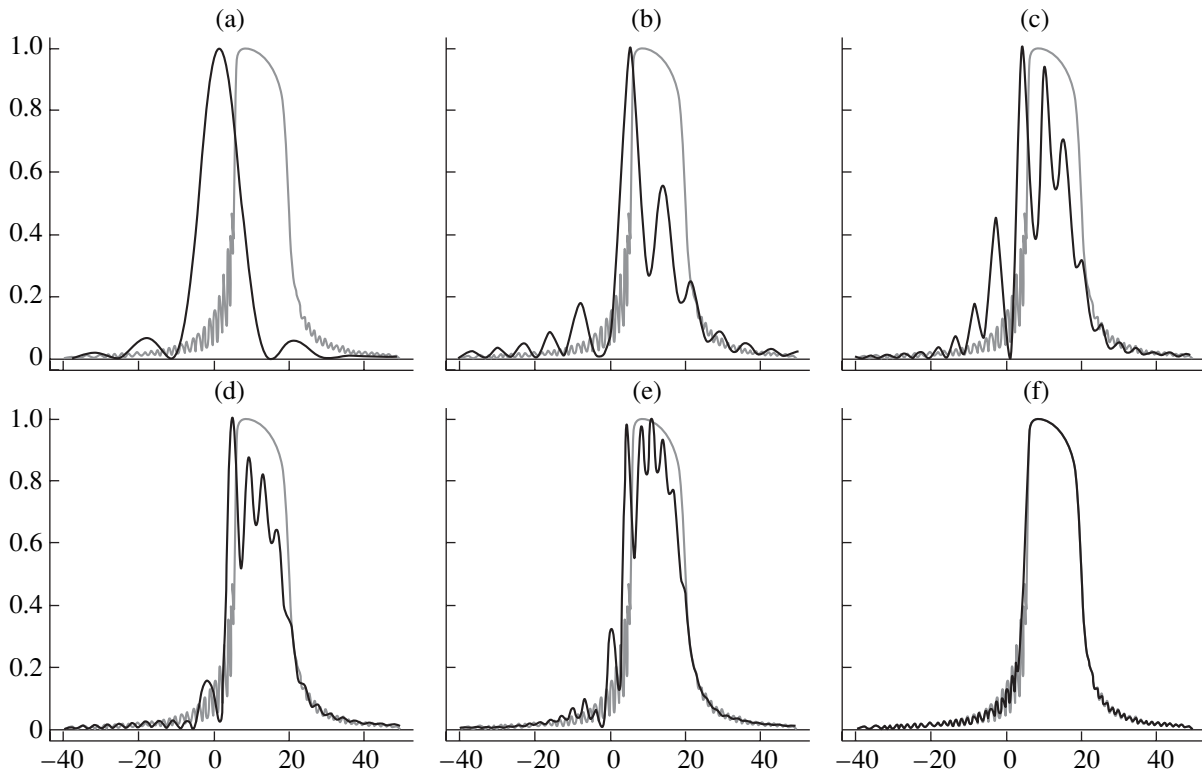


Fig. 4. Rocking curves for a crystal with $L_z = 10 \mu\text{m}$ at different values of L_x . The dotted line is the rocking curve for an infinite plane-parallel plate with $L_x =$ (a) 5, (b) 10, (c) 15, (d) 20, (e) 25, and (f) 150 μm .

observe a complete coincidence of the rocking curves. Deviations from the Bragg angle in seconds of arc are plotted on the abscissa axis and the reflection intensity in arbitrary units is plotted on the ordinate axis.

In Figs. 3 and 4, we show the rocking curves calculated by the Laplace transformation method for crystals 5 and 10 μm thick, respectively, with different widths along the OX axis. In these figures, we also show for comparison the rocking curves of a plane-parallel plate of corresponding thickness infinitely extended along the OX and OY axes. Deviations from the Bragg angle in seconds of arc are plotted on the abscissa axis. The reflection intensity in arbitrary units (for each curve, the maximum value is taken as unity) is plotted on the ordinate axis. It can be seen from Figs. 3 and 4 that, for a small extension of the crystal along the OX axis ($L_x/L_z \approx 1$), the rocking curves (Figs. 3a, 4a) differ in shape only slightly from the curves calculated in the kinematic approximation (Fig. 2). With an increase in the dimension L_x , the rocking curve shows additional oscillations caused by the interference of the waves coming from the lateral ($x = 0$) and upper ($z = 0$) surfaces of the crystal (Figs. 3b–3e, 4b–4e). With a further increase in L_x , the contribution of the waves entering the crystal through the lateral surface becomes smaller

in comparison to the contribution of the waves coming from the upper surface. As a result, the rocking curve asymptotically approaches the corresponding curve for the infinite plane-parallel plate (Figs. 3f, 4f).

ACKNOWLEDGMENTS

This study was supported by the Russian Foundation for Basic Research, project no. 03-02-16239.

REFERENCES

1. K. Nakashima and Y. Kawaguchi, *J. Appl. Phys.* **90** (7), 3255 (2001).
2. Th. Wiebach, M. Schmidbauer, M. Hanke, *et al.*, *Phys. Rev. B* **61** (8), 5571 (2000).
3. V. I. Punegov, *Poverkhnost*, No. 1, 77 (2002).
4. N. M. Olekhovich and A. I. Olekhovich, *Acta Crystallogr., Sect. A: Cryst. Phys., Diffr., Theor. Gen. Crystallogr.* **34**, 321 (1978).
5. G. Thorkildsen and H. B. Lersen, *Acta Crystallogr., Sect. A: Fundam. Crystallogr.* **55**, 840 (1999).

Translated by K. Kugel

DIFFRACTION AND SCATTERING OF IONIZING RADIATIONS

Study of Deformation Fields as a Function of the Temperature Gradient in the Mirror Block of an Interferometer

H. R. Drmeyan

Gyumri State Pedagogical Institute, Gyumri, Armenia

e-mail: converse@web.am

Received February 24, 2004; in final form, September 30, 2004

Abstract—The formation of moiré fringes in an X-ray interferometer is studied. It is shown experimentally that the well-known expression for calculating the period of moiré pattern cannot be always used to calculate the period of moiré patterns obtained in an X-ray interferometer. The change in the moiré period caused by the temperature gradient in the crystal block of an interferometer is calculated. © 2005 Pleiades Publishing, Inc.

It is well known [1] that dilatation (change in interplanar spacings) arises owing to the temperature gradient in a crystalline plate, which may give rise to structural distortions of the crystal.

It is also well known [2] that the interference patterns obtained in X-ray interferometers are very sensitive to the structural distortions (defects) of single crystals. Measuring the periods of interference patterns, one may calculate relative deformation (dilatation) with an accuracy of 10^{-8} and small rotations in the crystal lattice of the irradiated parts of an interferometer with an accuracy of 10^{-3} using the expressions [3]:

$$\Delta d/d = d/\Lambda_1, \quad (1)$$

$$\alpha = d/\Lambda_2, \quad (2)$$

where d is the lattice period; α is the angle between the diffracting gratings; and Λ_1 and Λ_2 are the periods of parallel (dilatation) and rotational moiré, respectively. The above expressions are widely used to study deformation fields arising around growth dislocations in a silicon-based interferometer [4] and transverse stresses caused by ion bombardment of silicon crystals in order to determine refractive indices of various materials [5], absolute values of structure factors with a very high accuracy [6], Burgers vectors [7], etc. Expressions (1) and (2) are correct only for double crystal systems [8–10], i.e., in those cases, where an X-ray wave is diffracted successively from two crystals with different periods or different orientations (Fig. 1). However, the nature of formation of moiré patterns in an X-ray interferometer is quite different. First, in an interferometer, four and not two regions are irradiated (Fig. 2) and, second, at the entrance surface of the last block (analyzer A), coherent waves are superimposed (phenomenon of interference). Thus, the use of Eqs. (1) and (2) for calculating relative deformations and rotations of crystal lattices/gratings, yields only the averaged values.

It was shown experimentally [2] that different components (blocks) of an interferometer give different contributions to the formation of a moiré pattern. If an interferometer is prepared from a perfect crystal, i.e., a single crystal having no internal stresses (crystal lattices have the same periods and are parallel to one another), no moiré fringes are formed because the phase difference is constant across the whole section of the superimposing beams. Now, assume that there are three irradiated regions (1, 2, and 3) having the same lattice period d_0 , whereas the lattice period of the fourth region (4) is d (Fig. 2). In this case, the moiré patterns are formed. Heating of region 4 changes the period of the moiré pattern (it increases if $d < d_0$ and decreases if $d > d_0$). Thus, it is obvious that the change of the moiré patterns (caused by the temperature gradient applied to the block of an X-ray interferometer) depends only on the redistribution of the internal stresses in this block.

Proceeding from the above, we decided to study moiré patterns as functions of the temperature gradient in the mirror block of an X-ray interferometer and to study the redistribution of stresses arising in the mirror

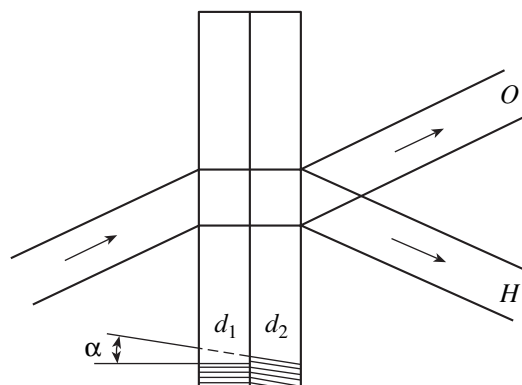


Fig. 1. Double-crystal system and X-ray path in it.

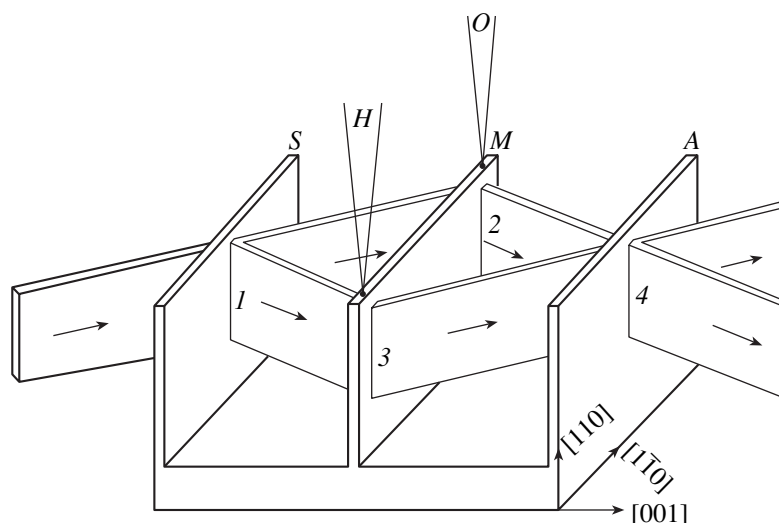


Fig. 2. X-ray interferometer according to Laue. X-ray path and location of heaters.

block of this interferometer during its heating. Although moiré topographs are specific two-dimensional projections of structural distortions in the blocks, they allow one to study deformations along the whole depth of the block under consideration.

EXPERIMENTAL

The experiments were performed in an KRS X-ray diffraction chamber with a scanning device (reciprocating motion). We used an X-ray tube with a copper anode and an URS-2 X-ray power unit.

An interferometer was manufactured from a dislocation-free silicon single crystal with the orientation shown in Fig. 2. The interferometer geometry (block dimensions and interblock distances) was such that the limit of scanning (reciprocating motion of interferometer with respect to the incident beam) was 10 mm.

First, we used scanning to obtain a moiré topograph from the whole working part of the interferometer (Fig. 3a). Then, we also obtained topographs from the heated mirror block of the interferometer successively at the points *O* and *H* (Figs. 3b and 3c). It is seen that with an increase of the current in a heater the moiré patterns (arrangement of moiré fringes) remained almost unchanged, but the periods of the patterns changed.

We studied the changes of the parallel moiré patterns as functions of the temperature gradient applied to the irradiated portions of the mirror block of the interferometer. Our studies show that not all the interferometers form moiré patterns, which indicates that the irradiated parts of the interferometers are always characterized by mutual rotations and certain scatter in interplanar spacings. This makes it difficult to evaluate the effect of various external factors such as irradiation,

temperature gradient, mechanical stresses, etc., on the changes in moiré patterns.

It is well known that the nonuniform heating gives rise to the redistribution of stresses in crystals. It is also well known [1] that heating of a crystalline plate gives rise to stresses determined by the equation

$$\sigma = \frac{\alpha ET}{1 - \nu}, \quad (3)$$

where σ is the internal stress, T is the temperature, $\alpha = 2.64 \times 10^{-6} \text{ }^\circ\text{C}^{-1}$ is the linear expansion coefficient of silicon, E is the Young modulus, and $\nu = 0.262$ is the Poisson ratio [9]. Taking into account that the relative deformation of the crystal lattice along the $[1\bar{1}0]$ direction changes the period of the dilatation moiré and using Eq. (1), we obtain

$$\sigma/E = \Delta d/d = d/\Lambda_1, \quad (4)$$

where Δd is the absolute change in the period of reflecting planes. Using Eqs. (3) and (4), we obtain

$$T = \frac{d(1 - \nu)}{\alpha \Lambda_1}. \quad (5)$$

As is seen from Eq. (5), the period of the parallel moiré pattern is inversely proportional to temperature.

To interpret the influence of thermal stresses on the changes in the moiré pattern we assumed that the initial moiré pattern (obtained without heating of the interferometer blocks) is caused by a certain temperature difference between the irradiated blocks of the interferometer. In other words, we assumed that the interferometer was manufactured from an ideal single crystal so that it could not give rise to the formation of a moiré pattern and that the moiré pattern was formed due to thermal stresses.

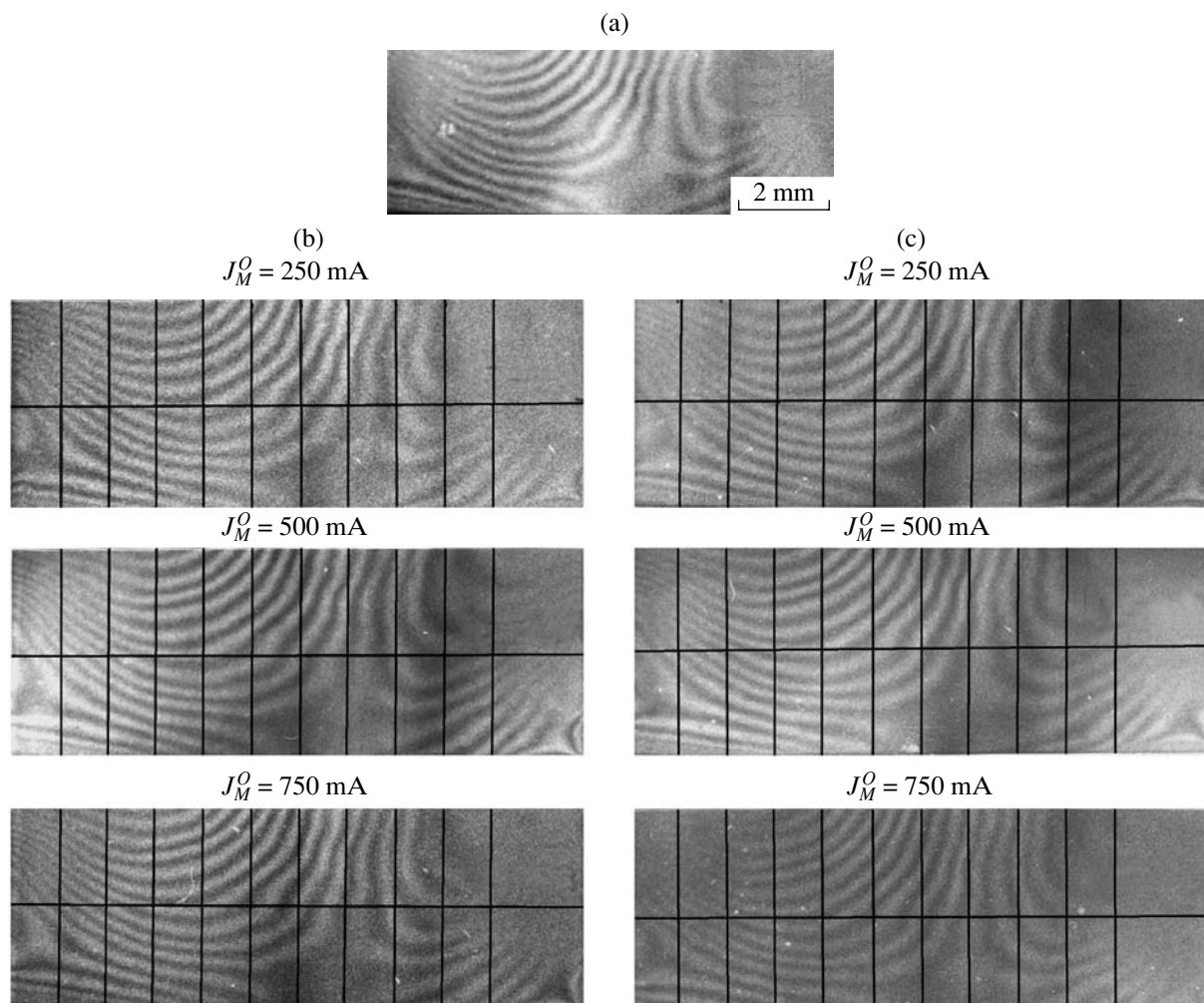


Fig. 3. (a) Initial moiré topograph obtained in an interferometer according to Laue geometry ($\times 6$). (b) Moiré topographs obtained in the heated interferometer in the region O ($\times 4$); the upper left point is heated. (c) Moiré topographs obtained during heating of region H of the interferometer ($\times 4$); the upper point is heated.

To calculate the changes in the moiré periods we divided all the topographs into two parts each (Fig. 3) and determined the periods of the moiré patterns at the boundaries between these parts. In Fig. 4, we plotted temperatures along the ordinate axis and the distances x of the moiré pattern from the left part of the topograph (left edge of the mirror block) along the abscissa. It is seen from the plot in Fig. 4 that the temperature regularly depends on the current in the heated region only in the region with x ranging within 0–1.8 mm: with an increase in the heater current, the temperature of this region decreases. This is evidence that moiré in this region ($x = 0$ –1.8 mm) depends on the difference between the interplanar spacings of the irradiated portions—the mirror and the splitter or the mirror and the analyzer, with the interplanar spacing of the mirror block being less than the interplanar spacing of the splitter or analyzer. However, the comparison of the experimental data from this region with the initial moiré pattern (no heating) shows that the temperature decreases

if the mirror block is heated in the region H and increases if the mirror block is heated in the region O . For the region $x = 2.5$ –3.0 mm, the heating of the mirror block in both O and H regions results in an increase of the moiré period (on the plot, this corresponds to lowering of the temperature). In the remaining parts of the plot, the change of the temperature due to heating of the mirror block does not obey Eq. (5). For example, heating of the mirror block in the region O results in an increase of the moiré period at the distance $x = 10$ mm at the heater current 250 mA, whereas at the currents 500 and 750 mA, it decreases. Heating of the region H at currents 250, 500, and 750 mA results in a decrease of the moiré period (on the plot, this corresponds to a lowering of the temperature). At the distances $x = 13.5$ –14.0 mm, an increase in the heater current gives rise to an increase of the moiré period (on the plot, this corresponds to lowering of the temperature), and at the heater current 750 mA in the region H , the moiré period

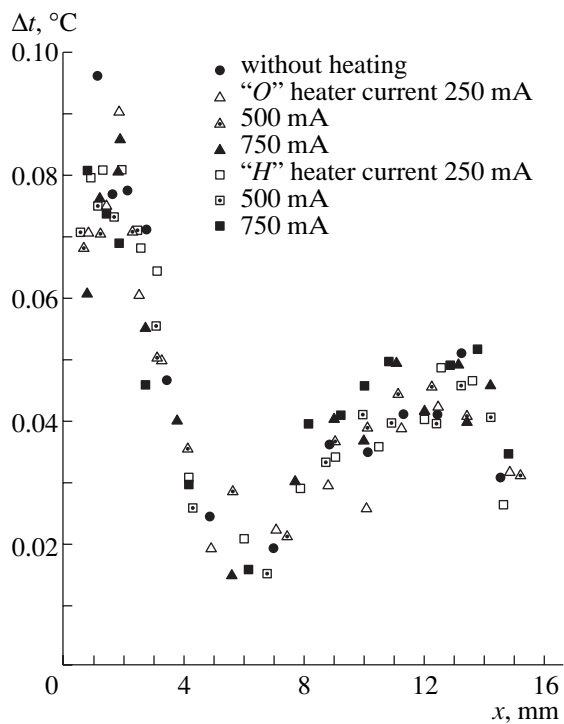


Fig. 4. Temperature as a function of the distance x of moiré from the left edge of the mirror block.

remains almost constant (0.0517 mm without heating and 0.0520 mm during heating).

Thus, the part of the moiré pattern continuously varying with the change of the temperature may be used for calculating the changes of the temperature (change of thermal stress) in the crystal block of the interferometer.

REFERENCES

1. S. P. Timoshenko, *Theory of Elasticity*, 3rd ed. (McGraw-Hill, New York, 1970; Akad. Nauk SSSR, Moscow, 1976).
2. S. A. Aladzhadzhyan, F. O. Éiramdzhyan, K. G. Truni, and P. A. Bezirganyan, *Mol. Nauchn. Rabot. Erev. Gos. Univ.* **2**, 76 (1974).
3. *Electron Microscopy of Thin Crystals*, Ed. by P. B. Hirsch, A. Howie, R. B. Nicholson, D. W. Pashley, and M. J. Whelan (Plenum, New York, 1965; Mir, Moscow, 1968).
4. G. Ghristiansen, L. Gerward, and A. A. Lindegaard Andersen, *Appl. Cryst.* **4**, 370 (1971).
5. U. Bonse and H. Hettkotfer, *Z. Phys.* **223**, 345 (1969).
6. N. Kato and S. Tanemura, *Phys. Rev. Lett.* **19**, 22 (1967).
7. M. Hart, *Philos. Mag.* **26** (4), 821 (1972).
8. A. R. Lang, *Nature* **220**, 652 (1968).
9. I. I. Wortman and R. A. Evans, *J. Appl. Phys.* **36**, 1953 (1965).
10. A. O. Aboyan, *Izv. Akad. Nauk Arm., Fiz.* **35** (4), 212 (2000).

Translated by L. Man

STRUCTURE OF INORGANIC COMPOUNDS

Crystal Structures of K- and Cs-Exchanged Forms of Zorite

N. V. Zubkova*, D. Yu. Pushcharovsky*, G. Giester**, I. V. Pekov*, A. G. Turchkova*,
N. V. Chukanov***, and E. Tillmanns**

* Faculty of Geology, Moscow State University, Vorob'evy gory, Moscow, 119992 Russia
e-mail: dmitp@geol.msu.ru

** Institute of Mineralogy and Crystallography, Geocenter, University of Vienna,
Althanstrasse 14, A-1090 Vienna, Austria

*** Institute of Problems of Chemical Physics, Russian Academy of Sciences,
Chernogolovka, Moscow oblast, 142432 Russia

Received October 1, 2004

Abstract—The crystal structures of K- and Cs-exchanged forms of zorite were studied by X-ray diffraction and IR spectroscopy: $K_{4.75}Na_{1.82}[Ti(Ti_{0.79}Nb_{0.20})_4Si_{12}O_{34}(O,OH)_{5.2}] \times 10.62 H_2O$ (sp. gr. *Cmmm*, $R = 0.0481$ for 516 independent reflections) and $Cs_{4.34}Na_{1.90}[Ti(Ti_{0.80}Nb_{0.18})_4Si_{12}O_{34}(O,OH)_5] \times 5.37 H_2O$ (sp. gr. *Cmmm*, $R = 0.0285$ for 621 independent reflections). Both structures retain the mixed polyhedral framework of zorite: $Na_6Ti(Ti,Nb)_4(Si_6O_{17})_2(O,OH)_5 \times nH_2O$, where $n \sim 11$. It is shown that the positions of the atoms located in the cavities of the frameworks of these compounds differ from those in the structures of zorite and its synthetic analogs. © 2005 Pleiades Publishing, Inc.

INTRODUCTION

Zorite $Na_6Ti(Ti,Nb)_4(Si_6O_{17})_2(O,OH)_5 \times nH_2O$, where $n \sim 11$, is a typical representative of natural microporous heteropolyhedral-framework silicates having pronounced zeolite properties. Zorite was described as a new mineral from the famous Yubileinaya pegmatite, a large hyperagpaitic pegmatite mined at Karnasurt Mountain of the Lovozero alkaline massif (Kola Peninsula, Russia) [1]. In the Yubileinaya pegmatite, zorite involved in the late hydrothermal assemblage is very abundant. This mineral is also present in several pegmatites at Karnasurt Mountain but has not been found anywhere else in the world. No known minerals have structures analogous to the crystal structure of zorite, which is based on a mixed framework formed by xonotlite-like $[Si_6O_{17}]$ ribbons consisting of eight-membered tetrahedral rings. The ribbons are extended along the [001] direction and are linked to each other by columns of vertex-sharing $(Ti,Nb)O_6$ octahedra and isolated $(Ti,Nb)O_5$ half-octahedra. The framework includes two systems of zeolite channels running along the [010] (the minimum diameter is 4.3 Å) and [001] (the minimum diameter is 4.6 Å) directions. These channels are randomly occupied by Na atoms and H_2O molecules. Sodium atoms occupy two nonequivalent positions and have, correspondingly, octahedral coordination formed by four O atoms and two H_2O molecules and sevenfold coordination formed by O atoms.

According to [2], the polyhedral framework of zorite contains two types of rods parallel to the [010] direction. The rods of the first type contain tilting zigzag columns of the $(Ti,Nb)O_6$ octahedra fastened by

$Si(1)O_4$ tetrahedra. This structural fragment of zorite corresponds to the 7.238-Å period along the *b* axis and resembles those observed in nenadkevichite $(Na,K)_{2-x}[(Nb,Ti)_2(Si_4O_{12})(O,OH)_2] \times 4H_2O$ [3] and other minerals of the labuntsovite group. The rods of the second type are formed by TiO_5 half-octahedra and half-occupied $Si(2)O_4$ tetrahedra. If these tetrahedra were completely occupied, the adjacent $Si(2)O_4$ tetrahedra along the [010] direction would be linked together by sharing faces. This fragment of the polyhedral framework, as well as the Na atoms and water molecules located in the channels of the framework, is responsible for possible doubling of the period along the *b* axis. The disordered arrangement of this fragment results in the absence of periodicity along the *a* and *c* axes and is responsible for the *OD* character of the structure as a whole [2].

In 1996, the first data on the synthetic analog of zorite were published. This analog was called ETS-4 (Engelhard Titanium Silicate-4). The synthesis was carried out under hydrothermal conditions, and the product was obtained as thin intergrowths of two titanosilicates, which are analogs of zorite (ETS-4) and “Tinenadkevichite” (korobitsynite, an orthorhombic Ti-dominant member of the labuntsovite group) [4, 5]. The Rietveld refinement of the ETS-4 structure confirmed its similarity to the zorite structure [6]. However, in contrast to zorite, both Ti atoms in ETS-4 have octahedral coordination. Later, the crystal structure of the Sr-exchanged form of ETS-4 was also studied by powder X-ray diffraction [7]. This structure was considered as a result of microintergrowth of four polymorphs, which

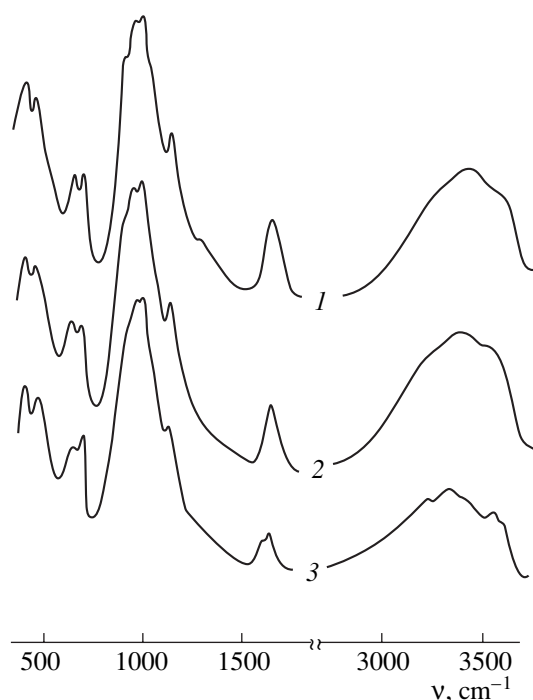


Fig. 1. IR spectra of the (1) starting, (2) K-exchanged, and (3) Cs-exchanged zorites.

differ in the symmetry and packing of the rods of the first type. In addition, the Ti(2) atom in this structure [7], in contrast to ETS-4 [6], was described as having fivefold coordination. In 2001, the crystal structures of the synthetic analogs of zorite—Na-(ETS-4) and the Sr-exchanged form of ETS-4—were studied by single-crystal X-ray diffraction [8]. The results of X-ray diffraction study and IR spectroscopy confirmed that Ti(2) atoms in these structures, like in zorite, have fivefold rather than sixfold coordination. It should be emphasized that the coordinates of water molecules and the occupancies of their positions reported in all publications devoted to zorite and its analogs differ substantially from each other. This fact is indicative of the disordered arrangement of water molecules in the polyhedral framework.

Nowadays, ETS-4 is considered to be one of the most promising mixed-framework “zeolites” from a practical standpoint. Because of its high cation-exchange properties, this compound was patented as a sorbent for radioactive Cs and Sr isotopes [9]. In addition, modified forms of ETS-4 were found to exhibit catalytic activity in reactions involving organic compounds [10].

Natural zorite forms crystals up to 3 mm in length suitable for single-crystal X-ray diffraction studies. The framework density of zorite (the number of Si, Ti, and Nb framework atoms per 1000 Å³) is 14.5. Hence, zorite is one of three (along with traskite and seidite-(Ce)) natural heteropolyhedral-framework silicates with the widest pores. We found that zorite exhibits

high ion-exchange properties with respect to K, Rb, Cs, Ca, Sr, and Pb even under room-temperature conditions. This fact gave impetus to studying the structure of the K- and Cs-exchanged forms of zorite. The results of this study are discussed below.

EXPERIMENTAL

Ion-exchange experiments were carried out using prismatic crystals of zorite (0.3–0.8 mm in length and 0.05–0.2 mm in thickness) from the Yubileynaya pegmatite. The crystals were soaked in 1 M KCl and CsCl solutions for four months, after which their compositions were determined by examining crystal cuts with an electron-probe X-ray microanalyzer. Study of the crystal-cut surface by reflection electron microscopy demonstrated a uniform distribution of K and Cs exchange cations throughout the bulk of the crystals. The starting zorite contained Na₂O (15.3 wt %) and K₂O (1.8 wt %) and did not contain Cs in amounts detectable by electron-probe X-ray microanalysis (i.e., <0.05–0.1 wt % of Cs). After soaking in a KCl solution, the Na₂O content in the samples decreased to 3.0–3.3 wt %, while the K₂O content increased to 14.8–17.2 wt %. After soaking in a CsCl solution, the Na₂O content decreased to 2.7–2.9 wt % and the K₂O content decreased to 0.00 wt %, whereas the Cs₂O content increased to 21.3–21.7 wt %.

Study of samples by IR spectroscopy demonstrated that different exchange cations differently affect the framework and water molecules in the zorite structure (Fig. 1). The wavenumbers of the band maxima in the IR spectrum of the starting zorite (cm⁻¹, sh is a shoulder) are as follows: 3570, 3420, 3260 sh (stretching vibrations of water molecules and OH groups); 1638 (bending vibrations of the water molecules); 1385 (a weak band that is, apparently, due to vibrations of H⁺ ions); 1136 (stretching vibrations of Si–O–Si bridges); 993, 962, 913 (Si–O–stretching vibrations); 702, 653 (Ti–O–stretching vibrations); and 462, 421 (Si–O–Si-bending vibrations). The replacement of Na with K does not lead to substantial changes in the IR spectrum (shifts of most of the bands are no larger than 3 cm⁻¹). A comparison of the IR spectra of the Na- and K-exchanged zorites allows us to conclude that H₂O molecules form somewhat stronger hydrogen bonds in the K-exchanged zorite, which manifests itself in red shifts of the O–H-stretching bands (3570 → 3500 and 3420 → 3375 cm⁻¹).

More substantial changes occur when Na is replaced with Cs. In this case, the absorption bands associated with the framework broaden and their intensities and frequencies change. This is indicative of significant distortions and polarization of the framework. The most considerable changes in the frequencies (cm⁻¹) are observed for the bands sensitive to the Si–O–Si and Ti–O–Ti angles: 1136 → 1131, 702 → 696, and

Table 1. Principal crystallographic characteristics and experimental data for the K- and Cs-exchanged forms of zorite

| Phases | K-exchanged phase | Cs-exchanged phase |
|--|---|---|
| Chemical formula | $\text{K}_{4.75}\text{Na}_{1.82}[\text{Ti}(\text{Ti}_{0.79}\text{Nb}_{0.20})_4\text{Si}_{12}\text{O}_{34}(\text{O}, \text{OH})_{5.2}] \times 10.62\text{H}_2\text{O}$ | $\text{Cs}_{4.34}\text{Na}_{1.90}[\text{Ti}(\text{Ti}_{0.80}\text{Nb}_{0.18})_4\text{Si}_{12}\text{O}_{34}(\text{O}, \text{OH})_5] \times 5.37\text{H}_2\text{O}$ |
| <i>M</i> | 1659.42 | 1948.13 |
| Sp. gr., <i>Z</i> | <i>Cmmm</i> ; 1 | <i>Cmmm</i> ; 1 |
| <i>a</i> , <i>b</i> , <i>c</i> , Å | 23.2620(15), 7.247(5), 6.966(5) | 23.189(5), 7.2489(14), 6.9376(14) |
| <i>V</i> , Å ³ | 1174.3(12) | 1166.2(4) |
| ρ_{calcd} , g/cm ³ | 2.346 | 2.774 |
| μ , mm ⁻¹ | 1.744 | 4.641 |
| <i>F</i> (000) | 825 | 911 |
| θ_{min} , θ_{max} , deg | 2.41, 24.68 | 2.94, 26.28 |
| Scan ranges | $-26 \leq h \leq 27$; $-8 \leq k \leq 8$; $-8 \leq l \leq 8$ | $-27 \leq h \leq 28$; $-8 \leq k \leq 9$; $-8 \leq l \leq 8$ |
| Number of independent reflections with $I > 2\sigma(I)$ | 516 | 621 |
| Number of parameters in refinement | 112 | 129 |
| <i>R_F</i> | 0.0481 | 0.0285 |
| <i>wR</i> (<i>F</i> ²) | 0.1224 | 0.0870 |
| <i>GOF</i> | 1.143 | 1.098 |
| $\Delta\rho_{\text{max}}/\Delta\rho_{\text{min}}$, e/Å ³ | 0.546/−0.561 | 0.539/−0.678 |

421 → 407. In the IR spectrum of the Cs-exchanged sample, the bands of H₂O are weaker than those observed in the IR spectrum of the starting sample. It should be noted that substantially different water molecules are present in this sample, which contains not only zorite-type H₂O molecules but also strongly polarized water molecules involved in very strong hydrogen bonds. The latter are characterized by absorption bands at 3220 and 1615 cm⁻¹. Strong diffusive absorption observed in the range 1200–1450 cm⁻¹ may be due to vibrations of H⁺ ions. However, the characteristic bands of H₃O⁺ ions are absent in the spectrum of the Cs-exchanged sample.

X-ray diffraction data were collected from single crystals of the K- and Cs-exchanged phases, with dimensions of 0.030 × 0.065 × 0.025 mm³ and 0.025 × 0.055 × 0.150 mm³, respectively. Three-dimensional sets of X-ray reflections were measured on a Nonius Kappa CCD diffractometer (MoK_α radiation, $\lambda = 0.71073$ Å). The absorption corrections were applied taking into account the crystal habit. All calculations were carried out using the SHELX97 program package [11]. The structures were refined using the atomic coordinates determined in [2] as the starting model within the sp. gr. *Cmmm* to *R*(*F*) = 0.0481 for 516 reflections with $I > 2\sigma(I)$ for the K-exchanged phase and to *R*(*F*) = 0.0285

for 621 reflections with $I > 2\sigma(I)$ for the Cs-exchanged phase. The refinement gave the following structural formulas: $\text{K}_{4.75}\text{Na}_{1.82}[\text{Ti}(\text{Ti}_{0.79}\text{Nb}_{0.20})_4\text{Si}_{12}\text{O}_{34}(\text{O}, \text{OH})_{5.2}] \times 10.62 \text{H}_2\text{O}$ for the K-exchanged phase and $\text{Cs}_{4.34}\text{Na}_{1.90}[\text{Ti}(\text{Ti}_{0.80}\text{Nb}_{0.18})_4\text{Si}_{12}\text{O}_{34}(\text{O}, \text{OH})_5] \times 5.37 \text{H}_2\text{O}$ for the Cs-exchanged phase. The cation distributions were established on the basis of the refinement of the electron contents of the cation positions and taking into account the requirements for retaining positive values of the thermal parameters and electroneutrality of the chemical formula.

The main characteristics of the crystals and details of the X-ray diffraction study are listed in Table 1. The figures were plotted using the ATOMS program [12].

The structure data for the K- and Cs-exchanged forms of zorite were deposited at the Inorganic Crystal Structure Database (ICSD) with the reference numbers 415042 and 415041, respectively.

DESCRIPTION AND DISCUSSION OF STRUCTURES

Both the structures under study retain the mixed polyhedral framework of zorite. The arrangement of the framework cations in the K- and Cs-exchanged forms of zorite differs from that observed in the zorite structure primarily in the shift of the O(7)=[O,OH] atom

Table 2. Coordinates of the framework atoms, their displacement parameters, and occupancies of the positions (Q) in the crystal structures of the K- and Cs-exchanged (the second row) forms of zorite

| Atom | x | y | z | U_{eq}^* | Q |
|--|--------------|--------------|--------------|-------------|-----------|
| Ti _{0.7897(1)} Nb _{0.2000} | 0.25 | 0.25 | 0 | 0.03474(1) | 0.9897(1) |
| Ti _{0.7958(9)} Nb _{0.1800} | 0.25 | 0.25 | 0 | 0.02348(7) | 0.9759(9) |
| Ti | 0 | 0.5 | 0.03835(3) | 0.04325(8) | 0.25 |
| Ti | 0 | 0.5 | 0.0558(2) | 0.0362(6) | 0.25 |
| Si(1) | 0.161801(2) | 0 | 0.269752(7) | 0.02830(1) | 1 |
| Si(1) | 0.161924(13) | 0 | 0.26908(4) | 0.01739(8) | 1 |
| Si(2) | 0.064132(4) | 0.093496(15) | 0 | 0.02777(3) | 0.50 |
| Si(2) | 0.06409(3) | 0.09722(9) | 0 | 0.01925(15) | 0.50 |
| O(1) | 0.154374(9) | 0 | 0.5 | 0.04044(6) | 1 |
| O(1) | 0.15431(6) | 0 | 0.5 | 0.0353(4) | 1 |
| O(2) | 0.096015(5) | 0 | 0.18846(2) | 0.03806(4) | 1 |
| O(2) | 0.09552(4) | 0 | 0.18922(14) | 0.0365(3) | 1 |
| O(3) | 0.194239(4) | 0.183702(13) | 0.201387(13) | 0.03528(3) | 1 |
| O(3) | 0.19435(3) | 0.18304(8) | 0.20108(10) | 0.03198(17) | 1 |
| O(4) | 0.219958(8) | 0.5 | 0 | 0.03061(5) | 1 |
| O(4) | 0.28070(5) | 0.5 | 0 | 0.0217(3) | 1 |
| O(5) | 0 | 0 | 0 | 0.03247(8) | 1 |
| O(5) | 0 | 0 | 0 | 0.0257(5) | 1 |
| O(6) | 0.059797(12) | 0.31203(4) | 0 | 0.04517(9) | 0.50 |
| O(6) | 0.05957(8) | 0.3166(3) | 0 | 0.0528(8) | 0.50 |
| O(7) | 0 | 0.5 | 0.30011(13) | 0.0545(3) | 0.3001(5) |
| O(7) | 0 | 0.5 | 0.3067(11) | 0.058(2) | 0.254(4) |

* The parameters U_{eq} were calculated from the corresponding anisotropic displacement parameters.

Table 3. Coordinates, displacement parameters, and occupancies of the positions (Q) of the cations located in cavities of the framework of the K-exchanged form of zorite

| Atom | x | y | z | U_{eq} | Q |
|------|--------------|-------------|--------------|-------------|-----------|
| K | 0.372960(5) | 0 | 0.253819(19) | 0.07438(4) | 0.5934(2) |
| Na | 0.25 | 0.25 | 0.5 | 0.04432(8) | 0.4561(3) |
| W(1) | 0.290746(17) | 0.05399(4) | 0.5 | 0.05916(13) | 0.4478(3) |
| W(2) | 0.05866(6) | 0.2979(2) | 0.5 | 0.1317(5) | 0.1879(4) |
| W(3) | 0 | 0.17315(19) | 0.5 | 0.1898(6) | 0.4720(7) |
| W(4) | 0.01370(11) | 0.11907(19) | 0.5 | 0.0693(8) | 0.0797(3) |
| W(5) | 0 | 0.6983(4) | 0.3372(4) | 0.1669(10)* | 0.1297(5) |
| W(6) | 0.39355(4) | 0.05662(13) | 0.12988(15) | 0.0391(3)* | 0.0857(2) |
| W(7) | 0 | 0.03874(14) | 0.5 | 0.0458(5) | 0.1493(4) |

* Isotropic displacement parameters.

occupying the fifth (apical) vertex of the Ti half-octahedron to a position in the (100) mirror plane. O(7) atoms in the structures of Na-(ETS-4) and its Sr-exchanged form [7, 8], as in the K- and Cs-exchanged analogs, do not deviate from the (100) symmetry plane. In the zorite

structure, as in the structures of the Na- and Sr-exchanged forms of ETS-4, the Ti–O(7) distance varies from 1.67 to 1.70 Å. In the K- and Cs-exchanged forms of zorite, this distance increases to 1.8235(16) and 1.741(8) Å, respectively. The coordinates of the frame-

Table 4. Coordinates, displacement parameters, and occupancies of the positions (Q) of the cations located in cavities of the framework of the Cs-exchanged form of zorite

| Atom | x | y | z | U_{eq} | Q |
|--|--------------|------------|------------|-------------|-----------|
| Cs _{0.2900(4)} Na _{0.2500(1)} | 0.314817(16) | 0 | 0.5 | 0.03017(10) | 0.5400(4) |
| Cs _{0.1289(4)} Na _{0.23000(2)} | 0.30183(3) | 0 | 0.5 | 0.0323(2) | 0.3589(4) |
| Cs(3) | 0 | 0.10519(8) | 0.5 | 0.03920(13) | 0.2652(4) |
| Cs(4) | 0 | 0 | 0.5 | 0.0381(3) | 0.1604(5) |
| Cs(5) | 0 | 0.1753(2) | 0.5 | 0.0569(6) | 0.0807(4) |
| Cs(6) | 0.33894(14) | 0 | 0.5 | 0.0492(12) | 0.0418(4) |
| Cs(7) | 0.40454(10) | 0 | 0.0693(10) | 0.118(3) | 0.0400(3) |
| Cs(8) | 0.40632(9) | 0.0437(3) | 0 | 0.0878(11) | 0.0597(3) |
| W(1) | 0.25 | 0.25 | 0.5 | 0.0201(10) | 0.301(3) |
| W(2) | 0.3738(4) | 0 | 0.1201(17) | 0.043(3) | 0.090(2) |
| W(3) | 0.36380(11) | 0 | 0.1977(6) | 0.0322(9) | 0.317(2) |
| W(4) | 0.4234(5) | 0 | 0.5 | 0.125(7) | 0.225(6) |

work atoms, their displacement parameters, and the occupancies of the positions for the K- and Cs-exchanged forms of zorite are given in Table 2.

Concerning the atoms occupying the cavities of the framework, it should be noted that Na atoms in the structure of the K-exchanged form of zorite occupy the position corresponding to the Na(1) atom in the zorite structure and to the Na atom in the ETS-4 structure, whereas K atoms partially occupy the position corresponding to the Na(2) atom in the zorite structure (and the Sr position in the Sr-exchanged form of ETS-4). By analogy with the Sr-exchanged form of ETS-4, the K atom is in eightfold coordination with seven K–O distances in the range 2.5984(9)–2.7984(13) Å, and the eighth apical atom, O(7), located at a distance of 2.9727(2) Å from K, which is in agreement with the generally accepted K–O distances. The O(7) atom was not included in either the environment of Na in the zorite structure or the environment of Sr in the Sr-exchanged form of ETS-4. However, the Na/Sr–O(7) distances are very large in both these structures. In addition, the environment of the K atom in these structures can also involve the W(6) water molecule. The position of this molecule is characterized by a low occupancy (0.09) and is located at a distance of 2.746(2) Å from the K atom. The Na atom in the K-exchanged form of zorite, as in zorite, occupies an octahedral position (Na–O distances vary from 2.3983(14) to 2.4981(12) Å).

In addition, the structures of the K- and Cs-exchanged forms of zorite differ from the structures of zorite and ETS-4 in the arrangement of water molecules. Only the W(1) water molecule was unambiguously localized in all these structures. On the whole, the positions of water molecules in the K-exchanged form

of zorite are characterized by low occupancies and strong disorder. The W(3) molecule found in zorite [2] is absent in the K-exchanged form (as in ETS-4). The coordinates of the Na and K positions and the water molecules, their occupancies, and atomic displacement parameters for the K-exchanged form of zorite are given in Table 3.

The arrangement of Cs and Na cations in the structure of the Cs-exchanged form of zorite differs significantly from that in zorite, its K-exchanged form, and the synthetic Na analog of ETS-4. In the Cs-exchanged form of zorite, the position corresponding to the Na position in the structure of the K analog is occupied by a water molecule. The position corresponding to the K position in the K-exchanged form position is substantially shifted and is also occupied by a water molecule. Cesium atoms, as well as water molecules, are strongly disordered and partially occupy eight positions, which have not been revealed previously (H₂O molecules occupy four nonequivalent positions). Two of these positions (Cs(1) and Cs(2)) are partially occupied by Na atoms and are located at a very short distance from each other (0.301 Å). Apparently, the positions occupied by these atoms should be considered as a result of splitting of the common (Cs,Na) position. The random substitution of Cs by Na cations in the Cs(1) and Cs(2) positions accounts for the unreasonably short (from 2.3544(4) Å for Cs,Na(1) and from 2.1746(5) Å for Cs,Na(2)) cation–water distances in the polyhedra of these cations. The Cs,Na(1), Cs,Na(2), and Cs(3) positions are characterized by the highest occupancies. The cations located in these positions have ninefold coordination (for the first two positions, the Cs,Na(1)–O distances are 2.3544(4)–3.1024(8) Å; Cs,Na(2)–O distances are 2.1746(5)–3.0964(8) Å) and twelfold coordination (for the Cs(3) atom, the Cs(3)–O distances

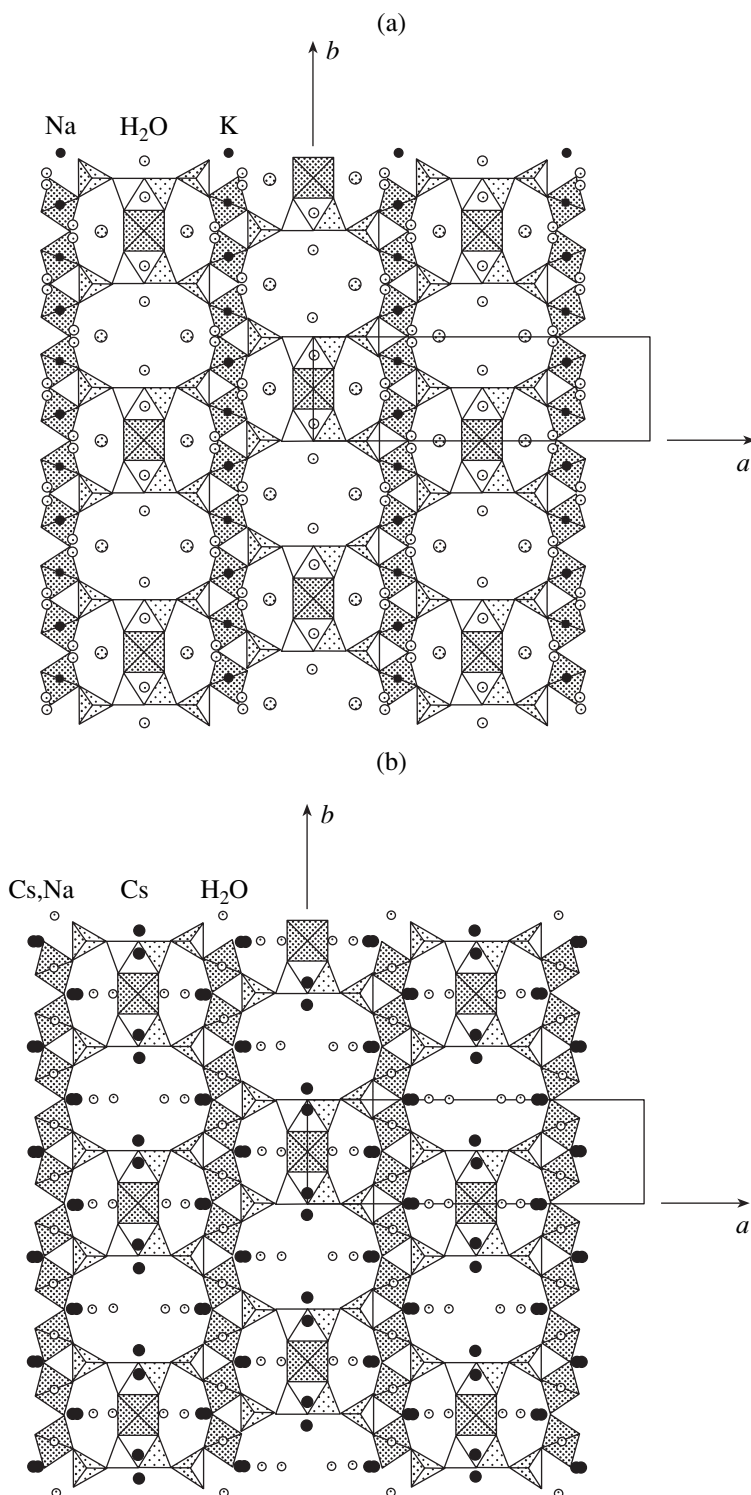


Fig. 2. Crystal structures of the (a) K-exchanged and (b) Cs-exchanged forms of zorite projected onto the (001) plane. The positions with occupancies higher than 0.20 are shown. The atoms located in the cavities of the framework are shown without consideration of ordering, unlike the framework groups formed by the Si(2) tetrahedra and Ti five-vertex polyhedra. The Ti polyhedra are shaded in gray and the Si tetrahedra are open.

are 3.161(3)–3.6585(16) Å). In addition, the W(2) water molecule with a partial occupancy (0.09) can be involved in the environment of the Cs,Na(1) and

Cs,Na(2) atoms. The distances from the W(2) molecule to the Cs,Na(1) and Cs,Na(2) atoms are 2.969(12) and 3.120(11) Å, respectively. The coordinates of the Cs

and Na positions and the water molecules, their occupancies, and atomic displacement parameters for the Cs-exchanged form of zorite are given in Table 4.

The crystal structures of the K- and Ce-exchanged forms of zorite projected onto the (001) plane are shown in Fig. 2.

In summary, we revealed the difference in the distribution of large K and Cs cations in cavities of the mixed framework of the zorite structure. New data on the ion exchange in zorite will provide a deeper insight into the relationship between the structural disorder and the chemical nature and properties of the Na cations replacing K and Cs cations.

ACKNOWLEDGMENTS

This study was supported by the Russian Foundation for Basic Research (project no. 03-05-64054), a joint grant from the Russian Foundation for Basic Research and the Austrian Exchange Service, Agency for International Cooperation in Education and Research (grant no. 03-05-20011BNTS_a), grant from the President of the Russian Federation for Support of Young Russian Scientists and Leading Scientific Schools of the Russian Federation (project no. MK-1046.2004.5), the Program for Leading Scientific Schools (project no. NSh-1642.2003.5), and the program "Universities of Russia."

REFERENCES

1. A. N. Mer'kov, I. V. Bussen, E. A. Goïko, *et al.*, *Zap. Vses. Miner. O-va* **102** (1), 54 (1973).
2. P. A. Sandomirskii and N. V. Belov, *Kristallografiya* **24** (6), 1198 (1979) [*Sov. Phys. Crystallogr.* **24**, 686 (1979)].
3. G. Perrault, Ch. Boucher, J. Vicat, *et al.*, *Acta Crystallogr., Sect. B: Struct. Crystallogr. Cryst. Chem.* **29**, 1432 (1973).
4. J. Rocha, P. Brandao, Z. Lin, *et al.*, *J. Phys. Chem.* **100** (36), 14978 (1996).
5. A. Philippou and M. W. Anderson, *Zeolites* **16** (2-3), 98 (1996).
6. G. Cruciani, P. Deluca, A. Nastro, and P. Patisson, *Micropor. Mesopor. Mater.* **21** (1-3), 143 (1998).
7. C. Braunbarth, H. W. Hillhouse, M. Tsapatsis, *et al.*, *Chem. Mater.* **12**, 1857 (2000).
8. S. Nair, H.-K. Jeong, A. Chandrasekaran, *et al.*, *Chem. Mater.* **13**, 4247 (2001).
9. A. Dyer, M. Pillinger, J. A. Newton, *et al.*, GB Patent WO 9,958,243, *Chem. Abstr.* **131**, 355540 (1999).
10. R. M. Krishna, A. M. Prakash, V. Kurshev, and L. Kevan, *Phys. Chem. Chem. Phys.* **1**, 4119 (1999).
11. G. M. Sheldrick, *SHELX97. Program for the Solution and Refinement of Crystal Structures* (Univ. of Göttingen, Germany, 1997).
12. E. Dowty, *Atoms 3.2. A Computer Program for Displaying Atomic Structures* (Kingsport, 1995), TN 37663.

Translated by T. Safonova

STRUCTURE
OF INORGANIC COMPOUNDS

Refinement of the Crystal Structure of Rhombohedral $KU_2(PO_4)_3$ as a Representative of Orthophosphates with the $NaZr_2(PO_4)_3$ Structure

E. R. Gobechiya*, Yu. K. Kabalov*, S. V. Tomilin**, A. N. Lukinykh**,
A. A. Lizin**, and A. I. Orlova***

* Faculty of Geology, Moscow State University, Vorob'evy gory, Moscow, 119992 Russia
e-mail: elgob@mail.ru

** Federal State Unitary Enterprise State Scientific Center of the Russian Federation,
Research Institute of Atomic Reactors, Dimitrovgrad, 433510 Russia
e-mail: xto@niiar.ru

*** Department of Chemistry, Nizhni Novgorod State University,
pr. Gagarina 23, Nizhni Novgorod, 603950 Russia
e-mail: oai@uic.nnov.ru

Received March 4, 2004

Abstract—The crystal structure of the high-temperature β modification of synthetic orthophosphate $KU_2(PO_4)_3$ was refined from powder X-ray diffraction data by the Rietveld method: sp. gr. $R\bar{3}c$, the unit-cell parameters $a = 9.113(1)$ Å and $c = 24.997(1)$ Å. The isotropic refinement converged to $R_{wp} = 6.15$, $R_B = 2.14$, $R_F = 3.52$, and $S = 0.42$. It was confirmed that β - $KU_2(PO_4)_3$ belongs to the structure type of sodium zirconium phosphate containing an actinide atom in a sixfold (octahedral) coordination formed by oxygen atoms, which is unusual for orthophosphates. The principal interatomic distances and bond angles in the structure are reported. © 2005 Pleiades Publishing, Inc.

INTRODUCTION

Crystalline anhydrous orthophosphates are considered to be promising matrices for immobilization of radioactive wastes of various chemical compositions [1–5]. Among a vast chemical and structural diversity of synthetic orthophosphates, several structure types are characterized by high chemical resistance and thermal and radiation stability, due to which they can be regarded as potential candidates for ceramic forms for immobilization of environmentally hazardous radionuclides [5]. Orthophosphates with structures of monazite, kosnarite, langbeinite, zircon, and some other minerals [6] are of greatest interest in this context. The structure type of sodium zirconium phosphate $NaZr_2(PO_4)_3$ (NZP) has attracted considerable attention of researchers and experts in waste immobilization. A natural analog of NZP is the mineral kosnarite with the idealized formula $KZr_2(PO_4)_3$ [7]. Due to a wide isomorphism, crystals of phosphates with the NZP structure can incorporate about two thirds of all elements of the periodic table [1], the phase homogeneity and high stability characteristics of the resulting compounds being retained. An analysis of the crystal-chemical parameters of a large number of orthophosphates with NZP structure showed that rather large actinide(III) and actinide(IV) cations are difficult to include in the

anionic framework of the NZP structure because of the size factor. Nevertheless, some data have been published [8, 9] on the synthesis and identification of the $KZr_{2-x}U_x(PO_4)_3$ ($0 \leq x \leq 0.2$) and $NaZr_{2-x}An_x(PO_4)_3$ limited solid solutions, where $An = Np$ or Pu ($0 \leq x \leq 0.2$ for Np and $0 \leq x \leq 0.4$ for Pu), with NZP structure. Moreover, actinide alkali metal orthophosphates of the $M^I An_2(PO_4)_3$ series exhibiting high-temperature polymorphism were synthesized and described [10, 11]. It was found that the phosphates $KU_2(PO_4)_3$ and $M^I An_2(PO_4)_3$, where $M^I = Na$ or K and $An = Np$ or Pu , can exist in at least two crystal modifications: a low-temperature (α) modification and a high-temperature (β) modification. The α modifications exist in a temperature range of 500–1100°C and crystallize in the structure type of well-known monoclinic sodium thorium phosphate $NaTh_2(PO_4)_3$ (NTP) belonging to a series of the isostructural $M^I Th_2(PO_4)_3$ compounds, where $M^I = Li, Na, K, Rb,$ or Cs [12]. The $\alpha \rightarrow \beta$ polymorphic transformation occurs at 1000–1200°C to form a rhombohedral modification, which was assigned (on the basis of the powder X-ray diffraction data) to the NZP-structure type [11]. In the temperature range under study (up to 1500°C), orthophosphates of this formula containing other combinations of actinides and alkali metals form exclusively either the α or β modification

(in some cases, individual γ or β' modifications additionally exist), but the $\alpha \rightarrow \beta$ phase transition is not observed [11]. The structure of the first coordination sphere of the central f - or d -metal atom in monoclinic NZP-type orthophosphates differs substantially from that in rhombohedral NZP-type phosphates. The coordination polyhedron of an actinide atom in monoclinic phosphates is a distorted tricapped trigonal prism formed by nine oxygen atoms [12]. The nearest environment of a d -metal atom in an NZP-type structure is an octahedron formed by six oxygen atoms of six isolated $[\text{PO}_4]^{3-}$ groups [13]. Therefore, the $\alpha \rightarrow \beta$ phase transition is accompanied by a very interesting phenomenon consisting in a decrease in the coordination number of an actinide atom from 9 to 6. It is known that low coordination numbers are untypical of rather large actinide(III) and actinide(IV) ions. Hawkins *et al.* [8] provided direct structural evidence (by the Rietveld method) that a certain number of uranium atoms are statistically involved in positions occupied by zirconium atoms (which are in an octahedral oxygen environment) in the anionic framework of an NZP-type structure. It was of obvious interest to obtain analogous evidence for the β modification of orthophosphate, in which zirconium is completely replaced with actinide. For this purpose, we synthesized $\beta\text{-KU}_2(\text{PO}_4)_3$ and refined its crystal structure by the Rietveld method.

EXPERIMENTAL

The synthesis of $\beta\text{-KU}_2(\text{PO}_4)_3$ was carried out by a high-temperature treatment of a suspension of stoichiometric amounts of the starting reagents. Electrolytically pure UO_2 , KH_2PO_4 (reagent grade), and a 1 M H_3PO_4 (reagent grade) solution were used as the starting compounds. The thermal treatment was performed stepwise in argon. The steps of the thermal treatment were alternated with grinding of the resulting powder: 150°C for 10 h, 350°C for 2 h, 800°C for 1 h, 1000°C for 2 h, and 1250°C for 3 h. After the last annealing step, the cell containing the powder was rapidly cooled (the cooling rate was higher than 50 K/min). The intermediates and final annealing products were analyzed by powder X-ray diffraction using the photographic method on a Debye–Scherrer camera.

An X-ray diffraction spectrum for the Rietveld refinement of the crystal structure was measured on an upgraded DRON-3M diffractometer in the angle range $10.00^\circ \leq 2\theta \leq 150.00^\circ$ with a step of 0.02° ; the exposure time at each point was 10 s (filtered $\text{CuK}\alpha$ radiation). The refinement was carried out using the WYRIET program (version 3.3) [14]. The peak profiles were approximated by the Pearson VII function. The peak asymmetry was refined at $2\theta < 60^\circ$. The ionic scattering curves were used for all elements. The crystal structure was refined by successively adding the parameters to be refined using graphical modeling of

Table 1. Unit-cell parameters and results of the Rietveld refinement of the crystal structure of $\beta\text{-KU}_2(\text{PO}_4)_3$

| | |
|------------------------------------|-----------------|
| a , Å | 9.113(1) |
| c , Å | 24.997(1) |
| V , Å ³ | 1797.94(7) |
| Space group, Z | $R\bar{3}c$, 6 |
| 2θ -scan range, deg | 10.00–150.00 |
| Number of reflections | 862 |
| Number of parameters in refinement | 25 |
| R_{wp} | 6.15 |
| R_B | 2.14 |
| R_F | 3.52 |
| S | 0.42 |

Note: $R_{wp} = [\sum w|I_{\text{obs}} - I_{\text{calcd}}|^2 / \sum w I_{\text{obs}}^2]^{1/2}$; $R_B = \sum |I'_{\text{obs}} - I'_{\text{calcd}}| / \sum I'_{\text{obs}}$, where I'_{obs} and I'_{calcd} are the observed and calculated integrated intensities of Bragg reflections, respectively; $R_F = \sum |F_{\text{obs}} - F_{\text{calcd}}| / \sum F_{\text{obs}}$.

Table 2. Coordinates and displacement parameters of the basis atoms in the $\beta\text{-KU}_2(\text{PO}_4)_3$ structure

| Atom | x | y | z | B_{iso} |
|------|-----------|----------|-----------|------------------|
| U | 0 | 0 | 0.1503(1) | 0.31(2) |
| K | 0 | 0 | 0 | 3.5(4) |
| P | −0.290(1) | 0 | 0.25 | 0.9(2) |
| O(1) | 0.318(2) | 0.467(2) | 0.2594(7) | 0.9(4) |
| O(2) | 0.195(2) | 0.236(2) | 0.1980(5) | 1.7(6) |

the background throughout the refinement until the R factors ceased to change.

The atomic coordinates of $\text{KZr}_2(\text{PO}_4)_3$ with sp. gr. $R\bar{3}c$ [13] were used as the starting model for the refinement of the $\beta\text{-KU}_2(\text{PO}_4)_3$ structure. Selected details of the X-ray data collection and the results of the structure refinement are given in Table 1. It should be noted that a low value of S (goodness of fit) is, apparently, associated with an insufficient exposure time at each point used in our experiment [15]. The atomic coordinates and isotropic displacement parameters for the refined $\beta\text{-KU}_2(\text{PO}_4)_3$ structure are listed in Table 2.

The experimental X-ray diffraction spectrum of $\beta\text{-KU}_2(\text{PO}_4)_3$ is shown in Fig. 1. Figure 2 shows the crystal structure of $\beta\text{-KU}_2(\text{PO}_4)_3$ projected onto the (001) plane, which was drawn using the ATOMS program [16].

RESULTS AND DISCUSSION

The results of this study confirmed that the crystal structure of the phosphate $\beta\text{-KU}_2(\text{PO}_4)_3$ belongs to the

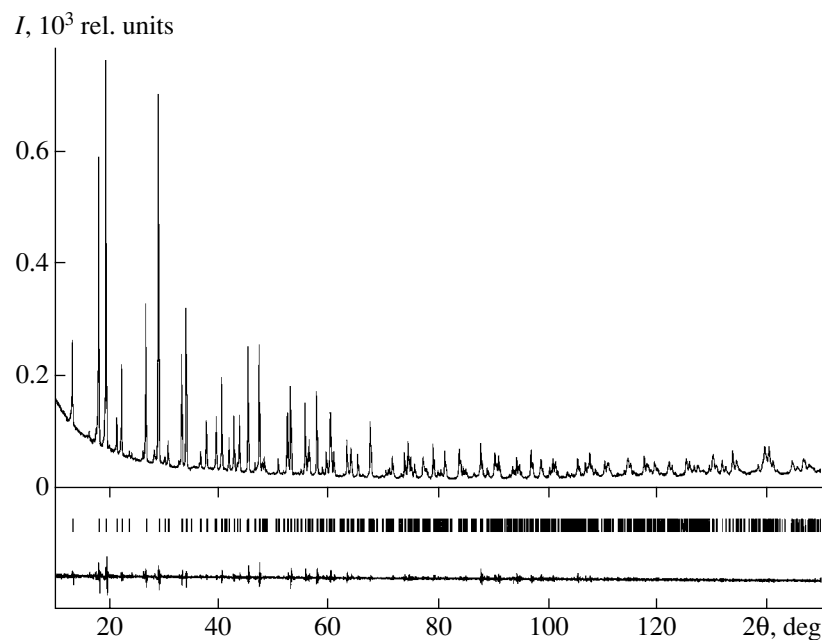


Fig. 1. Experimental X-ray diffraction spectrum of β - $\text{KU}_2(\text{PO}_4)_3$. The vertical bars indicate the positions of reflections of the theoretical X-ray diffraction pattern. The difference curve for the intensities of the experimental and theoretical spectra is shown in the bottom.

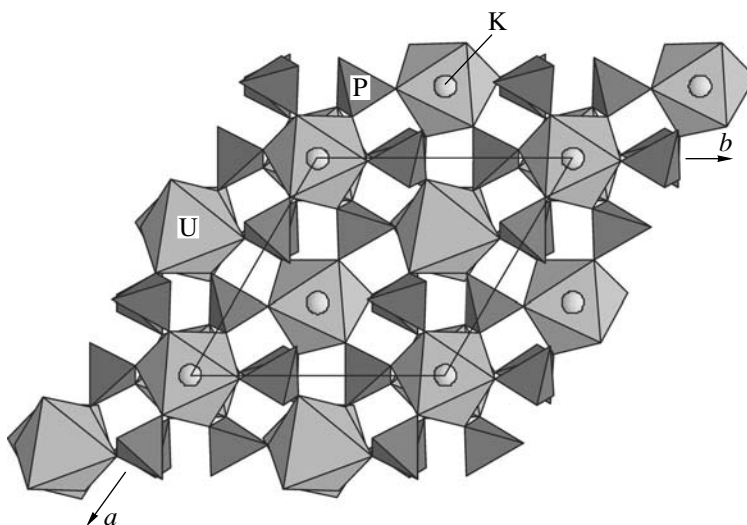


Fig. 2. Crystal structure of β - $\text{KU}_2(\text{PO}_4)_3$ projected onto the (001) plane.

NZP-structure type and is characterized by the presence of the complex three-dimensional anionic $[\text{U}_2(\text{PO}_4)_3]_\infty$ framework, whose cavities are occupied by K^+ cations. The anionic framework consists of U octahedra sharing oxygen vertices with P octahedra. Each uranium atom is surrounded by six oxygen atoms of six different isolated PO_4 groups. Each PO_4 group is coordinated to four uranium atoms. The uranium atoms are located on threefold axes in a slightly distorted octa-

hedral environment characterized by two groups of somewhat different interatomic distances ($\text{U}-\text{O}(1) \times 3 = 2.269(2) \text{ \AA}$ and $\text{U}-\text{O}(2) \times 3 = 2.320(2) \text{ \AA}$). The $\text{O}-\text{U}-\text{O}$ bond angles vary in the range $84.1(1)^\circ$ – $96.0(1)^\circ$. Therefore, the rms deviation of the UO_6 octahedron from the ideal geometry calculated according to procedures proposed in [17, 18] is 1.007. The potassium atom lies on an inversion center and is surrounded by six oxygen atoms occupying the vertices of a trigonal antiprism with six equivalent $\text{K}-\text{O}$ bonds ($2.907(3) \text{ \AA}$).

The phosphorus–oxygen distances in the PO_4 groups have nearly standard values: $\text{P–O}(1) \times 2 = 1.523(1) \text{ \AA}$ and $\text{P–O}(2) \times 2 = 1.500(3) \text{ \AA}$. The O–P–O angles vary from $103.83(7)^\circ$ to $126.6(2)^\circ$. Therefore, the rms deviation of the PO_4 octahedra from the ideal geometry is 1.018.

As expected, the uranium–oxygen interatomic distances in the β modification of $\text{KU}_2(\text{PO}_4)_3$ (2.46 \AA) are shorter than those in the α modification. It was demonstrated previously [8] that the $\alpha \rightarrow \beta$ transformation is accompanied not only by the rearrangement of the inner coordination sphere of the uranium atom and shortening of the U–O bond lengths but also by an increase in the shortest uranium–uranium distances from 4.11–4.20 \AA in the α modification to 4.984(4) \AA in the β modification. As a result, the packing of the polyhedral framework becomes looser (but more symmetrical), as evidenced by the 29% increase in the volume per formula unit (V/Z): from 231.5 \AA^3 in the α modification to 299.7 \AA^3 in the β modification.

Orthophosphates of tetravalent d metals (titanium, zirconium, and hafnium) and alkali metals of the general formula $M^I M_2^{\text{IV}}(\text{PO}_4)_3$ [12, 19] are typical representatives of the NZP-structural family. The unit-cell parameters a and c of the hexagonal lattice of these compounds increase linearly with an increase in the ionic radius of the d element. Our investigation and the previous study [20] demonstrated that the lattice parameters of actinide (U, Np, and Pu) orthophosphates with the NZP structure follow the same dependence. This dependence for the compounds of the above-mentioned d and f metals with the potassium cation is graphically shown in Fig. 3. Therefore, a change in the ionic radius of a tetravalent anion has the same effect on the lattice parameters in spite of the different chemical nature of the cations, which is a consequence of the fact that compounds are isostructural.

The temperature of the phase transition of the monoclinic modification of $\text{KU}_2(\text{PO}_4)_3$ to the rhombohedral modification is 1200°C [11]. It can be expected that at temperatures above 1200°C the region of existence of the $\text{KZr}_{2-x}\text{U}_x(\text{PO}_4)_3$ solid solution will be larger than that reported in [8], because both monoclinic $\text{KU}_2(\text{PO}_4)_3$ and solid solutions of zirconium uranium phosphates were synthesized in [8] at temperatures no higher than 1100°C. At temperatures above 1200°C, both end members of this series of solid solutions— $\text{KZr}_2(\text{PO}_4)_3$ and $\text{KU}_2(\text{PO}_4)_3$ —exist in the rhombohedral modification. Apparently, one should expect an analogous situation to occur in Zr–Np and Zr–Pu phosphates, in which the limits of existence of solid solutions were established also at temperatures below the phase-transition temperatures of the corresponding neptunium and plutonium phosphates [9, 11]. The occurrence of NZP-type crystal modifications for tetravalent actinide (U, Np, Pu) orthophosphates of the

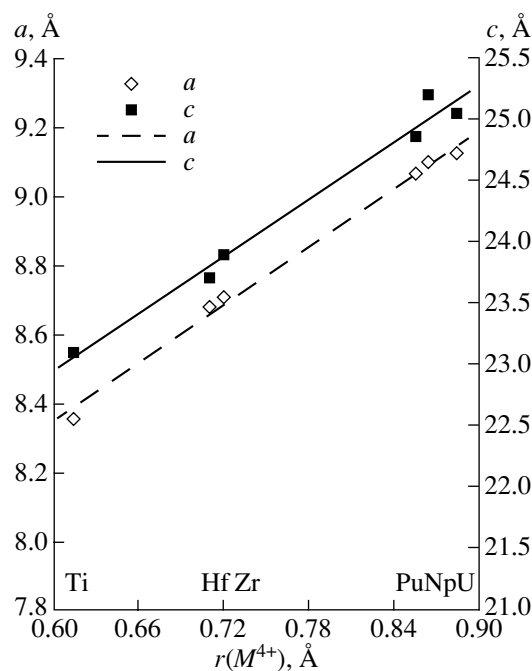


Fig. 3. Dependence of the parameters of the hexagonal unit cells of d - and f -metal orthophosphates with NZP structure of the composition $\text{KM}_2^{\text{IV}}(\text{PO}_4)_3$ on the ionic radius of M^{IV} (Shannon radii [21]).

general formula $M^I M_2^{\text{IV}}(\text{PO}_4)_3$ is a manifestation of the fact that the crystal chemistry of d and f elements has certain features in common. In addition to the purely scientific interest, this phenomenon is also of practical importance because of the possibility of concentrating and immobilizing an actinide fraction of radioactive wastes in homogeneous NZP-type phases. These phases, in principle, can be constructed on the basis of either actinide compounds or solid solutions of actinide zirconium orthophosphates. In the latter case, zirconium plays, apparently, a very important crystal-chemical role as the best stabilizer of NZP-type structures of all known framework-forming elements.

ACKNOWLEDGMENTS

This study was supported by the Russian Foundation for Basic Research, project no. 03-05-64054, and the program “Universities of Russia.”

REFERENCES

1. B. E. Sheetz, D. K. Agrawal, E. Breval, and R. Roy, *Waste Manage. Res.* **14** (6), 489 (1994).
2. A. I. Orlova, V. I. Pet'kov, O. V. Skiba, *et al.*, in *Proceedings of the International Conference of Future Nuclear Systems, Global'97* (Yokohama, Japan, 1997), Vol. 2, p. 1253.

3. Y. Hirose, A. Suzuki, T. Fukasava, *et al.*, in *Proceedings of the International Conference of Future Nuclear Systems, Global'97* (Yokohama, Japan, 1997), Vol. 2, p. 1181.
4. V. Brandel, N. Dacheux, and M. Genet, *Radiokhimiya* **43** (1), 16 (2001).
5. A. I. Orlova, *Radiokhimiya* **44** (5), 384 (2002).
6. Yu. F. Volkov, *Radiokhimiya* **41** (2), 161 (1999).
7. M. E. Brownfield, E. E. Foord, S. J. Sutley, and T. Botinelly, *Am. Mineral.* **78**, 653 (1993).
8. H. T. Hawkins, D. R. Spearing, D. K. Veirs, *et al.*, *Chem. Mater.* **11** (10), 2851 (1999).
9. A. I. Orlova, in *Abstracts of Third Russian Conference on Radiochemistry, Radiochemistry-2000* (St. Petersburg, 2000), p. 26.
10. A. A. Burnaeva, Yu. F. Volkov, A. I. Kryukova, and I. A. Korshunov, *Radiokhimiya* **34** (5), 12 (1992).
11. Yu. F. Volkov, R. F. Melkaya, V. I. Spiriyakov, and G. A. Timofeev, *Radiokhimiya* **36** (3), 205 (1994).
12. B. Markovic, B. Prodic, and M. Sljukic, *Bull. Soc. Chim. Fr.*, Special Issue 1777 (1968).
13. M. Sljukic, B. Makovic, B. Prodic, and D. Anderson, *Z. Kristallogr.* **130** (1–3), 148 (1969).
14. J. Schneider, in *Proceedings of International Workshop on the Rietveld Method* (Petten, 1989).
15. L. B. McCusker, R. B. Dreele, D. E. Cox, *et al.*, *J. Appl. Crystallogr.* **32**, 36 (1999).
16. E. Dowty, *Atoms 3.2. A Computer Program for Displaying Atomic Structures* (Kingport, 1995), TN 37663.
17. K. Robinson, G. V. Gibbs, and P. H. Ribbe, *Science* **172**, 567 (1971).
18. M. H. Hazen and L. W. Finger, *Comparative Crystal Chemistry* (Wiley, Chichester, 1982).
19. A. I. Kryukova, *Zh. Neorg. Khim.* **36** (8), 1962 (1991).
20. Yu. F. Volkov, S. V. Tomilin, A. I. Orlova, *et al.*, *Radiokhimiya* **45** (4), 289 (2003).
21. R. D. Shannon, *Acta Crystallogr., Sect. A: Cryst. Phys., Diffraction, Theor. Gen. Crystallogr.* **32**, 751 (1976).

Translated by T. Safonova

STRUCTURE OF INORGANIC COMPOUNDS

Numerical Dependence of the Unit-Cell Parameters of Minerals of the Lamprophyllite Group on the Cationic Composition in the Interlayer Position

V. A. Zaitsev

Vernadsky Institute of Geochemistry and Analytical Chemistry, Russian Academy of Sciences,
ul. Kosygina 19, Moscow, 119991 Russia
e-mail: woland@ok.ru; alkaline@geokhi.ru

Received February 17, 2004

Abstract—Analysis of the data on the unit-cell parameters of the chemically characterized minerals of the lamprophyllite group showed that the parameter c and the angle β are independent of the cationic composition in the interlayer position. The value of the parameter b correlates with the Ba content. It is shown that the parameter a linearly depends on the average ionic radius of cations in the interlayer position. The Ba and K contents can be estimated from the equations $K + Ba = 2.1431a - 41.091$ and $Ba = 17.764b - 125.36$. © 2005 Pleiades Publishing, Inc.

Layered titanosilicates (titanosilicate micas) form a specific group of minerals whose structure incorporates three-layer packages composed of an octahedral layer located between two titanium–silicon–oxygen nets. The thickness of such a package is 7–9 Å. In different minerals, there are ions, molecules, or even blocks (structural fragments) of other minerals between these packages. The width of the interlayer gap varies from 0 to 18 Å.

In the minerals of the lamprophyllite group, the distance between neighboring packages depends on the composition of cations filling the interpackage space. A change in this distance should affect the unit-cell parameter a since the x axis in the generally accepted orientation of crystals is nearly perpendicular to the package plane.

The relationship between the composition of interlayer cations in the minerals of the lamprophyllite group and the unit-cell parameter a was qualitatively ascertained in [1, 2].

For quantitative estimation of the dependence of the lattice parameters of lamprophyllite on its composition, we collected the results obtained by us and the data in the literature on the composition and unit-cell parameters for 16 samples of minerals of the lamprophyllite group. These samples include lamprophyllite and barytolamprophyllite polytypes 2M and 2O from the Khibina, Lovozero, and Murunsky massifs, from the White Sea coast and the Gardiner massif and nabalamprophyllite from the Inagli massif. The interlayer cation composition was determined from the structural interpretations or the data of microprobe and chemical analyses, recalculated per formula units with four Si + Al atoms [3]. These data were used to calculate the corre-

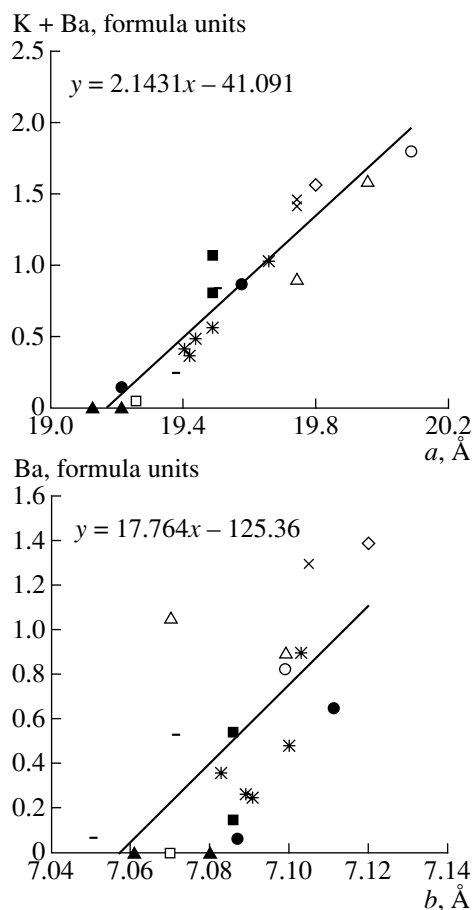


Fig. 1. Dependence of the unit-cell parameters a and b on the K and Ba contents in the minerals of the lamprophyllite group according to the data in the literature \square [1], \triangle [2], \blacksquare [4], \times [5], \circ [6], $*$ [7], \diamond [8], $-$ [9], and \bullet [10] and the data of this study \bullet .

Coefficients of correlation between the elemental composition in the interlayer position (in formula units) and the unit-cell parameters of the minerals of the lamprophyllite group (significant coefficients are marked in bold)

| Unit-cell parameter | Sr | K | Ba | Na | Sr + Ba | K + Ba | Na + Ba |
|---------------------|--------------|-------------|-------------|--------------|---------|-------------|---------|
| <i>a</i> | -0.81 | 0.64 | 0.85 | -0.69 | 0.20 | 0.95 | 0.50 |
| <i>b</i> | -0.54 | 0.06 | 0.67 | -0.31 | 0.37 | 0.56 | 0.53 |
| <i>c</i> | -0.27 | 0.13 | 0.21 | -0.17 | -0.11 | 0.23 | 0.20 |
| β | -0.22 | 0.21 | 0.24 | -0.31 | 0.07 | 0.28 | 0.11 |

lation coefficients,¹ which are listed in the table. It can be seen that the parameter *a* depends most strongly on the sum of the contents of potassium and barium, whereas the parameter *b* depends most strongly on the barium content. These dependences are shown in Fig. 1. For the parameter *c* and the angle β , all correlation coefficients are insignificant.

Using the least-squares method, we found the linear regression equations: $K + Ba = 2.1431a - 41.091$ and $Ba = 17.764b - 125.36$. The corresponding dependences are shown in Fig. 1. The total content of the elements can be estimated from the first of these formulas, whereas the barium content can be found from the second formula.

As a generalized characteristic of the composition, the value of the average atomic radius in the position M_1 can be used (for nabalamprophyllite, we took the average of the two values arising as a result of the position splitting). The use of the systems of Goldschmidt, Pauling, and Belov atomic radii leads to a unified picture: the dependence of the unit-cell parameter *a* on the average atomic radius in the M_1 position (Fig. 2) is

¹ The correlation coefficient is a measure of linear dependence between two values. More detailed data on this parameter can be found in textbooks on the probability theory and mathematical statistics.

clearly linear (for example, for the system of Pauling radii, the correlation coefficient is 94.8% and the curve is described by the equation $r_{av} = 0.3075a - 4.837$). The deviation is large only for the data of [4]. This could be explained by incomplete occupation of the interlayer position. However, the analysis carried out in [4], as well as the composition obtained by interpretation of the sample, indicate the absence of vacancies.

The use of the system of Shannon–Prewitt effective ionic radii [11] causes some difficulties because the corresponding data for Na, K, Sr, and Ba in the coordination 11 and Na in the coordination 12 are absent.

The radius of the Na ion in coordination 12 can be estimated from the interpretation [12] of the lueshite structure, in which Na occupies the same position. On the basis of the fact that the value of the ionic radius of Nb in octahedra is consistent with the value of 0.64 Å recommended by Shannon and Prewitt, the average radius of the oxygen ions must be 1.3455 Å and the radius of the sodium ion must be 1.44 Å. If we assume, as Shannon and Prewitt recommend, the oxygen radius in the sixfold coordination to be 1.40 Å, the average radius of the sodium ions will be 1.38 Å.

The linear approximation of the dependence of the effective ionic radius on the coordination number (Fig. 3) yields the following estimates of the ionic radii

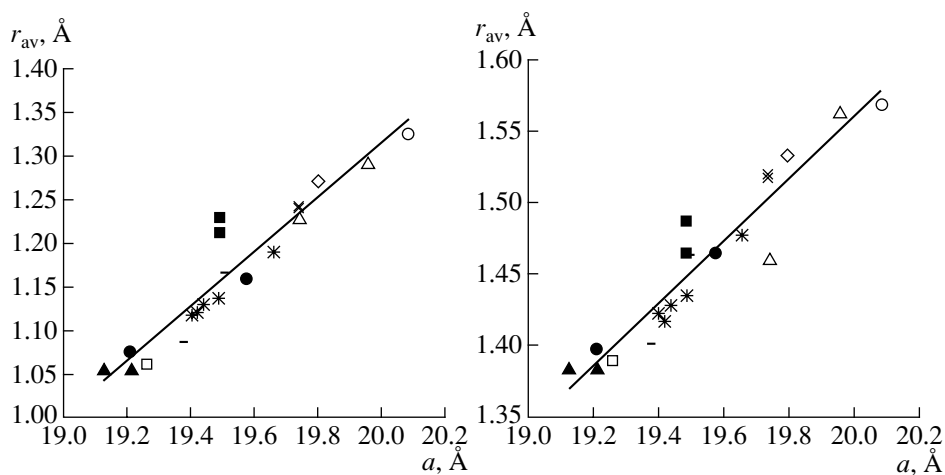


Fig. 2. Dependence of the unit-cell parameter *a* on the average radius of cations in the interlayer position. Designations are the same as in Fig. 1.

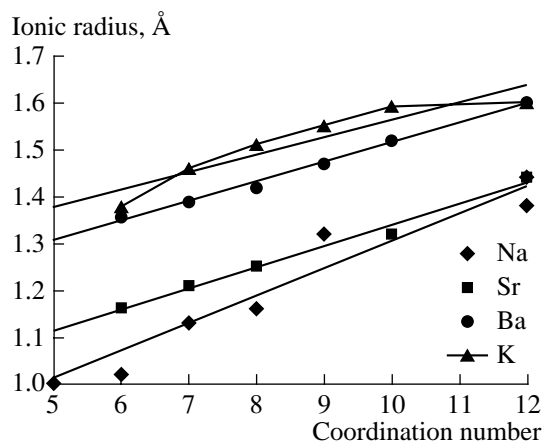


Fig. 3. Dependences of the ionic radii of K, Sr, Na, and Ba on the coordination number.

of Na, K, Sr, and Ba in coordination 11: 1.36, 1.60, 1.38, and 1.56, respectively. When these values are used, the deviation from the trend for the data of [4] decreases. The curve based on these values of the ionic radii is a straight line described by the equation $r_{av} = 0.217a - 2.7805$. The correlation coefficient is 95.0%.

The dependence of the parameter b on the average ionic radius is as follows: $r_{av} = 1.6512b - 10.245$. The correlation coefficient is 50.4%.

The linear dependence of the average atomic radius in the interlayer position and the unit-cell parameter a , which is sensitive to the occupation of the interlayer space, indicates the absence of volume mixing effects in the quaternary system lamprophyllite–barytolamprophyllite—their hypothetical potassium and sodium analogs.

ACKNOWLEDGMENTS

This study was supported by the Russian Foundation for Basic Research, project no. 02-05-64122, and

the program “Leading Scientific Schools,” project no. NSH-1087.2003.5.

REFERENCES

1. A. I. Komkov, G. P. Akimova, N. V. Kuznetsova, and A. D. Rudneva, *X-ray Diffractometry of Mineral Raw Materials and Its Applied Importance* (VIMS, Moscow, 1980), p. 133 [in Russian].
2. R. K. Rastsvetaeva and M. D. Dorfman, *Kristallografiya* **40** (6), 1026 (1995) [*Crystallogr. Rep.* **40**, 951 (1995)].
3. V. A. Zaitsev and L. N. Kogarko, *Geokhimiya*, No. 4, 1 (2002).
4. R. K. Rastsvetaeva, M. N. Sokolova, and A. I. Gusev, *Mineral. Zh.* **12** (5), 25 (1990).
5. R. K. Rastsvetaeva and N. V. Chukanov, *Dokl. Akad. Nauk* **386** (4), 492 (1999).
6. R. K. Rastsvetaeva, V. G. Evsyunin, and A. A. Konev, *Kristallografiya* **40** (3), 517 (1995) [*Crystallogr. Rep.* **40**, 472 (1995)].
7. O. Johnsen, T. F. D. Nielsen, and J. G. Ronsbo, *Neues Jahrb. Mineral., Monatsh.*, No. 7, 328 (1994).
8. K. A. Lazebnik, N. V. Zayakina, and G. P. Paukevich, *Dokl. Akad. Nauk* **361** (6), 799 (1998).
9. *Mineralogy of the Khibina Massif* (Nauka, Moscow, 1978), Vol. 2 [in Russian].
10. S. V. Krivovichev, T. Armbruster, V. N. Yakovenchuk, *et al.*, in *Proceedings of IV International Symposium “Mineralogical Museums”* (NIIZK SPbGU, St. Petersburg, 2002), p. 269.
11. R. D. Shannon and C. T. Prewitt, *Acta Crystallogr.* **25**, 925 (1969).
12. A. C. Sakowsky-Cowley, K. Lukaszewicz, and D. Megan, *Acta Crystallogr., Sect. B: Struct. Crystallogr. Cryst. Chem.* **25** (5), 851 (1969).

Translated by Yu. Sin'kov

STRUCTURE OF INORGANIC COMPOUNDS

X-ray Diffraction Study of Thiocarbamide Hydrochloride

Yu. P. Gladii

Kostroma State Technological University, ul. Dzerzhinskogo 17, Kostroma, 156005 Russia

e-mail: info@kstu.edu.ru

Received March 3, 2004

Abstract—Thiocarbamide hydrochloride single crystals forming a salt with the composition $[(\text{NH}_2)_2\text{CSH}]^+\text{Cl}^-$ are studied by the X-ray diffraction method. The tetragonal crystals have the unit-cell parameters $a = 7.556(1)$ Å and $c = 18.329(3)$ Å, $V = 1046.5$ Å³, $Z = 8$, $\rho_{\text{calcd}} = 1.436$ g/cm³, sp. gr. $P4_12_12$, and $R = 0.050$. Each chloride anion in the crystal forms five hydrogen bonds with three different cations. © 2005 Pleiades Publishing, Inc.

To study the problems of complex formation of amides with mineral acids, we determined the crystal and molecular structure of thiocarbamide hydrochloride with the composition $\text{CS}(\text{NH}_2)_2 \cdot \text{HCl}$.

The unit-cell parameters and integral intensities of reflections were measured on a DRON diffractometer (λMoK_α radiation, graphite monochromator, $\theta/2\theta$ scan, 369 crystallographically independent nonzero reflections with $\theta \leq 29^\circ$). The crystals have tetragonal symmetry and the unit-cell parameters $a = 7.556(1)$ Å and $c = 18.329(3)$ Å, $V = 1046.5$ Å³, $Z = 8$, and $\rho_{\text{calcd}} = 1.436$ g/cm³. We selected the group $P4_12_12$ of two pos-

sible enantiomorphous space groups $P4_12_12$ and $P4_32_12$. No attempts to determine the absolute configuration were made.

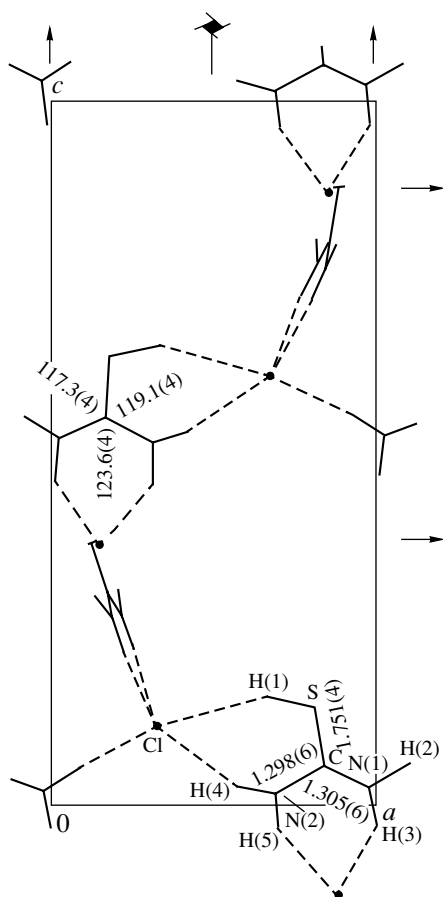
The structure was solved by direct methods. The coordinates of all the non-hydrogen atoms were determined from the E syntheses of electron density and refined by the least-squares method in the full-matrix approximation. Hydrogen atoms were localized from the difference electron-density syntheses in the isotropic approximation. The final value of the reliability factor is $R = 0.050$. All the computations were made using the AREN complex of programs [1]. The atomic coor-

Table 1. Coordinates of non-hydrogen ($\times 10^4$) and hydrogen ($\times 10^3$) atoms in the structure

| Atom | x/a | y/b | z/c | Atom | x/a | y/b | z/c |
|------|---------|---------|---------|------|----------|---------|--------|
| Cl | 3423(2) | 3591(2) | 1121(1) | H(1) | 655(11) | 337(12) | 125(6) |
| S | 8255(2) | 3746(2) | 1424(1) | H(2) | 1102(9) | 340(10) | 50(4) |
| N(1) | 9890(5) | 3037(6) | 197(3) | H(3) | 1000(11) | 251(10) | -33(6) |
| N(2) | 6857(5) | 3040(6) | 137(2) | H(4) | 564(12) | 337(12) | 39(6) |
| C | 8330(7) | 3227(6) | 493(2) | H(5) | 689(12) | 270(12) | -42(7) |

Table 2. Parameters of hydrogen bonds

| Bond | $D\cdots A$, Å | $D-H$, Å | $A\cdots H$, Å | $\angle DHA$, deg |
|--|-----------------|-----------|-----------------|--------------------|
| S-H(1) \cdots Cl (x, y, z) | 3.695(3) | 1.37(9) | 2.37(9) | 162(2) |
| N(1)-H(2) \cdots Cl ($x+1, y, z$) | 3.188(5) | 1.06(8) | 2.15(9) | 166(3) |
| N(1)-H(3) \cdots Cl ($y+1/2, -x+1/2, z-1/4$) | 3.245(2) | 1.04(9) | 2.32(9) | 147(3) |
| N(2)-H(4) \cdots Cl (x, y, z) | 3.187(6) | 1.05(9) | 2.16(8) | 165(3) |
| N(2)-H(5) \cdots Cl ($y+1/2, -x+1/2, z-1/4$) | 3.265(5) | 1.04(8) | 2.34(9) | 147(3) |



The structure projected onto the (010) plane.

dinates obtained are listed in Table 1; the parameters of hydrogen bonds are given in Table 2. The figure shows the structure projected onto the (010) plane.

It was established that the compound studied is a salt with the composition $[(\text{NH}_2)_2\text{CSH}]^+\text{Cl}^-$ formed owing to protonation of thiocarbamide molecules with the hydrogen atoms of hydrochloride. This is also indicated by the bond lengths for the cation: an increase in the C-S bond length up to 1.751(4) Å and a decrease (on the average to 1.302(6) Å) in the C-N bond lengths in comparison with the corresponding values 1.72 and 1.34 Å in nonprotonated thiocarbamide molecules in the crystal [2].

The molecular packing in the crystal is ensured by a three-dimensional system of hydrogen bonds with the participation of all the hydrogen atoms and with each chloride anion forming hydrogen bonds with three different cations.

REFERENCES

1. V. I. Andrianov, *Kristallografiya* **34** (6), 1387 (1989) [*Sov. Phys. Crystallogr.* **34**, 835 (1989)].
2. M. R. Truter, *Acta Crystallogr.* **22**, 566 (1967).

Translated by L. Man

STRUCTURE
OF INORGANIC COMPOUNDS

Analysis of Diffuse Background on the X-ray Diffraction Pattern
of Fullerite C₆₀

L. A. Aleshina, A. D. Fofanov, R. N. Osaulenko, and L. A. Lugovskaya

Petrozavodsk State University, pr. Lenina 33, Petrozavodsk, 185640 Karelia, Russia

e-mail: alkft@mail.ru

Received June 24, 2003; in final form, September 27, 2004

Abstract—Diffuse scattering on the X-ray diffraction pattern of fullerite C₆₀ is analyzed. The characteristics of the short-range order of the amorphous component of fullerite are determined by the Finbak–Warren method. It is established that the short-range order of the amorphous component is similar to the short-range order of lonsdaleite. © 2005 Pleiades Publishing, Inc.

X-ray studies of a powder fullerite C₆₀ sample were performed on an automated DRON-2 diffractometer using CuK_α radiation monochromitized by a pyrolytic graphite crystal. The scattering intensities were recorded at a step of 0.02° on the scale of scattering angles 2θ.

The X-ray diffraction pattern (Fig. 1) was indexed in the cubic system with the lattice parameter $a = 14.19 \pm 0.01$ Å, sp. gr. $Fm\bar{3}m$.

The characteristic feature of the diffraction patterns is the presence of the diffuse background, which indicates the existence of the amorphous component. This was first noticed in [1]. The present study was undertaken in order to establish the type of the short-range order of the amorphous component of a cubic fullerite C₆₀.

Full-profile (Rietveld) analysis of the X-ray diffraction pattern of fullerite C₆₀ showed that the maxima in the region of the 220–222, 331–511, and 333 reflections, which could have been considered as a diffuse background were in fact formed owing to superposition of the above groups of reflections (Fig. 2).

Nevertheless, we analyzed the background both with due regard for these maxima and ignoring them. Figure 3a shows the scattering intensities normalized by the Warren method for both instances and also, for comparison, the intensity distributions obtained in [2, 3] for amorphous carbon (Fig. 3b) and schungite (Fig. 3c). It is seen that the intensity distribution for the amorphous component of fullerite C₆₀, amorphous carbon, and schungite considerably differ.

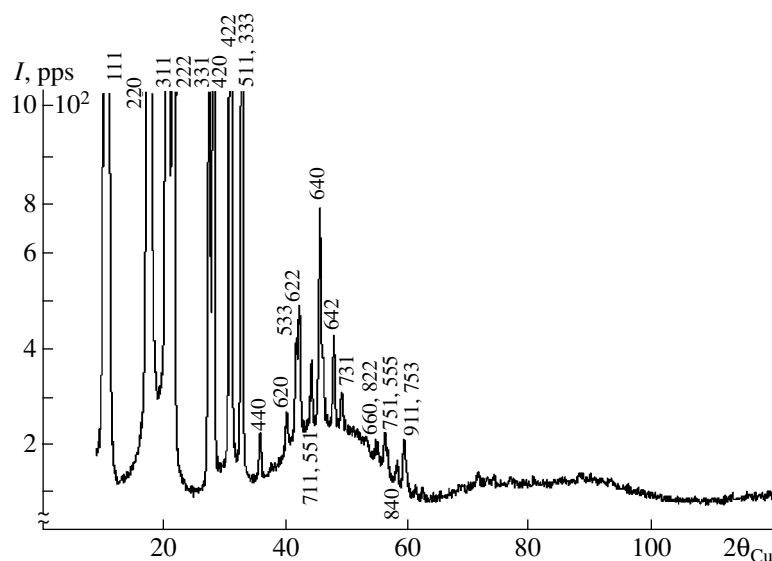


Fig. 1. X-ray diffraction patterns of the cubic fullerite C₆₀ obtained using copper radiation.

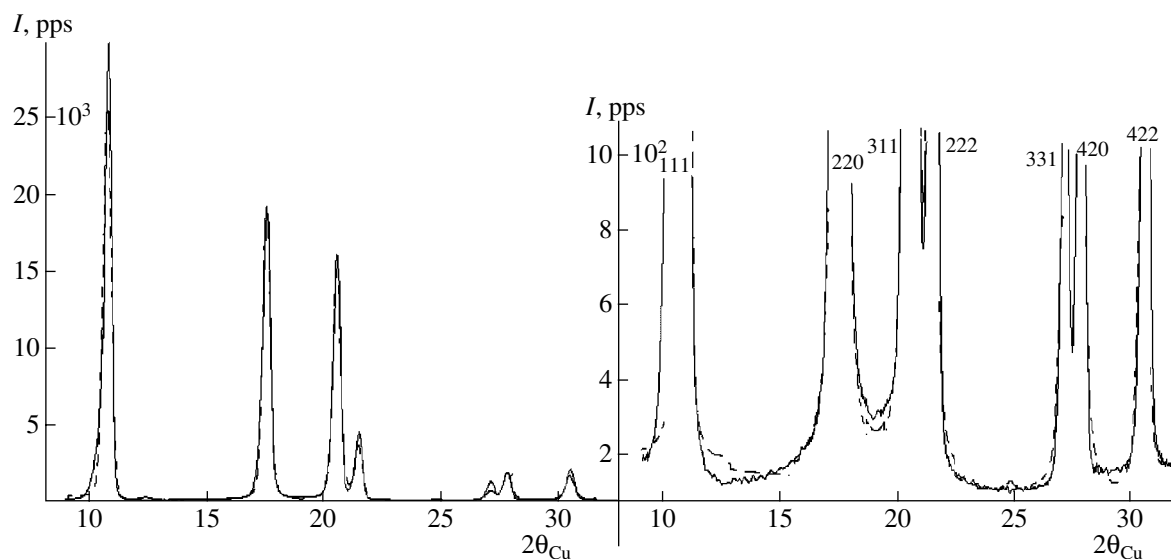


Fig. 2. Solid line is the experimental intensity distribution for fullerite C_{60} ; dashed line shows the result of the full-profile Rietveld analysis.

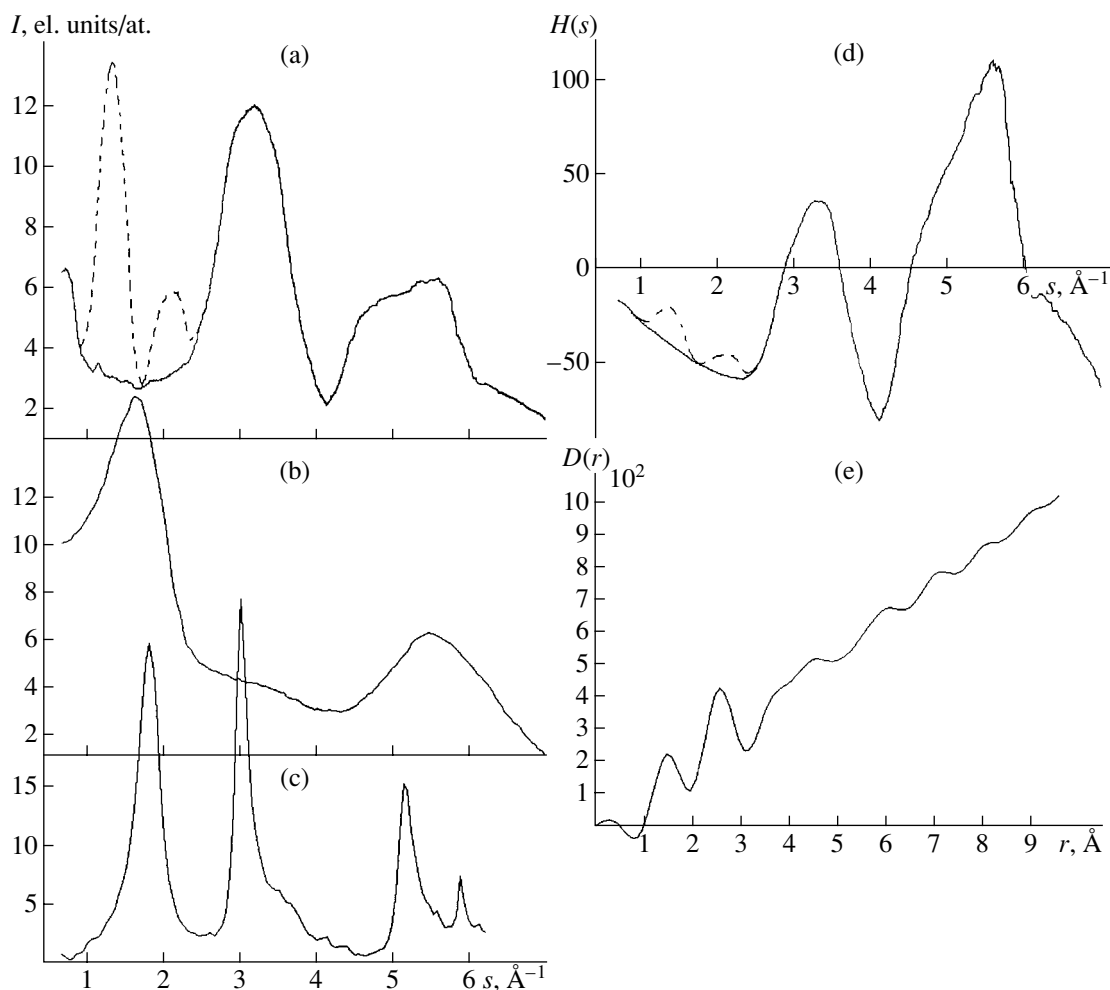


Fig. 3. Normalized diffuse-background intensity $I(s)$ on X-ray diffraction patterns of (a) fullerite, (b) amorphous carbon (carbon black), and (c) schungite. The intensities are calculated from (a): (d) is the s -weighted interference function $H(s)$; (e) is the distribution curve of the pair functions $D(r)$. Dashed lines indicate the maxima that disappeared after the Rietveld analysis.

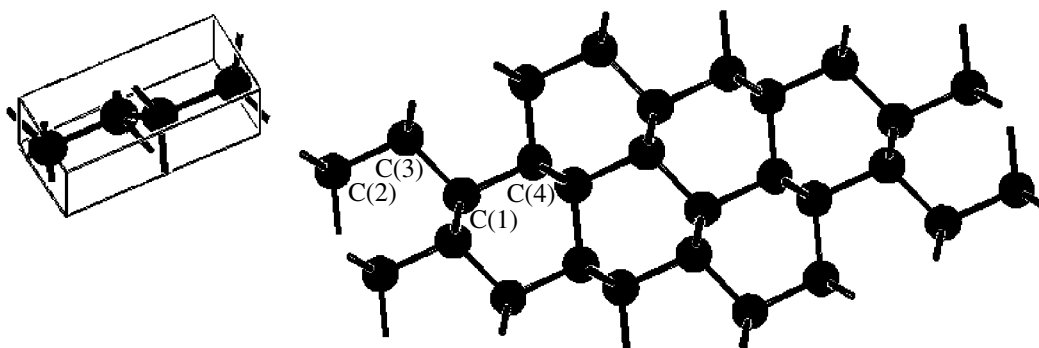


Fig. 4. Unit cell and bonding between tetrahedra in the lonsdaleite structure.

Using the normalized diffuse-scattering intensities of the X-ray diffraction pattern of fullerite C_{60} , we calculated the distribution curves for s , the weighted interference function $H(s)$ (Fig. 3d), and pair functions $D(r)$

(Fig. 3e), where $s = 4\pi \sin \theta / \lambda$ and λ is the incident-radiation wavelength. The method for calculation and analysis of the $D(r)$ curves was considered elsewhere [4, 5]. The spurious maxima on the $D(r)$ curve are rather low

Table 1. Calculated radii r_{ij} , spreading σ_{ij} of the coordination spheres, and coordination numbers N_{ij} for the amorphous component of fullerite C_{60} and the respective data for diamond and lonsdaleite

| Hexagonal graphite | | Diamond | | Lonsdaleite | | | | Amorphous component of fullerite C_{60} | | | Schungite [3] | | | | | | | | | | | | |
|----------------------|----------|----------------------|----------|----------------------|----------|----------------------|----------|---|---------------------------|---------------------|----------------------|---------------------------|-----------|-------------|------|------|-------|------|----------------|------|------|------|---------------|
| $r_{ij}, \text{\AA}$ | N_{ij} | $r_{ij}, \text{\AA}$ | N_{ij} | average | | | | experiment | | | * | | | | | | | | | | | | |
| | | | | $r_{ij}, \text{\AA}$ | N_{ij} | $r_{ij}, \text{\AA}$ | N_{ij} | $r_{ij}, \text{\AA}$ | $\sigma_{ij}, \text{\AA}$ | $N_{ij} \pm N_{ij}$ | $r_{ij}, \text{\AA}$ | $\sigma_{ij}, \text{\AA}$ | N_{obs} | N_{calcd} | | | | | | | | | |
| 1.42 | 3 | 1.54 | 4 | 1.544 | 3 | 1.54 | 4 | 1.53 | 0.23 | 4.0 ± 0.1 | 1.42 | 0.22 | 2.52 | 2.86 | | | | | | | | | |
| 2.46 | 6 | 2.52 | 12 | 1.545 | 1 | 2.52 | 13 | 2.49 | 0.39 | 12.7 ± 0.2 | 2.46 | 0.18 | 5.07 | 5.5 | | | | | | | | | |
| | | | | 2.520 | 6 | | | | | | | | | | | | | | | | | | |
| | | | | 2.522 | 6 | | | | | | | | | | | | | | | | | | |
| 2.84 | 3 | 2.95 | 12 | 2.575 | 1 | 2.96 | 9 | 2.92 | 0.37 | 8.2 ± 0.2 | 2.84 | 0.11 | 2.59 | 2.68 | | | | | | | | | |
| | | | | 2.955 | 3 | | | | | | | | | | | | | | | | | | |
| | | | | 2.956 | 6 | | | | | | | | | | | | | | | | | | |
| 3.35 | 1 | 3.56 | 6 | 3.565 | 6 | 3.58 | 12 | 3.56 | 0.28 | 11.9 ± 0.2 | 3.38 | 0.10 | 2.25 | 0.8 | | | | | | | | | |
| | | | | 3.603 | 6 | | | | | | | | | | | | | | | | | | |
| | | | | 3.64 | 9 | | | | | | | | | | 3.88 | 12 | 3.884 | 6 | 3.89 | 9 | 3.85 | 0.23 | 9.0 ± 0.2 |
| 3.75 | 6 | 3.888 | 3 | | | | | | | | | | | | | | | | | | | | |
| 4.15 | 6 | 4.120 | 2 | 4.12 | 2 | 4.12 | 0.00 | 2.1 ± 0.2 | 3.87 | 0.28 | 7.84 | 6.49 | | | | | | | | | | | |
| 4.25 | 6 | 4.36 | 24 | | | | | | | | | | 4.365 | 6 | 4.37 | 18 | 4.35 | 0.32 | 18.2 ± 0.2 | 4.26 | 0.14 | 5.24 | 4.82 |
| 4.39 | 9 | 4.62 | 16 | | | | | | | | | | 4.366 | 12 | | | | | | | | | |
| | | | | 4.630 | 6 | | | | | | | | | | | | | | | | | | |
| | | | | 4.633 | 3 | | | | | | | | | | | | | | | | | | |
| | | | | 4.830 | 12 | | | | | | | | | | | | | | | | | | |
| | | | | 4.858 | 3 | | | | | | | | | | | | | | | | | | |
| | | | | 4.91 | 6 | 5.04 | 12 | 5.040 | 6 | 5.16 | 30 | 5.20 | 0.43 | 30 ± 1 | 5.02 | 0.16 | 12.4 | 9.46 | | | | | |
| 5.03 | 18 | 5.068 | 6 | | | | | | | | | | | | | | | | | | | | |
| | | 5.271 | 6 | | | | | | | | | | | | | | | | | | | | |
| | | 5.271 | 6 | | | | | | | | | | | | | | | | | | | | |
| | | 5.274 | 6 | | | | | | | | | | | | | | | | | | | | |

Note: $\Delta\sigma_{ij} = \pm 0.01 \text{\AA}$, $\Delta r_{ij} = \pm 0.01 \text{\AA}$.

* N_{obs} indicates experimental data; N_{calcd} indicates the data calculation for a model.

Table 2. Interatomic distances r and the number N of atomic pairs located at the given distance in the configuration $1 \times 5 \times 5$ for lonsdaleite and diamond unit cell

| Lonsdaleite | | | | | | | | | |
|-----------------|-----|-----------------|-----|-----------------|-----|-----------------|-----|-----------------|-----|
| $r, \text{\AA}$ | N | $r, \text{\AA}$ | N | $r, \text{\AA}$ | N | $r, \text{\AA}$ | N | $r, \text{\AA}$ | N |
| 1.54 | 131 | 7.56 | 40 | 10.88 | 32 | 13.90 | 20 | 17.23 | 24 |
| 2.52 | 242 | 7.58 | 48 | 10.99 | 5 | 14.04 | 12 | 17.42 | 7 |
| 2.57 | 40 | 7.71 | 40 | 10.99 | 101 | 14.13 | 32 | 18.02 | 14 |
| 2.95 | 80 | 7.85 | 98 | 11.10 | 32 | 14.35 | 20 | 18.13 | 21 |
| 3.60 | 64 | 7.98 | 32 | 11.18 | 48 | 14.49 | 86 | 18.20 | 16 |
| 3.88 | 144 | 8.24 | 60 | 11.37 | 9 | 14.78 | 47 | 18.25 | 9 |
| 4.12 | 80 | 8.38 | 36 | 11.55 | 18 | 14.92 | 48 | 18.36 | 6 |
| 4.36 | 126 | 8.61 | 160 | 11.56 | 16 | 14.93 | 4 | 18.59 | 18 |
| 4.82 | 128 | 8.63 | 49 | 11.74 | 21 | 15.14 | 16 | 18.71 | 12 |
| 4.85 | 63 | 8.85 | 79 | 11.93 | 78 | 15.33 | 10 | 18.93 | 14 |
| 5.04 | 60 | 8.87 | 63 | 12.09 | 62 | 15.62 | 9 | 19.16 | 3 |
| 5.27 | 123 | 9.08 | 54 | 12.27 | 7 | 15.75 | 39 | 19.31 | 8 |
| 5.66 | 88 | 9.44 | 32 | 12.36 | 64 | 15.76 | 3 | 19.54 | 8 |
| 6.02 | 49 | 9.56 | 62 | 12.45 | 50 | 15.82 | 16 | 19.59 | 13 |
| 6.20 | 64 | 9.65 | 72 | 12.61 | 64 | 15.94 | 16 | 20.13 | 9 |
| 6.34 | 126 | 9.78 | 30 | 12.93 | 14 | 16.03 | 27 | 20.44 | 8 |
| 6.36 | 45 | 9.99 | 56 | 12.95 | 27 | 16.42 | 26 | 20.54 | 6 |
| 6.50 | 96 | 10.08 | 20 | 13.01 | 24 | 16.48 | 20 | 20.65 | 4 |
| 6.66 | 90 | 10.10 | 72 | 13.19 | 16 | 16.67 | 32 | 21.06 | 5 |
| 6.69 | 30 | 10.19 | 20 | 13.34 | 48 | 16.73 | 8 | 21.74 | 2 |
| 7.15 | 48 | 10.40 | 106 | 13.43 | 46 | 16.91 | 18 | 21.94 | 3 |
| 7.28 | 98 | 10.79 | 42 | 13.58 | 30 | 17.05 | 9 | 23.07 | 1 |
| 7.29 | 45 | 10.81 | 45 | 13.74 | 7 | 17.17 | 26 | | |
| Diamond | | | | | | | | | |
| 1.56 | 7 | 2.54 | 12 | 2.98 | 6 | 3.92 | 3 | | |

and correspond to the positions of the peaks appearing as a result of the termination effect of the experimental diffraction data at $s_{\max} = 7.05 \text{ \AA}^{-1}$. This indicates the absence of noticeable experimental errors that could have been formed when singling out the background scattering on the experimental diffraction pattern. The attained high accuracy was ensured by a small scanning step both in the regions of diffraction reflections and background scattering and also by high intensity of the background scattering: from 235 pps in the region of maxima up to 75 pps at the minimum. The curves of pair-function distribution calculated for both variants of the intensity distribution of the diffuse background on the X-ray diffraction pattern of fullerite C_{60} coincided within 2% accuracy.

The position of the first maximum on the $D(r)$ curve is 1.53 \AA , the first coordination number is 4, and the average electron density equals 1.05 \AA^{-3} . These values correspond to the analogous data for two other crystalline modifications of carbon: diamond and lonsdaleite

(often called hexagonal diamond) [6]. The shortest interatomic distance for fullerene equals 1.41 \AA ; the coordination number is 3. Table 1 lists the radii of the coordination spheres, coordination numbers, and spreading of the coordination spheres calculated from the experimental $D(r)$ curve in comparison with the analogous data for graphite, diamond, lonsdaleite, and schungite. Both electron density and coordination numbers for amorphous carbon are lower than for schungite. The radii of the coordination spheres and the coordination numbers calculated for the amorphous component of fullerite C_{60} correspond well to those calculated for lonsdaleite (Fig. 4). The coordination spheres show pronounced spreading; i.e., the configuration is considerably distorted. Almost zeroth spreading of the sphere with a radius of 4.12 \AA may be explained by the fact that only two atoms are located at this sphere. It should be noted that, in distinction from liquids, one cannot always expect for amorphous materials a regular increase in coordination-sphere spreading with an

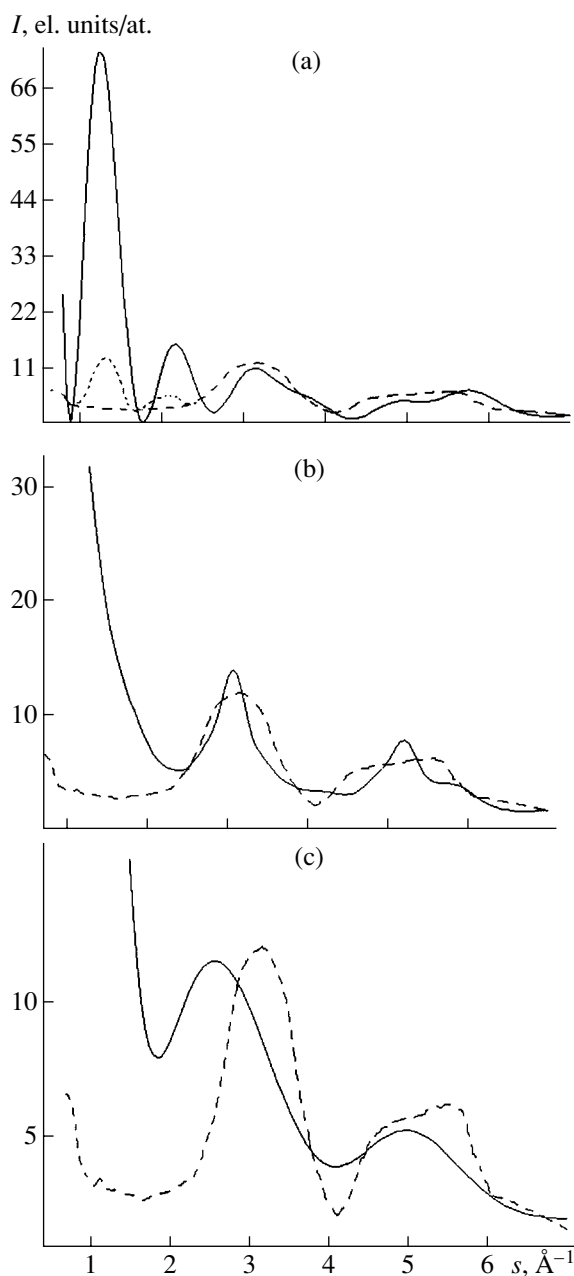


Fig. 5. Diffuse-scattering intensity distribution on the X-ray diffraction pattern of fullerite C_{60} (dashed line) and the data calculated by the Debye formula (solid curves).

increase of the radius. This is confirmed by numerous experimental data reviewed in [2] and by structure simulation by the methods of a disordered net for oxide systems and of curved nets for amorphous carbon materials [2, 3].

Figure 5 illustrates the calculation of diffraction patterns by the Debye formula (a) for one C_{60} molecule, (b) the atomic configuration corresponding to 25 unit cells of lonsdaleite with the dimensions $1 \times 5 \times 5$, and (c) the atomic configuration in one unit cell of diamond.

The number of atomic pairs and the distances between these pairs in a fullerite C_{60} molecule are consistent with the data in [1]. The corresponding data for lonsdaleite and diamond are listed in Table 2. It follows from Fig. 5 that the positions of the diffuse-background maxima on the experimental curve correspond to the data calculated for lonsdaleite. The attempts to fit the calculated intensity-distribution curves for fullerene fragments in the region of the first two maxima failed. Moreover, the next two maxima on the calculated curves for the fragments of fullerite C_{60} are shifted and have lower intensities.

Thus, the short-range order of the amorphous component of cubic fullerite C_{60} is of the same type as in lonsdaleite. This result is consistent with the known data. Thus, the analysis of the published experimental data [7] showed that the thermodynamic parameters of various mechanisms of diamond formation vary within wide ranges of pressure (from 10^{-7} to 10^6 bar) and temperature (from 20 to 4000°C). It is also indicated that products of synthesis are most often the intergrowth of diamond and non-diamond carbon. In [8], thin diamond films were synthesized by deposition during chemical reaction between H_2 and CH_4 proceeding under a pressure of 65–85 torr at temperatures of 700 – 800°C .

ACKNOWLEDGMENTS

This study was supported by the American Foundation for Civil Studies and Development for Independent States of former Soviet Union (USA), project no. PZ-013-02, and the Ministry of Education of the Russian Federation.

REFERENCES

1. Yu. M. Korolev, V. V. Kozlov, V. M. Polikarpov, and E. M. Antipov, *Dokl. Akad. Nauk* **374** (1), 74 (2000).
2. A. D. Fofanov, Doctoral Dissertation in Physics and Mathematics (Moscow State Univ., Moscow, 1998).
3. L. A. Aleshina, E. A. Nikitina, and A. D. Fofanov, in *Proceedings of I National Conference on Application of X-ray and Synchrotron Radiations, Neutrons, and Electrons to Study of Materials, RSNE-97* (Dubna, 1997), Vol. 2, p. 75.
4. L. A. Aleshina and A. D. Fofanov, *X-ray Diffraction Analysis of Amorphous Materials* (Petrozavod. Gos. Univ., Petrozavodsk, 1987) [in Russian].
5. L. A. Aleshina, V. P. Malinenko, A. D. Phouphanov, and N. M. Yakovleva, *J. Non-Cryst. Solids* **87**, 350 (1986).
6. T. G. Shumilova, *Diamond, Graphite, Fullerene, and Other Carbon Modifications* (Ural. Otd. Ross. Akad. Nauk, Yekaterinburg, 2002) [in Russian].
7. T. G. Shumilova, Doctoral Dissertation in Geology and Mineralogy (St. Petersburg, 2003).
8. C. J. Brooks, L. A. Powers, and R. E. Acosta, *J. Vac. Sci. Technol. B* **17** (6), 3144 (1999).

Translated by L. Man

STRUCTURE
OF INORGANIC COMPOUNDS

Diffractometric Study of Structural Transformations in $\text{Cu}_{1.70}\text{Cd}_{0.05}\text{S}$ Crystals

Yu. G. Asadov and R. B. Baikulov

*Institute of Physics, National Academy of Sciences of Azerbaijan,
pr. Dzhavida 33, Baku, 370143 Azerbaijan
e-mail: physic@physics.ab.az*

Received November 28, 2003; in final form, March 23, 2004

Abstract—The influence of the partial replacement of copper atoms by cadmium atoms on the real structure, phase formation, and temperatures of the structural transformations in $\text{Cu}_{1.75}\text{S}$ are studied by high-temperature X-ray diffractometry. It was shown that $\text{Cu}_{1.70}\text{Cd}_{0.05}\text{S}$ crystals at room temperature, unlike $\text{Cu}_{1.75}\text{S}$ and $\text{Cu}_{1.70}\text{In}_{0.05}\text{S}$ crystals, form not only orthorhombic anilite and monoclinic djurleite phases but also the respective metastable high-temperature fcc_1 and fcc_2 phases. © 2005 Pleiades Publishing, Inc.

It is shown [1] that a mineral of the composition $\text{Cu}_{1.75}\text{S}$ (anilite) is crystallized in the orthorhombic system with the lattice parameters $a = 7.89 \text{ \AA}$, $b = 7.84 \text{ \AA}$, and $c = 11.01 \text{ \AA}$, sp. gr. P_{nma} , $Z = 4$. It is established that the natural and synthetic anilite crystals have close compositions and are formed together with djurleite ($\text{Cu}_{1.96}\text{S}$), which crystallizes in the monoclinic system with the lattice parameters $a = 26.897 \text{ \AA}$, $b = 15.745 \text{ \AA}$, $c = 13.565 \text{ \AA}$, $\beta = 90.13^\circ$, sp. gr. $P2_1/n$, $Z = 8$ $\text{Cu}_{31}\text{S}_{16}$ [2]. Morimoto, Koto, and Shimazaki [1] failed to separate the $\text{Cu}_{1.75}\text{S}$ and $\text{Cu}_{1.96}\text{S}$ crystals.

A Bridgman-grown $\text{Cu}_{1.75}\text{S}$ compound was studied in [3] and it was shown that, at room temperature, this compound also contains crystals of anilite, its metastable fcc_1 phase with the lattice parameters $a = 5.542 \text{ \AA}$, sp. gr. $Fm\bar{3}m$, $Z = 4$, and djurleite. It was revealed that anilite and djurleite are transformed into the fcc_1 phase at the temperatures 308 ± 1 and $389 \pm 1 \text{ K}$, respectively. Figure 1 shows that the a parameter of the cubic phase undergoes no jump in the anilite transformation into the fcc_1 phase (in other words, in this case, the cubic phase plays the role of a ready nucleus), whereas in the djurleite $\longleftrightarrow \text{fcc}_1$ transformation, the parameter a undergoes some jumps. The reflection diffraction patterns from the (111), (222), and (333) planes of the fcc_1 phase also have the superimposed reflections from the (202), (404), and (606) planes of orthorhombic anilite and from the (333), (666), and (999) planes of monoclinic djurleite, which indicates that the lattices of these phases are crystallographically related. The transformations observed are reversible. However, it is unclear why djurleite does not undergo transformation into the respective fcc_2 phase.

To answer this question and establish the influence of the partial replacement of copper atoms in $\text{Cu}_{1.75}\text{S}$ by indium, iron, and cadmium atoms on the phase forma-

tion, stabilization of individual phases, and the mechanism of structural transformations, we studied the $\text{Cu}_{1.70}\text{In}_{0.05}\text{S}$, $\text{Cu}_{1.70}\text{Fe}_{0.05}\text{S}$, and $\text{Cu}_{1.70}\text{Cd}_{0.05}\text{S}$ compounds on a DRON-3M diffractometer ($\text{CuK}\alpha$ radiation, Ni filter) with a high-temperature URVT-2000 attachment in a 10^{-1}-Pa vacuum. The angular resolution was about 0.1° . We used the continuous scanning mode. The error in the angle determination did not exceed $\Delta\theta = \pm 0.02^\circ$. The growth method of these single crystals was described in [3].

$\text{Cu}_{1.70}\text{In}_{0.05}\text{S}$. The analysis of the diffraction patterns from a $\text{Cu}_{1.70}\text{In}_{0.05}\text{S}$ crystal recorded at room temperature in the angular range $10^\circ \leq 2\theta \leq 100^\circ$ showed that the crystal consists of the following phases: orthorhombic (anilite), monoclinic (djurleite), and metastable fcc_1 phases with the lattice parameter $a = 5.5593 \text{ \AA}$ [4]. It is established that at $362 \pm 1 \text{ K}$, anilite is transformed into its fcc_1 phase, whereas djurleite is also transformed into the fcc_1 anilite phase at $383 \pm 1 \text{ K}$.

Since the ionic radius of an In^{3+} ion (0.92) is very close to the ionic radii of mono- and divalent copper ions (0.98 for Cu^{1+} and 0.80 for Cu^{2+}), the partial replacement of copper by indium ions proceeds in such a way that the indium ions occupy the sites in the centers of the tetrahedra or triangles formed by sulfur atoms. In this case, in order to preserve the electrostatic balance in the crystal lattice, copper ions are replaced by indium ions, i.e., $\text{Cu}^{1+}\text{Cu}^{2+} \longleftarrow \text{In}^{3+}$ (heterovalent isomorphous substitution). An increase in the temperature of anilite and djurleite transformation into the fcc_1 phase in $\text{Cu}_{1.70}\text{In}_{0.05}\text{S}$ in comparison with this transformation in $\text{Cu}_{1.75}\text{S}$ seems to be explained by covalent bonding between indium and sulfur and a decrease in the number of vacancies in the lattice, where $\text{Cu}^{1+}\text{Cu}^{2+} \longleftarrow \text{In}^{3+}$ (i.e., each indium atom is related to two $\text{Cu}^{1+}\text{Cu}^{2+}$ vacancies). As is seen from Fig. 1, in this

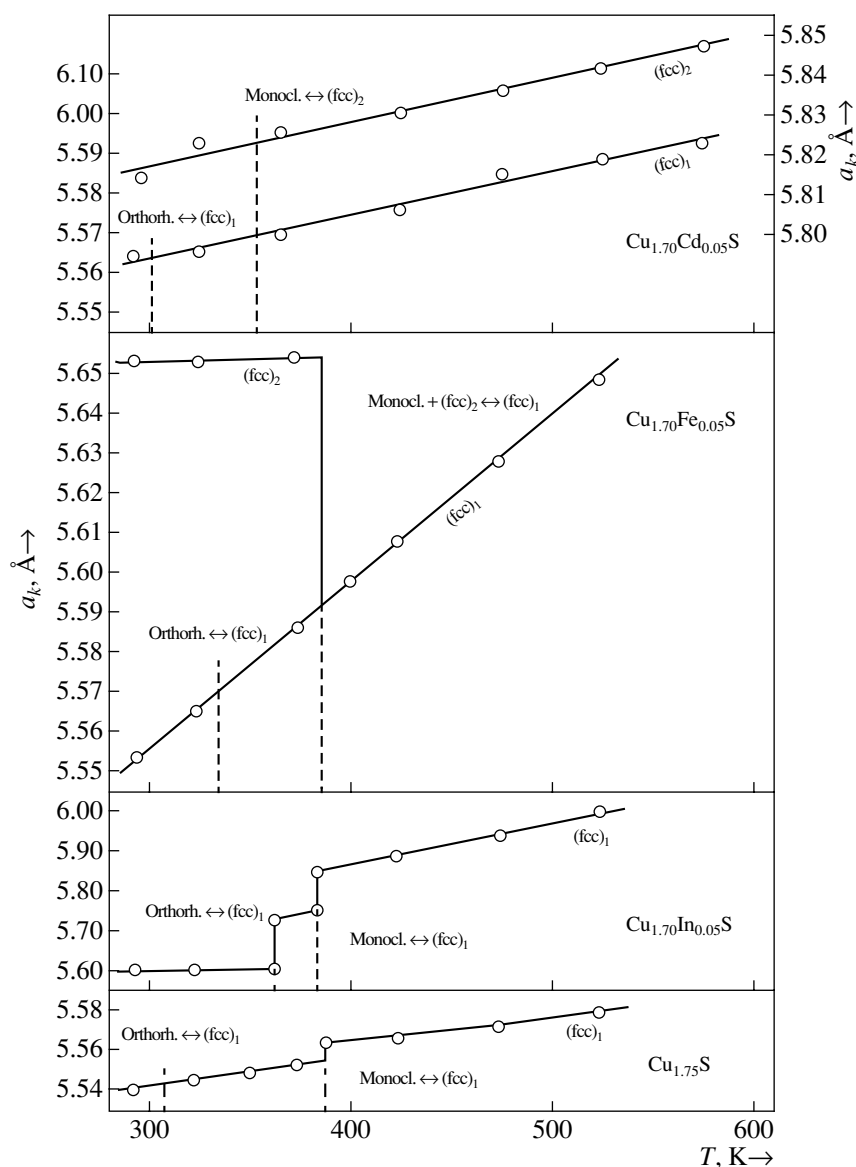


Fig. 1. Temperature dependences of the lattice parameter of the fcc_1 phase in the $\text{Cu}_{1.75}\text{S}$ and $\text{Cu}_{1.70}\text{In}_{0.05}\text{S}$ crystals, as well as of fcc_1 and fcc_2 phases in $\text{Cu}_{1.70}\text{Fe}_{0.05}\text{S}$ and $\text{Cu}_{1.70}\text{Cd}_{0.05}\text{S}$ crystals.

case, the lattice parameter of the fcc_1 phase has jumps in both transformations.

$\text{Cu}_{1.70}\text{Fe}_{0.05}\text{S}$. The analysis of the diffraction patterns from a $\text{Cu}_{1.70}\text{Fe}_{0.05}\text{S}$ crystal shows that, unlike $\text{Cu}_{1.75}\text{S}$ and $\text{Cu}_{1.70}\text{In}_{0.05}\text{S}$, the $\text{Cu}_{1.70}\text{Fe}_{0.05}\text{S}$ also includes the high-temperature metastable fcc_2 phase of djurleite. The fcc_1 and fcc_2 phases have different unit-cell parameters ($a_1 = 5.5473 \text{ \AA}$ and $a_2 = 5.6530 \text{ \AA}$, respectively) and, therefore, also different concentrations of metal atoms [4]. It is shown that at $343 \pm 1 \text{ K}$ anilite is transformed into its fcc_1 phase, whereas djurleite and its metastable fcc_2 phase are transformed into the fcc_1 phase at $385 \pm 1 \text{ K}$. In cooling of the $\text{Cu}_{1.70}\text{Fe}_{0.05}\text{S}$ phase, the diffraction patterns are restored in the opposite sequence. At several cycles of thermal

treatment, the number and the width of the diffraction reflections remain unchanged. The diffraction-maximum intensities (superimposed reflections of two phases) either increase or decrease after the transformation of one of these phases into the fcc phase.

The lattice framework of the fcc phases of $\text{Cu}_{1.70}\text{Fe}_{0.05}\text{S}$ consists of sulfur atoms with copper atoms being statistically distributed over the tetrahedral and triangular voids formed by two neighboring sulfur atoms lying one above the other. Since the ionic radii of Fe^{2+} and Cu^{2+} coincide ($\sim 0.8 \text{ \AA}$) with the ionic radius of divalent copper (80 for Cu^{2+}), the Fe^{2+} ions may isomorphously replace Cu^{2+} ions in sulfur triangles with the electrostatic balance in the crystal lattice being unchanged. However, as was shown by the nuclear

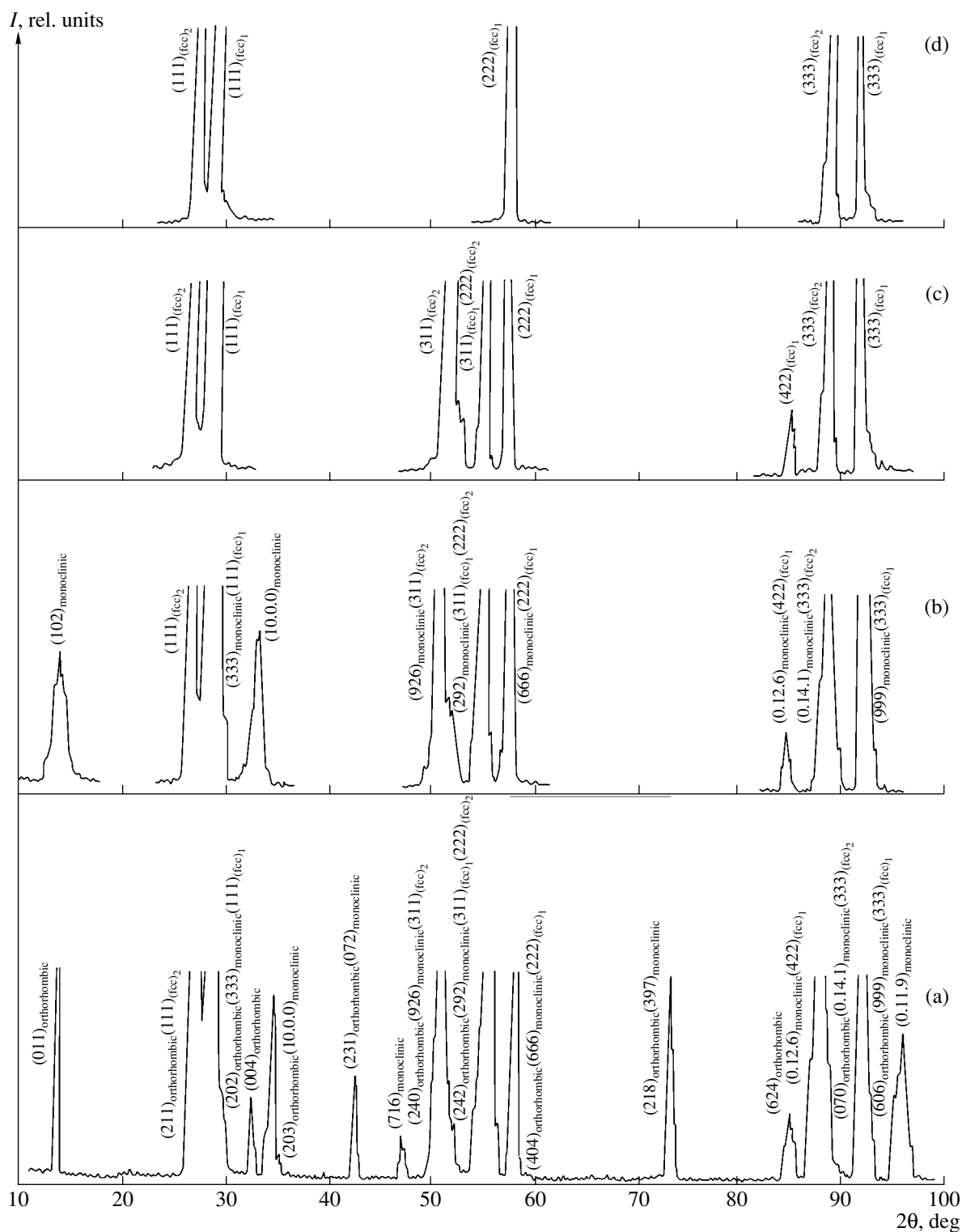


Fig. 2. Diffraction patterns from $\text{Cu}_{1.70}\text{Cd}_{0.05}\text{S}$ crystal at (a) 293, (b) 323, (c) 373, and (d) 773 K.

gamma-spectroscopy method, iron atoms enter the lattice in the trivalent state with the ionic radius 0.67 Å, i.e., less than the ionic radii of Cu^{1+} and Cu^{2+} . To preserve the electrostatic balance in this case, each Fe^{3+} ion

should bind two vacancies of copper atoms, i.e., $\text{Fe}^{3+} \rightarrow \text{Cu}^{1+}\text{Cu}^{2+}$, as in a $\text{Cu}_{1.70}\text{In}_{0.05}\text{S}$ crystal. This results in considerable reduction of the number of vacancies in the lattice.

Calculated diffraction patterns from $\text{Cu}_{1.70}\text{Cd}_{0.05}\text{S}$ crystal

| T_{exp} , K | θ | I/I_0 | d_{exp} , Å | Orthorhombic | | Monoclinic | | fcc ₁ | | fcc ₂ | | Lattice parameter, Å |
|-------------------------|----------|---------|-------------------------|---------------------------|----------|---------------------------|------------|---------------------------|----------|---------------------------|-----------------------|-------------------------|
| | | | | d_{calcd} , Å | hkl | d_{calcd} , Å | hkl | d_{calcd} , Å | hkl | d_{calcd} , Å | hkl | |
| 293 | 6°56' | 50 | 6.3869 | 6.3869 | 011 | | | | | | | Orthorhombic |
| | 13°17' | 90 | 3.3561 | 3.3563 | 211 | | | | | 3.3561 | 111 | $a = 7.9008$ |
| | 13°54' | 100 | 3.2094 | 3.2066 | 202 | 3.1982 | 333 | 3.2090 | 111 | | | $b = 7.8512$ |
| | 16°15' | 12 | 2.7551 | 2.7525 | 004 | | | | | | | $c = 11.0100$ |
| | 16°40' | 40 | 2.6879 | 2.6870 | 203 | 2.6897 | 1000 | | | | | |
| | 21°08' | 30 | 2.1384 | 2.1372 | 231 | 2.1349 | 072 | | | | | Monoclinic |
| | 23°31' | 10 | 1.9320 | | | 1.9319 | 716, 107 | | | | | $a = 26.897$ |
| | 26°04' | 70 | 1.7544 | 1.7553 | 240 | 1.7557 | 926 | | | 1.7524 | 311 | $b = 15.745$ |
| | 27°19' | 80 | 1.6798 | 1.6723 | 242 | 1.6763 | 475, 292 | 1.6751 | 311 | 1.6780 | 222 | $c = 13.565$ |
| | 28°38' | 80 | 1.6083 | 1.6033 | 404 | 1.5991 | 666 | 1.6045 | 222 | | | $\beta = 90.13^\circ$ |
| | 36°54' | 50 | 1.2839 | 1.2820 | 218 | 1.2849 | 397, 088 | | | | | fcc ₁ |
| | 42°43' | 40 | 1.1363 | 1.1357 | 624 | 1.1348 | 0126, 4108 | 1.1368 | 422 | | | $a_1 = 5.5654$ |
| | 43°25' | 70 | 1.1216 | 1.1210 | 454, 070 | 1.1208 | 0141, 2140 | | | 1.1187 | 333 | |
| | 46°06' | 100 | 1.0698 | 1.0689 | 606 | 1.0695 | 999 | 1.0696 | 333, 511 | | | fcc ₂ |
| 47°58' | 40 | 1.0378 | | | 1.0379 | 0119 | | | | | $a_2 = 5.8128$ | |
| 323 | 6°44' | 50 | 6.5720 | | | 6.5731 | 102 | | | | | Monoclinic |
| | 13°16' | 80 | 3.3605 | | | | | | 1.3619 | 111 | $a = 26.9080$ | |
| | 13°53' | 100 | 3.2134 | | | 3.2075 | 333 | 3.2151 | 111 | | $b = 15.7720$ | |
| | 16°39' | 12 | 2.6908 | | | 2.6909 | 1000 | | | | $c = 13.6083$ | |
| | 26°03' | 60 | 1.7552 | | | 1.7639 | 926 | | 1.7558 | 311 | $\beta = 90.13^\circ$ | |
| | 27°18' | 80 | 1.6810 | | | 1.6805 | 475, 292 | 1.6791 | 311 | 1.6810 | 222 | |
| | 28°37' | 80 | 1.6093 | | | 1.6038 | 666 | 1.6076 | 222 | | | |
| | 42°42' | 40 | 1.1409 | | | 1.1372 | 0126, 4108 | 1.1367 | 422 | | | $a_1 = 5.5689$ |
| | 43°24' | 70 | 1.1220 | | | 1.1227 | 0141, 2140 | | | 1.1207 | 333 | fcc ₂ |
| 46°05' | 100 | 1.0701 | | | 1.0691 | 999 | 1.0717 | 333 | | | $a_2 = 5.8232$ | |
| 373 | 13°15' | 60 | 3.3634 | | | | | | 3.3637 | 111 | | |
| | 13°52' | 100 | 3.2174 | | | | | 3.2158 | 111 | | | |
| | 26°02' | 50 | 1.7564 | | | | | | 1.7567 | 311 | fcc ₁ | |
| | 27°18' | 70 | 1.6809 | | | | | 1.6795 | 311 | 1.6819 | 222 | $a_1 = 5.5701$ |
| | 28°37' | 80 | 1.6104 | | | | | 1.6080 | 222 | | | fcc ₂ |
| | 42°42' | 40 | 1.1366 | | | | | 1.1370 | 422 | | | $a_2 = 5.8262$ |
| | 43°24' | 60 | 1.1222 | | | | | | 1.1212 | 333 | | |
| | 46°04' | 100 | 1.0703 | | | | | 1.0714 | 333 | | | |
| 773 | 13°08' | 60 | 3.3916 | | | | | | 3.3886 | 111 | fcc ₁ | |
| | 13°46' | 100 | 3.2404 | | | | | 3.2376 | 111 | | $a_1 = 5.6078$ | |
| | 28°26' | 80 | 1.6192 | | | | | 1.6188 | 222 | | | |
| | 43°05' | 60 | 1.1285 | | | | | | 1.1296 | 333 | fcc ₂ | |
| | 45°39' | 90 | 1.0780 | | | | | 1.0792 | 333 | | | $a_2 = 5.8694$ |

Note: CuK_α radiation ($\lambda_\alpha = 1.5418 \text{ \AA}$), Ni filter, mode: 35 kV, 10 mA.

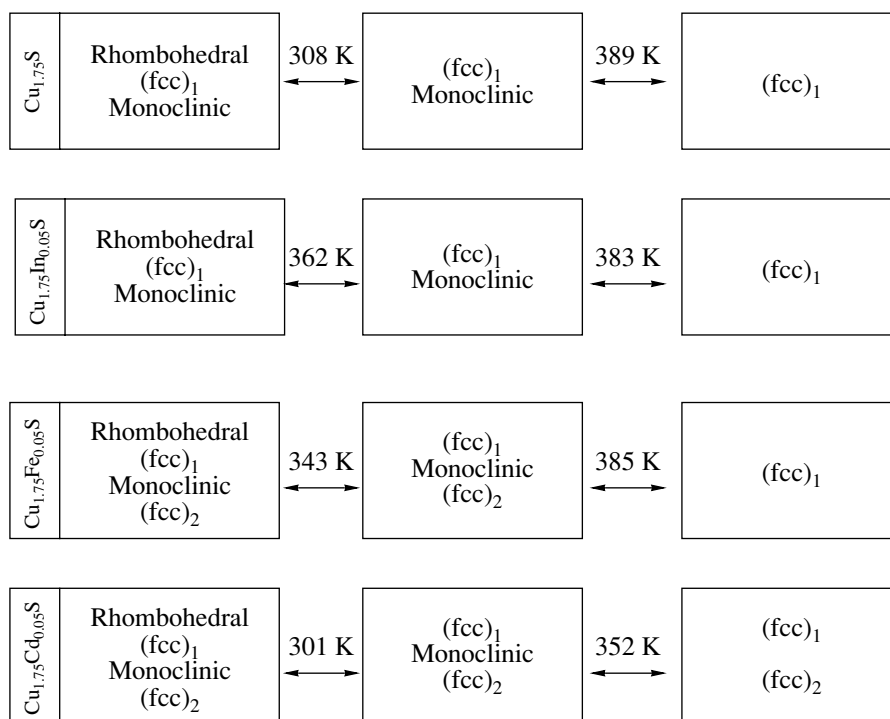


Fig. 3. Scheme of structural transformation in Cu_{1.75}S and Cu_{1.70}A_{0.05}S crystals (A = In, Fe, Cd).

Cu_{1.70}Cd_{0.05}S. The diffraction patterns of a Cu_{1.70}Cd_{0.05}S crystal have 15 diffraction reflections in the angular range $10^\circ \leq 2\theta \leq 100^\circ$ at room temperature (Table 1, Fig. 2a). This also confirms that the crystal contains anilite, djurleite, and their metastable fcc₁ and fcc₂ phases. After recording diffraction reflections from a Cu_{1.70}Cd_{0.05}S crystal at room temperature, we switched on a heater and recorded diffraction patterns after each increase of the temperature by 30 K. At 323 K, we recorded 10 diffraction reflections in the same angular range. As is seen from the table and Fig. 2b, the reflections from the (011) and (004) planes due to the anilite phase disappeared. It was established that the anilite phase is transformed at 301 ± 0.5 K into its fcc₁ phase. At 373 K, from 10 reflections in the same angular range, two reflections from the (102) and (1000) planes of the djurleite phase disappeared. The remaining eight reflections (table, Fig. 2c) belong either to the fcc₁ phase (111, 311, 222, 422, and 333 reflections) or to the fcc₂ phase (111, 311, and 333 reflections). At 352 ± 0.5 K, the monoclinic phase of djurleite is transformed into its fcc₂ phase. The subsequent crystal cooling resulted in the complete restoration of the diffraction pattern. The transformations are reversible and are of the single crystal single crystal type. After prolong heating, both fcc₁ and fcc₂ phases are preserved as individual phases. An increase in the annealing temperature to 773 K results in disappearance of the 311 and 422 reflections and 311 and 222

reflections from the diffraction patterns of the fcc₁ phase and fcc₂ phase, respectively.

As is seen from Fig. 1, in the phase transformations of anilite and djurleite, the temperature dependence of the lattice parameters of the fcc₁ and fcc₂ phases remains linear. Each cubic phase continues to grow

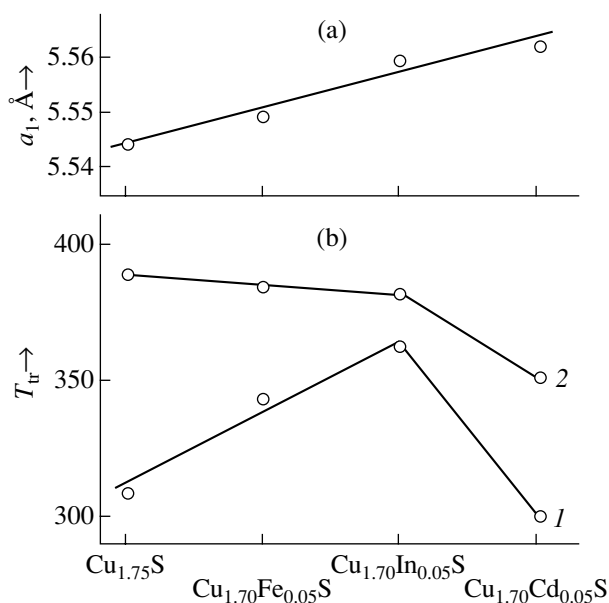


Fig. 4. Composition dependence of (a) the lattice parameter of the fcc₁ phases and (b) phase-transition temperatures in (1) anilite and (2) djurleite.

only at the expense of its low-temperature modifications.

Thus, the results obtained show that the structural transformations in the samples studied occur at significantly low temperatures in comparison with their growth temperatures. First, the crystals of the high-temperature fcc phase start to grow, which allows one to vary the number of cations in the unit cell. Cooling of the crystals to room temperature gives rise to the first cycle of phase transformations reducing to the formation of two low-symmetry modifications in $\text{Cu}_{1.75}\text{S}$, $\text{Cu}_{1.70}\text{In}_{0.05}\text{S}$, and $\text{Cu}_{1.70}\text{Fe}_{0.05}\text{S}$. As is seen from Fig. 3, the schemes of phase transformations in $\text{Cu}_{1.75}\text{S}$ and $\text{Cu}_{1.70}\text{In}_{0.05}\text{S}$ are the same: cooling of the high-temperature fcc₁ phase of anilite first leads to the formation of the monoclinic djurleite and then to orthorhombic anilite, so that, at room temperature, the $\text{Cu}_{1.75}\text{S}$ and $\text{Cu}_{1.70}\text{In}_{0.05}\text{S}$ crystals consist of three phases. The $\text{Cu}_{1.70}\text{Fe}_{0.05}\text{S}$ and $\text{Cu}_{1.70}\text{Cd}_{0.05}\text{S}$ crystals at room temperature consist of four phases because anilite and djurleite also possess the metastable fcc₁ and fcc₂ phases. At 385 K, a $\text{Cu}_{1.70}\text{Fe}_{0.05}\text{S}$ crystal consisting of the mixture of djurleite and fcc₂ phase is transformed into the fcc₁ phase. The anilite phase in $\text{Cu}_{1.70}\text{Cd}_{0.05}\text{S}$ is transformed, at 301 K, into its fcc₁ phase and, at 352 K, the djurleite phase is transformed into its fcc₂ phase.

As is seen from Fig. 4a, at 293 K, the unit-cell parameters of the metastable fcc₁ phases of anilite grow linearly despite the almost equal radii of cations. This seems to be associated with the change of chemical cation–cation and cation–anion bonds, which affects the temperatures of the structure transformations in anilite (Fig. 4b, curve 1) in the compounds $\text{Cu}_{1.75}\text{S}$, $\text{Cu}_{1.70}\text{Fe}_{0.05}\text{S}$, and $\text{Cu}_{1.70}\text{In}_{0.05}\text{S}$. In djurleite (Fig. 4b, curve 2), the picture is opposite. Anilite in $\text{Cu}_{1.70}\text{Cd}_{0.05}\text{S}$ is transformed into its fcc₁ phase, and djurleite is transformed into its fcc₂ phase, which results in a considerable decrease in the phase-transformation temperature.

REFERENCES

1. N. Morimoto, K. Koto, and Y. Shimazaki, *Am. Mineral.* **54**, 1256 (1969).
2. H. T. Evans, *Z. Kristallogr.* **150**, 299 (1979).
3. Yu. G. Asadov, K. M. Jafarov, and G. B. Gasyimov, *Phase Transit.* **7**, 281 (1986).
4. D. I. Ismailov, Yu. G. Asadov, and G. B. Gasyimov, *Cryst. Res. Technol.* **22** (12), 1459 (1987).

Translated by L. Man

STRUCTURE
OF ORGANIC COMPOUNDS

Disaccharide Nucleosides: The Crystal and Molecular Structure of 2'-O-β-D-Ribopyranosylcytidine

G. V. Gurskaya*, N. E. Zhukhlistova**, Yu. V. Nekrasov**, G. V. Bobkov*,
E. V. Efimtseva*, and S. N. Mikhailov*

* Engelhardt Institute of Molecular Biology, Russian Academy of Sciences,
ul. Vavilova 32, Moscow, 119991 Russia

e-mail: gurskaya@genome.eimb.relarn.ru; smikh@eimb.ru

** Shubnikov Institute of Crystallography, Russian Academy of Sciences,
Leninskii pr. 59, Moscow, 119333 Russia

Received May 25, 2004

Abstract—The crystal structure of a disaccharide nucleoside, 2'-O-β-D-ribofuranosylcytidine, is studied using X-ray diffraction (space group $P2_1$, $a = 6.827(2)$ Å, $b = 12.813(3)$ Å, $c = 9.532(2)$ Å, $\beta = 92.934(5)^\circ$, $V = 832.7(4)$ Å³, $Z = 2$). The stereochemical features of the molecular structure of 2'-O-β-D-ribofuranosylcytidine are analyzed, and the structural data are compared with those obtained for the previously studied disaccharide nucleoside 2'-O-β-D-ribofuranosyluridine. © 2005 Pleiades Publishing, Inc.

INTRODUCTION

Disaccharide nucleosides form an important group of natural compounds in which, unlike conventional nucleosides, a disaccharide rather than a monosaccharide is bound to the heterocyclic base. To date, more than a hundred disaccharide nucleosides and their derivatives have been isolated from various sources [1–3]. These compounds exhibit a wide spectrum of biological activities and possess antibacterial, fungicidal, herbicidal, insecticidal, antitumorigenic, and antiviral properties. Disaccharide nucleosides are not only low-molecular compounds but also structural units of biopolymers, such as poly(ADP-ribose) and tRNA [3, 4].

Recently [5–7], a convenient general method was developed for preparing 2'-O-β-D-ribofuranosyl nucleosides. This method involves the condensation of a tin tetrachloride-activated 1-O-acetyl-2,3,5-tri-O-benzoyl-β-D-ribofuranose with partially protected ribonucleosides. The proposed approach was also used to prepare 2'-O-α-D-arabinofuranosyl nucleosides, 2'-O-β-D-erythrofuransyl nucleosides, 2'-O-β-D-ribofuranosyl nucleosides, and other disaccharide compounds [7, 8]. Based on these compounds, we synthesized oligonucleotides and studied the parameters of their complex formation with complementary DNA and RNA. It was shown that oligonucleotides containing disaccharide nucleosides form stable complexes with RNA ($\Delta T_m = 0^\circ\text{C}$), whereas the melting temperatures of the complexes with DNA are somewhat lower than those of the natural compounds [8].

The effect of a 2'-O-β-D-ribofuranosyladenosine residue on the stability of the duplex formation was studied by high-resolution NMR spectroscopy and

molecular dynamics methods using a fragment of the double-chain RNA as an example [9]. It was shown that an additional bulky ribofuranose residue is located in a minor groove of an RNA double helix and has an insignificant effect on the RNA structure in a solution ($\Delta T_m = 0^\circ\text{C}$). The results obtained agree well with the X-ray diffraction data on the position of the minor nucleoside 2'-O-β-D-ribofuranosyladenosine in tRNA^{Met}₁ [10].

Continuing our investigations into the physicochemical properties of disaccharide nucleosides [6], we performed an X-ray diffraction analysis of 2'-O-β-D-ribofuranosylcytidine and compared the stereochemical features of its molecular structure with those of the 2'-O-β-D-ribofuranosyluridine studied earlier in [6].

EXPERIMENTAL

2'-O-β-D-Ribopyranosylcytidine was synthesized according to the following procedure. A solution of *N*₄-benzoyl-1-[2-O-(2,3,5-tri-O-acetyl-β-D-ribofuranosyl)-β-D-ribofuranosyl]cytosine (0.350 g, 0.58 mmol) [8] in 5 M ammonium solution (5 ml) in methanol was allowed to stand for 24 h at 20°C and was then evaporated under vacuum to dryness. The residue was dissolved in water (20 ml) and washed with methylene chloride (2 × 10 ml). The aqueous layer was evaporated under vacuum. The residue was treated with acetone and allowed to stand for 3 days at 0°C. The precipitate was filtered off, washed with acetone and ether, and dried. The yield was 180 mg (83%). UV, λ_{max} , nm (ϵ , M⁻¹ cm⁻¹): 280 (12 200) (pH 1), 270 (8400) (pH 7–13). ¹H NMR at 298 K in D₂O (400 MHz; *J*, Hz): 7.66 d

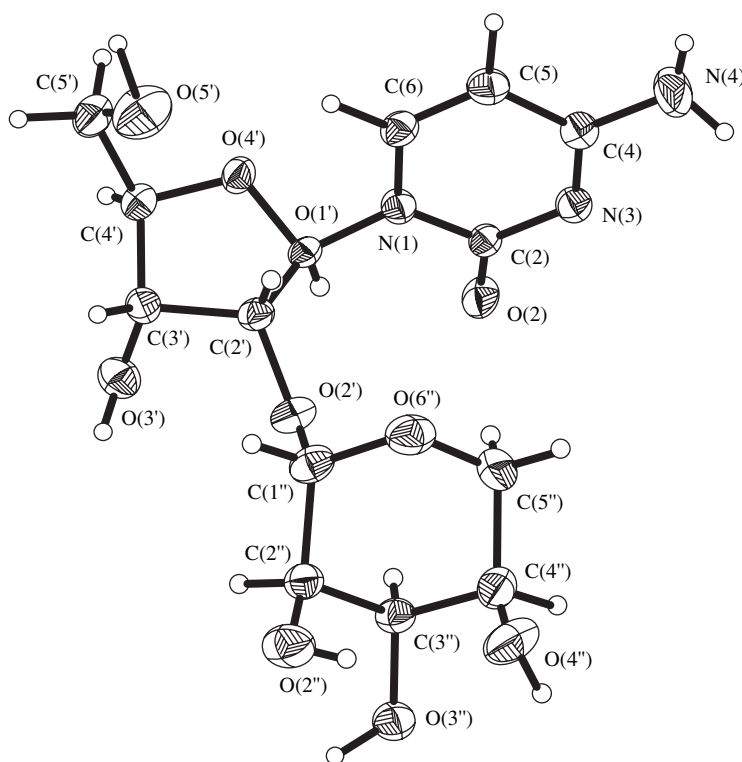


Fig. 1. Molecular structure of 2'-O- β -D-ribofuranosylcytidine.

(1H, $J_{6,5} = 7.6$, H6), 5.93 d (1H, H5), 5.92 d (1H, $J_{1',2'} = 5.6$, H1'), 4.76 d (1H, $J_{1'',2''} = 4.6$, H1''), 4.31 dd (1H, $J_{2',3'} = 5.4$, H2'), 4.22 dd (1H, $J_{3',4'} = 4.5$, H3'), 3.99 ddd (1H, $J_{4',5'a} = 3.1$, $J_{4',5'b} = 4.4$, H4'), 3.87 dd (1H, $J_{3'',2''} = 3.3$, $J_{3'',4''} = 3.1$, H3''), 3.72 dd (1H, $J_{5'a,5'b} = -12.8$, H5'a), 3.72 dddd (1H, $J_{4'',5'a} = 3.2$, $J_{4'',5'b} = 5.9$, $J_{4'',2''} = 1.0$, H4''), 3.66 dd (1H, H5'b), 3.61 ddd (1H, H2''), 3.52 dd (1H, $J_{5'a,5'b} = -12.0$, H5'a), 3.44 dd (1H, H5'b).

Colorless single crystals of 2'-O- β -D-ribofuranosylcytidine were grown at room temperature through slow evaporation of the solvent from a saturated water-alcohol solution of the compound. The crystals belong to the space group $P2_1$, and the unit cell parameters are as follows: $a = 6.827(2)$ Å, $b = 12.813(3)$ Å, $c = 9.532(2)$ Å, $\beta = 92.934(5)^\circ$, $V = 832.7(4)$ Å³, $Z = 2$, $\rho_{\text{calcd}} = 1.497$ g/cm³, and $M = 375.34$. The intensities of reflections were measured on a SYNTEX $P2_1$ four-circle diffractometer (CuK α radiation, graphite monochromator, $\theta/2\theta$ scan mode, $\theta_{\text{min}} = 4.64^\circ$, $\theta_{\text{max}} = 63.62^\circ$). The correction for absorption was introduced by a semiempirical method in accordance with the absorption curve. A total of 1548 unique reflections were collected, of which 1542 reflections with $I > 2\sigma(I)$ were used for the solution and refinement of the structure.

The structure was solved by direct methods and refined in the anisotropic approximation for the non-hydrogen atoms. All the hydrogen atoms were located from difference electron-density maps and refined iso-

tropically. All the calculations were performed with the SHELX97 program package [11]. The final value of the discrepancy factor R is equal to 3.91% for 1542 reflections with $I > 2\sigma(I)$.

RESULTS AND DISCUSSION

The molecular structure of 2'-O- β -D-ribofuranosylcytidine with the atomic numbering is shown in Fig. 1. The N, O, and C atoms are drawn as ellipsoids of thermal vibrations at the 50% probability level, and the hydrogen atoms are depicted as spheres of arbitrary radius.

The bond lengths and angles in the nucleoside fragment of the molecule are close to those in the previously studied structures of the cytidines modified in the carbohydrate fragment [12–14]. Therefore, we will dwell primarily on the conformational properties of 2'-O- β -D-ribofuranosylcytidine molecules.

Similar to molecules of many other cytidines modified in a carbohydrate group, the 2'-O- β -D-ribofuranosylcytidine molecule is characterized by an *anti* conformation about the N-glycoside bond; in this case, the $\chi[\text{O}(4')\text{—C}(1')\text{—N}(1)\text{—C}(2)]$ torsion angle is equal to $-132.3(2)^\circ$. The torsion angles about the C(4')—C(5') exocyclic bond of the nucleoside are $\gamma[\text{O}(5')\text{—C}(5')\text{—C}(4')\text{—C}(3')] = 50.6^\circ$ and $\phi[\text{O}(5')\text{—C}(5')\text{—C}(4')\text{—O}(4')] = -68.7(3)^\circ$, which corresponds to a *gauche*⁺ conformation of the sugar. The furanose ring in the 2'-O- β -D-

Table 1. Bond lengths (d , Å) and angles (ω , deg) in the pyranose fragment of the 2'-*O*- β -*D*-ribofuranosylcytidine molecule

| Bond | d | Bond | d | Angle | ω | Angle | ω |
|---------------|----------|---------------|----------|--------------------|----------|--------------------|----------|
| C(1'')–C(2'') | 1.530(4) | O(6'')–C(1'') | 1.400(3) | C(1'')C(2'')C(3'') | 110.3(2) | C(1'')C(2'')O(2'') | 109.9(2) |
| C(2'')–C(3'') | 1.523(3) | C(2'')–O(2'') | 1.428(3) | C(2'')C(3'')C(4'') | 110.5(2) | C(3'')C(2'')O(2'') | 112.0(2) |
| C(3'')–C(4'') | 1.523(3) | C(3'')–O(3'') | 1.413(3) | C(3'')C(4'')C(5'') | 107.5(2) | C(2'')C(3'')O(3'') | 112.2(2) |
| C(4'')–C(5'') | 1.520(4) | C(4'')–O(4'') | 1.428(4) | C(4'')C(5'')O(6'') | 110.9(2) | C(4'')C(3'')O(3'') | 109.8(2) |
| C(5'')–O(6'') | 1.442(4) | | | C(5'')O(6'')C(1'') | 114.4(2) | C(3'')C(4'')O(4'') | 111.3(2) |
| | | | | O(6'')C(1'')C(2'') | 113.6(2) | C(5'')C(4'')O(4'') | 108.8(2) |

Table 2. Geometric parameters of hydrogen bonds in the structure of 2'-*O*- β -*D*-ribofuranosylcytidine

| $D-H$ | $d(D-H)$ | $d(H\cdots A)$ | $\angle DHA$ | $d(D\cdots A)$ | A | Symmetry |
|----------------|----------|----------------|--------------|----------------|--------|-------------------------------|
| O(2'')–H(O2'') | 0.77(4) | 2.04(4) | 151(4) | 2.745(4) | O(4'') | [x, y, z] |
| N(4)–H(41) | 0.82(3) | 2.28(3) | 158(2) | 3.051(4) | O(4'') | [$-x + 1, y - 1/2, -z + 2$] |
| N(4)–H(41) | 0.82(3) | 2.50(3) | 107(2) | 2.845(3) | O(6'') | [$-x + 1, y - 1/2, -z + 2$] |
| N(4)–H(42) | 0.85(6) | 2.06(6) | 165(5) | 2.895(4) | O(3'') | [$-x, y - 1/2, -z + 2$] |
| O(3'')–H(O3'') | 0.85(6) | 2.14(6) | 174(5) | 2.982(3) | O(2) | [$-x, y + 1/2, -z + 1$] |
| O(5'')–H(O5'') | 0.92(5) | 2.17(5) | 153(5) | 3.014(3) | O(3'') | [$x + 1, y, z$] |
| O(3'')–H(O3'') | 0.90(5) | 1.89(5) | 174(4) | 2.787(3) | O(4'') | [$-x, y + 1/2, -z + 1$] |
| O(4'')–H(O4'') | 0.73(5) | 2.07(5) | 177(5) | 2.793(3) | N(3) | [$-x, y + 1/2, -z + 2$] |

Note: D is the donor, A is the acceptor, d is the distance (Å), and \angle is the angle (deg).

ribofuranosylcytidine molecule has an *envelope* (2E) conformation. The C(1''), C(3''), C(4''), and O(4'') atoms lie in the same root-mean-square plane, and the C(2'') atom deviates from this plane by 0.524(4) Å in the direction of the base. The phase angle of pseudorotation P is 157.9°, and the maximum amplitude of pseudorotation (the degree of twisting) Ψ_m is 34.5°.

The six-membered pyranose ring has a distorted chair conformation (1C_4). The C(2''), C(3''), C(5''), and O(6'') atoms lie in the same plane; the C(1'') atom deviates from this plane by 0.574(3) Å in the direction of the base; and the C(4'') atom deviates from the plane by 0.720(4) Å in the opposite direction. The O(2'')–H and O(4'') atoms of the pyranose fragment are linked by the intramolecular hydrogen bond: the O(2'')–H \cdots O(4'') distance is equal to 2.745(4) Å, and the O(2'')–H \cdots O(4'') angle is 151(4)°. The bond lengths and angles in the pyranose ring are given in Table 1. The C–O bonds in the hydroxyl groups [C(2'')–O(2'')H, 1.428(4) Å and C(4'')–O(4'')H, 1.428(4) Å], whose oxygen atoms are involved in the intramolecular hydrogen bond, are slightly longer than the C(3'')–O(3'')H bond [1.413(3) Å], whose O(3'') atom participates only in the intermolecular hydrogen bonds (Table 2).

In the nucleoside fragment of the disaccharide nucleoside 2'-*O*- β -*D*-ribofuranosyluridine (Fig. 2), which was studied earlier in [6], the molecule is characterized by an *anti* conformation about the *N*-glycoside bond, a *gauche-anti* conformation about the C(4'')–C(5'') exocyclic bond, and an 4E conformation of the

furanose ring ($P = 54.6^\circ$, $\Psi_m = 36.6^\circ$). The additionally attached 2'-*O*-ribofuranose fragment has a C(2'')-*exo*-C(3'')-*endo* (2T_3) conformation of the sugar ring ($P = 344.4^\circ$, $\Psi_m = 38.3^\circ$; the deviations of the C(2'') and C(3'') atoms are 0.543 and 0.051 Å, respectively) and a *gauche-trans* conformation about the C(4'')–C(5'') bond.

Comparison of the chemical shifts and spin-spin coupling constants in the 1H NMR spectra of 2'-*O*- β -*D*-ribofuranosylcytidine [6] and 2'-*O*- β -*D*-ribofuranosyluridine shows that, in water, the conformations of the nucleoside parts of the molecules are identical to each other and analogous to that of natural cytidine. It should be noted that, in the case of 2'-*O*- β -*D*-ribofuranosyluridine, the $S \rightleftharpoons N$ equilibrium is slightly shifted toward the S conformer. In a solution, the pyranose part of 2'-*O*- β -*D*-ribofuranosyluridine, like the molecule of methyl- β -*D*-ribofuranoside [15], is in an approximately equimolar ${}^4C_1 \rightleftharpoons {}^1C_4$ equilibrium.

The lengths of the *O*-glycoside bonds in the molecules of the disaccharides under investigation coincide to within the limits of 3σ . In the molecules of 2'-*O*- β -*D*-ribofuranosyluridine and 2'-*O*- β -*D*-ribofuranosyluridine [6], the O(2'')–C(1'') bonds are equal to 1.411(3) and 1.420(4) Å, respectively. However, the O(6'')–C(1'')–O(2'')–C(2'') and O(4'')–C(1'')–O(2'')–C(2'') torsion angles about these bonds slightly differ [$-81.6(2)^\circ$ and $-70.0(3)^\circ$, respectively] because of the different natures of the additional 2'-*O*-carbohydrate residues. Accordingly, there is a difference between the torsion

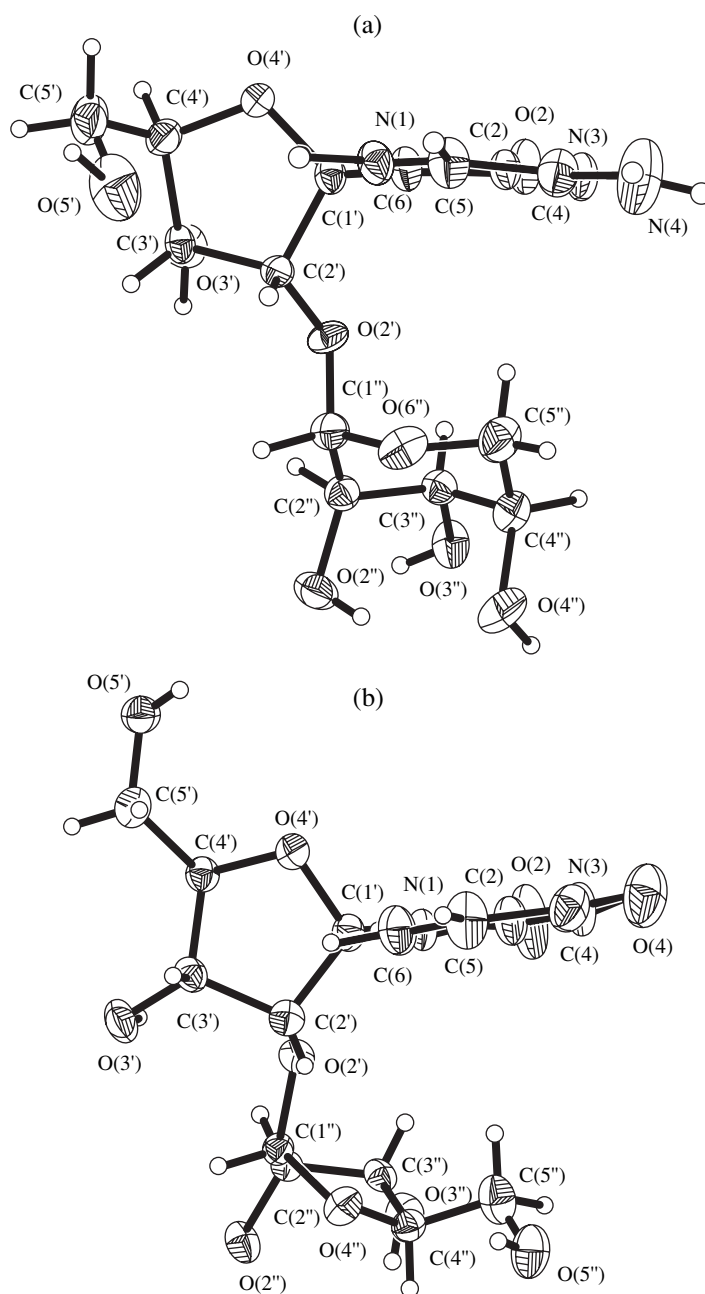


Fig. 2. Molecular conformations of (a) 2'-*O*- β -*D*-ribofuranosyluridine and (b) 2'-*O*- β -*D*-ribofuranosyluridine.

angles characterizing the orientation of the *O*-glycoside bonds with respect to the nucleoside fragments. For example, in the structure of 2'-*O*- β -*D*-ribofuranosyluridine, the C(1'')–O(2'')–C(2'')–C(3'') and C(1'')–O(2'')–C(2'')–C(1'') torsion angles are equal to $-105.7(2)^\circ$ and $139.7(2)^\circ$, respectively. In the structure of 2'-*O*- β -*D*-ribofuranosyluridine, the corresponding angles are $-93.0(3)^\circ$ and $155.3(3)^\circ$.

Nonetheless, as is seen from Figs. 2a and 2b, the molecules of disaccharide nucleosides have a common conformational feature; namely, the additional 2'-*O*-carbohydrate residues are rotated toward the bases in

such a way that they are oriented approximately (roughly) parallel to the heterocyclic bases in their proximity. This is especially pronounced in the case of 2'-*O*- β -*D*-ribofuranosyluridine. The angle between the root-mean-square planes through the heavy (O, N, C) atoms of the base and the atoms of the planar fragment of the pyranose ring [C(2''), C(3''), C(5''), O(6'')] is only $22.7(2)^\circ$. The C(6'')...O(6'') and O(2'')...O(6'') distances are equal to 4.124 and 4.416 Å, respectively. In the structure of 2'-*O*- β -*D*-ribofuranosyluridine, the corresponding angle between the base and the additional furanose ring is equal to $40.0(3)^\circ$ and the C(6'')...O(4'')

and O(2)···O(4'') distances are 5.037 and 5.021 Å, respectively.

Taking into account the general conformational similarity of the 2'-O-β-D-ribofuranosylcytidine and 2'-O-β-D-ribofuranosyluridine molecules, as well as the data on the stability of the oligonucleotide complexes containing these disaccharide nucleosides with single-chain RNA and DNA [8, 9], we can assume that there exists an analogy between the three-dimensional arrangements of their additional sugar fragments in the molecular duplexes of RNA and DNA.

In conclusion, we note that the crystal structure of 2'-O-β-D-ribofuranosylcytidine, like the structure of 2'-O-β-D-ribofuranosyluridine, is characterized by a saturated hydrogen-bond system; i.e., all oxygen and nitrogen atoms of the molecules are involved in hydrogen bonding (Table 2). In the structure of 2'-O-β-D-ribofuranosylcytidine, one of the hydrogen bonds [O(2'')-H···O(4'')] is intramolecular.

ACKNOWLEDGMENTS

This study was supported by the Council on Grants from the President of the Russian Federation (grant no. NSh-1781.2003.04) and the Russian Foundation for Basic Research and was performed in the framework of the program "Investigations and Elaborations in the Priority Trends of the Development of Science and Engineering (AIDS)."

REFERENCES

1. *Dictionary of Natural Products on CD-ROM: Version 9 : 2* (Chapman and Hall/CRC, 2001).

2. K. J. Isono, *Antibiotics* **41**, 1711 (1988).
3. E. V. Efimtseva and S. N. Mikhailov, *Usp. Khim.* **74**, 435 (2004).
4. E. V. Efimtseva and S. N. Mikhailov, *Biokhimiya* **67**, 1374 (2002).
5. S. N. Mikhailov, A. de Bruyn, and P. Herdewijn, *Nucleosides Nucleotides* **14**, 481 (1995).
6. S. N. Mikhailov, E. V. Efimtseva, G. V. Gurskaya, *et al.*, *J. Carbohydr. Chem.* **16**, 75 (1997).
7. S. N. Mikhailov and E. V. Efimtseva, *Collect. Symp. Ser.* **5**, 181 (2002).
8. E. V. Efimtseva, G. V. Bobkov, S. N. Mikhailov, *et al.*, *Helv. Chim. Acta* **84**, 2387 (2001).
9. I. Luyten, R. M. Esnouf, S. N. Mikhailov, *et al.*, *Helv. Chim. Acta* **83**, 1278 (2000).
10. R. Basavappa and P. B. Sigler, *EMBO J.* **10**, 3105 (1991).
11. G. M. Sheldrick, *SHELX97: Program for the Solution and Refinement of Crystal Structures* (Univ. of Göttingen, Germany, 1997).
12. G. V. Gurskaya, G. M. Javadova, and S. N. Mikhailov, *Cryst. Struct. Commun.* **11**, 1253 (1982).
13. G. V. Gurskaya, A. A. Zhdanov, S. N. Mikhailov, and E. N. Tzapkina, *Cryst. Struct. Commun.* **11**, 1245 (1982).
14. G. V. Gurskaya, G. M. Javadova, and S. N. Mikhailov, *Cryst. Struct. Commun.* **11**, 1259 (1982).
15. F. Franks, P. J. Lillford, and G. Robinson, *J. Chem. Soc., Faraday Trans. 1*, 2417 (1989).

Translated by I. Polyakova

STRUCTURE
OF ORGANIC COMPOUNDS

Crystal and Molecular Structures
of *trans*-2-(4'-Dimethylaminobenzylideneacetyl)-5,5-
Dimethylcyclohexane-1,3-dione

S. L. Bondarev*, A. S. Lyakhov**, A. N. Pyrko***, A. A. Govorova***,
I. I. Kalosha*, and V. N. Knyukshto*

* Institute of Molecular and Atomic Physics, National Academy of Sciences of Belarus,
pr. Franziska Skaryny 70, Minsk, 220072 Belarus

e-mail: bondarev@imaph.bas-net.by

** Research Institute of Physicochemical Problems, Belarussian State University,
Leningradskaya ul. 14, Minsk, 220050 Belarus

*** Institute of Bioorganic Chemistry, National Academy of Sciences of Belarus,
ul. Kuprevicha 5/2, Minsk, 220141 Belarus

Received February 9, 2004; in final form, September 24, 2004

Abstract—The crystal and molecular structures of a cyclic β -triketone, namely, *trans*-2-(4'-dimethylaminobenzylideneacetyl)-5,5-dimethylcyclohexane-1,3-dione (**I**), are determined using X-ray diffraction analysis. It is established that the compound in the crystalline state exists in a diketo–enol form stabilized by intramolecular hydrogen bonds. The specific features of the structure and the physicochemical and fluorescence properties of the compound are discussed. © 2005 Pleiades Publishing, Inc.

INTRODUCTION

Organic crystals have found wide application in nonlinear and laser optics [1]. Considerable attention has been focused on the search for new nonlinear optical materials based on organic crystals for use in the conversion of laser radiation frequency through the simultaneous absorption of two photons. Compounds with a high probability of two-photon light absorption occurring hold much promise because these materials can be used for visualization of laser IR radiation (through two-photon excitation fluorescence with a spectrum in the visible range) [2], optical recording of information [3], the design of laser devices [4], and photodynamic therapy [5].

The purpose of this work was to investigate the molecular and crystal structures of a cyclic β -triketone, namely, *trans*-2-(4'-dimethylaminobenzylideneacetyl)-5,5-dimethylcyclohexane-1,3-dione (**I**). Crystals of compound **I** are characterized by an intense two-photon excitation fluorescence spectrum in the wavelength range 550–700 nm upon excitation with the first harmonic of neodymium laser radiation at a wavelength $\lambda_{\text{exc}} = 1.06 \mu\text{m}$. The intensity of two-photon excitation fluorescence of a powdered polycrystalline sample of compound **I** is 70 times higher than the intensity of the second harmonic generated by the well-known nonlinear optical compound, namely, potassium titanyl phosphate. Owing to the high efficiency of IR radiation conversion, compound **I** can be considered a promising

nonlinear optical material for use in visualization of laser radiation at wavelengths up to 1.2 μm .

EXPERIMENTAL

trans-2-(4'-Dimethylaminobenzylideneacetyl)-5,5-dimethylcyclohexane-1,3-dione (**I**) was synthesized from 5,5-dimethylcyclohexane-1,3-dione (dimedone) in two stages. At the first stage, 2-acetyl-5,5-dimethylcyclohexane-1,3-dione was prepared through acylation of dimedone with acetic acid according to the procedure described in [6]. At the second stage, compound **I** was synthesized by the aldol–crotonic condensation of 2-acetyl-5,5-dimethylcyclohexane-1,3-dione with *para*-(dimethylamino)benzaldehyde. Single crystals were grown through slow evaporation of a saturated solution of compound **I** in ethyl alcohol at room temperature for two months.

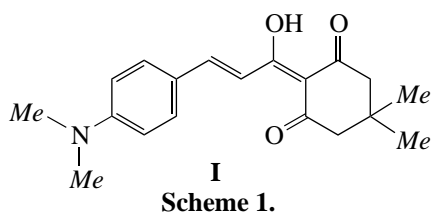
X-ray diffraction investigations were performed at room temperature on a Nicolet R3m diffractometer (MoK α radiation, graphite monochromator, $\omega/2\theta$ scan mode) [7]. The unit cell parameters were determined and refined using 25 reflections in the angle range $\theta = 10.0^\circ$ – 15.5° . The structure was solved by direct methods (SIR97 [8]). The hydrogen atoms were located from the difference Fourier synthesis. The refinement of the crystal structure was carried out using the full-matrix least-squares method with allowance made for the anisotropic displacement parameters of the non-hydrogen atoms (SHELX97 [9]). The positions of the hydrogen atoms of the hydroxyl groups and of the eth-

ylene fragments were refined in the isotropic approximation, whereas the positions of the remaining hydrogen atoms were refined within a riding model. The main crystallographic data and the parameters of the structure refinement are presented in Table 1. The figures were drawn with the PLATON program package [10]. The crystallographic data for the structure of compound **I** have been deposited with the Cambridge Structural Database (CCDC, no. 247719).

The steady-state fluorescence spectra obtained under one-photon and two-photon excitation were recorded on a wide-aperture instrument described in [11]. Two-photon excitation was accomplished using the first harmonic of a pulsed neodymium laser at a wavelength of 1.06 μm . The intensity of two-photon excitation fluorescence of powdered samples was measured according to the technique described in [12].

RESULTS AND DISCUSSION

Analysis of the structural data has revealed that, in the crystal, molecule **I** exists in the diketo-enol form stabilized by a strong intramolecular hydrogen bond and is characterized by the *trans* orientation of the substituents with respect to the C(8)=C(9) bond (see Fig. 1, Scheme 1).



In the crystal of compound **I**, the asymmetric cell contains two crystallographically independent molecules, which are designated as *A* and *B*. The atomic numbering in these molecules is given in Fig. 1. The selected geometric parameters of molecules *A* and *B* are listed in Tables 2 and 3. It can be seen from these tables and Fig. 2 that molecules *A* and *B* have very similar

Table 1. Crystal data, data collection, and refinement parameters for the structure of compound **I**

| | |
|---|---|
| Empirical formula | $\text{C}_{19}\text{H}_{23}\text{NO}_3$ |
| Molecular weight | 313.38 |
| Crystal system | Monoclinic |
| Space group and unit cell parameters | $P2_1/c$ |
| a , \AA | 25.389(5) |
| b , \AA | 10.660(2) |
| c , \AA | 12.743(3) |
| β , deg | 104.14(2) |
| V , \AA^3 | 3344.4(12) |
| Z | 8 |
| ρ_{calcd} , g/cm^3 | 1.245 |
| $\mu(\text{MoK}\alpha)$, cm^{-1} | 0.84 |
| $F(000)$ | 1344 |
| Crystal size, mm | $0.48 \times 0.36 \times 0.14$ |
| $\theta_{\text{min}}-\theta_{\text{max}}$, deg | 1.65–27.56 |
| Number of reflections measured/Number of unique reflections | 8002/7648 [$R_{\text{int}} = 0.0377$] |
| Goodness-of-fit (<i>GOOF</i>) on F^2 | 0.974 |
| R_1/wR_2 [$I > 2\sigma(I)$] | 0.0685/0.1761 |
| R_1/wR_2 (all data) | 0.1313/0.2242 |
| Extinction coefficient | 0.0080(14) |
| $\Delta\rho_{\text{max}}/\Delta\rho_{\text{min}}$, e \AA^{-3} | 0.376/–0.245 |

structures. For this reason, in what follows, we will imply that the data presented in this paper refer to both molecules if the letters *A* and *B* are absent in the atomic notation.

Although the enolization reaction can be accompanied by the formation of O(7)–H or O(1)–H hydroxyl groups, compound **I** undergoes enolization according

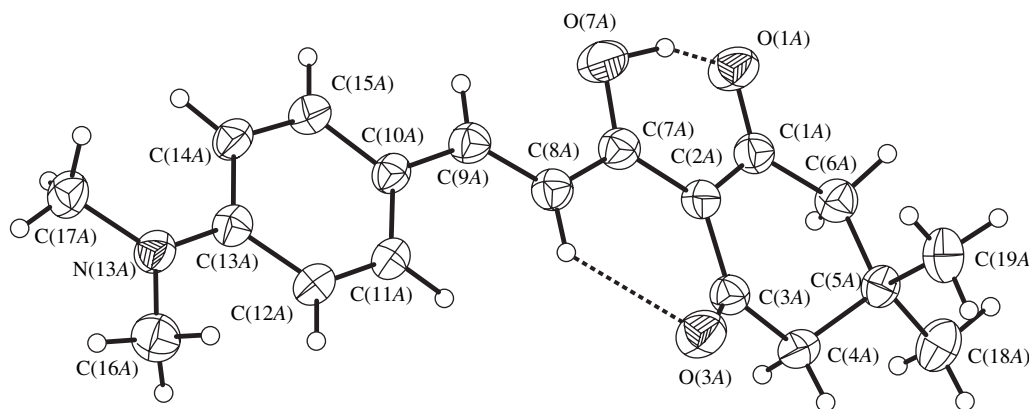


Fig. 1. Structure and atomic numbering of molecule *A* in the crystal structure of compound **I** (molecule *B* has a similar structure and atomic numbering). Dashed lines indicate hydrogen bonds.

Table 2. Selected bond lengths (Å) in molecules of compound **I**

| Bond | Molecule <i>A</i> | Molecule <i>B</i> | Bond | Molecule <i>A</i> | Molecule <i>B</i> |
|------------|-------------------|-------------------|-------------|-------------------|-------------------|
| C(1)–O(1) | 1.279(3) | 1.282(3) | C(7)–C(8) | 1.431(4) | 1.432(4) |
| C(1)–C(2) | 1.417(4) | 1.410(4) | C(8)–C(9) | 1.348(4) | 1.347(4) |
| C(1)–C(6) | 1.483(4) | 1.492(4) | C(9)–C(10) | 1.446(4) | 1.437(4) |
| C(2)–C(7) | 1.439(4) | 1.439(4) | C(10)–C(11) | 1.391(4) | 1.400(4) |
| C(2)–C(3) | 1.461(4) | 1.475(4) | C(10)–C(15) | 1.399(4) | 1.391(4) |
| C(3)–O(3) | 1.220(3) | 1.221(3) | C(11)–C(12) | 1.368(4) | 1.361(4) |
| C(3)–C(4) | 1.509(4) | 1.499(4) | C(12)–C(13) | 1.421(4) | 1.416(4) |
| C(4)–C(5) | 1.529(4) | 1.529(4) | C(13)–N(13) | 1.357(4) | 1.358(4) |
| C(5)–C(19) | 1.516(4) | 1.524(4) | C(13)–C(14) | 1.404(4) | 1.397(4) |
| C(5)–C(6) | 1.516(4) | 1.526(4) | N(13)–C(16) | 1.453(4) | 1.446(4) |
| C(5)–C(18) | 1.538(4) | 1.534(4) | N(13)–C(17) | 1.440(4) | 1.446(4) |
| C(7)–O(7) | 1.301(3) | 1.304(4) | C(14)–C(15) | 1.367(4) | 1.371(4) |

Table 3. Selected bond angles (deg) in molecules of compound **I**

| Angle | Molecule <i>A</i> | Molecule <i>B</i> | Angle | Molecule <i>A</i> | Molecule <i>B</i> |
|------------------|-------------------|-------------------|-------------------|-------------------|-------------------|
| O(1)–C(1)–C(2) | 121.7(3) | 121.6(3) | O(7)–C(7)–C(8) | 116.8(3) | 117.2(3) |
| O(1)–C(1)–C(6) | 115.4(3) | 115.7(3) | O(7)–C(7)–C(2) | 118.2(3) | 117.6(3) |
| C(2)–C(1)–C(6) | 122.9(3) | 122.6(3) | C(8)–C(7)–C(2) | 125.0(3) | 125.1(3) |
| C(1)–C(2)–C(7) | 118.1(3) | 118.3(3) | C(9)–C(8)–C(7) | 120.5(3) | 120.5(3) |
| C(1)–C(2)–C(3) | 118.7(2) | 118.6(3) | C(8)–C(9)–C(10) | 128.3(3) | 127.9(3) |
| C(7)–C(2)–C(3) | 123.2(2) | 123.0(2) | C(11)–C(10)–C(15) | 116.6(3) | 115.9(3) |
| O(3)–C(3)–C(2) | 124.0(3) | 123.3(3) | C(11)–C(10)–C(9) | 124.5(3) | 124.7(3) |
| O(3)–C(3)–C(4) | 119.4(3) | 119.6(3) | C(15)–C(10)–C(9) | 118.9(3) | 119.4(3) |
| C(2)–C(3)–C(4) | 116.6(2) | 117.1(2) | C(12)–C(11)–C(10) | 122.0(3) | 122.4(3) |
| C(3)–C(4)–C(5) | 113.5(2) | 114.3(2) | C(11)–C(12)–C(13) | 121.3(3) | 121.0(3) |
| C(19)–C(5)–C(6) | 111.0(2) | 110.1(3) | N(13)–C(13)–C(14) | 121.5(3) | 122.0(3) |
| C(19)–C(5)–C(4) | 109.8(2) | 110.5(3) | N(13)–C(13)–C(12) | 121.9(3) | 121.0(3) |
| C(6)–C(5)–C(4) | 108.1(2) | 107.0(2) | C(14)–C(13)–C(12) | 116.5(3) | 117.0(3) |
| C(19)–C(5)–C(18) | 109.4(3) | 109.7(3) | C(13)–N(13)–C(16) | 121.4(3) | 121.9(3) |
| C(6)–C(5)–C(18) | 109.4(2) | 109.9(2) | C(13)–N(13)–C(17) | 121.9(3) | 121.7(3) |
| C(4)–C(5)–C(18) | 109.1(2) | 109.6(3) | C(17)–N(13)–C(16) | 116.6(3) | 116.3(3) |
| C(1)–C(6)–C(5) | 115.9(2) | 114.8(2) | C(15)–C(14)–C(13) | 121.0(3) | 120.6(3) |
| | | | C(14)–C(15)–C(10) | 122.6(3) | 123.0(3) |

Table 4. Geometric parameters of hydrogen bonds in the structure of compound **I** (*d*, Å; ω , deg)

| <i>D</i> –H... <i>A</i> | <i>d</i> (<i>D</i> –H) | <i>d</i> (H... <i>A</i>) | <i>d</i> (<i>D</i> ... <i>A</i>) | ω (DHA) |
|--|-------------------------|---------------------------|------------------------------------|----------------|
| O(7 <i>A</i>)–H(7 <i>A</i>)...O(1 <i>A</i>) | 1.22(4) | 1.25(4) | 2.409(3) | 155(4) |
| O(7 <i>B</i>)–H(7 <i>B</i>)...O(1 <i>B</i>) | 1.13(4) | 1.31(4) | 2.396(3) | 158(4) |
| C(8 <i>A</i>)–H(8 <i>A</i>)...O(3 <i>A</i>) | 0.97(3) | 2.23(3) | 2.890(4) | 124(2) |
| C(8 <i>B</i>)–H(8 <i>B</i>)...O(3 <i>B</i>) | 0.95(3) | 2.21(3) | 2.868(4) | 125(2) |

to the first variant. This circumstance will be discussed below.

The benzene rings have a planar structure. The root-mean-square deviations of atoms from the planes in molecules *A* and *B* are equal to 0.006(2) and 0.007(2) Å, respectively. The N(13*A*) and N(13*B*) nitrogen atoms are characterized by a trigonal-planar configuration (for molecules *A* and *B*, the sums of the angles at these atoms are equal to 359.9°). Such a configuration is

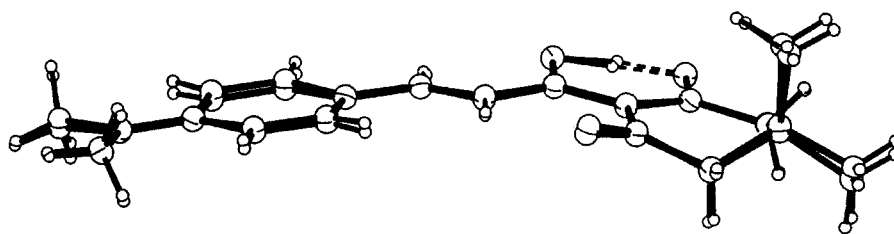


Fig. 2. Comparison of the geometries of molecules *A* and *B* by their superposition (PLATON program package [10]).

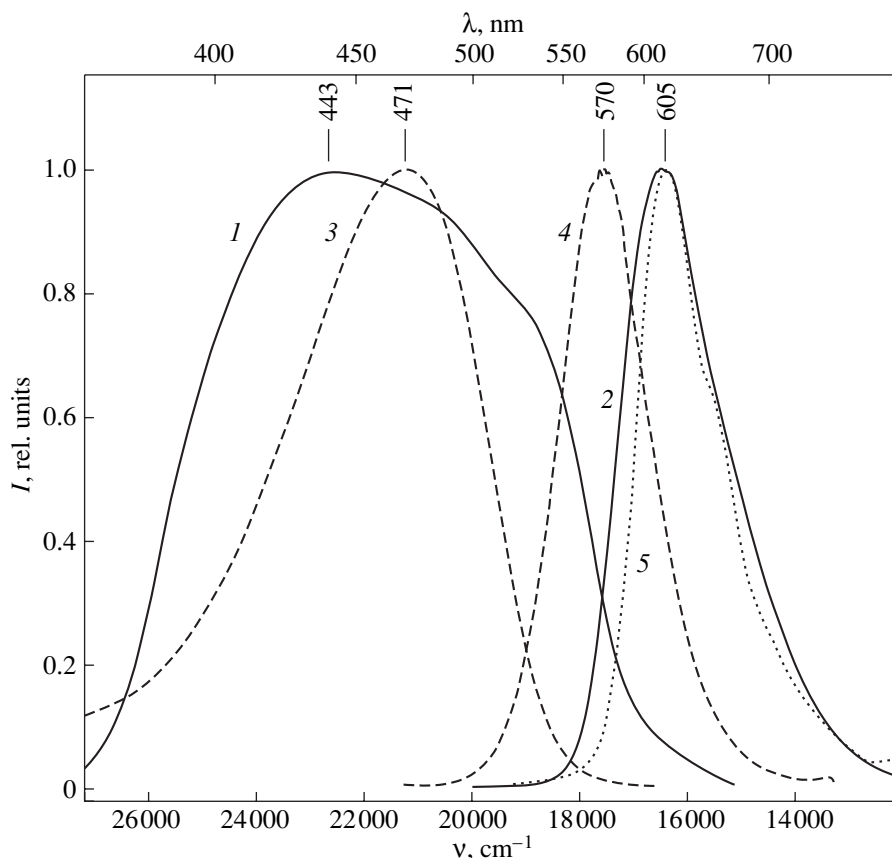


Fig. 3. (1, 3) Absorption and (2, 4, 5) fluorescence spectra of (3, 4) compound **I** in an ethanol solution and (1, 2, 5) polycrystals **I** upon (1–4) one-photon excitation and (5) two-photon excitation at room temperature. The concentration of compound **I** in ethanol is $C = 5 \times 10^{-6}$ mol/l. The positions of the maxima in the spectra are given in nanometers.

associated with the conjugation of the lone electron pair of the nitrogen atom with the π system of the benzene ring. The geometric characteristics of the benzene ring are close to the standard parameters. Nonetheless, there exist a number of specific features. First, the C(14)–C(15) and C(11)–C(12) bonds in the benzene fragment of compound **I** are slightly shortened (Table 2). Second, the endocyclic bond angles at the C(10) and C(13) carbon atoms are considerably smaller than the standard values, whereas the other angles of the benzene ring are somewhat larger (Table 3). This distortion is characteristic of benzene rings containing π -donor substituents in the *para* position [13, 14].

The conformation of the cyclohexane ring is determined by the system of C(7)=C(2), C(1)=O(1), and C(3)=O(3) conjugated bonds. This system of bonds is responsible for the planarity of the C(6)–C(1)–C(2)–C(3)–C(4) fragment in the cyclohexane ring. In this case, the root-mean-square deviations of atoms from the corresponding plane in molecules *A* and *B* are equal to 0.072(2) and 0.047(2) Å, respectively. The folding angle of the C(4)–C(5)–C(6) fragment from the aforementioned plane is equal to 42.4(2)° for molecule *A* and 45.0(2)° for molecule *B*. It should be noted that molecule **I** has a rather planar structure due to the formation of the system of conjugated bonds that encompass the

entire molecular skeleton (from the benzene ring to the cyclohexane ring).

The enol form of molecule **I** is stabilized by strong intramolecular hydrogen bonds. The geometric parameters of these bonds are presented in Table 4. The C(2)=C(7) and C(1)–C(2) bond lengths in the cycle formed through the intramolecular hydrogen bond are very close to each other (Table 2), because the hydrogen bond is involved in a single conjugated chain. This phenomenon is typical of β -diketones and β,β' -triketones and is referred to as resonance-assisted hydrogen bonding [15, 16]. These hydrogen bonds are relatively short, with the D–H and H...A distances being very close to each other. However, the proton is not located precisely at the midpoint between two oxygen atoms. Apart from the classical hydrogen bonds, intramolecular hydrogen bonds of the C–H...O type [17] also make a certain contribution to the stabilization of the structure of molecule **I**. The geometric parameters of these intramolecular hydrogen bonds are listed in Table 4. Thus, the crystal structure of compound **I** involves intramolecular hydrogen bonds alone, whereas molecules of this compound are bound through van der Waals interactions.

The results of analyzing the structural data obtained for cyclic β -triketones [14] have demonstrated that, as a rule, the carbonyl group located outside the cycle is subject to enolization, except for the compounds containing bulky substituents in a side chain when the carbonyl group of the cycle undergoes enolization. An example of the latter compounds is provided by 2-benzoyldimedone [18, 19]. This regularity is confirmed by the structural data obtained for compound **I**.

The absorption and fluorescence spectra of compound **I** in an ethanol solution and in a polycrystalline film applied to a quartz substrate by rubbing are depicted in Fig. 3. The absorption spectrum of the polycrystalline film (Fig. 3, curve 1) is substantially broadened as compared to the absorption spectrum of the ethanol solution of compound **I** (Fig. 3, curve 3). The half-widths $\Delta\nu$ of these spectra are equal to 7500 and 4200 cm^{-1} , respectively. The broadening of the absorption spectrum of the crystal is associated primarily with the exciton bands. The formation of these bands is governed, to a great extent, by the interactions of excitons with molecular vibrations in the crystal, i.e., with phonons [20]. Moreover, the absorption spectrum of the polycrystalline film of compound **I** can be inhomogeneously broadened because of the broad size distribution of microcrystals in the sample.

The one-photon excitation fluorescence spectrum (Fig. 3, curve 2; $\lambda_{\text{exc}} = 450 \text{ nm}$) and the two-photon excitation fluorescence spectrum (Fig. 3, curve 5; $\lambda_{\text{exc}} = 1.06 \mu\text{m}$) of compound **I** in the polycrystalline state almost coincide with each other. These spectra are bathochromically shifted and broadened as compared to the one-photon excitation fluorescence spectrum of the ethanol solution by 35 nm (1015 cm^{-1}) and

$\sim 400 \text{ cm}^{-1}$, respectively. It should be emphasized that the two-photon excitation fluorescence spectra of compound **I** in the single-crystal and polycrystalline states are identical to each other and that the one-photon excitation fluorescence spectra do not depend on the excitation wavelength.

Since the absorption spectrum of the polycrystalline film of compound **I** is significantly broadened, it becomes possible to visualize laser IR radiation over a wide spectral range (800–1200 nm) through two-photon excitation fluorescence with a spectrum in the wavelength range 550–700 nm. Another important feature of the broadened absorption spectrum is noteworthy. This feature is associated with the increase in the probability of two-photon absorption. In actual fact, the probability of two-photon absorption and, accordingly, the probability of two-photon excitation fluorescence occurring are proportional to the square of the one-photon transition dipole moment [21], i.e., to the integral of the absorption spectrum corresponding to the transition from the S_0 ground state to the S_1 excited state. Furthermore, an increase in the probability of two-photon absorption occurring is also favored by an extended system of conjugated bonds in the enol form of molecule **I**. This system is enhanced and stabilized by intramolecular hydrogen bonds.

ACKNOWLEDGMENTS

The authors acknowledge the support of the Russian Foundation for Basic Research in the payment of the license for using the Cambridge Structural Database, project no. 99-07-90133.

This work was supported in part by the Belarussian Foundation for Basic Research, project no. F02R-119.

REFERENCES

1. *Nonlinear Optical Properties of Organic Molecules and Crystals*, Ed. by D. S. Chemla and J. Zyss (Academic, New York, 1987; Mir, Moscow, 1989), Vol. 1.
2. W. Denk, J. H. Strickler, and W. W. Webb, *Science* **248** (4951), 73 (1990).
3. D. A. Parthenopoulos and P. M. Rentzepis, *Science* **245** (4345), 843 (1989).
4. G. S. He, R. Signorini, and P. N. Prasad, *Appl. Opt.* **37** (28), 5720 (1998).
5. H. Stiel, K. Tenchner, A. Paul, *et al.*, *J. Photochem. Photobiol. A* **80** (2), 289 (1994).
6. A. N. Pyrko, *Zh. Org. Khim.* **27** (10), 2237 (1991).
7. *Nicolet R3m Software* (Nicolet XRD, Cupertino, Cal., 1980).
8. A. Altomare, M. C. Burla, M. Camalli, *et al.*, *J. Appl. Crystallogr.* **32**, 115 (1999).
9. G. M. Sheldrick, *SHELX97: Program for the Solution and Refinement of Crystal Structures* (Univ. of Göttingen, Germany, 1997).
10. A. L. Spek, *J. Appl. Crystallogr.* **36**, 7 (2003).

11. E. A. Borisevich, V. N. Knyukshto, A. N. Kozyrev, and K. N. Solov'ev, *Opt. Spektrosk.* **74** (1), 210 (1993) [*Opt. Spectrosc.* **74**, 129 (1993)].
12. S. K. Kurtz and T. T. Perry, *J. Appl. Phys.* **39** (8), 3798 (1968).
13. *Accurate Molecular Structures: Their Determination and Importance*, Ed. by A. Domenicano and I. Hargittai (Oxford Univ. Press, Oxford, 1992; Mir, Moscow, 1997).
14. F. H. Allen, *Acta Crystallogr., Sect. B: Struct. Sci.* **58**, 380 (2002).
15. G. Gilli, F. Bellucci, V. Ferretti, and V. Bertolasi, *J. Am. Chem. Soc.* **111** (3), 1023 (1989).
16. V. Bertolasi, P. Gilli, V. Ferretti, and G. Gilli, *J. Am. Chem. Soc.* **113** (13), 4917 (1991).
17. G. R. Desiraju and T. Steiner, *The Weak Hydrogen Bond in Structural Chemistry and Biology* (Oxford Univ. Press, Oxford, 1999).
18. E. V. Borisov, T. S. Khlebnikova, and F. F. Lakhvich, *Zh. Org. Khim.* **26** (11), 2445 (1990).
19. E. V. Borisov, A. S. Lyakhov, A. A. Govorova, *et al.*, *Izv. Ross. Akad. Nauk, Ser. Khim.*, No. 6, 1074 (2000).
20. A. S. Davydov, *Theory of Molecular Excitons* (Nauka, Moscow, 1968; Plenum, New York, 1971).
21. T. Kogej, D. Beljonne, F. Meyers, *et al.*, *Chem. Phys. Lett.* **298** (1), 1 (1998).

Translated by O. Borovik-Romanova

STRUCTURE
OF ORGANIC COMPOUNDS

Crystal Structure of Bis[diethylenetriamine-*N'*-(3-Propionato)-*N,N',N'',O,O'*]dicopper(II) Diperchlorate, $[\text{Cu}_2(4\text{-Dtmp})_2](\text{ClO}_4)_2$

A. S. Antsyshkina*, G. G. Sadikov*, A. L. Poznyak**, and V. S. Sergienko*

* Kurnakov Institute of General and Inorganic Chemistry, Russian Academy of Sciences,
Leninskiĭ pr. 31, Moscow, 119991 Russia
e-mail: asants@igic.ras.ru

** Institute of Molecular and Atomic Physics, National Academy of Sciences of Belarus,
pr. Franziska Skaryny 70, Minsk, 220072 Belarus

Received April 17, 2004

Abstract—A complex of copper(II) with the diethylenetriaminemonopropionate ligand $[\text{Cu}_2(4\text{-Dtmp})_2](\text{ClO}_4)_2$ (**I**) is synthesized and characterized using X-ray diffraction. The crystals of compound **I** are monoclinic, $a = 7.740(2)$ Å, $b = 19.199(3)$ Å, $c = 8.449(2)$ Å, $\beta = 91.61(2)^\circ$, $Z = 2$, and space group $P2_1/n$. The structural units of crystal **I** are centrosymmetric dimeric cations and statistically disordered ClO_4^- anions. In the cation, the copper atom is coordinated by three N atoms [mean Cu–N, 2.01(1) Å] and two O atoms [Cu–O, 2.134(6) Å and 1.958(7) Å] of the pentadentate bridging–chelate *Dtmp* ligand, which occupy vertices of the trigonal bipyramid. The binuclear cations are linked via centrosymmetric pairs of hydrogen bonds into ribbons aligned parallel to the *a* axis of the crystal. The ClO_4^- anions form columns in the same direction. In the crystal, the cationic ribbons and anionic columns alternate in a chessboard fashion. © 2005 Pleiades Publishing, Inc.

INTRODUCTION

Among the so-called tripod ligands, which are potentially tetradentate, alkylcarboxylate derivatives of diethylenetriamine of the general formula $(\text{NH}_2\text{CH}_2\text{CH}_2)_2\text{N}(\text{CH}_2)_n\text{CO}_2^-$ have attracted particular research attention. The first three members of this series are of primary interest for coordination chemistry, because at $n > 3$, the closing of the eight-membered or more extended aminocarboxylate metallocycle is hardly probable. We designate the ligands with $n = 1, 2$, and 3 as $L^1 = 4\text{-Dtma}$, $L^2 = 4\text{-Dtmp}$, and $L^3 = 4\text{-Dtmb}$, respectively. The structures of a number of copper(II) complexes with the above ligands were studied earlier. In the polymeric chain structures $\text{Cu}(L^1)\text{X}$ ($X = \text{ClO}_4^-$ [1], NCS^- [2], Br^- [3], or NO_3^- [4]) and dimeric structures $[\text{Cu}_2(L^1)_2\text{Im}]\text{ClO}_4$ and $[\text{ZnCu}(L^1)_2\text{Im}]\text{ClO}_4$ [5–7], the 4-*Dtmp* ligand is tetradentate with respect to one copper atom (*Im* is the deprotonated imidazole anion). In the $[\text{Cu}(L^3)]\text{ClO}_4$ structure [8], the 4-*Dtmb* ligand is coordinated to the metal atom in the same way: in this case, the seven-membered aminobutyric metallocycle is closed. However, in the $[\text{Cu}(L^2)\text{NCS}]$ structure [2], the six-membered aminopropionate ring is not formed and the 4-*Dtmp* ligand is coordinated to a copper atom by three donor nitrogen atoms, whereas two oxygen atoms of the acetate group are coordinated to the neighboring copper atom. Possibly, the pentadentate bridg-

ing–chelate structural function of the 4-*Dtmp* ligand in this compound is governed by the coordination of the NCS^- ion to the copper atom.

In this paper, we report the results of the X-ray diffraction study of the crystals of bis[diethylenetriamine-*N'*-(3-propionato)-*N,N',N'',O,O'*]dicopper(II) diperchlorate (**I**).

EXPERIMENTAL

Synthesis

4-*Dtmp*[−] ions were obtained in a solution according to the procedure described earlier for the synthesis of the corresponding cobalt(III) complex [9]. First, *N,N*-bis(2-carbamoylethyl)aminopropionate was prepared from aminopropionic acid and acrylamide. Then, the propionamide groups were transformed into 2-aminoethyl groups according to the Hofmann reaction (oxidative destruction with hypobromite). The 4-*Dtmp* ligand was not isolated in a free state; instead, Cu^{2+} ions were added to the resultant reaction mixture. The $[\text{Cu}(4\text{-Dtmp})]^+$ complexes were isolated using gel filtration on a Sephadex G10 column and ion-exchange chromatography on a Sephadex SP25 cation exchanger. Crystals **I** precipitated after the complexes were eluted at the second stage with a 0.1 M NaClO_4 solution and the eluate was evaporated.

Bond lengths (d , Å) and angles (ω , deg) in the structure of compound **I**

| Bond | d | Bond | d | Angle | ω | Angle | ω |
|-------------|----------|-------------|----------|------------------|----------|-----------------|----------|
| Cu(1)–N(1) | 2.02(1) | Cu(1)–N(2) | 2.020(7) | N(1)–Cu(1)–N(2) | 85.5(4) | N(1)–Cu(1)–N(3) | 132.6(4) |
| Cu(1)–N(3) | 2.00(1) | Cu(1)–O(1) | 2.134(6) | N(1)–Cu(1)–O(1) | 111.7(4) | N(1)–Cu(1)–O(1) | 98.0(4) |
| Cu(1)–O(1) | 1.958(7) | N(1)–C(1) | 1.42(2) | N(2)–Cu(1)–N(3) | 86.2(4) | N(2)–Cu(1)–O(1) | 92.0(3) |
| N(2)–C(2) | 1.46(2) | N(2)–C(4) | 1.48(2) | N(2)–Cu(1)–O(1) | 169.9(3) | N(3)–Cu(1)–O(1) | 115.2(4) |
| N(2)–C(7) | 1.51(2) | N(3)–C(3) | 1.45(2) | N(3)–Cu(1)–O(1) | 98.2(4) | O(1)–Cu(1)–O(1) | 77.9(3) |
| O(1)–C(5) | 1.29(1) | O(2)–C(5) | 1.23(1) | Cu(1)–N(1)–C(1) | 108.7(8) | Cu(1)–N(2)–C(2) | 109.0(7) |
| C(1)–C(2) | 1.52(2) | C(3)–C(4) | 1.48(2) | Cu(1)–N(2)–C(4) | 104.7(7) | Cu(1)–N(2)–C(7) | 113.8(7) |
| C(5)–C(6) | 1.51(1) | C(6)–C(7) | 1.47(2) | C(2)–N(2)–C(4) | 110.9(9) | C(2)–N(2)–C(7) | 112(1) |
| Cl(1)–O(3) | 1.47(5) | Cl(1)–O(4) | 1.44(4) | C(4)–N(2)–C(7) | 105.8(9) | Cu(1)–N(3)–C(3) | 110.5(7) |
| Cl(1)–O(5) | 1.38(5) | Cl(1)–O(6) | 1.41(4) | Cu(1)–O(1)–Cu(1) | 102.1(3) | Cu(1)–O(1)–C(5) | 132.0(6) |
| Cl(1)–O(7) | 1.4(1) | Cl(1)–O(8) | 1.43(3) | Cu(1)–O(1)–C(5) | 124.9(6) | N(1)–C(1)–C(2) | 111(1) |
| Cl(1)–O(9) | 1.45(5) | Cl(1)–O(10) | 1.42(5) | N(2)–C(2)–C(1) | 112(1) | N(3)–C(3)–C(4) | 110(1) |
| Cl(1)–O(11) | 1.48(4) | Cl(1)–O(12) | 1.67(5) | N(2)–C(4)–C(3) | 113(1) | O(1)–C(5)–O(2) | 122.7(9) |
| Cl(1)–O(13) | 1.31(5) | Cl(1)–O(14) | 1.46(4) | O(1)–C(5)–C(6) | 116.7(9) | O(2)–C(5)–C(6) | 120.6(9) |
| Cl(1)–O(15) | 1.58(4) | Cl(1)–O(16) | 1.48(6) | C(5)–C(6)–C(7) | 118(1) | N(2)–C(7)–C(6) | 119(1) |
| Cl(1)–O(17) | 1.43(6) | Cl(1)–O(18) | 1.3(1) | | | | |

X-ray Diffraction Analysis

Crystals **I**, $[\text{Cu}_2(\text{C}_7\text{H}_{12}\text{N}_3\text{O}_2)_2](\text{ClO}_4)_2$, are blue in color and prismatic in shape. The X-ray diffraction

analysis was performed with a sample $0.08 \times 0.24 \times 0.30$ mm in size. The parameters of the monoclinic unit cell are $a = 7.740(2)$ Å, $b = 19.199(3)$ Å, $c = 8.449(2)$ Å, $\beta = 91.61(2)^\circ$, and $V = 1255.0(5)$ Å³; $F(000) = 692$,

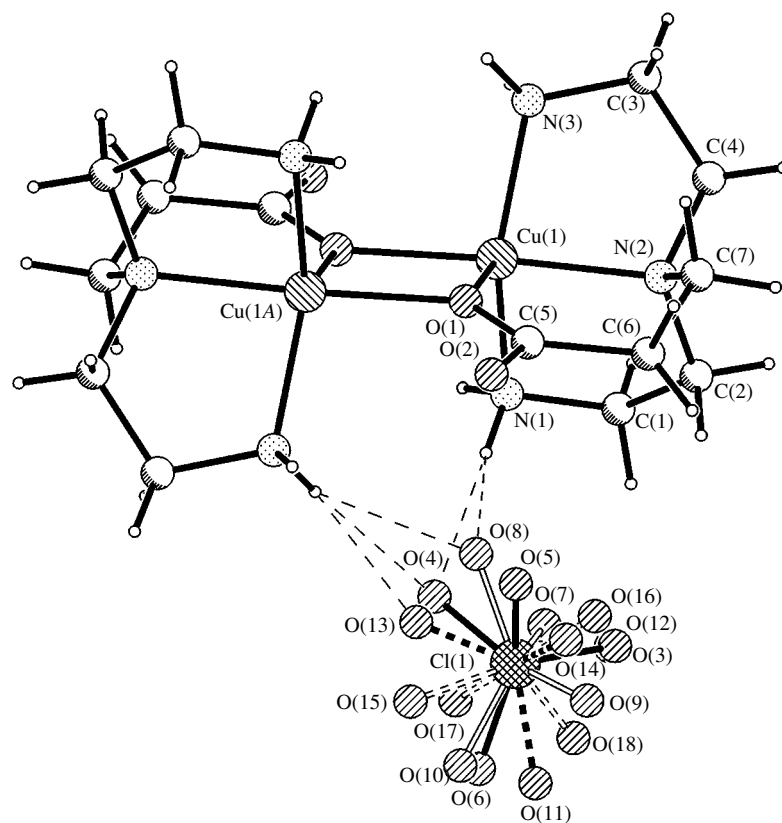


Fig. 1. Structure of the cation–anion group of compound **I** (four orientations of the disordered perchlorate anion are shown).

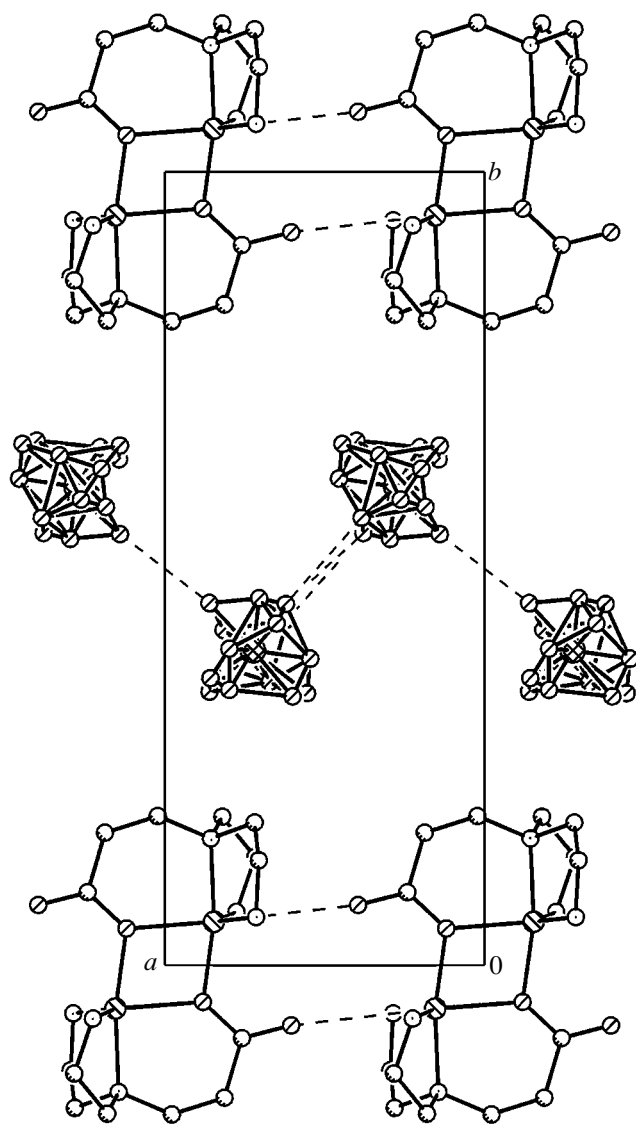


Fig. 2. Packing of the cationic ribbons and anionic columns in crystal **I** (projection onto the *ab* plane).

$\rho_{\text{calcd}} = 1.785 \text{ g/cm}^3$, $\mu = 1.98 \text{ mm}^{-1}$, $Z = 2$, and space group $P2_1/n$.

The experimental set of intensities of reflections was collected on an Enraf–Nonius CAD4 diffractometer at 293 K (MoK α radiation, graphite monochromator, $\omega/2\theta$ scan mode, $\theta = 28^\circ$). A total of 2967 unique nonzero reflections were measured.

The structure was solved by direct methods. In the course of the structure solution, we found that the oxygen atoms of the perchlorate group are disordered. The structure was refined by the full-matrix least-squares method in the approximation of anisotropic thermal vibrations of the non-hydrogen atoms (except for the O atoms of the ClO $_4$ anion, which were refined isotropically). The H atoms were refined within a riding model (N–H, 0.90 Å; C–H, 0.96 Å) with the thermal param-

eters exceeding the relevant value of U_C or U_N for the reference carbon or nitrogen atom by a factor of 1.2. The final parameters of the refinement are as follows: $R_1 = 0.0740$ and $wR_2 = 0.1663$ for 1050 reflections with $I > 2\sigma(I)$, $R_1 = 0.2454$ and $wR_2 = 0.2444$ for all reflections, 186 parameters refined, and $GOOF = 1.14$. The maximum and minimum residual electron densities are equal to 1.65 and -0.64 e \AA^{-3} , respectively.

All the calculations were performed with the SHELXS86 [10] and SHELXL93 [11] program packages. The bond lengths and angles are listed in the table. The CIF file has been deposited with the Cambridge Structural Database (no. 235797).

RESULTS AND DISCUSSION

Crystal **I** is built of centrosymmetric dimeric cationic complexes $[\text{Cu}_2(4\text{-Dtmp})_2]^{2+}$ and perchlorate anions in the general position (Fig. 1). In the binuclear cation, the O(1) oxygen atom of the propionate group of the 4-*Dtmp* ligand acts as a bridge. As a result, three nitrogen atoms [mean Cu–N, 2.01(1) Å] and two oxygen atoms [Cu–O, 2.134(6) Å and 1.958(7) Å] of the pentadentate bridging–chelate *Dtmp* ligand are coordinated to the copper atom through vertices of the irregular trigonal bipyramid.

The Cu and O atoms form a planar CuO $_2$ Cu four-membered ring; the O–Cu–O angle is 77.7° , and the Cu...Cu distance is 3.18 Å. In the absence of additional ligands, as was expected [8], the 4-*Dtmp* ligand forms three metalocycles with the Cu atom, namely, two five-membered and one six-membered rings.

Other metals also can form dimeric complexes via the carboxyl group of the amino-3-propionate fragment of a polydentate ligand. Examples are provided by $[(\text{H}_2\text{O})_2\text{Co}_2(\text{Npda})_2]^{2+}$ [12], $[(\text{H}_2\text{O})_2\text{Zn}_2(\text{Npda})_2]^{2+}$ [12], $[(\text{H}_2\text{O})_4\text{Ni}_2(\text{Mipa})_2]$ [13], and $[(\text{H}_2\text{O})_2\text{Ni}_2(\text{Heidp})_2]$ [14], where *Npda* is nitrilo-3-propionate-diacetate, *Mipa* is methyliminoacetate-3-propionate, and *Heidp* is 2-hydroxyethyliminodi(3-propionate). In these compounds, unlike compound **I**, metal atoms have an octahedral coordination.

In structure **I**, the dimeric cationic complexes related by a translation are linked via centrosymmetric pairs of the N(3)–H(2N3)...O(2) hydrogen bonds into ribbons aligned parallel to the *a* axis of the crystal (Fig. 2). The ClO $_4^-$ anions form columns in the same direction.

The perchlorate anions are orientationally disordered. Four orientations of the ClO $_4^-$ tetrahedron can be distinguished, namely, O(3)–O(6), O(7)–O(10), O(11)–O(14), and O(15)–O(18) (Fig. 1). The hydrogen atoms of the NH $_2$ groups and the oxygen atoms of the perchlorate anions most probably form labile hydrogen bonds capable of changing the acceptors, depending on the orientation of the ClO $_4^-$ anion: the N(3) atom is bonded

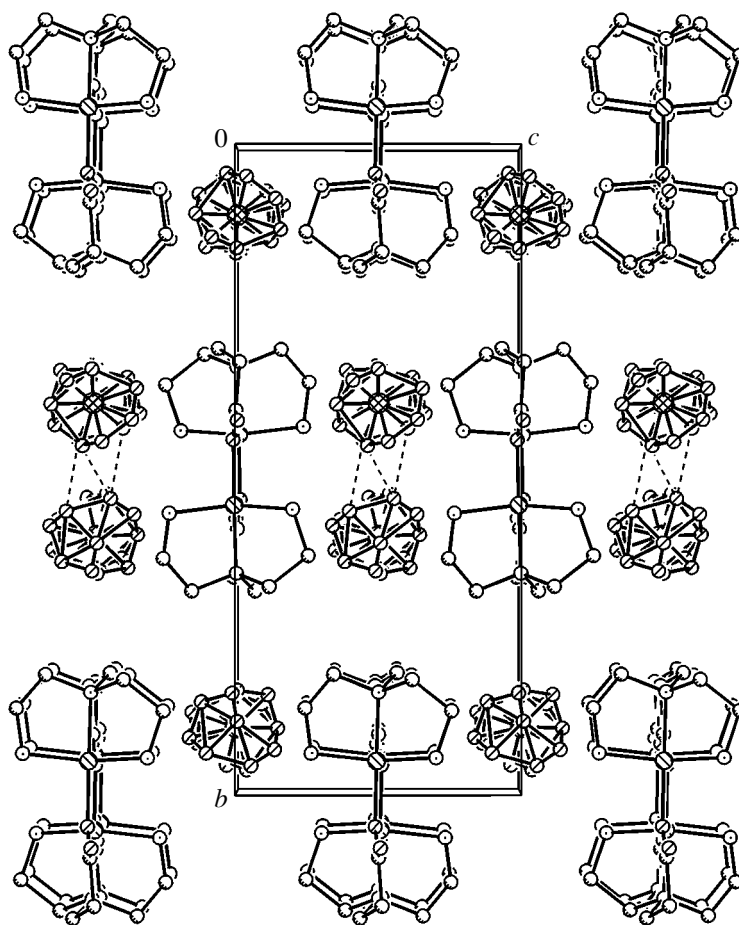


Fig. 3. Chessboard motif of the packing of the cationic ribbons and anionic columns (projection onto the bc plane).

to the O(4), O(8), or O(13) atom; and the N(1) atom is bonded to the O(4), O(7), or O(17) atom (Fig. 1). The centers of inversion that relate the perchlorate anions into columns are considered to be statistical. Some combinations of neighboring ClO_4^- anions are impossible for geometric reasons; the corresponding unreal contacts are shown by dashed lines in Fig. 2. The statistical disordering of the ClO_4^- anions allows them to be more densely packed into columns that fit the cationic formations: cationic ribbons and anionic columns are aligned parallel to each other and alternate in the crystal in a chessboard fashion (Fig. 3).

REFERENCES

1. A. B. Ilyukhin, L. M. Shkol'nikova, A. L. Poznyak, and N. M. Dyatlova, Dokl. Akad. Nauk SSSR **306** (1), 100 (1989) [Sov. Phys. Dokl. **34**, 393 (1989)].
2. A. B. Ilyukhin, L. M. Shkol'nikova, A. L. Poznyak, and N. M. Dyatlova, Koord. Khim. **16** (6), 811 (1990).
3. A. B. Ilyukhin and A. L. Poznyak, Koord. Khim. **19** (10/11), 855 (1993).
4. A. B. Ilyukhin, A. L. Poznyak, and V. S. Sergienko, Kristallografiya **40** (5), 934 (1995) [Crystallogr. Rep. **40**, 867 (1995)].
5. Z.-W. Mao, K. B. Yu, W.-X. Tang, *et al.*, Polyhedron **11** (2), 191 (1992).
6. Z.-W. Mao, D. Chen, W.-X. Tang, *et al.*, Chin. J. Chem. **10** (1), 45 (1992).
7. Z.-W. Mao, Polyhedron **12** (12), 1465 (1993).
8. I. F. Burshtein, V. I. Pavlovskii, and A. L. Poznyak, Koord. Khim. **24** (2), 140 (1998).
9. L. M. Shkol'nikova and A. L. Poznyak, Zh. Neorg. Khim. **40** (4), 604 (1995).
10. G. M. Sheldrick, *SHELXS86: Program for the Solution of Crystal Structures* (Univ. of Göttingen, Germany, 1986).
11. G. M. Sheldrick, *SHELXL93: Program for the Refinement of Crystal Structures* (Univ. of Göttingen, Germany, 1993).
12. J. M. Gonzales Perez, J. Niclos Gutierrez, N.-H. Dung, *et al.*, Inorg. Chim. Acta **184** (2), 243 (1991).
13. A. S. Antsyshkina, G. G. Sadikov, V. S. Sergienko, and A. L. Poznyak, Zh. Neorg. Khim. **42** (2), 238 (1997).
14. O. P. Gladkikh, A. L. Poznyak, T. N. Polynova, and M. A. Poraï-Koshits, Zh. Neorg. Khim. **42** (9), 1482 (1997).

Translated by I. Polyakova

STRUCTURE OF ORGANIC COMPOUNDS

Crystal Structure Analysis of Two Terpene Derivatives¹

V. K. Gupta¹, Rajnikant¹, B. Parsad¹, R. K. Thappa², S. G. Agarwal²,
B. Varghese³, and S. Goswami¹

¹ Laboratory of Crystallography, Postgraduate Department of Physics, University of Jammu,
Jammu Tawi, 180006 India

e-mail: vivek_gupta2k2@hotmail.com

² Division of Organic Chemistry, Regional Research Laboratory, Jammu, India

³ Regional Sophisticated Instrumentation Center, Indian Institute of Technology, Chennai, 600036 India

Received October 16, 2003; in final form, April 28, 2004

Abstract—The crystal structures of two terpene derivatives, 2,4,5,6,7,7a-hexahydro-7a-hydroxy-3,6-dimethyl-2-benzofuranone (compound **I**) and β -cyclolavandulic acid (compound **II**), were determined by single-crystal diffraction. Compound **I**, C₁₀H₁₄O₃, crystallizes in the orthorhombic space group $P2_12_12_1$ with the unit cell parameters $a = 6.715(1)$ Å, $b = 7.043(1)$ Å, $c = 20.292(3)$ Å, and $Z = 4$. The six-membered ring has an ideal chair conformation. The five-membered ring is planar. Compound **II**, C₁₀H₁₆O₂, crystallizes in the monoclinic space group $P2_1/n$ with the unit cell parameters $a = 8.446(1)$ Å, $b = 12.156(1)$ Å, $c = 9.901(1)$ Å, $\beta = 106.29(1)^\circ$, and $Z = 4$. The cyclohexene ring exhibits a half-chair conformation. Both the crystal structures are stabilized by intermolecular O–H...O hydrogen bonds. © 2005 Pleiades Publishing, Inc.

INTRODUCTION

The present study of the compounds 2,4,5,6,7,7a-hexahydro-7a-hydroxy-3,6-dimethyl-2-benzofuranone (**I**) and β -cyclolavandulic acid (**II**) is part of a series of investigations on the crystal structures of terpene derivatives [1–4]. Compound **I**, a monoterpenoid, has been isolated from the leaves of *Mentha piperate*. Compound **II**, also a monoterpenoid, has been isolated from the seeds of *Trachyspermum roxburghianum*. *Trachyspermum roxburghianum* fruits commonly known as *Ajmoda* are widely used in the Indian system of medicines for the treatment of various gastrointestinal and other ailments [5–9]. The chemical structures assigned to compounds **I** and **II** on the basis of IR, UV, NMR, and mass spectral data are shown in Fig. 1.

EXPERIMENTAL

The solvent loss technique has been employed for the growth of single crystals of compounds **I** and **II**. For both compounds, three-dimensional X-ray intensity data were collected on an Enraf–Nonius CAD4 diffractometer with CuK α radiation for the values of θ up to 70°. The data were corrected for Lorentz and polarization effects. Absorption and extinction corrections were not applied.

For both compounds structure solution was accomplished by direct methods using the SHELXS86 program [10], the SHELXL93 program used to refine structure [11], molecular graphics ORTEP-3 [12], and

software used to prepare material for publication PARST [13, 14]. In both compounds, all the hydrogen atoms were located from a difference Fourier map. The final refinement cycle converged at $R = 0.031$, $wR(F^2) = 0.092$ for compound **I** and $R = 0.047$, $wR(F^2) = 0.158$ for compound **II**. Atomic scattering factors were taken from *International Tables for X-ray Crystallography* (1992, Vol. C, Tables 4.2.6.8 and 6.1.1.4). The crystallographic data are summarized in Table 1.

RESULTS AND DISCUSSION

For both compounds, the atomic coordinates and equivalent isotropic displacement parameters are presented in Table 2. Selected bond distances, bond angles, and torsion angles are listed in Table 3. Figure 2 shows the molecular structure and the atom-labeling scheme

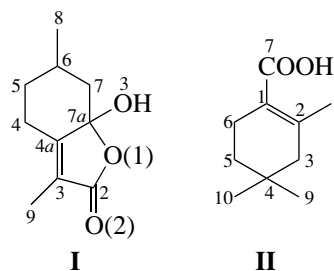


Fig. 1. Chemical structures of 2,4,5,6,7,7a-hexahydro-7a-hydroxy-3,6-dimethyl-2-benzofuranone (**I**) and β -cyclolavandulic acid (**II**).

¹ This article was submitted by the authors in English.

Table 1. Crystal data and other experimental details

| | Compound I | Compound II |
|---|--|---|
| Crystal description | Colorless rectangular | Colorless rhombohedral |
| Chemical formula | C ₁₀ H ₁₄ O ₃ | C ₁₀ H ₁₆ O ₂ |
| Molecular weight | 182.2 | 168.2 |
| Cell parameters | $a = 6.715(1) \text{ \AA}$, $b = 7.043(1) \text{ \AA}$, $c = 20.292(3) \text{ \AA}$ | $a = 8.446(1) \text{ \AA}$, $b = 12.156(1) \text{ \AA}$, $c = 9.901(1) \text{ \AA}$, $\beta = 106.29^\circ$ |
| Unit cell volume, \AA^3 | 959.68 | 975.72 |
| Number of molecules per unit cell, Z | 4 | 4 |
| Crystal system | Orthorhombic | Monoclinic |
| Space group | $P2_12_12_1$ | $P2_1/n$ |
| Density (calculated), Mg/m^3 | 1.261 | 1.145 |
| $F(000)$ | 392 | 368 |
| Refinement of unit cell | 25 reflections ($20^\circ < \theta < 30^\circ$) | 25 reflections ($20^\circ < \theta < 25^\circ$) |
| Number of measured reflections | 1105 | 2121 |
| Number of unique reflections | 1085 | 1843 |
| Number of observed reflections | 1043 [$F_o > 4\sigma(F_o)$] | 1428 [$F_o > 4\sigma(F_o)$] |
| Number of parameters refined | 175 | 173 |
| Final R -factor | 0.031 | 0.047 |
| $wR(F^2)$ | 0.092 | 0.158 |
| Weighting scheme | $1/[\sigma^2(F_o^2) + (0.0621P)^2 + 0.14P]$, where $P = [F_o^2 + 2F_c^2]/3$ | $1/[\sigma^2(F_o^2) + (0.1316P)^2 + 0.06P]$, where $P = [F_o^2 + 2F_c^2]/3$ |
| $GOOF(S)$ | 0.986 | 0.894 |
| Final residual electron density, $e \text{ \AA}^{-3}$ | $-0.12 < \Delta\rho < 0.16$ | $-0.18 < \Delta\rho < 0.16$ |
| $(\Delta/\sigma)_{\text{max}}$ in the final cycle | -0.076 [for $z \text{ H}(3O)$] | 0.409 [for $z \text{ H}(82)$] |

for **I**, and Fig. 3 shows the molecular structure and atom-labeling scheme for **II**.

The geometric parameters of the two molecules **I** and **II** are not very different from the values found in the literature for other terpene derivatives [15–18]. The

C=O and C(sp^3)–C(sp^3) bond lengths in both structures are comparable with the values found in the literature [19].

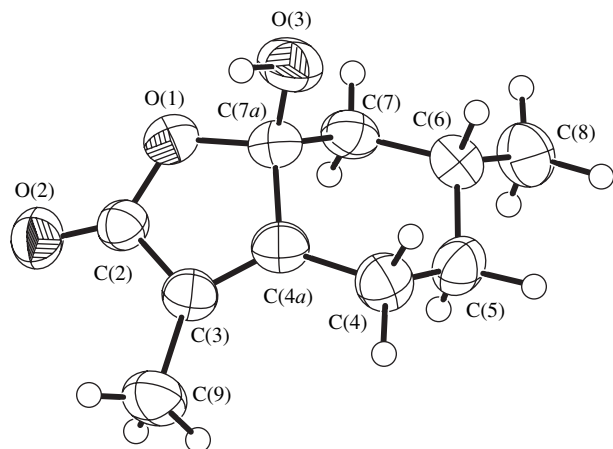


Fig. 2. The molecular structure of **I** with the atom-labeling scheme and 50% probability displacement ellipsoids. H atoms are displayed as small spheres of arbitrary radii.

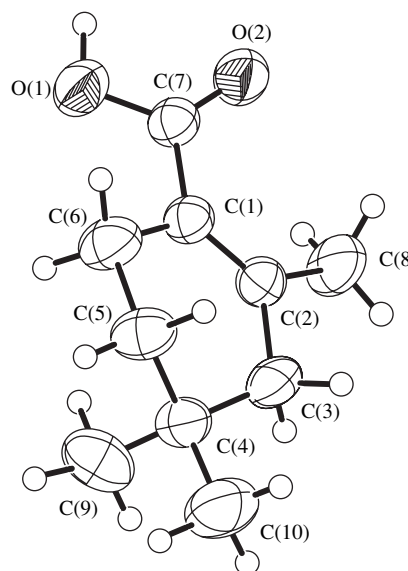


Fig. 3. The molecular structure of **II** with the atom-labeling scheme and 50% probability displacement ellipsoids. H atoms are displayed as small spheres of arbitrary radii.

Table 2. Atomic coordinates and equivalent isotropic thermal parameters (\AA^2) for non-hydrogen atoms (e.s.d.'s are given in parentheses)

| Atom | <i>x</i> | <i>y</i> | <i>z</i> | U_{eq}^* | Atom | <i>x</i> | <i>y</i> | <i>z</i> | U_{eq}^* |
|-------------------|-----------|-----------|-----------|-------------------|--------------------|-----------|-----------|-----------|-------------------|
| Compound I | | | | | Compound II | | | | |
| O(1) | 0.8925(2) | 0.7717(2) | 0.3065(1) | 0.0573(5) | O(1) | 0.2157(2) | 0.5038(1) | 0.0119(1) | 0.0664(5) |
| O(2) | 0.9136(2) | 0.8094(3) | 0.1979(1) | 0.0619(5) | O(2) | 0.0750(1) | 0.5535(1) | 0.1584(1) | 0.0732(6) |
| O(3) | 1.0030(3) | 0.5909(3) | 0.3950(1) | 0.0660(6) | C(1) | 0.3699(2) | 0.5718(1) | 0.2308(1) | 0.0415(4) |
| C(2) | 0.9980(3) | 0.7940(3) | 0.2507(1) | 0.0478(5) | C(2) | 0.3855(2) | 0.6491(1) | 0.3298(2) | 0.0456(5) |
| C(3) | 1.2127(3) | 0.7988(3) | 0.2655(1) | 0.0462(6) | C(3) | 0.5528(2) | 0.6778(2) | 0.4275(2) | 0.0591(6) |
| C(4) | 1.4046(3) | 0.8015(4) | 0.3756(1) | 0.0572(7) | C(4) | 0.7031(2) | 0.6382(1) | 0.3845(2) | 0.0483(5) |
| C(4a) | 1.2321(3) | 0.7818(3) | 0.3302(1) | 0.0451(5) | C(5) | 0.6696(2) | 0.5206(1) | 0.3314(2) | 0.0549(6) |
| C(5) | 1.3616(3) | 0.9627(4) | 0.4239(1) | 0.0572(7) | C(6) | 0.5155(2) | 0.5113(2) | 0.2068(2) | 0.0573(6) |
| C(6) | 1.1620(3) | 0.9415(3) | 0.4594(1) | 0.0511(6) | C(7) | 0.2079(2) | 0.5435(1) | 0.1319(2) | 0.0445(5) |
| C(7a) | 1.0307(3) | 0.7625(3) | 0.3621(1) | 0.0491(6) | C(8) | 0.2480(3) | 0.7154(2) | 0.3569(3) | 0.0710(9) |
| C(7) | 0.9928(3) | 0.9224(3) | 0.4098(1) | 0.0510(6) | C(9) | 0.7341(3) | 0.7119(2) | 0.2704(3) | 0.0715(7) |
| C(8) | 1.1264(4) | 1.1096(3) | 0.5056(1) | 0.0662(8) | C(10) | 0.8546(3) | 0.6391(2) | 0.5131(3) | 0.0750(8) |
| C(9) | 1.3644(4) | 0.8213(5) | 0.2125(1) | 0.0645(8) | | | | | |

$$*U_{\text{eq}} = (1/3) \sum_i \sum_j U_{ij} a_i^* a_j^* a_i a_j.$$

Table 3. Selected bond distances (\AA), bond angles (deg), and torsion angles (deg) for non-hydrogen atoms (e.s.d.'s are given in parentheses)

| Compound I | | | |
|-----------------------|----------|-----------------------|----------|
| O(1)–C(2) | 1.345(3) | C(4)–C(4a) | 1.486(3) |
| O(1)–C(7a) | 1.462(3) | C(7a)–C(7) | 1.507(3) |
| O(2)–C(2) | 1.217(3) | C(4a)–C(7a) | 1.505(3) |
| C(3)–C(4a) | 1.325(3) | | |
| O(3)–C(7a)–C(4a) | 113.8(2) | O(1)–C(7a)–C(4a) | 103.5(1) |
| O(1)–C(7a)–O(3) | 108.9(2) | C(4a)–C(7a)–C(7) | 111.1(2) |
| C(3)–C(4a)–C(4) | 133.0(2) | O(3)–C(7a)–C(7) | 108.5(2) |
| C(4)–C(4a)–C(7a) | 116.2(2) | O(1)–C(7a)–C(7) | 110.8(2) |
| C(3)–C(4a)–C(7a) | 110.2(2) | | |
| C(5)–C(4)–C(4a)–C(7a) | –52.5(2) | C(4a)–C(7a)–C(7)–C(6) | –52.8(2) |
| C(4)–C(5)–C(6)–C(7) | –55.5(2) | C(4a)–C(4)–C(5)–C(6) | 52.8(2) |
| C(5)–C(6)–C(7)–C(7a) | 54.5(2) | C(4)–C(4a)–C(7a)–C(7) | 53.6(2) |
| Compound II | | | |
| O(1)–C(7) | 1.301(2) | O(2)–C(7) | 1.228(2) |
| C(3)–C(4) | 1.526(3) | C(1)–C(2) | 1.337(2) |
| C(1)–C(6) | 1.508(3) | C(1)–C(7) | 1.428(2) |
| C(6)–C(1)–C(7) | 115.2(1) | C(3)–C(4)–C(5) | 107.7(1) |
| C(2)–C(1)–C(7) | 122.0(1) | C(9)–C(4)–C(10) | 109.6(2) |
| C(2)–C(1)–C(6) | 122.8(1) | C(5)–C(4)–C(10) | 109.0(1) |
| C(5)–C(4)–C(9) | 110.5(1) | | |
| C(1)–C(2)–C(3)–C(4) | 15.5(2) | C(4)–C(5)–C(6)–C(1) | –47.2(2) |
| C(2)–C(3)–C(4)–C(5) | –42.8(2) | C(5)–C(6)–C(1)–C(2) | 17.7(2) |
| C(3)–C(4)–C(5)–C(6) | 58.9(2) | C(6)–C(1)–C(2)–C(3) | –1.9(2) |

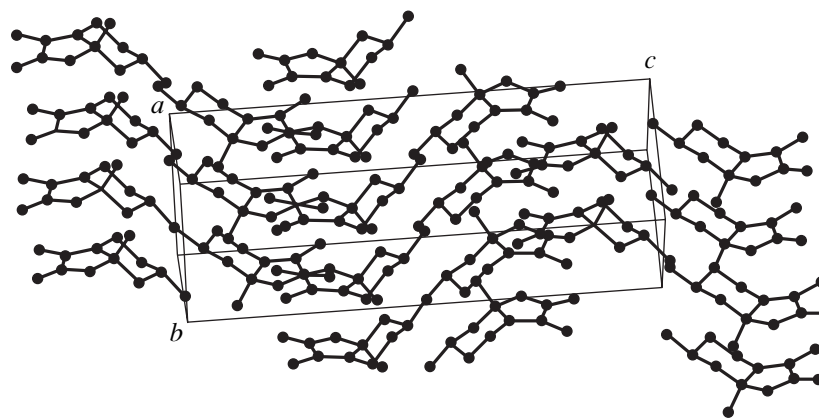


Fig. 4. Molecular packing in the unit cell (compound I).

In compound **I**, the six-membered ring has an ideal chair conformation with the best rotational axis bisecting C(4a)–C(7a) and C(5)–C(6) bonds and with the asymmetry parameter $\Delta C_2(C(4a)–C(7a)) = 1.25$ [20]. The best mirror plane passes through C(4a) and C(6) with $\Delta C_s(C(4a)) = 0.94$. The five-membered ring is planar with a maximum deviation of $-0.005(2)$ Å for C(2). The dihedral angle between the best least-squares planes through five- and six-membered rings is $142.9(1)^\circ$. In compound **II**, the cyclohexene ring exhibits a half-chair conformation in which the C(6)–C(1)–C(2)–C(3) group is planar and the other carbon atoms of the ring (C(4) and C(5)) are displaced on opposite sides of the plane by $0.328(2)$ and $-0.394(2)$ Å, respectively. The rotational axis passes through C(1)–C(2) and C(4)–C(5) bonds with asymmetry parameter $\Delta C_2(C(1)–C(2)) = 3.48$.

In compound **I**, an intermolecular hydrogen bond is observed between O(3) and O(2). The hydrogen-bond geometry is O(3)–H(3O) = 0.846 , H(3O)⋯O(2) =

1.953 , O(3)⋯O(2) = 2.793 Å, and O(3)–H(3O)⋯O(2) = 171.97° , and symmetry code: $2 - x, -0.5 + y, 0.5 - z$. The molecules in the unit cell are forming layers, and each layer is stacked one above the other giving rise to molecular sheets (Fig. 4). In compound **II**, the crystal structure is stabilized by an intermolecular O–H⋯O hydrogen bond [O(1)–H(1O) = 0.998 , H(1O)⋯O(2) = 1.673 , O(1)⋯O(2) = 2.652 Å, and O(1)–H(1O)⋯O(2) = 166.02° , and symmetry code: $-x, 1 - y, -z$]. The molecular layers appear to be extending diagonally in the unit cell (Fig. 5).

REFERENCES

1. V. K. Gupta, Rajnikant, K. N. Goswami, *et al.*, *Cryst. Res. Technol.* **28**, 359 (1993).
2. V. K. Gupta, K. N. Goswami, and K. K. Bhutani, *Cryst. Res. Technol.* **29**, 373 (1994).
3. Rajnikant, V. K. Gupta, A. Singh, *et al.*, *Mol. Mater.* **6**, 227 (1996).
4. Rajnikant, V. K. Gupta, V. D. Rangari, *et al.*, *Cryst. Res. Technol.* **36**, 93 (2001).
5. K. Raghunathan, *Pharmacopoeial Standards of Ayurvedic Formulations* (CCRIMH, New Delhi, 1976), p. 7.
6. *Pharmacopoeial Standards of Ayurvedic Formulations* (Central Council of Research in Ayurveda and Siddha, Ministry of Health and Family Welfare, Govt. of India, New Delhi, 1987), p. 37.
7. Report of the Work Done under the Project Central Scheme to Develop Pharmacopoeial Standards of ISM Drugs at RRL (Jammu, 1998–1999), p. 146.
8. *Wealth of India (Raw Materials): Publication and Information Directorate* (CSIR, New Delhi, 1976), Vol. 10, p. 271.
9. *Ayurvedic Formulary of India* (Govt. of India, Ministry of Family Planning, Dep. of Health, New Delhi, 1978), Part 1.
10. G. M. Sheldrick, *SHELX86. Program for Crystal Structures Determination* (Univ. of Göttingen, Germany, 1986).

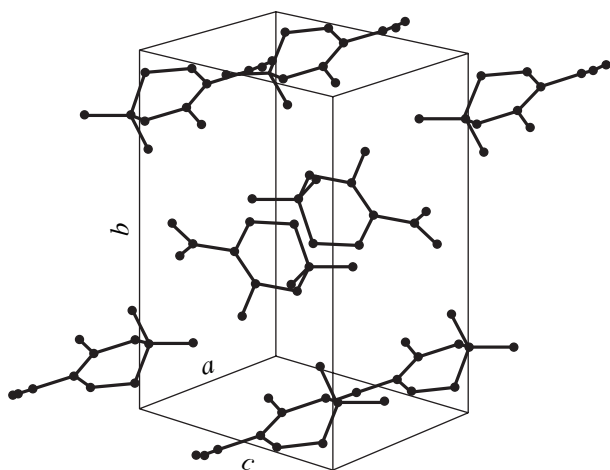


Fig. 5. Molecular packing in the unit cell (compound II).

11. G. M. Sheldrick, *SHELXL93. Program for the Refinement of Crystal Structures* (Univ. of Göttingen, Germany, 1993).
12. L. J. Farrugia, *J. Appl. Crystallogr.* **30**, 565 (1997).
13. M. Nardelli, *Comput. Chem.* **7**, 95 (1983).
14. M. Nardelli, *J. Appl. Crystallogr.* **28**, 659 (1995).
15. E. Diaz, A. F. Benitez, E. V. Villafrance, and C. K. Jankowski, *Acta Crystallogr., Sect. C: Cryst. Struct. Commun.* **50**, 2030 (1994).
16. T. Kiyotani, K. Masuda, H. Ageta, *et al.*, *Acta Crystallogr., Sect. C: Cryst. Struct. Commun.* **52**, 3216 (1996).
17. E. Bunuel, C. Cativiela, M. D. Diaz-de-Villegas, and J. A. Gálvez, *Acta Crystallogr., Sect. C: Cryst. Struct. Commun.* **52**, 1456 (1996).
18. I. K. Larsen and P. Trickey, *Acta Crystallogr., Sect. C: Cryst. Struct. Commun.* **51**, 125 (1995).
19. F. H. Allen, O. Kennard, D. G. Watson, *et al.*, *J. Chem. Soc., Perkin Trans. 2*, S1 (1987).
20. W. L. Duax and D. A. Norton, *Atlas of Steroid Structures* (Plenum, New York, 1975), Vol. 1.

STRUCTURE
OF ORGANIC COMPOUNDS

Electronic Nature of Substituents and the Structure
of 4,4'-Dipyridylum Dications: Crystal Structure
of *N,N'*-Di(2-Carboxyethyl)-4,4'-Dipyridylum Diperchlorate

A. P. Polishchuk, I. Yu. Polishchuk, G. V. Klimusheva, A. V. Gridyakina,
A. B. Bordyug, and L. G. Grineva

Institute of Physics, National Academy of Sciences of Ukraine, pr. Nauki 46, Kiev, 03650 Ukraine
e-mail: polyshchuk@stc.gov.ua

Received January 27, 2003

Abstract—The crystal structure of *N,N'*-di(2-carboxyethyl)-4,4'-dipyridylum diperchlorate, $C_{16}H_{18}Cl_2N_2O_{12}$, is determined using X-ray diffraction analysis at 293 K. The crystals are orthorhombic, $a = 20.084(4)$ Å, $b = 8.687(2)$ Å, $c = 11.725(2)$ Å, space group $Pna2_1$, and $Z = 4$; 1688 reflections measured; and $R = 0.056$ and $R_w = 0.059$ for 1244 reflections with $I > 3\sigma(I)$. It is found that, in the absence of charge transfer or short intramolecular $O\cdots N$ contacts, the nucleus of the dication adopts a twist conformation (the angle of rotation between the planes of the pyridine rings is equal to 23°). © 2005 Pleiades Publishing, Inc.

INTRODUCTION

Quaternary salts of 4,4'-dipyridylum (viologens) exhibit a great variety of physicochemical properties. These compounds are finding ever-widening application in practice as photosensitive materials for displaying and storing information. The photosensitive properties of viologens were discussed in detail in [1–6]. These properties are based on the ability of viologens to generate colored radical cations (for which the absorption spectrum lies in the visible range) under UV radiation or in response to an electric field applied to the cell [7]. However, the problem concerning the correlation between the structure of viologens and the mechanism of the formation of radical cations remains unsolved. It is known that the central nucleus of the radical cation is flattened [8]. It has been established that, in the crystalline state, charge-transfer complexes are characterized by a planar structure of the central dipyridylum fragment of the molecules [1–3]. In the absence of charge-transfer interaction, the dipyridylum skeleton of these molecules adopts a twist conformation, as is observed in *N,N'*-dimethyl-4,4'-dipyridylum tetrachloropalladate ($MD^{2+}PdCl_4^{2-}$) [9] and *N,N'*-diheptyl-4,4'-dipyridylum perchlorate ($HD^{2+}2ClO_4^-$) [1]. However, our recent structural studies of *N,N'*-di(2-dihydroxyethyl)-4,4'-dipyridylum diperchlorate ($HOEtD^{2+}2ClO_4^-$; $R = (CH_2)_2OH$) [5] and *N,N'*-di(carboethoxymethyl)-4,4'-dipyridylum diperchlorate ($CEMeD^{2+}2ClO_4^-$; $R = CH_2COOC_2H_5$) [6] have revealed that the dipyridylum skeleton can have a planar structure even in the absence of charge transfer but upon the formation of a short intramolecular $O\cdots N$ con-

tact due to the interaction between the π system of the dication and the lone electron pair of the oxygen atom involved in either an electron-donating or electron-withdrawing group.

In order to verify the important role played by the above interaction in the flattening of the nucleus of the dication, we performed an X-ray diffraction study of *N,N'*-di(2-carboxyethyl)-4,4'-dipyridylum diperchlorate (**I**) [$R = (CH_2)_2COOH$; $A = ClO_4^-$], which is characterized by both the absence of charge-transfer interaction and the inability of oxygen atoms, which are separated from the nitrogen atoms by three carbon atoms, to form short intramolecular $O\cdots N$ contacts.

EXPERIMENTAL

Compound **I** was synthesized according to the procedure described in [2]. Single crystals were grown through slow evaporation of an isopropanol solution. Transparent single crystals in the form of thin plates were obtained in the course of crystallization. The X-ray experiment was performed on an Enraf–Nonius CAD4 four-circle automated diffractometer (graphite monochromator, $\omega/2\theta$ scan mode) at room temperature.

The structure was solved by direct methods. The non-hydrogen atoms were refined in the anisotropic approximation by the full-matrix least-squares procedure. Unfortunately, we failed to reveal the carboxyl hydrogen atoms objectively because of the poor quality of the single crystals. The positions of all the other H atoms were determined geometrically and included in further refinement with fixed positional and thermal parameters. All the calculations were performed on an IBM AT personal computer with the CRYSTALS pro-

Table 1. Crystal data, data collection, and refinement parameters for the structure of compound **I**

| Parameter | I |
|---|--|
| Empirical formula | C ₁₆ H ₁₈ Cl ₂ N ₂ O ₁₂ |
| Molecular weight | 499.21 |
| Crystal system | Orthorhombic |
| Space group | <i>Pna</i> 2 ₁ |
| <i>Z</i> | 4 |
| <i>a</i> , Å | 20.084(4) |
| <i>b</i> , Å | 8.687(2) |
| <i>c</i> , Å | 11.725(2) |
| α , deg | 90 |
| β , deg | 90 |
| γ , deg | 90 |
| <i>V</i> , Å ³ | 2045.7(7) |
| ρ_{calcd} , g/cm ³ | 1.621 |
| μ , mm ⁻¹ | 0.382 |
| <i>F</i> (000) | 1025 |
| Diffractionmeter | Enraf–Nonius CAD4 |
| λ , Å | 0.71069 |
| <i>T</i> , K | 293 |
| θ_{max} , deg | 24 |
| Number of reflections measured | 1688 |
| Number of reflections with $I > 3\sigma(I)$ | 1244 |
| Refinement on | <i>F</i> |
| <i>R</i> | 0.056 |
| <i>R</i> _w | 0.059 |
| <i>S</i> | 1.1 |

grams [10]. Correction for absorption in the crystal was introduced using the azimuthal scan method [11] ($T_{\text{min}} = 0.65$, $T_{\text{max}} = 0.93$). The five-parametric (1.68, 1.50, 1.59, 0.408, and 0.367) Chebyshev weighting scheme [12] was used in the refinement. The main crystallographic and experimental parameters obtained at room temperature are summarized in Table 1. The atomic coordinates, interatomic distances, and bond angles are listed in Tables 2–4.

RESULTS AND DISCUSSION

In the crystal structure of compound **I**, the molecule occupies a general position with the characteristic arrangement of ClO₄⁻ anions above and below the dipyridylum rings (figure). The structure of molecule **I** differs significantly from those of the viologens studied earlier in [1–3, 5, 6], in which the molecules are located at the centers of symmetry. The latter molecules are characterized by a planar structure of the nucleus of the

Table 2. Coordinates ($\times 10^4$) and isotropic thermal parameters ($\text{\AA}^2 \times 10^3$) of the non-hydrogen atoms in the structure of compound **I**

| Atom | <i>x</i> | <i>y</i> | <i>z</i> | <i>U</i> _{eq} |
|-------|----------|-----------|----------|------------------------|
| Cl(1) | 4315(1) | 7864(3) | 2297(2) | 51(1) |
| Cl(2) | 3202(1) | -1309(3) | 6492(2) | 51(1) |
| O(1) | 3682(3) | 1445(9) | -413(6) | 63(5) |
| O(2) | 4194(3) | -661(8) | -914(6) | 60(4) |
| O(3) | 3190(3) | 6853(9) | 9972(7) | 69(5) |
| O(4) | 3767(3) | 5122(8) | 9040(6) | 57(4) |
| O(5) | 4335(4) | 6876(11) | 1341(7) | 95(7) |
| O(6) | 3941(5) | 9185(11) | 2029(9) | 113(8) |
| O(7) | 4972(4) | 8405(13) | 2505(7) | 99(6) |
| O(8) | 4018(5) | 7144(11) | 3257(7) | 97(6) |
| O(9) | 2606(3) | -1801(9) | 5938(6) | 63(4) |
| O(10) | 3595(4) | -390(10) | 5786(8) | 88(6) |
| O(11) | 3049(4) | -574(16) | 7522(9) | 128(8) |
| O(12) | 3580(4) | -2692(11) | 6740(10) | 103(6) |
| N(1) | 4543(3) | 3074(8) | 1650(6) | 38(4) |
| N(2) | 2993(3) | 3832(8) | 6938(6) | 39(4) |
| C(1) | 3967(4) | 3530(10) | 3747(7) | 40(5) |
| C(2) | 3597(4) | 3590(11) | 2758(7) | 42(5) |
| C(3) | 3888(4) | 3372(11) | 1722(8) | 45(5) |
| C(4) | 4926(4) | 3064(14) | 2606(8) | 56(6) |
| C(5) | 4648(4) | 3272(14) | 3632(8) | 59(4) |
| C(6) | 4866(4) | 2758(12) | 528(7) | 45(5) |
| C(7) | 4826(4) | 1106(11) | 173(7) | 42(5) |
| C(8) | 4167(4) | 0678(11) | -417(7) | 44(5) |
| C(9) | 3646(4) | 3731(11) | 4868(7) | 39(5) |
| C(10) | 3021(4) | 4458(12) | 4989(7) | 45(5) |
| C(11) | 2708(4) | 4478(12) | 6018(8) | 47(5) |
| C(12) | 3603(5) | 3214(11) | 6859(7) | 48(5) |
| C(13) | 3931(4) | 3159(12) | 5855(8) | 53(6) |
| C(14) | 2631(4) | 3798(12) | 8051(8) | 47(5) |
| C(15) | 2607(4) | 5356(12) | 8622(7) | 49(6) |
| C(16) | 3247(4) | 5738(12) | 9226(8) | 47(5) |

dication. In the structure studied, the dication nucleus has a twist conformation, with the angle of rotation between the planes of the pyridine rings being equal to 23° (the atomic deviations from the planes are within 0.02 Å). At the same time, despite the conformational changes, the bond lengths (Table 3) and angles (Table 4) in the dipyridylum skeleton of molecule **I** actually coincide with the corresponding values obtained for the planar molecules. In compound **I**, similar to the compounds HOEtD²⁺2ClO₄⁻ [5] and CEMeD²⁺2ClO₄⁻ [6], the dication has an S-shaped

Table 3. Bond lengths (Å) in the structure of compound **I**

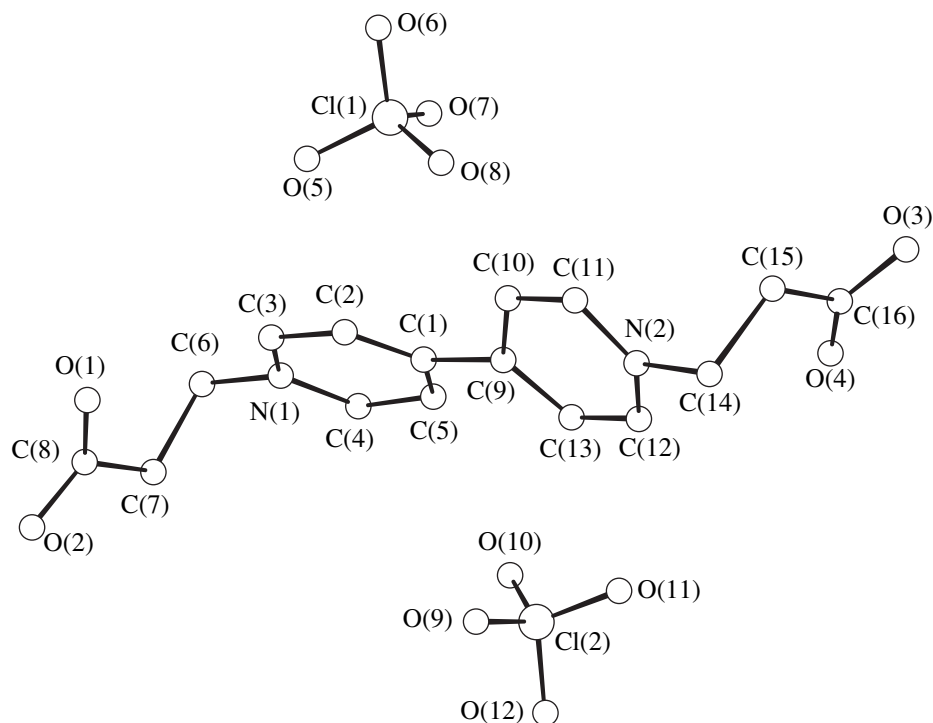
| Bond | <i>d</i> | Bond | <i>d</i> |
|-------------|-----------|-------------|-----------|
| Cl(1)–O(5) | 1.413(8) | N(2)–C(12) | 1.341(11) |
| Cl(1)–O(6) | 1.406(9) | N(2)–C(14) | 1.492(12) |
| Cl(1)–O(7) | 1.422(7) | C(1)–C(2) | 1.378(12) |
| Cl(1)–O(8) | 1.419(9) | C(1)–C(5) | 1.394(12) |
| Cl(2)–O(9) | 1.428(6) | C(1)–C(9) | 1.474(12) |
| Cl(2)–O(10) | 1.397(8) | C(2)–C(3) | 1.362(12) |
| Cl(2)–O(11) | 1.400(9) | C(4)–C(5) | 1.339(14) |
| Cl(2)–O(12) | 1.450(9) | C(6)–C(7) | 1.496(14) |
| O(1)–C(8) | 1.18(1) | C(7)–C(8) | 1.538(12) |
| O(2)–C(8) | 1.301(11) | C(9)–C(10) | 1.411(12) |
| O(3)–C(16) | 1.311(11) | C(9)–C(13) | 1.383(13) |
| O(4)–C(16) | 1.19(1) | C(10)–C(11) | 1.362(13) |
| N(1)–C(3) | 1.34(1) | C(12)–C(13) | 1.350(13) |
| N(1)–C(4) | 1.360(11) | C(14)–C(15) | 1.511(15) |
| N(1)–C(6) | 1.491(12) | C(15)–C(16) | 1.504(12) |
| N(2)–C(11) | 1.343(11) | | |

Table 4. Bond angles (deg) in the structure of compound **I**

| Angle | ω | Angle | ω |
|-------------------|----------|-------------------|----------|
| O(5)–Cl(1)–O(6) | 109.5(7) | C(1)–C(2)–C(3) | 120.9(8) |
| O(5)–Cl(1)–O(7) | 108.0(5) | N(1)–C(3)–C(2) | 120.3(7) |
| O(6)–Cl(1)–O(7) | 105.3(7) | N(1)–C(4)–C(5) | 120.2(8) |
| O(5)–Cl(1)–O(8) | 112.0(6) | C(1)–C(5)–C(4) | 121.2(8) |
| O(6)–Cl(1)–O(8) | 108.2(6) | N(1)–C(6)–C(7) | 113.5(7) |
| O(7)–Cl(1)–O(8) | 113.6(6) | C(6)–C(7)–C(8) | 113.8(7) |
| O(9)–Cl(2)–O(10) | 112.1(5) | O(1)–C(8)–O(2) | 122.7(8) |
| O(9)–Cl(2)–O(11) | 110.2(4) | O(1)–C(8)–C(7) | 124.8(9) |
| O(10)–Cl(2)–O(11) | 111.9(7) | O(2)–C(8)–C(7) | 112.5(8) |
| O(9)–Cl(2)–O(12) | 106.4(5) | C(1)–C(9)–C(10) | 122.0(7) |
| O(10)–Cl(2)–O(12) | 107.4(5) | C(1)–C(9)–C(13) | 121.6(8) |
| O(11)–Cl(2)–O(12) | 108.7(8) | C(10)–C(9)–C(13) | 116.4(8) |
| C(3)–N(1)–C(4) | 120.2(8) | C(9)–C(10)–C(11) | 120.3(8) |
| C(3)–N(1)–C(6) | 121.1(7) | N(2)–C(11)–C(10) | 120.7(8) |
| C(4)–N(1)–C(6) | 118.7(6) | N(2)–C(12)–C(13) | 121.3(8) |
| C(11)–N(2)–C(12) | 120.0(8) | C(9)–C(13)–C(12) | 121.0(8) |
| C(11)–N(2)–C(14) | 120.2(7) | N(2)–C(14)–C(15) | 112.6(7) |
| C(12)–N(2)–C(14) | 119.8(7) | C(14)–C(15)–C(16) | 112.3(8) |
| C(2)–C(1)–C(5) | 117.0(8) | O(3)–C(16)–O(4) | 122.0(8) |
| C(2)–C(1)–C(9) | 120.7(7) | O(3)–C(16)–C(15) | 113.7(8) |
| C(5)–C(1)–C(9) | 122.3(7) | O(4)–C(16)–C(15) | 124.2(9) |

structure (figure). In this case, however, the shortest intramolecular distance between the oxygen atoms of the carbonyl groups and the nitrogen atoms [O(1)⋯N(1), 3.293 Å; O(4)⋯N(2), 3.122 Å] is substantially larger than the intramolecular O⋯N contacts equal to 2.847 Å in HOEtD²⁺2ClO₄⁻ [5] and 2.780 Å in CEMeD²⁺2ClO₄⁻ [6]. This suggests that the lone elec-

tron pairs of the carbonyl groups in **I** do not interact with the electron-deficient π system of the pyridine

Structure of molecule **I** and the atomic numbering.

rings. Taking into account that compound **I** is characterized by the absence of charge transfer from the counterion (ClO_4^-) to the cation, the electronic effects on the structure of the dipyridylium nucleus can be considered to be insignificant. In this case, the twist conformation, which corresponds to the minimum conformational energy, is favored by the central part of the dication.

CONCLUSION

Thus, the X-ray diffraction study of compound **I**, which does not exhibit charge transfer or short O...N intramolecular contacts, showed that the nucleus of the dication has a twist conformation (the angle of rotation between the planes of the pyridine rings is equal to 23°). These data confirm the assumption that, in the crystals studied earlier ($\text{HOEtD}^{2+}2\text{ClO}_4^-$; $R = (\text{CH}_2)_2\text{OH}$ [5] and $\text{CEMeD}^{2+}2\text{ClO}_4^-$; $R = \text{CH}_2\text{COOC}_2\text{H}_5$ [6]), the electronic effects due to the O...N intramolecular contacts actually play a crucial role in the stabilization of the planar dipyridylium nucleus in these molecules.

REFERENCES

1. I. Yu. Polishchuk, L. G. Grineva, A. P. Polishchuk, and A. N. Chernega, *Zh. Obshch. Khim.* **66** (9), 1530 (1996).
2. I. Yu. Polishchuk, L. G. Grineva, A. P. Polishchuk, and A. N. Chernega, *Zh. Obshch. Khim.* **67** (11), 1893 (1997).
3. I. Yu. Polishchuk, L. G. Grineva, A. P. Polishchuk, and A. N. Chernega, *Zh. Obshch. Khim.* **68** (4), 647 (1998).
4. A. G. Iljin, G. V. Klimusheva, L. P. Yatsenko, *et al.*, *Proc. SPIE* **3488**, 16 (1998).
5. A. Yu. Vishnyakov, A. P. Polishchuk, I. Yu. Polishchuk, and L. G. Grineva, *Kristallografiya* **46** (3), 448 (2001) [*Crystallogr. Rep.* **46**, 398 (2001)].
6. A. Yu. Vishnyakov, A. P. Polishchuk, and I. Yu. Polishchuk, *Kristallografiya* **46** (6), 1049 (2001) [*Crystallogr. Rep.* **46**, 967 (2001)].
7. A. V. Vannikov and A. D. Grishina, in *Photochemistry of Polymeric Donor-Acceptor Complexes* (Nauka, Moscow, 1984) [in Russian].
8. T. M. Bokman and J. K. Kochi, *J. Org. Chem.* **55** (22), 4127 (1990).
9. C. K. Prout and P. Murrau-Rust, *J. Chem. Soc. A*, No. 10, 1520 (1969).
10. D. J. Watkin, C. K. Prout, J. R. Carruthers, and P. W. Betteridge, *CRYSTALS* (Chemical Crystallography Laboratory, Univ. of Oxford, 1996), Issue 10.
11. A. C. T. North, D. C. Phillips, F. Scott, and F. S. Mathews, *Acta Crystallogr., Sect. A: Cryst. Phys., Diffr., Theor. Gen. Crystallogr.* **24**, 351 (1968).
12. J. R. Carruthers and D. J. Watkin, *Acta Crystallogr., Sect. A: Cryst. Phys., Diffr., Theor. Gen. Crystallogr.* **35**, 698 (1979).

Translated by I. Polyakova

STRUCTURE OF ORGANIC COMPOUNDS

X-ray Crystallography of Cholest-3,5-Diene-7-One¹

Rajnikant*, Dinesh*, Anshu Sawhney*, Mousmi*, and Shafiullah**

* Condensed Matter Physics Group, Post Graduate Department of Physics,
University of Jammu, Jammu Tawi, 180006 India

e-mail: rkantverma@rediffmail.com

** Department of Chemistry, Aligarh Muslim University, Aligarh, India

Received October 3, 2003

Abstract—The molecular structure of cholest-3,5-diene-7-one (C₂₇H₄₂O) is determined by X-ray diffraction. The compound crystallizes in the orthorhombic crystal system (space group $P2_12_12_1$) with unit cell parameters $a = 11.281(5)$ Å, $b = 11.350(5)$ Å, $c = 18.518(5)$ Å, and $Z = 4$. The structure is solved by direct methods and refined to an R -value of 0.054 for 1070 observed reflections [$F_o > 4\sigma(F_o)$]. Ring A adopts a distorted half-chair conformation, ring B exists in sofa conformation, ring C acquires a chair conformation, and the five-membered ring D occurs in distorted half-chair conformation. The crystal structure is stabilized by van der Waals forces.
© 2005 Pleiades Publishing, Inc.

INTRODUCTION

Steroids perform some of the most fundamental biological functions. They are known to have multifaceted biological properties [1–3]. In continuation of our work on the single-crystal growth of X-ray diffraction quality crystals and crystallographic analysis of steroidal molecules [4–10], the crystal structure of cholest-3,5-diene-7-one is reported in this paper.

EXPERIMENTAL

The scheme of preparation for the title compound is as follows.

A solution of *t*-butyl chromate [*t*-butyl alcohol (60 ml), CrO₃ (30 g), acetic acid (84 ml), and acetic anhydride (10 ml)] was added at 0°C to a solution of cholest-5-ene (8 g, 21.62 mmol) in CCl₄ (150 ml), acetic acid (30 ml), and acetic anhydride (10 ml). The contents were refluxed for 3 h; then they were diluted with water, and the organic layer was washed with a NaHCO₃ solution (15%), water, and dried Na₂SO₄. Evaporation of the solvent under reduced pressure provided cholest-3,5-diene-7-one as an oil, which was crystallized from methanol. The solvent loss technique was then employed for the growth of transparent plate-shaped crystals (m.p. = 403 K) using acetone as the solvent system. The chemical structure, as shown in Fig. 1, has been assigned on the basis of IR, UV, NMR, and mass spectral data [11].

Three-dimensional crystal intensity data of cholest-3,5-diene-7-one were obtained from a computer-controlled single-crystal X-ray diffractometer (CAD4) [12] using MoK_α radiation ($\lambda = 0.71073$ Å), and the ω - 2θ scan mode was employed for data collection. The unit

cell parameters were refined from 25 accurately determined reflections in the range 5.54° to 13.34°. The cell measurement was carried out at 293(2) K and CAD4 programs were used for cell refinement. A total number of 2361 reflections were recorded in the θ range from 2.10° to 24.97°. From the number of reflections recorded, 2361 were found to be unique (with the index range $0 \leq h \leq 13$, $0 \leq k \leq 13$, $0 \leq l \leq 22$) and 1070 were treated as observed [$F_o > 4\sigma(F_o)$]. Two standard reflections (0 $\bar{1}$ 9 and 0 1 9) were monitored every 100 reflections to check for crystal deterioration, if any, during beam exposure to the sample. The data were corrected for Lorentz and polarization effects. The crystallographic data are listed in Table 1.

Direct methods have been employed for the structure determination by using SHELXS software [13]. All non-hydrogen atoms of the molecule were obtained from the E map. Refinement of the structure was carried out by the full-matrix least-squares method using the SHELXL93 program [14]. All the non-hydrogen atoms were refined anisotropically. The hydrogen atoms were fixed stereochemically. Further refinement converged the final R -factor to 0.054.

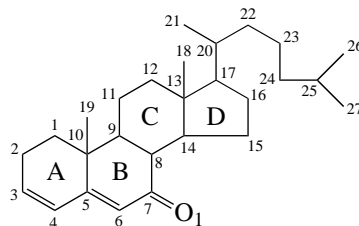


Fig. 1. Chemical structure of cholest-3,5-diene-7-one.

¹ This article was submitted by the authors in English.

Table 1. Crystal data and structure refinement details

| | |
|-------------------------------------|---|
| Crystal description | Transparent rectangular plates |
| Chemical formula | $C_{27}H_{42}O$ |
| Molecular weight | 382.63 |
| Crystal system, space group | Orthorhombic, $P2_12_12_1$ |
| Unit cell dimensions | $a = 11.281(5) \text{ \AA}$, $b = 11.350(5) \text{ \AA}$, $c = 18.518(5) \text{ \AA}$ |
| Volume | $2371.0(16) \text{ \AA}^3$ |
| Z, calculated density | 4, 1.077 Mg/m^3 |
| Radiation, wavelength (λ) | MoK_{α} , 0.71073 \AA |
| $F(000)$ | 848 |
| Crystal size | $0.30 \times 0.25 \times 0.20 \text{ mm}$ |
| Range θ for data collection | 2.10° – 24.97° |
| Limiting indices | $0 \leq h \leq 13$, $0 \leq k \leq 13$, $0 \leq l \leq 22$ |
| Reflections collected/unique | 2361/2361 |
| Data/restraints/parameters | 2361/2/254 |
| Goodness-of-fit on F^2 | 0.847 |
| Final R -factors | $R_1 = 0.054$, $wR_2 = 0.133$ |
| Largest diff. peak and hole | $-0.11 < \Delta\rho < 0.23 \text{ e \AA}^{-3}$ |

RESULTS AND DISCUSSION

The final positional and equivalent isotropic displacement parameters for all the non-hydrogen atoms are listed in Table 2. Bond distances and bond angles are presented in Table 3. A general view of the molecule in the atomic numbering scheme (thermal ellipsoids are drawn at 50% probability) is shown in Fig. 2 [15].

Bond distances and angles are in good agreement with some analogous structures [4, 9, 16–20] for the values in which the atoms C(2), C(3), C(13), C(17), C(20), C(22), C(23) were involved. The disagreement between some of the bond distances and angles of the present structure with its analogues could be due to the difference in the nature and position of substituents. The mean bond lengths, $C(sp^3)–C(sp^3) = 1.535(7) \text{ \AA}$, $C(sp^3)–C(sp^2) = 1.515(8) \text{ \AA}$, $C(sp^2)–C(sp^2) = 1.357(9) \text{ \AA}$, and $C(sp^2)=O = 1.240(7) \text{ \AA}$, are also quite close to the

standard values [21, 22]. The double bond character of C(3)=C(4) and C(5)=C(6) are confirmed by their distances of $1.317(10)$ and $1.332(8) \text{ \AA}$, respectively. The endocyclic bond angles in the steroid nucleus fall in the range from $105.3(4)^\circ$ to $126.6(5)^\circ$ [the average value being $114.4(7)^\circ$] for the six-membered rings and from $100.9(3)^\circ$ to $107.7(4)^\circ$ [the average value being $103.9(4)^\circ$] for the five-membered ring.

The ring *A* adopts a distorted half-chair conformation with the asymmetry parameter $\Delta C_2 = 9.32$ [23]. Ring *B* acquires a sofa conformation with $\Delta C_s = 3.45$. Ring *C* occupies a chair conformation with $\Delta C_2 = 4.85$ and $\Delta C_s = 1.21$ [23]. The five-membered ring *D* occurs in a distorted half-chair conformation with asymmetry parameter $\Delta C_2 = 7.03$, phase angle of pseudorotation $\Delta = -4.23^\circ$, and maximum angle of torsion $\phi_m = -45.3^\circ$ [24]. The methyl carbon C(18) is largely deviated below the mean plane of rings *C* and *D* [the deviation

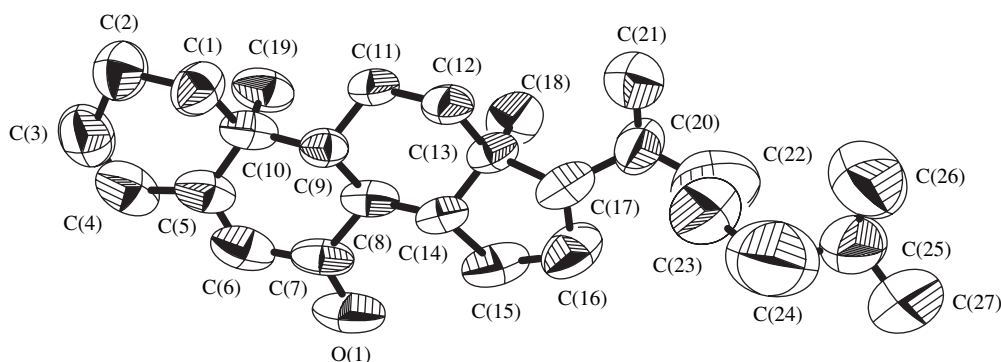
**Fig. 2.** General view of cholest-3,5-diene-7-one.

Table 2. Atomic coordinates and equivalent isotropic thermal parameters (\AA^2) for non-hydrogen atoms (e.s.d.'s are given in parentheses)

| Atom | <i>X</i> | <i>Y</i> | <i>Z</i> | U_{eq} |
|-------|------------|------------|------------|-----------------|
| O(1) | 0.7075(3) | 0.4686(3) | 0.1861(2) | 0.123(1) |
| C(1) | 0.6873(6) | 0.8646(4) | 0.3579(2) | 0.099(2) |
| C(2) | 0.6933(6) | 0.8590(5) | 0.4406(3) | 0.121(2) |
| C(3) | 0.7487(6) | 0.7353(8) | 0.4605(3) | 0.135(2) |
| C(4) | 0.7544(6) | 0.6473(6) | 0.4142(4) | 0.122(2) |
| C(5) | 0.7067(5) | 0.6500(4) | 0.3440(3) | 0.087(2) |
| C(6) | 0.7252(5) | 0.5615(5) | 0.2965(4) | 0.097(2) |
| C(7) | 0.6834(4) | 0.5555(4) | 0.2240(4) | 0.083(2) |
| C(8) | 0.6092(4) | 0.6569(3) | 0.1964(3) | 0.073(1) |
| C(9) | 0.6375(4) | 0.7692(3) | 0.2384(2) | 0.066(1) |
| C(10) | 0.6325(4) | 0.7541(4) | 0.3205(3) | 0.081(1) |
| C(11) | 0.5666(5) | 0.8741(4) | 0.2089(2) | 0.083(1) |
| C(12) | 0.5712(5) | 0.8886(3) | 0.1278(2) | 0.082(2) |
| C(13) | 0.5361(4) | 0.7762(4) | 0.0893(2) | 0.068(1) |
| C(14) | 0.6168(4) | 0.6761(3) | 0.1151(2) | 0.071(1) |
| C(15) | 0.5939(5) | 0.5767(4) | 0.0621(3) | 0.105(2) |
| C(16) | 0.5713(6) | 0.6385(4) | -0.0099(3) | 0.119(2) |
| C(17) | 0.5607(5) | 0.7737(4) | 0.0052(3) | 0.088(2) |
| C(18) | 0.4041(4) | 0.7504(5) | 0.1033(3) | 0.107(2) |
| C(19) | 0.5034(4) | 0.7371(5) | 0.3479(3) | 0.100(2) |
| C(20) | 0.4765(6) | 0.8322(5) | -0.0457(3) | 0.111(2) |
| C(21) | 0.4646(6) | 0.9644(5) | -0.0325(3) | 0.134(2) |
| C(22) | 0.4925(10) | 0.8121(8) | -0.1314(5) | 0.212(4) |
| C(23) | 0.6044(9) | 0.8496(9) | -0.1505(5) | 0.181(3) |
| C(24) | 0.6395(10) | 0.8225(10) | -0.2288(6) | 0.245(5) |
| C(25) | 0.5812(8) | 0.8516(7) | -0.2919(4) | 0.148(3) |
| C(26) | 0.5647(9) | 0.9829(8) | -0.2937(5) | 0.200(4) |
| C(27) | 0.6215(9) | 0.7958(8) | -0.3562(5) | 0.217(4) |

being $-1.763(5)$ \AA], and the methyl carbon C(19) is deviated above the mean plane of rings *A* and *B* [the deviation being $0.771(5)$ \AA]. Atoms C(18) and C(19) deviate unidirectionally from the mean *ABCD* plane. This is depicted in Figs. 2 and 3, respectively. The *A/B* ring junction is *quasi-trans*, while *B/C* and *C/D* are *trans*-fused. In view of the nonexistence of any substitution at rings *A*, *B*, and *C*, the magnitude of dihedral angles between the plane of rings *A* and *B*, *B* and *C*, and *C* and *D* is not very large. However, the chain of C_8H_{17} atoms at the C(17) position of the five-membered ring normally does not interfere in the conformation of this ring. It is because the group of atoms at C(17) is

Table 3. Bond distances (\AA) and bond angles (deg) for non-hydrogen atoms (e.s.d.'s are given in parentheses)

| | | | |
|------------------|----------|-------------------|-----------|
| C(1)–C(2) | 1.534(6) | C(12)–C(13) | 1.513(5) |
| C(1)–C(10) | 1.561(6) | C(13)–C(14) | 1.533(5) |
| C(2)–C(3) | 1.580(8) | C(13)–C(18) | 1.539(6) |
| C(3)–C(4) | 1.318(8) | C(13)–C(17) | 1.581(6) |
| C(4)–C(5) | 1.406(7) | C(14)–C(15) | 1.517(6) |
| C(5)–C(6) | 1.352(6) | C(15)–C(16) | 1.529(7) |
| C(5)–C(10) | 1.512(6) | C(16)–C(17) | 1.564(7) |
| C(6)–C(7) | 1.424(7) | C(17)–C(20) | 1.494(7) |
| C(7)–O(1) | 1.241(5) | C(20)–C(21) | 1.526(6) |
| C(7)–C(8) | 1.512(6) | C(20)–C(22) | 1.615(7) |
| C(8)–C(14) | 1.524(6) | C(22)–C(23) | 1.378(10) |
| C(8)–C(9) | 1.527(5) | C(23)–C(24) | 1.533(8) |
| C(9)–C(10) | 1.531(6) | C(24)–C(25) | 1.381(9) |
| C(9)–C(11) | 1.535(5) | C(25)–C(27) | 1.425(9) |
| C(10)–C(19) | 1.553(6) | C(25)–C(26) | 1.502(10) |
| C(11)–C(12) | 1.512(5) | | |
| C(2)–C(1)–C(10) | 115.3(4) | C(11)–C(12)–C(13) | 111.6(4) |
| C(1)–C(2)–C(3) | 106.7(5) | C(12)–C(13)–C(14) | 108.8(3) |
| C(4)–C(3)–C(2) | 122.8(5) | C(12)–C(13)–C(18) | 109.5(4) |
| C(3)–C(4)–C(5) | 124.5(6) | C(14)–C(13)–C(18) | 112.4(4) |
| C(6)–C(5)–C(4) | 121.7(5) | C(12)–C(13)–C(17) | 115.7(4) |
| C(6)–C(5)–C(10) | 118.6(5) | C(14)–C(13)–C(17) | 100.9(4) |
| C(4)–C(5)–C(10) | 119.7(5) | C(18)–C(13)–C(17) | 109.4(4) |
| C(5)–C(6)–C(7) | 126.7(5) | C(15)–C(14)–C(8) | 121.5(4) |
| O(1)–C(7)–C(6) | 119.9(5) | C(15)–C(14)–C(13) | 104.4(4) |
| O(1)–C(7)–C(8) | 122.3(6) | C(8)–C(14)–C(13) | 112.4(3) |
| C(6)–C(7)–C(8) | 117.8(5) | C(14)–C(15)–C(16) | 104.5(4) |
| C(7)–C(8)–C(14) | 114.3(4) | C(15)–C(16)–C(17) | 107.9(4) |
| C(7)–C(8)–C(9) | 110.3(4) | C(20)–C(17)–C(16) | 111.8(5) |
| C(14)–C(8)–C(9) | 111.8(3) | C(20)–C(17)–C(13) | 120.0(4) |
| C(8)–C(9)–C(10) | 113.9(3) | C(16)–C(17)–C(13) | 102.0(4) |
| C(8)–C(9)–C(11) | 111.0(3) | C(17)–C(20)–C(21) | 113.1(5) |
| C(10)–C(9)–C(11) | 114.9(4) | C(17)–C(20)–C(22) | 119.1(6) |
| C(5)–C(10)–C(9) | 110.7(4) | C(21)–C(20)–C(22) | 107.8(6) |
| C(5)–C(10)–C(19) | 109.2(4) | C(23)–C(22)–C(20) | 108.1(8) |
| C(9)–C(10)–C(19) | 111.9(4) | C(22)–C(23)–C(24) | 114.7(8) |
| C(5)–C(10)–C(1) | 106.2(4) | C(25)–C(24)–C(23) | 128.9(9) |
| C(9)–C(10)–C(1) | 109.7(4) | C(24)–C(25)–C(27) | 116.7(8) |
| C(19)–C(10)–C(1) | 109.0(4) | C(24)–C(25)–C(26) | 108.4(8) |
| C(12)–C(11)–C(9) | 114.8(4) | C(27)–C(25)–C(26) | 117.5(8) |

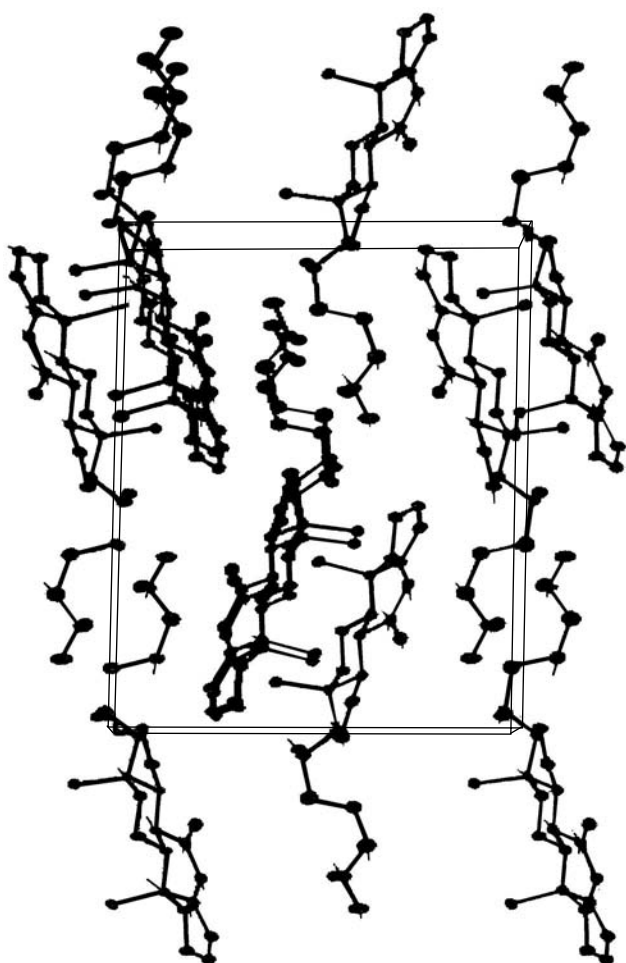


Fig. 3. Unit-cell molecular packing.

arranged in such a way that the atomic deviations of individual atoms provide some kind of balance to the chain. The free rotation of methyl groups, i.e., C(26) and C(27), could also have some kind of steric hindrances from the neighboring molecules, which may allow the C_8H_{17} chain to have a linear kind of character.

The packing of the molecules in the unit cell is shown in Fig. 3. The molecules in the unit cell have been plotted down the b axis, and they appear to exist in reversed orientations. The ring conformations as demonstrated by individual ring systems are quite distinctively depicted in the molecular packing. The crystal structure is stabilized by van der Waals interactions.

ACKNOWLEDGMENTS

The corresponding author (Rajnikant) is grateful to the Council of Scientific and Industrial Research, New

Delhi, for the financial support under Project no. 03(0927)/01/EMR-II.

REFERENCES

1. H. G. Williams-Ashman and A. H. Reddi, *Annu. Rev. Physiol.* **33**, 31 (1971).
2. E. V. Jensen and E. R. Desombre, *Annu. Rev. Biochem.* **41**, 203 (1972).
3. W. L. Duax, C. M. Weeks, and D. C. Roherer, *Topics of Stereochemistry*, Ed. by N. L. Allinger and E. L. Eliel (Wiley, New York, 1976), Vol. 9, p. 271.
4. A. Singh, V. K. Gupta, K. N. Goswami, *et al.*, *Mol. Mater.* **6**, 53 (1996).
5. Rajnikant, V. K. Gupta, J. Firoz, *et al.*, *Crystallogr. Rep.* **45**, 785 (2000).
6. Rajnikant, V. K. Gupta, J. Firoz, *et al.*, *Crystallogr. Rep.* **45** (5), 785 (2000).
7. Rajnikant, V. K. Gupta, J. Firoz, *et al.*, *Cryst. Res. Technol.* **2**, 215 (2001).
8. Rajnikant, V. K. Gupta, J. Firoz, *et al.*, *Cryst. Res. Technol.* **4** (5), 471 (2001).
9. Rajnikant, V. K. Gupta, E. H. Khan, *et al.*, *J. Chem. Crystallogr.* **32** (9), 325 (2002).
10. Rajnikant, Dinesh, Anshu, and Mousmi, *Cryst. Res. Technol.* **39** (4), 353 (2004).
11. Shafiullah, private communication (Aligarh Muslim Univ., Aligarh, 2003).
12. *Enraf-Nonius CAD4 Software. Version 5.0* (Enraf-Nonius, Delft, the Netherlands, 1989).
13. G. M. Sheldrick, *SHELXS86: Program for the Solution of Crystal Structures* (Univ. of Göttingen, Germany, 1986).
14. G. M. Sheldrick, *SHELXL93: Program for the Refinement of Crystal Structures* (Univ. of Göttingen, Germany, 1993).
15. L. J. Farrugia, *J. Appl. Crystallogr.* **30**, 565 (1997).
16. V. K. Gupta, Rajnikant, K. N. Goswami, and K. K. Bhutani, *Cryst. Res. Technol. A* **29**, 77 (1994).
17. V. K. Gupta, K. N. Goswami, K. K. Bhutani, and R. M. Vaid, *Mol. Mater. B* **4**, 303 (1994).
18. V. K. Gupta, Rajnikant, and K. N. Goswami, *Acta Crystallogr., Sect. C: Cryst. Struct. Commun.* **50**, 798 (1994).
19. A. Singh, V. K. Gupta, Rajnikant, and K. N. Goswami, *Cryst. Res. Technol. A* **29**, 837 (1994).
20. A. Singh, V. K. Gupta, Rajnikant, *et al.*, *Mol. Mater. B* **4**, 295 (1994).
21. L. E. Sutton, *Tables of Interatomic Distances and Configuration in Molecules and Ions* (Chemical Society, London, 1965), Special Publ. No. 18.
22. L. S. Bartell and R. A. J. Bonham, *J. Chem. Phys.* **32**, 824 (1960).
23. W. L. Duax and D. A. Norton, *Atlas of Steroid Structure* (Plenum, New York, 1975), p. 1.
24. C. Altona, H. J. Geise, and C. Romers, *Tetrahedron* **24**, 13 (1968).

REAL STRUCTURE OF CRYSTALS

Modeling of Layered Structures with Stacking Faults

V. A. Popenko

Research Institute, NPO Luch, Podolsk, Moscow oblast, 142116 Russia

e-mail: Lutch@Lotsia.com

Received February 9, 2004

Abstract—A method for modeling unit cells of layered structures containing stacking faults is considered by the example of silicon carbide. A rotating-crystal pattern is calculated by the proposed method for silicon carbide with pseudorandom violation of the sequence of close-packed layers. The results of the calculation show that the intensity and shape of reflections of an X-ray diffraction pattern of a layered structure is determined by the configuration of stacking faults. © 2005 Pleiades Publishing, Inc.

INTRODUCTION

Methods of computer simulation now find increasing application in X-ray diffraction analysis because they make it possible to simplify the interpretation and identification of X-ray diffraction patterns of materials studied. Varying the lattice parameters, one can calculate the diffraction pattern and directly trace changes in the diffraction spectrum. For most known inorganic materials, the unit cell contains from 10 to 100 atoms and completely identifies the lattice of an ideal crystal. Stacking faults change the lattice symmetry and make it impossible to calculate diffraction patterns based on the unit cell of an ideal structure. Since an individual crystallite about $0.1 \mu\text{m}$ in size contains no less than 10^9 atoms, it will hardly be possible to directly calculate the X-ray diffraction pattern of such a three-dimensional structure in the nearest future. Analytical calculation of diffraction effects in layered structures with stacking faults [1, 2] does not give a complete description of changes in the X-ray diffraction pattern. Nevertheless, the high operating speed of modern personal computers allows one to calculate X-ray diffraction patterns of such structures using a unit cell comparable in size with a real crystal. In what follows, we consider a method for calculating the coordinates of the basis atoms in the unit cell and the rotating-crystal diffraction pattern for crystal lattices with different configurations of stacking faults by the example of silicon carbide.

MODEL OF A UNIT CELL WITH STACKING FAULTS

In the crystal structure of SiC-type materials, a change in the stacking order of atomic layers leads to the occurrence of many polytype forms and is often accompanied by the formation of stacking faults, which impede interpretation of X-ray diffraction patterns. Presently, more than 100 SiC polytypes are known, whose crystal structures differ by the sequence of dou-

ble close-packed layers of Si and C atoms. The coordination polyhedron for all polytypes is a SiC_4 tetrahedron, at the center of which a Si atom is located.

The layers of tetrahedra can be arranged with respect to each other in two different ways: *a* and *b* (Fig. 1). Any polytype can be represented as a sequence of layers of such tetrahedra. In the case of the parallel packing of tetrahedra, the sequence of Si–C layers *aaaaa...* forms a cubic lattice. The sequence of the second type—*abab...*—corresponds to the hexagonal packing. This notation of the stacking order of layers, proposed by Wells in 1955, is most convenient for modeling a crystal structure with stacking faults, in contrast to the widely used notation proposed by Ramsdell in 1947.

The numerical values of the atomic coordinates in the *x*, *y*, *z* basis are determined by the type of packing (cubic or hexagonal) of close-packed Si–C layers. In the hexagonal coordinate system, with cubic packing of layers, the first layer is displaced with respect to the zero layer by $1/3, 2/3, 1/3$; the second layer is displaced with respect to the zero layer by $2/3, 1/3, 2/3$; and the third layer, located exactly above the zero layer, is displaced by $0, 0, 3/3$. When the unit cell contains *N* close-

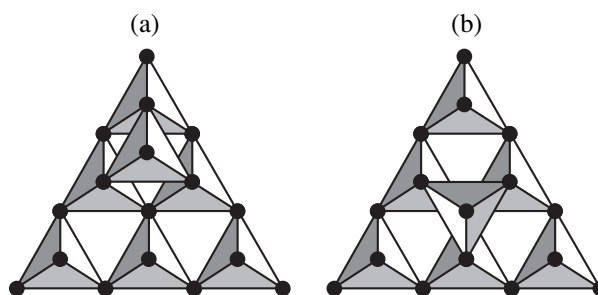


Fig. 1. (a) Cubic and (b) hexagonal packings of layers. The [0001] direction is perpendicular to the drawing plane.

packed layers, the coordinates x, y of the displacements of layers with respect to the zero layer will be cyclically repeated, as was indicated above, and the coordinate z will be determined by the layer number: $k - z_k = k/N$. Thus, for the cubic packing of layers, there are three possible sets of coordinates x, y to describe the displacement of close-packed layers with respect to the zero layer: (0, 0); (1/3, 2/3); and (2/3, 1/3). Let us denote the sequence of close-packed layers in the cubic lattice by the numbers 0, 1, 2, where the coordinates of the layer displacements are determined as was noted above. Then, the cubic packing is described by the cyclic sequence of the 012012... type, in which the upper and lower neighbors of each layer have different orientations. In the case of the hexagonal packing of layers, the coordinates x, y are repeated so that the upper and lower neighbors of each layer have the same orientation (for example, 0101... or 1212...). The z coordinate in the hexagonal packing is determined in the same way as for the cubic packing. If each layer contains atoms of the same type, the number of the basis atoms is equal to the number of layers incorporated into the unit cell and the atomic coordinates x, y are determined by the displacement of a layer with respect to the zero layer.

The silicon carbide lattice is constructed of alternating close-packed Si and C layers located one above another. If the stacking order of Si-C layers is set as a sequence of N Wells symbols, the coordinates of the basis atoms in the unit cell of silicon carbide can be found as follows. Let us calculate the displacement of each layer with respect to the zero close-packed Si-C layer using the recurrence relation

$$M_0 = 0;$$

$$M_k = (M_{k-1} + 1) \bmod(3) \text{ for symbol } a;$$

$$M_k = (M_{k-1} + 2) \bmod(3) \text{ for symbol } b;$$

where M_k denotes the type of displacement (012) of the k th layer ($k = 0-N-1$) with respect to the zero layer.

As a result, instead of a sequence of Wells symbols, we obtain a sequence of numbers 0, 1, 2, which determine the coordinates x, y of the displacement of a layer with respect to the zero layer, as was noted above. For example, for the SiC 6H polytype (aaabbb), the coordinates of Si atoms can be written as

| | | x^{Si} | y^{Si} | z^{Si} |
|-----------------|-----------------|-----------------|-----------------|-----------------|
| $a \rightarrow$ | $0 \rightarrow$ | 0 | 0 | 0 |
| $a \rightarrow$ | $1 \rightarrow$ | 1/3 | 2/3 | 1/6 |
| $a \rightarrow$ | $2 \rightarrow$ | 2/3 | 1/3 | 2/6 |
| $b \rightarrow$ | $1 \rightarrow$ | 1/3 | 2/3 | 3/6 |
| $b \rightarrow$ | $0 \rightarrow$ | 0 | 0 | 4/6 |
| $b \rightarrow$ | $2 \rightarrow$ | 2/3 | 1/3 | 5/6 |

Carbon atoms of the k th layer are displaced with respect to silicon atoms of the same layer along the

z axis by $3/(4N)$. Therefore, the coordinates of carbon atoms have the form

$$x_K^{\text{C}} = x_K^{\text{Si}}, \quad y_K^{\text{C}} = y_K^{\text{Si}}, \quad z_k^{\text{C}} = z_K^{\text{Si}} + 3/(4N).$$

Using the above algorithm, one can calculate the coordinates of the basis atoms in the unit cell of silicon carbide with an arbitrary packing of Si-C layers. For ideal structures, any sequence of alternating layers that does not violate the translational symmetry is allowable; i.e., the atomic coordinates x, y of the last layer should not coincide with the corresponding coordinates of the zero layer since any neighboring close-packed layers should be displaced with respect to each other and such combinations as 00, 11, and 22 are impossible.

The presence of stacking faults changes the sequence order of Wells symbols characteristic of the ideal structure. For example, the formation of a twin in a crystal of cubic silicon carbide will lead to the appearance of b -type layers in the sequence $aaaaa...: aaaaaba...$. In this case, a silicon carbide crystal with stacking faults can be regarded as a regular structure obtained by the translation along the a and b axes of the unit cell containing stacking faults and having the same size as that of the crystal along the c axis (Fig. 2). For a silicon carbide crystal with a size of 1 μm along the c axis, the unit cell will contain about 4000 double close-packed Si-C layers and 8000 Si and C atoms forming the basis of this cell. The coordinates of the basis atoms in this structure form a 3×8000 matrix, which makes it possible to calculate the X-ray diffraction pattern using modern computers.

The subsequent calculation of the diffraction pattern was performed using the model of stacking faults in SiC proposed in [3]. This model interprets a change in the width and intensity of reflections in the rotating-crystal pattern of cubic silicon carbide as a result of a displacement of a pair of adjacent layers of the 12 type, forming a stacking fault, in the (0001) plane. Analytical calculation of the intensity of diffraction reflections showed [3] that both diffuse and sharp reflections must be present in this case in the X-ray diffraction pattern, which is observed experimentally.

RESULTS OF THE CALCULATION

To calculate the rotating-crystal pattern, we chose a unit cell containing 2000 close-packed Si-C layers with cubic packing $aaa...$. Using the function *random* of the C programming language, we pseudorandomly chose 100 pairs of layers that had changed their orientation, $12 \Rightarrow 21$, which signifies the replacement $aaa \Rightarrow bbb$ in the sequence of Wells symbols. It should be noted that, according to [3], in the sequence of layers 012012..., only the layers of the 12 type change their orientation.

To calculate the atomic coordinates in the unit-cell basis, we used the hexagonal coordinate system. The

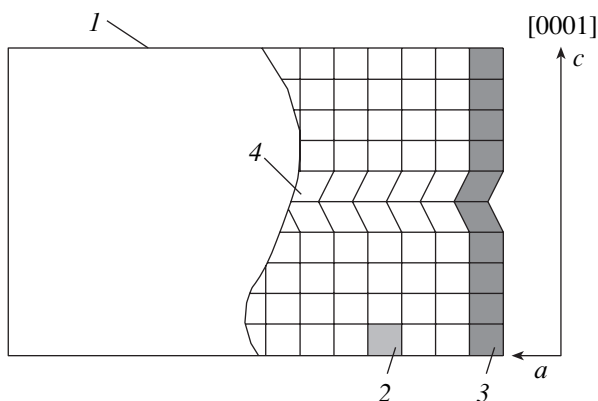


Fig. 2. (1) A crystal, a unit cell of (2) the ideal crystal and (3) a crystal with stacking faults, and (4) a lattice stacking fault.

distance between Si-C layers is 2.517 Å and the unit-cell parameters in the hexagonal coordinate system are $a = b = 3.078$ Å and $c = 5034$ Å. The method and the geometric parameters of the calculation correspond to the measurement of the X-ray diffraction pattern measured in NiK_α radiation on an RKV-86 standard chamber [4] with rotation of the crystal around the [0001] axis. In the X-ray diffraction pattern shown below, the reflections are indicated for which the calculated inten-

sity exceeds 0.01% of the maximum intensity for the reciprocal lattice sites covered by the Ewald sphere.

The calculation shows that the presence of double stacking faults leads to the appearance of a large number of weak closely located reflections at the layer lines of type II (Fig. 3a). The calculated intensity of these reflections is small (0.01% of the maximum intensity) and, owing to their mutual superposition in the diffraction pattern, they manifest themselves as a continuous weak line serving as a background for the main reflections. The enlarged fragment of the layer line of type II (Fig. 3b) shows that additional reflections may lead to the diffusion of the main reflection ($10\bar{1}$) in the X-ray diffraction pattern but do not change the size and shape of the ($10\bar{2}$) reflection, which is in agreement with the results of [3].

To compare the sensitivity of the size and shape of reflections to the configuration of stacking faults, a rotating-crystal pattern of cubic silicon carbide with another distribution of defects is shown in Fig. 4. In contrast to the previous case, the orientation of 200 arbitrarily chosen single layers was changed: $a \Rightarrow b$. Such a distribution of defects may be due, for example, to various fluctuations during the growth of a SiC crystal from the vapor phase. As follows from the results obtained (Fig. 4b), the main reflections of the ($10\bar{l}$) type are divided into several weaker reflections in this case, which should lead to their diffusion in the X-ray

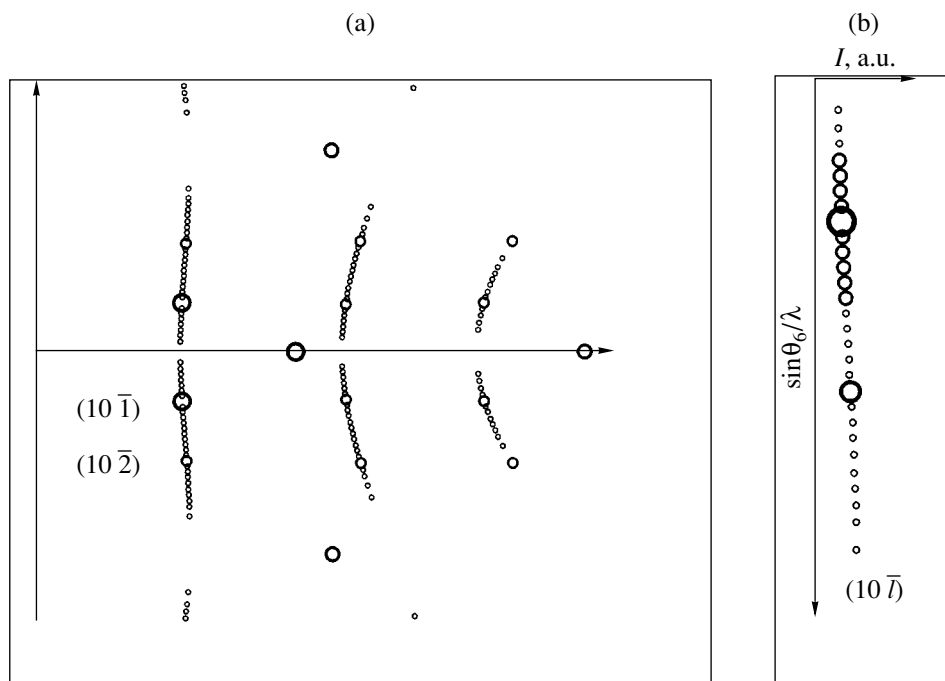


Fig. 3. (a) Rotating-crystal pattern of cubic SiC with double stacking faults and (b) a fragment of the layer line $10\bar{1}$.

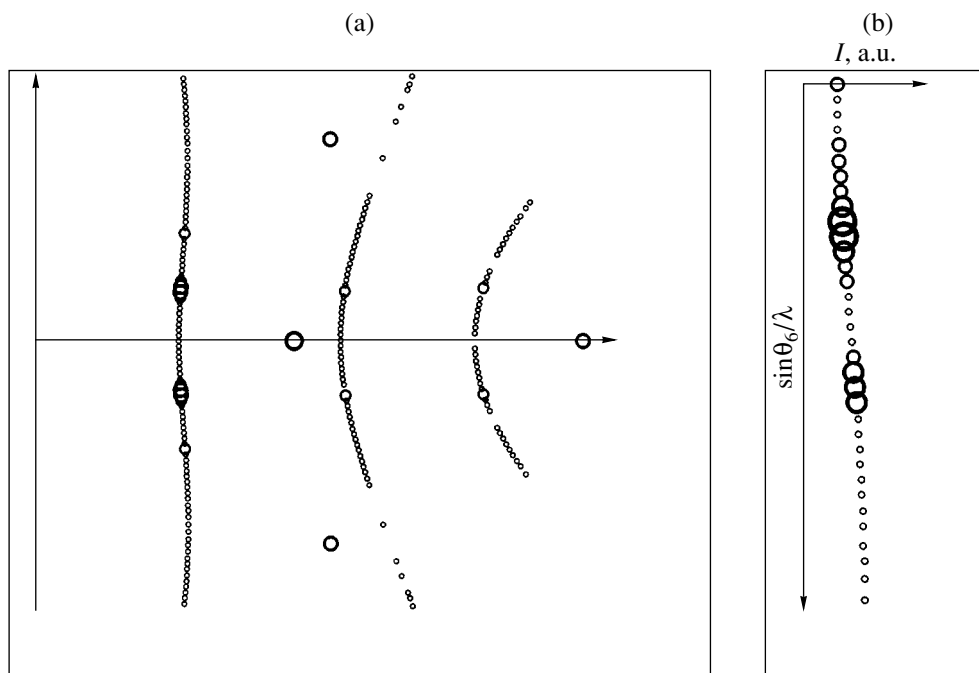


Fig. 4. (a) Rotating-crystal pattern of cubic SiC with single stacking faults and (b) a fragment of the layer line $10\bar{1}$.

diffraction pattern. A characteristic feature of both diffraction patterns is the absence of additional reflections near the main reflections of the (113) and (300) types

CONCLUSIONS

The proposed method for modeling stacking faults in layered structures can simplify the interpretation of experimentally obtained rotating-crystal patterns. The shape and size of the reflections in the X-ray diffraction pattern are determined to a large extent by the conditions and geometry of the pattern measurement. Therefore, as a reference for estimation of these factors for silicon carbides, one can use, for example, the (300) and (113) reflections, which, as can be seen from the results obtained, do not change.

REFERENCES

1. A. Plancon, B. A. Sakharov, Z. I. Gilan, and V. A. Drits, *Kristallografiya* **29** (4), 657 (1984) [*Sov. Phys. Crystallogr.* **29**, 389 (1984)].
2. A. Plancon, B. A. Sakharov, and V. A. Drits, *Kristallografiya* **29**, 663 (1984) [*Sov. Phys. Crystallogr.* **29**, 392 (1984)].
3. H. Jagodzinskiĭ, *Kristallografiya* **16** (6), 1235 (1971) [*Sov. Phys. Crystallogr.* **16**, 1081 (1971)].
4. S. S. Gorelik, L. N. Rastorguev, and Yu. A. Skakov, *X-ray and Electron-Optical Analysis* (Metallurgiya, Moscow, 1970) [in Russian].

Translated by Yu. Sin'kov

REAL STRUCTURE OF CRYSTALS

Analysis of a Random System of Dislocations in a Deformed Crystal

F. F. Satdarova

Moscow Institute of Steel and Alloys, Leninskiĭ pr. 4, Moscow, 117936 Russia

Received October 29, 2003

Abstract—Structure of deformed crystals is modeled by dislocation loops of random size nonuniformly randomly distributed in natural slip planes. This model is used to determine structure parameters from the harmonics of the diffraction line of a polycrystal. Practical analysis of the dislocation structure under real conditions of the diffraction experiment is performed. © 2005 Pleiades Publishing, Inc.

INTRODUCTION

It was theoretically proved by M.A. Krivoglaz that there is a fundamental possibility of determining the dislocation density in any dislocation structure from the diffraction pattern of a deformed crystal. The purpose of this study is to analyze the dislocation structures of the cellular type. Dislocation loops are elements of a random structure forming upon deformation of crystals. To mathematically describe this structure, dislocation loops of arbitrary shape are considered to be circular and their collective bonds are replaced by double bonds. These are necessary simplifications for the object model, on the basis of which an observation model of the object—a tool for studying its structure—is constructed.

MODEL OF DIFFRACTION OBSERVATIONS FOR DEFORMED CRYSTALS

The theoretical representation of the harmonics of the diffraction line of a deformed crystal $A_m = e^{-T(m)}$ ($m = 1, 2, \dots$) includes the effects of a random dislocation network T_0 , correlations in the distribution of dislocations over the crystal volume T_1 , and dislocation ordering with formation of subgrain boundaries T_2 . In an explicit form, e^{-T} is the result of averaging over a large ensemble of random dislocation systems with all possible arrangements of dislocation loops of specified type and size, at which the macroscopic parameters—density, correlation scale, and degree of order—remain invariable [1].

It is reasonable to suggest that in real crystals each of p slip systems has a random number L_α ($\alpha = 1, \dots, p$) of dislocation loops with random sizes and coordinates $\{\xi_j, \mathbf{r}_j\}$ ($j = 1, \dots, L_\alpha$). The loop type $\mathbf{e}_\alpha = (\mathbf{n}, \mathbf{b})_\alpha$, where \mathbf{n} is the unit vector normal to the loop plane and \mathbf{b} is the Burgers' vector of a dislocation, is completely determined by the slip system α .

Let us assume that all random variables describing the statistical ensemble of dislocation systems are mutually independent. To approach reality, we will continue to average e^{-T} over the ensemble that received additional degrees of freedom. First, let us find the mean $\langle e^{-T} \rangle$ over all possible L_α with the total number of loops in the crystal $L = \sum_{\alpha=1}^p L_\alpha$. The next operation of averaging of $\langle e^{-T} \rangle$ over random realizations $\xi(\mathbf{r})$ in the ensemble will be replaced by averaging over the distribution of loop sizes ξ in the crystal volume in accordance with the ergodic hypothesis [2].

At a large number of loops L , fluctuations in their concentrations and size distributions in random systems with respect to the ensemble means will be small. Fluctuations of the quantity T will be small as well; hence, we can write $\langle e^{-T} \rangle \approx e^{-\langle T \rangle}$ [3].

Let us assume that dislocation loops can be located with equal probability in all p slip systems in a crystal (which is close to reality for bcc crystals and may be true for fcc crystals with a high energy of stacking faults). The probability of the event when exactly L_α ($\alpha = 1, \dots, p$) loops from their total number L (obeying the Poisson distribution) are located in the slip system α is determined by the Bernoulli distribution $B_{1/p}(L, L_\alpha)$ [4]. For this distribution law, we have the following equation for the averaged component T_0 :

$$\langle T_0 \rangle = (a/2\pi)^3 q_i q_j \bar{c} (1/p) \sum_{\alpha=1}^p \Gamma_{ij}^{(\alpha\beta)} \langle \Phi_\alpha(\mathbf{R}, \xi) \rangle_\xi \delta_{\alpha\beta}, \quad (1)$$

$$\Phi_\alpha = (\xi/a) \int_{\mathbf{k}} \left(\frac{J_1(k'_\alpha \xi)}{k'_\alpha \xi} \right)^2 \frac{1}{k^2} (1 - \cos \mathbf{kR}) d\mathbf{k}.$$

Here, $|\mathbf{q}| = (2\pi/a) Q_{HKL}$, $|\mathbf{R}| = ma/Q_{HKL}$, $Q_{HKL} = [H^2 + K^2 + L^2]^{1/2}$, $\{HKL\}$ are the reflection indices, a is the lattice period, and $\bar{c} = L/N$ is the average concentration of loops in a crystal with the number of atoms N . The

tensor $\Gamma_{ij}^{(\alpha\beta)} = \Gamma_{ij}(\mathbf{e}_\alpha, \mathbf{e}_\beta)$ and the cylindrical Bessel function $J_1(x)$ (in its argument, $k'_\alpha = |\mathbf{k}'_\alpha|$, \mathbf{k}'_α is the projection of the wave vector \mathbf{k} onto the plane of a loop of type α) arise in the description of the distortions in the crystal caused by circular dislocation loops in the approximation of elastic isotropy of the crystal [1].

Harmonics of the diffraction line of order $1/\kappa \leq m \leq k_{\max}/\kappa$ can be determined experimentally. Here, $\kappa \ll 1$ is the ratio of the measurement interval of the diffraction line to the period in the reciprocal space and k_{\max} is the maximum number of reliable estimates $A_k > \sigma_k$, where σ_k is the measurement variance ($k = 1, 2, \dots$). In a limited range of values of m , the exact analytical expression for $\langle T(m) \rangle$ can be replaced by an approximate one.

For a small magnitude of the vector \mathbf{R} , when $m \ll \xi/a$, introducing the designation $\eta_\alpha = (\mathbf{R} \cdot \mathbf{n}_\alpha)/R$, we can write with accuracy to second-order terms

$$\Phi_\alpha \approx (\pi^2/a) \{ \eta_\alpha (R/a) (\xi/a)^2 - (1/2)(3\eta_\alpha^2 - 1)(R/a)^2 (\xi/a) \}.$$

Let us assume that the sizes ξ of all loops in the crystal have the same logarithmically normal distribution. The averaging of the approximate function $\Phi(\mathbf{R}, \xi)$ over ξ is reduced to determining the moments of this distribution. As a result, we have an approximation of Eq. (1) in the form

$$\langle T_0 \rangle \cong \bar{c} \{ Q_{HKL} m (\bar{\xi}/a)^2 [1 + (\sigma_\xi/\bar{\xi})^2] C_1^p - m^2 (\bar{\xi}/a) C_2^p \}.$$

Here, $(\bar{\xi}/a)$ and $(\sigma_\xi/\bar{\xi})$ are the average normalized loop radius and the coefficient of variance in their sizes, respectively, and (C_1^p, C_2^p) are the crystallogometrical first- and second-order coefficients, respectively. The numerical values of the coefficients (C_1^p, C_2^p) for calculation of scattering from a polycrystal are given below. For a bcc lattice and the slip set $\langle 111 \rangle \{ 110 \}$, $C_1^p = 8.769899$ and $C_2^p \sim 1.2$. For a bcc lattice and the slip set $\langle 111 \rangle \{ 112 \}$, $C_1^p = 9.493694$ and $C_2^p \sim 1.2$. For a fcc lattice and the slip set $\langle 110 \rangle \{ 111 \}$, $C_1^p = 6.265519$ and $C_2^p = 0$. As can be seen from the expression obtained for $\langle T_0 \rangle$, the size inhomogeneity of loops leads to an additional broadening of the diffraction line.

Let us now consider the correlation component T_1 . The number of loops (L_α, L_β) in the slip systems (α, β) for their total number L in the crystal is described by correlated random values obeying the two-dimensional (2D) Bernoulli distribution [4]. Assuming that the sizes ξ of all loops in the slip systems (α, β) are mutually independent random values, for $1 \ll L \ll N$, we obtain

the equation

$$\begin{aligned} \langle T_1 \rangle &= (a/2\pi)^3 q_i q_j \bar{c} (1/p^2) \\ &\times \sum_{\alpha=1}^p \sum_{\beta=1}^p \Gamma_{ij}^{(\alpha\beta)} \langle \Psi_{\alpha\beta}(\mathbf{R}, \xi) \rangle_\xi, \\ \Psi_{\alpha\beta} &= (\xi/a) \int_{\mathbf{k}} \left(\frac{J_1(k'_\alpha \xi)}{k'_\alpha \xi} \frac{J_1(k'_\beta \xi)}{k'_\beta \xi} \right) \\ &\times F_{\alpha\beta}(\mathbf{k}) \frac{1}{k^2} (1 - \cos \mathbf{kR}) d\mathbf{k}, \end{aligned} \quad (2)$$

where $F_{\alpha\beta}(\mathbf{k})$ is the Fourier transform of the correlation function, which depends on the distance $\boldsymbol{\rho}$ between the loop centers [1].

The effect of correlation in the slip plane is the most significant one. Correlation in parallel planes transforms the curve $T(m)$ at values of m close to zero; i.e., in the range $m < 1/\kappa$, which is inaccessible to measurements. In comparison with the effect of 2D correlation in the plane, we can neglect the effect of one-dimensional (1D) correlation along the normal to the plane in the observation model [1]. (The effect of correlation along the line of intersection of planes is of the same order of magnitude as that along the normal to the plane.)

Let us assume that the correlation decreases with an increase in the distance between the loop centers by the exponential law¹: $f(\boldsymbol{\rho}) \sim e^{-|\boldsymbol{\rho}|/\tau} \delta(\boldsymbol{\rho} \cdot \mathbf{n})$. Here, $\boldsymbol{\rho}'$ is the projection of the vector $\boldsymbol{\rho}$ on the loop plane with the normal \mathbf{n} and τ is the correlation radius, within which the probability of finding a pair of loops (α, β) exceeds that in the case of their random distribution over the crystal volume ($\delta(x)$ is the Dirac delta function).

The existence of large correlation radii is unrealistic.² If the diffraction line is observed when the dislocation density in a crystal is about 10^{10} cm^{-2} , the correlation radius τ cannot exceed $\sim 3b$, where b is the interatomic distance (otherwise, the line would be transformed into a diffuse background [1]).

When $(\tau/\xi) \ll 1$,

$$\Psi_{\alpha\beta} \approx 2\pi(\tau/b)^2 \Phi_\alpha(\mathbf{R}, \xi) \delta_{\alpha\beta},$$

where $(\tau/b)^2 = (\tau_1/b)^2 + \kappa(\tau_2/b)^2$ is the generalized correlation parameter at $\mathbf{n}_\alpha = \mathbf{n}_\beta$; i.e., for the dislocation

¹ If β arises at a distance $\boldsymbol{\rho}_1$ from α with a probability $f(\boldsymbol{\rho}_1)$ and γ arises at a distance $\boldsymbol{\rho}_2$ from β with a probability $f(\boldsymbol{\rho}_2)$, as a result of two independent random events, γ arises at the distance $\boldsymbol{\rho} = \boldsymbol{\rho}_1 + \boldsymbol{\rho}_2$ from α with the probability $f(\boldsymbol{\rho}) = f(\boldsymbol{\rho}_1)f(\boldsymbol{\rho}_2)$. It is the function $f(\boldsymbol{\rho}) \sim e^{h\boldsymbol{\rho}}$ (h is the coupling parameter) that satisfies this equation.

² The correlation radius τ determines the density of local loop clusters. The far range of bonds between loops (and their clusters) in the elastic stress field corresponds to the stability of the system as a whole.

loops with identical and different Burgers' vectors \mathbf{b} in the same slip plane ($\kappa = 0$ and ~ 0.2 for bcc and fcc lattices, respectively).

Therefore, the correlation component (2) can be approximately written as

$$\langle T_1 \rangle \approx (2\pi/p)(\tau/b)^2 \langle T_0 \rangle.$$

Thus, the deviation from the random distribution of loops in slip planes is equivalent to the increase in their concentration by a factor of about $[1 + (2\pi/p)(\tau/b)^2]$.

The formation of regular planar dislocation networks (as well as the walls of rectilinear dislocations) causes fluctuations of the diffraction intensity, which only weakly affect the diffraction line shape in the range accessible to measurements [1, 5]. Therefore, the component T_2 can be neglected in the analysis of measured harmonics $\{A_k\}$.

In the approximate expression for $\langle T_0 \rangle$, the component nonlinear with respect to m (when it is nonzero) is smaller than the linear one by an order of magnitude (in the range of practical interest, $m < \bar{\xi}/a$). This component can be assigned to the equation error, especially as real observations contain analogous systematic errors. The origin of these errors will be considered below.

Harmonic analysis of the X-ray diffraction line, which is a doublet of K_{α_1} - K_{α_2} radiation, yields the Fourier coefficients

$$A_k^d = A_k^s [w_1 + w_2 \cos(k\mu)],$$

$$B_k^d = A_k^s [w_2 \sin(k\mu)].$$

Here, μ is the ratio of the interdoubt spacing to the range of Fourier expansion and w_1 and w_2 are the weight fractions of the doublet components, whose profiles are described by the harmonics A_k^s . The expansion center is chosen, as usual, to correspond to the maximum intensity. Taking into account that $\mu \ll 1$, we have

$$(A_k^d)^2 + (B_k^d)^2 \approx (A_k^s)^2 [1 - (w_1 w_2 \mu^2) k^2].$$

Hence, the observations made in the analysis of the physical profile of the diffraction line can be written as

$$\ln A_k \approx \ln(A_k^s/A_0^s) - (1/2)(w_1 w_2 \mu^2) k^2,$$

where $k = \kappa m$. A shift of the expansion center does not affect the result.

Using the approximate representation $\langle T(m) \rangle$, we obtain the model of diffraction observations to study the structure of deformed crystals

$$g_k = \ln A_k + x_k \prod_{q=1}^4 \exp(\theta_q) + u_k = 0. \quad (3)$$

Here, $x_k = C_1^p Q_{HKL}(k/\kappa)$ is an independent variable and u_k is an auxiliary variable which takes into account the systematic errors of the model equation. The structural parameters enter the estimated vector θ :

$$\theta_1 = \ln[\bar{c}(\bar{\xi}/a)], \quad \theta_2 = \ln(\bar{\xi}/a),$$

$$\theta_3 = \ln[1 + (\sigma_{\bar{\xi}}/\bar{\xi})^2], \quad \theta_4 = \ln[1 + (2\pi/p)(\tau/b)^2].$$

Figure 1 shows by the example of Fe and Al crystals with specified parameters of dislocation structures the calculated deviations of the approximate equation from the exact one. The result of the calculation includes the error of averaging e^{-T} by the Monte Carlo method. The larger the variance of the logarithmically normal distribution ξ , the larger this error.

The obtained equation models the normalized harmonics of the diffraction line of a polycrystal when the dislocation loop size satisfies the relation $k_{\max}/\kappa \leq (\xi/a) \leq 0.1(\Xi/a)$ (Ξ is the crystal size). The limitation of (ξ/a) from below is related to the applicability of the approximate expressions for the model functions. The limitation of (ξ/a) from above is due to the effect of the size and shape of crystals, which leads to an asymmetry of the diffraction line (appearance of sine harmonics) [1].

According to the electron microscopy data, cells with sizes from 0.5 to 2 μm are observed in deformed crystals. The thickness of the cell walls is, on average, smaller by a factor of 5. Hence, dislocation loops in the walls may have sizes in the range $250 < (\xi/a) < 1000$. The experiment shows that the limiting coefficient of variance in loop sizes $(\sigma_{\xi}/\bar{\xi}) \leq 1/3$, when random values of logarithmically normally distributed (ξ/a) may differ by an order of magnitude.

As follows from the existing estimates of the dislocation density, $10^8 < \rho_d < 10^{13} \text{ cm}^{-2}$, where $\rho_d = (2\pi/a^2)\bar{c}(\bar{\xi}/a)$, and the average concentrations of loops in deformed crystals are in the range $10^{-8}(\bar{\xi}/a)^{-1} < \bar{c} < 10^{-3}(\bar{\xi}/a)^{-1}$. Estimation of the minimum of possible values of the number of loops L in the smallest existing crystals ($\Xi \sim 10 \mu\text{m}$) gives $L_{\min} \sim 10^3$. Therefore, the model assumptions, justified for a large statistical ensemble, can be applied to the object under consideration.

In practice, the number of reliably estimated harmonics of the diffraction lines of deformed crystals k_{\max} remains within one order of magnitude. Thus, one might expect that the region of real object parameters belongs to the limitation region of the observation model.

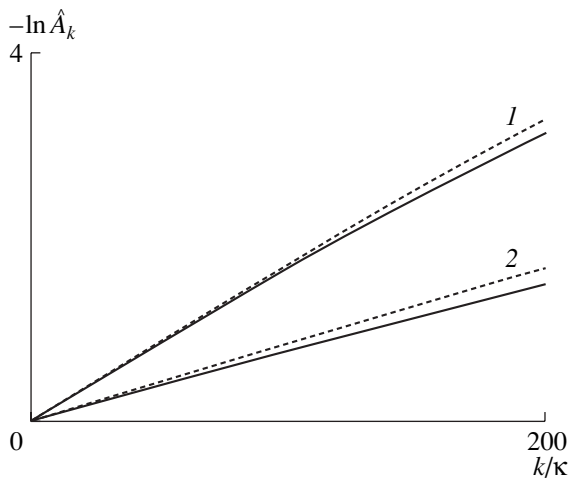


Fig. 1. Predicted harmonics of the diffraction lines of the model crystals with a specified dislocation structure: (1) {110} Fe ($\rho_d = 10^{10} \text{ cm}^{-2}$, $\bar{\xi}/a = 350$, $\sigma_{\bar{\xi}}/\bar{\xi} = 0.1$, $\tau/b = 2$) and (2) {111} Al ($\rho_d = 10^9 \text{ cm}^{-2}$, $\bar{\xi}/a = 500$, $\sigma_{\bar{\xi}}/\bar{\xi} = 0.2$, $\tau/b = 3$). The solid and dotted lines correspond to the theoretical and observation model equations, respectively.

DETERMINATION OF THE PARAMETERS OF THE DISLOCATION STRUCTURE OF DEFORMED CRYSTALS

The average characteristics of the real crystal structure form a parameter vector $\mathbf{\Omega} = (\rho_d, \bar{\xi}/a, \sigma_{\bar{\xi}}/\bar{\xi}, \tau/b)$, which enters the function $g_k(A_k, \mathbf{\theta}(\mathbf{\Omega}))$ of the model (3). It is necessary to find, based on the observations $\{A_k\}$, an estimate of $\mathbf{\theta}$ with minimum error to determine $\mathbf{\Omega}$. However, the form of the model (3) indicates its global nonidentifiability: the solution can satisfy an uncountable set of allowable vectors $\mathbf{\theta}$. In this situation, an unconventional method of statistical estimation of the parameters is required.

Let us represent the experimental results in a K -dimensional sample space ($K \equiv k_{\max}$). An observation vector $\mathbf{A} = (A_1, \dots, A_K)$ determines a point in the sample space. We will assume that there is a set of points $\{\mathbf{A}_r\}$ ($r = 1, \dots, n$) in the sample space and their number $n \geq l$, where l is the dimension of the parameter vector $\mathbf{\theta}$. (Independent repeated measurements of harmonics $\{A_k\}$ of the same diffraction line $\{HKL\}$ may serve as the set elements.) Then the problem of l -dimensional estimation of $\mathbf{\theta}$ can be reduced to l 1D problems of parallel componentwise estimation of $\{\theta_q\}$ ($q = 1, \dots, l$) at different points of the sample space $\{\mathbf{A}_r\}$. The estimate biases θ_q generated by the sampling can be limited by applying the randomized strategy: at each step of the optimizing sequence $\theta_q^{i+1} = \theta_q^i + \Delta\theta_q^i(\mathbf{A}_r, \mathbf{\theta}^i)$ ($i = 0, 1, \dots$), the point \mathbf{A}_r for θ_q is chosen randomly from the existing set $\{\mathbf{A}_r\}$ in the sample space.

Let us now represent the measurements $\mathbf{A} = \{A_k\}$ as initial approximations to "true" harmonics $\hat{\mathbf{A}} = \{\hat{A}_k\}$, for which the model equation $\mathbf{g}(\hat{\mathbf{A}}, \mathbf{\theta}) = 0$ is valid. Then, we associate each measurement vector from the set $\{\mathbf{A}_r\}$ ($r = 1, \dots, n$) with a random vector of auxiliary variables $\mathbf{u} = \{u_k\}$, which should automatically compensate the systematic errors of the model $\hat{\mathbf{u}} = \{\hat{u}_k\}$ when approaching the optimum.

Since the correlation of the variables (\mathbf{A}, \mathbf{u}) can be neglected, the solution (which realizes an asymptotically normal form of likelihood at limitations imposed on the parameters $\mathbf{\theta}$) will be a stationary point of the Lagrange function [6]:

$$\Lambda = \sum_{r=1}^n \left\{ \sum_{k=1}^K \left[\frac{1}{2} (\hat{A}_k - A_k)^2 / \sigma_{A_k}^2 + \frac{1}{2} (\hat{u}_k - u_k)^2 / \sigma_{u_k}^2 + \lambda_k g_k(A_k, \mathbf{\theta}) \right] \right\}_r,$$

where σ_{A_k} are the variances of the measurements A_k , whose estimates are found from experiment; σ_{u_k} are the variances of the variables u_k , which are to be estimated during the optimization; and $\{\lambda_k\}$ are the Lagrange multipliers. The initial point for searching the optimum can be chosen using linear regression analysis of the existing data.

Let us reduce the model (3) to the approximation equation for the observations $Y_k = -\ln A_k$:

$$\hat{Y}_k = h_1 z_{k1} + h_2 z_{k2},$$

where $z_{k1} = C_1^p Q_{HKL}(k/\kappa)$ and $z_{k2} = (k/\kappa)^2$ ($k = 1, \dots, k_{\max}$). We neglect the correlation $\{Y_k\}$. Using the condition for the minimum of squared deviations

$$U(\mathbf{h}) = \sum_{r=1}^n \left\{ \sum_{k=1}^K w_k [Y_k - \hat{Y}_k(\mathbf{h})]^2 \right\}_r,$$

with the weight $w_k = A_k^2 / \sigma_{A_k}^2$, we obtain an estimate for the vector of regression coefficients $\mathbf{h}^* = (h_1^*, h_2^*)$ with the covariance matrix

$$\mathbf{V}_h = \begin{bmatrix} \sigma_1^2 & \sigma_1 r_{12} \sigma_2 \\ & \sigma_2^2 \end{bmatrix}.$$

(If $U(\mathbf{h}^*) / (nK - 2) > 1 / (1 - P)$, there is a discrepancy between the model and the data with a reliability not lower than P , which requires critical analysis.)

Randomly chosen values $\{\theta_q\}$ from the ranges of allowable values $[\theta_q^{\min}, \theta_q^{\max}]$ ($q = 1, \dots, 4$), such that

$$\left| \prod_{q=1}^4 \exp(\theta_q) - h_1^* \right|^2 \leq \sigma_1^2,$$

form an allowable set of random starting points in the space of parameters θ .

The coefficient h_2^* is used to measure the average deviation from the linear dependence $Y_k \sim k$. Therefore, this coefficient is applicable for modeling the auxiliary variables $\{u_k\}$ on the assumption of their normal distribution with the mathematical expectation $\hat{u}_k \sim h_2^* z_k$ and the variance $\sigma_{u_k}^2 \sim \sigma_2^2 z_k^2$.

In order not to complicate the target function with the conditions for the optimization region, let us represent the model parameters θ as a limited function of some variable ω at an infinite interval:

$$\theta_q = \frac{1}{2}(\theta_q^{\max} + \theta_q^{\min}) + \frac{1}{2}(\theta_q^{\max} - \theta_q^{\min}) \sin \omega_q$$

$(q = 1, \dots, 4).$

(At $q = 3$, when θ_q varies in a very narrow range, ω_q must be reduced to the main values in the interval $(-\pi/2, \pi/2)$.)

To calculate the step of the iterative optimization process, we obtain the simple formulas

$$\Delta \omega_q = \left\{ \sum_{k=1}^K w_k e_k (\partial g_k / \partial \omega_q) \right\} / \left\{ \sum_{k=1}^K w_k (\partial g_k / \partial \omega_q)^2 \right\}$$

$(q = 1, \dots, l).$

Here, the quantities

$$e_k = (\hat{A}_k - A_k) / \hat{A}_k + (\hat{u}_k - u_k) - g_k,$$

$$w_k = (\sigma_{A_k}^2 / \hat{A}_k^2 + \sigma_{u_k}^2)^{-1}$$

are calculated at a random point r of the sample space. Initially, we take the measured values (\hat{A}_k, \hat{u}_k) for (A_k, u_k) . Then, using the Lagrange multipliers

$$\lambda_k = w_k [(\partial g_k / \partial \omega_q) \Delta \omega_q - e_k],$$

the current corrections to (\hat{A}_k, \hat{u}_k) ,

$$\Delta \hat{A}_k = -\{(\hat{A}_k - A_k) + \hat{A}_k^{-1} \lambda_k \sigma_{A_k}^2\},$$

$$\Delta \hat{u}_k = -\{(\hat{u}_k - u_k) + \lambda_k \sigma_{u_k}^2\},$$

are calculated for all points of the sample space ($r = 1, \dots, n$). Finally, we have to determine the derivatives of

the model functions:

$$(\partial g_k / \partial \omega_q) = x_k H_q \cos \omega_q,$$

where

$$H_q = \frac{1}{2}(\theta_q^{\max} - \theta_q^{\min}) \prod_{s=1}^4 \exp(\theta_s).$$

The estimate of the variance σ_{u_k} is refined at each iteration from the standard deviation \hat{u}_k at the points of the sample space :

$$\sigma_{u_k}^2 \approx \sum_{r=1}^n (\hat{u}_{k,r} - \bar{\hat{u}}_k)^2 / (n - 1),$$

where

$$\bar{\hat{u}}_k = \sum_{r=1}^n \hat{u}_{k,r} / n.$$

The iteration step ($i = 0, 1, \dots$), controlled by the coefficient $0 < \zeta^i \leq 1$, is considered to be allowable if at

$$\theta^{i+1} = \theta^i + \zeta^i \Delta \theta^i (\Delta \omega^i), \quad \hat{\mathbf{A}}^{i+1} = \hat{\mathbf{A}}^i + \zeta^i \Delta \hat{\mathbf{A}}^i,$$

$$\hat{\mathbf{u}}^{i+1} = \hat{\mathbf{u}}^i + \zeta^i \Delta \hat{\mathbf{u}}^i$$

we have

$$G^{i+1} < G^i = \sum_{r=1}^n \left\{ \sum_{k=1}^K w_k^i |g_k^i|^2 \right\}_r.$$

As a rule, the local minimum of G is obtained using three or four iterations. If deviations from the conditions for stationarity of the target function Λ in the local minimum are smaller than the allowable errors

$$\left\{ \left| \sum_{k=1}^K (\partial g_k / \partial \omega_q) \lambda_k \right|_r \right\} < \varepsilon \quad (q = 1, \dots, l),$$

$$\{(|\Delta \hat{A}_k|, |\Delta \hat{u}_k|)_r\} < \varepsilon \quad (k = 1, \dots, k_{\max}),$$

where $0 < \varepsilon \ll 1$, the optimum $\Lambda^* = \Lambda(\theta^*)$ is likely to be found. What is left to do is to check that the obtained values of $\hat{\mathbf{A}}$ lie within the confidence interval of measurements \mathbf{A} and that the residual deviations from the model equation $\mathbf{g}^* = \mathbf{g}(\hat{\mathbf{A}}, \theta^*)$ are insignificant.

To perform this check, let us calculate the statistical criteria

$$\eta_1 = (\zeta/n) \sum_{r=1}^n \left\{ \sum_{k=1}^K |\hat{A}_k - A_k|^2 / \sigma_{A_k}^2 \right\}_r,$$

$$\eta_2 = (\zeta/n) \sum_{r=1}^n \left\{ \sum_{k=1}^K |g_k^*|^2 / \sigma_{g_k}^2 \right\}_r$$

Table 1. Verification of the reliability of the estimates of the dislocation structure by the example of model crystals

| Model crystal | Specified exact values of the structure parameters | Approximate 90% confidence interval of the estimates |
|---------------|---|---|
| bcc-(Fe) | $\rho_d = 10^{10} \text{ cm}^{-2}$ $(\bar{\xi}/a) = 350$ $(\sigma_{\xi}/\bar{\xi}) = 0.1$ $(\tau/b) = 2.0$ | $[0.8; 1.2] \times 10^{10} \text{ cm}^{-2}$ [346; 451] [0.20; 0.24] [1.5; 2.0] |
| fcc-(Al) | $\rho_d = 10^9 \text{ cm}^{-2}$ $(\bar{\xi}/a) = 500$ $(\sigma_{\xi}/\bar{\xi}) = 0.2$ $(\tau/b) = 3.0$ | $[0.8; 1.4] \times 10^9 \text{ cm}^{-2}$ [477; 672] [0.23; 0.27] [2.1; 2.7] |

with the correction $\zeta = 2/(1 - 4/nK)$, which takes into account the presence of two inexact variables and four estimated parameters in the model equation [6]. The unknown variances σ_{g_k} will be estimated by the standard deviations of the residuals g_k from the means \bar{g}_k at n points of the sample space. For any distribution $\{A_k\}$, $\{g_k\}$, the solution is rejected with a reliability not smaller than P if either η_1 or η_2 exceeds $K/(1 - P)$.

The successful results of a search from random starting points can be regarded as independent realizations of a random vector $\omega^* = \omega(\theta^*)$. In fact, in a randomized computational experiment, we select a random sample $\{\omega_j^*\}$ ($j = 1, \dots, M$) from a completely unknown distribution (which is assumed to be the same for all j). Using this sample, confidence intervals for the parameters of the object model $\Omega(\theta^*)$ must be constructed.

For this purpose, we will use bootstrap confidence intervals, which are more exact than the standard ones and behave correctly at the transformations [7]:

$$\mathcal{R}(P) = \bar{y} \pm \sigma t(P) + \sigma v [2t(P)^2 + 1] / 6\sqrt{M}.$$

Here, $\sigma = [\mu_2/(M - 1)]^{1/2}$ is the variance of the sample mean \bar{y} ; $v = \mu_3/\mu_2^{3/2}$ is the sampling ratio, which contains the sample moments $\mu_\gamma = \sum_{j=1}^M (y_j - \bar{y})^\gamma / M$; and $t(P) = t_{(M-1), (1-\alpha/2)}$ are the percent points of the t distribution with $(M - 1)$ degrees of freedom for the given confidence probability $P = 1 - \alpha$.

Since no less than 90% of realizations of any distribution $y \equiv \{\omega_q^*\}$ ($q = 1, \dots, l$) will be between the boundary values of the sample (y_{\min}, y_{\max}) with a probability of ~ 99 and $\sim 61\%$ at $M = 60$ and 20 , respectively [3], we can assume $M = 60$ to be a sufficient sample and $M = 20$ to be a minimally necessary sample.

The properties of the obtained estimates $\Omega(\theta^*)$ were studied by the example of model crystals with bcc and

fcc lattices with specified parameters of dislocation structures. The initial data for the analysis were imitative measurements (of equal accuracy and uncorrelated) of the harmonics $\{A_k\}$. The normally distributed A_k with theoretically predicted mathematical expectations \hat{A}_k and accepted variance $\hat{\sigma}$ were modeled (see Fig. 1). Depending on a specified structure and the conditions of imitative experiments, different numbers of statistically significant (with a reliability of 95%) harmonics k_{\max} were obtained: for bcc (Fe), $\{110\}$ we have $\kappa = 0.10$, $\hat{\sigma} = 0.01$, and $k_{\max} = 22$ and for fcc (Al), $\{111\}$ we have $\kappa = 0.05$, $\hat{\sigma} = 0.03$, and $k_{\max} = 20$.

The parameters θ were estimated using a minimally necessary set of measurement vectors $\{\mathbf{A}_r\}$ ($r = 1, \dots, n$); i.e., when $n = l = 4$. (For the extended set $\{\mathbf{A}_{r+r'}\}$, including the vectors $\mathbf{A}_{r'}$ from the measurements for $\{112\}$ Fe or $\{200\}$ Al, no significant changes in the quality of the estimates were found.)

Some typical examples of approximate 90% confidence intervals for the structural parameters of the model crystals are listed in Table 1. The confidence intervals constructed from independent repeated samples of the vectors $\{\omega_j^*\}$ ($j = 1, \dots, 60$) mostly included the specified values of the initial parameters Ω .

As can be seen from Table 1, the estimates of the parameters are biased mainly to the center of the allowable range for the vector $\theta(\Omega)$. Note that at the sample volume $M = 20$ the estimate biases are smaller, but the confidence intervals are wider. The accuracy of approach to the optimum predominantly affected the bias of the estimate of the average loop size. The estimate of the dislocation density turned out to be most stable and the least biased one (see Table 1).

The results of the analysis of the imitative experiments with the model crystals show that the method verified gives acceptable estimates of the object parameters if the latter are far from the admissibility limits.

DIFFRACTION INVESTIGATION OF THE DISLOCATION STRUCTURE OF THE 01Kh5 STEEL

Two series of independent measurements of a sample and a reference are used for optimal estimation of the harmonics of the physical profile of a diffraction line. The data obtained provide a regularized solution for the inverse convolution problem: one sample–reference pair is used to calculate the harmonic vector $\mathbf{A} = \{A_k\}$ as a function of the regularization parameter, and the other pair is used to choose the optimal value of this parameter according to the measurement accuracy. Composing all possible sample–reference pairs from the data available, we obtain four independent estimates $\{\mathbf{A}_r\}$ with the least mean-square errors (which include squared biases of the estimates) [8].

The variances of the harmonics of the physical profile of a diffraction line $\{\sigma_{A_k}\}$ are estimated by the standard deviations $\{A_k\}$ from the means $\{\bar{A}_k\}$ for $n = 4$ points in the sample space. The distortions introduced into the first harmonic by the cutoff of the line tails, as well as the biases, which increase with increasing k , are automatically transformed into random errors.

The dislocation structure of a sample of 01Kh5 steel deformed by 50% was studied on the basis of the harmonics of the $\{110\}$ diffraction line measured in $\text{FeK}\alpha$ radiation (an annealed sample was used as a reference). The technique of the measurement (performed by Kozlov) was described in [8]. The ratio of the observation interval to the reciprocal lattice period of Fe was $\kappa = 0.1224$ and the fraction μ of the interdoublet spacing $K_{\alpha_1} - K_{\alpha_2}$ in the observation interval was $\mu = 0.0118$.

To separate the background, we chose 2ν boundary points of the observation interval, for which the weighted sum of squared deviations of the measured diffraction intensities from the line approximating the background is in the range $\chi_{2\nu}^2(1 - P) < \zeta U < \chi_{2\nu}^2(P)$ with the confidence probability $P = 0.95$ (in the approximation of the asymptotically normal distribution of primary measurements). Here, the χ^2 distribution with 2ν degrees of freedom is used and the correction $\zeta = 1/(1 - 2/2\nu)$ is taken into account in the estimation of two regression coefficients from 2ν measurement points. For various data, we obtained $4 \leq 2\nu \leq 6$.

After adding the errors in the background estimation, which are maximum at the ends of the observation interval, the statistical weight of the measurement points for a sample varied approximately by a factor of 2 and 6 for a sample and the reference, respectively. Therefore, the weight of the measurement points was taken into account in the harmonic analysis of the diffraction line.

The harmonics of the diffraction line of a sample were determined in the iterative search for a minimally necessary length of the Fourier series k_{\max} for an acceptable approximation of the measurement data preferentially by the smoothest possible curve. Such a procedure of stable statistical estimation of the data consistently minimizes the variances and biases of the obtained Fourier coefficients of the primary line profile [9]. (The number of harmonics of the reference line is limited by the condition for the lack of correlation between counts [8].)

For normalized measured harmonics of the diffraction lines of both the sample and reference, the variances were estimated from the pair differences in two series of experiments with a correction to the systematic deviation in the cases when it is statistically significant [8].

The sample oscillations of the optimal harmonics of the physical line profile $\{A_k\}_r$ ($r = 1, \dots, 4$) derived from

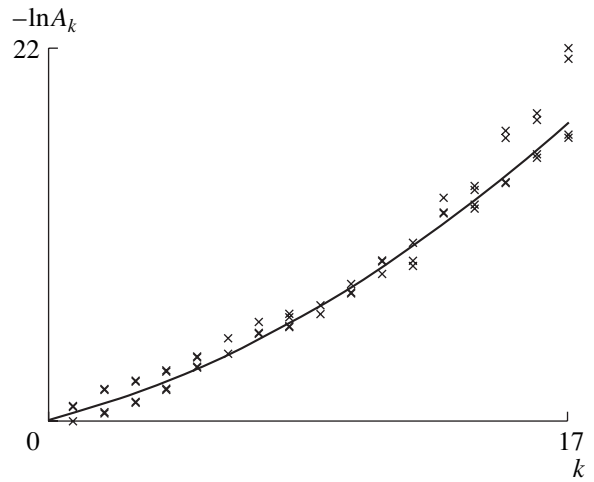


Fig. 2. Regression curve for the measured harmonics of the physical profile of the diffraction line $\{110\}$ of 01Kh5 steel deformed by 50%.

independent experiments can be seen in Fig. 2. The applicability of the approximation of the observations $Y_k = -\ln A_k$ in the interval $k \leq k_{\max} = 17$ by a second-order polynomial is not rejected by the statistical check: $U(\mathbf{h}^*) = 99.77 < 66/(1 - P)$ at $P = 0.5$. Figure 2 shows the deviations of the observations $\{Y_k\}$ from the polynomial regression line.

The data obtained on the physical profile of the measured diffraction line were used to construct approximate 90% confidence intervals for the parameters of the dislocation structure of a sample of 01Kh5 steel deformed by 50% (see Table 2). The estimation was performed for the model of bcc crystals, which assumes the dislocation distributions over two sliding sets to be equiprobable.

In reality, the shape of the diffraction line of deformed crystals is affected by other ignored parameters (for example, fluctuations of the dislocation line curvature). The presence of extra parameters, as well as deviations of measurement errors from the normal dis-

Table 2. Estimates of the parameters of the dislocation structure of 01Kh5 steel deformed by 50%

| Sample* | Approximate 90% confidence interval | | | |
|---------|--|-------------------------------------|--|-------------------------------|
| | dislocation density $\rho_d, 10^9 \text{ cm}^{-2}$ | average loop radius $(\bar{\xi}/a)$ | coefficient of variance $(\sigma_{\xi}/\bar{\xi})$ | correlation radius (τ/b) |
| 1 | [2.2; 2.7] | [408; 503] | [0.22; 0.26] | [1.7; 2.1] |
| 2 | [2.2; 2.8] | [452; 555] | [0.20; 0.25] | [1.6; 1.9] |
| 3 | [2.3; 3.1] | [421; 512] | [0.21; 0.25] | [1.5; 1.9] |
| 4 | [2.4; 3.3] | [417; 526] | [0.20; 0.25] | [1.5; 1.8] |
| 5 | [2.5; 3.3] | [395; 496] | [0.22; 0.26] | [1.5; 1.8] |

* Repeated series of computational experiments.

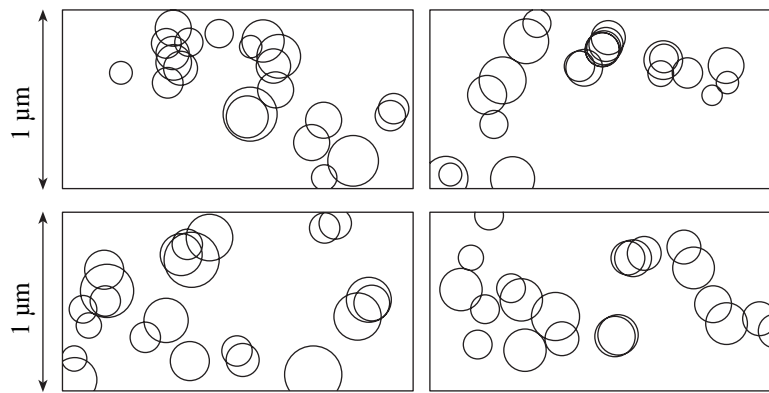


Fig. 3. Distribution of dislocation loops in a slip band $\sim 0.5 \mu\text{m}$ thick after 50% deformation. Statistical modeling with parameters randomly chosen from the confidence intervals of the estimates for 01Kh5 steel.

tribution, naturally increases the sample oscillations of the confidence intervals for the estimated parameters.

Table 2 contains the values of the intervals obtained from several series of computational experiments with the sample volume $M = 60$, which characterizes the degree of instability of the parameter estimates. The estimates are arranged in ascending order of confidence boundaries for the dislocation density. The random biases of the intervals are clearly correlated.

According to the data of Table 2 with a reliability of about 90%, the dislocation density in the sample under study is $\sim 3 \times 10^9 \text{ cm}^{-2}$. The width of the diffraction line reconstructed from its harmonics is $\rho_d \sim 10^{11} \text{ cm}^{-2}$ [10]. In other words, the dislocation density estimated from the diffraction line width is overestimated approximately by a factor of 30, which is furthered by the superposition of the effects of structure inhomogeneity (and the existing splitting of the $K_{\alpha_1}-K_{\alpha_2}$ doublet).

The found estimates of the structural parameters can be used for statistical modeling of the dislocation distribution. The random number of loops falling into one of the slip systems, with their average concentration in the crystal being known, is determined from probabilistic experiments according to the Bernoulli scheme. The propagation of loops over the acting slip planes is modeled by the Poisson flow. In this flow, the random distances between loops arriving one by one obey an exponential distribution law [3]. The smallest distance turns out to be the most probable one. The average distance is the quantity inverse to the flow density.

For the identified structure of deformed 01Kh5 steel, a graphical image of the dislocation loop distribution in a set of parallel slip planes (the distance between the acting slip planes was assumed to be $\sim 200 \text{ \AA}$) was obtained by statistical modeling. The dislocation structure pattern is similar to the expected one (Fig. 3).

The generation of Poisson flows of loops with densities corresponding to the parameters of the sample structure revealed frequent nucleation of extended random clusters of loops, randomly dividing pure regions

of the crystal. Figure 3 shows randomly implemented shapes of boundaries of multiply connected regions, which are characteristic of cellular structures.

In practice, analysis of the random dislocation system in deformed crystals gave a realistic quantitative description of the dislocation structure of a material with bcc crystals. In any case, the method provides a sufficient limitation of the parameters of an inhomogeneous structure for reliable estimation of the average dislocation density in a polycrystalline sample.

REFERENCES

1. F. F. Satdarova, *Fiz. Met. Metalloved.* **49** (3), 467 (1980).
2. L. D. Landau and E. M. Lifshitz, *Course of Theoretical Physics, Vol. 5: Statistical Physics*, 2nd ed. (Nauka, Moscow, 1964; Pergamon, Oxford, 1980).
3. G. A. Korn and T. M. Korn, *Mathematical Handbook for Scientists and Engineers* (McGraw-Hill, New York, 1968; Nauka, Moscow, 1974).
4. L. Janossy, *Theory and Practice of the Evaluation of Measurements* (Clarendon, Oxford, 1965; Mir, Moscow, 1968).
5. M. A. Krivoglaz, K. P. Ryaboshapka, and R. N. Barabash, *Fiz. Met. Metalloved.* **30** (6), 1134 (1970).
6. Y. Bard, *Nonlinear Parameter Estimation* (Academic, New York, 1974; Finansy i Statistika, Moscow, 1979).
7. B. Efron, *Nontraditional Methods of Multivariate Statistical Analysis*, Collection of Papers (Finansy i Statistika, Moscow, 1988).
8. F. F. Satdarova and D. A. Kozlov, *Zavod. Lab.* **48** (10), 53 (1982).
9. F. F. Satdarova and I. K. Kiselev, *Kristallografiya* **35** (1), 28 (1990) [*Sov. Phys. Crystallogr.* **35**, 14 (1990)].
10. M. A. Krivoglaz, *Theory of X-ray and Thermal Neutron Scattering by Real Crystals* (Nauka, Moscow, 1967; Plenum, New York, 1969).

Translated by Yu. Sin'kov

REAL STRUCTURE
OF CRYSTALS

Strain of Interatomic Bonds and Multiple-well Potential in Crystals with Perovskite Structure

N. M. Olekhovich

*Institute of Solid-State and Semiconductor Physics, Belarusian Academy of Sciences,
ul. Brovki 17, Minsk, 220072 Belarus*

e-mail: olekhnov@ifftp.bas-net.by

Received September 15, 2003

Abstract—A method for determining the strain characteristics of interatomic bonds in crystals of ABX_3 compounds with perovskite structure is developed. The bond strain energy ΔU_s is estimated. This energy is responsible for the formation of ordered lattice distortions related to the rotation of octahedra and/or the cooperative displacement of cations. It is shown that ΔU_s correlates with the characteristics of ordered distortions and the temperature of the phase transition of compounds to the cubic structure. It is ascertained that the interatomic-interaction potential in crystals with strained bonds is a local multiple-well potential, the form of which depends on the nature of interacting atoms. It is shown that the occurrence of the ferroelectric state in the noted crystals may be due to the presence of bond strains and the anisotropy of the covalent component of the cation–anion interaction. © 2005 Pleiades Publishing, Inc.

INTRODUCTION

It is well known that phase transitions in crystals of ABX_3 oxide and halide compounds with perovskite structure are accompanied by some ordered lattice distortions, which, depending on the nature of elements in their composition, may be related to the rotation of BX_6 octahedra the displacement of cations, or both these effects simultaneously. Such phase transitions are assigned to displacive transitions, the dynamics of which is characterized by the manifestation of soft modes, i.e., the softening of some normal vibrations, which are related to singularities in the Brillouin zone (see, for example, [1, 2]). It is believed that the high-temperature (cubic) and low-temperature phases in crystal systems showing displacive phase transitions are ordered in the ideal case and are both characterized by single-well interatomic interaction potentials that depend on anion–cation displacements.

However, there are some experimental data indicating that the phase transitions in crystals with perovskite structure show signs of order–disorder transitions. For example, the diffuse X-ray scattering [3], neutron scattering [4], and Raman scattering [5] investigations and the analysis of the X ray absorption fine structure (XAFS) [6] revealed local distortions, corresponding to clusters of the low-temperature phase, in the high-temperature cubic phases of some compounds with perovskite structure at temperatures much higher than the transition temperature T_c . The characteristics of such clusters were quantitatively estimated on the basis of the XAFS data and it was shown that macroscopic distortions in a crystal are determined mainly by the ordering of clusters rather than variation in their size.

The disorder of a system above T_c is a direct sign of the order–disorder phase transition. This transition means that the potential energy as a function of atomic displacements (without requirement for correlation of displacements in other cells) is a multiple-well (double-well in the one-dimensional case) temperature-independent potential [6]. A question arises about the nature of the multiple-well potential in such crystals.

The purpose of this work is to study the interatomic-bond strains and reveal the nature of the multiple-well potential and the character of ordered lattice distortions in crystals with perovskite structure. The bond strain energy is determined and its linear correlation with the phase transition temperature is established. It is shown that the occurrence of the multiple-well potential and ordered distortions, whose type depends on the character of interatomic interaction, is related to the bond strain energy. The relationship between the parameters of the multiple-well potential and the characteristics of the strain energy is considered for the case of ordered distortions related to the rotation of octahedra and displacements of cations.

BOND STRAIN ENERGY

In order to find out if bond strains exist in distorted perovskite-related structures ABX_3 or not, let us analyze the dependence of the potential energy of interatomic interaction U on the interionic distances $A-X$ and $B-X$. With this purpose, we can restrict our consideration in the first-order approximation to a cubic structure with the average parameter of the reduced cell $a = (V/p)^{1/3}$, where V is the unit-cell volume of the distorted structure and p is the number of formula units. The potential

energy of interatomic interaction in this system is expressed in the two-body approximation in terms of the sum of the sublattice energies

$$U = U_A(l_{AX}) + U_B(l_{BX}), \quad (1)$$

which depend on the average distances l_{AX} and l_{BX} , respectively.

At some values l_{0AX} and l_{0BX} , the components U_A (l_{AX}) and U_B (l_{BX}) reach the minimum values, which are the average unstrained-bond lengths.

Generally, the observed average interatomic distances

$$l_{AX} = a/\sqrt{2}, \quad l_{BX} = a/2 \quad (2)$$

differ from l_{0BX} and l_{0AX} and correspond to the strained state of bonds.

To estimate the potential energy of interatomic interaction for strained bonds, we can expand in series the components U_A and U_B , restricting ourselves to the second order of smallness and taking into account (2):

$$U = U_{0B} + U_{0A} + \frac{C_{BX}}{2} \left(\frac{a}{2} - l_{0BX} \right)^2 + \frac{C_{AX}}{2} \left(\frac{a}{\sqrt{2}} - l_{0AX} \right)^2, \quad (3)$$

where $C_{AX} = \left(\frac{d^2 U_A}{dl_{AX}^2} \right)_{l_{0AX}}$ and $C_{BX} = \left(\frac{d^2 U_B}{dl_{BX}^2} \right)_{l_{0BX}}$ are the force constants of the $A-X$ and $B-X$ bonds, respectively.

The condition $dU/da = 0$ yields the expression for the equilibrium parameter of the reduced cell:

$$a = \frac{1}{1+2\eta} 2l_{0BX} + \frac{2\eta}{1+2\eta} \sqrt{2}l_{0AX}, \quad (4)$$

where $\eta = C_{AX}/C_{BX}$.

Substituting (4) into (3), we can find the bond strain energy

$$\Delta U_s = \frac{C_{AX}}{1+2\eta} (l_{0BX} - l_{0AX}/\sqrt{2})^2, \quad (5)$$

which is the value by which the potential energy of the system increases owing to the deviation of the average unstrained-bond lengths l_{0AX} and l_{0BX} from the values satisfying the condition for the ideal perovskite structure

$$l_{0AX}/\sqrt{2}l_{0BX} = 1. \quad (6)$$

The values of l_{0AX} , l_{0BX} , and η , which enter (4) and (5), are estimated experimentally from the variation in the average parameter of the reduced cell in homologous series of ABX_3 compounds [7]. With this purpose, two type of such series are considered. Compounds with compositions differing only in the element B are grouped in homologous series of the first type (I). Each

series of type I is characterized by a particular element A . Compounds differing in the chemical element A are grouped in homologous series of the second type (II). Each series of type II is characterized by a particular element B .

It follows from (4) that

$$2l_{0BX} - a = \frac{4\eta}{1+2\eta} (l_{0BX} - l_{0AX}/\sqrt{2}), \quad (7)$$

$$a - \sqrt{2}l_{0AX} = \frac{2}{1+2\eta} (l_{0BX} - l_{0AX}/\sqrt{2}). \quad (8)$$

These relations describe the dependences of $2l_{0BX} - a$ on l_{0BX} and $a - \sqrt{2}l_{0AX}$ on $l_{0AX}/\sqrt{2}$ for series I and II at fixed values of l_{0AX} in (7) and l_{0BX} in (8). For the series with close values of the parameter η , relations (7) and (8) are linear.

On the basis of the analysis of relations (7) and (8) as applied to the above-mentioned homologous series, the average unstrained-bond lengths l_{0AX} and l_{0BX} and the parameter η were determined for the following families of compounds with perovskite structure: ABF_3 , $A^{1+}B^{5+}O_3$, $A^{2+}B^{4+}O_3$, $A^{3+}B^{3+}O_3$ [7]. The found values of l_{0AX} and l_{0BX} for most of these compounds turned out to be in agreement with the interatomic distances in crystals of the corresponding binary compounds. The relation between them, with rare exceptions, is determined by the inequality $l_{0AX}/\sqrt{2}l_{0BX} < 1$; i.e., it differs from the relation for the ideal perovskite structure (6). The difference between $l_{0AX}/\sqrt{2}$ and l_{0BX} is indicative of the bond strain in crystals with perovskite structure.

As can be seen from Fig. 1, the bond-strain energy ΔU_s in expression (5), estimated from the found values of l_{0AX} and l_{0BX} for the family of the investigated fluorides and oxides, systematically changes within each homologous series, reaching relatively large values with an increase in the difference $l_{0BX} - l_{0AX}/\sqrt{2}$.

The character of the change in the bond-strain energy in the homologous series of compounds corresponds to the character of the change in the phase transition temperature and the degree of ordered distortions. Let us compare ΔU_s with the cubic phase transition temperature T_c of the compounds. Figure 2 shows as an example the results of such comparison for a number of ABF_3 and $A^{1+}B^{5+}O_3$ compounds. The value of ΔU_s was estimated in relative units $\Delta U_s/C_{KF}$; i.e., the force constant for the noted compounds was determined with respect to its value for K-F bonds (C_{KF}) in the ion model approximation (the Madelung energy). It can be seen that the phase transition temperature T_c is proportional to the bond-strain energy or $(l_{0BX} - l_{0AX}/\sqrt{2})^2$. The proportionality factor depends on the nature of the atoms in the composition of the compound and the character of their interaction. This dependence

means that the phase transitions observed in crystals with perovskite structure are related to the bond-strain energy.

The increase in the bond-strain energy with increasing difference $l_{OBX} - l_{OAX}/\sqrt{2}$ can be related to the stability limit of the perovskite structure for the compounds in which a relatively small ion (for example, Li) serves as the *A* cation. Owing to the large value of ΔU_s , the perovskite structure turns out to be energetically unfavorable for such compounds and they are crystallized into another structure (e.g., LiNbO_3). For this reason, ionic compounds of this type, for example, LiBaF_3 , have the structure of inverse perovskite, in which *A* and *B* cations change their positions in the lattice, due to which the bond-strain energy decreases.

Expression (5) corresponds to the highest bond-strain energy since ordered lattice distortions were not taken into account in the approximation of a reduced cubic cell (which was used initially). As will be shown below, these distortions lead to a decrease in ΔU_s .

ORDERED STRUCTURAL DISTORTIONS AND THE MULTIPLE-WELL POTENTIAL

The cubic perovskite structure is unstable because of the bond strain. It can be transformed to a more stable state characterized by a lower energy ΔU_s owing to the occurrence of ordered lattice distortions. The distortion type is determined by the cation nature and the character of the cation–anion interaction. As was noted above, two main types of ordered distortions are distinguished: the rotation of octahedra and the displacement of cations.

Ordered distortions due to the rotation of octahedra occur mainly in ionic crystals with identical unstrained-bond lengths in the sublattices. In the crystals in which the interaction of *B* or (and) *A* cations with anions is determined to a large extent by the anisotropic covalent components, which result in different unstrained-bond lengths, distortions caused by the ordered displacement of cations may arise.

The potential energy of a perovskite structure with strained bonds depends in a certain way on the parameters of ordered distortions.

Let us consider the character of this dependence for the simplest cases of the above-mentioned types of distortions (the rotation of octahedra around one coordinate axis and the displacement of cations along one coordinate axis).

Ordered lattice distortions related to the rotation of octahedra manifest themselves in the cooperative displacement of anions perpendicular to the *B*–*X* bond lines, which lie in the plane perpendicular to the axis of rotation. At such displacements, the bond lengths become different in the different sublattices. Hence, the

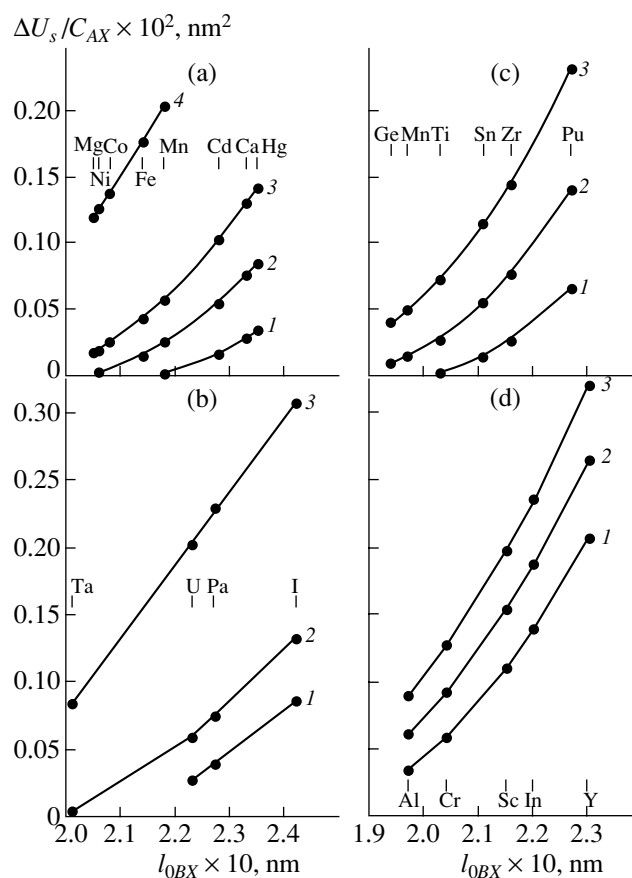


Fig. 1. Dependences of the relative value of the bond strain energy on the length of the *B*–*X* unstrained bond for a series of ABX_3 compounds: (a) ABF_3 (*A* = (1) Cs, (2) Rb, (3) K, and (4) Na), (b) $A^{1+}B^{5+}O_3$ (*A* = (1) Rb, (2) K, and (3) Na), (c) $A^{2+}B^{4+}O_3$ (*A* = (1) Ba, (2) Sr, and (3) Ca), and (d) $A^{3+}B^{3+}O_3$ (*A* = (1) La, (2) Sm, and (3) Yb).

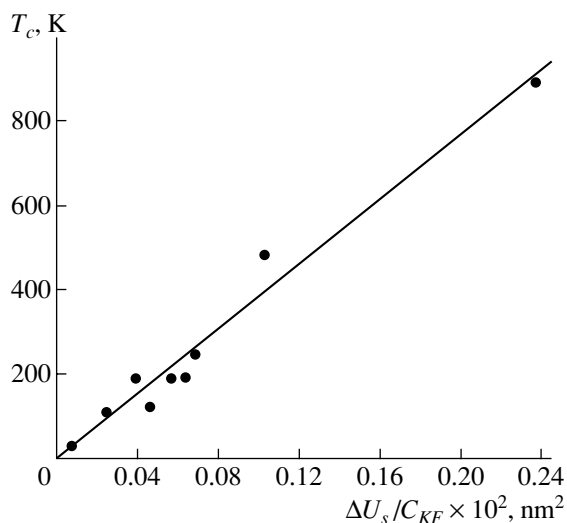


Fig. 2. Dependence of the cubic-phase transition temperature on the relative value of the bond-strain energy for ABF_3 and $A^{1+}B^{5+}O_3$ compounds.

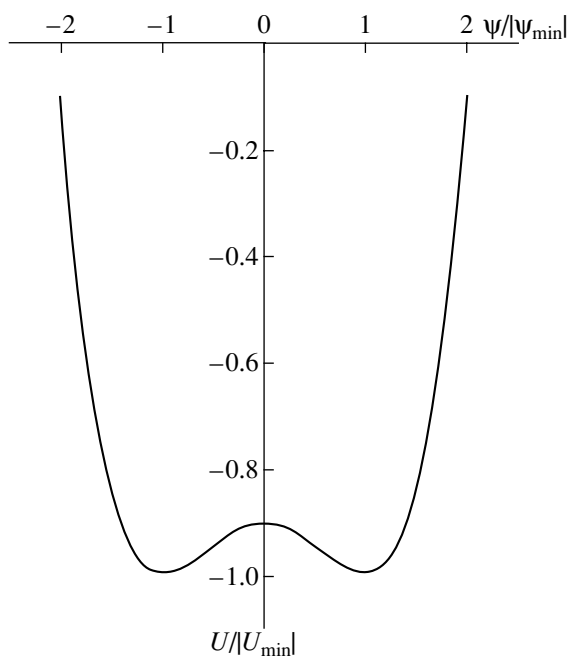


Fig. 3. Dependence of the potential energy of interatomic interaction in ABF_3 crystals with strained bonds on the angle of rotation of BX_6 octahedra around the coordinate axis.

potential energy of a distorted lattice, in contrast to (3), can be written as

$$U = U_0 + \frac{C_{BX}}{2} \left[\frac{1}{6} \sum_i^6 (l_{BX}^i - l_{0BX})^2 \right] + \frac{C_{AX}}{2} \left[\frac{1}{12} \sum_j^{12} (l_{AX}^j - l_{0AX})^2 \right] + \Delta U_r, \quad (9)$$

where ΔU_r is the contribution due to the ordered displacements of anions in the crystal lattice. Upon rotation of octahedra at some angle ψ around the z coordinate axis, the lengths l_{BX}^i and l_{AX}^j of the bonds lying in the xy plane and in the plane perpendicular to it can be expressed as follows:

for four bonds

$$l_{BX}^{xy} = l_{BX}(1 + \delta x)/\cos \psi, \quad (10)$$

for two bonds

$$l_{BX}^z = l_{BX}(1 + \delta z), \quad (11)$$

for four bonds

$$l_{AX}^{xy} = l_{BX}\sqrt{2}(1 + \delta x), \quad (12)$$

and for eight bonds

$$l_{AX}^z = (l_{BX}^2(1 + \delta z)^2 + l_{BX}^2(1 + \delta x)^2(1 \pm \tan \psi)^2)^{1/2}, \quad (13)$$

where $l_{BX} = a/2$ are the lengths of the $B-X$ bonds in the cubic reduced cell (2) and δx and δz are the relative changes in l_{BX} in the xy plane and along the z axis, respectively. These changes are due to the cooperative displacement of anions.

In view of the smallness of ψ , δx , and δz , expressions (10)–(13) can be represented by power polynomials and ΔU_r can be approximated by the sum

$$\Delta U_r = \frac{\alpha_\psi}{4} C_{BX} l_{BX}^2 \psi^4 + \alpha_x C_{BX} l_{BX}^2 \delta x \psi^2 + \alpha_z C_{BX} l_{BX}^2 \delta z \psi^2, \quad (14)$$

where α_ψ , α_x , and α_z are the approximation parameters.

Analysis of expression (9), taking into account (10)–(14), shows that the interaction potential, depending on the angle of rotation of octahedra, is a double-well one (Fig. 3). The solution of the system of equations

$\frac{\partial U}{\partial \psi} = 0$, $\frac{\partial U}{\partial \delta x} = 0$, $\frac{\partial U}{\partial \delta z} = 0$ shows that the maximum of U occurs at $\psi = 0$ and minima occur at

$$\psi_{1,2} = \pm \left(\alpha_1 \frac{l_{0BX} - l_{0AX}/\sqrt{2}}{l_{0BX} + \eta\sqrt{2}l_{0AX}} \right)^{1/2}, \quad (15)$$

$$(\delta x)_{\min} = \alpha_2 \psi_{1,2}^2, \quad (16)$$

$$(\delta z)_{\min} = \alpha_3 \psi_{1,2}^2, \quad (17)$$

where α_1 , α_2 , and α_3 are coefficients expressed in terms of α_ψ , α_x , α_z , and η . Note that $\alpha_2 < 0$ and $\alpha_3 > 0$

As follows from (9), with allowance for (15)–(17), the depth of the potential well is proportional to $(l_{0BX} - l_{0AX}/\sqrt{2})^2$. The data obtained suggest that, owing to the ordered distortions related to the rotation of octahedra, the system passes to a more stable state characterized by a lower potential energy. When octahedra are rotated around one coordinate axis (z), the lattice strain has a tetragonal character. The relation between the axes ($a_T < c_T$), which follows from (16) and (17), corresponds to the observed one [8].

In the general case, the potential (9) is multiple-well since octahedra can be rotated around any coordinate axis or simultaneously around several coordinate axes.

In the case of anisotropy of the covalent components of the anion–cation interaction, the unstrained-bond lengths in the two sublattices can generally be different. Let us consider the simplest case when the interaction between A and X ions is isotropic and the anisotropic covalent component plays an important role in the interaction between B and X ions. In this case, all lengths of unstrained bonds $A-X$ will be identical, whereas the lengths of $B-X$ bonds will be different. The bond strain in the crystal lattice affects the character of manifestation of the covalent components, facilitating the ordering of the orbitals of interacting atoms. As a

result, the covalent bond component directed along the ordering line (for example, along the z axis) increases owing to the displacement of both ions. The displacement of B cations from the centers of octahedra is due to the decrease in the bond-strain energy caused by the increase in the bond lengths in the plane perpendicular to the displacement direction. In this case, A cations may undergo some ordered displacement. As a result of such cooperative displacement of ions, the centers of gravity of the positive and negative charges in the unit cell do not coincide in the general case, which leads to the formation of a dipole moment. The ordering of bonds gives rise to the ordering of the dipole moments.

In this case, the potential interaction energy has the form

$$U = U_0 + \frac{C_{BX}}{2} \left[\frac{1}{6} \sum_{i=1}^6 (l_{BX}^i - l_{0BX}^i)^2 \right] + \frac{C_{AX}}{2} \left[\frac{1}{12} \sum_{j=1}^{12} (l_{AX}^j - l_{0AX}^j)^2 \right] + \Delta U_c + \Delta U_p + \Delta U_r, \quad (18)$$

where ΔU_c is the covalent component of the orbital ordering and ΔU_p is the dipole ordering energy.

Let us assume that the lengths of four unstrained bonds in an BX_6 octahedron are equal to $l_{0BX}^{(1)}$ and the lengths of the two other bonds are equal to $l_{0BX}^{(2)}$. Let the orbitals be ordered along the z axis. At relative displacements of A , B , and X ions along the z axis equal to Δ_A , Δ_B , and Δ_X , respectively, the expressions for strained bond lengths can be written as follows:

for four bonds

$$l_{BX}^{xy} = ((l_{BX}^a(1 + \delta x))^2 + (l_{BX}^c(1 + \delta z))^2 \Delta_B^2)^{1/2}, \quad (19)$$

for two bonds

$$l_{BX}^z = l_{BX}^c(1 + \delta z)(\pm \Delta_x \pm \Delta_B), \quad (20)$$

for four bonds

$$l_{AX}^{xy} = ((l_{BX}^a \sqrt{2}(1 + \delta x))^2 + (l_{BX}^c(1 + \delta z))^2 (\Delta_A - \Delta_X)^2)^{1/2}, \quad (21)$$

and for eight bonds

$$l_{AX}^z = ((l_{BX}^a \sqrt{2}(1 + \delta x))^2 + (l_{BX}^c(1 + \delta z))^2 (1 \pm \Delta_A)^2)^{1/2}, \quad (22)$$

where δx and δz are, respectively, the relative changes in l_{BX}^a and l_{BX}^c or the unit-cell parameters a and c , which are caused by the ordered distortions.

At $\Delta_A = \Delta_B = \Delta_X = 0$, the lengths l_{BX}^a and l_{BX}^c of the strained ordered B - X bonds are determined by the following expressions:

$$l_{BX}^a = \frac{l_{0BX}^a + \sqrt{2}\eta l_{0AX}}{1 + 2\eta} - \frac{\eta}{2(1 + 2\eta)(1 + \eta/2)} \Delta_{0BX}^c,$$

$$l_{BX}^c = \frac{l_{0BX}^c + \sqrt{2}\eta l_{0AX}}{1 + 2\eta} + \frac{\eta}{(1 + 2\eta)(1 + \eta/2)} \Delta_{0BX}^c,$$

where $\Delta_{0BX}^c = l_{0BX}^c - l_{0BX}^a$.

To reveal the character of the dependence of U (18) on the distortion parameters, we can restrict ourselves to the first-order approximation in estimating ΔU_c and ΔU_p :

$$\Delta U_c = \frac{\alpha_c}{2} C_{BX} (l_{BX}^c(1 + \delta z))^2 (\Delta_B - \Delta_X)^2, \quad (23)$$

$$\Delta U_p = \frac{\alpha_p}{2} C_{BX} (l_{BX}^c(1 + \delta z))^2 \times (n_A \Delta_A + n_B \Delta_B - n_X \Delta_X)^2, \quad (24)$$

where n_A , n_B , and n_X are the effective charges of the A , B , and X ions, respectively. ΔU_r is approximated by polynomials similar to (14).

Analysis of (18), taking into account (23) and (24), shows that the interatomic interaction potential in the case under consideration (cooperative displacements) is a double-well one.

It follows from the solution of the system of equations

$$\frac{\partial U}{\partial \Delta_B} = 0, \quad \frac{\partial U}{\partial \Delta_A} = 0, \quad \frac{\partial U}{\partial \Delta_X} = 0, \quad \frac{\partial U}{\partial \delta x} = 0, \quad \frac{\partial U}{\partial \delta z} = 0,$$

that the values $(\Delta_B)_{\min}$, $(\Delta_A)_{\min}$, and $(\Delta_X)_{\min}$, corresponding to the minimum of the energy U (18), are proportional to each other and expressed in terms of the unstrained-bond lengths.

In the general case, the potential (18), as in the case of the rotation of octahedra, is a multiple-well potential.

The data presented here suggest that the formation of the ferroelectric state in crystals with perovskite structure may be due to the presence of the bond strain and the anisotropy of the covalent component of the cation-anion interaction.

CONCLUSIONS

The method developed here for determining the characteristics of the interatomic bond strain in crystals of ABX_3 compounds with perovskite structure is based on the analysis of the dependence of the interaction potential energy on the cation-anion distances using the observable change in the average parameter of the reduced cell for different types of homologous series of

this class of compounds, including halides and oxides. The average lengths of $A-X$ and $B-X$ unstrained bonds (l_{0AX} and l_{0BX} , respectively), corresponding to the minima of the potential energy of interatomic interaction in the sublattices, are determined. It is shown that bonds are strained in crystals of this type. This strain is due to the fact that the values l_{0AX} and l_{0BX} do not satisfy the condition of existence of the ideal cubic structure ($l_{0AX}/\sqrt{2}l_{0BX} = 1$).

The bond-strain energy ΔU_s , which is proportional to $(l_{0BX} - l_{0AX}/\sqrt{2})^2$, systematically changes within the homologous series of compounds and can reach large values, at which the perovskite structure becomes unstable. This energy is responsible for the formation of ordered lattice distortions during the phase transitions related to the rotation of octahedra and/or the displacement of cations, since such distortions decrease the bond-strain energy and the system passes to a more stable state.

The value of the bond-strain energy correlates with the characteristics of ordered distortions. It should be noted that the temperature of the phase transition of the compounds to the cubic structure is proportional to ΔU_s .

In crystals with strained bonds, the anion-cation interaction energy as a function of the parameters of ordered distortions is a local multiple-well potential, whose form depends on the nature of interacting atoms. For the compounds with predominantly isotropic ionic type of interatomic bonds, ordered distortions are related to the rotation of octahedra. The position of the potential wells (the angles of rotation of octahedra) and their depth are determined by the difference $l_{0BX} - l_{0AX}/\sqrt{2}$.

When the covalent bond components are significant and have a certain anisotropy, cooperative displace-

ments of cations occur, leading generally to the formation of dipole moments in the reduced cells and their ordering. Therefore, the formation of the ferroelectric or antiferroelectric state in crystals with perovskite structure can be due to the presence of bond strain and anisotropy of the covalent component of the cation-anion interaction.

The formation of a local multiple-well potential due to the bond strain makes it possible to explain the observed conservation of local ordered lattice distortions at temperatures much higher than T_c and to describe the phase transitions in crystals with perovskite structure.

REFERENCES

1. M. E. Lines and A. M. Glass, *Principles and Application of Ferroelectrics and Related Materials* (Clarendon Press, Oxford, 1977; Mir, Moscow, 1981).
2. K. S. Aleksandrov, A. T. Anistratov, B. V. Beznosikov, and N. V. Fedoseeva, *Phase Transitions in Crystals of ABX_3 Haloid Compounds* (Nauka, Novosibirsk, 1981) [in Russian].
3. R. Comes, M. Lambert, and A. Guimier, *Acta Crystallogr., Sect. A: Cryst. Phys., Diffr., Theor. Gen. Crystallogr.* **26**, 244 (1970).
4. J. D. Axe, J. Harada, and G. Shirane, *Phys. Rev. B* **1**, 1227 (1970).
5. J. F. Scott, *Rev. Mod. Phys.* **B 46**, 83 (1974).
6. E. A. Stern and Y. Yacoby, *Phys. Chem. Solids* **57**, 1449 (1996).
7. N. M. Olekhovich, *Kristallografiya* **49** (5), 820 (2004) [*Crystallogr. Rep.* **49**, 733 (2004)].
8. M. Rousseau, J. Y. Gesland, and J. Julliard, *Phys. Rev. B* **12**, 1579 (1975).

Translated by Yu. Sin'kov

LATTICE DYNAMICS AND PHASE TRANSITIONS

Behavior of Ammonium Ion in β -LiRb $_{1-x}$ (NH $_4$) $_x$ SO $_4$ Mixed Crystals ($0.5 \leq x \leq 1.0$)

L. S. Smirnov^{1,2}, L. A. Shuvalov^{3,†}, M. L. Martinez Sarrion⁴,
L. Mestres⁴, and M. Herraiz⁴

¹ FSUE SSC RF Institute of Theoretical and Experimental Physics, Moscow, 117218 Russia

e-mail: lsmirnov@nf.jinr.ru

² Frank Laboratory of Neutron Physics, Joint Institute of Nuclear Research,
Dubna, Moscow oblast, 141980 Russia

³ Shubnikov Institute of Crystallography, Russian Academy of Sciences,
Leninskii pr. 59, Moscow, 117333 Russia

⁴ Department of Inorganic Chemistry, University of Barcelona, Barcelona, Spain

Received July 15, 2003; in final form, March 2, 2004

Abstract—The influence of replacement of an ammonium ion by rubidium on the x - T phase diagram in the concentration range $0.50 \leq x \leq 1.0$ has been studied by X-ray and neutron powder diffraction over a wide temperature range. It is shown that a decrease in the ammonium concentration is accompanied by an increase in the temperature of the II \leftrightarrow I phase transition and stabilization of phase II up to low temperatures (20 K). The changes occurring in the dynamics of mixed crystals are studied by inelastic incoherent neutron scattering. The spectra of the generalized vibrational density of states obtained allowed one to establish the difference in the phonon modes corresponding to phase III of β -LiNH $_4$ SO $_4$ and phase II of β -LiRb $_{1-x}$ (NH $_4$) $_x$ SO $_4$ mixed crystal with $x = 0.91$ and $x = 0.77$ at 20 K. It is shown that a mixed crystal with $x = 0.77$ at 20 K is in the orientational glass state. © 2005 Pleiades Publishing, Inc.

INTRODUCTION

The compounds β -LiNH $_4$ SO $_4$ (LAS) and LiRbSO $_4$ (LRS) belong to the family of AA'BX $_4$ crystals ($A, A' = \text{Li, Na, K, Rb, NH}_4, \text{Cs, N(CN)}_3$, etc.; $BX_4 = \text{SO}_4$,

SeO $_4$, ZnCl $_4$, ZnBr $_4$, BeF $_4$, MoO $_4$, WO $_4$, etc.) possessing ferroelectric properties [1]. As is well known, LAS undergo a number of the following phase transitions [2–4]:

$$\text{I} \Leftrightarrow 459.5 \text{ K [3]} \Leftrightarrow \text{II} \Leftrightarrow 283 \text{ K [2]} \Leftrightarrow \text{III} \Leftrightarrow 27 \text{ K [4]} \Leftrightarrow \text{IV.} \quad (1)$$

$T_1 \qquad \qquad \qquad T_2 \qquad \qquad \qquad T_3$

The crystal structure of phase I is orthorhombic, sp. gr. $Pm\bar{c}n-D_{2h}^{16}$, $Z = 4$, with the lattice parameters at 478 K equal to $a = 5.299(2)$, $b = 9.199(2)$, and $c = 8.741(3)$ Å [5]. The crystal structure of phase II is also orthorhombic, sp. gr. $P2_1cn-C_{2v}^9$, $Z = 4$ [6, 7] with the lattice parameters at $T = 298$ K equal to $a = 5.282(1)$, $b = 9.131(3)$, and $c = 8.780(2)$ Å [7]. The I \leftrightarrow II phase transition in LAS is a transition from the paraelectric to the ferroelectric state analogous to the paraelectric–ferroelectric phase transition in ammonium sulfate (NH $_4$) $_2$ SO $_4$. The latter compound and LAS enter a special group of ferroelectric crystals named “weak ferroelectrics” [8, 9].

The crystal structure of ferroelastic phase III [10, 11] is monoclinic and described by the sp. gr. $P2_1/c-C_{2h}^5$,

$Z = 8$ [7, 12] with the lattice parameters at $T = 190$ K equal to $a = 5.283(2)$ Å, $b = 9.121(5)$ Å, $c = 17.444(7)$ Å, and $\beta = 90.00(4)^\circ$ [7]. The crystal structures of phases II and III are shown in Fig. 1. It is seen that they are close to pseudo-hexagonal structures. Indeed, the unit cell of monoclinic phase III only slightly differs from orthorhombic, because the monoclinicity angle β is close to 90° and the a/b ratios in phases I–III are close to 1.73. Three SO $_4$ and three LiO $_4$ tetrahedra form a pseudo-hexagonal ring normal to the c axis. The SO $_4$ and LiO $_4$ tetrahedra in phase I occupy two configurational positions with equal probabilities or occupancies of 0.5. The NH $_4$ ions are located in the cavities of the rings between layered pseudo-hexagonal nets.

The crystal structure of phase IV is also monoclinic, sp. gr. Cc [4], and the phase transition III \leftrightarrow IV may result from condensation of the mode with the wave vector $k = (a^* + b^*)/2$ [4].

[†] Deceased.

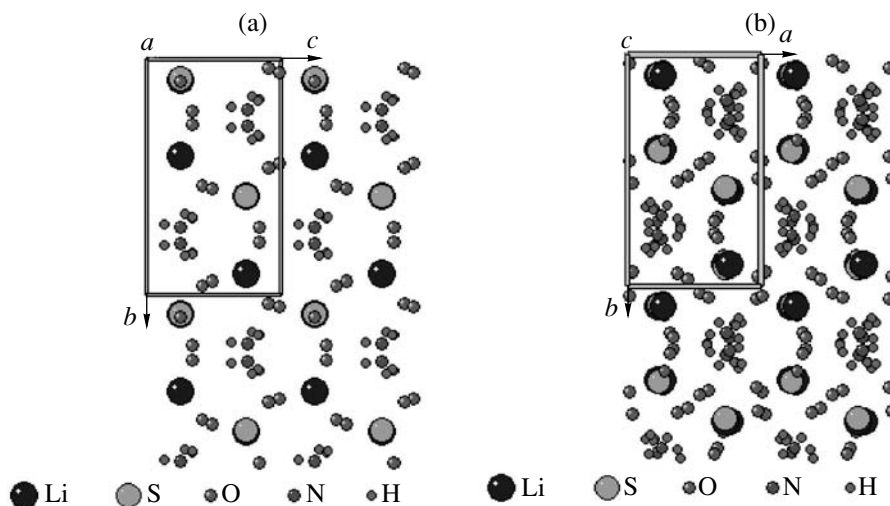
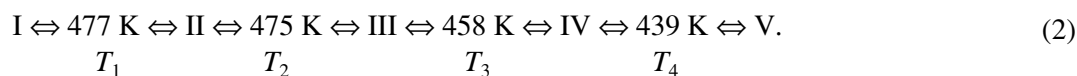


Fig. 1. Crystal structure of two phases of LiNH_4SO_4 : (a) phase II and (b) phase III.

The sequence of phase transitions in the compound LiND_4SO_4 (DLAS) is the same as in LAS, but the phase-transition temperatures in DLAS are shifted by several degrees in comparison with the phase-transition temperatures in LAS [13]. The DLAS structure was refined by the neutron powder diffraction (NPD) data

[14]. The SO_4 and ND_4 tetrahedra turned out to be irregularly distorted.

Similar to LAS, an LRS crystal has a pseudohexagonal structure inherent in the $AA'BX_4$ family [6, 15], but the sequence of phase transitions is somewhat different [16, 17]:



Crystal structures of various LRS phases are described in detail elsewhere [18]. Paraelectric phase I is orthorhombic, sp. gr. $Pm\bar{c}n-D_{2h}^{16}$, $Z = 4$, and the lattice parameters at 483 K are $a = 5.335 \text{ \AA}$, $b = 9.223 \text{ \AA}$, and $c = 8.742 \text{ \AA}$. Phase II is incommensurate (or almost commensurately modulated) because the unit-cell parameter c is almost equal to five unit-cell parameters c_0 of phase I. The LRS phases existing at lower temperatures have crystal structures described by different space groups: phase III, by sp. gr. $P2_1/c-C_{2h}^5$; ferroelectric phase IV, by sp. gr. $Pc-C_s^2$; and paraelectric phase V, by sp. gr. $P112_1/n-C_{2h}^5$.

Thus, the crystal structures of LAS and LRS in phase I are isomorphous and described by the sp. gr. $Pm\bar{c}n-D_{2h}^{16}$, whereas the crystal structures of all the remaining phases show no mutual correspondence. For example, LRS has phases II and IV with incommensurate structures that are intermediate between phases I and III and III and V. The first attempt to solve the problem of the transformation of the sequence of phase transitions from the side of LRS into the sequence of the phase transitions from the side of LAS

was made by Kawamura *et al.* [19] who studied in detail the x - T phase diagram of a $\beta\text{-LiRb}_{1-x}(\text{NH}_4)_x\text{SO}_4$ mixed crystals (LRAS) by X-ray diffraction. They obtained data on the influence of low concentrations of ammonium on the phase transitions in LRAS from the side of LRS ($0.0 \leq x \leq 0.2$) and the influence of low concentrations of rubidium ($0.90 \leq x \leq 1.0$) on the phase transitions in LRAS from the side of LAS and in the intermediate concentration region above 180 K.

Our aim was to study the influence of replacement of ammonium ions by rubidium on the phase transitions and the dynamics of ammonium ions in $\beta\text{-LiRb}_{1-x}(\text{NH}_4)_x\text{SO}_4$ mixed crystals in the concentration region from the side of ammonium $0.50 \leq x \leq 1.0$ over a large temperature range. The phase transitions were studied by X-ray and neutron powder diffraction (XPD and NPD, respectively); the effect of phase transitions on ammonium dynamics in these mixed crystals was studied by the method of inelastic incoherent neutron scattering (IINS).

EXPERIMENTAL AND RESULTS

The LAS were prepared by recrystallization of $(\text{NH}_4)_2\text{SO}_4$ and $\text{Li}_2\text{SO}_4 \cdot \text{H}_2\text{O}$ at 40°C . Both initial components were mixed in an aqueous solution in a stoichi-

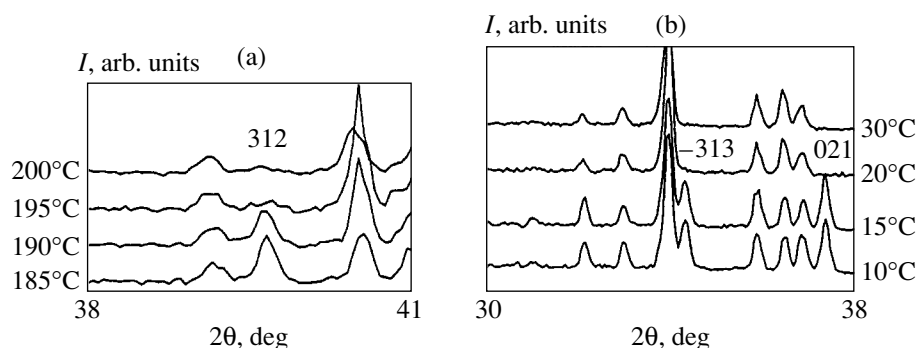


Fig. 2. (a) X-ray powder diffraction spectra of the I \leftrightarrow II and (b) II \leftrightarrow III phase transitions.

ometric proportion. As is well known, there are two crystalline modifications of the LAS compound: the α - and β -phases. The equilibrium between these LAS modifications is very labile. However, it is possible to shift the balance between these phases in the desirable direction by the dynamical method via stirring the solution during the recrystallization process at a constant temperature (40°C) [20, 21]. Colorless crystals of the β -LAS phase were several millimeters in length.

In a similar way, LiRbSO_4 crystals were also obtained from the stoichiometric aqueous solution of the initial $\text{Li}_2\text{SO}_4 \cdot \text{H}_2\text{O}$ and Rb_2SO_4 components after recrystallization by evaporation at 40°C.

$\beta\text{-LiRb}_{1-x}(\text{NH}_4)_x\text{SO}_4$ mixed crystals were obtained from aqueous solutions of $\text{Li}_2\text{SO}_4 \cdot \text{H}_2\text{O}$, $(\text{NH}_4)_2\text{SO}_4$, and Rb_2SO_4 mixed in stoichiometric ratios with subsequent slow evaporation at 40°C. The concentration composition of the final products of mixed crystals differed from the initial concentration compositions of the respective aqueous solutions. The composition of the grown crystals was determined by chemical analysis. The nitrogen and hydrogen concentrations were determined with the aid of a Carlo Erba EA 1108 microanalyzer; the concentration of Rb, with the aid of a Philips PV 9200X atomic absorption spectrophotometer; and the concentration of sulfur, by ICP analysis with the use of a Jobin Yvon analyzer.

The X-ray powder diffraction experiments on the prepared $\beta\text{-LiRb}_{1-x}(\text{NH}_4)_x\text{SO}_4$ mixed crystals were performed in a D500 automated powder diffractometer (Siemens) with $\text{CuK}\alpha$ radiation and with a secondary monochromator in the range of 2θ angles 10°–60°. The diffractometer was calibrated against silicon both before and after measurements. The temperature measurements were made in two ranges, 243–303 and 433–503 K. To perform temperature measurements, the samples were heated at a rate of 5 K/min, then both diffractometer and sample were kept for 10 min at the attained temperature to bring the system to the thermal equilibrium prior to the next measurement. The temperature measurements during lowering of the temperature were performed in a similar way. The X-ray powder

diffraction spectra thus obtained were indexed and the lattice parameters were determined using the AFFMAIL program [22].

The study of phase transitions in LAS and LRAS with $x = 0.91$ and 0.77 was performed by neutron powder diffraction in the temperature range from 300 to 20 K. The influence of phase transitions in LAS and LRAS on the ammonium dynamics was studied by the IINS method in the same temperature range. The NPD and IINS spectra in this temperature range at the concentrations $x = 1.0$, 0.91 , and 0.77 were obtained on a NERA-PR multicrystal inverted geometry spectrometer at the IBR-2 pulsed reactor at the Laboratory of Neutron Physics of the Joint Institute of Nuclear Research in Dubna [23].

The data obtained by X-ray powder diffraction on LAS showed that the temperatures T_1 and T_2 of the phase transitions turned out to be somewhat higher than the respective data indicated in literature. We determined the temperatures of phase transitions at a step of 5 K. The X-ray powder diffraction spectra used for the determination of the temperatures of the II \leftrightarrow I and III \leftrightarrow II phase transitions are shown in Figs. 2a and 2b, respectively. The II \leftrightarrow I phase transition was recorded from disappearance of the 312 reflection in the X-ray powder diffraction spectrum of phase II (Fig. 2a), and the phase transition III \leftrightarrow II was recorded from disappearance of the reflections $\bar{3}13$ and 021 in the X-ray powder diffraction spectrum of phase III (Fig. 2b).

The study of mixed crystals in the system $\beta\text{-LiRb}_{1-x}(\text{NH}_4)_x\text{SO}_4$ by X-ray powder diffraction at room temperature showed that, in the concentration range of ammonium $0.5 \leq x \leq 1.0$, monophasic crystals of the solid solution of the β -modification of LRAS are formed. It seems that the limited region of the solid solution in mixed LRAS crystals arises as a result of solution evaporation at 40°C, the temperature at which LAS and LRS have different crystal structures. The study of the influence of the variation of ammonium concentration on the transition temperature T_1 between phases II and I showed an increase in this temperature with a decrease in ammonium concentration at a rate of

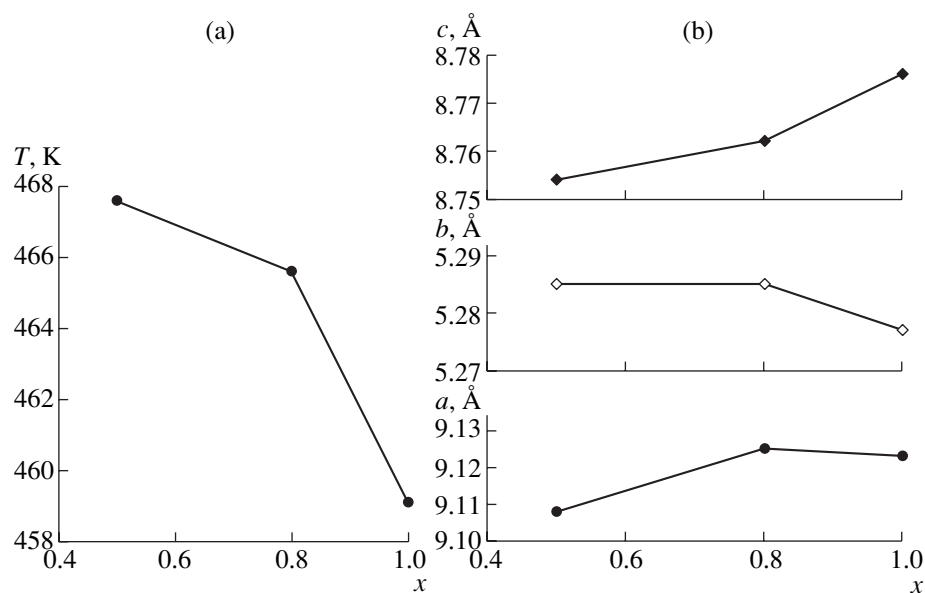


Fig. 3. (a) Concentration dependence of the temperature of the I \leftrightarrow II phase transition in LRAS crystals and (b) concentration dependence of the lattice parameters of phase II of LRAS crystals at room temperature.

0.17 K/at. % (Fig. 3a). The dependence of the lattice parameters of orthorhombic phase II of LRAS at the concentrations $x = 1.0$, 0.91, and 0.77 at room temperature is shown in Fig. 3b.

The NPD spectra of LAS at 294 K (phase II), 260 and 40 K (phase III), and 20 K (phase IV) are shown in Fig. 4 in the range of interplanar spacings $d = 1.9$ – 2.5 Å. The NPD spectrum at 260 K differs from that at 294 K by the presence of additional reflections indicating the occurrence of a structural phase transition. Slight differences between the spectra at 260 and 40 K reflect the influence of the temperature. The NPD spectra at 40 and 20 K are practically identical, although they should correspond to different phases. However, the temperature behavior of these spectra confirms the specificity of the III \leftrightarrow IV phase transition described in [4]. The temperature of this transition, $T_3 = 27$ K, also described in [4], corresponds to the middle point of the transition diffused over temperature. This phase transition is completed near 10 K.

The temperature dependence of the NPD spectra of LRAS crystals at $x = 0.91$ and 0.77 are shown in Fig. 5 together with the corresponding LAS spectrum at 294 K (phase II). The temperature variation from 260 to 20 K practically does not influence the family of NPD spectra for LRAS with $x = 0.91$ in the range of spacing variation d from 1.9 to 2.5 Å. On the other hand, the comparison of the NPD spectra of LAS at 294 K and LRAS with $x = 0.91$ in the temperature range from 260 to 20 K leads to a conclusion about the stability of phase II of LRAS (because its spectra are identical to the LAS spectrum). Thus the replacement of ammonium by 9% Rb in LAS stabilizes phase II down to low temperatures. The NPD spectrum of LRAS with $x =$

0.77 with 20 K, also shown in Fig. 5, demonstrates that it is identical to the analogous spectra of LAS and LRAS at $x = 0.91$ in phase II. The comparison of these spectra shows that the mixed LRAS crystals at the above concentrations preserve phase II down to low temperatures.

The IINS spectra of LAS measured on a NERA-PR spectrometer simultaneously with the NPD spectra at the same temperatures are shown in Fig. 6a. The generalized vibrational densities of states $G(E)$ calculated from these spectra in the incoherent one-phonon approximation by the program [24] are shown in Fig. 6b. The IINS spectra of LAS have some specific features: the presence of the contribution of a quasielastic incoherent neutron scattering (QINS) at 294 and 260 K, which does not noticeably vary in the II \leftrightarrow III phase transition. However, cooling in the temperature interval of phase III is accompanied by reduction of the QINS contribution up to its complete disappearance at 40 K. The considerable QINS contribution in the vicinity of the II \leftrightarrow III phase transition and its decrease with lowering of the temperature may be explained by a decrease in the frequency of ammonium-ion reorientation.

A decrease in anharmonicity and the QINS contribution with lowering of the temperature results in the formation of a fine structure of the $G(E)$ spectrum at 40 K. A slight difference between the $G(E)$ spectra at 40 and 20 K indicates the beginning of the III \leftrightarrow IV phase transition. The fine structure of the $G(E)$ spectrum allows one to determine the energy of the translation and librational modes of LAS in phases III and IV. The corresponding values and their comparison with the other known data are listed in the table.

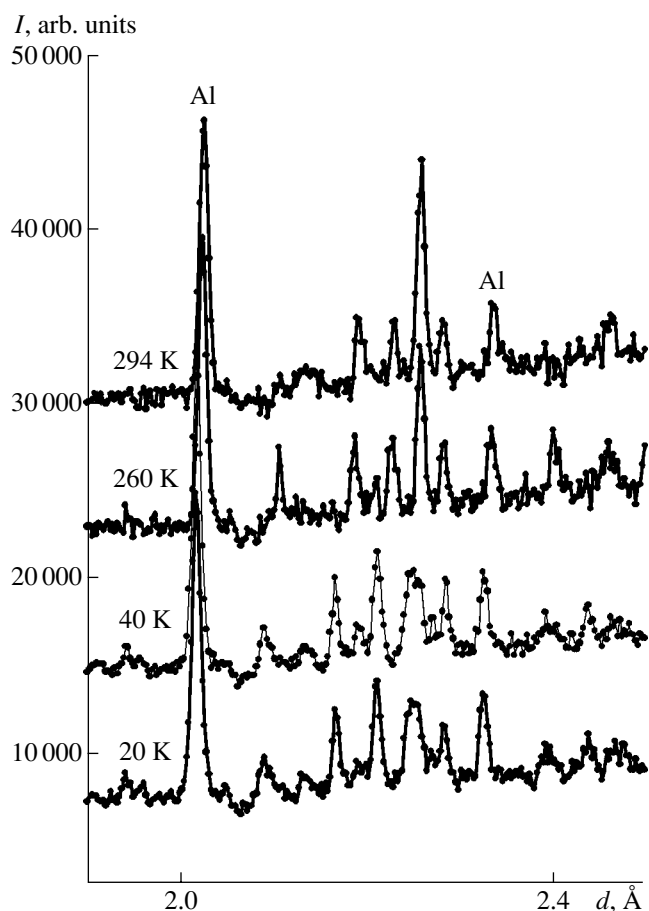


Fig. 4. Fragment of neutron powder diffraction spectra of β -LiNH₄SO₄ at various temperatures.

The identification of the translation (Σ) and librational (ν_6^+) modes of ammonium ions was made based on data [25, 26]. The resolution of the Raman scattering (RS) experiment is higher than the resolution of the IINS experiments and, therefore, the wide zones of the $G(E)$ spectra are compared in the table with narrow lines of the Raman spectra. It should be noted that the mode with the energy ~ 260 cm⁻¹ is absent in neutron scattering data [25]. In accordance with [13, 26], the librational modes in LAS spectra lie in the energy range 250–400 cm⁻¹. It should also be noted that the librational modes obtained for phase III satisfactory agree with the inelastic neutron scattering [25] and Raman scattering [13] data. The study of the influence of temperature on Raman scattering spectra from phase III of LAS showed [13] that the librational lines become narrower with cooling below T_2 , which is explained by a considerable reorientation amplitude of ammonium ions. With an approach to the temperature 40 K, the amplitude of librational vibrations decreases and ammonium ions are localized, which is accompanied by splitting and the appearance of well-resolved librational lines. A similar influence of the temperature on

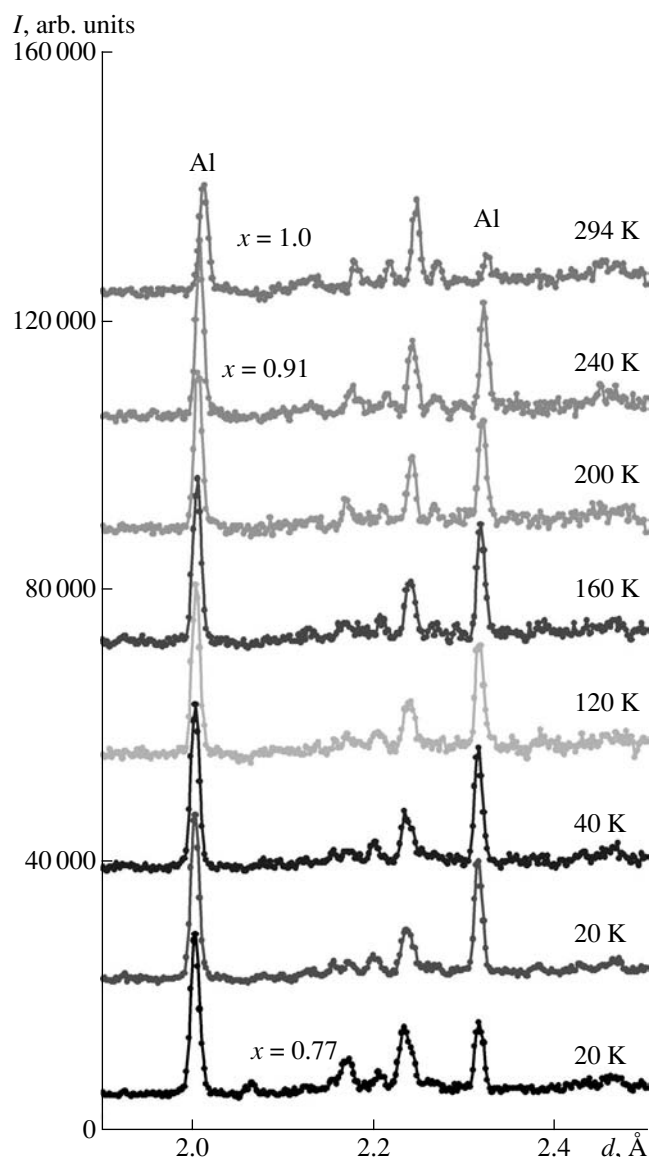


Fig. 5. Neutron powder diffraction spectra of β -LiRb_{1-x}(NH₄)_xSO₄ mixed crystals with $x = 0.77, 0.91,$ and 1.0 at various temperatures.

the $G(E)$ spectra was also observed in the case of inelastic incoherent neutron scattering, as has already been indicated above (comparison of the $G(E)$ spectra) at the temperatures 260 and 40 K in the range of existence of phase III (Fig. 6b).

It is also interesting to compare the identification of the modes observed by the IINS with the identification by the Raman scattering data for deuterated LAS, i.e., β -LiND₄SO₄ (DLAS) [27]. Thus, at a low temperature, the Raman spectra of DLAS showed the lines at 200 and 270 cm⁻¹ [27] which were compared with the lines at 200 and 370 cm⁻¹ in LAS spectra. Thus, the result obtained in [27] uniquely identifies the line at 200 cm⁻¹

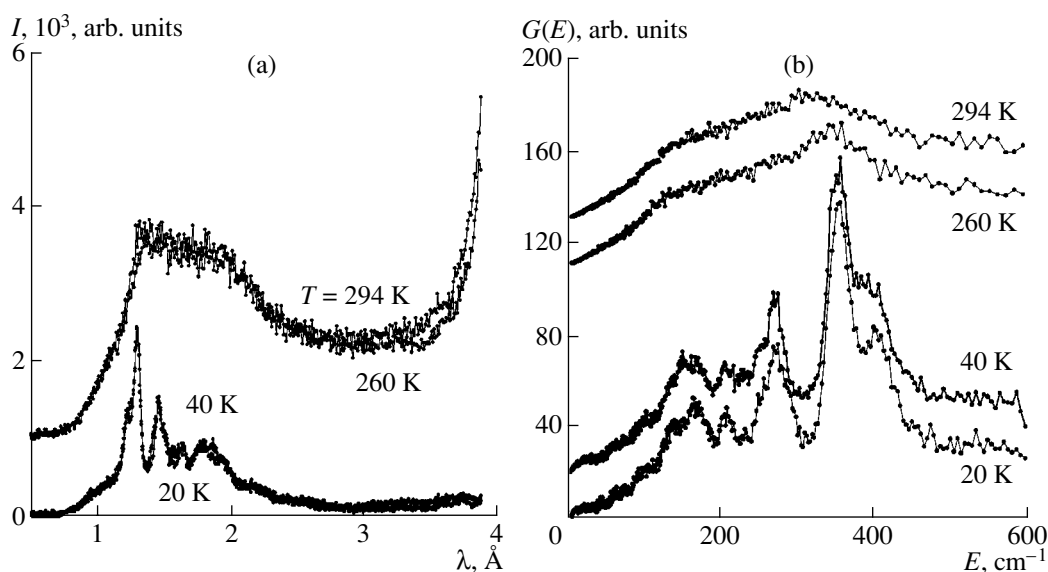


Fig. 6. β -LiNH₄SO₄: (a) IINS and (b) $G(E)$ spectra at various temperatures.

as the translation mode and the line at 370 cm⁻¹ as the librational mode of ammonium ions in LAS.

The temperature evolution of the IINS spectra from LiRb_{0.09}(NH₄)_{0.91}SO₄ is illustrated by Fig. 7a; the respective calculated $G(E)$ spectra are shown in Fig. 7b. The QINS contributions are observed in the IINS spectra of LiRb_{0.09}(NH₄)_{0.91}SO₄ at 240 and 200 K, monotonically decrease with lowering of the temperature, and disappear below 160 K.

The $G(E)$ spectrum from LiRb_{0.09}(NH₄)_{0.91}SO₄ at 240 K, which reflects the reorientation of ammonium ions and their anharmonicity, shows a broad maximum which is split into several maxima with lowering of the temperature, and at 20 K the $G(E)$ spectrum has a fine structure corresponding to phase II of the mixed crystal.

Comparison of the IINS and $G(E)$ spectra of mixed LRAS crystals with the corresponding spectra of LAS is illustrated by Figs. 8a and 8b at 20 K. It is seen that the vibrational spectra of LAS in phase III (or phase IV) and LRAS spectra of phase II are different. Thus, the mode with the energy in the vicinity of ~200 cm⁻¹ observed in phase III of LAS is not observed in the vibrational spectrum of phase II of LRAS mixed crystals with the ammonium concentrations $x = 0.91$ and 0.77. However, the IINS and $G(E)$ spectra of the LRAS mixed crystals in phase II with the ammonium concentration $x = 0.77$ at 20 K have broader maxima than the maxima of the respective spectra of LRAS at $x = 0.91$. Such a change in the IINS and $G(E)$ spectra of LRAS mixed crystals at $x = 0.77$ shows that, at low temperatures, these mixed crystals may be in the orientational glass state. In the $G(E)$ spectrum of LRAS crystals with $x = 0.77$, one broad librational maximum with the energy 340 cm⁻¹ is observed. This maximum combines the zones with the energies 353 and 402 cm⁻¹ of the

mixed crystals with $x = 0.91$ such that the FWHM of the librational maximum for $x = 0.77$ considerably exceeds the FWHM of the crystal with $x = 0.91$.

The comparison shows that the influence of concentration of rubidium substituting the ammonium ions on the x - T phase diagram of a LRAS mixed crystal on the dynamics of ammonium in this crystal is the same as for the [Rb_{1-x}(NH₄)_x]₃H(SO₄)₂ mixed crystal [28]. At the concentration of rubidium replacing ammonium ions higher than 10%, phase II is stabilized. At a low temperature, the maxima of the IINS and $G(E)$ spectra of phase II become wide, indicating the formation of the static disorder in orientations of ammonium ions. This, in turn, indicates the formation of the phase of orientational glass. Indeed, the phase with the orientational glass state on the x - T phase diagram of [Rb_{1-x}(NH₄)_x]₃H(SO₄)₂ mixed crystals was observed earlier by the method of dielectric spectroscopy [30].

The comparison of the x - T phase diagram of β -LiRb_{1-x}(NH₄)_xSO₄ in the region $0.5 < x < 1.0$ determined in the course of X-ray studies [7] and the neutron scattering data obtained in the present study is illustrated by Fig. 9. It should be noted that the regions of phases II and III were determined by both X-ray and neutron powder diffraction methods, whereas the orientational glass state of β -LiRb_{1-x}(NH₄)_xSO₄ with the ammonium concentration $x = 0.77$ was determined only by the inelastic incoherent neutron scattering.

DISCUSSION OF RESULTS

The results obtained on the behavior of ammonium ions in the β -LiRb_{1-x}(NH₄)_xSO₄ mixed crystals are compared with the results obtained by other authors who studied the crystal structure by X-ray single-crystal dif-

Energies (in cm^{-1}) of the modes revealed in several phases of LAS and LRAS crystals ($x = 0.91$ and 0.77) by different methods

| LAS | | LRAS, $x = 0.91$ | LRAS, $x = 0.77$ | LAS [25] | | LAS [26] | Mode |
|---------------|---------------|------------------|------------------|-------------|-------------|-------------|------------|
| phase IV | phase III | phase II | phase II | phase IV | phase III | phase III | |
| $G(E)$, 20 K | $G(E)$, 40 K | $G(E)$, 20 K | $G(E)$, 20 K | NS , 20 K | NS , 40 K | RS , 40 K | |
| 66.8 | 60 | 157 | 166 | | | 60 | Σ |
| | | | | | | 62 | |
| | | | | | | 74 | |
| | | | | | | 79 | |
| 100 | 104 | | | 96 | 96 | 85 | Σ |
| | | | | | | 93 | |
| | | | | | | 97 | |
| | | | | | | 107 | |
| | | | | | | 114 | |
| | | | | | | 118 | |
| | | | | | | 123 | |
| 135 | 136 | | | 136 | 136 | 127 | Σ |
| | 150 | | | | | 137 | |
| | | | | | | 148 | Σ |
| | | | | | | 155 | |
| 168 | 168 | | | 160 | 168 | 169 | Σ |
| | | | | | | 175 | |
| | | | | | | 179 | |
| 208 | 205 | 267 | 255 | 200 | 200 | 202 | Σ |
| | | | | | | 210 | |
| 263 | 257 | | | | | 230 | Σ^+ |
| 272 | 272 | | | 272 | 272 | 270 | ν_6^+ |
| 288 | | | | | | 280 | ν_6^+ |
| 353 | 352 | 353 | 340 | 344 | 360 | 342 | ν_6^+ |
| | | | | | | 356 | |
| | | | | | | 365 | |
| | | | | | | 369 | |
| 401.1 | 391.2 | 401.6 | | 400 | | 376 | ν_6^+ |
| | | | | | | 390 | |
| | | | | | | 400 | |
| | | | | | | 406 | |

fraction and physical properties by nuclear magnetic resonance NMR.

According to [7], the difference electron-density Fourier synthesis of phase II of LAS has six (i.e., more than four) peaks around a nitrogen atom. This fact formed the basis for the determination of the crystal structure of this phase with a partly disordered ammonium ion. According to [7], ammonium ions in phase III of LAS become ordered. The IINS spectra of LAS at 294 and 260 K corresponding to phases II and III, respectively, show that the QINS contribution to the IINS spectra is not considerably changed when inter-

secting the boundary between these phases. Such a temperature behavior of the IINS spectra may be explained under the assumption that ammonium ions in crystal structures of phases II and III may be reoriented with equal probabilities. In this case, the IINS spectra obtained are inconsistent with the results of X-ray structural studies reported in [7] and, therefore, the $\text{II} \Leftrightarrow \text{III}$ phase transition cannot be interpreted as a disorder-order phase transition.

The analysis of the ^7Li and ^2D NMR spectra of LAS over a wide temperature range [31] showed that ammonium ions are deformed and possess electric dipole

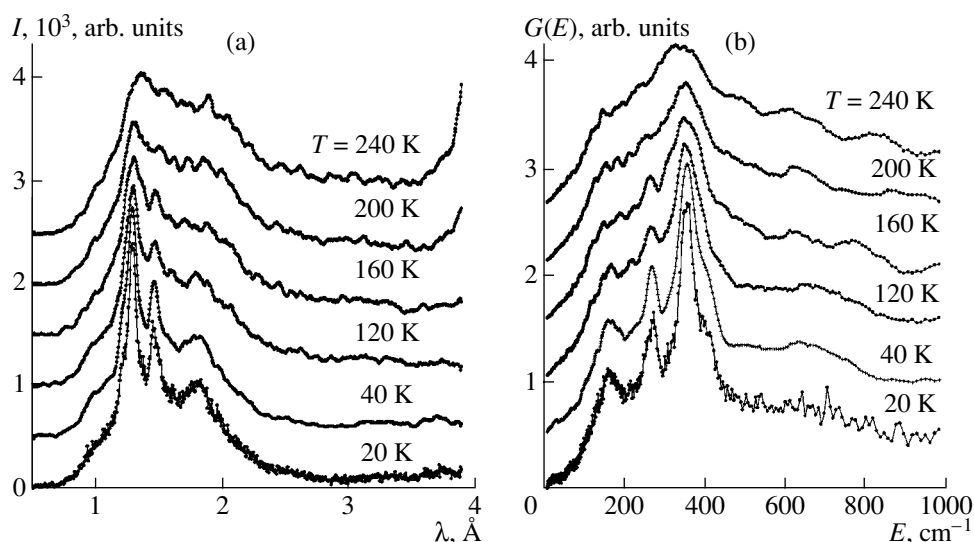


Fig. 7. β -LiRb_{0.09}(NH₄)_{0.91}SO₄: (a) IINS and (b) $G(E)$ spectra at various temperatures.

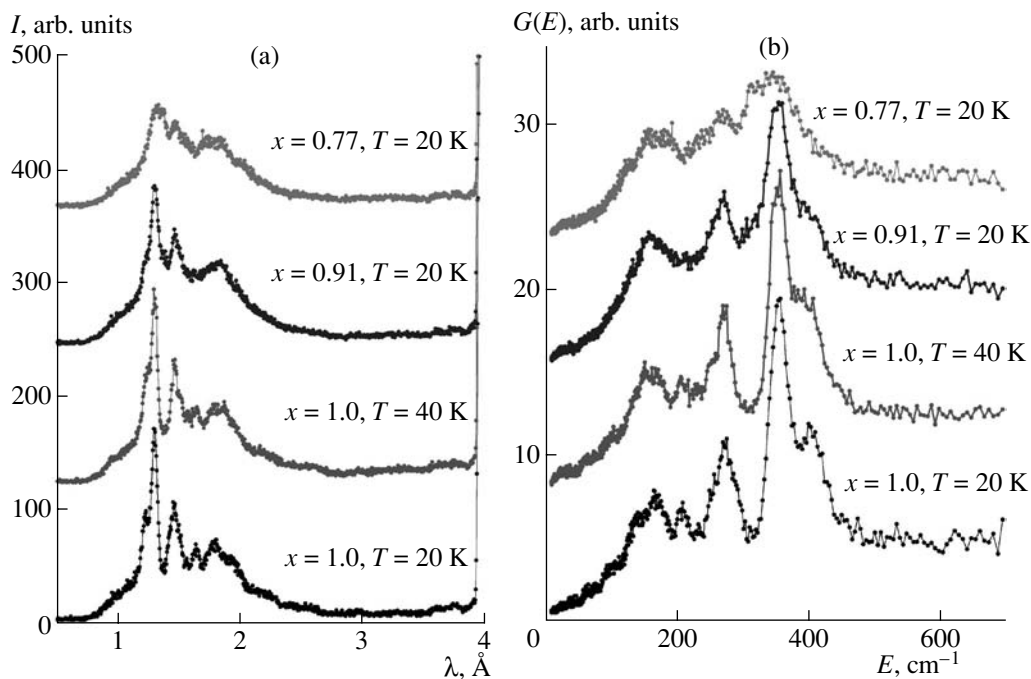


Fig. 8. β -LiRb_{1-x}(NH₄)_xSO₄ (a) IINS and (b) $G(E)$ spectra at low temperatures.

moments. The NMR studies of spin-lattice relaxation of LAS in the laboratory (T_1) and rotating ($T_{1\rho}$) coordinate systems in the range 400–77 K led Watton *et al.* [32] to the conclusion that they observed a phase transition in the vicinity of 133 K. Two singularities in the temperature dependence of both T_1 and $T_{1\rho}$ observed at 294 and 133 K indicated the existence of three different temperature regions: one from \sim 400 to 294 K in the region of phases II, where both T_1 and $T_{1\rho}$ decrease with lowering of the temperature with the activation

energy 1.9 ± 0.1 kcal/mol; the region between 294 and 133 K, where both T_1 and $T_{1\rho}$ decrease with lowering of the temperature with the activation energy 2.55 ± 0.05 kcal/mol; and the region below 133 K, where $T_{1\rho}$ continues decreasing with the activation energy 1.49 ± 0.05 kcal/mol, whereas T_1 passes through the minimum at 115 K.

It was shown [31] that the temperature dependences of T_1 and $T_{1\rho}$ may be explained by the reorientation of ammonium ions about the molecular axes C_2 and C_3

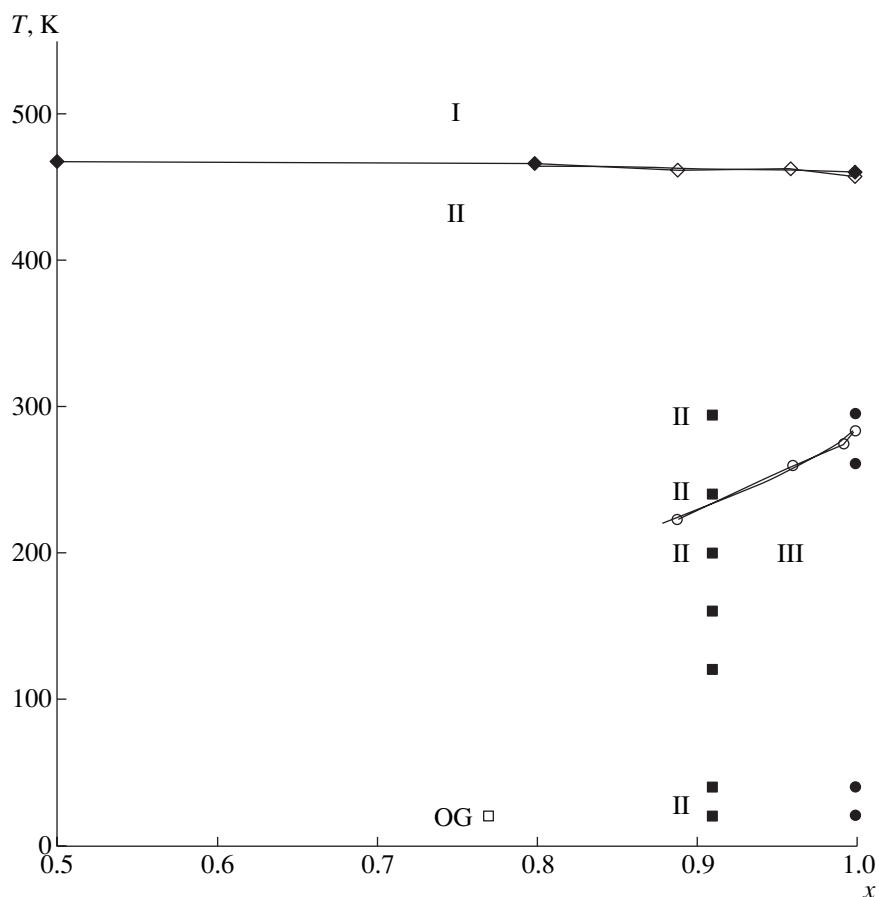


Fig. 9. x - T phase diagram of β -LiRb $_{1-x}$ (NH $_4$) $_x$ SO $_4$ in the concentration region of ammonium ions, $0.5 < x < 1.0$. Solid lines show the boundaries between the phases I \rightarrow II and II \rightarrow III, and the symbols \circ and \diamond correspond to the respective boundaries determined by X-ray diffraction studies [7]; the symbols \bullet , \blacklozenge , \blacksquare , and \square indicate the data obtained in the present study by the method of neutron diffraction scattering.

and it was assumed that the reorientation of ammonium ions is unimportant in the phase transitions at 284 and 133 K.

Lim *et al.* [33], studying the effect of temperature on the protonic magnetic resonance in LAS, confirmed the anomaly in spin-lattice relaxation at 133 K caused by a critical decrease in the soft mode, which is usually observed in structural phase transitions.

The conclusion drawn in [31] on the reorientation of ammonium ions about the molecular axes in the vicinity of the II \leftrightarrow III phase transition at 284 K is confirmed by the IINS spectra above and below the temperature of this phase transition (Fig. 6). However, the anomaly in LAS observed at 133 K [31] may be interpreted differently. The specificity of the temperature dependence of T_1 and $T_{1\rho}$ may result from the change in the reorientation of ammonium ions. A decrease in temperature gives rise to an increase in some potential barriers in the LAS crystal lattice, so that ammonium ions can reorient only about a limited number of molecular axes. A similar anomaly in the temperature dependence of the lattice parameters was observed in the monoclinic

NH $_4$ SCN phase [34]. The interpretation of the anomaly in the temperature dependence of T_1 and $T_{1\rho}$ at 133 K as a result of the phase transition is also inconsistent with the thermodynamic studies [27]. However, the above-mentioned studies [13] showed that the influence of reorientation of ammonium ions on the dynamic properties of LAS varies with lowering of the temperature. Thus, the detailed study of the influence of the temperature on the Raman spectra of LAS [13] demonstrated that with lowering of the temperature in the region of phase III below 200 K it becomes possible to observe the librational mode of ammonium with the energy increasing from ~ 250 cm $^{-1}$ at T_2 to ~ 275 cm $^{-1}$ at 40 K. Another librational mode splits below 200 K, with the energy increasing from ~ 300 cm $^{-1}$ at T_2 to ~ 360 cm $^{-1}$ at 40 K, although the energy of the doublet ~ 365 cm $^{-1}$ is almost constant in the temperature range from 200 to 40 K. It is possible to assume that both librational modes are observed in the $G(E)$ spectra at 40 K (table).

Analysis and comparison of the physical properties of LAS obtained by the above methods allow one to

suggest a model of behavior of an ammonium ion in $\beta\text{-LiRb}_{1-x}(\text{NH}_4)_x\text{SO}_4$ mixed crystals.

Both the structural [7] and NMR [31] data show that ammonium ions in phase II reorient. However, it is indicated in [7] that ammonium ions reorient about crystallographic axes, while in [31], they reorient about molecular axes. Possible reorientation of ammonium ions about crystallographic axes in phase II may give rise to formation of orientational glass in $\beta\text{-LiRb}_{1-x}(\text{NH}_4)_x\text{SO}_4$ mixed crystals during their cooling as a result of the rearrangement of the dynamic disorder in ammonium ion orientations into the static disorder. If ammonium ions are distorted, possess an electric dipole moment, and may reorient about molecular axes [31], cooling of the $\beta\text{-LiRb}_{1-x}(\text{NH}_4)_x\text{SO}_4$ mixed crystals will result in the formation of the state of dipole orientational glass. Thus, for better understanding of the nature of the orientational-glass state in $\beta\text{-LiRb}_{1-x}(\text{NH}_4)_x\text{SO}_4$ mixed crystals, one has to refine the crystal structure of phase II of LAS by methods of single-crystal neutron diffraction. X-ray studies of phase II of LAS showed that the difference Fourier maps have more than four peaks around the nitrogen peak, which corresponds to the electron charge-density distribution. However, only neutron diffraction can shed the light on the real distribution of nuclear density of hydrogen and answer the question about possible reorientation of ammonium ions in the crystal structure of phase II of LAS.

CONCLUSIONS

The results obtained in the study of the $\beta\text{-LiRb}_{1-x}(\text{NH}_4)_x\text{SO}_4$ mixed crystals by the methods of X-ray and neutron powder diffraction and inelastic incoherent neutron scattering show a considerable influence of rubidium on the x - T phase diagram. The X-ray powder diffraction study determined the region of the solid solution from the side of LiNH_4SO_4 and the influence of the rubidium concentration on the temperature of the $\text{II} \Leftrightarrow \text{I}$ phase transition. The powder neutron diffraction study shows that the replacement of ammonium ions by 9 and 23% of rubidium stabilizes phase II to a temperature of 20 K.

The inelastic incoherent neutron scattering study showed that rubidium influences the dynamics of ammonium ions. Analysis of the spectra of generalized vibrational density of states $G(E)$ of $\beta\text{-LiRb}_{1-x}(\text{NH}_4)_x\text{SO}_4$ mixed crystals showed that doping with rubidium of stabilized phase II results in disappearance of the mode with the energy in the vicinity of 200 cm^{-1} in the $G(E)$ spectrum at 20 K in comparison with the $G(E)$ spectrum of phase III in $\beta\text{-LiNH}_4\text{SO}_4$ at the same temperature. Broadening of the librational peaks in the $G(E)$ spectrum of the $\beta\text{-LiRb}_{0.23}(\text{NH}_4)_{0.77}\text{SO}_4$ mixed crystal indicates that this mixed crystal undergoes the transition to the phase of orientational glass.

The sequence of phase transitions in LAS is determined by the behavior of ammonium ions and their contribution to the propensity of the crystal lattice of this compound to the propensity of rearrangement because of the formation of hydrogen bonds of ammonium with neighboring atoms. With lowering of the temperature, the interaction of ammonium ions with their neighbors becomes more pronounced because of hydrogen bonding, which hinders the rotational motion of ammonium ions. Doping of LAS with rubidium, instead of ammonium, is accompanied by break of the net of hydrogen bonds formed via ammonium ions. This, in turn, considerably changes the propensity of the crystals to phase transitions.

Thus, when considering the x - T phase diagram of a LRAS mixed crystal at low temperature, one has must take into account the region of orientational glass, the concentration boundaries of which have not been established as yet.

It is also necessary to indicate that the nature of the state of orientation glass formed in LRAS has not been reliably established as yet. In order to determine possible reorientation of ammonium ions around crystallographic axes, it is necessary to refine the crystal structure of phase II of the LAS by the single-crystal neutron-diffraction data.

ACKNOWLEDGMENTS

The authors are grateful to I.V. Natkaniec for fruitful discussions and S.I. Bragin for his technical assistance in the neutron-scattering experiments. This study was supported by the Leading Scientific School of L.A. Shuvalov, project no. NSh-1514.2003.2, and the Russian Foundation for Basic Research, project no. 02-02-17330.

REFERENCES

1. S. Aleksovska, C. Nyburg, Li. Pejov, and V. M. Petrushevski, *Acta Crystallogr., Sect. B: Struct. Sci.* **54**, 115 (1998).
2. R. Pepinsky, K. Vedam, Y. Okaya, and S. Hoshino, *Phys. Rev.* **111**, 1467 (1958).
3. T. Mitsui, T. Oka, Y. Shiroishi, *et al.*, *J. Phys. Soc. Jpn.* **39**, 845 (1975).
4. T. Simonson, F. Denoyer, and R. Moret, *J. Phys. (Paris)* **45**, 125 (1984).
5. K. Itoh, H. Ishikura, and E. Nakamura, *Acta Crystallogr., Sect. B: Struct. Crystallogr. Cryst. Chem.* **37**, 664 (1981).
6. W. A. Dollase, *Acta Crystallogr., Sect. B: Struct. Crystallogr. Cryst. Chem.* **25**, 2298 (1969).
7. H. Mashiyama and H. Kasano, *J. Phys. Soc. Jpn.* **62**, 155 (1993).
8. A. K. Tagantsev, *Pis'ma Zh. Éksp. Teor. Fiz.* **45**, 352 (1987) [*JETP Lett.* **45**, 447 (1987)].
9. V. I. Torgashev and L. T. Latush, *Kristallografiya* **42**, 696 (1997) [*Crystallogr. Rep.* **42**, 636 (1997)].

10. K. S. Aleksandrov, I. R. Aleksandrova, L. I. Zherebtsova, and A. I. Kruglik, *Izv. Akad. Nauk SSSR, Ser. Fiz.* **39**, 943 (1975).
11. B. O. Hildmann, Th. Hahn, L. E. Cross, and R. E. Newnham, *Appl. Phys. Lett.* **27**, 103 (1975).
12. A. I. Kruglik, M. A. Simonov, and K. S. Aleksandrov, *Kristallografiya* **23**, 494 (1978) [*Sov. Phys. Crystallogr.* **23**, 274 (1978)].
13. V. I. Torgashev, Yu. I. Yuzyuk, F. Smutny, and M. Polomska, *Phys. Status Solidi B* **135**, 93 (1986).
14. P. Fischer, I. Sosnowska, and T. Wroblewski, *Physica B (Amsterdam)* **156–157**, 118 (1989).
15. A. Kunishige and H. Mashiyama, *J. Phys. Soc. Jpn.* **56**, 3189 (1987).
16. Y. Shiroishi, A. Nakata, and S. Sawada, *J. Phys. Soc. Jpn.* **40**, 911 (1976).
17. Y. Shiroishi and S. Sawada, *J. Phys. Soc. Jpn.* **46**, 148 (1979).
18. H. Mashiyama, K. Hasebe, S. Tanisaki, *et al.*, *J. Phys. Soc. Jpn.* **47**, 1198 (1979).
19. K. Kawamura, A. Kuramashi, H. Nakamura, *et al.*, *Ferroelectrics* **105**, 279 (1990).
20. I. Sosnowska, B. Hilczer, and P. Piskunowicz, *Solid State Commun.* **74**, 1249 (1990).
21. M. Polomska, B. Hilczer, and J. Baran, *J. Mol. Struct.* **325**, 105 (1994).
22. J. Stewart, *AFFMAIL. Computer Program for Cell Parameters Refinement* (Univ. of Bourdeaux, France, 1970). Modified by Comberton, 1970; Filhol, 1972 and 1978; and J. Rodriguez, 1985.
23. I. Natkaniec, S. I. Bragin, J. Brankowski, and J. Mayer, in *Proceedings of the ICANS XII Meeting*, Ed. by U. Steigenberger *et al.* (Abingdon, 1993), RAL Report No. 94-025, Vol. 1, p. 89.
24. E. L. Bokhenkov, I. Natkaniec, and E. F. Sheka, *Sov. Phys. JETP* **43**, 536 (1976).
25. I. Sosnowska, J. Sosnowski, and M. Prager, in *Phonons 89*, Ed. by S. Hunklinger *et al.* (World Sci., 1990), Vol. 1, p. 148.
26. Yu. I. Yuzyuk, V. I. Torgashev, I. Gregora, and A. H. Fuiith, *J. Phys.: Condens. Matter* **11**, 889 (1999).
27. P. Kumara Acharya and P. S. Narayanan, *Indian J. Pure Appl. Phys.* **11**, 514 (1973).
28. K. Chhor, L. Abello, and C. Pommier, *J. Phys. Chem. Solids* **50**, 423 (1989).
29. L. S. Smirnov, A. I. Baranov, L. A. Shuvalov, *et al.*, *Fiz. Tverd. Tela (St. Petersburg)* **43**, 115 (2001) [*Phys. Solid State* **43**, 117 (2001)].
30. A. I. Baranov, V. V. Dolbinina, E. D. Ykushkin, *et al.*, *Ferroelectrics* **217**, 285 (1998).
31. K. S. Aleksandrov, I. P. Aleksandrova, A. T. Anistratov, and V. F. Shabanov, *Izv. Akad. Nauk SSSR, Ser. Fiz.* **41**, 599 (1977).
32. A. Watton, E. C. Reynhardt, and H. E. Petch, *J. Chem. Phys.* **69**, 1263 (1978).
33. A. R. Lim, J. K. Jung, and S.-Y. Jeong, *J. Phys. Chem. Solids* **63**, 625 (2002).
34. M. Dlouha, S. Vratislav, I. Natkaniec, and L. S. Smirnov, *Kristallografiya* **43**, 237 (1998) [*Crystallogr. Rep.* **43**, 202 (1998)].

Translated by L. Man

LATTICE DYNAMICS AND PHASE TRANSITIONS

Molecular Dynamics Simulation of Premelting Effect in AgBr

A. K. Ivanov-Schitz*, G. N. Mazo**, E. S. Povolotskaya*, and S. N. Savvin**

* Shubnikov Institute of Crystallography, Russian Academy of Sciences,
Leninskii pr. 59, Moscow, 119333 Russia

e-mail: ivanov@ns.crys.ras.ru

** Moscow State University, Vorob'evy gory, Moscow, 119992 Russia

Received April 5, 2004

Abstract—The effect of premelting in silver bromide crystals has been simulated for the first time. It is shown that at the temperature about 150°C lower than the melting point of silver bromide, a considerable increase in the mobility in the cationic sublattice is observed, whereas the (self-)diffusion coefficient of silver ions attains values exceeding 10⁻⁶ cm²/s. The assumption about the superionic nature of conductivity in the region of premelting is confirmed by the break of the long-range order in the cationic subsystem, which, in turn, is confirmed by the comparison of the pair cation–cation correlation functions far from and in the vicinity of the melting point. It is established that the premelting effect correlates with the experimentally observed effect of a considerable increase in ionic conductivity in the vicinity of the melting point. It is shown that the premelting effect in AgBr is similar to the diffuse superionic phase transition in anionic conductors of the MF₂ family (*M* = Ca, Ba, Sr, and Pb). © 2005 Pleiades Publishing, Inc.

COMPUTER SIMULATION

As is well known, silver bromide and silver chloride demonstrate the so-called premelting effect: at high temperatures (150–200°C below the melting point), the conductivity dramatically increases and starts deviating from the Arrhenius behavior characteristic of ionic crystals [1–3]. It should be noted that AgBr does not undergo any structural phase transformations up to the melting point ($T_m = 701$ K), but prior crystal melting, its conductivity attains a value of about 1.3 Ω⁻¹ cm⁻¹, i.e., becomes comparable with the conductivity of typical superionics [4]. This effect is accompanied by a considerable increase in the concentration of mobile interstitial Ag⁺ ions (up to 2%), which, in turn, gives rise to high ionic conductivity in AgBr. The premelting effect is observed in many materials and is characterized by the anomalous behavior of various physical–chemical characteristics such as specific heat and surface disordering (surface melting) [5–9].

Silver bromide possessing a simple crystal structure (fcc lattice, NaCl structure type, sp. gr. $Fm\bar{3}m$) may serve as a model system for studying unusual behavior of ionic transport in solids by computer simulation. The present article describes the study of the thermodynamic, transport, and structural characteristics of silver bromide in the temperature range from 300 to 1500 K, i.e., over a wide temperature range below and above the melting point.

Molecular dynamics simulation was performed using the modified program complex Moldy [10] designed for computation of characteristics of condensed matter in the canonical *NPT* ensemble, which

allowed us to study the phase transitions accompanied by the change of the unit-cell dimensions. Atomic motion was calculated using the Beeman algorithm. The electrostatic (Coulomb) interactions were calculated by the Ewald method [11, 12]. The computational box consisted of 1000 particles (500 cations and 500 anions), i.e., was a 5 × 5 × 5 supercell, in which the anions were distributed over the positions of the fcc lattice, and the cations occupied the centers of the unit cells and the middle points of the their edges. The Ag⁺ ions were placed into octahedra sharing their edges and formed by Br⁻ ions.

The model pair-additive potentials $U_{ij}(r)$ were selected in the form

$$U_{ij}(r) = \frac{z_i z_j e^2}{r} + U_{ij}^{sh}(r), \quad (1)$$

where r is the distance between the interacting particles of species i and j , z_i and z_j are their effective charges, e is the electron charge, and $U_{ij}^{sh}(r)$ is the short-range (non-Coulomb) component of the potential. The Vashishti–Rahman short-range potential is written in the form

$$U_{ij}^{sh}(r) = \frac{H_{ij}}{r^6} - \frac{P_{ij}}{r^4} - \frac{C_{ij}}{r^6}, \quad (2)$$

where the first term describes the repulsion energy due to overlapping of electron shells and the second and third terms describe the attraction energy of van der Waals interactions (dipole–dipole interactions).

As was shown in [13], if cation–cation and cation–anion pairs in simple ionic salts are considered, it is possible to ignore van der Waals interactions because these interactions only slightly influence calculated thermodynamic and some kinetic characteristics. Considering cation–cation interactions, one may ignore polarization effects. The set of the parameters of the pair-interaction potential [14, 15] used in our computations is indicated in the table.

The effective ion charges were taken to be equal to $z(\text{Ag}^+) = 0.66$ and $z(\text{Br}^-) = -0.66$ e; the cut-off radius was taken to be equal to a half-side of the computational block. A time step of 5×10^{-15} s ensured the stability of the total energy of the computational system within the accuracy 0.2%. The particle velocities at the initial moment were assumed to be zero; then, the system temperature was brought to the given level using the thermalization mechanism. The characteristics of the simulated system were determined from the results obtained after 2×10^4 iterations (100 ps).

RESULTS AND DISCUSSION

The information on the structural characteristics of the simulated system may be extracted from the partial radial distribution functions $g_{ij}(r)$. Using these functions, one may characterize the degree of disorder of one or the other ionic sublattice of the crystal. Figure 1 shows different $g_{ij}(r)$ functions calculated for 200 configurations of the simulated thermodynamically stable system. At low temperatures, all the $g_{ij}(r)$ curves show well-resolved narrow peaks; the curve between these peaks goes to almost zero, which is characteristic of conventional solids. The distances between the centers of the peaks correspond to the respective distances between the ionic positions in the crystal lattice. With an increase in the temperature, the peaks broaden because of the intensification of atomic thermal vibrations around the centers of the atomic positions.

The cation–cation distribution function $g_{\text{Ag–Ag}}$ slightly changes with an increase in the temperature, so that at $T > 1000$ K, only the first well-pronounced peak characterizing the arrangement of the nearest neighbors is observed, whereas all the other peaks are leveled. Such a form of the pair distribution functions is characteristic of the superionic state in $\alpha\text{-AgI}$ [16]. As is seen from the $g_{\text{Br–Br}}$ curves, at $T = 1095$ K, the long-range order in the anionic subsystem is also broken; i.e., the crystal starts melting. The melting temperature is somewhat higher than the real melting point (701 K), which seems to be associated with insufficiently accurate selection of the pair potential.

The coefficients of particle self-diffusion can be determined by analyzing the mean-square displacements of ions $\langle r_k^2(t) \rangle$ if the following relationship is

Parameters of ionic interactions

| Type of pair $i-j$ | H_{ij}^* | P_{ij}^* | C_{ij}^* |
|-----------------------------|------------|------------|------------|
| $\text{Ag}^+ - \text{Ag}^+$ | 0.300 | 0.0 | 0.0 |
| $\text{Ag}^+ - \text{Br}^-$ | 7.432 | 0.9060 | 0.0 |
| $\text{Br}^- - \text{Br}^-$ | 59.456 | 1.812 | 7.785 |

* In $\text{e}^2/\text{\AA}$ ($=14.39$ eV) units.

fulfilled

$$\lim_{t \rightarrow \infty} \langle r_k^2(t) \rangle = 6D_k t + B_k, \quad (3)$$

where D_k is the diffusion coefficient of a particle of the k species and B_k is the Debye–Waller factor.

The molecular dynamics computations of the mean-square displacements of silver cations and bromine anions are illustrated by Fig. 2. The $\langle r_k^2(t) \rangle$ curves indicate that, at $T \geq 1000$ K, only the Ag^+ cations participate in the translational motion, whereas the Br^- anions

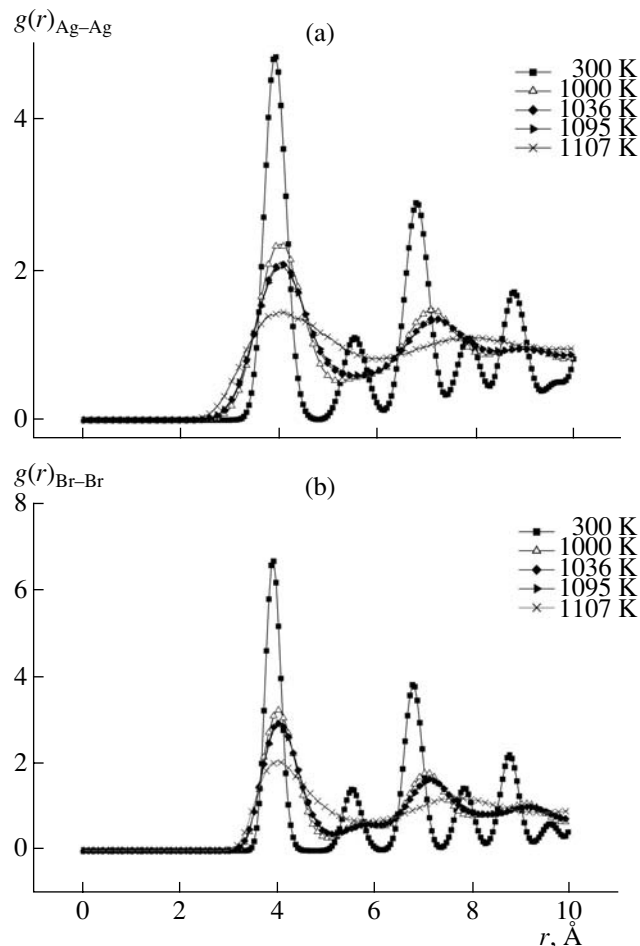


Fig. 1. Radial distribution functions at different temperatures: (a) for cation–cation and (b) for anion–anion pairs.

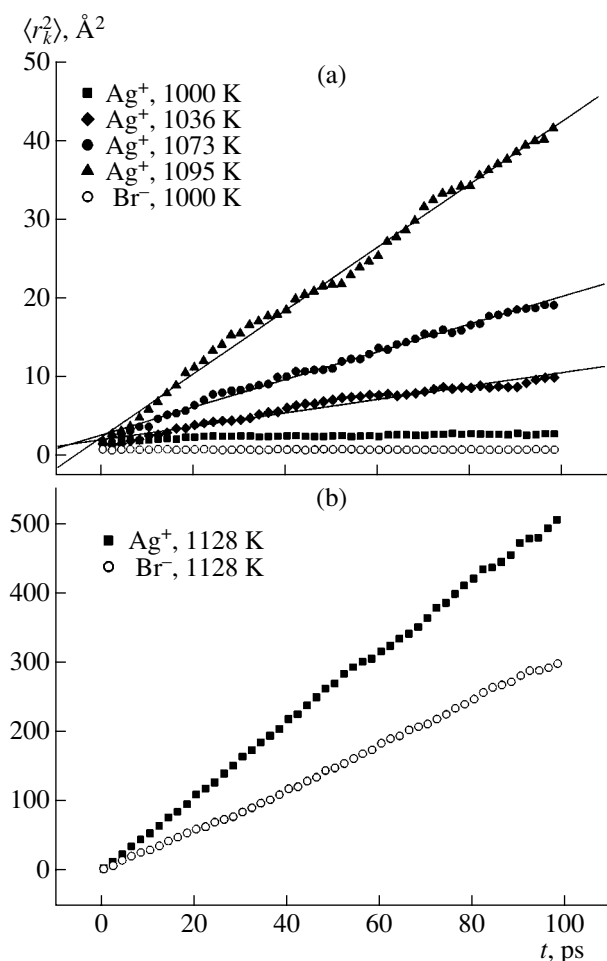


Fig. 2. Time dependences of the mean-square displacements of cations $\langle r_k^2(t) \rangle$ calculated at different temperatures (a) for Ag^+ and Br^- ions in the premelting region and (b) for Ag^+ and Br^- ions in the melt at 1128 K.

oscillate around their equilibrium positions. Only at elevated temperatures (above 1095 K), the anions leave their regular sites and are displaced for macroscopic distances, which corresponds to complete melting of the crystal. The temperature curves of the diffusion coefficient D_{Ag} of silver cations calculated by Eq. (3) are shown in Fig. 3. For comparison, Fig. 3 also shows the experimental values of the diffusion coefficient of cations obtained by the method of radioactive tracers [17–20]. It is seen from Fig. 3 that, close to the melting point, the calculated and experimental D_{Ag} values agree quite well.

Taking into account the above specificity of the behavior of the pair distribution functions in the vicinity of the melting point of the crystal and high values of the diffusion coefficient ($D_{\text{Ag}} = 3.34 \times 10^{-6}$ at 1095 K), one may draw the conclusion about the correlated motion of silver cations. The dynamics of disordering of Ag^+ cations indicates melting of the cationic sub-

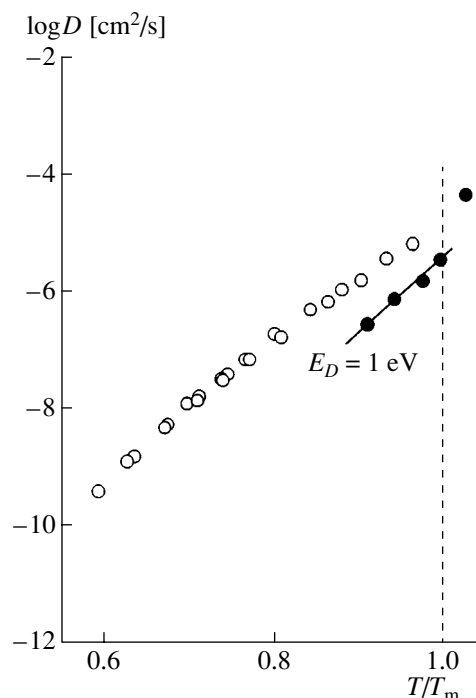


Fig. 3. Arrhenius plots of the diffusion coefficient of AgBr crystals. \circ Experiment [17–19], \bullet molecular dynamics computation.

system, which is analogous to the diffuse phase transition observed in the MF_2 fluorites ($M = \text{Ca}, \text{Ba}, \text{Sr},$ and Pb) [4], which results in the formation of a high conducting state. However, it is well known that the superionic state is characterized by low activation energies (of the order of 0.1 eV) and, therefore, a high value of the activation energy of diffusion (1.05 eV) indicates that the premelting effect in AgBr may be associated only with the initial stage of the transition to the superionic state.

ACKNOWLEDGMENTS

This study was supported by the Russian Foundation for Basic research, project no. 02-03-33353.

REFERENCES

1. A. B. Lidiard, *Ionic Conductivity* (Springer, Berlin, 1957; Inostrannaya Literatura, Moscow, 1962), in *Handbuch der Physik*, Ed. by S. Flugge, p. 246.
2. K. Aboagye and R. J. Friauf, *Phys. Rev. B* **11**, 1654 (1975).
3. P. A. Varotsos and K. Alexopoulos, *J. Phys. Chem. Solids* **39**, 759 (1978).
4. A. K. Ivanov-Schitz and I. V. Murin, *Ionics of Solid State* (S.-Peterb. Gos. Univ., St. Petersburg, 2001) [in Russian].
5. W. Hayes, *Contemp. Phys.* **27** (6), 519 (1986).
6. J. P. Hamilton, *Adv. Phys.* **37**, 359 (1988).

7. B.-E. Mellander and D. Lazarus, *Phys. Rev. B* **29** (4), 2148 (1984).
8. W. Andreoni and M. P. Tosi, *Solid State Ionics* **11**, 49 (1983).
9. M. A. S. M. Barrera, J. F. Sanz, L. J. Alvarez, and J. A. Odriozola, *Phys. Rev. B* **58** (10), 6057 (1998).
10. K. Refson, Moldy Code (Department of Earth Sciences, Univ. of Oxford, UK).
11. *Molecular Dynamics Method in Physical Chemistry*, Ed. by Yu. K. Tovbin (Nauka, Moscow, 1996) [in Russian].
12. D. W. Heermann, *Computer Simulation Methods in Theoretical Physics* (Springer, Berlin, 1986; Nauka, Moscow, 1990).
13. M. P. Allen and D. J. Tildesley, *Computer Simulation of Liquids* (Clarendon, Oxford, 1987).
14. P. D. Mitev, M. Saito, and Y. Waseda, *J. Non-Cryst. Solids* **312–314**, 443 (2002).
15. C. Tasseven, J. Trullas, O. Alcaraz, *et al.*, *J. Chem. Phys.* **106** (17), 7286 (1997).
16. A. K. Ivanov-Schitz, B. Yu. Mazniker, and E. S. Povolotskaya, *Kristallografiya* **47** (1), 125 (2002) [*Crystallogr. Rep.* **47**, 117 (2002)].
17. A. S. Miller and R. J. Maurer, *J. Phys. Chem. Solids* **4**, 196 (1958).
18. M. D. Weber and R. J. Friauf, *J. Phys. Chem. Solids* **30**, 407 (1969).
19. N. L. Peterson, L. W. Barr, and A. D. Le Claire, *J. Phys. C: Solid State Phys.* **6**, 2020 (1973).
20. A. P. Batra and L. M. Slifkin, *J. Phys. C: Solid State Phys.* **9**, 947 (1976).

Translated by L. Man

LATTICE DYNAMICS AND PHASE TRANSITIONS

Specific Features of Twinning in Divalent Nitrates

E. F. Dudnik* and A. G. Kolomoets**

* Dnepropetrovsk State University, Dnepropetrovsk, 49050 Ukraine

** Zaporozh'e State University, Zaporozh'e, Ukraine

e-mail: koloms@rambler.ru

Received August 7, 2003

Abstract—The etch patterns similar to those found previously for strontium nitrate $\text{Sr}(\text{NO}_3)_2$ were revealed on the surface of barium nitrate $\text{Ba}(\text{NO}_3)_2$ and lead nitrate $\text{Pb}(\text{NO}_3)_2$. The geometry of these patterns is studied. It is suggested that these etch patterns correspond to the translation twins occurring in divalent nitrates at the $Pm3 \rightarrow Pa3$ phase transition. © 2005 Pleiades Publishing, Inc.

It has been shown previously [1, 2] that strontium nitrate $\text{Sr}(\text{NO}_3)_2$, barium nitrate $\text{Ba}(\text{NO}_3)_2$, and lead nitrate $\text{Pb}(\text{NO}_3)_2$ undergo the $Pm3 \rightarrow Pa3$ phase transition at temperatures 588–603, 303–318, and 463–468 K, respectively. According to [3], crystals undergoing a similar transition are nonferroic, and the order parameter arising in the asymmetric phase is described by a macroscopic value. The domain structure of nonferroic crystals cannot be observed visually in a polarization microscope but, in some cases, can be visualized by chemical etching.

Etching the (111) surface of $\text{Sr}(\text{NO}_3)_2$ crystals in dilute solutions of nitric acid, we revealed previously characteristic patterns in the form of steps [4]. However, the question of existence of similar etch patterns for barium and lead nitrates was open at that time and the geometry of these etch patterns was unknown. We found using an MII-4 microinterferometer that these etch patterns are triangular pits with a vertex angle

ranging from 114° to 117° . We also found similar etch patterns on the (111) surface of barium nitrate (Fig. 1) and lead nitrate crystals (Fig. 2).

Distilled water and glycerin were used as etchants for barium and lead nitrates, respectively. The dimensions of the etch pits increased by an order of magnitude in the sequence $\text{Ba}(\text{NO}_3)_2$ – $\text{Pb}(\text{NO}_3)_2$ – $\text{Sr}(\text{NO}_3)_2$. It was found that such etch patterns can be reproduced at any point of the crystal volume, independent of the crystal thickness. Apparently, these etch patterns may correspond to translation twins formed owing to the $Pm3 \rightarrow Pa3$ phase transition in the divalent nitrates studied. The shape of etch patterns must be related to the internal crystal structure and account for the structure of the high-temperature phase.

It has been established [2, 5] that barium, strontium, and lead nitrates undergo another transition to the $P2_13$ phase at low temperatures. In other words, a sequence

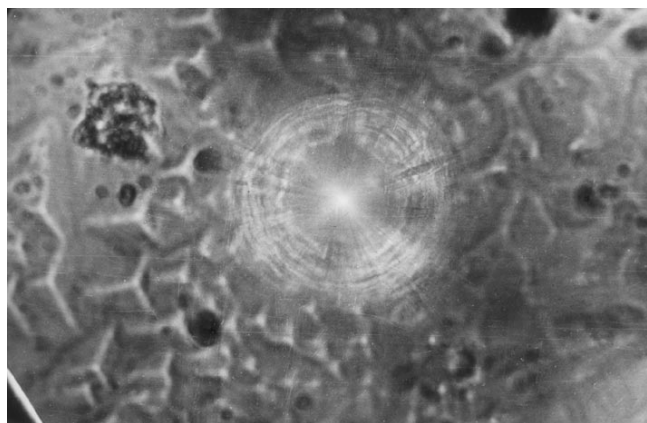


Fig. 1. Etch patterns on the (111) surface of barium nitrate $\text{Ba}(\text{NO}_3)_2$ crystals; $\times 1225$.

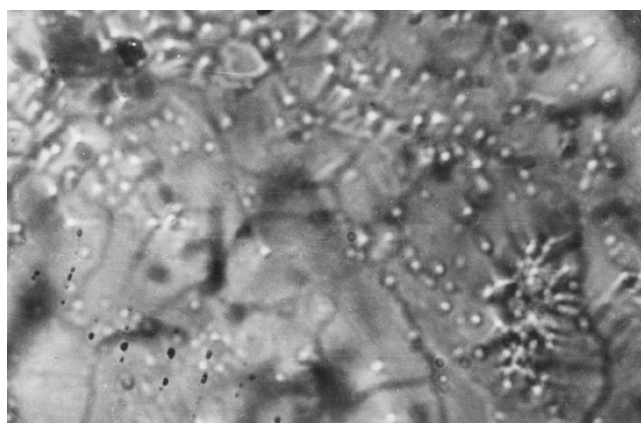


Fig. 2. Etching patterns on the (111) surface of lead nitrate $\text{Pb}(\text{NO}_3)_2$ crystals; $\times 360$.

of phase transitions $Pm3 \rightarrow Pa3 \rightarrow P2_13$ is realized in these crystals.

At the $Pm3 \rightarrow P2_13$ phase transition, a spontaneous thermodynamic quantity described by a third-rank tensor should arise in the asymmetric phase. The piezoelectric tensor seems to be appropriate (this transition is characteristic of ferroelastoelectrics). However, we failed to find the piezoelectric effect in the $P2_13$ phase. It is possible that accumulation of piezoelectric charges at the transition to the $P2_13$ phase occurs on the walls of translation twins, which already exist in the $Pa3$ phase. Therefore, the observation of the piezoelectric effect in the $P2_13$ phase becomes impossible.

REFERENCES

1. E. F. Dudnik, A. G. Kolomoets, and E. V. Bondarenko, *Ferroelectrics* **130**, 351 (1992).
2. E. F. Dudnik, A. G. Kolomoets, V. F. Katkov, and V. N. Moiseenko, *Izv. Ross. Akad. Nauk, Ser. Fiz.* **62**, 1526 (1998).
3. P. Toledano and J. C. Toledano, *Phys. Rev. B* **25**, 1946 (1982).
4. E. F. Dudnik, A. G. Kolomoets, I. V. Gařdar, and V. N. Moiseenko, *Kristallografiya* **36**, 1207 (1991) [*Sov. Phys. Crystallogr.* **36**, 683 (1991)].
5. O. F. Dudnik, G. G. Kolomoets, and V. F. Katkov, *Ukr. Fiz. Zh.* **42**, 593 (1997).

Translated by T. Dmitrieva

LATTICE DYNAMICS
AND PHASE TRANSITIONS

Exchange of Sodium and Silver Ions in $\text{Na}_3\text{Sc}_2(\text{PO}_4)_3$ Single Crystals

G. V. Shilov and L. O. Atovmyan

*Institute of Problems of Chemical Physics, Russian Academy of Sciences,
Institutskii pr. 18, Chernogolovka, Moscow oblast, 142432 Russia*

e-mail: gshilov@icp.ac.ru

Received August 11, 2003

Abstract—Sodium- and silver-ion exchange in single crystals of two polymorphous modifications of the $\text{Na}_3\text{Sc}_2(\text{PO}_4)_3$ compound has been studied. It is established that in the process of ion exchange, the samples undergo phase transitions similar to the well-known temperature transformations observed in these systems. It is shown that the phases with ferroelectric, ionic, and superionic properties may simultaneously coexist in one sample. © 2005 Pleiades Publishing, Inc.

It is well known that $\text{Na}_3\text{Sc}_2(\text{PO}_4)_3$ single crystals at room temperature exist in two polymorphous modifications—ferroelectric monoclinic (α phase) and ionic rhombohedral (β phase). Being heated, monoclinic crystals undergo two phase transitions—the $\alpha \rightarrow \beta$ transition at the temperature close to 50°C and the $\beta \rightarrow \gamma$ transition at the temperature close to 150°C , where γ is the superionic rhombohedral phase. In terms of X-ray diffractometry, the difference between the latter states reduces to disappearance of the superstructural reflections in the diffraction field in the course of the $\beta \rightarrow \gamma$ transition [1–8]. The crystals of the rhombohedral modification were reported to undergo only one transition ($\beta \rightarrow \gamma$) in the vicinity of 160°C [5]. Later, we revealed one more phase transition in the rhombohedral phase at about 240 K accompanied by a small jump in the c period in the hexagonal setting and disappearance of superstructural reflections in the diffraction field of the single crystals. We also performed the studies of $\text{Ag}_3\text{Sc}_2(\text{PO}_4)_3$ single crystals at different temperatures and revealed two phase transitions at 30°C ($\alpha \rightarrow \beta$) and at 180–170 K ($\beta \rightarrow \gamma$) [9]. The $\text{Ag}_3\text{Sc}_2(\text{PO}_4)_3$ single crystals were obtained by the replacement of Na by Ag in $\text{Na}_3\text{Sc}_2(\text{PO}_4)_3$ single crystals in aqueous solution of AgNO_3 . The $\text{Ag}_3\text{Sc}_2(\text{PO}_4)_3$ single crystals manifest the properties similar to those of $\text{Na}_3\text{Sc}_2(\text{PO}_4)_3$ single crystals at lower temperatures; in particular, the $\beta \rightarrow \gamma$ phase transition takes place practically at room temperature. Therefore, we believe that the information on the purity of the single crystal obtained after the ion exchange and on the conditions at which the samples of necessary quality are obtained seems to be useful. In the final analysis, all these facts brought us to the idea to study the processes occurring in single crystals during ion exchange by the method of single crystal diffractometry.

The study was performed on single crystals no larger than 0.3 mm at 19°C on a single-crystal KM-4 diffractometer produced by KUMA DIFFRACTION (Poland) with the use of the monochromatic MoK_α radiation. We studied the unit-cell parameters, intensities of X-ray diffraction reflections, and symmetry. The study was performed on specially selected high-quality $\text{Na}_3\text{Sc}_2(\text{PO}_4)_3$ single crystals. The unit-cell parameters and the reflection intensities are indicated in the hexagonal setting. The study was performed as follows. A single crystal on a goniometric head was fixed on a diffractometer. The unit-cell parameters and their intensities were measured and refined using a set of 15 reflections. Then the single crystal on the goniometric head was taken away from the diffractometer and placed for a certain time into an aqueous AgNO_3 solution of given concentration. Then the single crystal was taken away from the solution and placed back onto the diffractometer. Since we did not remove the crystal from the goniometric head which is rigidly fixed on the diffractometer, the unit-cell was refined by the set of reflections obtained earlier. When studying phase transformations, we determined a number of reflections typical of a certain state of the single crystal. Thus, the α state was characterized by the (0 1 5), (1 -1 5) and (-1 0 5) reflections which almost disappeared in the transition to the β phase irrespective of the crystal composition— $\text{Na}_3\text{Sc}_2(\text{PO}_4)_3$ or $\text{Ag}_3\text{Sc}_2(\text{PO}_4)_3$. We also considered the 113 reflection and its symmetric equivalents since they had high intensities and were present in the diffraction field of $\text{Na}_3\text{Sc}_2(\text{PO}_4)_3$ single crystals both in the α and β phases. In the α – β phase transition, the intensities of these reflections slightly increased; however, after the ion exchange in $\text{Ag}_3\text{Sc}_2(\text{PO}_4)_3$ single crystals of the β phase, their intensity decreased by more than an order of magnitude.

Figure 1a shows the dependence of the relative intensity I/I_0 of the (113) reflection on time t of the presence of a rhombohedral $\text{Na}_3\text{Sc}_2(\text{PO}_4)_3$ crystal in the AgNO_3 aqueous solution with the concentration $N = 2.535 \text{ g/cm}^3$. Since the intensity of an X-ray diffraction reflection is proportional to the volume of a scattering single crystal, $I \sim V$, the ratio of the current intensity of a certain reflection to the initial intensity of this reflection measured prior to ion exchange, I/I_0 , allows one to estimate the fraction of the remained initial phase.

We performed our study on a 0.3-mm-long crystal-line sample with an irregular shape. It is seen from the plot that the ion exchange was completed within 330 min. The superstructural diffraction reflections disappeared 30 min after the beginning of the exchange process. It should be indicated that in the course of the study of the phase transitions in rhombohedral $\text{Na}_3\text{Sc}_2(\text{PO}_4)_3$ single crystals we established the low-temperature phase transition at 240 K, which was accompanied by a small jumplike decrease in the c parameter and disappearance of the superstructural reflections. If we take into account that lowering of the sample temperature is equivalent to an increase in the external pressure applied to the sample, it is possible to explain the disappearance of the superstructural reflections. Indeed, the unit-cell volume of the initial rhombohedral $\text{Na}_3\text{Sc}_2(\text{PO}_4)_3$ crystal is 1533 \AA^3 and the unit-cell volume of the $\text{Ag}_3\text{Sc}_2(\text{PO}_4)_3$ crystal is 1573 \AA^3 ; thus, the difference amounts to 40 \AA^3 . Since the ion exchange proceeds first in the upper blocks of the single crystal, they create the pressure necessary for the phase transition in the remaining part of the crystal. Since the ion exchange in deeper layers of the single crystal requires overcoming of the pressure caused by the external parts of the sample, the rate of ion exchange should decrease with time, which is observed in the plot.

A somewhat different character of Na and Ag ion exchange is observed in monoclinic $\text{Na}_3\text{Sc}_2(\text{PO}_4)_3$ crystals. Figure 1b shows the dependence of the I/I_0 of the (1)–(15) (curve 1) and (1 1 3) (curve 2) reflections on t . The ion exchange was performed in a single crystal having the shape of a small cube with a 0.15-mm edge in an AgNO_3 aqueous solution of the same concentration as earlier. Curve 1 illustrates disappearance of the initial monoclinic phase about 30 min after the beginning of the ion exchange process. Curve 2 at the segment 0–10 min shows approximately the same rate of the I/I_0 variation as curve 1; in other words, at this segment, the monoclinic $\text{Na}_3\text{Sc}_2(\text{PO}_4)_3$ modification is transformed into the rhombohedral $\text{Ag}_3\text{Sc}_2(\text{PO}_4)_3$ modification. At the segment 10–20 min, the rate of the variation of curve 1 is higher than the rate of the variation of curve 2, because in the initial phase, the monoclinic $\text{Na}_3\text{Sc}_2(\text{PO}_4)_3$ phase is actively transformed into the rhombohedral $\text{Na}_3\text{Sc}_2(\text{PO}_4)_3$ phase against the background of Na replacement by Ag. At the segment 20–

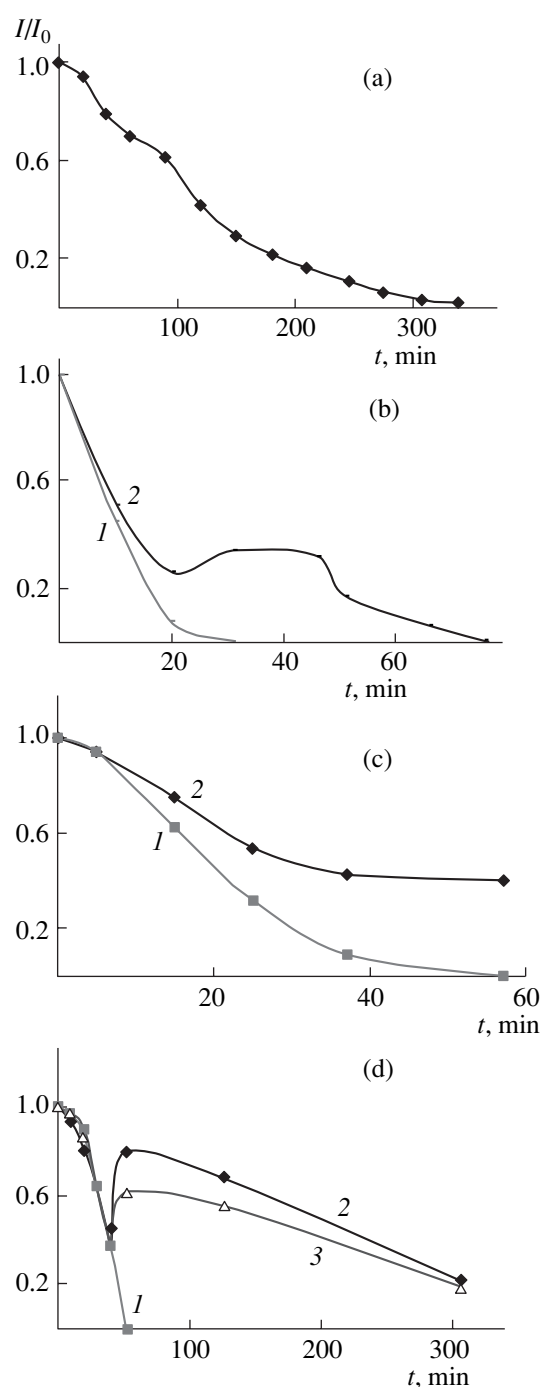


Fig. 1. Relative intensity I/I_0 of reflections as a function of the time of the presence of the α - and β - $\text{Na}_3\text{Sc}_2(\text{PO}_4)_3$ single crystals in AgNO_3 aqueous solutions with various concentrations N : (a) (1 1 3) reflection, β phase, $N = 2.535 \text{ g/cm}^3$; (b) (1) (1–1 5) and (2) (1 1 3) reflections, α phase, $N = 2.536 \text{ g/cm}^3$; (c) (1) (1–1 3) and (2) (1 1 3) reflections, α phase, $N = 5.070 \text{ g/cm}^3$; (d) (1) (1–1 5), (2) (1 1 3) reflections, and (3) (1–2 3) reflections, α phase, $N = 0.634 \text{ g/cm}^3$.

30 min, the transformation of the remaining initial α phase into the β phase having the same composition prevails over the exchange process. At the segment 30–

80 min, the crystalline sample consists of two β phases with the compositions $\text{Ag}_3\text{Sc}_2(\text{PO}_4)_3$ and $\text{Na}_3\text{Sc}_2(\text{PO}_4)_3$. At the end of this process, the superstructural reflections are formed in the diffraction field. During the ion exchange, the sample undergoes a number of transformations: from $\alpha\text{-Na}_3\text{Sc}_2(\text{PO}_4)_3$ to $\beta\text{-Ag}_3\text{Sc}_2(\text{PO}_4)_3$; from $\alpha\text{-Na}_3\text{Sc}_2(\text{PO}_4)_3$ to $\beta\text{-Na}_3\text{Sc}_2(\text{PO}_4)_3$ and $\beta\text{-Ag}_3\text{Sc}_2(\text{PO}_4)_3$, and from $\beta\text{-Na}_3\text{Sc}_2(\text{PO}_4)_3$ to $\beta\text{-Ag}_3\text{Sc}_2(\text{PO}_4)_3$. As is well known, the α phase is a ferroelectric, whereas in the β phase the dipole moment disappears and the sample becomes an ionic conductor. We believe that all these transformations are caused by the directional effect of the process and different volumes of each of the phases. Ion exchange proceeds from the external to the internal layers of the single crystal. The volume of the monoclinic unit cell is about 1555 \AA^3 ; the volume of the rhombohedral sodium-containing phase, about 1533 \AA^3 ; and the volume of the silver-containing phase, about 1570 \AA^3 . With an increase of the amount of the silver-containing phase, the upper layers of the crystal increase their volume and exert pressure onto the internal part of the initial sample. Finally, this gives rise to the $\alpha \rightarrow \beta$ phase transition in the sample. In the first 10 min of the process, the volume of the effective unit cell increases, in the next 20 min it decreases to the minimum value, and then it increases again and attains the maximum value. This dependence of the effective unit-cell volume of the crystal on the degree of ion exchange is in good accord with the scheme of the exchange of Na and Ag ions. The change in the unit-cell parameters during the ion exchange in the rhombohedral crystal proceeds according to the scheme in Fig. 1a—the parameters increase from the known the unit-cell parameters of $\beta\text{-Na}_3\text{Sc}_2(\text{PO}_4)_3$ to the known parameters of $\beta\text{-Ag}_3\text{Sc}_2(\text{PO}_4)_3$. We also studied the exchange processes in $\alpha\text{-Na}_3\text{Sc}_2(\text{PO}_4)_3$ crystals. Figures 1c and 1d show the curves that describe the exchange process at a Ag concentration in the solution lower and higher than the concentration N . In both cases, all the stages described above are also observed with the only difference that at higher concentrations the process proceeds at a higher rate and an increase in the amount of the

rhombohedral $\text{Na}_3\text{Sc}_2(\text{PO}_4)_3$ phase shows no maximum. In other words, the rate of ion exchange and the rate of the formation of the sodium-containing β phase are comparable. It should be noted that at high Ag ion concentration in aqueous solutions, the rate of ion exchange may be even higher, but the crystal thus grown would be of poorer quality and may be fractured because of the stresses which arise because the blocks of the single crystal do not have enough time to get rearranged. If ion exchange takes place in the solutions of lower concentrations, the process takes more time and an increase in the amount of the sodium-containing β phase becomes more obvious.

Thus, the study of the exchange of Na and Ag ions in $\text{Na}_3\text{Sc}_2(\text{PO}_4)_3$ single crystals in the aqueous solutions with low AgNO_3 concentrations showed that it is possible to obtain simultaneously within one crystalline sample the phases possessing the ferroelectric, ionic, and superionic properties.

REFERENCES

1. V. A. Efremov and V. B. Kalinin, *Kristallografiya* **23**, 703 (1978) [*Sov. Phys. Crystallogr.* **23**, 393 (1978)].
2. B. M. Lazoryak, V. B. Kalinin, S. Yu. Stefanovich, *et al.*, *Dokl. Akad. Nauk SSSR* **250**, 861 (1980) [*Sov. Phys. Dokl.* **25**, 67 (1980)].
3. L. O. Atovmyan, V. V. Tkachev, V. I. Ponomarev, *et al.*, *Zh. Strukt. Khim.* **20**, 940 (1979).
4. S. Yu. Stefanovich and V. B. Kalinin, *Fiz. Tverd. Tela (Leningrad)* **23** (11), 3509 (1981) [*Sov. Phys. Solid State* **23**, 2043 (1981)].
5. L. O. Atovmyan, N. G. Bukun, V. I. Kovalenko, *et al.*, *Elektrokhimiya* **19**, 933 (1983).
6. D. Tran Qui, J. J. Capponi, M. Condrand, *et al.*, *Solid State Ionics*, No. 5, 305 (1981).
7. L. Boehm, C. J. Delbecq, E. Hutchinson, *et al.*, *Solid State Ionics*, No. 5, 311 (1981).
8. G. Collin, R. Comes, J. P. Boilot, *et al.*, *J. Phys. Chem. Solids* **47** (9), 843 (1986).
9. G. V. Shilov, L. O. Atovmyan, and V. I. Kovalenko, *Kristallografiya* (2005).

Translated by L. Man

PHYSICAL PROPERTIES
OF CRYSTALS

Circular Dichroism Spectra of Synthetic Amethyst Crystals

V. I. Burkov*, A. V. Egorysheva**, Yu. F. Kargin**,
A. A. Mar'in***, and E. V. Fedotov*

* *Moscow Institute of Engineering Physics, Kashirskoe sh. 31, Moscow, 115409 Russia*
** *Kurnakov Institute of General and Inorganic Chemistry, Russian Academy of Sciences,
Leninskii pr. 31, Moscow, 119907 Russia*
e-mail: anna_egorysheva@rambler.ru

*** *All-Russia Research Institute for Synthesis of Mineral Raw Materials,
Aleksandrov, Moscow oblast, Russia*

Received October 10, 2003; in final form, March 22, 2004

Abstract—The axial circular-dichroism spectrum of a synthetic amethyst crystal has been studied for the first time. Bands both of the positive and negative signs are revealed. New information on the color centers of amethyst and their electronic structure is obtained. © 2005 Pleiades Publishing, Inc.

INTRODUCTION

Amethyst is a semiprecious stone; it is, in fact, quartz with color varying from bluish lilac to reddish violet. Amethyst is widespread in nature. At present, there are several methods to grow crystals of synthetic amethyst [1]. Recent exhaustive studies [1, 2] showed that amethyst acquires its color under the influence of X-ray or gamma radiation only in the crystals containing trivalent iron as a structural impurity. The nature of color centers of amethyst crystals has been repeatedly discussed in literature on the basis of various suggested models of color centers [2]. These models were created proceeding mainly from the experimental EPR data and optical spectra. However, none of these models could satisfactorily explain all the sets of experimental data.

The absorption spectra of various oxide matrices containing tetrahedrally coordinated iron (Fe^{2+} and Fe^{3+}) and the absorption spectra of amethyst turned out to be different [3]. Therefore, it was assumed that, under the action of the ionizing radiation, the trivalent iron ions initially present in quartz acquire a higher degree of oxidation +4. The $[\text{FeO}_4]^{4-}$ centers thus formed contribute to amethyst color. The EPR spectra of irradiated quartz crystals, which, being irradiated, acquired the amethyst color, contained three lines characteristic of the system with the spin $S = 2$ [4]. Such spectra are observed in the case of the $3d^6$ (Fe^{2+}) and $3d^4$ (Fe^{4+}) configurations. It is natural that Cox [4] had to consider the alternative when interpreting the EPR spectra. Taking into account the results obtained in [3], he preferred the Fe^{4+} configuration.

Obviously, the parallel increase in the color intensity and a decrease in the intensity of the primary EPR spectrum cannot give unique information about the formation in the crystal of the centers of only one type, namely, $[\text{FeO}_4]^{4+}$ centers. Indeed, the attempts to inter-

pret the amethyst absorption spectra within the framework of $[\text{FeO}_4]^{4+}$ color centers gave somewhat ambiguous results [2, 5]. There are no reliable data on the experimental absorption spectra of the $[\text{FeO}_4]^{4+}$ complex either [6], because oxidation degree +4 is quite unusual for iron ions.

Thus, the only prerequisite indicating the presence of Fe^{4+} ions in amethyst are the EPR data. Publication [4] triggered numerous studies of EPR spectra of amethyst (see, e.g., [2]) and, although these studies gave some useful information on the fine structure of the EPR spectra, no other data directly related to the assumed color centers have been published. This leads to the assumption that the information obtained by the EPR methods is insufficient and one has to invoke some other physical methods to study color centers in amethyst. In particular, the degree of iron oxidation was studied by X-ray spectral analysis [7]. This study was dedicated to the X-ray absorption spectrum of amethyst and revealed the transitions to the $2s$ and $2p$ orbitals. The results obtained were somewhat surprising. No traces of Fe^{4+} ions were found in the spectrum; it was also established that two thirds of iron impurities are in the Fe^{2+} state. Another promising method of studying the iron state is Mössbauer spectroscopy. Synthetic quartz diffusely doped at high temperature with the ^{57}Co isotope decomposed with the formation of ^{57}Fe [8]. It was established that most of iron in quartz has the oxidation degree +2.

The above short review leads to the conclusion that the problem of the structure of amethyst color centers in quartz has not been completely solved as yet.

To obtain new information on amethyst color centers and their electronic structure, we used the method of circular dichroism spectroscopy.

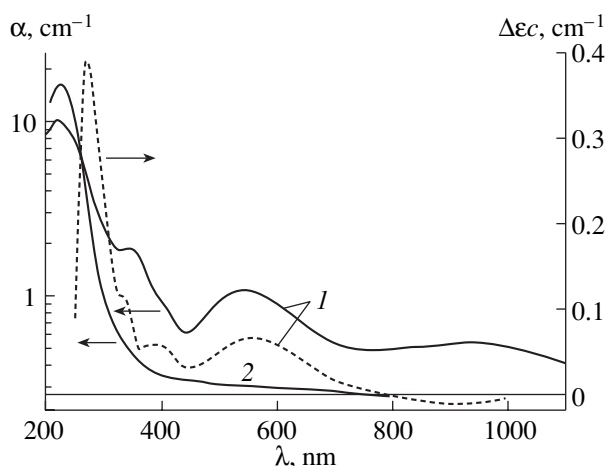


Fig. 1. Axial absorption (solid line) and circular dichroism (dashed line) spectra of (1) the initial amethyst crystal and (2) the amethyst crystal annealed in air at $T = 400^\circ\text{C}$.

The absence of published data on the gyrotropic characteristics of amethyst is explained by the fact that, in distinction from quartz (uniaxial optically active crystal), natural amethyst crystals are biaxial. The angle $2V$ between the optic axes of amethyst (both natural and synthetic) was determined in [9–11]. The measurements were performed on both colorless and colored parts of the crystals. Biaxiality was revealed only in the colored parts of the crystals, and the angle $2V$ ranged from 0° to 12° [10]. According to [11], the $2V$ angles measured on natural amethyst ranged within 8° – 12° . It is commonly accepted that formation of biaxiality in amethyst crystals is associated with the nonuniform arrangement of iron over the equivalent positions of the unit cell with the symmetry C_2 [2]. The nonuniform iron distribution also gives rise to pleochroism of amethyst crystals [2, 12].

We measured experimental axial absorption spectra and circular dichroism of the samples of synthetic amethyst crystals grown by the method described elsewhere [1]. The study of these crystals in polarized light gave conoscopic figures that revealed no noticeable biaxiality. The measurements were performed on the 0.3–1.0-mm-thick z -cuts of amethyst crystals. The absorption spectra were recorded on Specord M-40 and Lambda spectrophotometers; the circular dichroism spectra, on a Mark 3S (Jobin Yvon) dichrograph.

RESULTS AND DISCUSSION

The axial absorption spectra (Fig. 1, solid line 1) showed a number of bands with the maxima in the vicinity of 930, 540, 400, 350, and 230 nm. The positions of the band maxima differ from the positions of the respective bands in orthoaxial absorption spectra [2, 5, 13]. The maxima of the dichroism spectra (dashed line 1) also shown in Fig. 1 are considerably displaced with respect to the absorption maxima. The

spectrum has a band with the maximum at $\lambda_1 \sim 920$ nm of the negative sign and the bands of the positive sign with the maxima at $\lambda_2 \sim 560$, $\lambda_3 \sim 400$, $\lambda_4 \sim 330$, and $\lambda_5 \sim 270$ nm.

Naturally, a problem arises—how to interpret these bands and establish their relation to the respective electron transitions. If one assumes that the amethyst color is determined by the electron transitions of tetravalent iron with the configuration $3d^4$, then, according to the Orgel and Tanabe–Sugano diagrams, there should exist only one spin-allowed transition in the crystal field within the framework of the symmetry T_d , namely, ${}^5T_2 \rightarrow {}^5E$. Other transitions are spin-forbidden, and the corresponding bands should have intensities much lower than the intensities of the respective absorption bands. However, the experimental data (Fig. 1) show that the intensities of the bands in the near IR and visible range of the spectra have comparable values. It is assumed [5] that the band with the maximum at $\lambda \sim 935$ nm in the orthoaxial absorption spectrum is caused by the transition in the crystal field, or, more exactly, by the transition from the components of the state T split by the crystal field to the components of the split E state, whereas the bands of shorter wavelengths are caused by the transitions accompanied by charge transfer. In this case, the intensities of the bands caused by charge transfer are considerably higher than the intensity of the band caused by transition in the crystal field. Usually, the intensities of the absorption bands caused by transitions accompanied by charge transfer exceed the intensities of the bands caused by transitions in the crystal field by 2–3 orders of magnitude. It should be noted that sometimes [1] the ${}^5T_2 \rightarrow {}^5E$ transition is associated with the appearance of the band with the maximum at $\lambda \sim 540$ nm. The intense absorption bands observed (350, 400, and 930 nm) are attributed to the centers not related to Fe^{4+} ions. Thus, the following scheme was suggested in [11]: a broad absorption band with the maximum at 930 nm is caused by the transition from the split levels of the state 5T to the sublevels of the only quintet state 5E of an interstitial Fe^{2+} ion ($3d^6$). These ions (centers I6) may have appeared due to irradiation. However, the last statement contradicts the data obtained from circular dichroism spectra since the non-structured impurities cannot give any contribution to the optical activity of crystals. In turn, the band in the vicinity of 350 nm is associated with the ${}^6A \rightarrow {}^4E({}^4A)$ transition of trivalent iron $\text{Fe}^{3+}(3d^5)$ [14].

If one takes into account that the identification of the band having the maximum at $\lambda = 930$ nm with the ${}^5T_2 \rightarrow {}^5E$ transition of tetravalent iron is correct and uses the splitting scheme of the T_d states and the positions of their split components, then the behavior of circular dichroism in the region of this transition becomes consistent with the interpretation made in [5].

Indeed, the shift of the maximum of the circular dichroism band with respect to the maximum of the

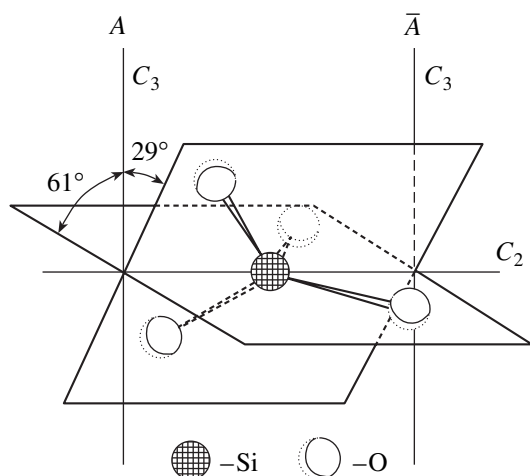


Fig. 2. Orientation of a SiO_4 tetrahedron in quartz [11].

corresponding absorption spectrum band to the region of shorter wavelengths indicates that the *A* state possesses the maximum energy among the split *A* and two *B* components of the excited tetrahedral states. In the case of the ground state, the picture is opposite; i.e., the *A* component possesses the minimum energy. The data on the quartz structure whose fragment is shown in Fig. 2 indicates that the C_2 axis of a $[\text{SiO}_4]$ tetrahedron is directed normally to the C_3 axis of the crystal [11]. In this case, the *A*–*A* transitions would give the maximum contribution to the axial circular dichroism spectrum because the polar vector of the electric dipole and the axial vector of the magnetic dipole of the above electron transition are directed along the C_2 axis.

Therefore, the rotation force of the transition (intensity of the circular dichroism band) determined by the pseudoscalar product of the projections of these vectors onto the plane normal to the wave vector directed along the C_3 axis has the maximum value. In the case of the *A*–*B* transitions, the electric and magnetic moments lie in the plane parallel to the C_3 axis. These moments are not determined by the symmetry conditions and may have arbitrary directions. The maximum value is attained if the rotation force of these transitions is comparable with the rotation force of the *A*–*A* transitions and if these vectors are collinear and orthogonal to the C_3 and C_2 axes of the unit cell. Thus, the result obtained confirms the arrangement of the split component of the *T* states suggested in [5].

It should be noted that the band intensities in the circular dichroism spectrum are very high. Thus, the crude estimation for the transition in the vicinity of 560 nm yields the anisotropy factor $g = \Delta\epsilon/\epsilon = 5 \times 10^{-2}$. This result indicates that the centers responsible for amethyst color are incorporated into the crystal lattice.

Heating of an amethyst crystal in air up to 400°C almost completely discolors the crystal. The long-

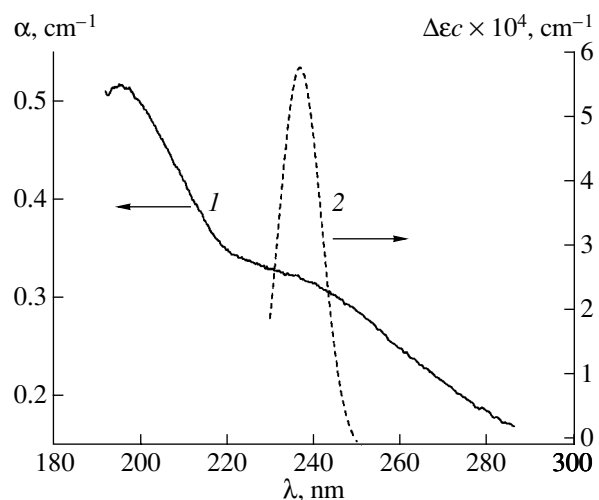


Fig. 3. (1) Absorption and (2) circular-dichroism spectra of undoped synthetic quartz crystals.

wavelength bands in the absorption spectra disappear (Fig. 1, solid line 2). A dramatic increase in absorption in the region $\lambda < 300$ nm caused by the transitions accompanied by charge transfer of tetrahedral Fe^{3+} did not allow us to perform measurements in the short-wavelength range of the spectrum. Therefore, we measured absorption and circular dichroism of nonirradiated plates of synthetic quartz with much lower Fe^{3+} concentrations. The absorption spectra (Fig. 3, curve 1) showed the bands with the maxima at $\lambda'_1 = 240$ nm and $\lambda'_2 = 195$ nm caused by the transitions accompanied by charge transfer of tetrahedrally coordinated Fe^{3+} , whereas the circular dichroism spectrum showed the band with the maximum at $\lambda \sim 237$ nm (Fig. 3, curve 2).

It was also assumed [15] that absorption spectra determining amethyst color are associated with electron transitions of several centers. This assumption seems to be quite reasonable if one takes into account the data on the absorption spectrum of X-ray-irradiated quartz-like berlinite crystal (AlPO_4) [16]. Comparing the absorption spectra of an irradiated berlinite crystal with the absorption spectra of an amethyst crystal, one may see rather good correspondence in the location of the band maxima in the region 560–310 nm (see table). Therefore, there are grounds to believe that, similar to berlinite, absorption in amethyst in this spectrum range is associated with electron transitions in defects formed

Positions of the absorption-band maxima (λ_{max}) in spectra of amethyst and irradiated berlinite crystals

| Crystal | λ_{max} , nm | | | | |
|------------------------|-----------------------------|-----|-----|-----|---------|
| | 936 | 540 | 400 | 350 | 225–195 |
| Amethyst | | | | | |
| Berlinite (irradiated) | | 520 | 394 | 310 | 220 |

due to replacement of a silicon atom by a foreign atom and a hole at the π orbital of oxygen.

As was indicated above, the transition in the vicinity of 930 nm in the circular dichroism spectrum manifests itself as a band of the negative sign, which makes it unique among other transitions. It is well known that, as a rule, the bands in the crystal field of the complexes of 3d elements have the same sign determined by the absolute configuration of the crystal lattice [16]. The opposite sign of circular dichroism bands with respect to the sign of the band at ~920 nm in the visible and near UV range of the spectrum may be an indication of the fact that the former bands and the band at ~930 nm are of different nature. It is possible to assume that the band with the maximum at 930 nm is caused by the ${}^5T_2 \rightarrow {}^5E$ transition of a tetravalent iron in the crystal field [5], whereas the bands in the visible and near UV range of the spectra are caused by the transitions with charge transfer of other centers. The role of such centers in amethyst may be played by the defects analogous to the defects in an irradiated berlinite crystal; the models of such centers are suggested in [15].

CONCLUSIONS

The axial circular dichroism spectra of synthetic amethyst crystals obtained by irradiation of iron-containing quartz crystals and preserving the optical uniaxiality of pure quartz have been studied for the first time. The results obtained allowed us to formulate additional criteria for constructing a model (or, possibly, a set of models) of the structural color centers in amethyst. The diversity of these centers characterized by different concentrations determines the real color of amethyst crystals.

REFERENCES

1. V. S. Balitskiĭ, V. E. Khadzi, B. A. Dorogovin, *et al.*, *Synthesis of Minerals* (VNIISIMS, Aleksandrov, 2000), Vol. 1.
2. G. R. Rossman, *Rev. Mineral.* **29**, 433 (1994).
3. G. Lehmann, *Z. Naturforsch. A* **22** (12), 2080 (1967).
4. R. T. Cox, *J. Phys. C: Solid State Phys.* **9**, 3355 (1976).
5. R. T. Cox, *J. Phys. C: Solid State Phys.* **10** (22), 4631 (1977).
6. V. I. Burkov, A. V. Egorysheva, and Yu. F. Kargin, *Zh. Neorg. Khim.* **48** (4), 620 (2003).
7. G. Cressey, C. M. B. Henderson, and G. van der Lann, *Phys. Chem. Mineral.* **20**, 111 (1993).
8. M. F. Vereshchak, A. K. Zhetbaev, D. K. Kaipov, and K. K. Satpaev, *Fiz. Tverd. Tela (Leningrad)* **14** (10), 3082 (1972) [*Sov. Phys. Solid State* **14**, 2638 (1972)].
9. C. Frondel, *The System of Mineralogy*, 7th ed. (Wiley, New York, 1962), Vol. 3.
10. N. M. Melankholin and L. I. Tsinober, *Kristallografiya* **7** (1), 110 (1963) [*Sov. Phys. Crystallogr.* **7**, 97 (1963)].
11. T. I. Barry, P. McNamara, and W. J. Moore, *J. Chem. Phys.* **42** (7), 2599 (1965).
12. S. Pancharatnam, *Proc. Indian Acad. Sci., Sect. A* **40** (6), 196 (1954).
13. L. G. Chentsova, L. I. Tsinober, and M. I. Samoĭlovich, *Kristallografiya* **11** (2), 236 (1966) [*Sov. Phys. Crystallogr.* **11**, 219 (1966)].
14. A. Lever, *Inorganic Electronic Spectroscopy* (Elsevier, Amsterdam, 1984; Mir, Moscow, 1987), Part 1.
15. L. E. Halliburton, L. A. Kappers, A. F. Armington, and J. Larkin, *J. Appl. Phys.* **51** (4), 2193 (1980).
16. V. A. Kizel' and V. I. Burkov, *Crystal Gyrotropy* (Nauka, Moscow, 1980) [in Russian].

Translated by L. Man

PHYSICAL PROPERTIES
OF CRYSTALS

On the Optical Properties of Anisotropic Media in the Presence of Negative Components of Dielectric and (or) Magnetic Tensors

O. S. Eritsyun

Yerevan State University, ul. A. Manukyan 1, Yerevan, 375049 Armenia

e-mail: heritsyan@ysu.am

Received October 21, 2003

Abstract—The studies of the media with an open surface of wave vectors (SWV) undertaken by the author in the 1970s are continued. A number of new specific features of these media are revealed. It is shown, in particular, that the focusing upon refraction at a plane boundary (a phenomenon that has recently attracted much attention and is related to the media whose permittivity and permeability are simultaneously negative) can also be realized in a nonmagnetic medium with an open SWV. The boundary problem for a plate and a semi-infinite crystal with an open SWV is solved, and the qualitative differences from the media with a closed SWV are revealed. Biaxial nonmagnetic media and nonmagnetic media in the presence of negative components of the dielectric and magnetic tensors are briefly considered. © 2005 Pleiades Publishing, Inc.

1. INTRODUCTION

Traditional optics deals with the media for which all components of the dielectric tensor ϵ_{ij} are positive. The surface of wave vectors (SWV), the Fresnel surface, and the characteristic surfaces of the tensors ϵ_{ij} and ϵ_{ij}^{-1} are all closed [1–3].

The uniaxial media for which one component of the dielectric tensor ϵ_{ij} is negative were considered in [4–7]. The presence of a negative component does not rule out the possibility of the wave propagation without attenuation, but only limits the range of directions in which an undamped extraordinary wave can propagate. In this case, the SWV and the two above-mentioned surfaces are open (namely, they are hyperboloids) rather than closed, as in traditional optics. In particular, the Fresnel ellipsoid is transformed into a hyperboloid. One more feature revealed (to be used in Section 2) is that the wave vector \mathbf{k}_e and the Poynting vector \mathbf{S}_e of a refracted extraordinary wave are on different sides with respect to the normal to the boundary.

Recent attention to the development of isotropic media with simultaneously negative ϵ and μ [8, 9] is related, in particular, to the problem of focusing of a diverging beam upon its refraction at a plane boundary. The focusing is due to the antiparallel orientation (ascertained in [10]) of the \mathbf{k} and \mathbf{S} vectors in these media [11].

In Section 2 of this study, it is shown that the focusing upon refraction at a plane boundary occurs also in nonmagnetic uniaxial anisotropic media (considered in [4]) with one negative component of the ϵ_{ij} tensor. The focusing is possible due to the above-mentioned

unusual mutual orientation of the wave vector and the Poynting vector. In Section 3, the anisotropic media for which both ϵ_{ij} and μ_{ij} tensors have negative components are briefly considered. At the end of Section 3, the preparation of uniaxial anisotropic structures with such tensors ϵ_{ij} and μ_{ij} is discussed. Section 4 is devoted to brief consideration of biaxial nonmagnetic media. In Section 5, the boundary problems for the MgF₂ crystal, whose tensor ϵ_{ij} has a negative component [12], are considered. Finally, it is worth noting study [13], which is also devoted to the specific features of crystals in the presence of a negative component of the dielectric tensor.

2. UNIAXIAL MEDIA WITH AN OPEN SURFACE OF WAVE VECTORS

Consider an optically uniaxial medium. When the components ϵ_{\perp} and ϵ_{\parallel} of the tensor ϵ_{ij} along the directions perpendicular (ϵ_{\parallel}) and parallel (ϵ_{\perp}) to the optical axis have different signs, the SWV equation for an extraordinary wave

$$(k_{ex}^2 + k_{ey}^2)\epsilon_{\parallel}^{-1} + k_{ez}^2\epsilon_{\perp}^{-1} = (\omega/c)^2 \quad (1)$$

describes a hyperboloid rather than the traditional ellipsoid. Let the z axis be parallel to the optical axis of the medium. Figure 1 shows the section of the hyperboloid (1) by the plane $y = 0$.

Let a plane wave be incident on the medium boundary from vacuum:

$$\mathbf{E}(r, t) = \mathbf{E} \exp i(k_x x + k_z z - \omega t). \quad (2)$$

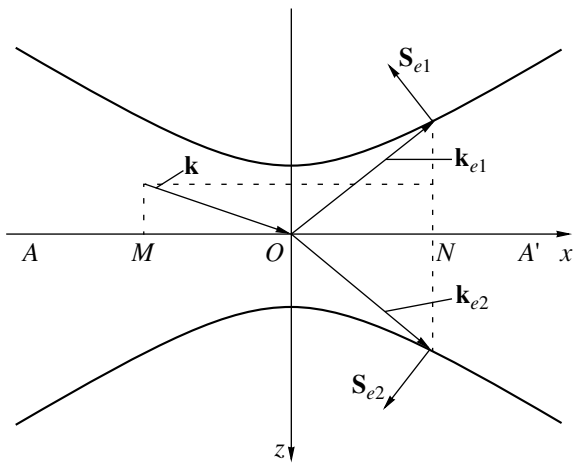


Fig. 1. SWV shape and the determination of the directions of the wave vector \mathbf{k}_e and the Poynting vector \mathbf{S}_e . The hyperbolas are the lines of intersection of the surface of extraordinary-wave vectors by a plane passing through the optical axis (z axis) of the medium at $\epsilon_{\perp} > 0$ and $\epsilon_{\parallel} < 0$. \mathbf{k} is the incident-wave vector, and $MO = ON = k_x$ is the tangential component of all wave vectors (of the incident, reflected, and refracted waves; the reflected-wave vector is not shown). The z axis is directed into the medium. The interface is perpendicular to the optical axis. The absorption is absent.

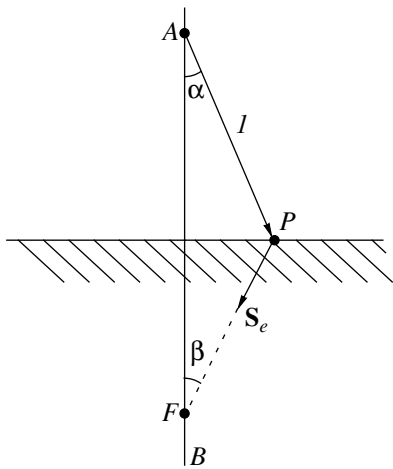


Fig. 2. The incident ray is denoted by I . The energy of the refracted ray flows towards the AB normal.

The requirement that the tangential components of the incident, reflected, and refracted waves should be equal results in the following expression for the normal component k_{ez} of the wave vector of the refracted extraordinary wave:

$$k_{ez} = \pm \{ [(\omega/c)^2 + (k_x^2/|\epsilon_{\parallel}|)] \epsilon_{\perp} \}^{1/2}, \quad (|\epsilon_{\parallel}| = -\epsilon_{\parallel}). \quad (3)$$

Two signs in Eq. (3) correspond to two refracted-wave vectors \mathbf{k}_{e1} and \mathbf{k}_{e2} in Fig. 1. The sign in front of the root is chosen on the basis of the requirement that the

refracted-wave energy flow from the boundary into the medium rather than to the boundary. The wave vector \mathbf{k}_{e2} complies with this requirement because the Poynting vector (whose direction is determined as the direction of the external normal to the SWV surface) is directed into the medium specifically when \mathbf{k}_{e2} (rather than \mathbf{k}_{e1}) is taken as the refracted-wave vector (see also formulas (4) below). Hence, the Poynting vector of the refracted wave is \mathbf{S}_{e2} (rather than \mathbf{S}_{e1}). Figure 1 corresponds to the case when the imaginary parts of ϵ_{ij} and \mathbf{k}_e are absent, $\epsilon'_{\parallel} = \epsilon_{\parallel} < 0$, and $\epsilon'_{\perp} = \epsilon_{\perp} > 0$.

The calculation taking into account the imaginary parts of ϵ_{ij} results in the following expression for the Poynting vector components averaged over the light wave period (the wave is incident from vacuum, $k''_x = 0$):

$$\bar{S}_{ez} = (\epsilon'_{\perp} k'_{ez} + \epsilon''_{\perp} k''_{ez}) f, \quad \bar{S}_{ex} = |\epsilon_{\perp}/\epsilon_{\parallel}|^2 \epsilon'_{\parallel} k'_x f, \quad (4)$$

$$f = \omega(8\pi|k_{ez}|^2)^{-1} |E_{ex}|^2 \exp(-k''_{ez} z),$$

where E_{ex} is the amplitude of the tangential component of the electric field of the refracted wave (single and double primes indicate the real and imaginary parts of the corresponding values, respectively). Under the assumption that $\bar{S}_{ez} > 0$, the requirement that $\epsilon'_{\perp} > 0$ is satisfied at $k'_{ez} > 0$, i.e., by choosing the vector \mathbf{k}_{e2} (rather than \mathbf{k}_{e1}) as the refracted-wave vector. For our choice of the signs of ϵ'_{ij} ($\epsilon'_{\parallel} < 0$, $\epsilon'_{\perp} > 0$), the tangential component of the Poynting vector \bar{S}_{ex} is, according to (4), negative.

On the basis of this mutual arrangement of \mathbf{k}_e and \mathbf{S}_e (revealed in [4]), let us consider how a beam diverging from a point source is focused upon refraction at a plane boundary.

Since $\bar{S}_{ez} > 0$ and $\bar{S}_{ex} < 0$, the energy of the beam incident from a point source A (Fig. 2; the index "2" in \mathbf{S}_e is omitted) at an angle α on a given point P of the boundary flows, after refraction, towards the normal AB to the boundary and the refracted ray intersects the normal at the point F at a certain angle β .

To make the rays originating from a point source and incident from vacuum on different points of the boundary converge at one point (F) upon refraction, the ratio $\tan \alpha / \tan \beta$ must be independent of α . This leads to the relation

$$(1 - \sin^2 \alpha)^{-1/2} |\epsilon_{\parallel}|^2 |\epsilon_{\perp}|^{-2} \times (\epsilon'_{\perp} \cos \phi + \epsilon''_{\perp} \sin \phi) (\epsilon'_{\parallel})^{-1} (a^2 + b^2)^{1/4} = \text{const}, \quad (5)$$

where

$$\varphi = \frac{1}{2} \arctan(b/a),$$

$$a = [(1 - |\varepsilon_{\parallel}|^{-2} \varepsilon_{\parallel}' \sin^2 \alpha) \varepsilon_{\perp}' - |\varepsilon_{\parallel}|^{-2} \varepsilon_{\parallel}'' \varepsilon_{\perp}' \sin^2 \alpha], \quad (6)$$

$$b = [(1 - |\varepsilon_{\parallel}|^{-2} \varepsilon_{\parallel}' \sin^2 \alpha) \varepsilon_{\perp}'' + |\varepsilon_{\parallel}|^{-2} \varepsilon_{\parallel}'' \varepsilon_{\perp}' \sin^2 \alpha].$$

The constancy of the left-hand side of relation (5) can be satisfied at small angles of incidence. Figure 3 shows the dependence of the ratio $\tan \beta / \tan \alpha$ on the angle of incidence.

Thus, in the media with an open SWV, focusing occurs, which is due to specific mutual orientation of the wave vector and the Poynting vector, this orientation being, in turn, related to the open character of the SWV.

When absorption is taken into account (this was done in the above consideration), the SWV is not a hyperboloid but is closed near the asymptotes, existing in the absence of absorption [5]. However, the concave character inherent in the hyperboloid is retained. Therefore, a medium will be referred to as a medium with an open SWV even in the case that the SWV, although being actually closed, has concave regions. It is the concavity that results in the specific mutual orientation of the vectors \mathbf{k}_e and \mathbf{S}_e .

3. MEDIA WITH NONZERO MAGNETIC SUSCEPTIBILITY

Isotropic media with simultaneously negative scalar ε and μ were considered in [10]. The properties of such a medium are identical for any polarization of a wave, while the wave vector is antiparallel to the Poynting vector. We showed that the antiparallel orientation of \mathbf{k}_e and \mathbf{S}_e can also be implemented in the media in which the permittivity and permeability have different signs along different directions. In this case, the implementation of the antiparallel orientation of the above two vectors depends on the wave polarization.

In fact, the dispersion equation for the medium with the tensors ε_{ij} and μ_{ij} has the form

$$\begin{aligned} & (\omega/c)^2 \{ \varepsilon_3 \mu_3 k_z^4 + \varepsilon_2 \mu_2 k_y^4 + \varepsilon_1 \mu_1 k_x^4 \\ & + [(\varepsilon_1 \mu_3 + \varepsilon_3 \mu_1) k_x^2 k_z^2 + (\varepsilon_3 \mu_2 + \varepsilon_2 \mu_3) k_y^2 k_z^2 \\ & + (\varepsilon_1 \mu_2 + \varepsilon_2 \mu_1) k_x^2 k_y^2] \} \\ & - (\omega/c)^4 \{ \varepsilon_3 \mu_3 (\varepsilon_1 \mu_2 + \varepsilon_2 \mu_1) k_z^2 \\ & + \varepsilon_2 \mu_2 (\varepsilon_1 \mu_3 + \varepsilon_3 \mu_1) k_y^2 + \varepsilon_1 \mu_1 (\varepsilon_2 \mu_3 + \varepsilon_3 \mu_2) k_x^2 \} \\ & + (\omega/c)^6 \varepsilon_1 \varepsilon_2 \varepsilon_3 \mu_1 \mu_2 \mu_3 = 0, \\ & \varepsilon_1 = \varepsilon_{xx}, \quad \varepsilon_2 = \varepsilon_{yy}, \quad \varepsilon_3 = \varepsilon_{zz}, \\ & \mu_1 = \mu_{xx}, \quad \mu_2 = \mu_{yy}, \quad \mu_3 = \mu_{zz}. \end{aligned} \quad (7)$$

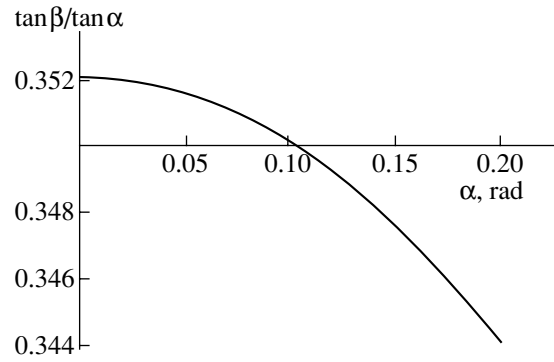


Fig. 3. Dependence of the ratio $\tan \beta / \tan \alpha$ on the angle of incidence at $\varepsilon_{\parallel} = -7.3 + 0.9982i$ and $\varepsilon_{\perp} = 6.8629 + 0.273i$. In the range $0 \leq \alpha \leq 0.1$ rad, this ratio is constant accurate to 0.7%.

In the simplest case $k_x = k_y = 0$, for two mutually perpendicular polarizations, we have for k_{ez}

$$k_{ez1}^2 = (\omega/c)^2 \varepsilon_1 \mu_2, \quad k_{ez2}^2 = (\omega/c)^2 \varepsilon_2 \mu_1. \quad (8)$$

Let us assume that $\varepsilon_1 < 0$, $\mu_2 < 0$, $\varepsilon_2 > 0$, and $\mu_1 > 0$. Then, both \mathbf{k}_{ez1} and \mathbf{k}_{ez2} are real. For the wave with $\mathbf{k}_{ez} = \mathbf{k}_{ez1}$ ($E_x \neq 0$, $E_{y,z} = 0$, $H_y \neq 0$, $H_{x,z} = 0$), the wave vector and the Poynting vector are antiparallel. For the wave with $\mathbf{k}_{ez} = \mathbf{k}_{ez2}$ ($E_{x,z} = 0$, $E_y \neq 0$, $H_{y,z} = 0$, $H_x \neq 0$), the noted vectors are parallel. Thus, for the same propagation direction, the handedness of the same medium is different for different wave polarizations.

The medium discussed in this Section can be prepared artificially using artificial media with $\varepsilon < 0$ and $\mu < 0$ that were developed in [8, 9]. Let us consider briefly this possibility.

It is known that a structure composed of different alternating isotropic layers is anisotropic [14]. Let ε_1 and ε_2 and l_1 and l_2 be, respectively, the permittivities and thicknesses of the layers of the first and second types. Then, the permittivities of the structure along the direction normal to the layers and along the directions parallel to them are [14]

$$\begin{aligned} \varepsilon^{\perp} &= \varepsilon_1 \varepsilon_2 (l_1 + l_2) / (\varepsilon_1 l_2 + \varepsilon_2 l_1), \\ \varepsilon^{\parallel} &= (\varepsilon_1 l_1 + \varepsilon_2 l_2) / (l_1 + l_2). \end{aligned} \quad (9)$$

Similar relations are easily obtained for the corresponding permeabilities:

$$\begin{aligned} \mu^{\perp} &= \mu_1 \mu_2 (l_1 + l_2) / (\mu_1 l_2 + \mu_2 l_1), \\ \mu^{\parallel} &= (\mu_1 l_1 + \mu_2 l_2) / (l_1 + l_2) \end{aligned} \quad (10)$$

(μ_1 and μ_2 are the permeabilities of the layers with the thicknesses l_1 and l_2 , respectively). If, for example, $\varepsilon_1 > 0$, $\mu_1 > 0$, $\varepsilon_2 < 0$, $\mu_2 < 0$, and $l_1 = l_2$, then $\varepsilon^{\perp} < 0$ and $\mu^{\parallel} < 0$ when $|\varepsilon_1| > |\varepsilon_2|$ and $|\mu_1| < |\mu_2|$. In this case, according to Section 3, in a wave with the electric field perpendic-

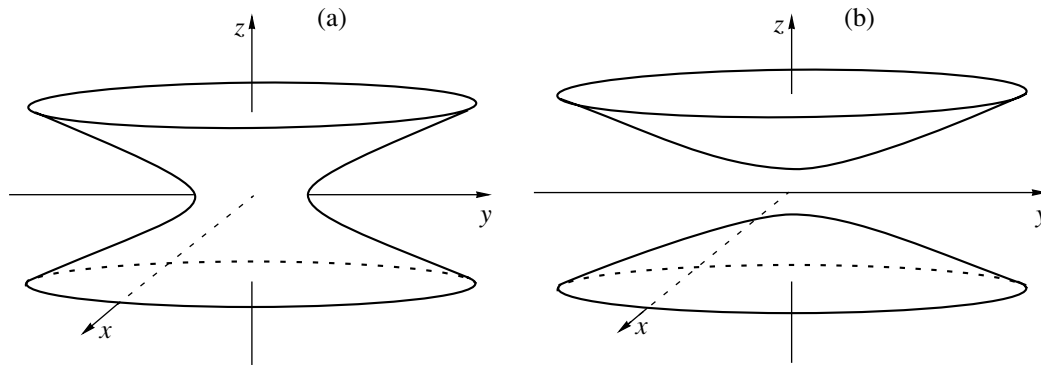


Fig. 4. (a) SWV shape for an extraordinary wave and (b) the characteristic surface of the tensor ϵ_{ij} in the case when $\epsilon_{xx} < 0$ and $\epsilon_{zz} > 0$.

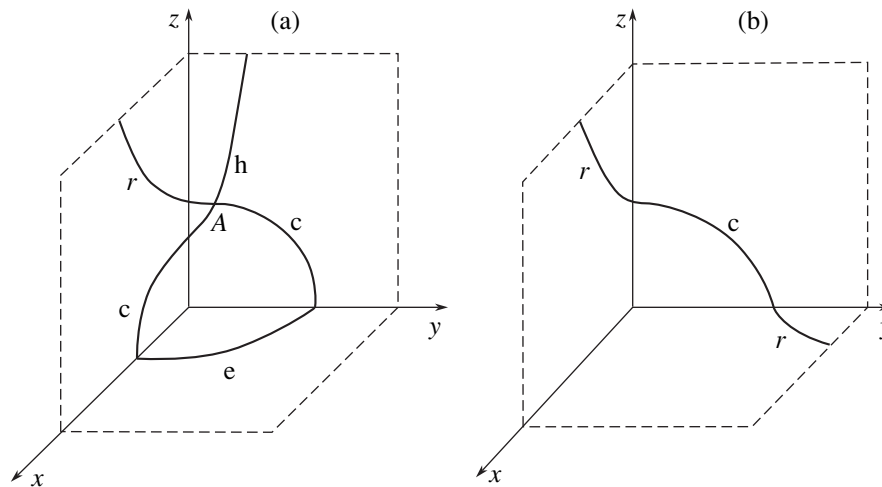


Fig. 5. Section of the SWV by coordinate planes for (a) $\epsilon_{xx} > 0$, $\epsilon_{yy} > 0$, and $\epsilon_{zz} < 0$ and (b) $\epsilon_{xx} > 0$, $\epsilon_{yy} < 0$, and $\epsilon_{zz} < 0$. For (a) and (b), $|\epsilon_{xx}| > |\epsilon_{yy}| > |\epsilon_{zz}|$.

ular to the layers the wave vector and the Poynting vector are antiparallel.

For $\mu_1 = \mu_2 = \mu$, we obtain an anisotropic structure with permeability μ and the permittivities (9). Providing opposite signs of ϵ^\perp and ϵ^\parallel , we obtain a dielectrically anisotropic medium with an open SWV.

4. BIAXIAL MEDIA

Before considering the SWV and the characteristic surfaces of biaxial crystals, we present, for completeness, these surfaces for uniaxial crystals. Figure 4 shows the shapes of (a) the SWV and (b) the characteristic surface of the tensor ϵ_{ij} for a uniaxial crystal. The characteristic surface of ϵ_{ij}^{-1} (not shown in Fig. 4) has the same shape as that of the tensor ϵ_{ij} . The characteristic surface of the tensor ϵ_{ij} , which is closed at $\epsilon_{ij} > 0$, also proves to be open: the Fresnel ellipsoid is transformed into a hyperboloid.

We now turn to biaxial crystals. Let us consider two cases: (1) $\epsilon_{xx} > 0$, $\epsilon_{yy} > 0$, $\epsilon_{zz} < 0$; (2) $\epsilon_{xx} > 0$, $\epsilon_{yy} < 0$, and $\epsilon_{zz} < 0$. Figure 5 shows the sections of the SWV by coordinate planes in the first octant. The letters c, e, and h denote circle, ellipse, and hyperbola, respectively. As can be seen from the figures, there are directions along which only one wave can propagate in the medium. In Fig. 5a, such a direction lies in the yz plane and passes through the origin of coordinates and the point A, at which the circle and the hyperbola intersect. Because of the symmetry, there is a direction that is symmetrical to the above-mentioned direction with respect to the xz plane. In Fig. 5b, only one wave can propagate in any direction. It is worth noting that a situation when only one wave can propagate in one direction occurs also in single-refracting media [1]. However, the physical pictures in single-refracting media and in the media considered here are different. In single-refracting media, the phase velocity is independent of the polarization; therefore, there is no birefringence. In the media under consideration, the birefringence occurs, but one of the

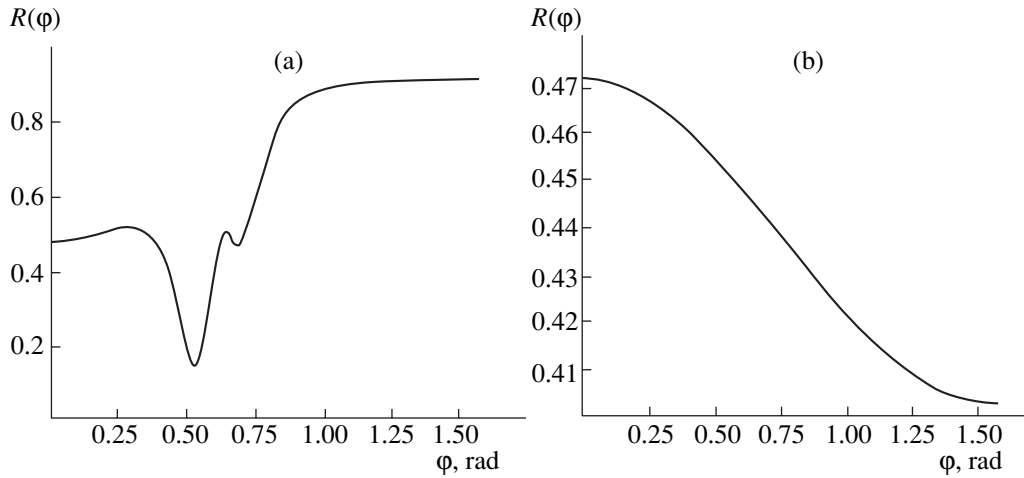


Fig. 6. Dependence of the power reflectivity R on the angle φ between the optical axis of the crystalline plate and the normal to its boundaries: (a) $\epsilon_{\parallel} = 7.3 + 0.9982i$ and $\epsilon_{\perp} = 6.8629 + 0.2973i$ (open SWV) and (b) $\epsilon_{\parallel} = 7.3 + 0.9982i$ and $\epsilon_{\perp} = 6.8629 + 0.2973i$ (closed SWV). In both cases, the plate thickness is 10^{-3} cm.

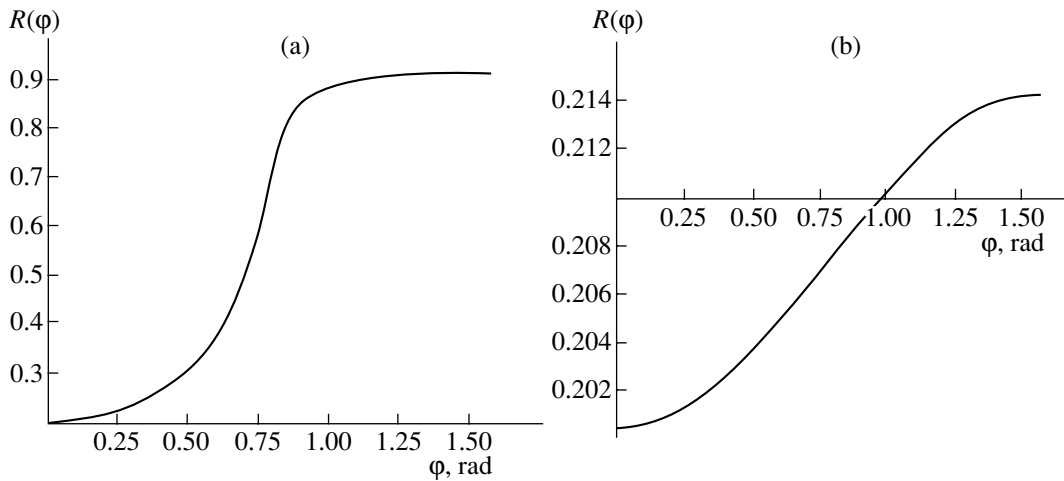


Fig. 7. Dependence of the power reflectivity R on the angle φ between the optical axis of a semi-infinite crystal and the normal to its boundary. All parameters (except d) are the same as in Fig. 6.

waves is a damped wave. Note also that Fig. 5 corresponds to no absorption.

5. BOUNDARY PROBLEM FOR A PLATE AND SEMISPACe

Consider light (electromagnetic wave) propagation through a layer of an optically uniaxial medium with different signs of the components of the real part of the tensor ϵ_{ij} in the case of the normal incidence for different orientations of the optical axis with respect to the normal. Specifically, we consider the MgF_2 crystal. Let the plate occupy the region $0 \leq z \leq d$ and the wave

$$\mathbf{E}^{ext}(z, t) = \mathbf{E}^{ext} \exp i((\omega/c)z - \omega t) \quad (11)$$

be incident from the region $z < 0$ (vacuum) on the boundary $z = 0$. The plane of incidence is the xz plane;

the electric field vector of the incident wave and the optical axis of the crystal lie in the same plane. Thus, only an extraordinary wave will be excited in the plate; specifically it is this wave that will exhibit the specific features discussed above.

For the electric fields of the transmitted and reflected waves (\mathbf{E}^t and \mathbf{E}^r , respectively), we have

$$\begin{aligned} E_x^t &= 2E_x^{ext}(A_2 - A_3) \\ &\times \exp i(k_{ez1} - k_{ez2})d / ((1 + A_2)(1 - A_3) \exp i k_{ez1}d \\ &\quad - (1 - A_2)(1 + A_3) \exp i k_{ez2}d), \\ E_x^r &= (1 - A_2)(1 + A_3)(2(A_2 - A_3))^{-1} E_x^t, \\ A_2 &= (c/\omega)k_{ez2}, \quad A_3 = (c/\omega)k_{ez1}, \\ k_{ez1,2} &= \mp(\omega/c)((\cos^2 \varphi/\epsilon_{\perp}) + (\sin^2 \varphi/\epsilon_{\parallel}))^{-1/2}, \end{aligned} \quad (12)$$

where φ is the angle between the optical axis of the crystal and the normal to the crystal boundary.

Figure 6 shows the dependences of the power reflectivity R on φ for the plates cut from the crystals with the open and closed SWVs. In going from one crystal to the other, the quantities ε_{ij}'' and the magnitudes of ε_{ij}' do not change; what changes is the sign of one of the ε_{ij}' components.

Figure 7 shows the same dependences as in Fig. 6 but for a semi-infinite crystal. Comparison of the curves shows that the presence of the negative component (responsible for the SWV concavity) qualitatively affects the behavior of the $R(\varphi)$ curves. In particular, when ε_{ij} has a negative component, new extrema appear in the region of rapid variation in $R(\varphi)$ as compared with the case which all ε_{ij}' components are positive. In the presence of a negative component of ε_{ij} , the quantity $R(\varphi)$ takes values close to unity as φ approaches $\pi/2$ (although the incidence is normal). In this context, it should be noted that, at $\varepsilon_{\parallel}'' = 0$, $\varepsilon_{\parallel}' < 0$, and $\varphi = \pi/2$, we would have a complete reflection at normal incidence: the permittivity at the boundary would be real and negative for the field of the incident wave. Note also that for an open SWV $R(\varphi)$ varies within a much wider range than in the case of the medium with a closed SWV (compare Figs. 6a, 6b and Figs. 7a, 7b).

REFERENCES

1. F. I. Fedorov, *Optics of Anisotropic Media* (Akad. Nauk BSSR, Minsk, 1958) [in Russian].

2. L. D. Landau and E. M. Lifshitz, *Course of Theoretical Physics*, Vol. 8: *Electrodynamics of Continuous Media*, 2nd ed. (Nauka, Moscow, 1982; Pergamon, Oxford, 1984).
3. A. Yariv and P. Yeh, *Optical Waves in Crystals: Propagation and Control of Laser Radiation* (Wiley, New York, 1984; Mir, Moscow, 1987).
4. O. S. Eritsyán, *Kristallografiya* **23**, 461 (1978) [*Sov. Phys. Crystallogr.* **23**, 255 (1978)].
5. O. S. Eritsyán, *Optics of Gyrotropic Media and Cholesteric Liquid Crystals* (Añastan, Yerevan, 1988) [in Russian].
6. O. S. Eritsyán, *Izv. Nats. Akad. Nauk Arm., Fiz.* **38**, 312 (2003).
7. O. S. Eritsyán and O. M. Arakelyán, *Izv. Nats. Akad. Nauk Arm., Fiz.* **39**, 107 (2004).
8. J. B. Pendry, A. J. Holden, W. J. Stewart, and J. Youngs, *Phys. Rev. Lett.* **76**, 4773 (1996).
9. D. R. Smith, W. J. Padilla, D. C. Vier, *et al.*, *Phys. Rev. Lett.* **84**, 4184 (2000).
10. V. G. Veselago, *Usp. Fiz. Nauk* **87**, 517 (1967) [*Sov. Phys. Usp.* **10**, 509 (1968)].
11. J. B. Pendry, *Phys. World* **27** (2000).
12. V. V. Bryksin, D. N. Mirlin, and I. I. Reshina, *Fiz. Tverd. Tela (Leningrad)* **15**, 1118 (1973) [*Sov. Phys. Solid State* **15**, 760 (1973)].
13. M. I. Ryazanov, *Zh. Éksp. Teor. Fiz.* **103**, 1840 (1993) [*JETP* **76**, 910 (1993)].
14. M. Born and E. Wolf, *Principles of Optics*, 4th ed. (Pergamon, Oxford, 1969; Nauka, Moscow, 1970).

Translated by A. Zolot'ko

LIQUID CRYSTALS

Threshold Spatially Periodic Structure of the Director in a Nematic Flexoelectric Cell with Finite Anchoring Energy

M. F. Lednei and I. P. Pinkevich

Shevchenko National University, Kiev, 03022 Ukraine

e-mail: lednei@univ.kiev.ua

Received April 17, 2004

Abstract—The influence of the finiteness of the anchoring energy of a director and the value of flexoelectric polarization on the threshold of a spatially periodic reorientation of the director and the period of the arising structure is considered for a planar nematic cell. The threshold and the period are calculated numerically and the corresponding analytical expressions are obtained for the case of a strong anchoring of the director. It is shown that for a finite azimuthal anchoring energy the range of admissible values of the flexoelectric parameter ν widens, while for a finite polar anchoring energy this range narrows as compared to the case of an absolutely rigid orientation of the director at the cell surface. © 2005 Pleiades Publishing, Inc.

INTRODUCTION

An interest in the phenomena of the director reorientation in nematic liquid crystals (NLCs) under an external electric field, in particular, in the threshold reorientation (the Freedericksz effect), is related to their wide application in various optoelectronic devices. The theory of these phenomena has been developed quite well [1–3]. It was shown that in a number of cases a spatially periodic structure of the director field is generated at the threshold reorientation in the plane of an NLC cell. This phenomenon was considered in [4, 5] for the planar alignment of the director in an NLC with flexopolarization. It was shown in [6] that a periodic structure of the director field may occur even without flexopolarization, provided that the Frank elastic constants differ significantly. The above studies used the model of an infinitely rigid anchoring of the director at the cell surface. However, although these orientational transitions are bulk effects, their characteristics, such as the threshold field and the degree of the director reorientation, depend significantly on the interaction between the nematic and the cell surface. The influence of the cell surface is so significant that a so-called “spontaneous” transition, or, more exactly, the Freedericksz transition induced by changing conditions at the surface, may occur [7–10].

The influence of the surface on the threshold spatially periodic reorientation of the director by an electric field was considered in [11] for a homeotropically aligned cell. The threshold field and the spatial period of the director were found in terms of the anchoring energy of the director at the surface and flexoelectric coefficients of NLC. In this study, we consider the influence of the surface on the threshold spatially periodic director reorientation in a planar flexoelectric NLC. In this case, the flexoelectric polarization enters

not only the equations for the director (as in the homeotropic case) but also the boundary conditions for it.

EQUATIONS FOR THE DIRECTOR

Consider a plane-parallel flexoelectric NLC cell bounded by the planes $z = -L/2$ and $z = L/2$ with initial planar orientation along the Ox axis subjected to an external dc electric field $E = (0, 0, E)$.

In the one-constant approximation, the free energy of the NLC cell can be written as

$$F = F_{el} + F_E + F_d + F_S,$$

$$F_{el} = \frac{K}{2} \int_V \{(\operatorname{div} \mathbf{n})^2 + (\operatorname{curl} \mathbf{n})^2\} dV,$$

$$F_E = -\frac{\varepsilon_a}{8\pi} \int_V (\mathbf{nE})^2 dV, \quad (1)$$

$$F_d = -\int_V \{e_1(\mathbf{nE}) \operatorname{div} \mathbf{n} + e_3([\operatorname{curl} \mathbf{n} \times \mathbf{n}]E)\} dV,$$

$$F_S = -\frac{W_\phi}{2} \int_{S_{1,2}} \cos^2 \phi dS - \frac{W_\theta}{2} \int_{S_{1,2}} \cos^2 \theta dS,$$

$$W_\phi > 0, \quad W_\theta > 0.$$

Here, \mathbf{n} is the director; F_{el} is the Frank elastic energy; F_E and F_d are, respectively, the anisotropic and flexoelectric contributions to the interaction energy of the NLC with an electric field; F_S is the surface free energy of the NLC taken in the form of the Rapini potential [12]; $\varepsilon_a = \varepsilon_{\parallel} - \varepsilon_{\perp} > 0$ is the static dielectric anisotropy; e_1 and e_3 are the flexoelectric coefficients; W_θ and W_ϕ

are, respectively, the polar and azimuthal anchoring energies of the director at the cell surface; and θ and φ are the deviation angles of the director in the planes xz and xy , respectively.

In planar geometry, the threshold director reorientation results in the formation of a spatially periodic structure along the Oy axis [4, 5]. Hence, the director will be sought in the form

$$\mathbf{n} = \mathbf{i} \cos \theta(y, z) \cos \varphi(y, z) + \mathbf{j} \cos \theta(y, z) \sin \varphi(y, z) + \mathbf{k} \sin \theta(y, z), \quad (2)$$

where \mathbf{i} , \mathbf{j} , and \mathbf{k} are the unit vectors of the Cartesian coordinate system.

For small deformations of the director ($|\varphi|, |\theta| \ll 1$), minimization of the free energy (1) with respect to θ and φ yields the following steady-state equations:

$$K \left(\frac{\partial^2 \theta}{\partial y^2} + \frac{\partial^2 \theta}{\partial z^2} \right) + \epsilon E^2 \theta + eE \frac{\partial \varphi}{\partial y} = 0, \quad (3)$$

$$K \left(\frac{\partial^2 \varphi}{\partial y^2} + \frac{\partial^2 \varphi}{\partial z^2} \right) - eE \frac{\partial \theta}{\partial y} = 0,$$

with the boundary conditions

$$\left[(W_\theta \mp e_0 E) \theta \pm K \left(\frac{\partial \theta}{\partial z} + \frac{\partial \varphi}{\partial y} \right) \right]_{z=\pm L/2} = 0, \quad (4)$$

$$\left[W_\varphi \varphi \pm K \left(\frac{\partial \varphi}{\partial z} - \frac{\partial \theta}{\partial y} \right) \right]_{z=\pm L/2} = 0,$$

where $\epsilon = \frac{\epsilon_a}{4\pi}$, $e_0 = e_1 + e_3$, and $e = e_1 - e_3 \neq 0$.

If we take into account the symmetry of system of equations (3), the solution to it is sought in the form

$$\begin{aligned} \theta(y, z) &= \cos(qy) \theta_1(z), \\ \varphi(y, z) &= \sin(qy) \varphi_1(z), \end{aligned} \quad (5)$$

where the functions $\theta_1(z)$ and $\varphi_1(z)$ satisfy the following equations:

$$\begin{pmatrix} Kq^2 - K \frac{d^2}{dz^2} - \epsilon E^2 & -eEq \\ -eEq & Kq^2 - K \frac{d^2}{dz^2} \end{pmatrix} \begin{pmatrix} \theta_1(z) \\ \varphi_1(z) \end{pmatrix} = 0. \quad (6)$$

Setting

$$\begin{pmatrix} \theta_1(z) \\ \varphi_1(z) \end{pmatrix} = e^{ipz} \begin{pmatrix} \theta_{10} \\ \varphi_{10} \end{pmatrix} \quad (7)$$

in (6), we arrive at a homogeneous system of two algebraic equations to determine the unknown coefficients θ_{10} and φ_{10} . The condition for nontrivial solution of this

system gives the equations for the values of p :

$$(Kq^2 + Kp^2)^2 - \epsilon E^2 (Kq^2 + Kp^2) - (eEq)^2 = 0. \quad (8)$$

Solving (8), we obtain $p = \pm p_1, \pm ip_2$, where p_1 and p_2 are real quantities:

$$p_1 = \sqrt{\frac{1}{2K} (\epsilon E^2 + \sqrt{(\epsilon E^2)^2 + (2eEq)^2}) - q^2}, \quad (9)$$

$$p_2 = \sqrt{q^2 - \frac{1}{2K} (\epsilon E^2 - \sqrt{(\epsilon E^2)^2 + (2eEq)^2})}.$$

We also find from (6) that

$$\frac{\varphi_{10}}{\theta_{10}} = \frac{eEq}{Kq^2 + Kp^2} \equiv \alpha(p).$$

Then, the general solution to system of equations (6) is

$$\begin{aligned} \theta_1(z) &= a_1 \cos p_1 z + a_2 \sin p_1 z \\ &\quad + b_1 \cosh p_2 z + b_2 \sinh p_2 z, \\ \varphi_1(z) &= \alpha_1 (a_1 \cos p_1 z + a_2 \sin p_1 z) \\ &\quad + \alpha_2 (b_1 \cosh p_2 z + b_2 \sinh p_2 z), \end{aligned} \quad (10)$$

where

$$\alpha_1 = \alpha(p = \pm p_1) = \frac{2eEq}{\epsilon E^2 + \sqrt{(\epsilon E^2)^2 + (2eEq)^2}},$$

$$\alpha_2 = \alpha(p = \pm ip_2) = \frac{2eEq}{\epsilon E^2 - \sqrt{(\epsilon E^2)^2 + (2eEq)^2}}.$$

Here, a_i and b_i ($i = 1, 2$) are arbitrary constants determined from the boundary conditions (4).

INFLUENCE OF THE FINITENESS OF AZIMUTHAL ANCHORING ENERGY

Let us assume that the polar anchoring energy W_θ of the director at the cell surface is infinitely high ($W_\theta = \infty$), while the azimuthal anchoring energy W_φ can be arbitrary. In this case, the boundary conditions (4) take the form

$$\theta_1|_{z=\pm L/2} = 0,$$

$$\left[W_\varphi \varphi_1 \pm K \frac{d\varphi_1}{dz} \right]_{z=\pm L/2} = 0. \quad (11)$$

Substituting solution (10) into the boundary conditions (11), we obtain a homogeneous system of four algebraic equations to determine the coefficients a_i and b_i ($i = 1, 2$). The condition for nontrivial solution of this

system yields the equation

$$\begin{aligned} & \cos \frac{p_1 L}{2} \cosh \frac{p_2 L}{2} \left\{ 2W_\varphi \sqrt{(\epsilon E^2)^2 + (2eEq)^2} \right. \\ & \left. + Kp_1 (\epsilon E^2 - \sqrt{(\epsilon E^2)^2 + (2eEq)^2}) \tan \frac{p_1 L}{2} \right. \\ & \left. + Kp_2 (\epsilon E^2 + \sqrt{(\epsilon E^2)^2 + (2eEq)^2}) \tanh \frac{p_2 L}{2} \right\} = 0. \end{aligned} \quad (12)$$

Solving this equation together with relations (9), we obtain the electric field E as a function of the parameter q .

In the limiting case of absolutely rigid anchoring of the director at the substrate, $W_\varphi = \infty$, we find from Eq. (12) that $p_1 = \frac{\pi}{L}$ (the lowest nonzero value of p).

Accordingly, the dispersion dependence $E^\infty(q)$ is derived from (9):

$$E^\infty(q) = \frac{q^2 + \left(\frac{\pi}{L}\right)^2}{\sqrt{q^2 + \nu \left(q^2 + \left(\frac{\pi}{L}\right)^2\right)}} \frac{K}{e}, \quad (13)$$

where $\nu = \frac{\epsilon K}{e^2} > 0$.

The instability threshold is determined by the minimum in the curve $E^\infty(q)$. Minimizing dependence (13), we obtain

$$E_c^\infty = E^\infty(q_c^\infty) = \frac{2\pi K}{|e|(1+\nu)L}, \quad (14)$$

where the wave number of the forming structure of the director is

$$q_c^\infty = \frac{\pi}{L} \sqrt{\frac{1-\nu}{1+\nu}}, \quad (15)$$

which coincides with the result of [4]. It can be seen that in the case of absolutely rigid anchoring of the director at the cell surface the instability associated with the formation of the periodic structure of the director can arise only when $\nu < 1$.

For strong (but not absolutely rigid) anchoring ($\epsilon_\varphi = \frac{W_\varphi L}{K} \gg 1$), the solution to Eq. (12) is sought in

the form $p_1 = \frac{\pi}{L} - x$, where $x \ll \frac{\pi}{L}$. Restricting our-

selves in Eq. (12) to the terms linear in $\frac{1}{\epsilon_\varphi}$, we arrive at

$$p_1 = \frac{\pi}{L} \left(1 + \frac{1}{\epsilon_\varphi} \frac{\epsilon E^2 - \sqrt{(\epsilon E^2)^2 + (2eEq)^2}}{\sqrt{(\epsilon E^2)^2 + (2eEq)^2}} \right).$$

Accordingly, we find from (9) that

$$E(q) = E^\infty(q) \left\{ 1 - \frac{2}{\epsilon_\varphi} \frac{q^2 \left(\frac{\pi}{L}\right)^2}{\left(q^2 + \left(\frac{\pi}{L}\right)^2\right) \left[q^2 + \nu \left(q^2 + \left(\frac{\pi}{L}\right)^2\right) \right]} \right\}. \quad (16)$$

Minimizing the latter expression with respect to q , we obtain the threshold value of the electric field in the approximation linear in $\frac{1}{\epsilon_\varphi}$:

$$E_c = E(q_c) = E_c^\infty \left(1 - \frac{1-\nu}{\epsilon_\varphi} \right), \quad (17)$$

where the corresponding wave number is

$$q_c = q_c^\infty \left(1 + \frac{1}{\epsilon_\varphi} \frac{3\nu-1}{1-\nu} \right), \quad (18)$$

if $\nu < 1$ and $\epsilon_\varphi(1-\nu) \gg 1$, or

$$q_c = \frac{\pi}{\sqrt{2}L} \sqrt{\frac{4}{\epsilon_\varphi} + 1 - \nu}, \quad (19)$$

if $|1-\nu| \ll 1$.

It can be seen that the threshold field always decreases with a decrease in the azimuthal anchoring energy ϵ_φ . At the same time, at $\nu < 1$, the wave number corresponding to this threshold can both decrease (if $0 < \nu < 1/3$) and increase (if $1/3 < \nu < 1$) with decreasing ϵ_φ . It is noteworthy that, as can be seen from (19), at a finite anchoring energy ϵ_φ the periodic structure of the director appears also at the parameter ν greater than unity (depending on the anchoring energy ϵ_φ , specifically, at $\nu < 1 + \frac{4}{\epsilon_\varphi}$).

To determine the threshold values of E_c and q_c for an arbitrary azimuthal anchoring energy ϵ_φ , one has to solve Eq. (12) numerically. However, it should be noted that the condition of the appearance of the threshold periodic structure of the director field is as follows:

$$\left. \frac{dE}{dq} \right|_{q=0} < 0. \quad (20)$$

Then, differentiating Eq. (12) with respect to q at the point $q = 0$ and performing some algebraic transforma-

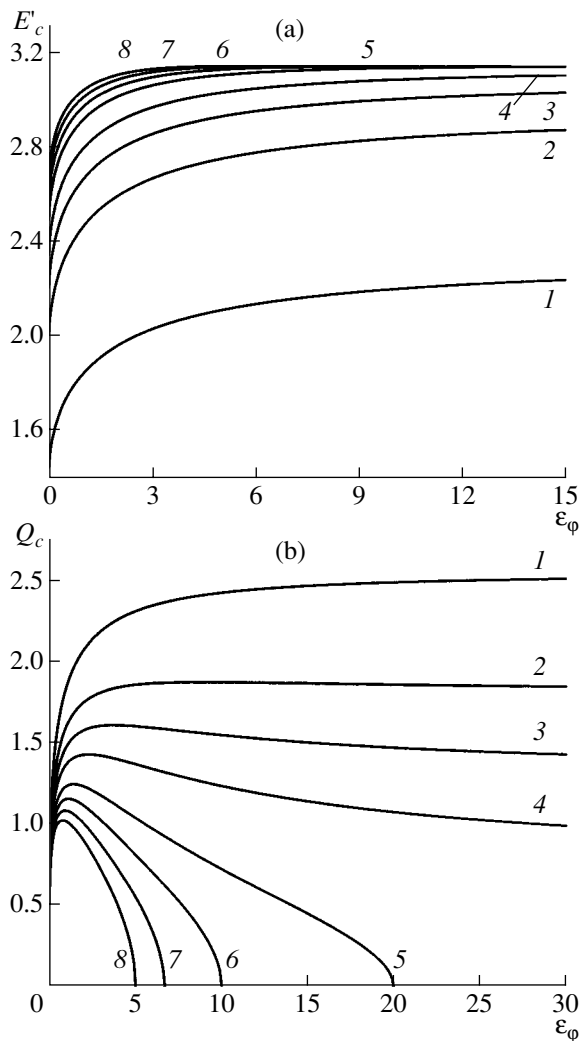


Fig. 1. Dependences of (a) the threshold field E'_c and (b) the wave number Q_c on the azimuthal anchoring energy ε_ϕ for $\nu = (1) 0.2, (2) 0.5, (3) 0.7, (4) 0.9, (5) 1.2, (6) 1.4, (7) 1.6,$ and $(8) 1.8$.

tions, we arrive at the inequality

$$\nu < 1 + \frac{4}{\varepsilon_\phi} \equiv \nu_{th}, \quad (21)$$

which is valid for arbitrary values of the anchoring energy ε_ϕ . Thus, the range of the flexoelectric parameter ν in which the periodic structure of the director exists depends strongly on the anchoring energy. At $\varepsilon_\phi \rightarrow 0$, the values of ν can be practically arbitrary.

Figure 1 shows the numerically calculated dependences of the threshold field $E'_c = \sqrt{\frac{\varepsilon}{K}} E_c L$ and the corresponding wave number $Q_c = q_c L$ on the azimuthal anchoring energy ε_ϕ of the director at the cell surface for different values of the flexoelectric parameter ν . In numerical calculations, we used the following values of

the NLC parameters: $\varepsilon_a = 0.2$ and $K = 0.7 \times 10^{-6}$ d. The flexoelectric coefficients e_1 and e_3 were taken from the range $(0.7-2.5) \times 10^{-4}$ d^{1/2}.

As expected, the threshold electric field E_c increases with an increase in the anchoring energy ε_ϕ of the director at the cell surface and with increasing parameter ν (Fig. 1a). For the values of the flexoelectric parameter in the range $0 < \nu < 1/3$, the period $\lambda_c = \frac{2\pi}{q_c} = \frac{2\pi L}{Q_c}$ of the forming spatial structure of the director monotonically decreases as the anchoring energy ε_ϕ increases (Fig. 1b). However, for the flexoelectric parameter $\nu > 1/3$, the dependence of the period λ_c of the spatial structure of the director on the anchoring energy ε_ϕ becomes nonmonotonic: as the energy ε_ϕ increases, λ_c first decreases to a certain minimal value and then increases. In the limiting case of absolutely rigid anchoring, $\varepsilon_\phi \rightarrow \infty$, the period approaches (for the values of the flexoelectric parameter in the range $0 < \nu < 1$) a certain constant value $\lambda_c^\infty = \frac{2\pi}{q_c}$ specified by expression (15).

It can be seen from Fig. 1b that for each given value $\nu > 1$ there is a finite critical value of the azimuthal anchoring energy $\varepsilon_{\phi th} = \frac{4}{\nu - 1}$ specified by inequality (21) (the values of ε_ϕ corresponding to $Q_c = 0$). At $\varepsilon_\phi < \varepsilon_{\phi th}$, the Fredericksz transition associated with the formation of a periodic structure occurs, while at $\varepsilon_\phi > \varepsilon_{\phi th}$ the ordinary Fredericksz transition with a homogeneous (along the 0y axis) director field is only possible.

Figure 2 shows the calculated dependences of the threshold field E_c and the wave number q_c on the flexoelectric parameter ν for different azimuthal anchoring energies ε_ϕ . The period λ_c of the forming spatial structure of the director, as well as the corresponding value of the threshold electric field E_c , increase with an increase in the parameter ν . It can be seen from Fig. 2b that for each given anchoring energy ε_ϕ there is a critical value of the flexoelectric parameter ν_{th} determined by inequality (21) (the values of ν corresponding to $Q_c = 0$): at $\nu < \nu_{th}$ the Fredericksz transition with the formation of a periodic structure of the director occurs, while at $\nu > \nu_{th}$ the ordinary Fredericksz transition is observed.

INFLUENCE OF THE FINITENESS OF POLAR ANCHORING ENERGY

Now, let us assume that the azimuthal anchoring energy of the director at the substrate is infinitely high ($W_\phi = \infty$), while the polar anchoring energy W_θ is arbitrary.

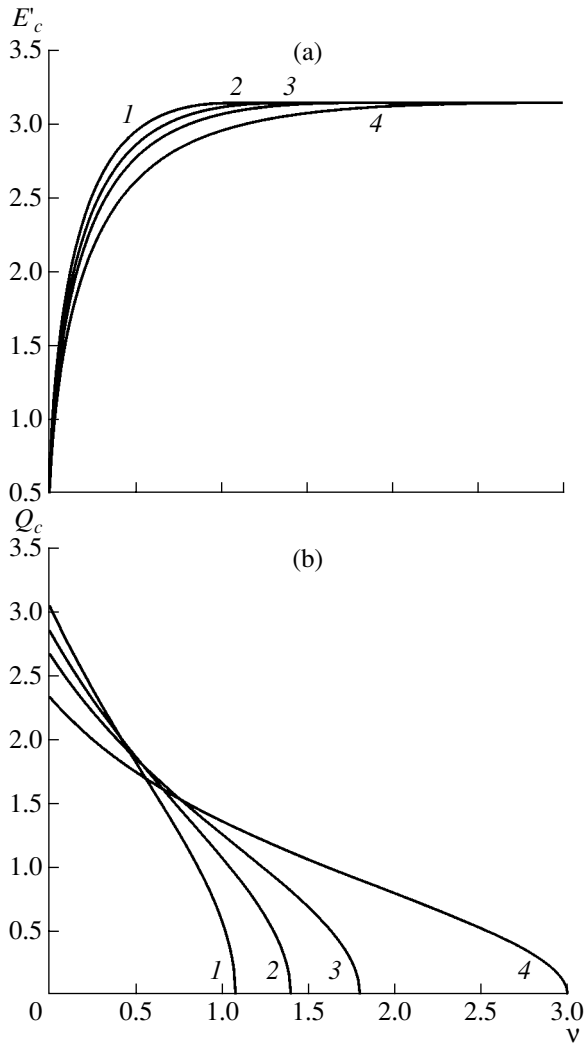


Fig. 2. Dependences of (a) the threshold field E'_c and (b) the wave number Q_c on the parameter v for $\epsilon_\phi = (1)$ 50, (2) 10, (3) 5, and (4) 2.

bitrary. In this case, the boundary conditions (4) take the form

$$\left[(W_\theta \mp e_0 E) \theta_1 \pm K \frac{d\theta_1}{dz} \right]_{z=\pm L/2} = 0, \quad (22)$$

$$\Phi_1|_{z=\pm L/2} = 0.$$

Substituting solution (10) into the boundary conditions (22), we obtain a homogeneous system of four algebraic equations for the coefficients a_i and b_i ($i = 1, 2$). The condition for nontrivial solution of this system yields the following equation:

$$[AB - (e_0 E)^2 ((\epsilon E^2)^2 + (2eEq)^2)] \times \cos \frac{p_1 L}{2} \sin \frac{p_1 L}{2} \cosh \frac{p_2 L}{2} \sinh \frac{p_2 L}{2} = 0, \quad (23)$$

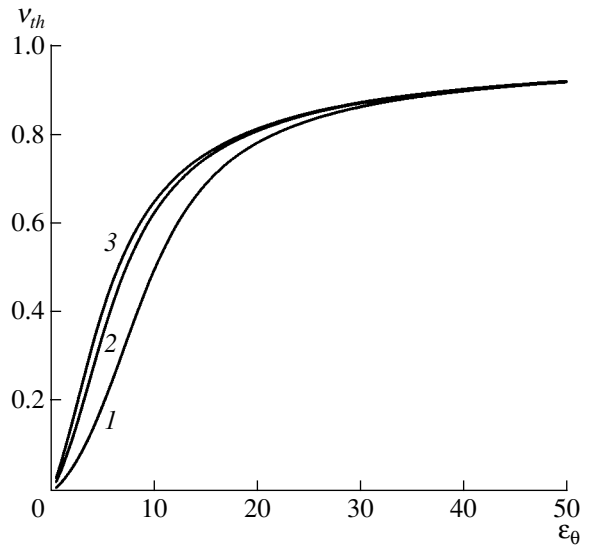


Fig. 3. Dependence of the critical value of the parameter v_{th} on the polar anchoring energy ϵ_θ for $v_0 = (1)$ 0.1, (2) 0.3, and (3) 0.5.

where

$$A = W_\theta \sqrt{(\epsilon E^2)^2 + (2eEq)^2} - \frac{1}{2} K p_1 (\epsilon E^2 + \sqrt{(\epsilon E^2)^2 + (2eEq)^2}) \tan \frac{p_1 L}{2} - \frac{1}{2} K p_2 (\epsilon E^2 - \sqrt{(\epsilon E^2)^2 + (2eEq)^2}) \tanh \frac{p_2 L}{2}, \quad (24)$$

$$B = W_\theta \sqrt{(\epsilon E^2)^2 + (2eEq)^2} + \frac{1}{2} K p_1 (\epsilon E^2 + \sqrt{(\epsilon E^2)^2 + (2eEq)^2}) \cot \frac{p_1 L}{2} - \frac{1}{2} K p_2 (\epsilon E^2 - \sqrt{(\epsilon E^2)^2 + (2eEq)^2}) \coth \frac{p_2 L}{2}.$$

In the limiting case of absolutely rigid anchoring $W_\theta = \infty$, we find from Eq. (23) that $p_1 = \frac{\pi}{L}$ and the previously obtained result (14), (15).

In the case of strong anchoring ($\epsilon_\theta = \frac{W_\theta L}{K} \gg 1$), Eq. (23) is solved similarly to the previous case by setting $p_1 = \frac{\pi}{L} - x$, where $x \ll \frac{\pi}{L}$. Restricting ourselves to the terms linear in $\frac{1}{\epsilon_\theta}$, we arrive at

$$p_1 = \frac{\pi}{L} \left(1 - \frac{1}{\epsilon_\theta} \frac{\epsilon E^2 + \sqrt{(\epsilon E^2)^2 + (2eEq)^2}}{\sqrt{(\epsilon E^2)^2 + (2eEq)^2}} \right).$$

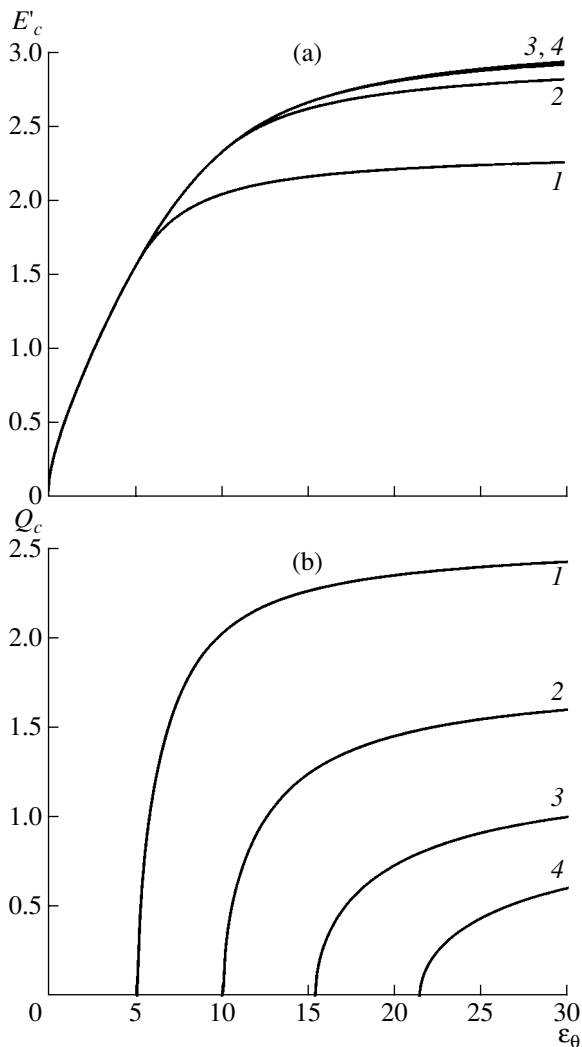


Fig. 4. Dependences of (a) the threshold field E'_c and (b) the wave number Q_c on the polar anchoring energy ϵ_θ for $v_0 = 0.1$ and $v = (1) 0.2, (2) 0.5, (3) 0.7,$ and $(4) 0.8$.

Accordingly, we find from (9) the dispersion dependence with accuracy up to the first-order terms

$$E(q) = E^\infty(q) \left\{ 1 - \frac{2 \left(\frac{\pi}{L} \right)^2}{\epsilon_\theta q^2 + \left(\frac{\pi}{L} \right)^2} \right\}. \quad (25)$$

Minimizing expression (25), we obtain the threshold field

$$E_c = E(q_c) = E_c^\infty \left(1 - \frac{1+v}{\epsilon_\theta} \right), \quad (26)$$

where the wave number is

$$q_c = q_c^\infty \left(1 - \frac{1+v}{\epsilon_\theta} \right) \quad (27)$$

at $v < 1$ and $\epsilon_\theta(1-v) \gg 1$ or

$$q_c = \frac{\pi}{\sqrt{2}L} \sqrt{1-v - \frac{4}{\epsilon_\theta}} \quad (28)$$

at $|1-v| \ll 1$.

It can be seen from here that both the threshold field E_c and the corresponding wave number q_c decrease with a decrease in the polar anchoring energy ϵ_θ . To form the periodic structure of the director, the flexoelectric parameter v must satisfy the inequality

$$v < 1 - \frac{4}{\epsilon_\theta}.$$

For arbitrary values of ϵ_θ , we failed to obtain the criterion (20) of the formation of the periodic structure in an analytical form. The results of the numerical calculations of the parameter v as a function of the energy ϵ_θ are shown in Fig. 3 for several values of the parameter

$$v_0 = \frac{\epsilon K}{e_0^2}.$$

Here, the range $v < v_{th}$ is the region of existence of a periodic structure of the director. As can be seen from Fig. 3, the finiteness of the polar anchoring energy results in the narrowing of the range of the flexoelectric parameter v in which the periodic structure exists.

Figure 4 shows the dependences of the threshold field and the corresponding wave number on the polar anchoring energy ϵ_θ calculated numerically by solving (23) for several values of the parameter v . As for the strong anchoring, the threshold field and the wave number increase monotonically with an increase in the anchoring energy ϵ_θ for all values of the parameter v . The flexoelectric parameter v_0 was set in this case to be equal to 0.1. The values of v_0 only slightly affect the obtained dependences $E_c(\epsilon_\theta)$ and $q_c(\epsilon_\theta)$.

CONCLUSIONS

Thus, in the case of the initial planar orientation of the director, the anchoring energy of the director at the cell surface significantly affects not only the threshold electric field and the period of the forming structure of the director field but also the range of admissible values of the flexoelectric parameter v . For a finite azimuthal anchoring energy, the range of admissible values of the parameter v widens, while for a finite polar anchoring energy this range narrows (as compared to the range of v in the case of infinitely rigid director anchoring).

REFERENCES

1. *The Physics of Liquid Crystals*, Ed. by P. de Gennes (Clarendon, Oxford, 1974; Mir, Moscow, 1977).
2. L. M. Blinov, *Electro-Optical and Magneto-Optical Properties of Liquid Crystals* (Nauka, Moscow, 1978; Wiley, New York, 1983).
3. A. S. Sonin, *Introduction to the Physics of Liquid Crystals* (Nauka, Moscow, 1983) [in Russian].
4. Yu. P. Bobylev and S. A. Pikin, Zh. Éksp. Teor. Fiz. **72** (1), 369 (1977) [Sov. Phys. JETP **45**, 195 (1977)].
5. Y. P. Bobylev, V. G. Chigrinov, and S. A. Pikin, J. Phys. Colloid. Chem. **40** (C3), 331 (1979).
6. F. Lonberg and R. B. Meyer, Phys. Rev. Lett. **55** (7), 718 (1985).
7. A. N. Chuvyrov, Kristallografiya **25**, 326 (1980) [Sov. Phys. Crystallogr. **25**, 188 (1980)].
8. A. M. Blinov and A. A. Sonin, Zh. Éksp. Teor. Fiz. **87**, 476 (1984) [Sov. Phys. JETP **60**, 272 (1984)].
9. V. G. Nazarenko and O. D. Lavrentovich, Phys. Rev. E **49**, 990 (1994).
10. I. P. Pinkevich and M. F. Lednei, Proc. SPIE **2651**, 167 (1996).
11. V. P. Romanov and G. K. Sklyarenko, Zh. Éksp. Teor. Fiz. **116** (2), 543 (1999) [JETP **89**, 288 (1999)].
12. A. Rapini and M. Papolar, J. Phys. Colloid. Chem. **30**, 54 (1969).

Translated by A. Zolot'ko

Mechanochemical Synthesis of Nonstoichiometric Fluorite $\text{Ca}_{1-x}\text{La}_x\text{F}_{2+x}$ Nanocrystals from CaF_2 and LaF_3 Single Crystals

B. P. Sobolev*, I. A. Sviridov**, V. I. Fadeeva**, S. N. Sul'yanov*, N. I. Sorokin*,
Z. I. Zhmurova*, P. Herrero***, A. Landa-Canovas***, and R. M. Rojas***

* Shubnikov Institute of Crystallography, Russian Academy of Sciences,
Leninskii pr. 59, Moscow, 119333 Russia
e-mail: sobolevb@yandex.ru

** Moscow State University, Moscow, 119992 Russia

*** Instituto de Ciencia de Materiales de Madrid, Madrid, Spain

Received December 29, 2004

Abstract—The nonstoichiometric $\text{Ca}_{1-x}\text{La}_x\text{F}_{2+x}$ phase ($x \geq 0.1$) is obtained by mechanochemical synthesis from CaF_2 and LaF_3 single crystals. This phase is the first representative of fluorite fluorides obtained by mechanochemical synthesis in the $\text{MF}_m\text{—RF}_n$ systems ($m < n \leq 4$). The average grain size ranges within 10–30 nm. The temperature dependence of ionic conductivity of the mechanochemically synthesized phase pressurized at 600 MPa (at its high-temperature portion at temperatures exceeding 200–250°C) coincides with the conductivity of the single crystals of the same composition ($\text{Ca}_{0.8}\text{La}_{0.2}\text{F}_{2.2}$). The activation energy of ionic conductivity (0.95 eV) corresponds to migration of interstitial fluoride ions in the crystal bulk. Mechanochemical synthesis of a multicomponent fluoride material with nanometer grains opens a new chapter in the chemistry of inorganic fluorides. A decrease of the sintering temperature of the powders with nanometer grains is very important for preparing dense fluoride ceramics of complicated compositions and other polycrystalline forms of fluoride materials. © 2005 Pleiades Publishing, Inc.

INTRODUCTION

In its applied aspect, mechanochemistry studying the influence of mechanical deformation on inorganic materials and their chemical reactions is closely related to synthesis of materials with high reactivity. This is explained by the fact that mechanochemical synthesis often yields materials with nanometer particles (nanoparticles) which are characterized by the considerable contribution of the surface layer to their properties and chemical behavior. Mechanochemical synthesis is one of the important modern methods for production of nanomaterials.

Up to now, mechanochemical synthesis has not been used for obtaining multicomponent materials consisting of inorganic fluorides, of which the most important for practice are nonstoichiometric fluorite phases of the composition $M_{1-x}R_x\text{F}_{2+x}$. These phases form only a small part of all the known nonstoichiometric phases of the composition $M_{1-x}R_x\text{F}_{m(1-x)+nx}$ formed in binary $\text{MF}_m\text{—RF}_n$ systems ($m < n \leq 4$; M and R are 34 different metals) [1–5]. However, the physicochemical characteristics of the $M_{1-x}R_x\text{F}_{2+x}$ phase are of great practical interest. The defect structure of these phases, which controls the bulk properties, has been studied in good detail. Therefore, we selected the family of the $M_{1-x}R_x\text{F}_{2+x}$ phases as the first type of multicomponent fluoride materials to be obtained by mechanochemical synthesis.

We selected as the first object of this family the nonstoichiometric $\text{Ca}_{1-x}\text{La}_x\text{F}_{2+x}$ phase with the fluorite structure. This phase is a typical representative (with respect to both its defect structure and the related specific properties) of a large family of 80 $M_{1-x}R_x\text{F}_{2+x}$ crystals with varying qualitative (elemental) chemical composition ($M = \text{Ca, Sr, Ba, Cd, Pb}$; R are rare earth elements, namely, Sc, Y, La–Lu). The equilibrium phase diagrams of these phases are characterized by extended homogeneity regions (up to 50 ± 2 mol % RF_3 under standard pressure). These phases are related to the type of heterovalent solid solutions with a varying number of atoms in the unit cell [6]. Their formation is accompanied by unusually high concentrations of structural defects such as anionic vacancies and interstitial fluoride ions. One of the consequences of high defect concentration is the appearance of superionic conductivity of fluoride ions [7, 8] and other properties.

The main structural characteristic of the $M_{1-x}R_x\text{F}_{2+x}$ phases is grouping of the defects in the anionic and cationic sublattices into clusters. Single clusters have nanometer dimensions, which allows one to consider the $M_{1-x}R_x\text{F}_{2+x}$ crystals as the first nanostructured fluorides having their own place in the classification of the known nanostructured materials [9]. The unique properties of the $M_{1-x}R_x\text{F}_{2+x}$ crystals controllable over a wide range (by varying their compo-

sition and defect structure) make these crystals very promising for modern technologies [1–5].

As a rule, the $M_{1-x}R_xF_{2+x}$ fluorides are used in practice in the form of single crystals synthesized from melts by various modifications of the method of directed crystallization [10]. Much less popular are their ceramic forms, including multicomponent optical fluoride ceramics [11]. The use of high temperatures in all the methods of synthesis of the $M_{1-x}R_xF_{2+x}$ phases (from 1550°C in growth from melts, up to 700–900°C in synthesis of ceramics) is accompanied by the fluoride reaction with water vapor (pyrohydrolysis) observed above 450–500°C [12]. The incorporation of oxygen into fluorides results in several negative effects of which the most important is uncontrollable change of some physical characteristics and, first of all, of crystal transparency.

In addition to pyrohydrolysis, the use of high temperatures also imposes severe limitations on the choice of fluorides as the components of complex fluoride materials [5]. These limitations are associated with different melting points of the components, their vapor pressures, thermal decomposition, and other factors. Mechanochemical synthesis has some obvious advantages and is characterized, first of all, by relatively low temperatures increasing the possibilities of synthesis of multicomponent fluoride materials, including nonstoichiometric ones.

The present study was aimed at the establishment of the possibility of preparing nonstoichiometric fluoride phases of the $M_{1-x}R_xF_{2+x}$ composition from the crystalline MF_2 and RF_3 components by mechanochemical synthesis of the phase $Ca_{1-x}La_xF_{2+x}$.

EXPERIMENTAL

Choice of the $Ca_{1-x}La_xF_{2+x}$ solid solution as the object of our study was dictated by a number of reasons. This solid solution is formed from the components possessing the highest melting points among all the MF_2 and RF_3 compounds ($1418 \pm 5^\circ\text{C}$ for CaF_2 and $1500 \pm 10^\circ\text{C}$ for LaF_3). The CaF_2 – LaF_3 system has the simplest phase composition among all the MF_2 – RF_3 systems and has no other phases except for the $Ca_{1-x}La_xF_{2+x}$ and $La_{1-y}Ca_yF_{3-y}$ -based solid solutions crystallized in the fluorite (CaF_2) and tysonite (LaF_3) structure types, respectively. This system is also of a simple eutectic type. At the eutectic temperature (1311°C), the solubility limit of LaF_3 in CaF_2 is 46 mol % ($x = 0.46$) and the solubility limit of CaF_2 in LaF_3 is 23 mol % ($y = 0.23$).

The phase diagram of the system is well studied up to 800°C [13–15]; the subsolidus region extends up to 600°C [16]. Thus, the study of the products of the fluoride reaction in the CaF_2 – LaF_3 system under the condition of mechanochemical synthesis is facilitated by its simple and well-studied phase composition in the tem-

perature range from the melting point up to 600°C . At the same time, it is also possible to establish to what extent the phase relationships known for this system under the equilibrium conditions would be preserved or change under the a priori nonequilibrium conditions of mechanochemical synthesis.

Starting materials were CaF_2 crystals with an oxygen content of 0.025 wt % (wastes of optical single crystals produced by the Vavilov State Optical Institute). Lanthanum trifluoride crystals were grown from melt in the atmosphere of the products of Teflon pyrolysis with an oxygen content of 0.052 wt % (method of vacuum melting [17]).

The starting mechanical mixtures, (1) 90 mol % CaF_2 and 10 mol % LaF_3 and (2) 80 mol % CaF_2 and 20 mol % LaF_3 (mixture compositions are indicated in mol %, whereas formulas indicate molar fractions x), consisted of single-crystal fragments with a diameter up to 1 mm. The components were mixed in a planetary ball mill without preliminary milling.

Mechanochemical synthesis was performed by milling the mixtures of CaF_2 and LaF_3 fragments in a MAPF-2M water-cooled planetary ball mill in a protective argon atmosphere. The drum and ball were manufactured from ShKh-15 steel. The initial loading of the component mixture was 10 g. The ratio of the ball weight to the component weight was 6 : 1. The milling energy estimated by the method suggested in [18] with due regard for the reagent weights, the number and diameter of the balls, and the velocity of the drum rotation was 10 W/g.

X-ray phase analysis of the products of mechanochemical synthesis was performed on a KARD-6 diffractometer with a two-dimensional detector based on a planar proportional camera (reflection geometry, CuK_α radiation, graphite monochromator). Reflection intensity as a function of the diffraction angle, $I(2\theta)$, was calculated over the whole detector area by the method suggested in [19]. The lattice parameters, the weight fractions of phases in the mixture, and the percentage of Ca and La atoms in the fluorite and tysonite phases were determined by the Rietveld method using the Full-Prof program [20].

Chemical composition of the $Ca_{1-x}La_xF_{2+x}$ solid solution was evaluated from the linear dependence of the cubic lattice parameter $a = 5.46296 + 0.56333x$ on the composition in the whole homogeneity region [21]. In [15, 22], the following equation is given: $a = a_0 + 0.591x - 0.134x^2$. We failed to establish the cause of the difference in the dependence of the lattice parameter on composition. In what follows, we use the linear dependence almost coinciding with the nonlinear dependence in the region with the LaF_3 content up to 30 mol %.

The lattice parameter a was calculated by the Rietveld method. The angular accuracy of the calculated peak positions was $\sim 0.02^\circ$, whence the relative error in the determined lattice parameter is ~ 0.0004 ,

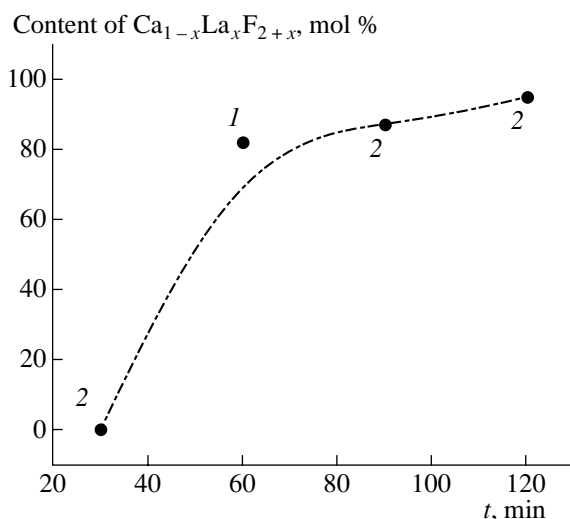


Fig. 1. Content of the fluorite $\text{Ca}_{1-x}\text{La}_x\text{F}_{2+x}$ phase in the products of mechanochemical synthesis as a function of the milling time. The starting materials: (1) 90 mol % CaF_2 + 10 mol % LaF_3 and (2) 80 mol % CaF_2 + 20 mol % LaF_3 .

which considerably exceeds the standard deviations calculated by the program [20]. The dependence of the unit-cell parameter on the composition is determined with a high accuracy in [15, 21]. Therefore, the content of LaF_3 in the solid solution may also be calculated from the value of the lattice parameter a calculated by the Rietveld method with a higher accuracy than the LaF_3 content obtained in the direct structure refinement. Both values obtained in our experiment agree quite well. Below, we refer to the values obtained by the first method.

Particle shape and size and diffraction from microcrystals of the products of synthesis were studied in a JEOL 2000FX electron microscope at an accelerating voltage 200 kV. The samples for electron microscopy studies were obtained by dispersion of the product of mechanochemical synthesis in *n*-butanol with the subsequent application of the suspension onto a copper grid coated with graphite.

Behavior of the product of mechanochemical synthesis during its heating to 1000°C was studied in a Seiko TG/DTA 6300 setup for differential thermal analysis (DTA) in a platinum crucible in an argon flow (100 ml/min). The powder was pressurized into tablets under a pressure of 600 MPa. The heating and cooling rates were 10°C/min.

Ionic conductivity of the product of mechanochemical synthesis (performed for 1.5 h) of the nominal composition $\text{Ca}_{0.8}\text{La}_{0.2}\text{F}_{2.2}$ was studied by the method of impedance spectroscopy (Tesla BM507 impedance meter, frequency range 5 to 5×10^5 Hz, resistance range 1 to 10^7 Ω). The starting powder was pressed (600 MPa) into tablets 3 mm in diameter and 1.6- to

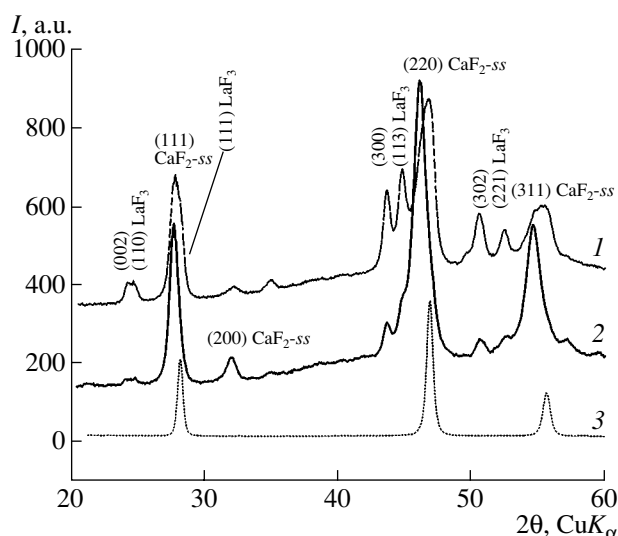


Fig. 2. X-ray powder diffraction patterns of the products of (1) 60-min-milling of the 90 mol % CaF_2 + 10 mol % LaF_3 mixture, (2) 120-min-milling of the 80 mol % CaF_2 + 20 mol % LaF_3 mixture, and (3) CaF_2 ; ss indicates solid solution.

1.7-mm thick. The tablets were supplied with graphite electrodes (DAG-580 paste) applied to their end surfaces. Electrophysical measurements were performed in a $\sim 10^{-1}$ Pa vacuum in the temperature range 60–530°C.

EXPERIMENTAL RESULTS

Kinetics of formation of the $\text{Ca}_{1-x}\text{La}_x\text{F}_{2+x}$ solid solution during mechanochemical synthesis. Kinetics of mechanochemical synthesis of the nonstoichiometric fluorite phase was studied for two mechanical mixtures: (1) 90 mol % CaF_2 + 10 mol % LaF_3 and (2) 80 mol % CaF_2 + 20 mol % LaF_3 . The samples for quantitative X-ray phase analysis were selected after 30-, 45-, 60-, 90-, and 120-min milling. X-ray diffraction patterns from the samples were treated by the Rietveld method to determine the content of each phase in the products of mechanochemical synthesis. The content of the $\text{Ca}_{1-x}\text{La}_x\text{F}_{2+x}$ solid solution (in mol %) in the product of mechanochemical synthesis as a function of the milling time t is shown in Fig. 1. The numerals in parentheses correspond to mixtures (1) and (2).

X-ray powder diffraction pattern from the product of 60-min milling of mixture (1) (diffraction pattern 1) and 120-min milling of mixture (2) (diffraction pattern 2) are shown in Fig. 2. For comparison, Fig. 2 also shows the diffraction pattern of CaF_2 (3) milled in a conventional ball mill.

Our studies showed that 30-min milling is not sufficient to initiate the reaction of mechanochemical synthesis (Fig. 1). The lattice parameter of the fluorite phase is close to that of pure CaF_2 ; however, milling

gives rise to noticeable broadening of the diffraction reflections.

Figure 2 (curve 1) shows that 60-min milling of mixture (1) results not only in broadening of the diffraction reflections of the fluorite lattice but also in the displacement of the reflections to small angles, i.e., in the formation of the mixture of solid-solution particles having different compositions.

The 60-min milling of the initial mixture (1) showed that the solid-solution content in the product of mechanochemical synthesis was equal to 82 mol % for the phase composition $\text{Ca}_{0.9}\text{La}_{0.1}\text{F}_{2.1}$. The 90-min milling of mixture (2) yielded a content equal to 87 mol % for the phase composition $\text{Ca}_{0.84}\text{La}_{0.16}\text{F}_{2.16}$ (the compositions were determined from the unit-cell parameters). Thus, the yield of the fluorite $\text{Ca}_{1-x}\text{La}_x\text{F}_{2+x}$ solid solution is practically independent of the mixture composition in the range of LaF_3 content 10–20 mol %.

Thus, 120-min mechanochemical synthesis with the milling energy indicated above shows almost complete (95 mol % of the fluorite phase) proceeding of the reaction between the mixture of the crystalline 80% CaF_2 and 20% LaF_3 with the formation of the nonstoichiometric $\text{Ca}_{0.8}\text{La}_{0.2}\text{F}_{2.2}$ phase.

Determination of chemical composition of the nonstoichiometric fluorite $\text{Ca}_{1-x}\text{La}_x\text{F}_{2+x}$ phase formed in mechanochemical synthesis. As a result of 120-min milling of mixture (2), the $\text{Ca}_{1-x}\text{La}_x\text{F}_{2+x}$ solid solution is formed (diffraction pattern 2 in Fig. 2). Its composition was determined by two independent methods. The first one reduced to the calculation of the composition from the dependence of the lattice parameter on composition [15, 21, 22] and the parameter determined by the Rietveld method. For the mixture indicated above, the lattice parameter was determined as $a = 5.579(2)$ Å, which corresponds to the LaF_3 content 20.6 mol %.

Mixture (2) subjected to 90-min milling yielded the solid solution with the lattice parameter $a = 5.553(2)$ Å corresponding to the composition $\text{Ca}_{0.84}\text{La}_{0.16}\text{F}_{2.16}$ (determined from the dependence of the lattice parameter on composition [21]). Assuming the formation of the $\text{Ca}_{1-x}\text{La}_x\text{F}_{2+x}$ solid solution, we obtained the close composition by the Rietveld method, $\text{Ca}_{0.86}\text{La}_{0.14}\text{F}_{2.14}$ ($R_{\text{Br}} = 1.09\%$). The above data show that the LaF_3 content in the solid solution increases during milling simultaneously with an increase of the brutto content of the fluorite $\text{Ca}_{1-x}\text{La}_x\text{F}_{2+x}$ phase.

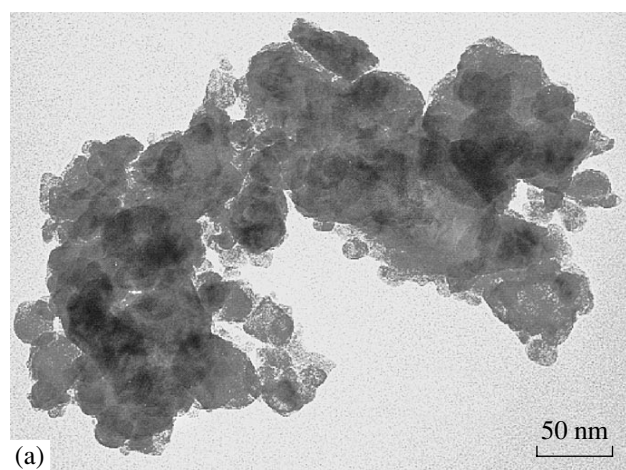
The composition of the fluorite $\text{Ca}_{0.794}\text{La}_{0.206}\text{F}_{2.206}$ phase obtained after 120-min milling is close within the accuracy of its determination from the lattice parameter ($\pm 0.5\%$ LaF_3) to the charge composition (20 mol % LaF_3). However, this is insufficient to draw a unique conclusion on the complete proceeding of the reaction in mixture (2) subjected to 2 h milling. As is seen from X-ray diffraction pattern 2 in Fig. 2, some amount of

the phase with the tysonite structure is also seen on the respective diffraction pattern. Because of the low intensity of the respective reflections and weak dependence of the lattice parameters of the tysonite phase on the composition, it is difficult to come to a decisive conclusion whether the phase obtained is a $\text{La}_{1-y}\text{Ca}_y\text{F}_{3-y}$ solid solution or pure LaF_3 . In our calculations, we used the following composition of the tysonite phase $\text{La}_{0.97}\text{Ca}_{0.03}\text{F}_{2.97}$. The amount of this phase determined by the Rietveld method is ~ 5.0 mol %.

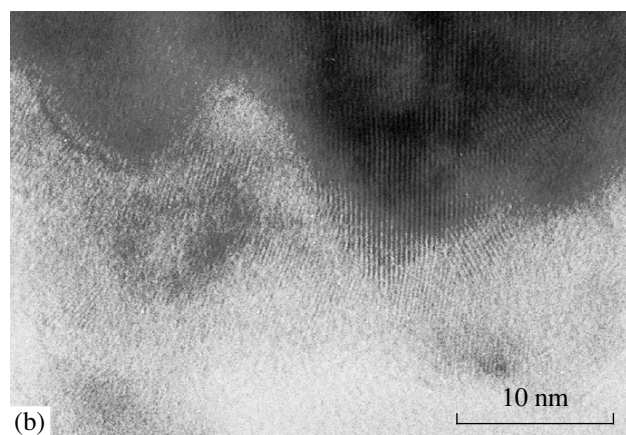
The presence of unreacted LaF_3 (or a solid solution based on it) may be associated with the design of the mill drum with a rectangular bottom with dead zones. The possible capture of large grains into the dead zones was also facilitated by the fact that we made no preliminary milling of the components, so that the grains sometimes were 1 mm in diameter. The grains of such size were also observed in an optical microscope.

Dispersion and homogeneity of the product of mechanochemical synthesis were studied by the optical method in a MIN-8 microscope. We observed component grains up to 1 mm in diameter. It seems that some crystalline grains captured into the dead zones preserved their initial size after milling. This indicates the necessity of the preliminary milling of the whole starting mixture of the components and constant stirring of the products of mechanochemical synthesis instead of manually stirring only every 15 min of milling.

The product dispersion can be estimated from the width of the diffraction lines on the powder diffraction patterns. The dependence of the diffraction-line width on the diffraction angle for the phases studied is complicated. Line broadening considerably increases with an increase in the diffraction angle and is determined not only by dispersion but, probably, also by strong second-order lattice distortions. Below, we indicate the dimensions of the coherent-scattering blocks calculated from broadening of the diffraction lines with the minimum diffraction angle made as estimated by the Selykov–Scherrer formula for spherical particles, $L = 0.89\lambda/(\cos\theta\Delta(2\theta))$. We used the Gaussian approximation for both instrumental function and the recorded line. Here $\Delta(2\theta) = (B^2 - b^2)^{1/2}$, where B and b are the measured and standard values of the half-width at the half-height and λ is the wavelength of the radiation. For 30-min milling of mixture (2), we obtained the composition CaF_2 80 mol % + LaF_3 20 mol %, in which no solid solution has been formed as yet. The CaF_2 phase has the size of a coherent-scattering block, $L = \sim 108$ Å. After 60-min-milling of initial mixture (1) 90 mol % CaF_2 + 10 mol % LaF_3 , the product of mechanochemical synthesis $\text{Ca}_{0.9}\text{La}_{0.1}\text{F}_{2.1}$ was characterized by $L = 91$ Å. A close value was also obtained after 90-min milling of mixture (2), $L = 81$ Å.



(a)



(b)

Fig. 3. (a) Product of mechanochemical synthesis of $\text{Ca}_{0.8}\text{La}_{0.2}\text{F}_{2.2}$ and (b) high-resolution micrographs of $\text{Ca}_{0.8}\text{La}_{0.2}\text{F}_{2.2}$ nanoparticles.

After 120-min milling of mixture (2) CaF_2 80 mol % + LaF_3 20 mol %, the size of the coherent-scattering blocks of the fluorite phase was $L = 108 \text{ \AA}$.

The above data indicate that the intense process of formation of the $\text{Ca}_{1-x}\text{La}_x\text{F}_{2+x}$ solid solution begins (at the given milling energy) only after 40–50 min of milling. The rate of formation of the nonstoichiometric fluorite phase weakly depends on the initial ratio of the components (in the range of 10–20 mol % LaF_3). The size of coherent-scattering blocks of the fluorite solid solution is independent of the initial charge composition (in the range indicated above) and the milling time and, according to the estimate made by the Rietveld method, is about 10 nm.

X-ray estimation of the size of coherent-scattering blocks of the fluorite solid solution qualitatively agrees with the electron-microscopy data.

Transmission electron microscopy study showed that the products of mechanochemical synthesis consist of particles with the size ranging from 5 to 50 nm, with the average size ranging within 20–30 nm (Fig. 3a). At higher magnification it was also seen that large parti-

cles are, in fact, the aggregates of smaller ones. Small particles are mosaic and contain differently oriented coherent-scattering regions with a well-formed set of atomic planes (Fig. 3b). Electron diffraction study confirmed the crystallinity of the sample, its fluorite structure, and its rather high stability to electron irradiation.

Changes in the product of mechanochemical synthesis during heating. The $\text{Ca}_{0.8}\text{La}_{0.2}\text{F}_{2.2}$ solid solution obtained is metastable under the conditions of mechanochemical synthesis because below 600°C the equilibrium solubility of LaF_3 in CaF_2 is close to zero. Heating the nonequilibrium $\text{Ca}_{0.8}\text{La}_{0.2}\text{F}_{2.2}$ product to temperatures giving rise to volume diffusion, one may expect some phase transformations. In accordance with the phase diagram, the transformations may be expected in the high-temperatures range. However, possible non-equilibrium processes may also give rise to the formation of metastable phases.

The heating curves of $\text{Ca}_{0.8}\text{La}_{0.2}\text{F}_{2.2}$ demonstrate some thermal effects. Heating to $120\text{--}180^\circ\text{C}$ is accompanied by weight losses slightly exceeding 1 wt %. Conditionally, this loss may explain a very weak endothermic effect. A more obvious but also weak endothermic effect is observed at 480°C . The corresponding phase transformation takes place against the background of continuing loss of weight attaining, at 1000°C , a value of about 2.5%.

The loss of weight (0.5%) continues during sample cooling from 1000 to 400°C . The repeated cooling may result in further loss of weight within tenths of a percent; then the sample weight is practically stabilized. The nature of the weight loss observed is still unclear. Its monotonic character over the wide temperature range indicates the occurrence of partial hydrolysis rather than gas desorption from the surface.

At 784°C , the pronounced endothermic effect is observed. The transformation is irreversible and is not observed during cooling and repeated heating. The phase equilibria in the subsolidus region below 800°C in the $\text{CaF}_2\text{--LaF}_3$ system have been studied insufficiently. Therefore, the nature of the effect observed at 784°C is still unknown and may only be assumed.

According to [16], this temperature is close to the temperature of formation of $\text{Ca}_{0.8}\text{La}_{0.2}\text{F}_{2.2}$ from the components. In the temperature range $690\text{--}917^\circ\text{C}$, no experimental points are observed on the solidus curve and its run in this interval has not been established. If one assumes that the curve of the formation (decomposition) of the solid solution of the composition indicated above is intersected at 784°C , above this temperature, the remaining unreacted components (CaF_2 and LaF_3) should start reacting. As a result, a composition is formed which is saturated, in the general case, with the tysonite phase $\text{La}_{1-y}\text{Ca}_y\text{F}_{3-y}$ at the maximum attained temperature (in our case, 1000°C).

X-ray diffraction study of the sample subjected to DTA showed that at least three processes occurred in

the sample: recrystallization of the main compound of the composition $\text{Ca}_{0.8}\text{La}_{0.2}\text{F}_{2.2}$ and formation of two fluorite phases, $\text{Ca}_{0.52}\text{La}_{0.48}\text{F}_{2.48}$ and $\text{Ca}_{0.94}\text{La}_{0.06}\text{F}_{2.06}$ (the compositions were determined from the dependences of the lattice parameters [21]). The composition $\text{Ca}_{0.52}\text{La}_{0.48}\text{F}_{2.48}$ is close to the composition of the saturated solid solution at the eutectic temperature (1310°C) in the CaF_2 – LaF_3 system (46 ± 2 mol % [13–16]). The second composition is close to the composition of the CaF_2 component. The main part of the product consists of the recrystallized $\text{Ca}_{0.8}\text{La}_{0.2}\text{F}_{2.2}$ solid solution characterized by narrow reflections on the diffraction pattern.

The LaF_3 content in the newly formed $\text{Ca}_{0.52}\text{La}_{0.48}\text{F}_{2.48}$ phase considerably exceeds its content in the equilibrium saturated solid solution for the isotherm 1008°C studied earlier (~ 37 mol % LaF_3 according to [16]). This deviation from the equilibrium solubility may serve as an indication of the fact that the reaction of nanodispersed phases (components of the system and the fluorite solid solution) gives rise to the formation of a metastable product at the reaction temperature under the DTA conditions (at temperatures up to 1000°C). The formation of metastable states in mechanochemical synthesis in oxide systems is well known and is often observed [23, 24]. For fluoride systems, this problem should be studied separately.

Measurements of ionic conductivity. Up to now, studying the conductivity of numerous fluorite phases of the composition $M_{1-x}R_x\text{F}_{2+x}$ ($M = \text{Ca}, \text{Sr}, \text{Ba}, \text{Cd}, \text{Pb}$; $R = \text{Sc}, \text{Y}, \text{La-Lu}$) [7, 8, 25, 26], we have never encountered a phase with such a high degree of dispersion as $\text{Ca}_{0.8}\text{La}_{0.2}\text{F}_{2.2}$ obtained by mechanochemical synthesis. Moreover, studying the ionic transport in nonstoichiometric fluorides, we always tried to synthesize single crystals, which minimized the contribution of the surface component to the total conductivity and diminished the probability of sample degradation during heating because of the occurrence of the pyrohydrolysis reaction.

Analysis of impedance hodographs (complex resistivity) of electrochemical cells with graphite electrodes allowed us to separate the total bulk resistivity R_b characterizing all the processes of defect migration in the materials studied. Conductivity was calculated by the formula $\sigma = h/R_b S$, where h is the sample thickness and S is the electrode area. The activation energy E_a determined by the migration mechanism of charge carriers was found from the Arrhenius–Frenkel equation $\sigma T = A \exp(-E_a/kT)$, where A is the preexponential factor of electrical conductivity.

Temperature dependence of conductivity of one of the samples of the $\text{Ca}_{0.8}\text{La}_{0.2}\text{F}_{2.2}$ solid solution obtained by mechanochemical synthesis is shown in Fig. 4a for four temperature modes. Figure 4b shows the $\sigma(T)$ curves for three samples in the mode of the first cooling. To facilitate comparison of Figs. 4a and 4b, we also

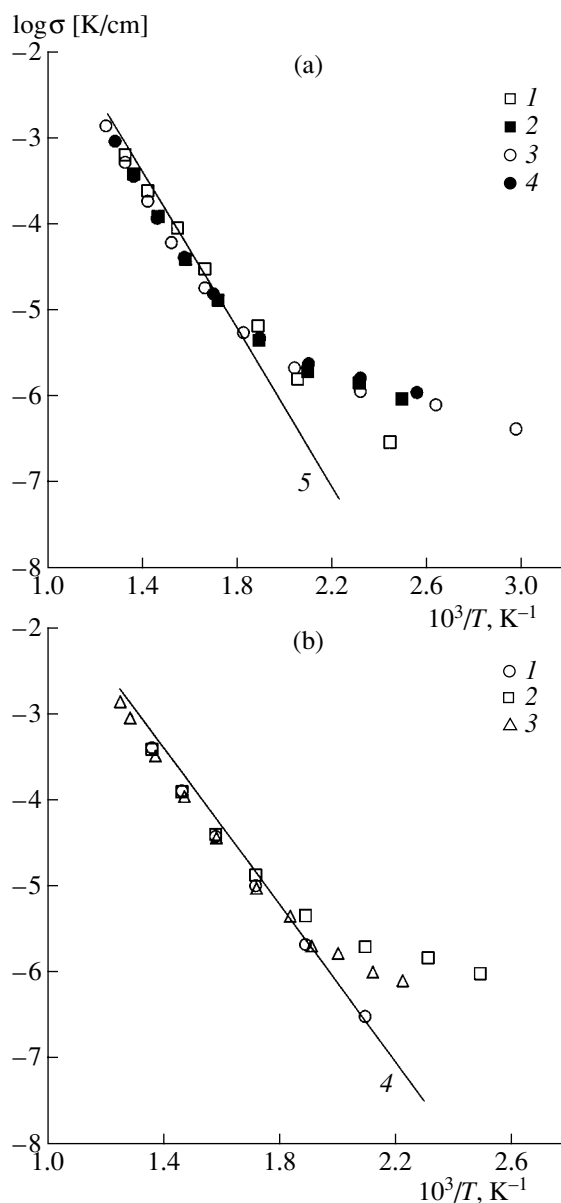


Fig. 4. Temperature curves of conductivity σ of the $\text{Ca}_{0.8}\text{La}_{0.2}\text{F}_{2.2}$ solid solution obtained by mechanochemical synthesis (a) in different thermal modes: ceramic (1) first heating, (2) first cooling, (3) second heating, (4) second cooling, and (5) the $\text{Ca}_{0.8}\text{La}_{0.2}\text{F}_{2.2}$ single crystal grown from melt; (b) temperature dependence of conductivity σ for (1, 2, 3) three different ceramic samples obtained in the mode of the first cooling and (4) the melt-grown $\text{Ca}_{0.8}\text{La}_{0.2}\text{F}_{2.2}$ single crystal.

show the temperature dependence of ionic conductivity of a $\text{Ca}_{0.8}\text{La}_{0.2}\text{F}_{2.2}$ single crystal obtained in [8]. The conductometric data for all the samples were reproducible in both heating and cooling modes (except for the first low-temperatures heating), so that the discrepancy in the data did not exceed $\pm 5\%$.

Temperature dependences of conductivity of the solid-solution samples obtained by mechanochemical

synthesis have two portions. The high-temperature portions of the $\sigma(T)$ curves begin at 200–250°C, depending on the sample, and completely coincide with the ionic conductivity of the respective single crystal. The activation energy $E_a = 0.95$ eV corresponds to migration of interstitial fluoride ions in the bulk of the fluorite $\text{Ca}_{0.8}\text{La}_{0.2}\text{F}_{2.2}$ solid solution.

The transition from the high- to low-temperature portion of the curves at 200–250°C is accompanied by a considerable decrease in the activation energy E_a , which indicates the change of the conductivity mechanism. At the low-temperature portions, the activation energy has the value $E_a = 0.2$ eV characteristic of migration anionic vacancies in the fluoride materials.

Thus, mechanochemical synthesis allowed us to obtain, for the first time, the nonstoichiometric nanocrystalline fluorite $\text{Ca}_{1-x}\text{La}_x\text{F}_{2+x}$ phase with the electrophysical characteristics not worse than those known for the single-crystal sample.

CONCLUSIONS

For the first time, mechanochemical synthesis was used to give rise to the reaction between single-crystal CaF_2 and LaF_3 starting materials resulting in the formation of nonstoichiometric $\text{Ca}_{0.8}\text{La}_{0.2}\text{F}_{2.2}$ fluoride with 10- to 30-nm-large grains and the defect structure of the CaF_2 type. The starting materials were refractory inorganic fluorides, which opens possibilities for mechanochemical synthesis of other multicomponent fluoride materials from less refractory fluorides.

A considerable increase in the number of possible components in mechanochemical synthesis—simple metal fluorides that may be used to obtain multicomponent fluoride materials—is explained by relatively “mild” temperature conditions of mechanochemical synthesis. A number of multicomponent fluoride materials cannot be obtained by traditional methods (such as crystallization from melts, solid-phase synthesis, and hot pressing) because of the high volatility, thermal dissociation, pyrohydrolysis, and other unfavorable characteristics of some initial components, which are difficult to combine with refractory, nonvolatile, and thermally stable initial components. In mechanochemical synthesis, similar limitations either completely remove or influence the result only to a minor degree. Mechanochemical synthesis in application to inorganic fluorides opens a new chapter in the chemistry of fluorides and the respective field of materials science.

Solid solutions of the fluorides with multicomponent compositions and nanoparticles are characterized by a reduced sintering temperature and possible formation of dense polycrystalline materials (ceramics).

Mechanochemical synthesis of fluorite $M_{1-x}R_x\text{F}_{2+x}$ phases is important for studying structural mechanisms of nonstoichiometric formation. The characteristics of the defect (cluster) structure of these phases are usually

studied on melt-grown crystals, which inherit the defects of the real structure formed during growth (non-equilibrium process) and uncontrollable cooling. Concentration of such defects may attain high values, which can mask the true mechanism of nonstoichiometric formation.

As was indicated in [23], the application of mechanochemical synthesis to multicomponent oxide systems often results in the formation of fluorite and perovskite phases. The estimates made in the present study may be extended to the $M\text{F}_m\text{--}R\text{F}_n$ fluoride systems with $m < n \leq 4$, and M and R are 34 metals. In these systems, the main products of high-temperature chemical reactions between the fluorides of the cations of different valence are the nonstoichiometric fluorite $M_{1-x}R_x\text{F}_{m(1-x)+nx}$ phases which amount to about 50% of all the two-component phases revealed in these systems [1–5].

ACKNOWLEDGMENTS

This study was supported by the Russian Foundation for Basic Research, project no. 04-02-16241, International Scientific–Technological Center, project no. 2136, and the Presidential Foundation of the Russian Federation for Support of Scientific Schools, project nos. NSh 1642.2003.2 and NSh 1954.2003.2. The authors are grateful to B.A. Popovkin for his interest in this study.

REFERENCES

1. B. P. Sobolev, *Zh. Vses. Khim. O–va im. D. I. Mendeleeva* **36** (6), 726 (1991).
2. B. P. Sobolev, *Butll. Soc. Catalana Cien. Fis. Quim. Mat.* **12** (2), 275 (1991).
3. B. P. Sobolev, in *Crystal Growth* (Nauka, Moscow, 1990), Vol. 18, p. 233 [in Russian].
4. B. P. Sobolev, in *Crystals. Growth, Structure, Properties* (Nauka, Moscow, 1993), Vol. 18, p. 167 [in Russian].
5. B. P. Sobolev, *The Rare Earth Trifluorides, Part 2: Introduction to Materials Science of Multicomponent Metal Fluoride Crystals* (Inst. d’Estudis Catalans, Barcelona, 2001).
6. V. M. Goldschmidt, T. Barth, G. Lunde, and W. Zachariasen, *Skr. Nor. Vidensk. Akad. 1: Mat.–Naturvidensk. Kl.* **1** (2), 1 (1926).
7. A. K. Ivanov-Shits, N. I. Sorokin, P. P. Fedorov, and B. P. Sobolev, *Solid State Ionics* **37** (1–2), 125 (1990).
8. A. K. Ivanov-Shitz, N. I. Sorokin, P. P. Fedorov, and B. P. Sobolev, *Solid State Ionics* **31** (4), 269 (1989).
9. B. P. Sobolev, A. M. Golubev, and P. Herrero, *Kristallografiya* **48** (1), 148 (2003) [*Crystallogr. Rep.* **48**, 141 (2003)].
10. B. P. Sobolev, Z. I. Zhmurova, V. V. Karelin, *et al.*, in *Crystal Growth* (Nauka, Moscow, 1988), Vol. 16, p. 58 [in Russian].

11. E. G. Chernevskaya, G. V. Anan'eva, T. I. Merkulyaeva, *et al.*, *Izv. Akad. Nauk SSSR, Neorg. Mater.* **26** (3), 658 (1990).
12. B. P. Sobolev, *Crystallogr. Rep.* **47** (Suppl. 1), 563 (2002).
13. P. P. Fedorov, Yu. G. Sizganov, and B. P. Sobolev, in *Abstracts of IV All-Union Symposium on Chemistry of Inorganic Fluorides, Dushanbe, 1975* (Nauka, Moscow, 1975), p. 30.
14. B. P. Sobolev and P. P. Fedorov, *J. Less-Common Met.* **60** (1), 33 (1978).
15. P. P. Fedorov and B. P. Sobolev, *J. Less-Common Met.* **63** (1), 31 (1979).
16. M. Svantner, E. Mariani, P. P. Fedorov, and B. P. Sobolev, *Krist. Tech.* **14** (3), 365 (1979).
17. G. G. Glavin and Yu. A. Karpov, *Zavod. Lab.* **30** (3), 306 (1964).
18. E. V. Shelekhov and T. A. Sviridova, *Materialovedenie*, No. 10, 13 (1999).
19. S. N. Sulyanov, A. N. Popov, and D. M. Kheiker, *J. Appl. Crystallogr.* **27**, 934 (1994).
20. J. Rodriguez-Carvajal, *Program FullProf* (Lab. Leon Brillouin, France, 2004).
21. O. Greis and M. Kieser, *Z. Anorg. Allg. Chem.* **479**, 165 (1981).
22. P. P. Fedorov and B. P. Sobolev, *Kristallografiya* **37** (5), 1210 (1992) [*Sov. Phys. Crystallogr.* **37**, 651 (1992)].
23. V. V. Zyryanov and N. F. Uvarov, *Neorg. Mater.* **40** (7), 835 (2004).
24. V. V. Zyryanov, *Neorg. Mater.* **39** (11), 1347 (2003).
25. N. I. Sorokin, M. V. Fominykh, E. A. Krivandina, *et al.*, *Fiz. Tverd. Tela* (St. Petersburg) **41** (4), 638 (1999) [*Phys. Solid State* **41**, 573 (1999)].
26. N. I. Sorokin, M. V. Fominykh, E. A. Krivandina, *et al.*, *Kristallografiya* **41** (2), 310 (1996) [*Crystallogr. Rep.* **41**, 292 (1996)].

Translated by L. Man

Physical and Physicochemical Processes Accompanying Powder Synthesis, Growth of PbMoO_4 Crystals, and Their Annealing in Various Media: II. Shape of the Crystal–Melt Interface Caused by Melt Evaporation and Supercooling

V. T. Gabrielyan^{1,2}, O. S. Grunskii¹, and A. V. Denisov¹

¹ Russian Center of Laser Physics of St. Petersburg State University, St. Petersburg, 198504 Russia
e-mail: tigran@home.rclph.spbu.ru

² Institute for Physical Research, Academy of Sciences of Armenia, Ashtarak, 138410 Armenia

Received November 20, 2003; in final form, October 12, 2004

Abstract—The temperature distribution in a melt of PbMoO_4 is investigated using a modified thermocouple and a scanning device. It is shown that the PbMoO_4 melt whose thermal field is significantly inhomogeneous at different depths demonstrates a strong (below the melting temperature) supercooling at the surface due to the evaporation. The position of the isotherm corresponding to the melting temperature of PbMoO_4 in the melt is determined by the degree of the melt supercooling at different growth parameters. The results obtained show that the conditions of mass and heat exchange in the melt are mainly determined by convection. The free convection remains dominant even at intense rotation of a crystal and the most thorough thermal isolation of the crystallization unit. © 2005 Pleiades Publishing, Inc.

INTRODUCTION

The temperature field in the volume of a melt for growing crystals by the Czochralski method is a complex function of several parameters characterizing and decisively determining the crystal growth. In addition to the well-known molecular heat transfer, convective heat transfer also occurs and plays a key role in melts (especially melts of oxides). The latter type of heat transfer is due to various reasons. Nonuniform temperature distribution in the crystallization unit results in an inhomogeneous field of densities in the melt, whose interaction with the gravitational field leads to the occurrence of a convective flow referred to as free convection. For melts with high vapor pressure, free convection is the dominant and, in fact, main mechanism of heat transfer. No thermal isolation in the crystallization unit, however effective, can reduce the free convection due to the evaporation from the melt surface, which causes, in turn, very large superheating of crucible walls.

It is well known that melts of most high-temperature nonvolatile oxides, showing no significant supercooling, are often superheated above the melting point, or, at least, have a surface temperature close to the melting point. Therefore, when a seed of a crystallized material is brought into contact with a melt to choose the growth conditions, an extended liquid-drop column of melt (meniscus) is observed in most cases, whose boundary coincides with the melting point isotherm. The above-

described conditions are not observed, however, in the growth of the compounds whose melts have very high volatility (PbMoO_4 , PbWO_4 , CaMoO_4 , CaWO_4 , Al_2O_3 , TeO_2 , and so on). The most typical situation for the melts of these compounds is an almost complete absence of the meniscus under the conditions similar to the growth conditions. In this case, the crystal tends to decrease the supercooling caused by the melt evaporation, growing into the melt in the form of a tapered protrusion (Fig. 1). In fact, the latent crystallization heat, which is generally removed upwards through the growing crystal in the absence of the direct melt evaporation, is spent in the case under consideration to compensate the melt supercooling under the crystal. The depth of penetration of the crystallization front into the melt can serve as an indicator of the degree of supercooling, since the crystal growth below the melt level will cease at the point where the tip of the tapered protrusion reaches the melting point isotherm of the compound grown.

In this paper, we report the results of the investigation of the temperature distribution in the PbMoO_4 melt and the shape of the crystal–melt interface, which are related to the melt supercooling. It should be noted that the thermal supercooling caused by the melt evaporation is meant rather than the constitutional supercooling which is known to be due to the rejection of impurities and their accumulation near the crystallization front.

EXPERIMENTAL TECHNIQUES

In order to reduce the measurement inertia to a minimum, it is preferable to measure temperature and its relative distribution in the melt volume with uncovered thermocouples. However, the following experimental difficulties may arise in this case:

(i) a chemical reaction is possible between the melt and the material of a thermocouple (the rhodium element of Pt/Pt–Rh thermocouples often reacts with many melts of oxides, for example, with LiNbO_3 , LiTaO_3 , and others, coloring the melts and the crystals grown orange-yellow);

(ii) it is difficult to fix the thermojunction at a required depth and move the thermocouple in the melt volume without rigid insulating ceramic tubes.

Another important fact is that the use of uncovered thermocouples is justified mainly in the case of a significant difference in the conductivities of the melt and the thermocouple material. At the same time, the use of thermocouples in protective thermowells also has some serious drawbacks since thermocouples are not in direct contact with the melt in this case, which inevitably results in a high inertia. The latter circumstance hinders measurements of relative variations in temperature from point to point and decreases the thermocouple sensitivity and the measurement accuracy.

A Modified Thermocouple and Scanning Device¹

The design of the modified thermocouple fabricated taking into account the above considerations and being, in fact, an analog of a conventional Pt/Pt–Rh thermocouple, is shown in Fig. 2.

The platinum thermowell *1*, which serves simultaneously as one of the thermoelectrodes and, with corresponding grounding, a high-frequency shield, is made in the form of a thin-wall cylindrical tube with conical narrowing at one of its ends. In accordance with the experimental conditions, the thermowell length is equal to or slightly exceeds the maximum depth of immersion into the melt. The thermowell is connected with the second wire Pt–Rh thermoelectrode *2* with the formation of the working junction in the conical part. With this purpose, the second thermoelectrode is inserted into the first one (the platinum thermowell) and, accordingly, isolated from it by a single-channel ceramic tube *3*. The continuation of the first thermoelectrode (thermowell) is a platinum wire from a conventional thermocouple, which is welded to the thermowell basis as a second free end of the thus modified thermocouple.

In order to move the modified thermocouple and measure temperature at any point in the melt volume, a special scanning device with a thermocouple holder was developed [1].

¹ Designed and fabricated by O.A. Arakelov at the Institute for Physical Research, Ashtarak, Armenia.

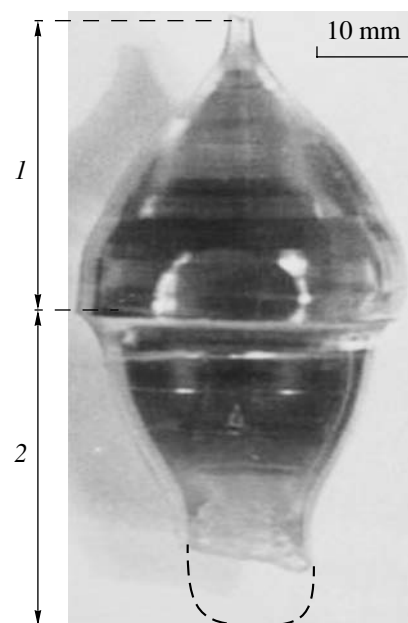


Fig. 1. PbMoO_4 crystal: (1) the part grown by pulling and (2) the tapered protrusion grown by thermal supercooling of the melt.

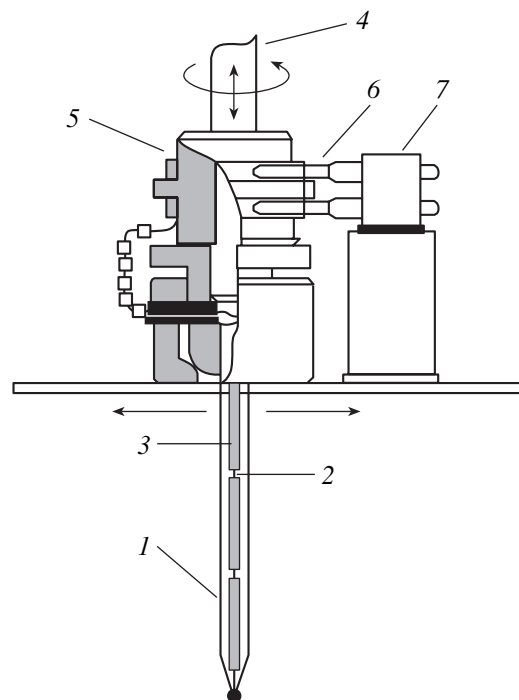


Fig. 2. Modified thermocouple: (1) platinum thermoelectrode (thermowell), (2) Pt–Rh thermoelectrode, (3) ceramic tube, (4) shaft of the pulling mechanism, (5) collector, (6) loop contacts, and (7) tightening mechanism.

The crucible with molten PbMoO_4 is installed on a ceramic support in the growth chamber. The mechanism of vertical motion is connected with the mobile part of the scanning device that is rigidly fixed on a

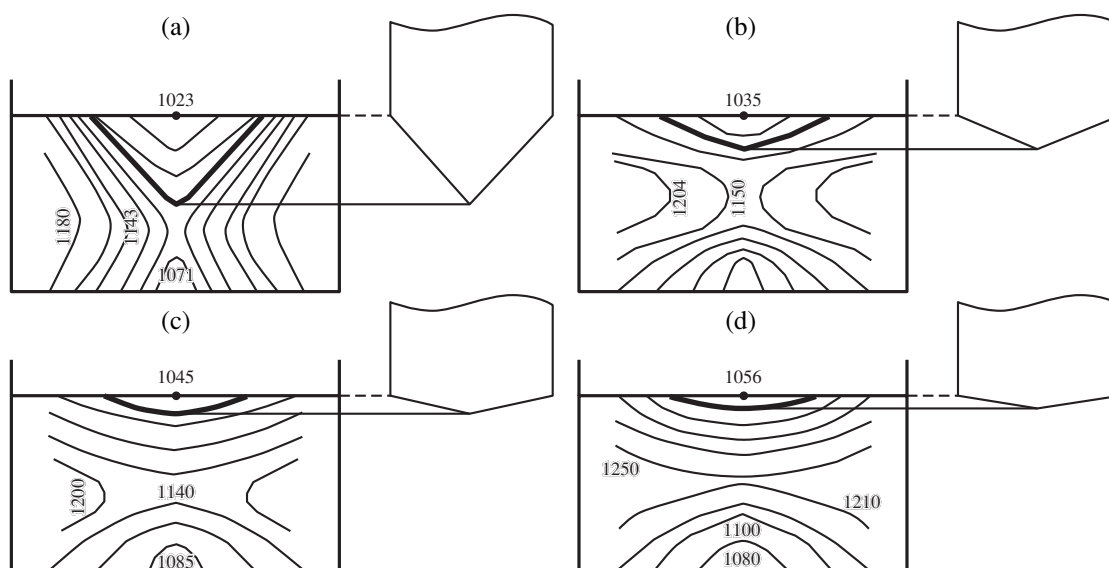


Fig. 3. Temperature distributions in the PbMoO_4 melt at different rotation speeds of the thermocouple (crystal): $\omega =$ (a) 0, (b) 3, (c) 25, and (d) 50 rpm. The dotted line shows the melt level. The thick solid line is the isotherm t_{melt} (1065°C). Numbers at the isotherms (thin solid lines) indicate temperature in $^\circ\text{C}$.

flange joint of the growth chamber. The shaft of the mechanism of vertical motion 4 is rigidly connected with the modified thermocouple immersed into the crucible with the melt. The shaft rotates, rotating the thermocouple around its axis; the scanning device shifts the thermocouple in the horizontal plane of the crucible; and the vertical mechanism shifts the thermocouple in the vertical direction. Thus, the modified thermocouple can move throughout the crucible volume, imitating by the rotation around its own axis (when the vertical motion is possible) the rotation of a growing single crystal with simultaneous measurement of temperature at any point of the melt. The ends of the modified thermocouple are connected to the collector 5 and brought out to the tightening mechanism 7 through the loop contacts 6. A bush and a guide are used to fix the bearing disc.

Measurements

The temperature distribution in the PbMoO_4 melt was studied using the modified thermocouple and the scanning device under the conditions similar to the standard crystal growth conditions.

The modified thermocouple is immersed into the crucible with melt through the pulling mechanism and the scanning device. First, the temperature on the melt surface at the center of the crucible was measured. Then, shifting the thermocouple towards the crucible wall, temperature was measured with a step of 5 mm. The thermocouple was stopped and kept at each point for ~ 20 min (the relaxation time). Near the crucible wall, the thermocouple was immersed into the melt by the pulling mechanism for 5 mm and, after measuring

the temperature, was shifted to the center. Thus, repeating the operations of shift and immersion, we obtained the values of temperature at different depths in the melt in the crucible only in one half of the melt volume. Taking into account the circular symmetry of the thermal field in the melt and using the data obtained, we plotted the entire temperature distribution in the melt for a crucible 70 (diameter) $\times 50$ (height) $\times 3$ (wall thickness) mm^3 in size at different rotation speeds of the thermocouple. Crystals 15 – 20 mm in diameter were grown under the same conditions. Note that all temperature measurements and growth processes were performed with the crystallization unit kept open (without upper thermal shields over the crucible).

RESULTS AND DISCUSSION

Figure 3 shows the distributions of the thermal fields in the PbMoO_4 melt and the positions of the growth isotherms at different rotation speeds of the thermocouple (and, respectively, the crystal). It can be clearly seen that in the absence of rotation and at low rotation speeds the surface of the PbMoO_4 melt shows a significant supercooling below the melting point (1060 – 1070°C) (Figs. 3a, 3b). The growth isotherms and the crystallization front of the crystal are at a rather large distance from the melt surface. With an increase in the rotation speed, the degree of the melt supercooling decreases as a result of the transition from the conditions of dominant free convection to the mixed convection mode. The growth isotherm and the crystallization front maximally approach the melt surface in this case (Figs. 3c, 3d).

Analysis of the data characterizing the behavior of the volatile PbMoO_4 melt (the temperature distribution and the position of the growth isotherm) shows that the melt evaporation caused by the high tension of the melt vapor and the vapor of the oxide components is accompanied by significant supercooling of the melt, which was described in the literature. It was reported in [2] that molybdates and tungstates of divalent metals are prone to supercooling. In this context, when the DTA method is used, it is recommended to set the position of the liquidus curve in the phase equilibrium diagram only under heating conditions. Under the growth conditions, the noted supercooling leads to the formation of a crystallization front strongly bulged into the melt. As a result, stresses arise in the grown crystals, often leading to their plastic deformation. Hence, the search for possibilities and methods of controlling the shape of the crystallization front during the crystal growth is important from both scientific and practical points of view.

CONCLUSIONS

The PbMoO_4 melt, whose thermal field is significantly inhomogeneous at different depths, has the following specific features.

(i) Under the experimental conditions similar to the growth conditions, the PbMoO_4 melt shows significant supercooling, which, depending on the rotation speed, ranges from 10 to 40°C.

(ii) The position of the melting point isotherm in the PbMoO_4 melt is actually determined by the degree of melt supercooling under different experimental conditions.

(iii) An increase in the rotation speed of the thermocouple (and, respectively, the crystal) facilitates the formation of a rising flow in the central zone of the crucible and the corresponding upward shift (closer to the melt surface) of the melting point isotherm of PbMoO_4 and decreases the degree of supercooling of the melt surface.

(iv) At low rotation speeds of the thermocouple and crystal (0–3 rpm), the motion in the melt is determined mainly by free convection; therefore, the rising flow under the crystal almost does not occur.

(v) The region occupied by the rising flow formed at high rotation speeds (25–50 rpm) is relatively small; it is located directly under the growing crystal.

The results of measurements suggest that the conditions of mass and heat exchange in the PbMoO_4 melt are determined mainly by the convection. Free (natural) convection for this compound is dominant even at sufficiently high rotation speeds. Obviously, it is a difficult problem to obtain a planar crystallization front even with the most thorough thermal isolation of the crystallization unit.

REFERENCES

1. V. T. Gabrielyan, Candidate's Dissertation in Physics and Mathematics (Inst. of Crystallography, USSR Academy of Sciences, Moscow, 1978).
2. T. M. Yanushkevich, Candidate's Dissertation in Chemistry (Ural State Univ., Sverdlovsk, 1973).

Translated by Yu. Sin'kov

CRYSTAL
GROWTH

Mathematical Modeling and Experimental Investigation of the Effect of Temperature Gradients on Crystallization Processes under Terrestrial and Space Conditions

V. I. Strelov*, B. G. Zakharov*, V. S. Sidorov*, I. Zh. Bezbakh*,
and V. I. Folomeev**

* *Space Materials Research Center, Institute of Crystallography,
Russian Academy of Sciences, Kaluga, 248640 Russia*
e-mail: zakharov@kaluga.rosmail.com

** *Institute of Physics and Power Engineering, pl. Bondarenko 1,
Obninsk, Kaluga oblast, 249039 Russia*

Received April 17, 2004

Abstract—Mathematical modeling of the processes of heat and mass transfer during directed crystallization under terrestrial and space conditions is performed on the basis of experimental data on the temperature distribution (boundary conditions). Convective processes are described by the system of Oberbeck–Boussinesq equations together with the heat-conduction equation (the Stefan problem). A dependence of the intensity of thermal gravitational convection on the radial and axial temperature gradients is established. It is shown that one of the necessary conditions for the growth of homogeneous semiconductor crystals under both terrestrial and zero-gravity (on board spacecraft) conditions is the absence of the free surface of a melt (the Marangoni convection) and optimization of the temperature gradients (first of all, the radial gradient). © 2005 Pleiades Publishing, Inc.

INTRODUCTION

Theoretical description of crystal growth based on mathematical modeling makes it possible to establish relationships between the properties of crystals and the conditions of their growth. In addition, the development of a model of a growth process based on a mathematical apparatus of differential equations makes it possible to independently optimize the process parameters of growth systems, which is very difficult to do experimentally [1, 2].

Processes of heat and mass transfer (HMT) occurring in a melt during its crystallization are one of the decisive factors for the homogeneity of properties of the crystal grown. Depending on the structure and intensity of these processes, the crystal growth is determined by diffusive, convective, or both of these HMT processes. The main decisive factor for the occurrence and intensity of thermal gravitational convection under terrestrial conditions is the radial temperature gradient ΔT_r in a melt. Under the conditions of microgravity, the decisive factor is the Marangoni convection [3]. Optimization of HMT processes with velocities of convective flows approaching the diffusive mode makes it possible to grow single crystals with highly uniform properties under both terrestrial and space conditions.

The convective processes occurring in melts during the growth of semiconductor crystals by the Bridgman method under terrestrial and space conditions were described by us using a system of Navier–Stokes equations in the Oberbeck–Boussinesq approximation [4].

The purpose of this study is to investigate the processes of formation of microinhomogeneities during the growth of Ge(Ga) crystals by directed crystallization under terrestrial and space conditions, depending on the intensities of thermal gravitational convection and Marangoni convection.

DETERMINATION OF THERMAL BOUNDARY CONDITIONS

Mathematical modeling of HMT processes under terrestrial and space conditions was carried out for the real growth of Ge(Ga) single crystals; i.e., we used the thermal boundary conditions determined by thermostating of the crystal–melt system. Figure 1 schematically shows a block diagram of the arrangement of temperature-sensitive elements (calibrated Chromel–Alumel microthermocouples) for the system under study. The thermocouple readings with a discreteness of an hour from the beginning to the end of the crystallization process are listed in the table. However, it should be noted that we fixed and used a continuous

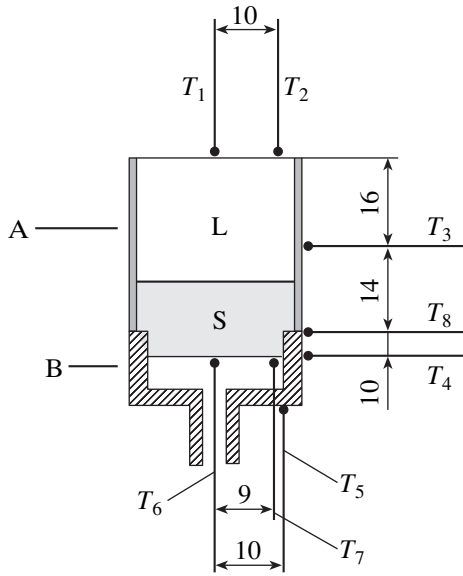


Fig. 1. Schematic block diagram of the arrangement of temperature-sensitive elements: (T_1 – T_7) microthermocouples, (S) seed, (L) melt, (A) graphite crucible, and (B) crystal holder.

spectrum of measured temperatures in calculations (to introduce the boundary conditions).

MATHEMATICAL AND COMPUTATIONAL MODELS

To describe the processes of thermal convection in a melt during the crystal growth, we used a system of Oberbeck–Boussinesq equations together with the heat-conduction equation (the Stefan problem) [5].

The heat-conduction equation (the Stefan problem) in the dimensionless form with respect to V_0 and L in the (R,Z) geometry can be written as

$$\frac{\partial \rho h}{\partial t} = -V_r \frac{\partial \rho h}{\partial r} - V_z \frac{\partial \rho h}{\partial z} + \frac{1}{\text{PrRe}} \left(\frac{\partial \lambda \partial T}{\partial r^2} + \frac{\partial \lambda \partial T}{\partial z^2} + \frac{\lambda \partial T}{r \partial r} \right), \tag{1}$$

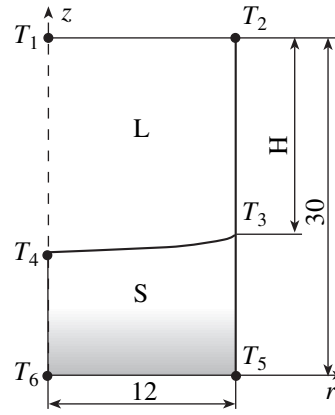


Fig. 2. Model region (dimensions are in mm).

where h is the enthalpy, $\rho = \rho(h)$ is the density, $T(h)$ is temperature, and $\lambda = \lambda(h)$ is the thermal conductivity coefficient.

At the moving phase boundary, the Stefan condition is satisfied:

$$h_0(V_f, n) = Q^+ - Q^-, \tag{2}$$

where h_0 is the specific heat of the phase transition, V_f is the velocity of a point at the phase boundary, n is the unit vector normal to the boundary, Q^+ is the normal heat flow from the phase with a lower specific enthalpy, and Q^- is the normal heat flow to the phase with a higher specific enthalpy.

To describe the liquid phase, we used the following equations (in the dimensionless form with respect to V_0 and L in the (R,Z) geometry): the momentum equations in the Boussinesq approximation

$$\frac{\partial V_r}{\partial t} = -V_r \frac{\partial V_r}{\partial r} - V_z \frac{\partial V_r}{\partial z} - \frac{\partial P}{\partial r} + \frac{1}{\text{Re}} \left(\frac{\partial^2 V_r}{\partial z^2} + \frac{\partial^2 V_r}{\partial r^2} + \frac{1}{r} \frac{\partial V_r}{\partial r} - \frac{V_r}{r^2} \right), \tag{3}$$

Readings of microthermocouples during the crystal growth

| Growth time, h | Temperature measured by control microthermocouples, °C | | | | | | | |
|----------------|--|-------|-------|-------|-------|-------|-------|-------|
| | T_1 | T_2 | T_3 | T_4 | T_5 | T_6 | T_7 | T_8 |
| 0 | 986 | 987 | 961 | 850 | 866 | 900 | 892 | 881 |
| 1 | 977 | 978 | 952 | 850 | 873 | 900 | 892 | 879 |
| 2 | 969 | 970 | 944 | 850 | 880 | 900 | 892 | 876 |
| 3 | 961 | 962 | 936 | 850 | 888 | 900 | 892 | 872 |
| 4 | 952 | 953 | 927 | 850 | 896 | 900 | 892 | 867 |
| 5 | 942 | 943 | 917 | 850 | 905 | 900 | 892 | 860 |
| 6 | 932 | 933 | 906 | 850 | 915 | 900 | 892 | 852 |

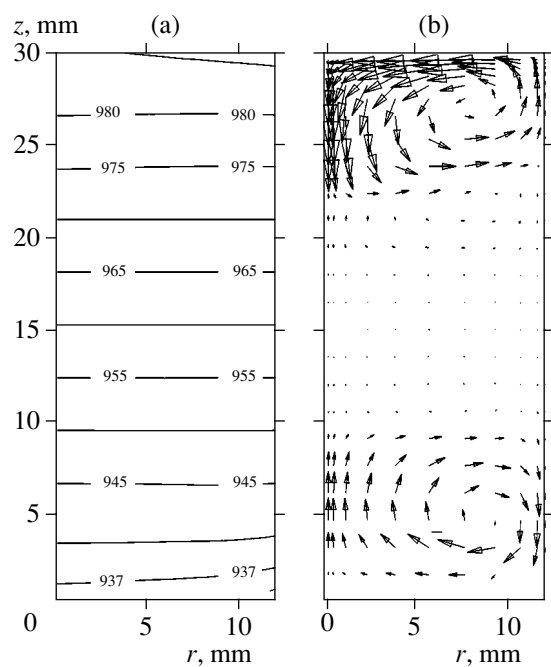


Fig. 3. (a) Temperature isolines and (b) the structure of convective flows in a melt 600 s after the onset of crystallization ($\Delta T_r = 2$ K/cm, $Mn = 0$).

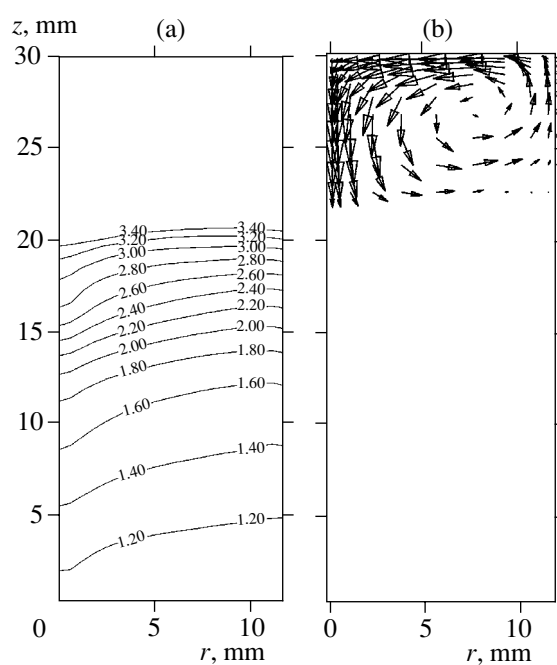


Fig. 4. (a) Dopant (Ga) concentration isolines in a crystal and (b) the structure of convective flows in a melt 15600 s after the onset of crystallization ($\Delta T_r = 2$ K/cm, $Mn = 0$).

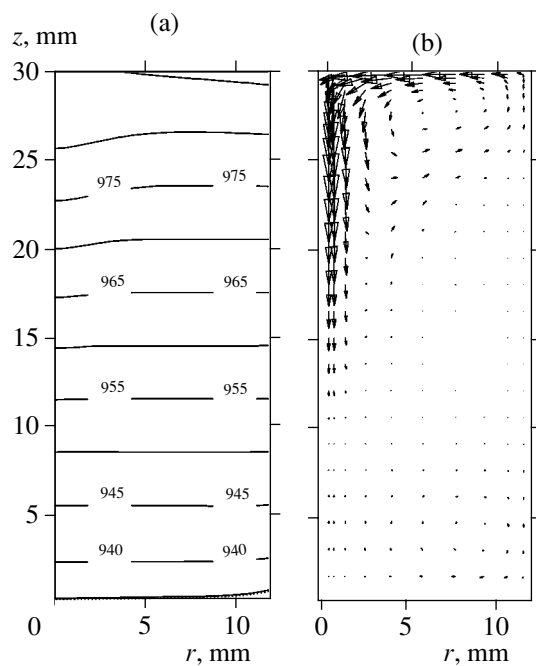


Fig. 5. (a) Temperature isolines and (b) the structure of convective flows in a melt 600 s after the onset of crystallization in the presence of Marangoni convection ($\Delta T_r = 2$ K/cm).

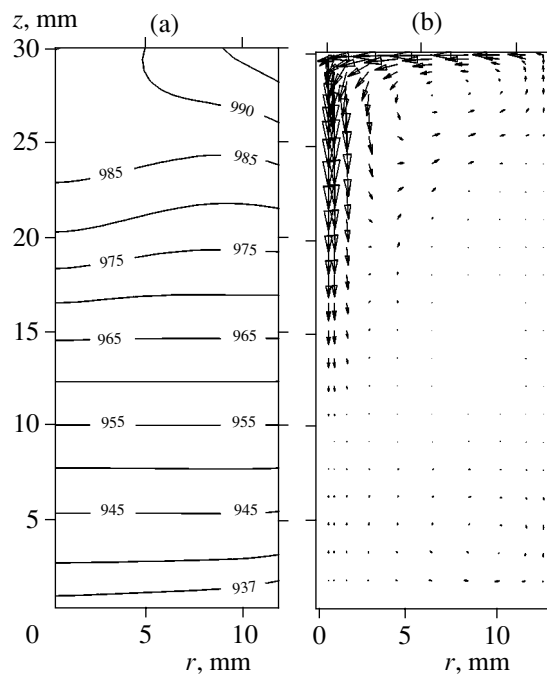


Fig. 6. (a) Temperature isolines and (b) the structure of convective flows in a melt 600 s after the onset of crystallization ($\Delta T_r = 5$ K/cm, $Mn = 0$).

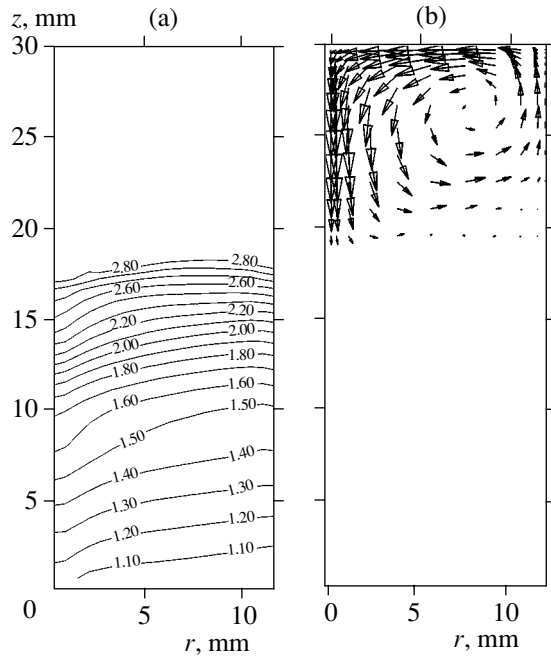


Fig. 7. (a) Dopant (Ga) concentration isolines in a crystal and (b) the structure of convective flows in a melt 14200 s after the onset of crystallization ($\Delta T_r = 5$ K/cm, $Mn = 0$).

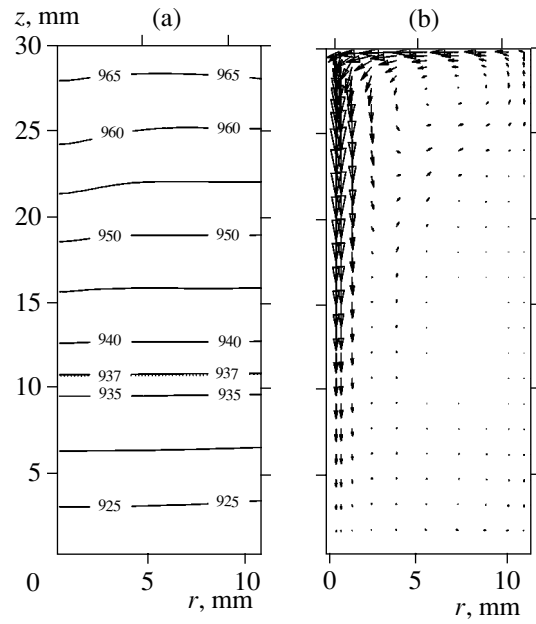


Fig. 8. (a) Temperature isolines and (b) the structure of convective flows in a melt 600 s after the onset of crystallization in the presence of Marangoni convection ($\Delta T_r = 5$ K/cm).

$$\frac{\partial V_z}{\partial t} = -V_r \frac{\partial V_z}{\partial r} - V_z \frac{\partial V_z}{\partial z} - \frac{\partial P}{\partial z} + \frac{1}{\text{Re}} \left(\frac{\partial^2 V_z}{\partial z^2} + \frac{\partial^2 V_z}{\partial r^2} + \frac{1}{r} \frac{\partial V_z}{\partial r} \right) + \frac{\text{Gr}_T}{\text{Re}^2} T + \frac{\text{Gr}_C}{\text{Re}^2} C; \quad (4)$$

the continuity equation

$$\frac{\partial V_r}{\partial r} + \frac{\partial V_z}{\partial z} + \frac{V_r}{r} = 0; \quad (5)$$

and the dopant transport equation

$$\frac{\partial C}{\partial t} = -V_r \frac{\partial C}{\partial r} - V_z \frac{\partial C}{\partial z} + \frac{1}{\text{ReSc}} \left(\frac{\partial^2 C}{\partial r^2} + \frac{\partial^2 C}{\partial z^2} + \frac{1}{r} \frac{\partial C}{\partial r} \right), \quad (6)$$

where V_r is the radial velocity component, V_z is the axial velocity component, C is the dopant concentration, V_0 is the characteristic velocity, L is the characteristic size, ν is the kinematic viscosity, D is the dopant diffusion coefficient, $\text{Re} = \frac{V_0 L}{\nu}$ is the Reynolds number, $\text{Sc} = \frac{\nu}{D}$ is the Schmidt number, $\text{Pr} = \frac{\nu}{a}$ is the Prandtl number, $\text{Gr}_T = g \beta_{\rho_r} L^3 \Delta T / \nu^2$ is the Grashof temperature number, and $\text{Gr}_C = g \beta_{\rho_C} L^3 C_0 / \nu^2$ is the Grashof concentrational number.

The boundary conditions are as follows. At $r = 0$,

$$\frac{\partial T}{\partial r} = \frac{\partial C}{\partial r} = \frac{\partial V_r}{\partial r} = \frac{\partial V_z}{\partial r} = 0; \quad (7)$$

at $r = R_0$,

$$\frac{\partial C}{\partial r} = 0, \quad V_r = 0, \quad V_z = 0, \quad T = f_z(z, t); \quad (8)$$

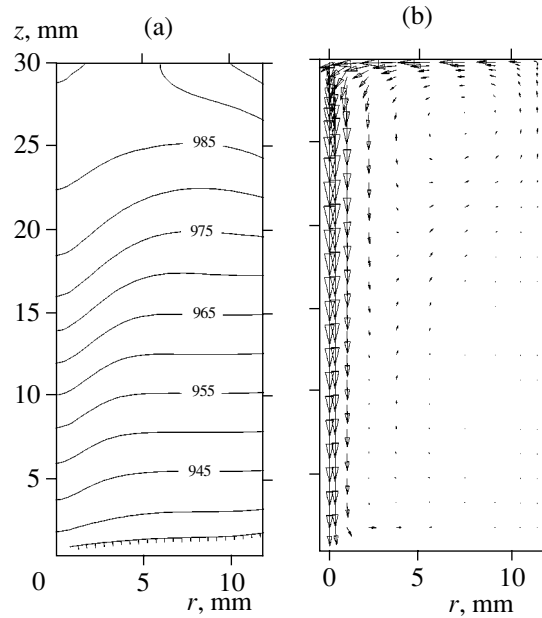


Fig. 9. (a) Temperature isolines and (b) the structure of convective flows in a melt 1172 s after the onset of crystallization in the presence of Marangoni convection ($\Delta T_r = 15$ K/cm).

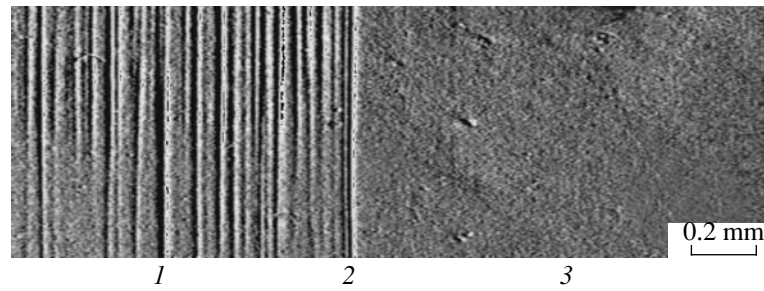


Fig. 10. Micrograph of the surface of a crystal cut parallel to the growth axis $\langle 111 \rangle$ after selective chemical etching ($\Delta T_r = 2$ K/cm, the melt surface is covered): (1) seed, (2) phase boundary, and (3) part of the grown crystal.

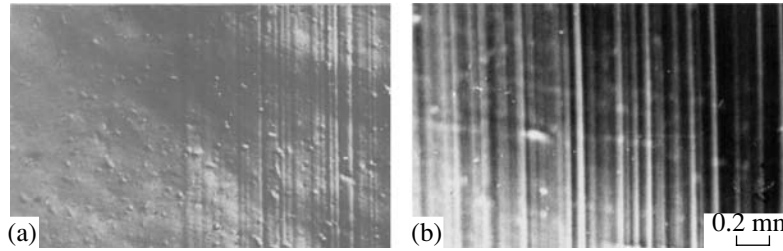


Fig. 11. Micrograph of the surface of a crystal cut parallel to the growth axis $\langle 111 \rangle$ after selective chemical etching ($\Delta T_r = 5$ K/cm): growth with (a) a covered and (b) a free melt surface.

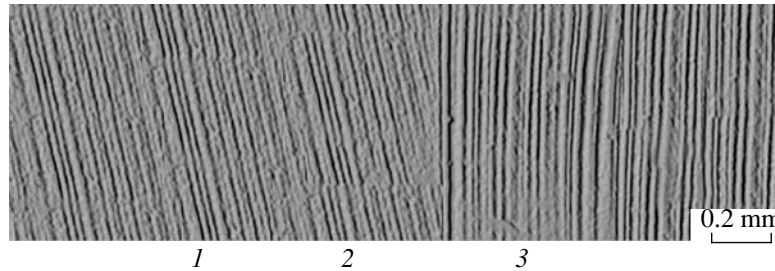


Fig. 12. Micrograph of the surface of a crystal cut parallel to the growth axis $\langle 111 \rangle$ after selective chemical etching ($\Delta T_r = 15$ K/cm): (1) seed, (2) phase boundary, and (3) part of the grown crystal.

at $z = 0$,

$$T = f_{r1}(r, t); \quad (9)$$

at $z = H$ (at the crystallization front),

$$\begin{aligned} V_z = V_{fz}, \quad V_r = 0, \quad T = T_m, \\ -\frac{1}{Sc} \frac{\partial C}{\partial z} = (k_0 - 1) Re_b C; \end{aligned} \quad (10)$$

and, at $z = Z_0$,

$$\begin{aligned} V_z = 0, \quad T = f_{r2}(r, t), \quad \frac{\partial C}{\partial z} = 0, \\ \frac{\partial V_r}{\partial z} = \frac{Mn_T}{PrRe} \frac{\partial T}{\partial r}, \end{aligned} \quad (11)$$

where V_{fz} is the velocity of the crystallization front,

$Re_b = \frac{V_{fz} L}{\nu}$ is the Reynolds number with respect to the

crystal growth rate, and $Mn_T = \frac{\sigma \beta_{\sigma} \Delta T L}{\rho \nu a}$ is the

Marangoni temperature number. For a more detailed description of the mathematical model, see [5].

The model region for the real process of directed crystallization is shown in Fig. 2. The crystallization region has a cylindrical shape with a rotation axis (T_1, T_0) and consists of two phases: solid (S) and liquid (L) (crystal and melt, respectively). The velocity of the crystallization front is $V_f = 5$ mm/h. The initial concentration of gallium dopant in germanium in the solid phase is $C = 10^{19}$ cm $^{-3}$. A temperature difference of 3 K is specified at the crystallization front.

The temperature at the point T_1 is determined experimentally. At the initial instant of time, it is 986°C. Dur-

ing the growth, T_1 changes by the law $T_1 = T_0 - V_T t$ (T_0 is the temperature in the initial stage of the crystal growth; t is the current time; and V_T is the rate of temperature change, which is set by a certain algorithm according to the results of measurements). At the points T_2 , T_5 , and T_6 , temperature is determined experimentally. T_4 is a point at the crystallization front, which moves from T_6 to T_1 at a specified velocity during the growth. The temperature at the point T_3 is determined by the curvature of the crystallization front, specified by carrying out calculations or found experimentally.

Calculations were carried out on a grid (22×50) with a logarithmic decrease in the grid step to the boundaries of the model region. The minimum and maximum radius steps were 0.0885 and 1 mm, respectively. The minimum and maximum height steps were 0.077 and 0.74 mm, respectively. The maximum time step was 0.5 s. The minimum time step was chosen automatically according to the convergence criteria for the iterative processes; it was no smaller than 0.005 s.

RESULTS AND DISCUSSION

On the basis of the experimental data on the temperature distributions determined above (the boundary conditions) during the growth of Ge(Ga) single crystals, we first performed mathematical modeling of the HMT processes in the Bridgman method for different radial temperature gradients at a fixed axial gradient (the axial temperature gradient in a melt was assumed to be ~ 16 K/cm in the calculations, which corresponded to the real experiment) for terrestrial and space conditions.

Figures 3–9 show the results of calculations for the terrestrial conditions (g_0): the temperature and dopant concentration distributions in the crystal and the structure of convective flows in a melt during the crystallization for real (experimental) values of $\Delta T_r = 2, 5,$ and 15 K/cm with a covered melt surface (the absence of Marangoni convection) and with a free melt surface (the presence of Marangoni convection).

The calculations performed show that in the experiments with $\Delta T_r = 2$ K/cm and $\Delta T_z = 16$ K/cm at the melt surface in the absence of Marangoni convection the conditions of reduced thermal gravitational convection are implemented during the growth. The velocity of convective flows is ~ 0.15 cm/s at the melt surface and ~ 0.00072 cm/s near the phase boundary (for a planar isotherm at the crystallization front). In the presence of Marangoni convection, the velocity of motion at the melt surface increases to ~ 0.65 cm/s but still does not significantly affect the velocity of convective flows at the crystallization front (~ 0.006 cm/s). This was also confirmed experimentally. Analysis of the microhomogeneity (by selective chemical etching) of single crystals grown under these conditions showed uniform (without striations) dopant distribution over the entire length and diameter of the samples (Fig. 10).

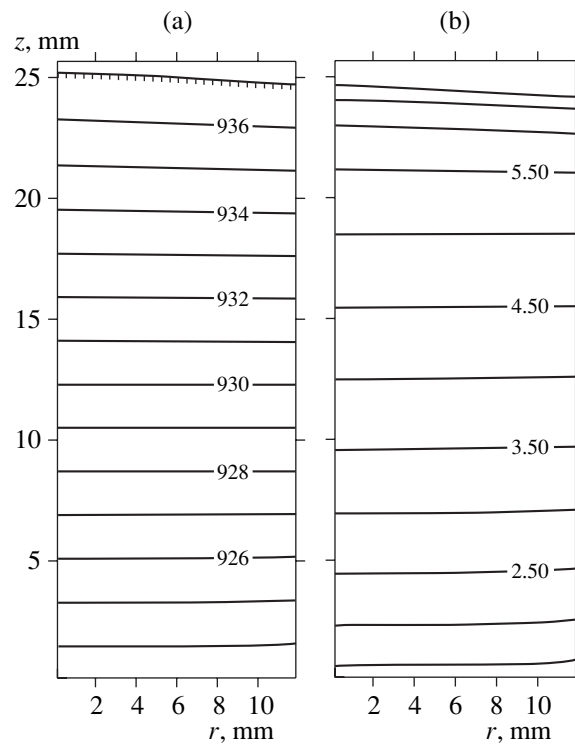


Fig. 13. Isolines of (a) the temperature in the melt and (b) the dopant concentration in the crystal grown at $g = 10^{-5} g_0$ ($Mn = 0$).

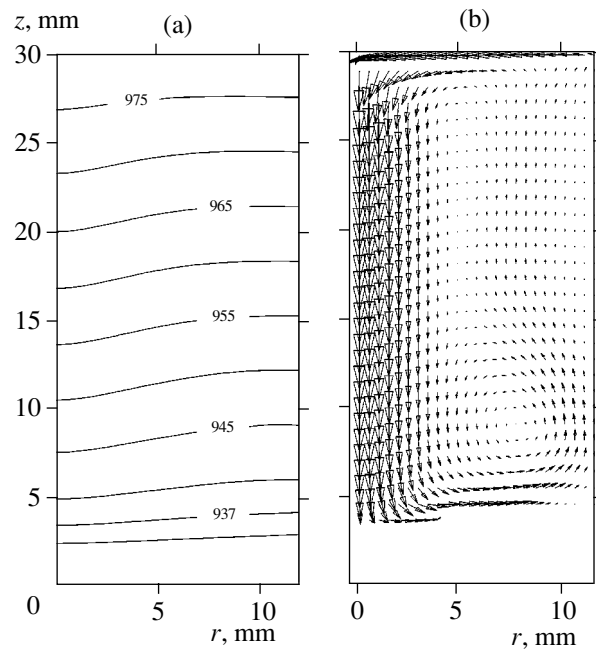


Fig. 14. (a) Temperature isolines and (b) the structure of convective flows in a melt 3000 s after the onset of crystallization in the presence of Marangoni convection ($g = 10^{-5} g_0$).

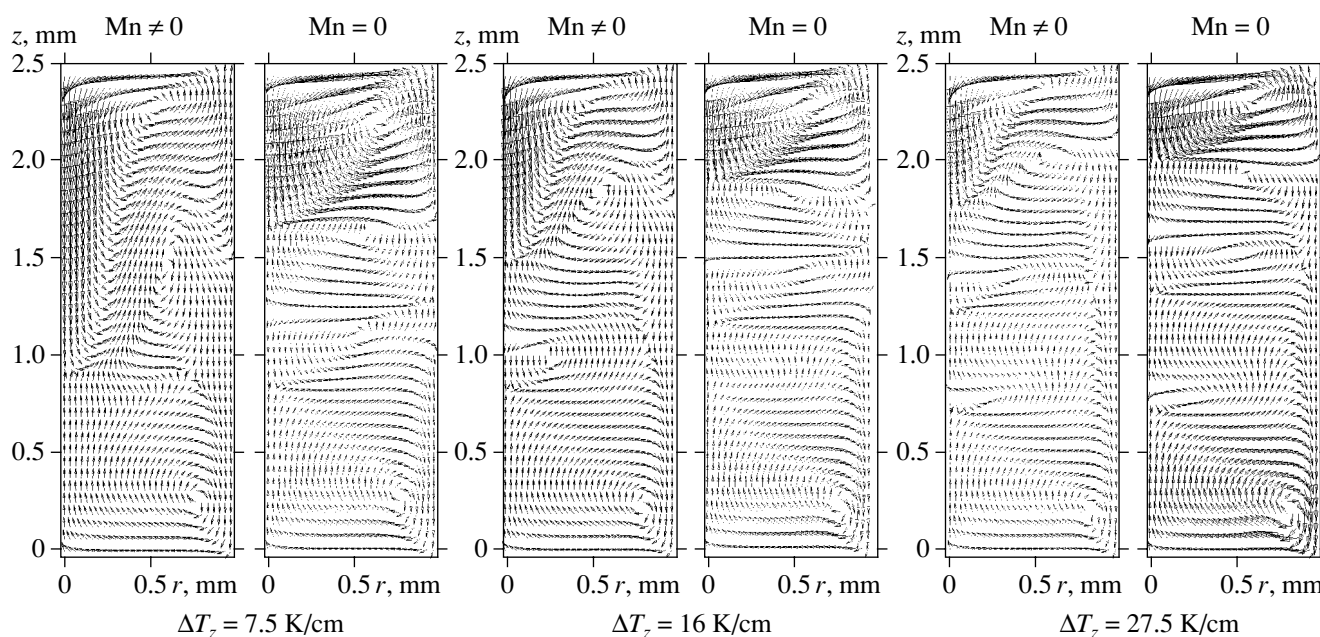


Fig. 15. Effect of the axial temperature gradient on the structure of convective flows in a melt (for all variants, $\Delta T_r = 2$ K/cm, $g = g_0$).

The increase in the radial temperature gradient to 5 K/cm leads to a significant increase in the intensity of thermal gravitational convection. In the absence of Marangoni convection (Fig. 6), the velocity of convective flows at the melt surface reaches ~ 1.02 cm/s (~ 0.025 cm/s at the crystallization front) and begins to affect the temperature distribution near the phase boundary. In the presence of Marangoni convection (Fig. 8), the flow velocity at the melt surface reaches ~ 1.76 cm/s and significantly affects the processes occurring near the crystallization front. This is confirmed by the experiments with the crystals grown with a covered melt surface (Fig. 11a): striations were found in some samples and, in the case of a free melt surface (Fig. 11b), striations were always present in all samples.

Further increase in the radial temperature gradient to 15 K/cm (which is characteristic of conventional methods of crystal growth with lateral heat supply) leads to a significant increase in the intensity of thermal gravitational convection and the formation of a multi-vortex structure of flows. In this case, even in the absence of Marangoni convection (Fig. 9), the velocity of convective flows at the melt surface becomes as high as ~ 2.85 cm/s (~ 0.34 cm/s at the crystallization front) and, in the presence of Marangoni convection, the velocity of flows is ~ 3.76 cm/s. Investigations of the microhomogeneity of the dopant distribution in the crystals grown under these thermal conditions showed the presence of striations throughout the entire length of the crystals (Fig. 12). Obviously, during the growth, with a decrease in the melt level near the crystallization front, constant rearrangement of the structure of flows occurs, which leads to variations in temperature at the

phase boundary. This, in turn, leads to uncontrolled variations in the crystallization rate and gives rise to striations. Calculations showed that the intensity of thermal gravitational convection depends strongly on the radial temperature gradient at the melt surface during the crystallization. In this case, even under terrestrial conditions with intense thermal gravitational convection, Marangoni convection makes a significant contribution to the HMT processes.

Thus, the calculations performed by us showed that under the conditions of zero-gravity, with a significant reduction of thermal gravitational convection, the structure and intensity of convective flows is determined only by Marangoni convection.

Figures 13 and 14 show the results of calculations for microgravity conditions ($g = 10^{-5}g_0$). With the radial and axial temperature gradients $\Delta T_r = 2$ K/cm and $\Delta T_z = 16$ K/cm, respectively, at a covered melt surface, diffusive mass transfer is observed (Fig. 13). The diffusive mode provides uniform dopant distribution over the crystal diameter. Quite another picture is observed in the presence of Marangoni convection (free melt surface). In this case, even at small radial temperature gradients ($\Delta T_r = 2$ K/cm), the structure and intensity of convective flows significantly change (Fig. 14). The velocity of flows reaches ~ 1.53 cm/s at the melt surface and ~ 0.5 cm/s near the crystallization front and becomes comparable with the conventional level of thermal gravitational convection under terrestrial conditions, leading to the violation of the stationary structure of convective flows and, accordingly, to a nonuniform dopant distribution. The calculations also showed that under the conditions of microgravity the structure

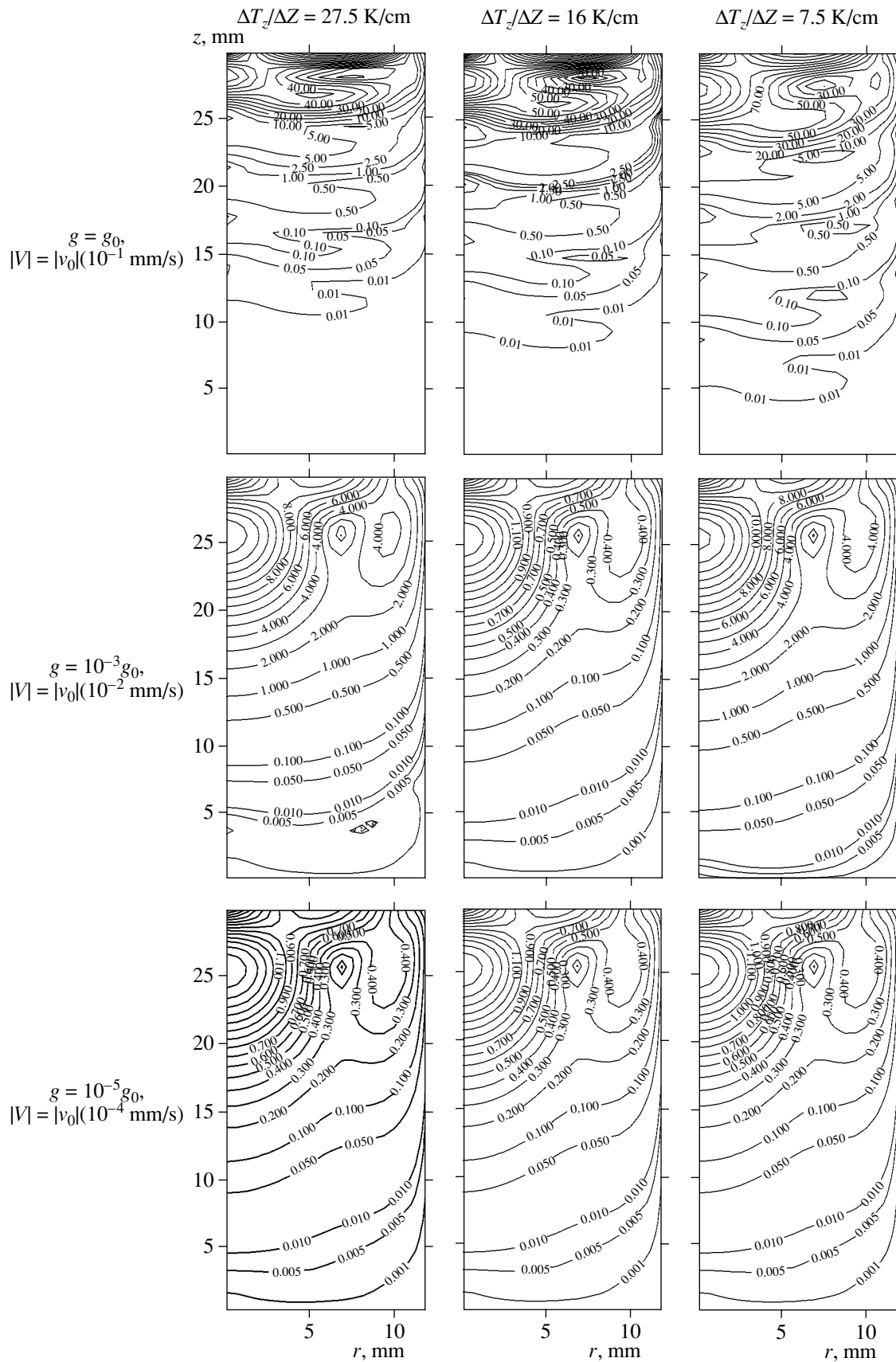


Fig. 16. Isolines of the absolute velocity of convective flows at different values of gravity and ratios $\Delta T_z/\Delta Z$ ($\Delta T_r = 2 \text{ K/cm}$, $Mn = 0$).

and velocity of convective flows in a melt is also affected (although to a lesser extent than in the case of Marangoni convection) by the radial temperature gradient at the melt surface. At $\Delta T_r = 2$ K/cm, the velocity of convective flows at the melt surface and near the phase boundary is $\sim 3 \times 10^{-5}$ and $\sim 5 \times 10^{-9}$ cm/s, respectively. At $\Delta T_r = 15$ K/cm, these values are $\sim 1.6 \times 10^{-4}$ and 1.4×10^{-8} cm/s, respectively.

The results obtained allow to conclude that one of necessary conditions for the growth of homogeneous semiconductor crystals under zero-gravity conditions (on board spacecraft) is the absence of the free melt surface (Marangoni convection).

The calculations performed showed that, along with the radial temperature gradient, the axial temperature gradient in the melt also affects the intensity of thermal gravitational convection. It was established by calculations that a decrease in the axial temperature gradient leads to a decrease in the radial temperature gradient and the radial component of the melt flow velocity near the crystallization front. However, the penetration depth of the thermal gravitational convection and the Marangoni convection into the melt increases in this case; i.e., the flow from the melt surface comes nearer to the crystallization front. With an increase in ΔT_z , an inverse dependence is observed. Figure 15 shows the results of calculations for the terrestrial conditions (g_0) on the effect of the axial temperature gradient in the melt at $\Delta T_z = 7.5, 16$ K/cm (this value is used in crystal growth), and 27.5 K/cm (at the radial temperature gradient $\Delta T_r = 2$ K/cm) on the structure of convective flows (Marangoni convection was taken into account). It can be seen that, for example, a decrease in ΔT_z from 27.5 to 7.5 K/cm leads to an increase in the penetration depth of the Marangoni convection from 5 to 16 mm (Fig. 15). It should be noted that such a significant effect occurs even at small radial temperature gradients ($\Delta T_r = 2$ K/cm), i.e., at low convection intensities. However, the calculations demonstrated that this dependence decreases with a decrease in gravity. Figure 16 shows the results of calculations of the effect of the axial temperature gradient (disregarding Marangoni convection) on the structure and intensity of convective flows at $g = g_0, 10^{-3}g_0$, and $10^{-5}g_0$.

CONCLUSIONS

The calculations carried out in this study made it possible to determine the velocity of convective flows in the melt volume and near the phase boundary for the growth of Ge(Ga) single crystals by directed crystallization as functions of the radial temperature gradient at the melt surface and the axial temperature gradient under terrestrial and space conditions.

It is shown theoretically and confirmed experimentally that Marangoni convection significantly affects the HMT processes under both terrestrial and space conditions. It is shown that under zero-gravity conditions Marangoni convection is the main factor violating the diffusive HMT mode, which leads to unregulated and uncontrolled processes in the melt during the crystal growth.

ACKNOWLEDGMENTS

This study was supported by the Federal Target Program "Integration" (contract no. I0876/909).

REFERENCES

1. V. I. Polezhaev, A. V. Buné, N. A. Verezub, G. S. Glushko, V. L. Gryaznov, K. G. Dubovik, S. A. Nikitin, A. I. Prostomolotov, A. I. Fedoseev, and G. G. Cherkasov, *Mathematical Modeling of Convective Heat and Mass Transfer on the Basis of Navier–Stokes Equations* (Nauka, Moscow, 1987) [in Russian].
2. G. Müller, *Convection and Inhomogeneities in Crystal Growth from the Melt* (Springer, Berlin, 1988; Mir, Moscow, 1991).
3. B. G. Zakharov, P. K. Volkov, V. I. Strelov, *et al.*, *Poverkhnost*, No. 9, 49 (2001).
4. P. K. Volkov, B. G. Zakharov, and Yu. A. Osip'yan, *Dokl. Akad. Nauk* **367** (1), 35 (1999) [*Dokl. Phys.* **44**, 404 (1999)].
5. V. I. Strelov, B. G. Zakharov, V. S. Sidorov, and V. I. Folomeev, *Poverkhnost*, No. 6, 75 (2003).

Translated by Yu. Sin'kov

CRYSTAL
GROWTH

Dendritic Growth of Snow Crystals

L. G. Gorbich and L. M. Martyshev

*Institute of Industrial Ecology, Ural Division, Russian Academy of Sciences,
ul. S. Kovalevskoi 20A, Yekaterinburg, GSP-594, 620219 Russia*

e-mail: mlm@ecko.uran.ru

Received April 21, 2004

Abstract—The hypothesis that allows the interpretation of dendritic growth of a snow crystal in terms of diffusion-limited aggregation is criticized. The results of simulation of growth of quasi-two-dimensional crystals in two- and three-dimensional media based on the classical two-parametric model of diffusion-limited aggregation are used as an argument in this criticism. It is established that the model dimensionality considerably influences morphology of the grown crystal. The mechanism of dendritic growth of a snow crystal in which the main part is played by the surface processes at the ice/water interface is suggested. © 2005 Pleiades Publishing, Inc.

INTRODUCTION

Dendritic growth of snow (ice) crystals whose aggregation results in the formation of snow flakes have long been studied because of their importance for both physics of the atmosphere (thermal–physical, optical, etc. properties) and ecology (shape of snow flakes strongly influences scavenger of atmospheric impurities) [1–9]. However, despite a large number of experimental and theoretical studies, this problem is still unclear. In particular, it is still unknown why snow crystals possess the dendritic (skeletal) structure. The most widespread standpoint is that dendritic form is associated with diffusion limitations taking place during crystal growth [2–4, 9]. The main arguments supporting this hypothesis are as follows.

It is usually accepted that ice crystals grow in an atmosphere of saturated (with respect to water) vapor: a supercooled cloud of droplets [2–4]. Since the pressures of saturated vapors of ice and water are different, the crystals exist under a considerable supersaturation (the maximum absolute supersaturation above ice at the saturation above water is observed at -12°C) [3]. The estimates [3–7, 10] show that growth of crystals up to a size of 50–300 μm proceeds mainly by the diffusion mechanism (in an immobile medium where one may ignore coagulation of cloud particles). The estimation according to the dimensionless criterion bR/D (where b is the kinetic crystallization coefficient, R is the characteristic dimension of the crystal, and D is the diffusion coefficient of water molecules in air) [11] and data [12, 13] yield a value of the order of 10^3 . Thus, the growth mode of a snow crystal is limited by diffusion. The loss of the morphological stability in this growth mode and dendritic growth have been studied rather well [14]. Qualitatively, these phenomena are explained by the fact that a ledge formed on the crystal surface is under

favorable growth conditions (is located in the region highly supersaturated with water vapor) and, therefore, develops at a higher rate than its environment. An additional argument in favor of this mechanism is that dendritic growth is observed at temperatures close to -12°C , i.e., under the maximum possible supersaturation in the cloud with respect to ice.

The experiments performed under laboratory conditions show that ice crystals are morphologically stable if they grow in a vacuum-processed vessel and become skeletal or dendritic when air is let into the chamber. In this case, the critical stability size is inversely proportional to the air pressure, i.e., is proportional to the diffusion coefficient [15].

The results of the numerical calculation [16] and computer simulation [17, 18] also showed that snow crystals may have dendritic form during diffusion growth. The numerical calculation of the stationary diffusion equation in an immobile medium was performed using the empirically established parameters of the ice/water/air system. The computer simulation was performed on the basis of a relatively simple model of diffusion-limited aggregation (DLA model).

However, the arguments in favor of the diffusion mechanism of dendritic growth are far from being ideal. Consider these arguments critically. The size of the observed snow dendrites most often exceeds 100 μm and attains lengths of 1 mm or more [1, 2]. In other words, the prevailing growth mechanism is the gravitational, turbulent, etc., coagulation [2–7] with 10- μm and even larger water microparticles [5]. Dendritic crystals may also be observed during precipitation from convective clouds [1], where a crystal does not have enough time to grow by the diffusion mechanism to the above size within the time of the cloud existence [2–4]. It is indicated [2] that the most branched crystals can grow only in a highly supersatu-

rated water cloud in the presence of numerous drops. It should also be noted that dendrite growth is most often observed for the prismatic faces of a snow crystal, whereas the basal faces are practically always relatively smooth, even in those cases where mainly these faces develop (in the temperature ranges from -4 to -10°C and from -20 to -35°C). This indicates the importance of the role of surface processes in dendrite formation in comparison with the role of bulk processes.

The results of the growth experiments in air and in vacuum show, first of all, that air (the whole mixture, its individual gaseous components, or present microscopic impurities) considerably influences the crystal stability. Obviously, the higher the air pressure, the more pronounced this influence and the sooner the crystal is transformed into the dendritic form. The possible mechanism of this influence will be considered later.

The known numerical and model computations of growth of snow crystals in the atmosphere has only one essential shortcoming: they are two-dimensional. We consider growth of snow crystals with the invocation of the diffusion-limited aggregation model [17, 18]. As has been already indicated, the formation of the dendritic form is explained only by the specificity of diffusion of water vapor from the ambient air to the crystal surface. In the traditional DLA approach, diffusion is modeled by multiple launches of randomly moving particles from the system periphery. A particle that during its random walk reached the crystal surface, is attached to this crystal. Naturally, the crystal part close to the starting position of particles is under the conditions more favorable for growth because of a strongly inhomogeneous concentration field. However, this mechanism may play the leading role only during crystal growth in a two-dimensional medium. The use of a three-dimensional model of water-vapor diffusion to an almost plane snow flake (the ratio of its diameter to its thickness equals 100 or even more) makes the diffusion limitations less severe.

The aim of the present study is the demonstration of this effect.

DESCRIPTION OF MODELS

To simulate growth of a quasi-two-dimensional crystal corresponding to natural growth in the temperature range from -10 to -20°C , we used the models of three types:

(1) the classical two-dimensional (2D) DLA model. Particles start their motion at a random point on the circumference described around the net (with the lattice parameter $a = 1$) and move along a random broken line with the length of each rectilinear segment being L . In order to diminish the stochastic action of individual particles, a certain averaging critical threshold H is selected (the number of particles that have to come into the given boundary cell of the crystal). The attainment of this threshold indicates the cell of an ambient

medium is "transformed" into the cell of the crystal. At the initial moment of simulation, a crystal is represented by the unit cell located in the net center (coinciding with the center of the initial circumference). In simulation, we used a flat hexagonal net.

(2) a three-dimensional (3D) DLA model with adsorption at the basal face. Unlike the model of the first type, here particles that started at a random site of surface randomly move inside a three-dimensional sphere. The crystal thickness is assumed to be equal to a . It is also assumed that the basal face of the crystal adsorbs all the particles reaching this surface, but no growth along this direction is possible (since the growth rate of the prismatic face is several times higher than the growth rate of the basal face [5, 13], this approximation is quite justified). If a particle enters the boundary cells of the prismatic (side) faces, growth proceeds in the same way as in the first model.

(3) a three-dimensional DLA model with the particle reflection from the basal face. Unlike the second model, the particles in this model are elastically scattered from the basal plane and not adsorbed.

RESULTS AND DISCUSSION

The computation based on the first model showed that the snow-flake-like structures correspond to relatively high values of the parameter H (exceeding 10). At low values of this parameter, more stochastic fractal-like structures are formed. The parameter L is responsible for porosity (looseness) of the structure. With an increase in the parameter L , the structure becomes denser. More detailed results of the simulation based on the first model are reported in [19].

Figure 1 illustrates the results of simulation based on three types of models. It is seen that the transition to the 3D models with preservation of the remaining parameters results in formation of more compact clusters. This may be explained by the fact that the particles that diffuse from the 3D environment to a quasi-two-dimensional object can always reach the central regions of the crystal and, thus, the growth defects formed earlier can always be healed, whereas in particle diffusion in the 2D space, this is principally impossible. An additional factor that influences the profile of the diffusion field and, as a consequence, also the morphology of the cluster formed is the considerable difference of the fraction of particles participating in growth from the total number of diffusing particles in the 3D and 2D cases. Diffusion-imposed limitations are even less important if the particles are not adsorbed but scattered by the basal face (model of the third type) and, thus, increase the effective concentration at the surface. As a result, the structures of the third type are even more compact than the aggregates obtained on the basis of the second model. Figure 2 shows the profile of the concentration field obtained in the 2D and 3D simulation. It is seen that, in the second case, the vapor concentra-










| | Model 1 | Model 2 | Model 3 |
|-----------|---|---|---|
| $L = 1$ |  |  |  |
| $L = 10$ |  |  |  |
| $L = 100$ |  |  |  |

Fig. 1. Results of the simulation based on three models at different values of the parameter L . The 301×347 net. Each cluster consists of 5000 cells. $H = 50$.

tion has practically the same value far from the crystal and close to it, which indicates the absence of the diffusion-imposed limitations during growth.

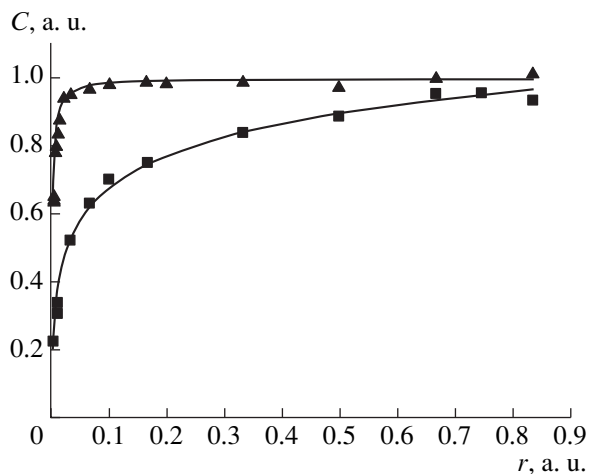


Fig. 2. Concentration field C as a function of the distance from the crystal center, r . At the initial circumference, $C = 1$ and $r = 1$ (concentrations are given with respect to the concentration at the initial circumference; the distances are given with respect to the circumference radius): ■ is the computation based on the 2D DLA model, ▲ is the computation based on the 3D DLA model.

Thus, it is shown that the use of the three-dimensional DLA models yields results which differ from the results for dendrite-like structures formed in the computations based on the two-dimensional DLA model [17–19] and from the results of analysis of the real shape of snow crystals [1, 2]. On the one hand, the latter fact makes the use of the DLA model for studying formation of snow flakes in atmosphere rather dubious and, on the other hand, is one more argument against the diffusion-limited mechanism of formation of snow dendrites. To solve the problem, it is necessary to create new three-dimensional DLA models (e.g., with growth in the basal plane) and also some alternative models, including those based on other growth mechanisms.

CONCLUSIONS

If one abandons the existing hypothesis, what mechanism is responsible for the dendritic growth of a snow crystal? This growth may be the consequence of the interaction between the surface of a growing crystal and various impurities in the mother medium, inclusions, etc., which are pushed away, are accumulated, and hinder growth of some sites of the surface. All this results in the preferable development of crystal angles and dendrite-like growth (for details see [20, 21]). The growth mechanism may be represented in the following way. Because of diffusion, small ice crystals attain a

size of the order of 100 μm . Then, the most important mechanism of their growth becomes coagulation with water drops in the cloud. If one assumes that the colliding water particles immediately solidify, this may result only in the formation of irregular crystalline aggregates (hail, snow pellets, or grained crystals). Therefore, it is possible to assume that drops spread over the surface and cover it with a thin layer (solidification time τ_{sol} considerably exceeds the time of drop spreading, τ_{spr}). The film thus formed has a small thickness, differing by several times in the center of the crystal and at its vertex. Thus, crystal growth proceeds not via vapor sublimation but via solidification of supercooled water (a hypothesis of a film-growth mechanism is also suggested in [5]). It should be noted that a liquid film on the ice surface in a cloud may also be formed for some other reasons, i.e., by too low an impurity content (e.g., the content of 10 ppm is sufficient for formation of a 0.009-mm-thick film [22] on an ice particle of 1 mm radius at a temperature of -10°C) or by the action of sunlight [22]. Thus, the growth mechanism described above may explain the appearance of dendrites also at crystal size less than 100 μm when coagulation is unimportant.

A growing crystal creates microinhomogeneities at the ice/water interface, which give rise to the formation of a dendrite. Obviously, in this case, the relaxation time of inhomogeneities τ_{rel} should exceed τ_{sol} . The times τ_{sol} , τ_{spr} , and τ_{rel} are determined by the thickness of a water film and the thermophysical characteristics of the ambient medium; the relaxation time τ_{rel} is also determined by the nature of the inhomogeneity under consideration.

What is the nature of the inhomogeneities? It seems that such an inhomogeneity is not a specific impurity contained in air or in water vapor. Although it is well known that even the lowest quantities of some substances contained in air may considerably influence the shape of a snow crystal (e.g., butyl alcohol [2]), the numerous observations and experiments performed under different conditions [2, 9, 23] do not support this mechanism (e.g., the results obtained in [23] show that crystallization in a nitrogen, oxygen, or air atmosphere do not change the morphology). At present, one can indicate two obvious reasons for formation of inhomogeneities. The first one is air bubbles (or bubbles of a gas constantly present in the atmosphere) forming at the ice/water interface (air solubility in ice is approximately 100 times lower than in water [22, 24]). The bubbles are accumulated in the central parts of the faces and hinder their further growth. The second possible reason of the loss of morphological stability is the appearance of an electrical potential difference (amounting to hundreds of volts) in solidification at the moving ice/water interface (thermoelectric effect) [24–26]. It was shown [26] that specific electric energy

of a double layer formed at the crystallization front is comparable with the surface energy of the water/ice interface and, therefore, may considerably affect the morphological instability of ice. No doubt, these speculations are only a working hypotheses which should be verified both theoretically and experimentally.

REFERENCES

1. A. D. Zamorskii, *Atmospheric Ice, Hoarfrost, Glaze, Snow, and Hail* (Akad. Nauk SSSR, Moscow, 1955) [in Russian].
2. B. J. Mason, *The Physics of Clouds*, 2nd ed. (Clarendon, Oxford, 1971; Gidrometizdat, Leningrad, 1961).
3. N. S. Shishkin, *Clouds, Precipitations, and Thunderstorm Electricity* (Gidrometizdat, Leningrad, 1961) [in Russian].
4. R. R. Rogers, *A Short Course in Cloud Physics*, 2nd ed. (Pergamon, Oxford, 1979; Gidrometeoizdat, Leningrad, 1979).
5. I. P. Mazin and S. M. Shmeter, *Clouds: Structure and Physics of Formation* (Gidrometeoizdat, Leningrad, 1983) [in Russian].
6. L. T. Matveev, *Course of General Meteorology. Atmospheric Physics* (Gidrometeoizdat, Leningrad, 1984) [in Russian].
7. *Handbook of Snow: Principles, Processes, Management, and Use*, Ed. by D. M. Gray and D. H. Male (Blackburn, Caldwell, N.J., 2004; Gidrometeoizdat, Leningrad, 1986) [in Russian].
8. L. M. Martyushev, I. E. Kuznetsova, and A. V. Verevchikov, in *Abstracts of VIII International Ecological Symposium* (Yekaterinburg, 2000), p. 163.
9. K. G. Libbrecht, *Eng. Sci.*, No. 1, 10 (2001).
10. Yu. S. Sedunov, *Physics of Formation of Liquid Droplet Phase in the Atmosphere* (Gidrometeoizdat, Leningrad, 1972) [in Russian].
11. A. A. Chernov, E. I. Givargizov, Kh. S. Bagdasarov, et al., in *Modern Crystallography*, Vol. 3: *Crystal Growth*, Ed. by B. K. Vainshtein, A. A. Chernov, and L. A. Shuvalov (Nauka, Moscow, 1980; Springer, Berlin, 1984).
12. K. G. Libbrecht and V. M. Tanusheva, *Phys. Rev. E* **59** (3), 3253 (1999).
13. K. G. Libbrecht, *Phys. Rev. E* **60** (2), 1967 (1999).
14. S. R. Coriell and G. B. McFadden, in *Handbook of Crystal Growth*, Ed. by D. T. J. Hurle (North-Holland, Amsterdam, 1993), Vol. 1, Part B, p. 785.
15. D. Nenov and V. Stoyanova, *J. Cryst. Growth* **41** (1), 73 (1977).
16. E. Yokoyama and T. Kuroda, *Phys. Rev. A* **41**, 2038 (1990).
17. J. Nittman and H. E. Stanley, *J. Phys. A: Math. Gen.* **20**, L1185 (1987).
18. S. Miyazima and T. Tanaka, *J. Phys. Soc. Jpn.* **56** (2), 441 (1987).

19. L. M. Martyshev and L. G. Gorbich, *Pis'ma Zh. Tekh. Fiz.* **29** (13), 36 (2003) [*Tech. Phys. Lett.* **29**, 544 (2003)].
20. D. D. Saratovkin, *Dendritic Crystallization* (Metalurgizdat, Moscow, 1957) [in Russian].
21. L. M. Martiouchev, V. D. Seleznev, and S. A. Skopinov, *J. Stat. Phys.* **90** (5/6), 1413 (1998).
22. N. Maeno, *The Science of Ice* (Hokkaido Univ. Press, Sapporo, 1984; Mir, Moscow, 1988).
23. K. Isono, *Nature* **182** (1), 1221 (1958).
24. L. G. Kachurin and V. G. Morachevskii, *Kinetics of Phase Transitions in Atmospheric Water* (Leningr. Gos. Univ., Leningrad, 1965) [in Russian].
25. A. A. Shibkov, Yu. I. Golovin, M. A. Zheltov, *et al.*, *Kristallografiya* **44** (5), 924 (1999) [*Crystallogr. Rep.* **44**, 863 (1999)].
26. Yu. I. Golovin, A. A. Shibkov, and M. A. Zheltov, *Mater. Élektron. Tekh.*, No. 4, 36 (1999).

Translated by L. Man

Hydrothermal Crystallization in the $\text{KOH-ZrO}_2\text{-GeO}_2\text{-H}_2\text{O}$ System under 0.1 GPa Pressure at 500°C: Phase Relationships for Zr Germanates and Modeling of $\text{K}_2\text{ZrGe}_2\text{O}_7$ Crystal Structure

G. D. Ilyushin

*Shubnikov Institute of Crystallography, Russian Academy of Sciences,
Leninskii pr. 59, Moscow, 119333 Russia*

Received January 15, 2003; in final form, November 11, 2003

Abstract—Formation of germanium dioxide of the composition $R\text{-GeO}_2$ (rutile structure type), Zr germanate of the composition $\text{Zr}^{[8]}\text{Ge}^{[4]}\text{O}_4$ (scheelite structure type), $\text{K,Zr}^{[6]}$ germanates of the compositions $\text{K}_2\text{Zr}^{[6]}\text{Ge}_3^{[4]}\text{O}_9$ (wadeite structure type) and $\text{K}_2\text{Zr}^{[6]}\text{Ge}_2^{[4]}\text{O}_7$, $\text{K,Ge}^{[6]}$ germanate of the composition $\text{K}_2\text{Ge}^{[6]}\text{Ge}_3^{[4]}\text{O}_9$, and the $\text{K,Ge}^{[6]}$ hydroxo germanate of the composition $\text{K}_3\text{HGe}_4^{[6]}\text{Ge}_3^{[4]}\text{O}_{16} \cdot 4\text{H}_2\text{O}$ is established in the $\text{KOH-ZrO}_2(\text{nanocrystalline})\text{-GeO}_2(\text{quartz structure type})\text{-H}_2\text{O}$ system under the pressure 0.1 GPa at the temperature 500°C (the superscripts indicate the coordination numbers of Zr and Ge atoms with respect to oxygen). It is shown that crystallization of K,Zr germanates under hydrothermal conditions depends on the molar $\text{ZrO}_2/\text{GeO}_2$ ratio and KOH concentration. The phases synthesized are subjected to crystallochemical analysis. The specific characteristics of the matrix assembly of the $\text{K}_2\text{ZrGe}_2\text{O}_7$ structure from suprapolyhedral structural units (SSU) are considered. The $\text{K}_2\text{ZrGe}_2\text{O}_7$ structure having the MT_2 framework built by M octahedra of the composition ZrO_6 and T tetrahedra of the composition GeO_4 is considered as a packing of SSU precursors of the composition $\text{K}_2M_2T_4$. The chemical composition of the SSU precursor of the composition $\text{K}_2M_2T_4$ with $M : T = 1 : 2$ determines the lower boundary of germanium content in the three-dimensional framework structures of K,Zr germanates as $\text{Ge/Zr} = 2$. © 2005 Pleiades Publishing, Inc.

Earlier, studying hydrothermal crystallization in the $\text{KF-ZrO}_2\text{-GeO}_2\text{-H}_2\text{O}$ system at 500–550°C, we revealed the formation of K,Zr germanate of the composition $\text{K}_x\text{Zr}_y\text{Ge}_p\text{O}_g$ (presumably, of the wadeite structure type), K germanate of the composition $\text{K}_2\text{Ge}_4\text{O}_9$, and K,Zr fluoride of the composition K_3ZrF_7 [1].

Two new isostructural phases, $\text{K}_2\text{ZrGe}_2\text{O}_7$ and $\text{K}_2\text{HfGe}_2\text{O}_7$, were synthesized hydrothermally from the concentrated KOH solutions at 500°C [2]. In [3], $\text{K}_2\text{ZrGe}_2\text{O}_7$ germanate was synthesized from a 6.6 M KOH solution at 170°C and its structural determination was performed. It was assumed [3] that the $\text{K}_x\text{Zr}_y\text{Ge}_p\text{O}_g$ phase synthesized in [1] is a solid solution with a wide homogeneity region.

The family of closely related (with respect to their composition and structure) K,Zr silicates includes the three dehydrated phases $\text{K}_2\text{ZrSi}_2\text{O}_7$ [4], $\text{K}_2\text{ZrSi}_3\text{O}_9$ [5], and $\text{K}_2\text{ZrSi}_6\text{O}_{15}$ [6] and the two hydrated phases $\text{K}_2\text{ZrSi}_3\text{O}_9 \cdot \text{H}_2\text{O}$ [7] and $\text{K}_4\text{Zr}_2\text{Si}_6\text{O}_{18} \cdot 2\text{H}_2\text{O}$ [8] having topologically different MT frameworks built by M octahedra of the composition ZrO_6 and T tetrahedra of the composition SiO_4 sharing their vertices.

The conditions of formation of K,Zr silicates were studied in [9–13]. It was shown [10] that the chemical composition, structure, and number of crystal-forming phases in the $\text{KOH-ZrSiO}_4\text{-H}_2\text{O}$, $\text{KOH-ZrO}_2(\text{crystalline})\text{-SiO}_2\text{-H}_2\text{O}$, and $\text{KOH-ZrO}_2(\text{nanocrystalline})\text{-SiO}_2\text{-H}_2\text{O}$ systems depend on the nature of the Zr component.

The present study was undertaken with the aim to identify the structure types of germanates formed in the $\text{KOH-ZrO}_2(\text{nanocrystalline})\text{-GeO}_2\text{-H}_2\text{O}$ system under the pressure 0.1 GPa at 500°C and to perform the crystallochemical analysis and model the matrix assembly of the $\text{K}_2\text{ZrGe}_2\text{O}_7$ structure from suprapolyhedral structural units (SSU precursors).

This study continues our previous investigations [2, 7–10, 14–18] dedicated to synthesis, analysis of geometrical-topological characteristics of formation of crystalline phases, and modeling of the processes of self-organization in the $\text{AOH-MO}_2\text{-TO}_2\text{-H}_2\text{O}$ systems ($A = \text{Li, Na, and K}$; $M = \text{Zr, Ti, Hf, Si}^{[6]}, \text{Ge}^{[6]}, \text{and Sn}$; $T = \text{Si}^{[4]} \text{ and } \text{Ge}^{[4]}$) at the suprapolyhedral level.

Table 1. Experimental data on phase formation in the KOH–ZrO₂–GeO₂–H₂O system at 500°C

| Experiments | KOH, wt % | $\alpha = \text{ZrO}_2 : \text{GeO}_2$, molar ratio | $\beta = \text{KOH} : \text{GeO}_2$ | Phase composition | | | | |
|-------------|-----------|--|-------------------------------------|---|--|--------------------|---|---|
| | | | | K germanates | | Zr germanates | | |
| | | | | K ₂ GeGe ₃ O ₉ | K ₃ HGe ₄ Ge ₃ O ₁₆ ·4H ₂ O | ZrGeO ₄ | K ₂ ZrGe ₃ O ₉ | K ₂ ZrGe ₂ O ₇ |
| 1 | 5 | 1 : 2 | 0.48 | + | + tr * | + | tr + | – |
| 2 | 10 | 1 : 2 | 1.00 | – | + | – | + | – |
| 3 | 20 | 1 : 2 | 2.19 | – | – | – | + | – |
| 4 | 35 | 1 : 2 | 4.33 | – | – | – | – | + |
| 5 | 5 | 1 : 3 | 0.42 | + | + | + | + | – |
| 6 | 10 | 1 : 3 | 0.88 | + | + | + | + | – |
| 7 | 20 | 1 : 3 | 1.91 | – | – | – | + | – |
| 8 | 35 | 1 : 3 | 3.79 | – | – | – | – | + |
| 9 | 5 | 1 : 6 | 0.34 | + | + | + | + | – |
| 10 | 10 | 1 : 6 | 0.73 | + | + | + | + | – |
| 11 | 20 | 1 : 6 | 1.59 | – | – | – | + | – |
| 12 | 35 | 1 : 6 | 3.14 | – | – | – | – | + |
| 13 | 5 | 1 : 9 | 0.33 | + | + | + | + | – |
| 14 | 10 | 1 : 9 | 0.69 | + | + | – | + | – |
| 15 | 20 | 1 : 9 | 1.49 | – | – | – | + | – |
| 16 | 35 | 1 : 9 | 2.96 | – | – | – | – | + |

* The abbreviation tr indicates trace amounts.

EXPERIMENTAL

Hydrothermal synthesis of crystals was performed by the temperature-gradient method [14]. Copper ampules with a diameter of 8 mm and a working volume of 15 cm³ were filled with the mixture of the starting components. Then, the sealed ampules were placed into 170-cm³ autoclaves with cylindrical shutters of the self-sealing type and annealed in a bottom-heated furnace.

Hydrothermal crystallization in the KOH–ZrO₂–GeO₂–H₂O system was studied at a temperature in the dissolution zone of 500°C under the pressure 0.1 GPa under the condition of the temperature gradient ranging within 1.5–2.0 K/cm along the vertical axis of the autoclave. The pressure was estimated from the *p*–*t* diagram of water given in [19]. The accuracy of the automated maintaining of the temperature along the external wall of the autoclave was ±2 K. The charge consisted of chemically pure components: GeO₂ (with quartz structure), KOH, and quickly dissolving ZrO₂ (nanocrystalline) obtained by the sol–sol method according to the technology described in [20]. The experiment duration was 240 h. Several runs of the experiment (Table 1) differed by the weight and the ratio of the oxides introduced into solution and the concentrations of the hydroxide KOH.

Insoluble solid products of high-temperature chemical interaction were washed with hot water, dried, and then analyzed.

The phases synthesized were identified by X-ray phase analysis (DRON-2 and Rigaku D-Max 1500 diffractometers, CuK_α radiation) with the invocation of the data from the ICDD (International Center for Diffraction Data) [21] and ICSD (Inorganic Crystal Structure Database) [22].

RESULTS

The products of hydrothermal crystallization were fine powders or colorless transparent single crystals with the linear dimension ranging within 0.1–2.0 mm. The phase composition of the crystallization field and the molar ratio $\beta = \text{KOH} : \text{GeO}_2$ are indicated in Table 1.

In the KOH–ZrO₂–GeO₂–H₂O system under 0.1 GPa pressure at 500°C, the compounds of four different crystallochemical groups are crystallized, which have different coordination numbers (c.n.) of Ge and Zr atoms, namely, (1) GeO₂ dioxide (rutile structure type with c.n. 6); (2) ZrO₂ dioxide (structure of monoclinic baddeleyite ZrO₂ with c.n. 7); (3) ZrGeO₄ germanate (structure built by dodecahedra with c.n. 8 and tetrahedra with c.n. 4); (4) *MT* structures built by *M* octahedra (Zr or Ge) and *T* tetrahedra (Ge), namely, K,Ge^[6] ger-

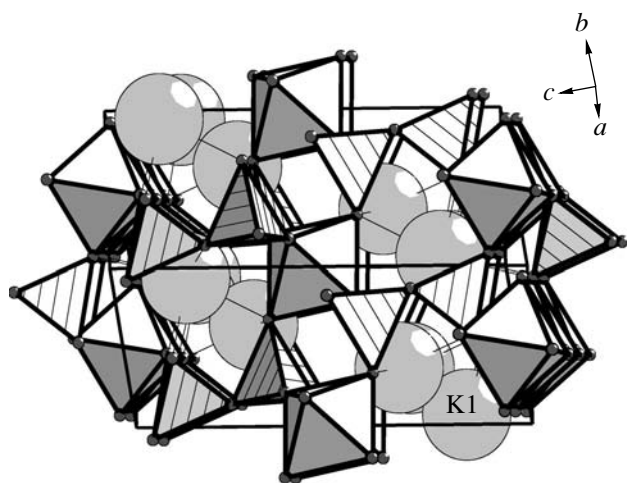


Fig. 1. Framework of the $K_2ZrGe_2O_7$ structure consisting of M octahedra linked by Ge_2O_7 or diortho groups; MT are the voids occupied by K atoms (large spheres).

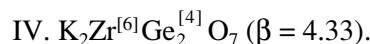
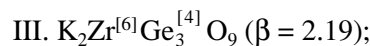
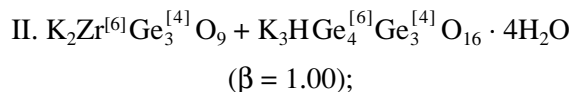
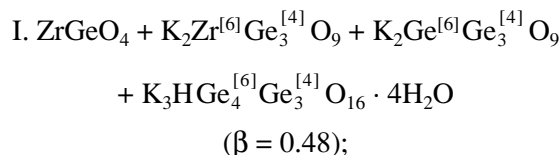
manate of the composition $K_2Ge^{[6]}Ge_3^{[4]}O_9$, $K,Ge^{[6]}$ hydroxo germanate of the composition $K_3HGe_4^{[6]}Ge_3^{[4]}O_{16} \cdot 4H_2O$, and $K,Zr^{[6]}$ germanates of the compositions $K_2Zr^{[6]}Ge_3^{[4]}O_9$ and $K_2Zr^{[6]}Ge_2^{[4]}O_7$.

In all the experiments, we obtained the compound $K_2ZrGe_3O_9$ corresponding to the phase of an unknown composition, $K_xZr_yGe_pO_g$, observed in [1]. This germanate is an analog of the silicate wadeite having the composition $K_2ZrGe_3O_9$ [5] with the framework topology *WAD* [17]. Single crystals of the $K_2ZrGe_3O_9$ germanate are not solid solutions as was assumed in [3], since our experiments revealed neither shift nor broadening of the respective X-ray diffraction lines. It should be indicated that up to now no examples of germanate structures representing the $A_xM_yGe_pO_g$ solid solutions are known in which the same A positions (in framework voids) are occupied by K and Zr atoms or the same octahedral M positions are occupied with Zr and Ge atoms. All the structures of such type (zirconium germanates, zirconium silicates, and their analogs [17]) have *MT* frameworks. The alkali metals A (occupying the voids of the *MT* frameworks) and the framework-forming $Zr(M)$ and $Ge(T)$ atoms perform different functions. Below we consider the functions of K, Zr, and Ge atoms by an example of the matrix assembly of $K_2ZrGe_2O_7$ and $K_2ZrGe_3O_9$ structures.

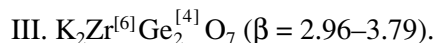
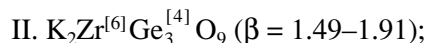
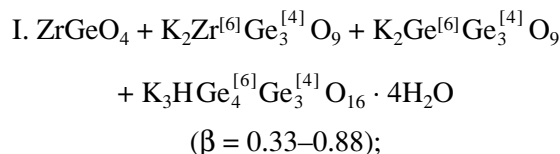
SPECIFIC CHARACTERISTICS OF PHASE FORMATION

The variation of the KOH concentration in all the runs with $ZrO_2 : GeO_2 = 1 : 2$ (runs 1–4) resulted in the change of the phase composition of the crystallization products. There are four characteristic crystallization

fields:



At $ZrO_2 : GeO_2 = 1 : 3-1 : 9$ (runs 5–16), an increase in the KOH concentration gave rise to the formation of the following crystallization fields with different compositions:



Thus, unlike the $KF-ZrO_2-GeO_2-H_2O$ system [1] in which only one K,Zr germanate of the composition $K_xZr_yGe_pO_g$ was formed at $500^\circ C$, the replacement of KF and slowly dissolving crystalline ZrO_2 (monoclinic modification, baddeleyite type) by KOH and quickly dissolving nanocrystalline ZrO_2 (with the surface area $\sim 100 \text{ m}^2/\text{g}$), respectively, initiated the formation of the following phases:

Zr -germanate of the compositions $ZrGeO_4$ with the scheelite structure as the primary Zr,Ge phase formed at a low KOH concentration, and

two $K,Zr^{[6]}$ germanates of the compositions $K_2ZrGe_3O_9$ (Ge wadeite) and $K_2ZrGe_2O_7$ with the phase transition from $K_2ZrGe_3O_9$ to $K_2ZrGe_2O_7$ with an increase in the KOH concentration.

Below, we consider the structural mechanism of the formation of $K_2Zr^{[6]}Ge_2^{[4]}O_7$ within the model of matrix assembly and interpret the sequence of formation of K,Zr germanates with an increase in the KOH concentration (C_{KOH}) at the suprapolyhedral level.

MATRIX ASSEMBLY OF THE STRUCTURE OF $K_2ZrGe_2O_7$ GERMANATE

The method for determining a crystal-forming SSU precursor from the known structural data and the algorithm of the reconstruction of three-dimensional structures based on the principle of maximum connectivity

in the transition to a higher level of the structural self-organization of the system are considered in detail elsewhere [14–16].

General structural characteristics. The monoclinic $K_2ZrGe_2O_7$ structure is described by the sp. gr. $C12/c1$ (no. 15 [23]) and has the lattice parameters $a = 9.961 \text{ \AA}$, $b = 5.557 \text{ \AA}$, $c = 12.955 \text{ \AA}$, and $\beta = 105.17^\circ$ [3]. The framework of the $K_2ZrGe_2O_7$ structure is formed by isolated M octahedra of the composition ZrO_6 linked by Ge_2O_7 (diortho) groups (Fig. 1); the K atoms occupy the MT voids. Two atoms of the unit cell are in the special positions: Zr is located at the center of inversion ($4d$ Wyckoff position) with the coordinates (0.25, 0.25, 0.5) [23], and the $O_{(4)}$ atom connecting two tetrahedra of diortho groups occupies the $4e$ position on the twofold axis with the coordinates (0, y , 0.25) [23]. Five remaining atoms occupy the general $8f$ position.

Polyhedral structure of an SSU. An SSU precursor of germanate (Fig. 2) is a cyclic-type cluster consisting of six linked polyhedra (D type, according to the topological classification of SSU precursors [14]). In this cluster, two ZrO_6 octahedra are linked via the Ge_2O_7 diortho groups. The K atoms are located above and under the plane of a six-membered M_2T_4 ring. The center of the SSU precursor is located in the general position $8f$ [23] with the coordinates (0.25, 0.48, 0.25). The MT fragments of the cyclic SSU precursor (Zr octahedron and Ge_2O_7 diortho group) are related by the 2_1 axis (Fig. 2).

Structural mechanism of assembly. Stable cyclic-type MT fragments of the composition $K_2M_2T_4$ control all the processes of further development of a crystal-forming MT complex and ensure the formation of a SSU of a higher level of the structural self-organization of the system. The coincidence of the cationic composition of the SSU precursor with $2ZrO_6 : 4GeO_4 = 1 : 2$ with the composition of the SSU precursor with $Zr : Ge = 1 : 2$ in the three-dimensional $K_2ZrGe_2O_7$ structure indicates that their packing according to the self-assembling mechanism most rapidly reconstructs the topology of the whole structure.

The mechanism of the reconstruction of the global (three-dimensional) topology proceeding from the local fragment of the structure via complementary connection of SSU precursors with one another has the following characteristics.

Assembly of primary MT chains of the framework. The one-dimensional periodic MT chains are formed owing to centrosymmetric connection of SSU precursors $K_2M_2T_4$ sharing two vertices along the short diagonal of the unit cell in the xz plane (Fig. 2). The symmetry center is located in the position $4a$ ($1/2, 1/2, 1/2$). The index of complementary connectivity of SSU precursors in the chain is 2.

Assembly of an MT layer. Connected MT chains form a layer consisting of four $K_2M_2T_4$ clusters, which are shown in Fig. 4. The index of complementary con-

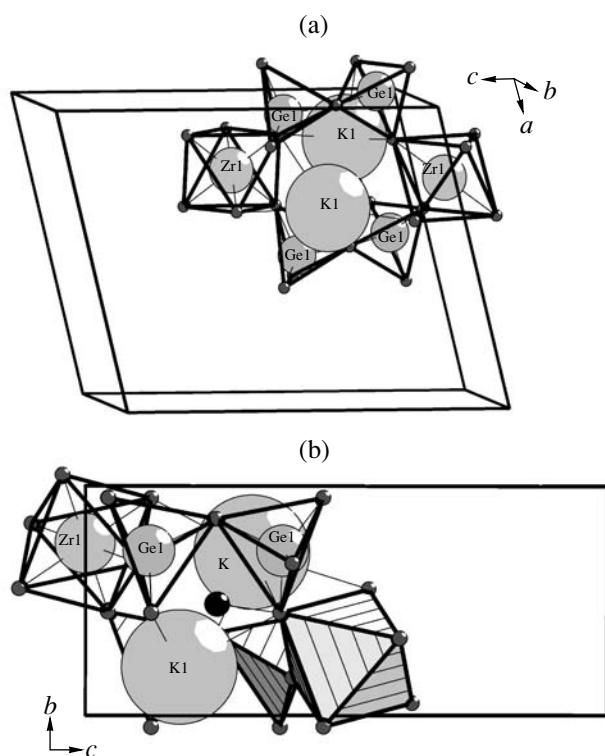


Fig. 2. SSU precursor of the $K_2ZrGe_2O_7$ structure projected along the (a) b and (b) a axes. The black sphere indicates the center of the SSU precursor.

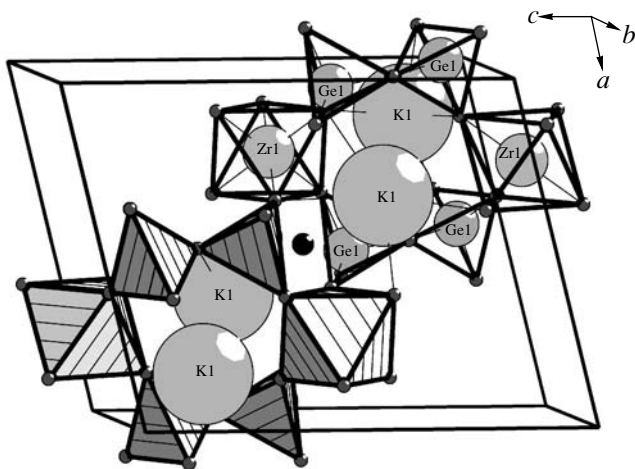


Fig. 3. Assembly of a chain of SSU precursors. The black sphere is the center of the cluster of SSU precursors.

nectivity of the chains consisting of SSU precursors is four. The distance between the centers of the SSU precursors consisting of parallel chains (Fig. 3) determines two largest translations in the germanate structure: $c = 12.955 \text{ \AA}$ in the direction along which the SSU precursors are connected by Ge_2O_7 diortho groups of neighboring SSU precursors practically parallel to the z axis and $a = 9.961 \text{ \AA}$ in the direction along which the SSU

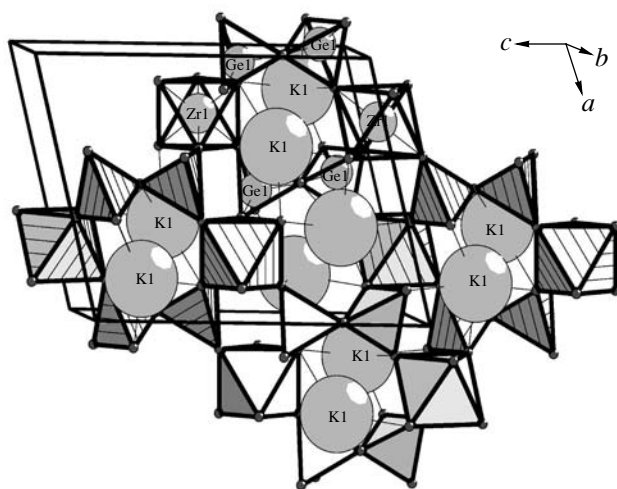


Fig. 4. Assembly of a layer consisting of two chains.

precursors are connected by the octahedra of the neighboring SSU.

Filling of all the geometrically equivalent voids by K atoms in a newly formed *MT* layer changes the layer composition from $K_2M_2T_4$ to $K_4M_2T_4$ (2 : 1 : 2), which, on the whole, corresponds to the chemical composition of the $K_2ZrGe_2O_7$ germanate (2 : 1 : 2). Two additional K atoms occupying the position in the center of the *MT* layer are shown in Fig. 4.

Assembly of the *MT* framework. The linear dimension of the separated slab (Fig. 4) determines the value of the third shortest translation $b = 5.557 \text{ \AA}$ in the direction along which the translation-related SSU precursors are linked (Fig. 5). As a result, the oxygen atoms at the slab boundaries are translation-equivalent. Condensation of germanate layers (Figs. 4 and 5) results in the assembly of a three-dimensional structure.

The two-dimensional layer-slabs separated in the process of modeling from the three-dimensional germanate structure are translation-equivalent and, therefore, the $K_2ZrGe_2O_7$ germanate represents the simplest *1L* type of the structure, where the notation *1L* indicates that the translation multiplication of the layer reconstructs the structure of a three-dimensional *MT* framework [16].

Thus, the $K_2ZrGe_2O_7$ structure with the *MT* framework MT_2 consisting of *M* octahedra and *T* tetrahedra is represented as packing of the SSU precursors of the composition $K_2M_2T_4$. The chemical composition of an SSU precursor of the composition $K_2M_2T_4$ with $M : T = 1 : 2$ determines the lower boundary of germanium content in structures of *K,Zr* germanates with three-dimensional frameworks with $q = Ge/Zr = 2$. Another *K,Zr* germanate $K_2ZrGe_3O_9$ of the composition obtained in this system is characterized by $q = 3$.

Structural analogs of $K_2ZrGe_2O_7$ germanate among the compounds with *MT* frameworks. Using

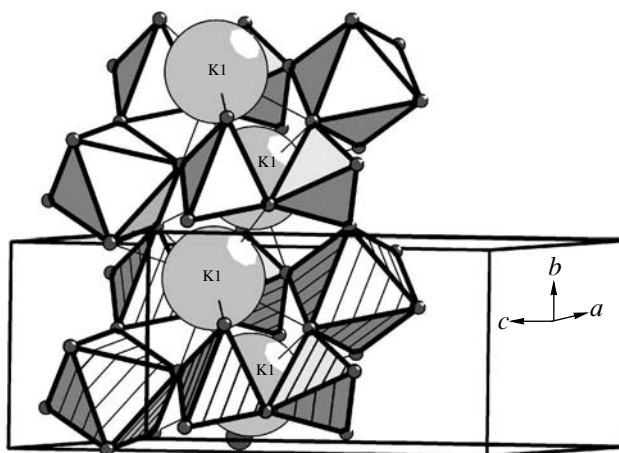


Fig. 5. Assembly of translationally equivalent SSU precursors along the y axis.

the TOPOS 3.2 package of programs [24], we searched in the ICSD-2002 database for the phases of the $A_2MT_2O_7$ composition possessing the *MT* frameworks consisting of *M* and *T* polyhedra topologically equivalent to the framework of the $K_2ZrGe_2O_7$ germanate.

As in [7, 18], the algorithms for search and analysis of the crystal structures consisted of the following stages:

formation of a database of crystal structure for the $A_2MT_2O_7$ compounds (we found 120 such compounds);

calculation of the connectivity matrix of atoms for each structure using the AutoCN program. We took into account only the strong interatomic contacts corresponding to the main faces of the Voronoi–Dirichlet polyhedra with the solid angles $\Omega > 5\%$ of the total solid angle equal to 4π steradians. When calculating the connectivity matrix by the methods of intersecting sectors, we used the Slater atomic radii;

calculation of *coordination sequences* $\{N_k\}$ for all the topological representations of the structures and their subsequent comparison using the IsoTest program. The coordination sequence is a set of numbers $\{N_k\}$, where N_k is the number of network sites in the k th coordination sphere of the atom selected as the central one. In order to determine the individual topologic characteristics of the sites in the *MT* frameworks in the calculation of the $\{N_k\}$ values, we removed the alkali metal atoms $A = Li-Cs$ from the structure and performed the further calculation only for the atoms forming the *M*, *T*, O framework.

We determined three families of structures, which are described by different symmetry groups: the triclinic parakeldyshite type, $Na_2ZrSi_2O_7$, described by the sp. gr. $P\bar{1}$ with group order 2; the monoclinic khibinskite type, $K_2ZrSi_2O_7$, described by the sp. gr. $P112_1/b$ with group order 4; and the high-pressure mon-

Table 2. Crystallographic data for various representatives of three crystallochemical families described by the general formula $A_2MT_2O_7$ with topologically equivalent MT frameworks built by octahedra and tetrahedra

| Compound | Sp. gr. | Z | Wyckoff position | Lattice parameters $a, b, c, \text{Å};$ $\alpha, \beta, \gamma, \text{deg}$ | $V, \text{Å}^3$ | Code in the ICSD | R, % |
|---|------------|---|------------------|---|-----------------|------------------|-------|
| Triclinic modification, parakeldyshite type | | | | | | | |
| $\text{Na}_2\text{ZrSi}_2\text{O}_7$ palakeldyshite | $P\bar{1}$ | 2 | $i12$ | 6.660, 8.830, 5.420, 92.75, 94.25, 72.33 | 302.8 | 24866 | 0.145 |
| $\text{Na}_2\text{ZrGe}_2\text{O}_7$ | $P\bar{1}$ | 2 | $i12$ | 5.630, 6.677, 9.108, 70.60, 88.85, 87.04 | 322.5 | 65808 | 0.055 |
| Monoclinic modification, khiminskite type | | | | | | | |
| $\text{K}_2\text{MnP}_2\text{O}_7$ | $P12_1/n1$ | 4 | $e12$ | 12.649, 5.527, 9.571, 90.00, 104.45, 90.00 | 648.0 | 74600 | 0.041 |
| $\text{K}_2\text{ZrSi}_2\text{O}_7$ khibinskite | $P112_1/b$ | 4 | $e12$ | 9.540, 14.260, 5.600, 90.00, 90.00, 116.52 | 681.7 | 20100 | 0.140 |
| $\text{K}_2\text{SrP}_2\text{O}_7$ | $P12_1/c1$ | 4 | $e12$ | 9.168, 5.712, 14.720, 90.00, 105.79, 90.00 | 741.8 | 39468 | 0.062 |
| $\text{K}_2\text{CaAs}_2\text{O}_7$ | $P12_1/c1$ | 4 | $e12$ | 9.222, 5.835, 14.698, 90.00, 105.84, 90.00 | 760.9 | 12116 | 0.056 |
| Monoclinic modification, $\text{Na}_2\text{Si}^{[6]}\text{Si}_2\text{O}_7$ type | | | | | | | |
| $\text{Na}_2\text{Si}^{[6]}\text{Si}_2\text{O}_7$ high pressure phase | $C12/c1$ | 4 | $f5ed$ | 8.922, 4.849, 11.567, 90.00, 102.64, 90.00 | 488.3 | 81134 | 0.020 |
| $\text{K}_2\text{CdP}_2\text{O}_7$ | $C12/c1$ | 4 | $f5ec$ | 9.737, 5.548, 12.766, 90.00, 106.50, 90.00 | 661.2 | 12117 | 0.067 |
| $\text{K}_2\text{ZrGe}_2\text{O}_7$ | $C12/c1$ | 4 | $f5ed$ | 9.962, 5.558, 12.955, 90.00, 105.17, 90.00 | 692.3 | 88843 | 0.037 |
| $\text{Rb}_2\text{SrP}_2\text{O}_7$ | $C12/c1$ | 4 | $f5ed$ | 10.270, 5.867, 14.413, 90.00, 116.48, 90.00 | 777.3 | 39506 | 0.073 |
| $\text{Cs}_2\text{SrP}_2\text{O}_7$ | $C12/c1$ | 4 | $f5ed$ | 10.528, 6.081, 14.766, 90.00, 118.34, 90.00 | 832.0 | 39507 | 0.088 |

oclinic $\text{Na}_2\text{Si}^{[6]}\text{Si}_2\text{O}_7$ phase described by the sp. gr. $C12/c1$ with group order 8.

The representatives of these families are alkali silicates (germanates) and phosphates (arsenates) with $M(4+) = \text{Si}$ and Zr , $M(2+) = \text{Mn}$, Cd , Ca , Sr , and Ba , and $A = \text{Na}$, K , Rb , and Cs (Table 2). It should be noted that the constant chemical composition $A_2MT_2O_7$ of all the phase-analogs allowed us to single out only three of the above families.

The topological-equivalence condition of the structures with the MT frameworks in the above three families of crystal structures $A_2MT_2O_7$ results in the equivalence of programs of their assembly from suprapolyhedral cyclic SSU precursors. This is explained by the fact that the connectivity indices of suprapolyhedral SSU precursors consisting of M and T polyhedra calculated for these families based on the same model of assembly are always the same.

The structure of the $\text{K}_2\text{ZrGe}_2\text{O}_7$ germanate relates to the $\text{Na}_2\text{Si}^{[6]}\text{Si}_2\text{O}_7$ family described by the sp. gr. possessing the maximum order. As was indicated for

$\text{K}_2\text{ZrGe}_2\text{O}_7$, the M polyhedra in the crystal structure preserve the center of inversion while the tetrahedra are related by a twofold rotational axis. In other families, all the atoms in structure occupy the general positions: $12i$ in $\text{Na}_2\text{ZrSi}_2\text{O}_7$ and $e12$ in $\text{K}_2\text{ZrSi}_2\text{O}_7$ (Table 2).

The $\text{Na}_2\text{Si}^{[6]}\text{Si}_2\text{O}_7$ family is more numerous. In addition to the $\text{Na}_2\text{Si}^{[6]}\text{Si}_2\text{O}_7$ silicate and isostructural $\text{K}_2M\text{Ge}_2\text{O}_7$ germanates ($M = \text{Zr}$ and Hf [2]), it includes three phosphates with large atoms M ($M = \text{Cd}$ and Sr) and alkali metals A ($A = \text{K}$, Rb , and Cs). The data on the chemical composition (A , M , and T atoms) of the $A_2MT_2O_7$ oxides (Table 2) reflect the dimensional relationships of the framework-forming M and T polyhedra, which impose some steric hindrances on the alkali metal atoms. The atoms A should correspond to the sizes of the MT voids of the framework formed during structure assembly. For comparison, the volume ratio of the unit cells of $\text{Na}_2\text{Si}^{[6]}\text{Si}_2\text{O}_7$ silicate with the smallest Si octahedron (488.3 Å^3) and of $\text{Cs}_2\text{SrP}_2\text{O}_7$ phosphate with the largest Sr octahedron (832.0 Å^3) equals 0.59.

Table 3. Coordination sequences N_k of $K_2ZrGe_2O_7$ [3] and $Na_2ZrGe_2O_7$ germanates [25]. Topologically equivalent framework-forming atoms are characterized by the equivalent $\{N_k\}$ sequences

| Framework-forming atoms | | Coordination sequences N_k ($k = 1-11$) | | | | | | | | | | |
|-------------------------|----------------------|---|---|----|----|----|----|-----|-----|-----|-----|-----|
| $K_2ZrGe_2O_7$ | $Na_2ZrGe_2O_7$ | 1 | 2 | 3 | 4 | 5 | 6 | 7 | 8 | 9 | 10 | 11 |
| O(4) | O(2) | 2 | 6 | 6 | 30 | 24 | 60 | 30 | 102 | 68 | 198 | 84 |
| O(1)–O(3) | O(1)–O(3), O(5)–O(7) | 2 | 8 | 8 | 26 | 19 | 62 | 38 | 114 | 61 | 164 | 89 |
| Ge | Ge(1), Ge(2) | 4 | 4 | 18 | 15 | 48 | 27 | 78 | 49 | 156 | 76 | 198 |
| Zr | Zr | 6 | 6 | 18 | 12 | 42 | 30 | 102 | 50 | 122 | 74 | 222 |

The coordination sequences N_k of the framework-forming atoms in $K_2ZrGe_2O_7$ and $Na_2ZrGe_2O_7$ germanates are listed in Table 3. The groups of topologically equivalent atoms (prevailing in the MT frameworks with the same sets of N_k) are separated. Oxygen atoms with different N_k are differentiated into the bridging atoms (connecting T tetrahedra into diortho groups) and end atoms (connecting M and T polyhedra). Numbering of the atoms in $K_2ZrGe_2O_7$ and $Na_2ZrGe_2O_7$ corresponds to their numbering in structure determinations [3, 25]. The equivalent groups of framework-forming O and T atoms in the germanate structures with different symmetries perform the equivalent functions in the process of structure assembly (i.e., are functionally equivalent).

It should be indicated that the model of khibinskite $K_2ZrSi_2O_7$ formation (the second family of structures in Table 2) based on three-membered polyhedral cluster consisting of an M octahedron connected to a Si_2O_7 diortho group was suggested in 1973 [26]. It was suggested in 1985 [27] to use as a *fundamental structural block* in parakeldyshite–keldyshite $Na_2ZrSi_2O_7$ (the first family of triclinic structures, Table 2) a three-membered polyhedral cluster consisting of an octahedron and two tetrahedra in the *cis* position.

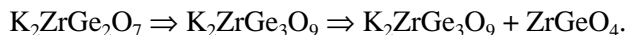
To determine a crystal-forming SSU precursor cluster, one has to consider instead of the M site topology in MT frameworks [26, 27] the correlation between the M sites, i.e., to analyze the local regions of the MT framework at higher levels of structural self-organization [28, 29].

We shall show later that it is possible to establish the invariance of the structure of an SSU precursor in the topologically different $K_2ZrGe_2O_7$ and $K_2ZrGe_3O_9$ structures and the bifurcation of the paths of their evolution (points of structural branching) in the system during the formation of three-dimensional periodic structures.

SEQUENCE OF FORMATION OF Zr GERMANATES

In the $KOH-ZrO_2-GeO_2-H_2O$ system studied, a decrease in C_{KOH} resulted in the successive formation of

the following Zr-germanate phases:



Consider in more detail the roles played by the structural and chemical factors in the formation of this sequence of the Zr,Ge phases in the system and the specific characteristics of the structural transition from the $K_2ZrGe_2O_7$ to $K_2ZrGe_3O_9$ phase.

Structure factor. The germanate with the $K_2ZrGe_2O_7$ structure is the phase formed in the system with the highest KOH concentration. The matrix assembly of the $K_2ZrGe_2O_7$ crystal structure from cyclic SSU precursors is the fastest because of the coincidence of the MT composition of the SSU precursor, M_2T_4 , and of the MT_2 framework of the germanate. Therefore, the packing of SSU precursors according to the mechanism of self-assembly quickly reproduces the structure topology. Lowering the KOH concentration, one may attain a certain threshold concentration (20% KOH) resulting in the crystallization of $K_2ZrGe_3O_9$ germanate. Similar to the $K_2ZrSi_3O_9$ silicate with the wadeite structure, the isostructural $K_2ZrGe_3O_9$ germanate has the SSU precursor with the same topology $K_2M_2T_4$ [16] as the $K_2ZrGe_2O_7$ germanate.

However, the assembly of the $K_2ZrGe_3O_9$ germanate is more complicated than the assembly of $K_2ZrGe_2O_7$. The $K_2ZrGe_3O_9$ germanate is characterized by an elevated germanium concentration in the MT framework. The structural transition from $K_2ZrGe_2O_7$ (MN framework) to $K_2ZrGe_3O_9$ (MT_3 framework) is ensured in solution by free $[Ge(OH)_4]^0$ tetrahedra modifying the primary MT chain and, thus, increasing the total number of Ge atoms in the structure.

Such free $[Ge(OH)_4]^0$ tetrahedra link the SSU precursors of $K_2M_2T_4$ [16]. The general connectivity index of SSU in the T -modified MT chain increases from 2 to 4. To modify the chain, the vertices of the M octahedra linking the centers should lie at a distance of ~ 2.6 Å comparable with the length of the tetrahedron edge. In other words, there should exist a geometric correspondence of these fragments to one another or a complementary equality (Fig. 6a).

The free vertices of M octahedra of various SSU precursors in the primary MT chain of the structure of

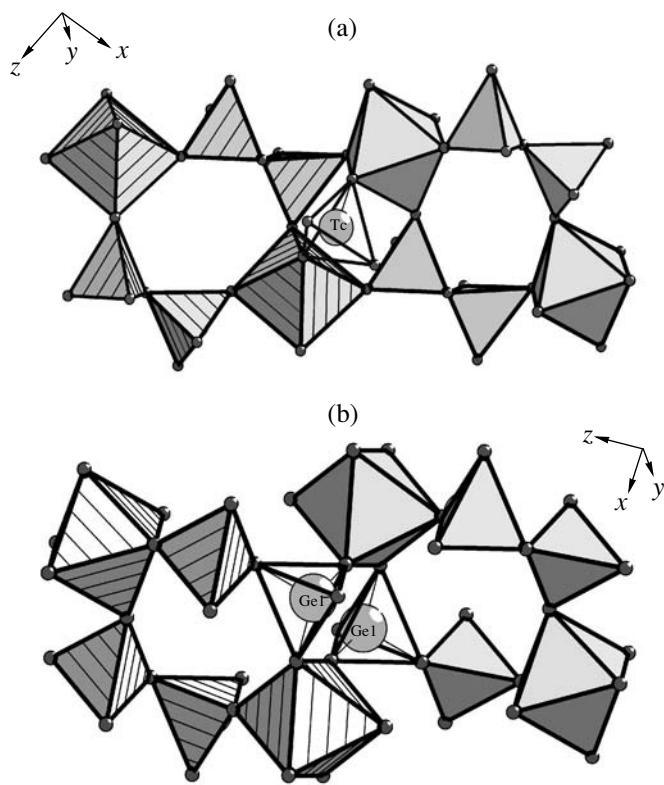


Fig. 6. Topologically different types of *MT* chains: (a) $\text{K}_2\text{ZrGe}_3\text{O}_9$ (T_c is a tetrahedron linking SSU precursors) and (b) $\text{K}_2\text{ZrGe}_2\text{O}_7$.

the $\text{K}_2\text{ZrGe}_2\text{O}_7$ germanate (Fig. 6b) show no such complementary equality contrary to the *MT* chain in $\text{K}_2\text{ZrGe}_3\text{O}_9$ (Fig. 6a). This signifies that there exists no continuous combinatorially topological transformation such that the vertices of the *M* octahedra in different SSU in the *MT* chain lie at a distance of 2.6 Å.

The symmetry elements relating invariant SSU precursors in *MT* chains are different: the center of inversion for $\text{K}_2\text{ZrGe}_2\text{O}_7$ (Fig. 6b) and the rotation axis for $\text{K}_2\text{ZrGe}_3\text{O}_9$ (Fig. 6a).

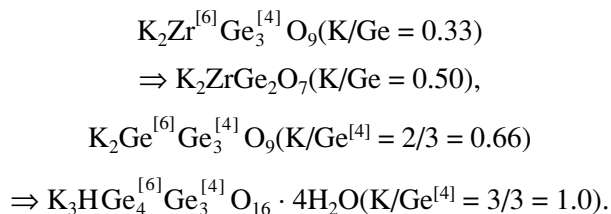
Thus, the matrix-assembly mechanisms in the $\text{K}_2\text{ZrGe}_2\text{O}_7$ and $\text{K}_2\text{ZrGe}_3\text{O}_9$ structures consisting of the same invariant SSU precursors are different even at the early stage of the system evolution, i.e., assembly of the primary *MT* chain.

Chemical factor. With lowering of the KOH concentration in the system, the fraction of $[\text{Ge}(\text{OH})_4]^{0-}$ tetrahedra linking *M* octahedra increases, on the one hand, and, on the other hand, the number of K atoms forming with *M* and *T* polyhedra a cyclic SSU precursor $\text{K}_2\text{ZrGe}_3\text{O}_9$ decreases. The latter process results in a decrease in the total number of K-containing SSU precursors and the evolution of other SSU precursors spontaneously formed in the system. Therefore, in the solutions with 10% KOH, one observes the joint crystallization of $\text{K}_2\text{ZrGe}_3\text{O}_9$ and alkali-free ZrGeO_4 germanate

formed on the basis of four-membered polyhedral cyclic SSU precursor [28]. In other words, two topologically different types of SSU precursors are spontaneously formed in the system.

The formation of SSU precursors of the composition ZrGeO_4 proceeds without participation of K atoms and is accompanied by an increase in the coordination number of Zr atoms from 6 to 8. Like in $\text{K}_2\text{ZrGe}_2\text{O}_7$, the assembly of the ZrGeO_4 structure [28] from SSU precursors proceeds very quickly because of the same stoichiometric compositions of four polyhedral SSU precursors with $2[\text{ZrO}_8] : 2[\text{GeO}_4] = 1 : 1$ and the SSU precursor with $\text{Zr} : \text{Ge} = 1 : 1$ in the three-dimensional ZrGeO_4 structure.

Concluding the article, we would like to note that, similar to the germanate and silicate $\text{AOH}-\text{MeO}_2-\text{TO}_2-\text{H}_2\text{O}$ systems studied earlier [2, 9, 14–16], an increase in the solvent concentration C_{AOH} in the systems results in the regular formation of K, Zr and K, Ge germanates with an increasing alkali metal content corresponding only to the *T* component of the crystals



CONCLUSIONS

It is established that formation of Zr germanates under hydrothermal conditions depends on the molar ratio $\text{ZrO}_2/\text{GeO}_2$ and the KOH concentration. The established sequence of Zr germanates formed with an increase in KOH concentration has the form $\text{ZrGeO}_4 + \text{K}_2\text{ZrGe}_3\text{O}_9 \Rightarrow \text{K}_2\text{ZrGe}_3\text{O}_9 \Rightarrow \text{K}_2\text{ZrGe}_2\text{O}_7$.

The specific features of the matrix assembly of $\text{K}_2\text{ZrGe}_2\text{O}_7$ and $\text{K}_2\text{ZrGe}_3\text{O}_9$ from invariant suprapolyhedral structural units of the cyclic type $\text{K}_2\text{M}_2\text{T}_4$ with K atoms being located above and under the plane of the ring are considered. The $\text{K}_2\text{ZrGe}_2\text{O}_7$ structure formed in the solution with 35% KOH is represented as a packing of SSU precursors $\text{K}_2\text{M}_2\text{T}_4$; the chemical composition of the SSU precursor $\text{K}_2\text{M}_2\text{T}_4$ with $M : T = 1 : 2$ determines the lower boundary of germanium content in three-dimensional framework structures of K, Zr germanates: $q = \text{Ge}/\text{Zr} = 2$.

Formation of the $\text{K}_2\text{ZrGe}_3\text{O}_9$ germanate in the solutions with 20% KOH and an elevated content of germanium atoms in the structure (*M* : *T* ratio increases from 1 : 2 to 1 : 3) is ensured by free $[\text{Ge}(\text{OH})_4]^{0-}$ tetrahedra modifying the *MT* chain and representing the tetrahedra linking SSU precursors.

With a decrease in the KOH concentration to 5 and 10%, the joint crystallization of $\text{K}_2\text{ZrGe}_3\text{O}_9$ and alkali

free $ZrGeO_4$ germanate with a new type of cyclic four-membered polyhedral SSU precursor takes place (without participation of K atoms and with an increase in the coordination number of Zr atoms from 6 to 8 and the preservation of the tetrahedral coordination of Ge atoms).

The model of the matrix assembly of the crystal structure of the $K_2ZrGe_2O_7$ germanate is applicable to the representatives of three crystallochemical families: alkali silicates (germanates) and phosphates (arsenates) with the chemical composition $A_2MT_2O_7$ and $M(4+) = Si, Zr, Hf, M(2+) = Mn, Cd, Ca, Sr, Ba$, and $A = Na, K, Rb, Cs$. The complementary assembly of the structures from cyclic SSU precursors proceeds very quickly because of the coincidence of the MT composition, M_2T_4 , of the SSU precursor and the MT_2 framework.

ACKNOWLEDGMENTS

The author is grateful to L.N. Demianets for discussion of the results and V.A. Blatov for supplying us with the TOPOS 3.2 package of programs. This study was supported by the Russian Foundation for Basic Research, project no. 02-02-16861.

REFERENCES

1. N. A. Nosyrev, L. N. Dem'yanets, V. V. Ilyukhin, *et al.*, *Kristallografiya* **19** (2), 432 (1974) [*Sov. Phys. Crystallogr.* **19**, 271 (1974)].
2. G. D. Ilyushin and L. N. Demianets, in *Proceedings of 4th International Symposium on Hydrothermal Reactions* (Nancy, 1993), p. 95.
3. P. Pertierra, M. A. Salvado, S. Garcia-Granda, *et al.*, *J. Solid State Chem.* **148** (1), 41 (1999).
4. A. N. Chernov, B. A. Maksimov, V. V. Ilyukhin, and N. V. Belov, *Dokl. Akad. Nauk SSSR* **193** (6), 1293 (1970) [*Sov. Phys. Dokl.* **15**, 711 (1970)].
5. D. Henshaw, *Miner. Mag.* **30** (2), 585 (1955).
6. S. Fleet, *Z. Kristallogr.* **121** (5–6), 349 (1965).
7. G. D. Ilyushin, *Neorg. Mater.* **29** (7), 971 (1993).
8. G. D. Ilyushin, Z. V. Pudovkina, A. A. Voronkov, *et al.*, *Dokl. Akad. Nauk SSSR* **257** (3), 608 (1982) [*Sov. Phys. Dokl.* **26**, 257 (1982)].
9. G. D. Ilyushin and L. N. Demianets, in *Crystal Growth*, Ed. by E. I. Givargisov and A. M. Melnikova (Consultant Bureau, New York, 1996), Vol. 20, p. 89.
10. G. D. Ilyushin and L. N. Dem'yanets, *Neorg. Mater.* **38** (6), 739 (2002).
11. S. R. Jale, A. Ojo, and F. R. Fitch, *Chem. Commun.*, No. 5, 411 (1999).
12. D. M. Poojary, A. I. Bortun, L. N. Bortun, and A. Clearfield, *Inorg. Chem.* **36** (14), 3072 (1997).
13. P. Ferreira, A. Ferreira, J. Rocha, *et al.*, *Chem. Mater.* **13** (2), 355 (2001).
14. G. D. Ilyushin and L. N. Dem'yanets, *Tetravalent Metal Germanates* (VINITI, Moscow, 1989) [in Russian].
15. G. D. Ilyushin and L. N. Dem'yanets, *Physics of Crystallization* (Fizmatlit, Moscow, 2002), pp. 92–184 [in Russian].
16. G. D. Ilyushin and L. N. Dem'yanets, *Zh. Neorg. Khim.* **47** (9), 1480 (2002).
17. G. D. Ilyushin and B. A. Blatov, *Acta Crystallogr., Sect. B: Struct. Sci.* **58** (2), 198 (2002).
18. G. D. Ilyushin, B. A. Blatov, and Yu. A. Zakutkin, *Acta Crystallogr., Sect. B: Struct. Sci.* **58** (6), 948 (2002).
19. B. N. Litvin and V. I. Popolitov, *Hydrothermal Synthesis of Inorganic Compounds* (Nauka, Moscow, 1984) [in Russian].
20. G. D. Ilyushin and L. N. Dem'yanets, *Hydrothermal Synthesis and Growth of Single Crystals* (Nauka, Moscow, 1982), pp. 229–243 [in Russian].
21. International Center for Diffraction Data (ICDD), *Acta Crystallogr., Sect. B: Struct. Sci.* **58**, 333 (2002).
22. Inorganic Crystal Structure Database (ICSD), *Acta Crystallogr., Sect. B: Struct. Sci.* **58**, 364 (2002).
23. *International Table for X-ray Crystallography*, Vol. 1: *Symmetry Groups*, Ed. by N. F. M. Henry and K. Lonsdale (Kynoch, Birmingham, 1952).
24. V. A. Blatov, A. P. Shevchenko, and V. N. Serezhkin, *J. Appl. Crystallogr.* **33** (4), 1193 (2000).
25. G. D. Ilyushin, *Kristallografiya* **34** (4), 846 (1989) [*Sov. Phys. Crystallogr.* **34**, 506 (1989)].
26. A. A. Voronkov, R. G. Sizova, V. V. Ilyukhin, and N. V. Belov, *Kristallografiya* **18** (1), 112 (1973) [*Sov. Phys. Crystallogr.* **18**, 67 (1973)].
27. F. C. Hawthorne, *Am. Mineral.* **70** (5–6), 455 (1985).
28. G. D. Ilyushin, *Kristallografiya* **48** (6), 1117 (2003) [*Crystallogr. Rep.* **48**, 1047 (2003)].
29. G. D. Ilyushin, *Simulation of Self-Organization Processes in Crystal-Forming Systems* (URSS, Moscow, 2003) [in Russian].

Translated by L. Man

**CRYSTAL
GROWTH**

On Calculation of the Transformation Kinetics for Models with the Diffusional Law of Growth of New-Phase Precipitates

M. P. Shepilov

Vavilov State Optical Institute, Birzhevaya liniya 12, St. Petersburg, 199034 Russia

e-mail: nitiom@goi.ru

Received March 1, 2004

Abstract—A method of calculation of the transformation kinetics for the geometric probability model with continuous nucleation and diffusional growth of new-phase precipitates is described. Previously, this method made it possible to calculate very exactly (with a level of error no greater than 0.00011) the evolution of the volume fraction of the non-transformed phase. It is shown that the upper bounds for the volume fraction of the nontransformed phase published recently for this model are much less accurate. The theoretical basis of the proposed calculation method is discussed. © 2005 Pleiades Publishing, Inc.

The geometric probability model of crystallization was proposed by Kolmogorov [1]. We will refer to it as the K model. Within this model, Kolmogorov derived a formula that exactly describes the dependence of the volume fraction q of the noncrystalline phase on time t . A rigorous and detailed analysis of the K model is given in the monograph of Belen'kiĭ [2]. This monograph provides an excellent basis for understanding the geometric probability description of phase transformations and is frequently cited below.

Let us discuss the geometric probability model with the diffusional law of crystal growth (we will refer to it as the D model), which is one of the most important models of such kind [2, 3]. It is based on the following assumptions [2]: (i) crystallization occurs in an infinite medium; (ii) the nucleation of crystals in the noncrystallized region obeys the Poisson law with the nucleation rate $\alpha(t)$ ($\alpha(t) = 0$ at $t < 0$); (iii) nuclei have a spherical shape before they undergo impacts and the growth cessation occurs in the radial directions passing through the impact points; and (iv) the radius of growing crystals follows the diffusional law

$$R(t_1, t) = \sqrt{g(t-t_1)}, \quad (1)$$

where t_1 and t are the times of nucleation and observation, respectively.

According to Eq. (1), the crystals nucleated at different times have different growth rates at time t . This is a specific feature of the D model in contrast to the K model.

Let us treat $q(t)$ as the probability for a randomly chosen point X to be in the noncrystallized region by a time t [1]. Using the terminology of [2], we refer to an aggressor as the crystal nucleated at time t_1 ($0 \leq t_1 < t$) that is able to crystallize the point X before time t provided there are no obstacles. The spatial region occupied at a time t by the crystal nucleated at the time t_1 at

the point X will be denoted as $Z(X, t_1, t)$ and the volume of this region will be denoted as $V(t_1, t)$. It was shown in [2] that the region $Z^*(X, t_1, t)$ of possible nucleation of an aggressor at the time t_1 is obtained by the inversion of the region $Z(X, t_1, t)$ with respect to the point X and has the volume $V(t_1, t)$.

Belen'kiĭ demonstrated that the following two statements are valid for the K model. They play the key role in the derivation of the Kolmogorov formula.

Statement 1. The nucleation of an aggressor inevitably causes the crystallization at a point X before time t ; i.e., a non-aggressor cannot shield the point X from the aggressor.

Statement 2. It follows from the condition of the absence of aggressors before the time t_1 that the region of possible nucleation of an aggressor at the time t_1 is not crystallized.

Statement 1 was proved in [2] for the general D model, in which similarly oriented crystals of a specified convex shape grow according to the diffusional law. It was noted in [4] that the proof reported in [2] is incomplete, and an example was given to demonstrate the violation of Statement 1 for the general D model.

However, for the D model with spherical crystals considered here, Statement 1 was proved [4]. The validity of Statement 1 means that the probability $q(t)$ for the point X to be noncrystallized by the time t is the probability of the absence of nucleation for the aggressor. Let $\mu(t_1, t)dt_1$ be the conditional probability of nucleation for the aggressor in the time interval $[t_1, t_1 + dt_1]$ if no aggressor nucleation occurred before the time t_1 . Then, we obtain

$$q(t) = \exp \left[- \int_0^t dt_1 \mu(t_1, t) \right]. \quad (2)$$

In our opinion, the derivation of formula (2) given in [2] is incorrect (see [5]). Therefore, we used another method to derive Eq. (2) [5].

According to its definition, $\mu(t_1, t)$ is calculated in the absence of any aggressors before the time t_1 . In the case of the K model, this condition ensures the absence of crystalline phase in the region of possible nucleation of an aggressor at the time t_1 (Statement 2) and Eq. (2) transforms into the Kolmogorov formula.

If Statement 2 is invalid, the crystalline phase of non-aggressors can penetrate the region $Z^*(X, t_1, t)$ of possible nucleation of an aggressor. In other words, there is a certain probability that the points in this region will fall into the crystalline phase. This reduces the probability of the nucleation of an aggressor. Let us introduce an unknown function $q_1(\mathbf{r}_1, t_1)$ defined as the probability that the point \mathbf{r}_1 of possible nucleation of an aggressor ($\mathbf{r}_1 \in Z^*(X, t_1, t)$) is not crystallized by the time t_1 provided that at previous time points t_2 ($t_2 < t_1$) the nucleation of an aggressor, i.e., a crystallite in the region $Z^*(X, t_2, t)$, does not occur. The dependence of $q_1(\mathbf{r}_1, t_1)$ on t is implied. Then, the product of the probability $q_1(\mathbf{r}_1, t_1)$ for the point \mathbf{r}_1 to be in the noncrystallized region and the probability $\alpha(t_1)d^3\mathbf{r}_1dt_1$ for the nucleation of a crystal in a noncrystallized volume element $d^3\mathbf{r}_1$ in the time interval $[t_1, t_1 + dt_1]$ gives the probability of nucleation of an aggressor in the absence of aggressors at the previous times. Integrating this probability over the volume of the region $Z^*(X, t_1, t)$, we find the desired conditional probability $\mu(t_1, t)dt_1$. Substituting it into Eq. (2), we obtain the formula

$$q(t) = \exp \left[- \int_0^t dt_1 \alpha(t_1) \int_{Z^*(X, t_1, t)} d^3\mathbf{r}_1 q_1(\mathbf{r}_1, t_1) \right], \quad (3)$$

which is applicable to any model where Statement 1 holds true. In the case of the K model, for which Statement 2 is valid, $q_1(\mathbf{r}_1, t_1) = 1$ and the integration over the region $Z^*(X, t_1, t)$ gives its volume $V(t_1, t)$; i.e., Eq. (3) reduces to the Kolmogorov formula. If only Statement 1 is fulfilled in a model, Eq. (3) contains an unknown function $q_1(\mathbf{r}_1, t_1)$. Using the D model as an example, we will demonstrate below that this formula can provide upper and lower bounds for $q(t)$.

In the D model, the region where the nucleation of an aggressor is possible at the time t_1 is a sphere $S_1(X, t_1, t)$ with the radius $R(t_1, t)$ (see Eq. (1)) centered at the point X (see the paragraph where the definition of an aggressor is given). Any crystal nucleated within this sphere at the time t_1 will crystallize the material at the point X before the time t . It is easy to show that the maximum penetration of the crystalline phase of a non-aggressor into the sphere $S_1(X, t_1, t)$ ($t_1 \in [0, t]$) occurs for the non-aggressor that nucleates at $t_1 = 0$ at the surface of the sphere $S_1(X, 0, t)$, i.e., at the distance $r_1 =$

\sqrt{gt} from the point X . The minimum distance from the point X to the crystallization front (surface) of such a crystal at the time t_1 is equal to

$$R_2(t_1, t) = \sqrt{gt} - \sqrt{gt_1}. \quad (4)$$

This means that the crystalline phase of non-aggressors does not penetrate into the sphere $S_2(X, t_1, t)$ with the radius $R_2(t_1, t)$ and can penetrate into the spherical layer $S_3(X, t_1, t) = S_1(X, t_1, t) - S_2(X, t_1, t)$; i.e.,

$$q_1(\mathbf{r}_1, t_1) = 1 \quad \text{at} \quad \mathbf{r}_1 \in S_2(X, t_1, t) \\ \text{and} \quad q_1(\mathbf{r}_1, t_1) \leq 1 \quad \text{at} \quad \mathbf{r}_1 \in S_3(X, t_1, t). \quad (5)$$

Using Eq. (5), we can represent Eq. (3) for the D model in the form

$$q(t) = \exp \left\{ - \int_0^t dt_1 \alpha(t_1) \right. \\ \left. \times \left[V_2(t_1, t) + \int_{S_3(X, t_1, t)} d^3\mathbf{r}_1 q_1(\mathbf{r}_1, t_1) \right] \right\}, \quad (6)$$

where $V_2(t_1, t)$ is the volume of the sphere with the radius $R_2(t_1, t)$ given by Eq. (4).

If we replace $q_1(\mathbf{r}_1, t_1)$ in Eq. (6) by its upper (lower) bound, we can find the lower (upper) bound for $q(t)$. The simplest estimates could be found if we take into account that $0 \leq q_1(\mathbf{r}_1, t_1) \leq 1$ in accordance with the probability definition. Replacing in [6] $q_1(\mathbf{r}_1, t_1)$ by unity, we obtain

$$q(t) \geq \exp \left[- \int_0^t dt_1 \alpha(t_1) V(t_1, t) \right] \equiv Q_1(t). \quad (7)$$

The expression for $Q_1(t)$ is equivalent to the Kolmogorov formula, but in the D model this expression gives the lower bound for $q(t)$, in contrast to the K model. The substitution of zero instead of $q_1(\mathbf{r}_1, t_1)$ leads to the upper bound $Q_2(t)$ for $q(t)$. Both these bounds were found by Belen'kiĭ [2]. The interval between the two bounds turns out to be too wide and makes it impossible to characterize the behavior of $q(t)$ [6].

To refine the upper bound for $q(t)$, we can use the inequalities

$$q_1(\mathbf{r}_1, t_1) \geq q(t_1) \geq Q_1(t_1). \quad (8)$$

The left-side inequality is a consequence of the conditional character of the probability $q_1(\mathbf{r}_1, t_1)$ and the right-side one is the bound given by Eq. (7). When $\alpha(t) = \text{const}$, we can reduce by about a factor of 4 the uncertainty range for $q(t)$ as compared to the situation when we use the bound $Q_2(t)$. However, the uncertainty remains significantly large (about 0.12 at $q \approx 0.1$).

Let us now give more detailed bounds for $q_1(\mathbf{r}_1, t_1)$. In calculations of $q_1(\mathbf{r}_1, t_1)$, it is necessary to take into

account the possibility of nucleation of crystals in the region $S_{11}(t_2)$ at times t_2 ($0 \leq t_2 < t_1$). This region includes the set of points of the sphere $S_1(\mathbf{r}_1, t_2, t_1)$ not belonging to sphere $S_1(X, t_2, t)$ (according to the definition of $q_1(\mathbf{r}_1, t_1)$). Following the reasoning similar to that used in the derivation of Eq. (6), we find

$$q_1(\mathbf{r}_1, t_1) = \exp \left\{ - \int_0^{t_1} dt_2 \alpha(t_2) \left[V_{21}(t_2) + \int_{S_{31}(t_2)} d^3 \mathbf{r}_2 q_2(\mathbf{r}_2, t_2) \right] \right\} \quad (9)$$

Here, $V_{21}(t_2)$ is the volume of the region $S_{21}(t_2)$ including the set of points of the sphere $S_2(\mathbf{r}_1, t_2, t_1)$ not belonging to the sphere $S_1(X, t_2, t)$ and $S_{31}(t_2)$ is the part of the spherical layer supplementing the region $S_{21}(t_2)$ to the region $S_{11}(t_2)$. The unknown function $q_2(\mathbf{r}_2, t_2)$ is treated as the probability of the absence of crystallization at the point \mathbf{r}_2 at the time t_2 provided that crystallization did not occur at the previous times t_3 ($0 \leq t_3 < t_2$) in the regions $S_1(X, t_3, t)$ and $S_{11}(t_3)$. This condition reliably ensures that the region $S_{21}(t_2)$ is not crystallized at the time t_2 . It is necessary to take into account that $q_2(\mathbf{r}_2, t_2)$, $S_{11}(t_2)$, and so on, also depend on t , t_1 , and \mathbf{r}_1 .

Let us now find new bounds for $q(t)$ on the basis of Eqs. (6) and (9). The reasoning similar to that used in the derivation of Eq. (8) leads to the inequality $q_2(\mathbf{r}_2, t_2) \geq Q_1(t_2)$. In the left-hand side of this inequality, we take the sphere $S_1(\mathbf{r}_2, t_3, t_2)$ having the volume $V(t_3, t_2)$ as the region where a nucleation of a crystal is possible at the time t_3 , which leads to the crystallization at the point \mathbf{r}_2 by the time t_2 . It can be shown that the condition in the definition of $q_2(\mathbf{r}_2, t_2)$ makes it possible to use a two-times smaller volume in the estimation of this quantity and to find a stronger bound:

$$q_2(\mathbf{r}_2, t_2) \geq \exp \left[-0.5 \int_0^{t_2} dt_3 \alpha(t_3) V(t_3, t_2) \right]. \quad (10)$$

Substitution of the expression from the right-hand side of inequality (10) into Eq. (9) instead of $q_2(\mathbf{r}_2, t_2)$ leads to a new upper bound for $q_1(\mathbf{r}_1, t_1)$. The use of this bound in Eq. (6) leads to a new lower bound for $q(t)$, $q(t) \geq Q_3(t)$. Similarly, the bound $q_2(\mathbf{r}_2, t_2) \leq 1$ leads to a new upper bound for $q(t)$: $q(t) \leq Q_4(t)$. The problem of determining $Q_3(t)$ and $Q_4(t)$ involves the calculation of some integrals. Note that even in the case of a simple dependence $\alpha(t)$ it is not possible to avoid the double numerical integration. Here, we should pay special attention to the choice of integration steps to obtain sufficiently exact results.

For the most interesting case of the constant nucleation rate, $\alpha = \text{const}$, we performed calculations [6] (see table) using the dimensionless time $t_0 = \alpha^{2/5} g^{3/5} t$. It can

Upper and lower bounds of the noncrystallized volume fraction $q(t)$ for the model with the diffusional growth law (1) and with the constant nucleation rate α for crystals: $Q_1(t) \leq Q_3(t) \leq q(t) \leq Q_4(t)$ ($Q_1(t)$ corresponds to the Kolmogorov formula)

| $\alpha^{2/5} g^{3/5} t$ | $Q_1(t)$ | $Q_3(t)$ | $Q_4(t)$ |
|--------------------------|----------|----------|----------|
| 0.1 | 0.99472 | | 0.99472 |
| 0.2 | 0.97047 | | 0.97048 |
| 0.3 | 0.9207 | | 0.92082 |
| 0.4 | 0.8440 | | 0.84440 |
| 0.5 | 0.7436 | | 0.74460 |
| 0.6 | 0.6267 | 0.62872 | 0.62873 |
| 0.7 | 0.5031 | 0.50654 | 0.50657 |
| 0.8 | 0.3832 | 0.38825 | 0.38831 |
| 0.9 | 0.2760 | 0.28241 | 0.28252 |
| 1.0 | 0.1872 | 0.19456 | 0.19472 |
| 1.1 | 0.1193 | 0.12676 | 0.12696 |
| 1.2 | 0.0711 | 0.07802 | 0.07824 |
| 1.3 | 0.0396 | 0.04532 | 0.04554 |
| 1.4 | 0.0205 | 0.02483 | 0.02503 |
| 1.5 | 0.0099 | 0.01283 | 0.01299 |
| 1.6 | 0.0044 | 0.00625 | 0.00637 |
| 1.7 | 0.0018 | 0.00287 | 0.00295 |

be seen from the table that the difference between the upper and lower bounds $Q_4(t) - Q_3(t) \leq 2.2 \times 10^{-4}$, i.e., the error of approximation $q(t) \cong (Q_4(t) + Q_3(t))/2$ does not exceed 1.1×10^{-4} . It can also be seen that the error due to the use of the Kolmogorov formula does not exceed 0.0077. In addition, it was found in [6] that the Avrami exponent n [3] decreases during the crystallization from $n = 2.5$ at $q = 1$ to $n \cong 2.37$ at $q = 0.01$. The results of the calculations [6] yield an almost exact value of $q(t)$ and agree well with the results of numerical simulation [7].

Upper bounds for $q(t)$ were recently reported in [8] for the case when the growth rate of a nucleus decreases with an increase in the age of nuclei. For the D model with $\alpha = \text{const}$, the maximum difference between the determined upper bound and the values calculated using the Kolmogorov formula (the maximum uncertainty in the determination of $q(t)$) was 1.4×10^{-2} and 2.2×10^{-2} in two- and three-dimensional cases, respectively. The accuracy of these bounds is much lower than that of both analytical bounds [6] and the bounds following from the numerical simulation of $q(t)$ performed for the three- [7] and two-dimensional [9] D models.

To guarantee the rigorous applicability of the methods considered in [8] and in this paper, Statement 1 should be valid. As far as the models with the diffusional crystal growth are concerned, Statement 1 was proved only in the case of spherical crystals obeying the

growth law given by Eq. (1) [4]. This issue was not discussed in [8], although the applicability range of the suggested method is considered to be quite wide: from growth laws more general than Eq. (1) to the case of an arbitrary shape of crystals.

Putting aside the problem of validity for Statement 1, we can argue that our model can be applied without any fundamental changes to the cases when the growth rate decreases with an increase in the age of the crystal. Moreover, it was applied to such a model characterized by a finite size of the critical nucleus [10]. The calculations demonstrated that the bounds $Q_3(t)$ and $Q_4(t)$ can be more or less accurate depending on the parameters of the model. When the interval between these bounds is considerably large, the results of numerical simulation for $q(t)$ [11] are close to $(Q_4(t) + Q_3(t))/2$.

One of the applications for the results obtained is the description of the nucleation kinetics for particles during the phase separation in glasses [12, 13].

In conclusion, on the basis of the rigorous analysis of the crystallization model characterized by the diffusional crystal growth, we presented a method which allowed us to perform nearly exact calculations of the kinetics of phase transformations within this model.

ACKNOWLEDGMENTS

This study was supported by the Program of the President of the Russian Federation for the Support of Leading Scientific Schools, grant no. NSh-1405.2003.3, and the Russian Foundation for Basic Research, project no. 04-03-32657.

REFERENCES

1. A. N. Kolmogorov, *Izv. Akad. Nauk SSSR, Ser. Mat.*, No. 3, 355 (1937).
2. V. Z. Belen'kiĭ, *Geometric Probabilistic Models of Crystallization: Phenomenological Approach* (Nauka, Moscow, 1980) [in Russian].
3. J. W. Christian, *The Theory of Transformations in Metals and Alloys* (Pergamon, Oxford, 1975; Mir, Moscow, 1978).
4. M. P. Shepilov, *Fiz. Khim. Stekla* **24** (6), 780 (1998) [*Glass Phys. Chem.* **24**, 557 (1998)].
5. M. P. Shepilov and D. S. Baik, *J. Non-Cryst. Solids* **171** (2), 141 (1994).
6. M. P. Shepilov, *Fiz. Khim. Stekla* **12** (1), 110 (1986).
7. M. P. Shepilov and V. B. Bochkarev, *Kristallografiya* **32** (1), 25 (1987) [*Sov. Phys. Crystallogr.* **32**, 11 (1987)].
8. N. V. Alekseechkin, *Kristallografiya* **48** (4), 760 (2003) [*Crystallogr. Rep.* **48**, 707 (2003)].
9. V. B. Bochkarev and M. P. Shepilov, *Kristallografiya* **33** (6), 1516 (1988) [*Sov. Phys. Crystallogr.* **33**, 902 (1988)].
10. M. P. Shepilov, *Fiz. Khim. Stekla* **13** (5), 791 (1987) [*Glass Phys. Chem.* **21**, 161 (1995)].
11. V. B. Bochkarev and M. P. Shepilov, *Fiz. Khim. Stekla* **14** (2), 284 (1988).
12. M. P. Shepilov, *Fiz. Khim. Stekla* **21** (2), 137 (1995).
13. M. P. Shepilov, *J. Non-Cryst. Solids* **208** (1–2), 64 (1996).

Translated by K. Kugel

CRYSTALLOGRAPHIC SOFTWARE

Division of Hydrate Frameworks into Cavities

E. V. Grachev and Yu. A. Dyadin[†]

*Institute of Inorganic Chemistry, Siberian Division, Russian Academy of Sciences,
pr. Akademika Lavrent'eva 3, Novosibirsk, 630090 Russia*

e-mail: grachev@che.nsk.su

Received June 12, 2003; in final form, October 8, 2003

Abstract—The algorithms for analysis of shape and size of a cavity in a hydrate framework are considered. As an example, the framework structure of cubic structure II is analyzed. © 2005 Pleiades Publishing, Inc.

INTRODUCTION

There exists a wide class of clathrate hydrates [1] in which water molecules linked by hydrogen bonds form a three-dimensional framework with various cavities occupied by “guest” molecules. In some hydrate structures, the atoms of guest molecules may also take part in framework formation. At present, the following types of hydrate frameworks are known: cubic structures I and II; hexagonal structures I, II, and III; tetragonal structures I, II, and III; and the orthorhombic structure. Analysis of these structures showed the presence of *D*, *D'*, *T*, *H*, *P*, and *E* cavities. All these structures and the respective cavities are considered in detail in [2]. Recently, tetragonal structure IV with a cavity of an unknown type has also been discovered [3]. However, it seems that the structural types are not limited to the ones mentioned above. Thus, there exist eight compounds with different stoichiometries in the $\text{Bu}_4\text{NH}(\text{CH}_2)_{10}\text{CO}_2/\text{H}_2\text{O}$ system whose structures are still unknown [4]. The structures have complicated frameworks and, therefore, the division of these frameworks into cavities is a rather labor- and time-consuming process. Analysis of hydrate structures is also complicated by ordering of the guest component and possible formation of superstructures [2]. Since the discovery of new hydrate structures has not been completed as yet, one constantly encounters the problem of their analysis. The present study is aimed at designing software which would allow one to use the crystallographic data on the frameworks of hydrate structures and perform the automatic division of these frameworks into cavities to facilitate analysis of all types of cavities in these frameworks.

It should be indicated that all the developed algorithms are valid for a hydrate framework in which each molecule is linked to four neighboring molecules by hydrogen bonds. The algorithm becomes invalid for

hydrate structures whose frameworks do not possess this property.¹

SOME NECESSARY DATA FROM THE GRAPH THEORY

The algorithms designed are based on construction of graphs [5]. Let us introduce some definitions.

Definition 1. A simple graph—or simply a graph—is a set of points V and a set of edges E such that each edge connects two points of the set V . A graph with the set of vertices V and a set of edges E is denoted as $G(V, E)$. If $V_1 \subset V$ and $E_1 \subset E$, the graph $G(V_1, E_1)$ is called a subgraph of the graph $G(V, E)$. If the edge $e \in E$ connects the vertices $v_1, v_2 \in V$, we write that $e = (v_1, v_2)$.

Definition 2. A path between the vertices v_1 and v_n is a set of edges e_1, e_2, \dots, e_{n-1} such that $e_1 = (v_1, v_2)$, and $e_2 = (v_2, v_3), \dots, e_{n-1} = (v_{n-1}, v_n)$. This path is often denoted as v_1, v_2, \dots, v_n . A path is called simple if all the vertices entering it are different, the only possible exception being the first and last vertices. A simple path in which the first and last vertices coincide is called a simple cycle. It should be noted that each face of a certain cavity is a simple cycle. This fact is used in the algorithms for cavity construction.

Definition 3. A graph with any two vertices that are connected by a certain path is called a connected graph. To check the graph connectedness, it is sufficient to check the possibility of connecting by a path any vertex of the graph with all the remaining vertices.

Definition 4. If two graph vertices are connected by an edge, these vertices are called adjacent. For a given vertex $v \in V$, the number of vertices adjacent to it is called the vertex degree. If the degrees of all the graph vertices are equal, the graph is called regular.

¹ The algorithms described here are applicable not only to hydrate frameworks but also for other frameworks possessing this property, for example, for the framework built from SiO_2 molecules.

[†] Deceased

Definition 5. The maximum connected subgraph of a certain graph is called a connected graph component. The subgraph maximality is understood in the sense that it is impossible to add even a single vertex to the subgraph without breaking its connectedness.

Definition 6. A graph edge is called a bridge if its removal increases the number of the connected components.

Definition 7. In 1741, the famous mathematician L. Euler solved the problem formulated as follows. It is necessary to go out from a certain graph vertex, pass all its edges once, and return to the initial vertex. This graph circuit is called Euler's circuit.

Euler's theorem. If a graph is to have an Euler's circuit, it is necessary and sufficient that this graph is connected and that the degrees of each of its vertices are even.

Now, consider a hydrate framework and construct on its basis a graph in such a way. Let the molecules forming the framework play the role of graph vertices.² Two graph vertices can be connected by an edge if and only if the corresponding molecules form a hydrogen bond. Now, the conditions imposed onto the framework may be formulated in terms of the graph theory in the following way:

- (1) A framework should form a connected graph.
- (2) The degree of each framework vertex should be 4.

The fulfillment of the above conditions is a necessary but not sufficient condition for constructing cavities. The sufficient condition is formulated in such a way: a hydrate framework should be a union of closed polyhedra.

PROBLEM FORMULATION

The problem of hydrate-framework division into cavities is formulated in terms of the graph theory in the following way. There exists a graph with vertices set by the coordinates of the points in a space and satisfying conditions (1) and (2). It is necessary to construct all the closed polyhedra with the vertices located at the given points.

ALGORITHMS

The problem of framework division into cavities is solved using the following three algorithms:

- (1) an algorithm for constructing edges,
- (2) an algorithm for constructing faces,
- (3) an algorithm for constructing cavities.

Algorithms (1) and (2) are performed only once. Algorithm (3) is iterated several times until all the cavities are constructed.

² For water molecules, the graph vertex is set in the center of the oxygen atom, and for a monatomic molecule, in the center of the respective atom.

ALGORITHM FOR CONSTRUCTING EDGES

It is well known that, in hydrate structures, the distance between oxygen atoms forming hydrogen bonds varies from 2.3 to 3.3 Å [6]. Knowing the coordinates of the atoms forming the framework, one may calculate the distances between all the atomic pairs. A pair of atoms will be connected by an edge if and only if the distance between these atoms is less than a certain given value.

ALGORITHM FOR CONSTRUCTING FACES

As was indicated above, each face of a cavity is a simple cycle. However not every simple cycle of a framework is a cavity face. One has to bear in mind the following. Each vertex of the framework is adjacent to four edges. Each of these four edges belongs to different faces of certain cavities. Each pair of adjacent edges belongs to one and only to one face of a certain cavity. Now, let us construct a minimum simple cycle containing these edges for each pair of adjacent edges. To avoid the construction of the same face several times, it is necessary to label all the pairs of adjacent edges which enter the face constructed. Now, consider a still-unlabeled pair of adjacent edges and construct a new face on its basis. This process is continued until all the pairs of adjacent edges become labeled, which signifies that the process of face construction is completed. We say that two faces are of the same type if they have the same number of edges.

ALGORITHM FOR CONSTRUCTING CAVITIES

Let the algorithm for constructing faces be performed. Two faces are called adjacent if they share one edge. It should be noted that each face belongs to two cavities, but any two adjacent faces belong only to one cavity. Thus, a certain cavity can be constructed on the basis of two adjacent faces.

Consider two adjacent faces and add to them new faces to construct a cavity in the following way. Let several faces be already added. Now add any face still not considered to the already existing faces if and only if this face is adjacent to any pair of the already-added adjacent faces but along different edges. The cavity is considered to be constructed no more faces can be added. To check whether the cavity thus constructed is a closed polygon, it is sufficient to check whether each edge of the cavity belongs only to two faces. After the completion of the cavity construction, we have to label each pair of the adjacent faces of this cavity. Then an unlabeled pair of adjacent faces is taken to construct a new cavity. The process is continued until all the pairs of adjacent faces are labeled. Then the process of framework division into cavities is considered to be complete.

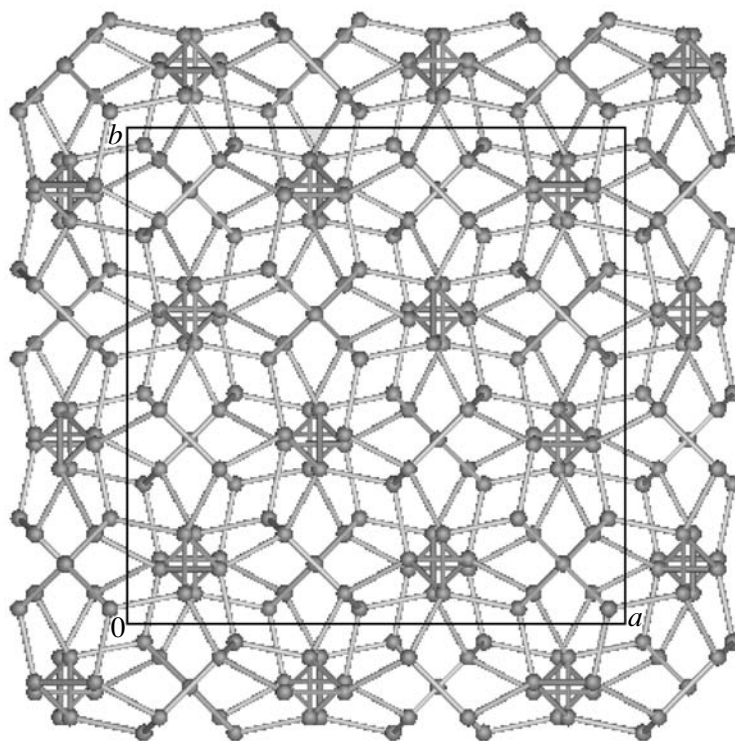


Fig. 1. Cubic structure II projected onto the (001) plane.

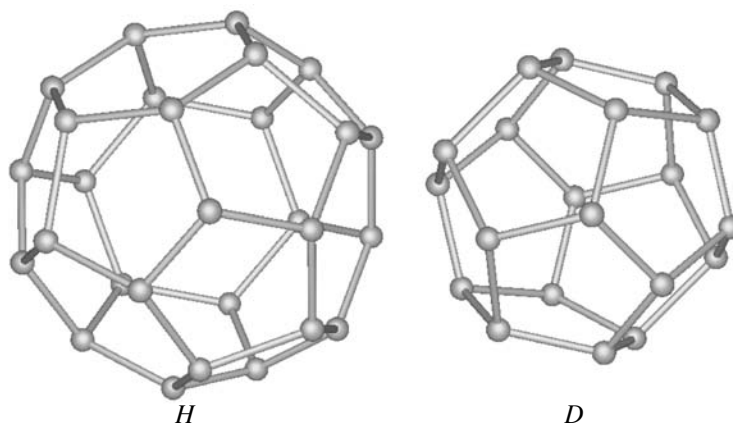


Fig. 2. Cavities *H* and *D* in cubic structure II.

CALCULATION OF POSITIONS OF HYDROGEN ATOMS

The user may calculate one of the variants of the arrangement of hydrogen atoms in a hydrate complex. The formulation of the problem reduces to the following: to calculate positions of hydrogen atoms in such a way that each oxygen atom is linked with two hydrogen atoms and each bond has only one hydrogen atom.

This problem is solved with the aid of Euler's circuit of the graph. When going out of a vertex, we shall attach to it a hydrogen atom. Using Euler's circuit, we go out of each vertex twice and enter this vertex again also twice. Thus, two hydrogen atoms are attributed to each oxygen atom. Since in Euler's circuit all the edges are passed only once, each bond will be occupied only by one hydrogen atom.

Euler's theorem ensures that a hydrate complex satisfying conditions (1) and (2) has Euler's circuit; how-

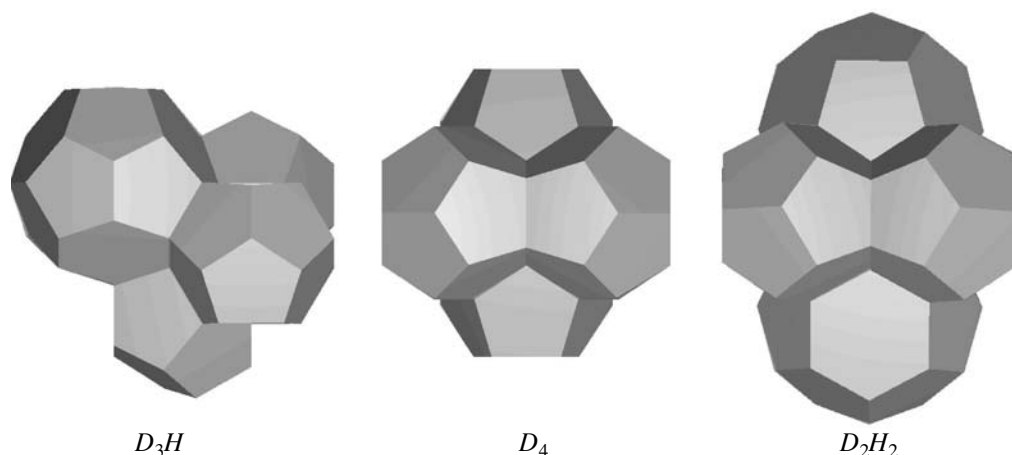


Fig. 3. Four-section cavities D_3H , D_4 , and D_2H_2 in cubic structure II.

ever, it gives no ideas about the algorithm of its implementation. The algorithm for constructing such a circuit reduces to the following.

Let us start the circuit with an arbitrary vertex v . Assume that we have already passed several graph edges and now are at the vertex u . After the removal from the graph of the already passed edges, we arrive at the subgraph G' . Now, let us find for the vertex u in the graph G' such an adjacent edge e which is not a bridge. Then continue our motion along the edge e . The algorithm is considered to be complete when all the graph edges have been passed.

Note. The above algorithm yields a certain random distribution of hydrogen atoms in a hydrate structure. This distribution may be modified in such a way that it will have a certain physical meaning; e.g., that the dipole moment of the structure will be close to zero. It is very difficult to sort all the variants of the arrangement of hydrogen atoms. (Theoretically, such a procedure is possible but requires sorting of a large number of variants. Thus, for a D cavity built by 20 water molecules, there are 3 600 000 possible variants of arrangement of hydrogen atoms [7].) However, it is possible to select a sufficiently large number of such variants and choose from them the variant with the minimum dipole-moment modulus.

DESCRIPTION OF THE PROGRAM

The above algorithms underlie the program Cavities. The program reads the unit-cell parameters a , b , c , α , β , and γ of a hydrate structure and the coordinates of the atoms forming the hydrate framework which are stored in a file in the Shexls form.

The program divides the hydrate framework into cavities and outputs following information for each cavity:

- the coordinates of atoms forming the cavity,
- the number of faces and vertices in the cavity,

- the coordinates of the cavity center, the cavity volume (i.e., the volume of a polyhedron forming the cavity), and

- the free volume of the cavity (i.e., polyhedron volume minus the volume of the molecules located inside the cavity).

For each type of face forming the cavity, the program outputs the number of edges of each face and the number of faces of each type.

The possible options are:

- output only of the information on the cavities whose centers are located inside the unit cell of the crystal,
- output only of the information about the cavities of different types,
- calculation of the positions of hydrogen atoms for each cavity,
- output of the list of adjacent cavities,
- output of the information on the multisection cavities.³

The program is appropriated for the operation systems Windows 95, Windows 98, and Windows NT.

The program was tested on six well-known structures of clathrate hydrates. These are cubic structures I and II, tetragonal structures I and II, hexagonal structure III, and the orthorhombic structure [1].

As an example, we consider here the structure of cavities in cubic structure II [1, 8]. Figure 1 shows this structure projected onto the (001) plane. The structure consists of 8 polyhedra faceted with 16 faces (the so-called H cavities) and 16 polyhedra faceted with 12 faces (D cavities). An H cavity is formed by 4 regular hexagons and 12 pentagons, and a D cavity is formed by 12 pentagons. The volume of the H cavity equals 308.62 \AA^3 and the volume of the D cavity equals 156.56 \AA^3 . It is well known that the average volumes of

³ Separation of multisection cavities is important, e.g., for selecting the "host" framework in hydrates of quaternary ammonium salts.

these cavities are 290 and 168 Å³, respectively [2]. Thus, the volume of the *H* cavity in cubic structure II is somewhat higher and the volume of the *D* cavity is somewhat lower than their average volumes. Figure 2 schematically depicts these cavities. The study of this structure shows that it contains three types of four-section cavities: *D*₃*H*, *D*₄, and *D*₂*H*₂ cavities (Fig. 3).

REFERENCES

1. Yu. A. Dyadin, K. A. Udachin, and I. V. Bondaryuk, *Clathrate Compounds* (Novosib. Gos. Univ., Novosibirsk, 1988) [in Russian].
2. Yu. A. Dyadin and K. A. Udachin, *Zh. Strukt. Khim.* **28** (3), 75 (1987).
3. A. V. Kurnosov, A. Yu. Manakov, V. Yu. Komarov, *et al.*, *Dokl. Akad. Nauk* **381** (5), 649 (2001).
4. Yu. A. Dyadin and L. S. Aladko, *Mendeleev Commun.*, No. 6, 239 (1995).
5. V. A. Emelichev, O. I. Mel'nikov, V. I. Sarvanov, and R. I. Tyshkevich, *Lectures on Graph Theory* (Nauka, Moscow, 1990) [in Russian].
6. G. A. Jeffrey, *An Introduction to Hydrogen Bonding* (Oxford Univ. Press, New York, 1997).
7. M. V. Kirov, *Zh. Strukt. Khim.* **37** (1), 98 (1996).
8. R. K. McMullan and A. Kvick, *Acta Crystallogr., Sect. B: Struct. Sci.* **46**, 390 (1990).

Translated by L. Man

CRYSTALLOGRAPHIC
SOFTWARE

Program for Analysis of Intermolecular Contacts in Organic Crystals

P. M. Zorkii and A. A. Stukalin

Moscow State University, Vorob'evy gory, Moscow, 119992 Russia

e-mail: PMZorky@phys.chem.msu.ru

Received December 29, 2003

Abstract—The ICA (Intermolecular Contacts Analysis) computer program was developed for statistical analysis of intermolecular atom–atom contacts in organic crystals. At present, the program allows one to examine homomolecular crystals belonging to monosystem structural classes. The analysis involves the following steps: selection of supporting contacts (i.e., contacts sufficient for the formation of a three-dimensional framework of intermolecular “touches”), construction of their distributions over atom–atom distances, approximation of the distribution curves by Gaussians, and calculations of the average (most probable) length of the contacts of a particular type and the variance of the distribution. The van der Waals radii of the most important organogenic elements were refined on the basis of the data on approximately 7800 crystal structures retrieved from the Cambridge Structural Database. © 2005 Pleiades Publishing, Inc.

INTRODUCTION

According to the theory of close packing of molecules [1, 2], whose first postulate [3], in fact, justifies the concept of a van der Waals radius (WR) [4], each molecule in an organic crystal forms supporting contacts, thus providing a stable equilibrium arrangement of molecules in the space. It should be emphasized that the sum of the van-der-Waals radii of the corresponding atoms ($R_X + R_Y$) or twice the geometric mean of these radii $2\sqrt{R_X R_Y}$ has a sense of the most probable interatomic distance, but only for supporting [4] van-der-Waals atom–atom contacts. Therefore, the correct evaluation of WRs requires two necessary conditions to be met. First, WR can be determined only by averaging based on statistical processing of experimental crystallographic data for numerous crystal structures. Second, to determine the optimal WRs, only the distances r_{ij} corresponding to supporting atom–atom contacts must be used. This requires a thorough selection of only those contacts that are actually supporting.

However, the first condition was not satisfied in all early determinations of WRs [1, 2, 5, 6] (optimal WRs were estimated on the basis of very limited structural data). Although extensive data retrieved from the Cambridge Structural Database (CSD) were used in [7, 8], the second condition was ignored in these studies. A reliable procedure for selecting supporting contacts and a statistical approach were used in [9], but the crystallographic data on only several tens of structures were analyzed, which is obviously inadequate to solve this problem. Thus, in fact, reliable information on the optimal van-der-Waals radii of organogenic elements has been lacking.

In this study, we describe the ICA (Intermolecular Contacts Analysis) program for analysis of intermolecular contacts in organic crystals (using the CSD data). The program was used to determine the van der Waals radii of important organogenic elements (C, H, O, N, and Cl).

MAIN PRINCIPLES OF THE PROGRAM

The program processes successively a set of crystal structures, which are retrieved from the CSD and categorized according to structural classes [10]. Recall that a structural class is a set of structures belonging to a particular space group, in which molecules (more precisely, their centers of mass) occupy one or several particular systems of equivalent positions (orbits).

A list of structural classes is formed by a user and introduced as a sequence of folders containing data on the structures belonging to the chosen structural classes. Each folder contains characteristics of a particular structural class and a sequence of files. Each file corresponds to a particular entry in the SCD, i.e., to a crystalline compound studied under certain conditions (in accordance with the data from a particular X-ray diffraction study), and is characterized by a refcode [11] and an empirical formula of the chemical compound. A set of folders (together with their content) formed for an investigation is called the main data array.

The program consists of several steps, which are specified by a user and include the following subroutines.

Step 1 involves a test for completeness of the data on the coordinates of the atoms present in the crystal tak-

ing into account the empirical formula and a test for the presence (or the absence) of partial disorder in the crystal. This step can also involve checking the files for particular additional criteria.

Step 2 involves a check for the compliance of the files with the following characteristic parameters specified in accordance with the purpose of the investigation:

(1) elemental compositions of chemical compounds;

(2) a class of chemical compounds and the presence of particular molecular fragments or functional groups;

(3) exclusion of duplicate data (the corresponding criteria are specified: for example, analyses performed at different temperatures, similar results obtained by different authors, and so on);

(4) selection of files according to the criteria that are of interest for a particular study (for example, the number of atoms in molecules), selection of low-temperature studies, and so on.

In steps 1 and 2, the main data array for the investigation is refined (corrected). The conditions accepted for the investigation are stored in the starting file, which also includes selected calculation parameters listed below.

Step 3 involves calculations of intermolecular atom–atom distances r_{ij} and a search for supporting (structure-forming) atom–atom contacts. In the case of a monosystem crystal, i.e., a crystal, in which all molecules are symmetrically related, the i th atom belongs to the starting molecule denoted I-000, and the j th atom belongs to one of the molecules involved in the nearest environment of the starting molecule and denoted N - HKL .¹ For each I-000– N - HKL pair, r_{ij} and $\Delta r_{ij} = r_{ij} - 2\sqrt{R_i R_j}$ are calculated, where R_i and R_j are the starting WRs.² In this study, we used the van-der-Waals radii proposed in [4, 9] as the starting values. Hereinafter, these radii are referred to as WR(ZZ). Then the minimum value of Δr_{ij} (Δr_{\min}) is found for each I-000– N - HKL pair. Finally, m smallest Δr_{\min} , i.e., m supporting contacts, are selected for each compound under investigation.

¹ The rational symbols N - HKL of molecules have been described in different publications (see, for example, [10, 12]). In this symbol, the letter N (which, generally, corresponds to a Roman numeral) denotes the orientation of the molecule, and H, K, L are integers corresponding to translation shifts along the coordinate axes. By varying N and the integers H, K, L (within specified limits) permissible for a particular space group, one can consider all molecules in the vicinity of the starting molecule. The calculations are performed within a restricted area specified by the limiting values of H, K, L (they are specified as parameters in the starting file).

² One would expect it to be more reasonable to use the difference $r_{ij} - (R_i + R_j)$ to determine Δr_{ij} . However, it was demonstrated previously [4, 9] and confirmed here that more self-consistent data are obtained using twice the geometric mean. Nevertheless, the ICA program allows for the use of any of the above approaches.

The aim of step 4 is to reveal specific contacts (and, probably, erroneous atomic coordinates). Each supporting contact thus revealed is compared with the lower limit of the distances $AB(\min)$, which are considered to be allowable for a particular combination of the A and B elements in the case of a van-der-Waals (nonspecific) $A\cdots B$ contact. A set of the accepted lower limits for the lengths of $A\cdots B$ van-der-Waals contacts is specified in the starting file. If the file contains an r_{ij} distance shorter than $r_{AB}(\min)$, this file is excluded from the main data array (a correction of the data array). The files discarded in this step are stored in a special data array, which can be used for studying shortened specific intermolecular contacts (after testing for the absence of evident errors in the atomic coordinates).

In step 5, the data array of the supporting contacts is supplemented with the r_{ij} distances for which Δr_{ij} differ only slightly (by no more than δ , which is specified in the starting file and generally taken equal to 0.1 Å) from Δr_{\min} . This step can be excluded at will from the general sequence of the steps of investigation.

In the final step 6, the chosen supporting contacts are sorted by AB combinations, i.e., $C\cdots C$, $C\cdots H$, $H\cdots H$, $O\cdots O$, $C\cdots O$, $H\cdots O$, etc., contacts are distinguished. The program compiles $AB.txt$ files, which are used to plot histograms characterizing the distribution of the supporting contacts of a particular AB type and statistically process these distributions. To follow the course of investigations and record the results of calculations, a report.txt file is compiled, in which the starting (specified) parameters are stored, the calculations are recorded, and the main results are saved. A corresponding code is assigned to each investigation. This code is used to label the starting file, the $AB.txt$ file, the report.txt file, the main and special data arrays, and all histograms plotted.

In conclusion, note that an analysis of various structural classes sometimes requires the use of special subroutines. For example, an analysis of intermolecular contacts in crystals containing molecules in special positions (on inversion centers, on twofold axes, etc.) is performed with the use of a structural formula determined by a connectivity matrix. A crystal-chemical analysis of polysystem crystals also presents certain problems.

DESCRIPTION OF THE INVESTIGATIONS

In the first investigations carried out using the ICA program, we used the structural data retrieved from the Cambridge Structural Database (CSD, release 2001) and corresponding to the most well studied structural classes of homomolecular organic crystals: $P2_12_12_1$, $Z = 4(1)$, and $P2_1/c$, $Z = 4(1)$. Only structures in which disorder is absent and which are characterized by the reliability factor R lower than 0.10 were considered.

Characterization of the investigations

| Investigation | Restrictions on the elemental composition | Total number of structures | Among them | | | |
|---------------|---|----------------------------|-------------------------|------------------------------|---------------|-------------------|
| | | | with shortened contacts | erroneous or incomplete data | repeated data | used in our study |
| 1 | C, H, O | 6548 | 1492 | 1553 | 562 | 2941 |
| 2 | C, H, O, N | 8526 | 2533 | 1852 | 327 | 3814 |
| 3 | C, H, O, N, Cl | 1662 | 281 | 397 | 48 | 936 |

We performed three investigations (1–3) with the following restrictions imposed on the elemental composition:

(1) the necessary presence of C and O atoms; the presence of H atoms is permissible;

(2) the necessary presence of C and N atoms; the presence of H and O atoms is permissible;

(3) the necessary presence of C and Cl atoms; the presence of H, O, and N atoms is permissible.

As mentioned above, the aim of this study was to obtain information on the distribution of supporting contacts and the statistical values of WRs for the most important organogenic elements (C, H, N, O, and Cl). The van-der-Waals radii determined in these three investigations are denoted WR(1), WR(2), and WR(3), respectively. Selected characteristics of the data used in these investigations are given in the table.

The main aim of investigation 1 was to determine WRs(1) of carbon, oxygen, and hydrogen (using the ZZ radii as the initial approximation). In investigation 2, most attention was concentrated on the determination of WR(2) of nitrogen. However, if WR(2) of carbon, oxygen, and hydrogen differ substantially (by more than 0.01 Å) from the corresponding WR(1), it would be reasonable to repeat the procedure for choosing the optimal WRs of carbon, oxygen, and hydrogen. However, as will be shown below, we did not encounter this problem. The main aim of investigation 3 was to determine WR(3) of chlorine. In investigations 2 and 3, WR(1) were used as the initial approximation. When selecting the supporting contacts, their minimum number (m) was assumed to be 6.

The histograms of the length distributions for the C···C, H···H, C···H, and C···O contacts determined in investigation 1 are shown in Fig. 1. The length distributions for all (except for H···H) contacts are approximately Gaussian. From the distributions of the C···C and H···H lengths, we obtain $R_C = 1.73_5$ Å and $R_H = 1.18_5$ Å. These values are larger than the starting WRs of carbon and hydrogen by 0.01₅ Å. It is noteworthy that the corresponding value of $2\sqrt{R_C R_H} = 2.87$ Å is exactly equal to the average-statistical length of C···H contacts. Hence, the formula $\bar{r}_{12} = 2\sqrt{R_C R_H}$ was valid as previously [9]. From the distribution of the C···O lengths, we obtained $R_O = 1.34$ Å assuming that $R_C =$

1.73₅ Å. This value of R_O is substantially larger than the starting radius $R_O(ZZ)$.

The results of investigation 2 are shown in Fig. 2. The distributions of the C···C and H···H lengths confirm the value of R_C of 1.73₅ Å obtained in investigation 1 and give $R_H = 1.17_5$ Å, which is equal (within 0.01 Å) to R_H determined in investigation 1. The same is true for the result of the statistical processing of the C···H-length distribution. The R_O radius (1.34 Å) was exactly reproduced. In addition, the C···N-length distribution obtained in investigation 2 gave $R_N = 1.52$ Å, which is somewhat larger than 1.50 Å (WR(ZZ) of nitrogen).

The distribution of the N···H lengths introduces an uncertainty into the results of the determination of the R_N radius. According to this distribution, R_N is 1.46 Å assuming that $R_H = 1.18_5$ Å. However, C–H···N hydrogen bonds seem to make a particular contribution here. We believe that the value of $R_N = 1.52$ Å is correct (although the number of supporting C···N contacts is smaller than the number of the supporting N···H contacts revealed).

The results of investigation 3 are shown in Fig. 3. Here, we did not use the distributions of the C···C, C···H, and H···H lengths because of their low representativeness and took into account only the van-der-Waals sizes of Cl atoms. In this case, we obtained different R_{Cl} radii from different distributions: 1.78 Å (from Cl···Cl contacts), 1.80₅ Å (from C···Cl contacts), and 1.82 Å (from Cl···H contacts). This fact may indicate that the van-der-Waals size of Cl depends on the type of the supporting contacts formed. However, much more extensive statistical data are desirable to justify this conclusion.

Thus, we obtained the following average lengths of the supporting van-der-Waals contacts: $\bar{r}_{C···C} = 3.47$ Å, $\bar{r}_{H···H} = 2.37$ Å, $\bar{r}_{C···H} = 2.87$ Å, $\bar{r}_{C···O} = 3.05$ Å, $\bar{r}_{C···N} = 3.25$ Å, $\bar{r}_{C···Cl} = 3.54$ Å, $\bar{r}_{Cl···H} = 2.93$ Å, and $\bar{r}_{Cl···Cl} = 3.54$ Å. The following van-der-Waals radii of the most important organogenic elements were determined from these contact lengths: $R_C = 1.73_5$ Å, $R_H = 1.18_5$ Å, $R_N = 1.52$ Å, $R_O = 1.34$ Å, $R_{Cl} = 1.78$ Å (Cl···Cl), 1.80₅ Å (C···Cl), and 1.82 Å (Cl···H); the starting $R_{Cl}(ZZ)$ radius was 1.90 Å. It should be noted that the Cl···Cl and Cl···H contacts, according to the conventional views, can be considered as specific interactions, whereas this

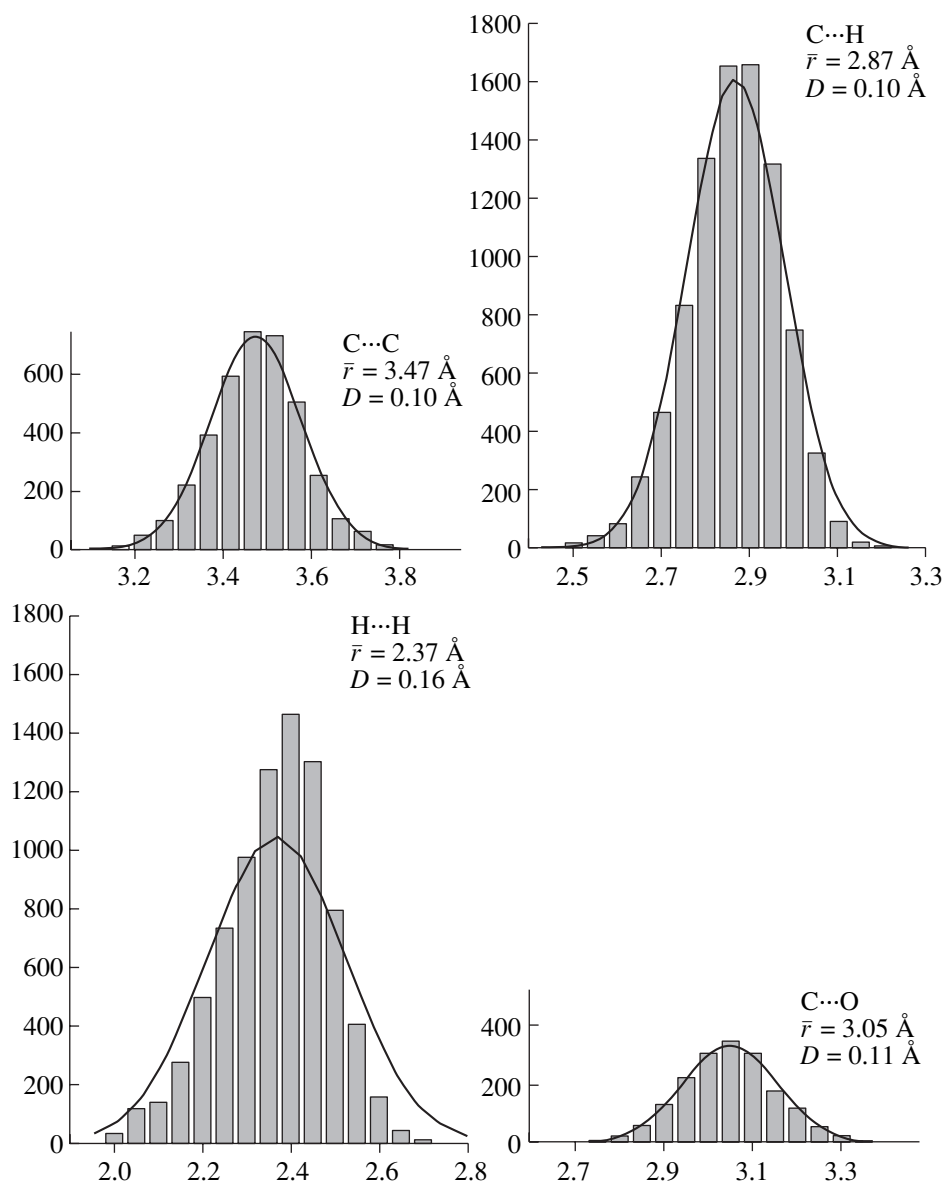


Fig. 1. Results of investigation 1: histograms of the length distribution for the supporting C...C, C...H, H...H, and C...O contacts. Hereinafter, the r_{ij} distance (in Å) and the number of contacts are plotted on the abscissa and ordinate, respectively. The reduced radii \bar{r} were calculated (with an accuracy of 0.005 Å) directly from the data on all supporting contacts revealed. The optimal Gaussian and the variance D depend, although weakly, on the step used to plot the histogram.

does not seem to be true for C...Cl contacts. However, the van-der-Waals radius of chlorine was determined from the latter contacts in [9]. Hence, the average-statistical value of R_{Cl} is somewhat unexpected, although the R_{Cl} radii varying in the narrow range 1.75–1.80 Å were determined from Cl...Cl contacts in a number of studies [1, 5, 13].

RESULTS AND DISCUSSION

It is of interest to consider the variances D shown in Figs. 1–3. Generally, D varies in the range 0.10–0.12 Å. However, the variances D for the H...H and N...H contacts are 0.13 and 0.14 Å, respectively. The distribution

of the Cl...Cl lengths is substantially broadened and is characterized by $D = 0.19$ Å. The latter fact is consistent with the assumption that there is no universal constant value of R_{Cl} .

A similar conclusion was previously drawn in [14], where a statistical analysis of van-der-Waals Cl...Cl contacts was carried out. However, the conclusion drawn in [14] was based on the polymodality of the distribution of $r_{Cl...Cl}$ (three split maxima). In this study, we also obtained a bimodal distribution of the supporting Cl...Cl contacts using small samples. However, using a sample containing more than a thousand of such contacts, we managed to obtain a unimodal distribution.

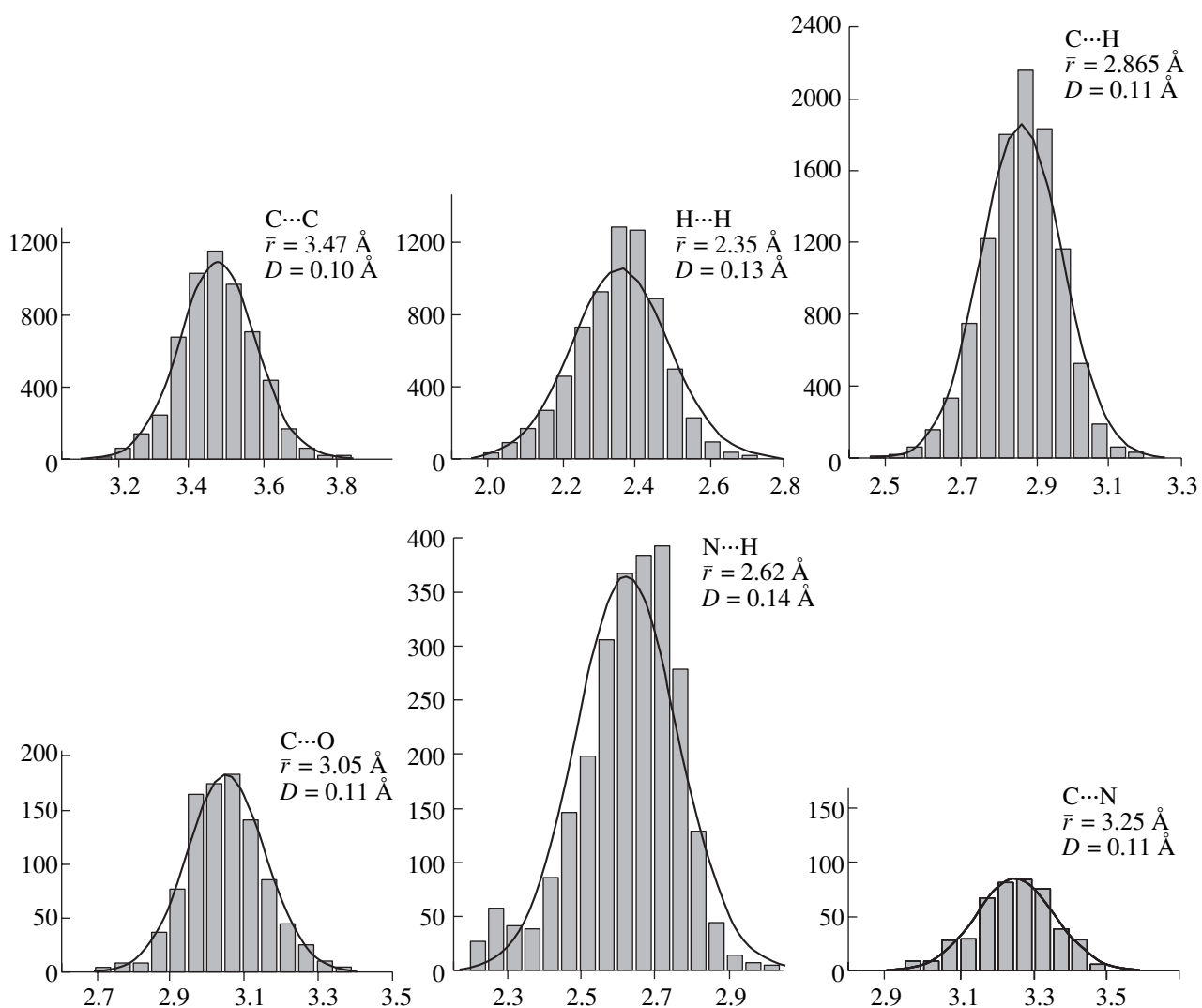


Fig. 2. Results of investigation 2 histograms of the length distribution for the supporting C...C, H...H, C...H, C...O, N...H, and C...N contacts. Compared to Fig. 1, the ordinate scale for the distributions of the C...C, C...H, and H...H lengths is decreased by 25%, and the ordinate scale for the distributions of C...O, N...H, and C...N is increased by a factor of 2.

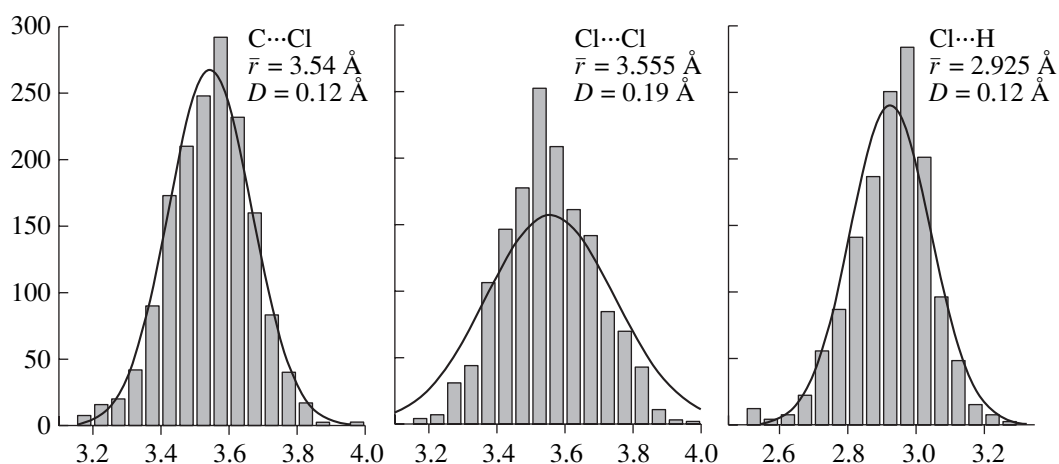


Fig. 3. Results of investigation 3 histograms of the length distribution for the supporting C...Cl, Cl...Cl, and Cl...H contacts. Compared to Fig. 1, the ordinate scale is increased by a factor of 3.

On the basis of the above results, we recommend the following van-der-Waals radii (RW(ZZ) be given for comparison).

| | H | C | O | N | Cl |
|-----------|-------------------|-------------------|------|------|-----------|
| WR, Å | 1.17 ₅ | 1.73 ₅ | 1.34 | 1.52 | 1.78–1.82 |
| WR(ZZ), Å | 1.16 | 1.72 | 1.29 | 1.50 | 1.90 |

The systematic increase in the van-der-Waals radii obtained here, as compared to WRs(ZZ), can be explained by the fact that we assumed the number of supporting contacts $m = 6$ to be the optimal value (providing the stability of the framework of intermolecular “touches”), whereas four supporting contacts ($m = 4$) were considered in [9] for molecules occupying general positions of the space group. For more detailed investigation of this problem, we plan to consider histograms plotted at $m = 8$ in the future.

The above results support, essentially, the theory of close packing proposed by A.I. Kitaigorodsky: more strictly, the first and main postulate of this theory about the existence of invariant van-der-Waals radii of organogenic elements. It should be noted that a reliable statistical verification of this postulate became possible only in the last few years owing to the increase in the amount of structural data available in the CSD. Our study of supporting contacts in organic crystals is, apparently, much more thorough than all previous studies concerning this problem. Nevertheless, we felt that in some cases it is desirable to extend the range of compounds under consideration.

There are two possible ways of extending the information used for statistical processing. First, one can examine data on heteromolecular organic crystals and molecular crystals containing shielded metals and semimetals with retention of the van-der-Waals character of intermolecular contacts. This approach, however, presents problems because of a vast diversity and a complex organization of heteromolecular and semiorganic crystals, whose structures are stored in the CSD [15]. Second, one can consider a larger number of structural classes of homomolecular organic crystals, which will at least double the volume of data on the supporting structural contacts.

The use of the ICA program in systematic studies of specific intermolecular interactions is of considerable interest. In this study, specific contacts were revealed and excluded from consideration. However, these contacts can be the focus of attention in solving other prob-

lems. The ICA program also offers other attractive possibilities. For example, it is of interest to elucidate whether WRs depend on the structural class of the crystals. At first glance, such a dependence is unlikely. However, some preliminary data demonstrate that this dependence does occur. There is also another evident problem associated with examination of the temperature dependence of the van-der-Waals radii.

ACKNOWLEDGMENTS

We are grateful to O.V. Grineva for helpful discussion.

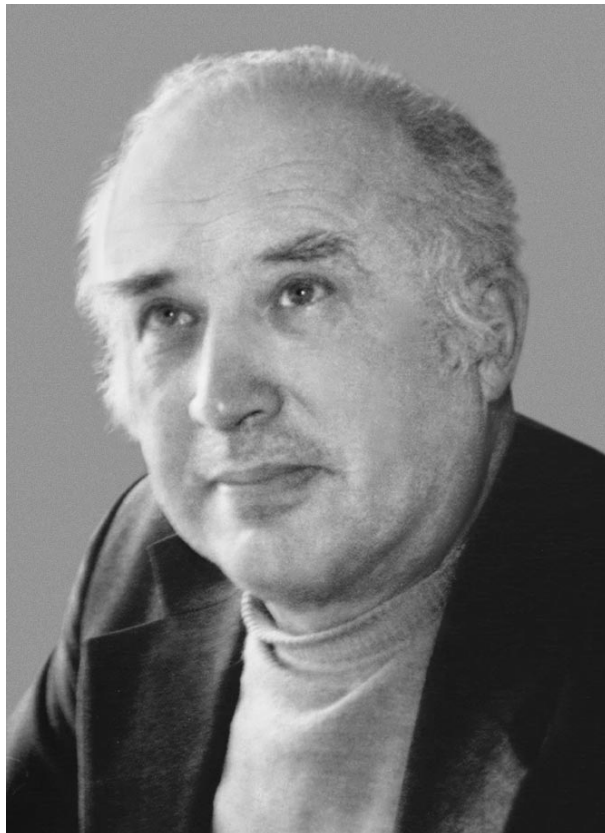
This study was supported by the Russian Foundation for Basic Research (project no. 03-03-32882) and the State Program of Support for Leading Scientific Schools of the Russian Federation (project no. NSh-1275.2003.3).

REFERENCES

1. A. I. Kitaigorodsky, *Organic Crystal Chemistry* (Akad. Nauk SSSR, Moscow, 1955) [in Russian].
2. A. I. Kitaigorodsky, *Molecular Crystals* (Nauka, Moscow, 1971) [in Russian].
3. P. M. Zorkii, *Zh. Fiz. Khim.* **68** (6), 966 (1994).
4. Yu. V. Zefirov and P. M. Zorkii, *Usp. Khim.* **58** (5), 713 (1989).
5. A. Bondi, *J. Phys. Chem.* **68** (3), 441 (1964).
6. S. S. Batsanov, *Neorg. Mater.* **17** (9), 1031 (2001).
7. S. C. Nyburg and C. H. Faerman, *Acta Crystallogr., Sect. B: Struct. Sci.* **41**, 274 (1985).
8. R. S. Rowland and R. Taylor, *J. Phys. Chem.* **100** (18), 7384 (1996).
9. Yu. V. Zefirov and P. M. Zorkii, *Zh. Strukt. Khim.* **15** (1), 118 (1974).
10. P. M. Zorky, *J. Mol. Struct.* **374**, 9 (1996).
11. Cambridge Structural Database, www.ccdc.cam.ac.uk.
12. P. M. Zorkii and O. N. Zorkaya, *Zh. Strukt. Khim.* **166** (1), 128 (1998).
13. L. Pauling and P. Pauling, *Chemistry* (Freeman, San Francisco, 1975; Nauka, Moscow, 1978).
14. A. É. Masunov and P. M. Zorkii, *Zh. Fiz. Khim.* **66** (1), 60 (1992).
15. P. M. Zorkii and P. N. Oleinikov, *Zh. Fiz. Khim.* **74** (11), 1944 (2000).

Translated by T. Safonova

OBITUARIES



Lev Aleksandrovich Shuvalov (November 15, 1923–December 6, 2004)

Lev Aleksandrovich Shuvalov, a leading researcher at the Shubnikov Institute of Crystallography of the Russian Academy of Sciences, a doctor of physics and mathematics, a professor, an Honored Scientist of the Russian Federation, and a winner of the State Prize of the Soviet Union, died on December 6, 2004.

The scientific career of Shuvalov was preceded by participation in the Great Patriotic War. Immediately after graduating from school, he entered the Red Army on a Komsomol assignment. He took part in the battles of Moscow, Stalingrad, and Kursk. For his merits in battle, Shuvalov was awarded the Order of the Red Star and several medals, including the Medal of Valor. Guards Sergeant Major Shuvalov's wartime experience ended near Prague. After returning to Moscow, he passed his university entrance exams and, in March 1946, entered the Faculty of Physics of Moscow State University. He graduated with distinction in 1950. Then Shuvalov worked for five years at the Hydroproject Institute while studying as a postgraduate student at the

Institute of Crystallography under the guidance of A.V. Shubnikov, who greatly influenced the formation of Shuvalov's scientific interests.

In 1956, Shuvalov started working at the Institute of Crystallography. He defended his candidate's thesis in 1961 and his doctoral thesis in 1971. For 20 years Shuvalov headed the Laboratory of Phase Transitions. He had more than 700 scientific publications and 20 inventor's certificates.

Shuvalov lived a long life full of creative achievements. He carried out a number of fundamental studies that played a key role in the development of the symmetry approach in crystallography and crystal physics of ferroelectrics. He investigated pulse switching in ferroelectrics. The results of his investigations had great importance for the use of this phenomenon in memory devices.

Shuvalov proposed an elegant solution to the problems associated with the change in the symmetry at ferroelectric, ferroelastic, and ferromagnetic phase transi-

tions on the basis of the Curie principle. His works devoted to the establishment of the general regularities in the domain structure of ferroelectrics and the domain structure's effect on the macroscopic properties of crystals, as well as the crystallophysical classification of ferroelectrics, have become classics. Shuvalov was one of the fathers of ferroelectric physics.

Shuvalov was awarded the Fedorov prize of the Russian Academy of Sciences for his cycle of investigations of the statics and dynamics of domains in collinear ferroelectrics based on the use of nematic liquid crystals and the determination of the most important regularities of switching in such ferroelectrics. These investigations formed the basis of practical application of such crystals in pyroelectric vidicons and other devices.

Shuvalov discovered and studied in detail a new large family of ferroelectrics and ferroelastics: alkaline trihydrosulfates (and selenates), which have unique physical properties.

Thanks to Shuvalov's influence in the scientific community, he organized a body in which scientists from the Soviet Union and other countries worked in cooperation studying superprotonic compounds with anomalously high conductivity.

The scientific enthusiasm and the organizational talent of Shuvalov enabled him to organize a number of research groups at Tver State University, Voronezh State Technical University, the Volgograd State Academy of Architecture and Building, and Rostov State University. Shuvalov's scientific school was formed and has developed until now. Shuvalov was also engaged in the scientific and organizational activity in Russia and abroad. He was a deputy chairman of the

division "Physics of Ferroelectrics and Insulators" of the Scientific Council on Condensed Matter Physics of the Russian Academy of Sciences, the editor in chief of the journal *Kristallografiya* (*Crystallography Reports*), one of the organizers of national conferences on ferroelectricity, and the chairman of the organizing committees of all national seminars on ferroelastics.

Shuvalov was very active in establishing international cooperation with scientists from Japan, the United States, Slovenia, Poland, the Czech Republic, Lithuania, Ukraine, Germany, and other countries. He was the organizer of bilateral Russian–American and Russian–Japanese symposia and a member of the editorial boards of the international journals *Ferroelectrics*, *Ferroelectrics Letters*, *Zeitschrift für Kristallographie*, *Crystallography Reviews*, and *Condensed Matter News*. Shuvalov was an honorary doctor of Martin Luther University (Germany) and an associate member of the Jozef Stefan Institute (Slovenia).

Among Shuvalov's various interests and passions, which delighted all who knew him, we should note his love for painting, cinema, literature, poetry, and Russian history. Shuvalov's colleagues, friends, and students highly appreciated his invariable optimism, benevolence, straightforwardness, and wisdom. He was always sincerely glad to hear about scientific success of his colleagues, friends, and students.

The name of Lev Aleksandrovich Shuvalov will remain forever in the history of domestic and world crystallography. Many people will remember this remarkable man in their hearts.

Translated by Yu. Sin'kov